

HIGH-VALENT IRON COMPLEXES SUPPORTED WITH TETRADENTATE AND PENTADENTATE LIGANDS BASED ON THE TRIAZACYCLONONANE SCAFFOLD

Gerard Sabeña Vila

Per citar o enllaçar aquest document:

Para citar o enlazar este documento:

Use this url to cite or link to this publication:

<http://hdl.handle.net/10803/406145>

ADVERTIMENT. L'accés als continguts d'aquesta tesi doctoral i la seva utilització ha de respectar els drets de la persona autora. Pot ser utilitzada per a consulta o estudi personal, així com en activitats o materials d'investigació i docència en els termes establerts a l'art. 32 del Text Refós de la Llei de Propietat Intel·lectual (RDL 1/1996). Per altres utilitzacions es requereix l'autorització prèvia i expressa de la persona autora. En qualsevol cas, en la utilització dels seus continguts caldrà indicar de forma clara el nom i cognoms de la persona autora i el títol de la tesi doctoral. No s'autoritza la seva reproducció o altres formes d'explotació efectuades amb finalitats de lucre ni la seva comunicació pública des d'un lloc aliè al servei TDX. Tampoc s'autoritza la presentació del seu contingut en una finestra o marc aliè a TDX (framing). Aquesta reserva de drets afecta tant als continguts de la tesi com als seus resums i índexs.

ADVERTENCIA. El acceso a los contenidos de esta tesis doctoral y su utilización debe respetar los derechos de la persona autora. Puede ser utilizada para consulta o estudio personal, así como en actividades o materiales de investigación y docencia en los términos establecidos en el art. 32 del Texto Refundido de la Ley de Propiedad Intelectual (RDL 1/1996). Para otros usos se requiere la autorización previa y expresa de la persona autora. En cualquier caso, en la utilización de sus contenidos se deberá indicar de forma clara el nombre y apellidos de la persona autora y el título de la tesis doctoral. No se autoriza su reproducción u otras formas de explotación efectuadas con fines lucrativos ni su comunicación pública desde un sitio ajeno al servicio TDR. Tampoco se autoriza la presentación de su contenido en una ventana o marco ajeno a TDR (framing). Esta reserva de derechos afecta tanto al contenido de la tesis como a sus resúmenes e índices.

WARNING. Access to the contents of this doctoral thesis and its use must respect the rights of the author. It can be used for reference or private study, as well as research and learning activities or materials in the terms established by the 32nd article of the Spanish Consolidated Copyright Act (RDL 1/1996). Express and previous authorization of the author is required for any other uses. In any case, when using its content, full name of the author and title of the thesis must be clearly indicated. Reproduction or other forms of for profit use or public communication from outside TDX service is not allowed. Presentation of its content in a window or frame external to TDX (framing) is not authorized either. These rights affect both the content of the thesis and its abstracts and indexes.



Doctoral Thesis

**HIGH – VALENT IRON
COMPLEXES SUPPORTED WITH
TETRADENTATE AND
PENTADENTATE LIGANDS BASED
ON THE TRIAZACYCLONONANE
SCAFFOLD**

GERARD SABEÑA VILA

2017

DOCTORAL PROGRAMME IN CHEMISTRY

Supervised by: Dr. Miquel Costas Salgueiro and Dr. Julio Lloret Fillol

Tutor: Dr. Miquel Costas Salgueiro

Presented in partial fulfilment of the requirements for a Doctoral Degree from the
University of Girona



Dr Miquel Costas Salgueiro, from Universitat de Girona and Julio Lloret Fillol, from Institut Català d'Investigació Química,

WE DECLARE:

That the thesis entitled “High – valent iron complexes supported with tetradentate and pentadentate ligands based on the triazacyclononane scaffold”, presented by Gerard Sabeña Vila to obtain a doctoral degree, has been completed under our supervision and meets the requirements to opt for an International Doctorate.

For all intents and purposes, we hereby sign this document.

Dr. Miquel Costas Salgueiro

Dr. Julio Lloret Fillol

Girona, May 12th, 2017

‘Gold is for the mistress — silver for the maid!
Copper for the craftsman cunning at his trade.’
‘Good!’ said the Baron, sitting in his hall,
‘But Iron — Cold Iron — is master of them all!’
—Rudyard Kipling, *Rewards and Fairies*

“Tomorrow's illiterate will not be the man who can't read; he will be the man who has
not learned how to learn.”
—Herbert Gerjuoy

EN MEMÒRIA DE LA MARE
DEDICAT A LA MEVA FAMÍLIA I EN
ESPECIAL A LA SANDRA

LIST OF PUBLICATIONS

Publications derived from this thesis:

From Chapter III:

Triggering the Generation of an Iron (IV) – Oxo Compound and Its Reactivity toward Sulfides by Ru^{II} Photocatalysis. A. Company, G. Sabenya, M. González – Béjar, L. Gómez, M. Clémancey, G. Blondin, A.J. Jasniewski, M. W.R. Browne, J.M. Latour, L. Que Jr., M. Costas, J. Pérez – Prieto, J. Lloret-Fillol. *J. Am. Chem. Soc.*, **2014**, 136, 4624 – 4633.

Oxygen Atom Exchange between H₂O and Non – Heme Oxoiron (IV) Complexes: Ligand Dependence and Mechanism. M. Puri, A. Company, G. Sabenya, M. Costas, L. Que Jr. *Inorg. Chem.* **2016**, 55, 5818 – 5827.

From Chapter VI:

Iron and Manganese Catalysts for the Selective Functionalization of Arene C(sp²) – H Bonds by Carbene Insertion. A. Conde,[‡] G. Sabenya,[‡] M. Rodríguez,[‡] V. Postils, J.M. Luis, M. Mar Díaz – Requejo, M. Costas, P. J. Pérez. *Angew. Chem. Int. Ed.* **2016**, 55, 6530 – 6534.

[‡]Authors contributed equally to this work.

These papers have been published in journals that belong to the first quartile according to JRC.

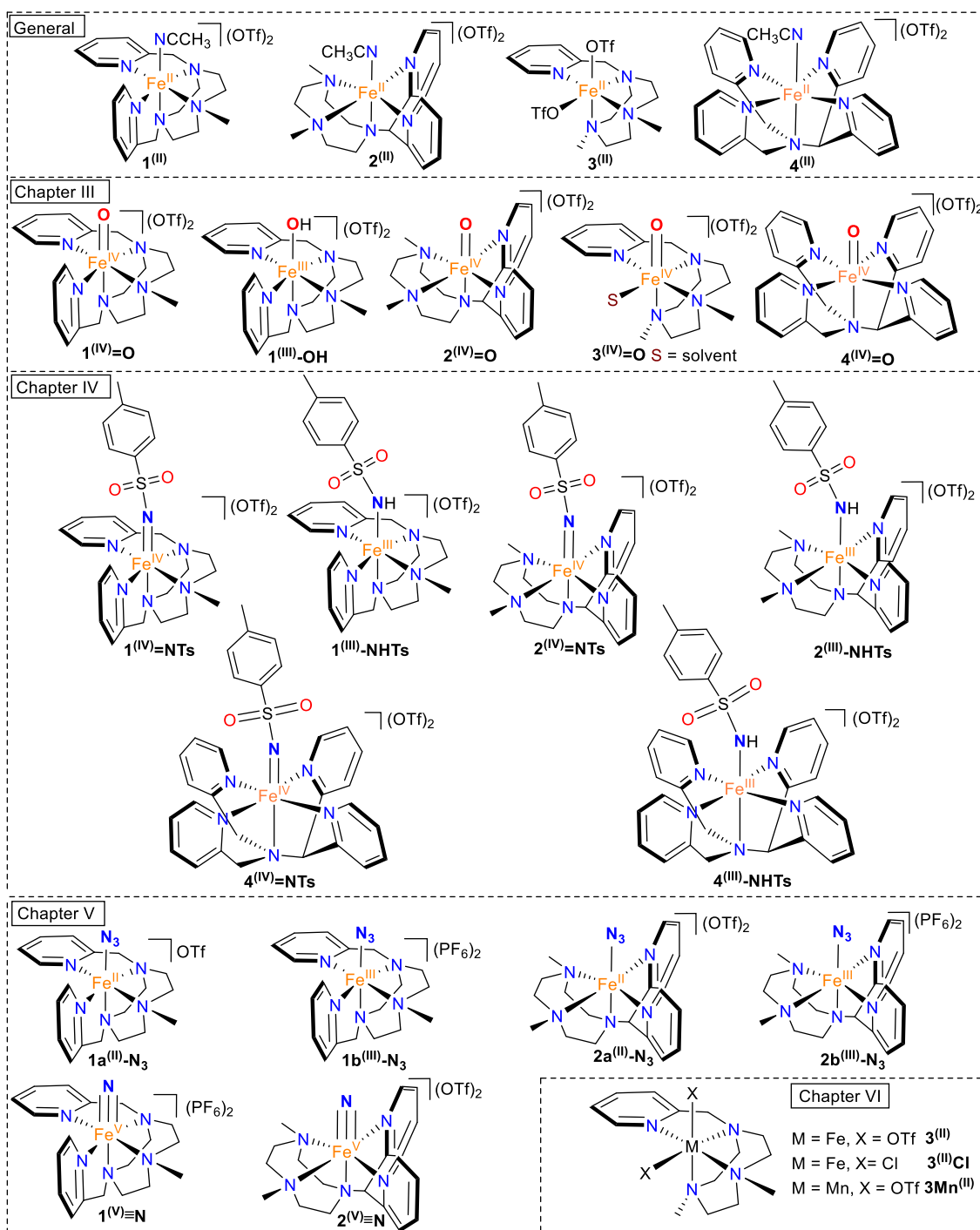
Work from Chapters IV and V is ongoing and will be published in the future.

LIST OF ABBREVIATIONS

1°, 2°, 3°	Primary, Secondary, Tertiary
Å	Angstrom
Abs	Absorbance
AcOEt	Ethyl Acetate
Asp	Asparagine Residue
BDE	Bond Dissociation Energy
bpy	2,2' – bipyridine
CAN	Ceric Ammonium Nitrate
CHD	1,4 – cyclohexadiene
Cp	Cyclopentadienyl anion
Cpd	Compound
CSI – MS	Cryospray Ionisation Mass Spectrometry
CV	Cyclic Voltammetry
Cyt	Cytochrome
DCM	Dichloromethane
DFT	Density Functional Model
DHA	9, 10 – dihydroanthracene
EDA	Ethyl Diazoacetate
<i>ee</i>	Enantiomeric Excess
EPR	Electron Paramagnetic Resonance
Eq. or equiv.	Equivalent
ESI – MS	Electrospray Ionisation Mass Spectrometry
Et	Ethyl
Et ₂ O	Diethyl Ether
EXAFS	Extended X – ray Absorption Fine Structure
FT – IR	Fourier Transform Infrared spectroscopy
GC	Gas Chromatography
GC – MS	Gas Chromatography Mass Spectroscopy
Glu	Glutamate Residue
HAT	Hydrogen Atom transfer
HR – MS	High Resolution Mass Spectrometry
His	Histidine Residue
HOMO	Highest Occupied Molecular Orbital
KIE	Kinetic isotope Effect
LED	Light – Emitting Diode
LMCT	Ligand to Metal Charge Transfer

LUMO	Lowest Occupied Molecular Orbital
<i>m</i> CPBA	<i>meta</i> – Chloro Perbenzoic Acid
Me	Methyl
MeCN	Acetonitrile
min	Minute
MLCT	Metal to Ligand Charge Transfer
MMO	Methane Mono Oxygenase
Na(NAr _F) ₄	Sodium tetrakis(bis – 3,5 – trifluoromethylphenyl)borate
NMR	Nuclear Magnetic Resonance
NRVS	Synchrotron – based nuclear resonance vibrational spectroscopy
OAT	Oxygen Atom Transfer
ORTEP	Oak Ridge Thermal – Ellipsoid Plot
OTf	Triflate (Trifluoromethanesulfonate) Anion
PCET	Proton – Coupled Electron transfer
Ph	Phenyl
PhIO	Iodosylbenzene, iodosobenzene
PhINTs	4 – methyl – N – (phenyl – λ ³ – iodanylidene)benzenesulfonamide
RDS	Rate determining Step
Ref.	Reference
rR	Resonance Raman
r.t.	Room Temperature
s	Seconds
SCE	Saturated Calomel Electrode (Reference)
SQUID	Superconducting quantum interference device (Magnetic Measurement)
T	Temperature
TACN or tacn	1,4,7 – triazacyclononane
TAML	Tetra – amido macrocyclic ligand
TEMPO	2,2,6,6 – Tetramethylpiperidine 1 – oxyl
THF	Tetrahydrofuran
Ts	Tosyl group, p – toluenesulfonyl group (CH ₃ (C ₆ H ₄)SO ₂)
UV – vis	Ultraviolet Visible Spectroscopy
XANES	X – ray Absorption Near Edge Structure
XAS	X – ray Absorption Spectroscopy
X – ray	X – ray diffraction Spectroscopy

ABBREVIATIONS OF COMPLEXES



Ligand abbreviations used: M^nX

M: 1 = MePy₂tacn

2 = Me₂(CHPy₂)tacn

3 = Me₂Pytacn

4 = N4Py

n is the oxidation state of the metal and X the ligand on labile positions

General abbreviation of complexes:

$[M^n(X)(L)](X)$ where M is the metal, n the oxidation state, L the ligand and X the counterions.

LIST OF FIGURES

Figure I.1. Structures of active centres of enzymatic reactions. (Top left) Cytochrome P450; (Top right) structure of Rieske oxygenases centre; (Below) intermediate Hred of soluble methane – monooxygenase (sMMO). His: histidine, Asp: asparagine, Glu: glutamic acid.	8
Figure I.2. Schematic representation of active centre of Rieske oxygenases; on the right oxygenase component showing 2 – His – 1 carboxylate facial triad and on the left the Fe ₂ S ₂ reductase component. .	13
Figure I.3. Suggested structure for the spectroscopically characterised intermediate Q from MMO enzymes. Carboxylates may not be bridging between both iron atoms. ¹⁷	13
Figure I.4. Structure of [Fe ^{IV} = O(TMP·)] ⁺ and different porphyrin ligands from literature.	15
Figure I.5. (Top left) Structure and ORTEP plot of [Fe ^{IV} (O _{anti})(TMC)(MeCN)] ²⁺ and [Fe ^{IV} (O _{syn})(OTf)(TMC)] ⁺ , extracted from ref. 65 and 70 (Top right) Structure of tetradentate N ₄ – donor R ₄ – cyclam family of ligands. Below structure of selected iron (IV) – oxo species in low spin and iron (III) – oxo.	17
Figure I.6. (Top) synthetic pathway for η^2 – peroxy species in Fe – TMC system (A: proton – assisted heterolytic pathway; B: homolytic pathway). (Below) X – ray structure of η^2 – [Fe ^{III} (OO)(TMC)] ²⁺ extracted from ref. 127 (30 % ellipsoid probability; Fe – O ₁ = 1.906 Å, Fe – O ₂ = 1.914 Å, O – O = 1.463 Å).....	19
Figure I.7. High – spin (S = 2) iron (IV) – oxo complexes.	21
Figure I.8. ORTEP structures of crystallographically characterised non – heme iron (IV) – oxo complexes (50 % probability ellipsoids with counterions not shown for commodity).	22
Figure I.9. Iron (V) – oxo species characterised in solution (Top) and detected by mass spectroscopy (Middle). (Below) Structure of oxo – acetate species [Fe ^V (O)(OAc)(PyNMe ₃)] ²⁺	26
Figure I.10. Spectroscopically characterised iron (IV) – imido complexes with structural data. ND: Not determined, spectroscopic data suggest a low spin (S = 1) species. ^a Value from EXAFS. ^b Values from DFT calculations.	31
Figure I.11. (Left) Crystallographically characterised iron (V) – bis(imido) species; (right) dimeric species formed from reaction of iron (I) precursor with (2, 5 – mesityl)phenyl azide.	34
Figure I.12. Catalytically competent iron species involved in the formation of C – N bonds and representative reactions suggested to be mediated by high – valent iron – imido species.	35
Figure I.13. Structure of the iron – molybdenum cofactor (FeMoco) of the nitrogenase enzyme with a central carbide atom and proposed intermediates in the N ₂ activation process (figure extracted from ref. 55).	36
Figure I.14. First and second row, reported high – valent iron – nitrido species. Third row, high – spin iron (III) complexes prepared by Barry and co – workers ²⁰⁰ and Wieghardt and co – workers. ^{198,205}	39
Figure I.15. Selected structures of reported iron porphyrin complexes used to prepare iron – carbene species.	42
Figure I.16. Buchner reaction catalysed by [Fe ^{III} (Cl)(TPP)].	45
Figure I.17. C – H insertion reactivity of [Fe ^{III} (Cl)(TPP)] and [Fe ^{III} (Cl)(F ₂₀ – TPP)].	46
Figure I.18. Non – heme complexes and ligands used in the decomposition of diazoacetate compounds.	47

Figure III.1. UV – vis spectrum of 1^(II) (blue) and 2^(II) (orange) in acetonitrile.....	57
Figure III.2. ¹ H – NMR spectroscopy of complex 1^(II) (top) and 2^(II) (below) in CD ₃ CN at 400 MHz at 298 K.....	58
Figure III.3. Ortep representation at 50 % of probability of X – ray structure of 1^(II) and 2^(II) , triflate anions and hydrogens are omitted for clarity.....	59
Figure III.4. UV – vis spectra of complexes 1^{(IV)=O} (green) and 2^{(IV)=O} (red) in acetonitrile prepared with PhIO as oxidant.....	61
Figure III.5. ¹ H – NMR and bidimensional COSY spectra of complex 1^{(IV)=O} and 2^{(IV)=O} in CD ₃ CN at 25 °C.....	63
Figure III.6. ESI – MS spectra of complex 1^{(IV)=O} in acetonitrile.....	64
Figure III.7. Experimental EXAFS data (black line) and best fit (red line). Unfiltered data shown in the inset and corresponding Fourier transform of 1^{(IV)=O} . <i>k</i> range = 2 – 15 Å ⁻¹ ; back – transform range, ≈ 0.83 – 3.0 Å.....	65
Figure III.8. Mössbauer spectrum of 1^{(IV)=O} recorded at 80 K with zero applied field. Hatched bars are the experimental data and the solid lines the contributions of Fe ^{IV} (O) (black line) and dimeric decomposition (grey line).....	65
Figure III.9. UV – vis 1^(III) – OH (0.4mM in MeCN) synthesised from 1^(II) with 2 eq H ₂ O ₂	66
Figure III.10. EPR spectrum of [Fe ^{III} (OH)(MePy ₂ tacn)](OTf) ₂ 1^(III) – OH recorded at 5 K with the following parameters: microwave frequency = 9.6551 GHz, microwave power = 0.317 mW, receiver gain = 3.99·10 ³ , time constant = 40.96 ms, modulation frequency = 100 kHz, modulation amplitude = 0.5 mT. The <i>g</i> – values are indicated.....	66
Figure III.11. Mössbauer spectrum of [Fe ^{III} (OH)(MePy ₂ tacn)](OTf) ₂ 1^(III) – OH recorded at 4.2 K under a magnetic field of 7 T applied parallel to the γ – rays. The spectrum was simulated under the assumption of slow relaxation by taking into account 92% of <i>S</i> = 1/2 species (red line) and 8% of 1^(II) (blue line).....	67
Figure III.12. Cyclic voltammetry of 1^(II) . 1 mM in MeCN, 0.1 M TBAPF ₆ . Scanrate 0.1 V/s. GC working electrode, Pt counter electrode and SCE reference electrode.....	68
Figure III.13. Plot of <i>E</i> _{1/2} vs pH of 1^(II) in H ₂ O (2mM, 0.1 M KNO ₃ , scan rate = 100 mV/s).....	69
Figure III.14. Cyclic Voltammetry of 1^(II) in H ₂ O (2 mM, 0.1 M KNO ₃ , scan rate = 100 mV/s). (A) Initial conditions. (B) CV initial conditions some minutes after preparation of the sample. (C) Addition of 1 μmol of HOTf (pH = 3.30). (D) Addition of 5 μmol of HOTf (pH = 2.60). (E) Addition of 10 μmol of HOTf (pH = 2.36). (F) Addition of 70 μmol of HOTf (pH = 1.57). (G) Addition of 130 μmol of HOTf (pH = 1.30). (H) Addition of 190 μmol of HOTf (pH = 1.14).....	70
Figure III.15. Spectroelectrochemistry of complex 1^(II) (14 mM in H ₂ O, 0.1 M KNO ₃ , scan rate = 5 mV/s). (A) Cyclic voltammetry of 1^(II) in H ₂ O. (B) UV – vis of the redox processes observed on the cyclic voltammetry spectrum. (C) Traces of the UV – vis evolution in front of the potential (Fe ^{II} , Fe ^{III} , and Fe ^{IV} at 420 nm, 305 nm and 720 nm, respectively).....	72
Figure III.16. <i>E</i> _{1/2} of iron (IV) – oxo species in the literature.(ref. 83).....	73
Figure III.17. Comparison of cyclic voltammetry spectra of complex 1^(II) (14 mM, 0.1 M KNO ₃ , scan rate = 5 mV/s) in H ₂ O (blue line) and MeCN:H ₂ O (1:3) (green line).....	73

Figure III.18. Plot of H ₂ ¹⁸ O concentration dependence for ¹⁸ O incorporation rate in 1^(IV)=O (0.5 mM, filled blue triangles at 50 °C), 2^(IV)=O (0.5 mM, filled pink squares at 50 °C) and 3^(IV)=O (open and filled purple circles at 22 °C, filled red circles at 0 °C), in MeCN solution. Open purple circles are from ref 77.	75
Figure III.19. Eyring plot for complex 3^(IV)=O linear regime (red circles) and saturated regime (green circles). Open circles are data from ref 77.	76
Figure III.20. UV – vis spectrum of the decay of complexes 1^(IV)=O (left) and 2^(IV)=O (right) upon addition of 50 eq of thioanisole at 20 °C, insets show the decay of 738 and 748 nm bands.	79
Figure III.21. (Left) Comparison plot of <i>k</i> _{obs} vs [<i>p</i> – ^X PhSMe] concentration for complexes 1^(IV)=O (solid lines) and 2^(IV)=O (dashed lines). (Right) Hammett plot of 1^(IV)=O (yellow circles) and 2^(IV)=O (red squares).	80
Figure III.22. UV – vis spectrum of the decay of complexes 1^(IV)=O and 2^(IV)=O upon addition of 500 eq. of cumene substrate were added at 20°C (insets show the traces of 738 and 748 nm features respectively).	82
Figure III.23. Oxidation products ratio for reaction of 1^(IV)=O and cumene under anaerobic conditions with ¹⁸ O ₂	85
Figure III.24. Plot of the pseudo – first order rate constants, <i>k</i> _{obs} (s ⁻¹), against substrate concentration to determine second – order rate constants, <i>k</i> ₂ (M ⁻¹ s ⁻¹), for the reaction of 1^(IV)=O and 2^(IV)=O with alkylbenzenes in CH ₃ CN at 25°C. Complex 1^(IV)=O are circles with solid line and 2^(IV)=O are squares with dashed line.	85
Figure III.25. Plot of log(<i>k</i> ₂ ') vs BDE (1^(IV)=O solid line with yellow circles; 2^(IV)=O dashed line with red squares). <i>k</i> ₂ values were normalised by the number of H available on the substrate to obtain the corresponding <i>k</i> ₂ ' (2 for ethylbenzene and 3 for toluene).	86
Figure III.26. Eyring plot for cumene and thioanisole on oxidation with complex 1^(IV)=O	89
Figure III.27. Kinetic trace at 715 nm corresponding to the reaction mixture containing 1^(II) (0.4 mM), 5 mol% [Ru ^{II} (bpy) ₃]Cl ₂ (0.02 mM) and Na ₂ S ₂ O ₈ (4 mM, 10 equiv) under N ₂ atmosphere at 25 °C. Labels on the figure indicate the initial (ON) and final (OFF) points of irradiation (λ = 447 ± 20 nm) as well as the addition of 1 equiv of ^{MeO} PhSMe.	93
Figure III.28. (Left) Hammett plot representing log(<i>k</i> _{rel}) against the Hammett parameter (σ _p) for the reaction of 1^(IV)=O with <i>p</i> – X – thioanisole in CH ₃ CN:H ₂ O 1:3 in the presence of 5 mol% [Ru ^{II} (bpy) ₃]Cl ₂ with 447 nm – light irradiation at 298 K. <i>k</i> _{rel} values were calculated by dividing <i>k</i> _{obs} of <i>p</i> – X – thioanisoles by <i>k</i> _{obs} of thioanisole obtained with 10 equiv. substrate. (Right) Hammett plot representing log(<i>P</i> _X / <i>P</i> _H) against the Hammett parameter (σ _p) for competition experiments corresponding to the simultaneous reaction of 1^(IV)=O with thioanisole and <i>p</i> – X – thioanisole in CH ₃ CN:H ₂ O 1:3 in the presence of 5 mol% [Ru ^{II} (bpy) ₃]Cl ₂ with 447 nm – light irradiation at 298 K. <i>P</i> _X corresponds to the amount of <i>p</i> – substituted phenylmethylsulfoxide obtained at the end of the reaction (determined by GC – FID or NMR). Competition experiments were run in the presence of 5 equiv thioanisole and 5 equiv <i>p</i> – X – thioanisole.	96
Figure IV.1. Top, Mössbauer spectrum of 1^(IV)=NTs (left) in acetonitrile recorded at 80K and Mössbauer spectrum of 2^(IV)=NTs (right) prepared in acetone and recorded at 80K. Experimental data are hatched bars and solid line represent the contributions of 1^(IV)=NTs and 2^(IV)=NTs . Centre, UV – vis spectrum of oxidation of 1^(II) to 1^(IV)=NTs in CH ₃ CN and kinetic trace that shows the evolution of 750 nm feature.	

Below, HR – MS spectrum of $1^{(IV)}=NTs$ prepared in CH_3CN exhibiting a base peak at m/z 275.09; inset show amplification of major peak for $[Fe^{IV}(NTs)(MePy_2tacn)]^{2+}$ species. Proper simulation of the peak requires inclusion of $\approx 10\%$ of $[Fe^{III}(NHTs)(MePy_2tacn)]^{2+}$ in the isotopic pattern corresponding to $[Fe^{IV}(NTs)(MePy_2tacn)]^{2+}$	106
Figure IV.2. 1H – NMR and bidimensional COSY spectra of (top) complex $1^{(IV)}=NTs$ in D_6 – acetone at 0 °C and (below) $2^{(IV)}=NTs$ in D_6 acetone at 25 °C (small peaks at 32 and -9 ppm belong to $<5\%$ of $[Fe^{IV}(O)(Me_2(CHPy)_2tacn)]$). Spectra recorded in a 400 MHz spectrometer.	108
Figure IV.3. Enhanced Raman spectra for complex $1^{(IV)}=NTs$ (top) and $2^{(IV)}=NTs$ (below) upon excitation at 488 nm.	109
Figure IV.4. Iron K – edge X – ray absorption spectra of: top left, $1^{(IV)}=NTs$ (red) and $1^{(III)} – NHTs$ (blue); top right: $2^{(IV)}=NTs$ (red) and $2^{(III)} – NHTs$ (blue). Below, non – phase shift corrected Fourier transforms for $1^{(IV)}=NTs$ (left) and $2^{(IV)}=NTs$ (right) with insets showing the k – space data and fits. Experimental data are shown in black and fits in red.	110
Figure IV.5. Computationally derived geometries and quasi – restricted orbitals (0.05 isovalue) showing the Fe d manifold for $1^{(IV)}=NTs$ (left) and $2^{(IV)}=NTs$ (right). (TPSSh/def2 – TZVP//TPSS/def2 – TZVP).	112
Figure IV.6. Selected structures of spectroscopically characterised iron (IV) – imido complexes. Ad = adamantane, $B(ArF)_4 = [B(3, 5 - (CF_3)_2C_6H_3)_4]^-$. ^{165,166,169,170,172}	113
Figure IV.7. Top, ORTEP structure of isolated ferric complex $1^{(III)} – NHTs/SbF_6$, 50% ellipsoid probability, counterions omitted for clarity.	114
Figure IV.8. Structures of reported iron (III) – amido/imido complexes. Ad = adamantane	115
Figure IV.9. Spectroscopic data of isolated $1^{(III)} – NHTs/OTf$ (left) and $2^{(III)} – NHTs/OTf$ (right). (Top) Zero Field Mössbauer spectra at 80 K. (Below) Mössbauer spectra at 4.2 K and 7T.	116
Figure IV.10. UV – vis spectra corresponding to the reaction of $1^{(IV)}=NTs$ and $2^{(IV)}=NTs$ upon addition of an excess of $p - Me^O$ PhSMe (reaction at 20 °C with 100 and 50 eq of substrate added respectively, $[Fe] = 0.25$ mM in MeCN). Spectra correspond to the first rapid phase of the reaction.	118
Figure IV.11. HR – MS monitoring of evolution of 0.25 mM solutions of $1^{(IV)}=NTs$ (top) and $2^{(IV)}=NTs$ (below) in MeCN upon addition of 100 and 50 eq of $p - Me^O$ PhSMe, respectively. Insets on the left show expanded region for iron (III) – tosylimido/tosylamido species. $m/z = 275.09$ ($[Fe^{IV}(NTs)L]^{2+}$), $m/z = 275.59$ ($[Fe^{III}(NHTs)L]^+$), $m/z = 550.18$ ($[Fe^{III}(NTs)L]^{2+}$). *Traces of unreacted PhINTs.....	119
Figure IV.12. Spectroscopic properties of iron(III) – tosylamido compounds resulting from reaction of $1^{(IV)}=NTs$ and $2^{(IV)}=NTs$ with $p - Me^O$ PhSMe. Mössbauer spectra of $1^{(III)} – NHTs$ (left) and $2^{(III)} – NHTs$ (right) formed after reaction of respective iron (IV) species with Me^O PhSMe.	121
Figure IV.13. (Top) Titration of $1^{(IV)}=NTs$ with ascorbic acid, initial iron (IV) is successively reduced to iron (III), $1^{(III)} – NHTs$, and iron (II), $1^{(II)}$. (Below) Titration of $1^{(III)} – NHTs$ with ascorbic acid after reaction of $1^{(IV)}=NTs$ with Me^O PhSMe.....	123
Figure IV.14. (Left) Decay profile of $1^{(IV)}=NTs$ (750 nm feature) upon addition of 100 eq of Me^O PhSMe. (Right) Rate dependence on substrate concentration.....	124
Figure IV.15. Hammett plot representing $\log(k_X/k_H)$ against Hammett parameter (σ_p) for the reaction of $1^{(IV)}=NTs$ (left) and $2^{(IV)}=NTs$ (right) with $p - X -$ thioanisoles in acetonitrile at 293 K. k_X values correspond	

to the second order rate constants obtained by measuring k_{obs} values at different $p - X -$ thioanisole concentrations.....	125
Figure IV.16. UV – vis monitoring for reactivity of $[\text{Fe}^{\text{IV}}(\text{NTs})\text{N4Py}]^{2+}$ ($\mathbf{4}^{\text{IV}}=\text{NTs}$) with MeOPhSMe at different temperature and complex and substrate conditions.	127
Figure IV.17. Mechanism proposal for the reactions of iron (IV) – tosylimido complexes with thioanisole substrates.	129
Figure IV.18. Plot of iron (III) formed depending on $[\mathbf{1}^{\text{IV}}=\text{NTs}]$	129
Figure IV.19. Sulfanylidene product ($\text{MeOPhS}(\text{NTs})\text{Me}$) vs. $[\mathbf{1}^{\text{IV}}=\text{NTs}]$	130
Figure V.1. (Top left) ORTEP representation on 50% of probability of the X – ray diffraction analysis of $\mathbf{1a}^{\text{III}} - \text{N}_3$ at 298 K (Top right), $\mathbf{1b}^{\text{III}} - \text{N}_3$ (Top right) and $\mathbf{2a}^{\text{III}} - \text{N}_3$ (Below left) at 100 K. Protons, hexafluorophosphate (PF_6^-) and trifluoromethanesulfonate (CF_3SO_3^-) anions were omitted for clarity. Table shows selected bond distances and angles for these compounds.....	138
Figure V.2. Zero – field Mössbauer spectra of $\mathbf{1a}^{\text{III}} - \text{N}_3$ recorded at 80 K (top left) and 297 K (top right). The green and blue lines are Lorentzian doublets accounting for low – spin (LS) and high – spin (HS) components with parameters given in the text; the red line in the top left spectrum is the superposition of the subspectra. The asymmetry of the top right spectrum results from a difference in line widths, not relative intensities, which presumably reflects a slight heterogeneity of iron (II) sites in the powder sample at room temperature. Below left spectrum shows Mössbauer data of $\mathbf{2a}^{\text{III}} - \text{N}_3$ at 80 K under zero – applied magnetic field. Temperature dependence of the magnetic susceptibility of $\mathbf{1a}^{\text{III}} - \text{N}_3$ (χT vs. T). Experimental data (open circles) are corrected for underlying diamagnetism. The blue and green line represent spin Hamiltonian simulations for the iron(II) high – spin species (HS) with $S = 2$, $D = 5 \text{ cm}^{-1}$, $g = 2.1$ and with ca. 100% abundance found above 295 K and ca. 7% abundance below 100 K. The red line is a simulation of an incomplete $S = 0$ to $S = 2$ phase transition, obtained with Sorai’s domain model ^{319,320} for which the high – spin fraction is given by $x = 0.07 + 1/(1 + \exp[(n\Delta H/R) - (1/T - 1/T_c)])$. There T_c is the transition temperature, $T_c = 194 \text{ K}$, and $n\Delta H$ is an enthalpy term, $n\Delta H = 917 \text{ cm}^{-1}$ for a domain size n , which determines the width of the transition.	139
Figure V.3. Zero – field Mössbauer spectra of $\mathbf{1b}^{\text{III}} - \text{N}_3$ (Top left) and $\mathbf{2b}^{\text{III}} - \text{N}_3$ (Top right) at 80 K. Below EPR spectra of $\mathbf{1b}^{\text{III}} - \text{N}_3$ (Below left) and $\mathbf{2b}^{\text{III}} - \text{N}_3$ (Below right) in a frozen acetone solution at 10 K. The Mössbauer spectrum for $\mathbf{2b}^{\text{III}} - \text{N}_3$ was fitted with three Lorentzian doublets accounting for i) Iron (III) LS ($\mathbf{2b}^{\text{III}} - \text{N}_3$, 50%, in blue) and ferrous impurities ii) Iron (II) HS $\mathbf{2a}^{\text{III}} - \text{N}_3$ (29%, in green), and iii) Iron (II) LS $[\text{Fe}^{\text{II}}(\text{MeCN})\text{Me}_2(\text{CHPy}_2)\text{tacn}](\text{PF}_6)_2$ (21%, in yellow).	142
Figure V.4. (Top) High resolution mass spectra of $\mathbf{1b}^{\text{III}} - \text{N}_3$ in acetone, insets are ions for $\text{Fe}^{\text{II}}(\text{L})$, $\text{Fe}^{\text{III}}(\text{N}_3)(\text{L})$ and $\text{Fe}^{\text{V}}(\text{N})(\text{L})$, with simulated peaks. (Below) High resolution mass spectra of $\mathbf{1b}^{\text{III}} - ^{15}\text{N}_3$ in acetone, below are shown simulated ions of $[\text{Fe}^{\text{II}}(\text{L})]^{2+}$, $[\text{Fe}^{\text{III}}(^{14/15}\text{N}_3)(\text{L})]^{2+}$ and $[(\text{Fe}^{\text{V}}(\text{N})(\text{L}))]^{2+} / [\text{Fe}^{\text{V}}(^{15}\text{N})(\text{L})]^{2+}$ species. $\text{L} = \text{MePy}_2\text{tacn}$	144
Figure V.5. (Left) Zero – field Mössbauer spectrum of solid complex $\mathbf{1b}^{\text{III}} - \text{N}_3$ after 4.5 h photolysis at 77 K with a 470 nm (blue) LED, and (Right) EPR spectrum recorded at 10 K ($T = 10 \text{ K}$, frequency 9.6459 GHz, power 0.2 mW, modulation 0.75 mT / 100 kHz). The EPR derivative amplitudes are given in arbitrary units, consistent with those of Figure V.3. The green and blue lines in left spectrum are Lorentzian doublets accounting for a new low – spin iron (II) species (Fe(II) LS) and the high – valent photo – product ($\mathbf{1}^{\text{V}}\Xi\text{N}$);	

the red is the superposition of the subspectra. The extended asymmetry of the subspectrum from ($\mathbf{1}^{(V)}\Xi\mathbf{N}$) presumably results from intermediate spin relaxation. The red line in EPR spectrum is a simulation with g values $g_1 = 1.38$ and $g_2 = 1.33$, $g_3 = 1$ (fixed) and Lorentzian line of the widths = $56 \cdot 10^{-4} \text{ cm}^{-1}$ for the g_{\perp} directions, and fixed $1000 \cdot 10^{-4} \text{ cm}^{-1}$ for g_{\parallel} , respectively.	146
Figure V.6. (Left) Zero – field Mössbauer spectrum of solid complex $\mathbf{1b}^{(III)} - \mathbf{N}_3$ after 5 h photolysis at 77 K with a 530 nm (green) LED, and (Right) EPR spectrum of a similar sample photolysed in a sealed EPR tube under vacuum ($T = 10 \text{ K}$, frequency 9.6468 GHz, power 0.2 mW, modulation 0.75 mT / 100 kHz). The EPR derivative amplitudes are given in arbitrary units, consistent with those of Figures V.3 and V.4. The Mössbauer spectrum was fitted with four Lorentzian doublets accounting for i) Iron (III) starting material ($\mathbf{1b}^{(III)} - \mathbf{N}_3$, 1%, in pink), ii) ferrous impurity, iron (II) HS (4%, in dark blue), and the photoproducts iii) Iron (II) LS (6%, in blue), and iv) the high – valent photo – product ($\mathbf{1}^{(V)}\Xi\mathbf{N}$, 89%, in green). The red line in EPR spectrum is a simulation with g values $g_1 = 1.37$ and $g_2 = 1.33$, $g_3 = 1$ (fixed) and Lorentzian line of the widths 56, 149, and $1000 \cdot 10^{-4} \text{ cm}^{-1}$	147
Figure V.7. (Left) Iron K – edge X – ray absorption spectra of $\mathbf{1a}^{(III)} - \mathbf{N}_3$ (blue), $\mathbf{1b}^{(III)} - \mathbf{N}_3$ (black) and $\mathbf{1}^{(V)}\Xi\mathbf{N}$ (red). The inset is an expansion of the pre – edge region. (Right) Fourier transformed EXAFS spectra of $\mathbf{1}^{(V)}\Xi\mathbf{N}$ (inset: k^3 -weighted unfiltered EXAFS spectra (Data: black circles; Fits: red line).	149
Figure V.8. Molecular orbital picture for compound $\mathbf{1}^{(V)}\Xi\mathbf{N}$	150
Figure V.9. Reactivity of $\mathbf{1b}^{(III)} - \mathbf{N}_3$ upon irradiation, percentages are the N_2 amounts generated after photolysis (percentage in parentheses are the combination of B.1 and B.2).	151
Figure V.10: Evolution of the relative composition of the nitrogen gas isotopes ($^{14}\text{N} - ^{14}\text{N}$ yellow line, $^{14}\text{N} - ^{15}\text{N}$ blue line and $^{15}\text{N} - ^{15}\text{N}$ green line) green line at the headspace of a solution of complex $\mathbf{1}^{(V)}\Xi\mathbf{N}$, generated by irradiation of a solution of $\mathbf{1b}^{(III)} - \mathbf{N}_3$ (4 mM) in acetone solution at 530 nm LED for 3.5 hours under Ar at 77 K while slowly melting.....	151
Figure VI.1. (Top) Metal – catalysed reaction of benzene with EDA and complexes used in this work ($X = \text{OTf, Cl}$).	160
Figure VI.2. Substrate scope for reaction of arenes with EDA and $\mathbf{3}^{(II)}$ (8 eq. of $\text{Na}(\text{BAr}_F)_4$). Yields were isolated and isomer ratios were determined by $^1\text{H} - \text{NMR}$ and are normalised by the number of positions available (2 <i>ortho</i> , 2 <i>meta</i> and 1 <i>para</i>). ^a Work performed by Mònica Rodriguez. ^b Combined yield of C – H and C – O functionalisation, see text for details.	161
Figure VI.3. Hammett plot from competition experiments for functionalisation of benzene with EDA and $[\text{M}(\text{OTf})_2(\text{Me}_2\text{Pytacn})]$ complexes. k_X/k_H = ratio of insertion products on benzene and $X - \text{C}_6\text{H}_5$ ($X = \text{MeO, Me, Cl}$ and CF_3), calculated by GC.	164
Figure VI.4. Competitive experiments for functionalisation of benzene and deuterated benzene with EDA and $[\text{M}(\text{OTf})_2(\text{Me}_2\text{Pytacn})]$ complexes. k_H/k_D = ratio of insertion products on benzene and deuterated benzene, calculated by GC.	165
Figure VI.5. Functionalisation of cyclopropylbenzene with EDA and $\mathbf{3}^{(II)}$. Ratio of isomers normalised to the number of carbons available (2 <i>ortho</i> , 2 <i>meta</i> and 1 <i>para</i>).	165
Figure VI.6. Proposed mechanism for arene functionalisation with EDA catalysed by non – heme iron and manganese complexes. The oxidation state for these species is not easily defined due to the highly covalent character of the bonds.....	166

Figure SIII.1. ^1H – NMR, bidimensional COSY and ^{13}C – NMR spectra of $\mathbf{1}^{\text{III}}$ in CD_3CN at 273 K. ...	202
Figure SIII.2. Top left: UV – vis spectrum of $\mathbf{1}^{\text{IV}}=\text{O}$ obtained upon reaction of $\mathbf{1}^{\text{III}}$ (0.4 mM) with 2 equiv $[\text{Ru}^{\text{III}}(\text{bpy})_3](\text{PF}_6)_3$ in water. Top right: UV – vis spectrum of $\mathbf{1}^{\text{IV}}=\text{O}$ obtained after reaction of $\mathbf{1}^{\text{III}}$ (0.4 mM) with 15 equiv ceric ammonium nitrate (CAN) in $\text{CH}_3\text{CN}:\text{H}_2\text{O}$ 1:3. Below: UV – vis evolution of photochemical oxidation of $\mathbf{1}^{\text{III}}$ (0.4 mM in $\text{MeCN}:\text{H}_2\text{O}$ (1:3), 0.02 mM of $[\text{RuCl}_2(\text{bpy})_3]$ and 4 mM $\text{Na}_2\text{S}_2\text{O}_8$) to generate $\mathbf{1}^{\text{IV}}=\text{O}$ upon irradiation (447 nm). Inset shows the kinetic trace of 715 nm. The lack of 414 nm band of initial $\mathbf{1}^{\text{III}}$ is due to its previous oxidation to $\mathbf{1}^{\text{III}}-\text{OH}$ upon addition of $\text{Na}_2\text{S}_2\text{O}_8$ before irradiating. Immediate consumption of band at 450 nm after starting irradiation indicates the fast oxidation of Ru^{II} to Ru^{III} . Complex $\mathbf{1}^{\text{IV}}=\text{O}$ was not formed in absence of $\text{Na}_2\text{S}_2\text{O}_8$ or $[\text{Ru}^{\text{II}}\text{Cl}_2(\text{bpy})_3]$. It was observed a solvatochromic effect when water was added to $\mathbf{1}^{\text{IV}}=\text{O}$, for example in a mixture 1:3 $\text{MeCN}:\text{H}_2\text{O}$ the 738 nm band (in MeCN) blue – shifted about 20 nm, to obtain a feature with a maximum at 715 nm with no significant change in the absorption coefficient. Such behaviour was also observed in related complexes such as $\mathbf{2}^{\text{IV}}=\text{O}$ or $[\text{Fe}^{\text{IV}}(\text{O})(\text{N4Py})]^{2+}$	203
Figure SIII.3. ESI – MS spectrum of complex $\mathbf{2}^{\text{IV}}=\text{O}$ in MeCN prepared with excess of PhIO	204
Figure SIII.4. OTTLE cell system used for spectrochemical measurements. See ref 371 and https://www.reading.ac.uk/chemistry/research/chem-spectroelectrochemistry.aspx	205
Figure SIII.5. Cyclic Voltammetry spectra of $\mathbf{1}^{\text{III}}$ (green line) and $\mathbf{2}^{\text{III}}$ (red line) in MeCN , 0.1 mM of TBAPF_6	205
Figure SIII.6. UV – vis traces of redox processes of $\mathbf{1}^{\text{III}}$ (14 mM in H_2O , 0.1 M KNO_3 , scanrate = 5 mV/s) followed by spectroelectrochemistry. $\text{Fe}(\text{II})$ was monitored at 423 nm, $\text{Fe}(\text{III})$ at 305 nm and $\text{Fe}(\text{IV})$ at 715 nm.....	206
Figure SIII.7. Spectroelectrochemistry of complex $\mathbf{1}^{\text{III}}$ (14 mM in $\text{MeCN}:\text{H}_2\text{O}$ (1:3), 0.1 M KNO_3 , scanrate = 5 mV/s). (A) Cyclic voltammetry of $\mathbf{1}^{\text{III}}$. (B) Evolution of the UV – vis in front of the potential. (C) UV – vis traces for the oxidation and reduction processes observed vs potential. $\text{Fe}(\text{II})$ was monitored at 420 nm, $\text{Fe}(\text{III})$ at 310 nm and $\text{Fe}(\text{IV})$ at 720 nm.	207
Figure SIII.8. Experiments between ^{18}O – labeled $\mathbf{3}^{\text{IV}}=\text{O}$ (generated from reaction of ^{16}O – labelled $\mathbf{3}^{\text{IV}}=\text{O}$ and 0.14 M H_2^{18}O , 1.0 mM) and H_2^{16}O or D_2^{16}O at 0 °C (Top 1.57 M, Center 0.74 M and Below 0.42 M of H_2O or D_2O) at 0 °C, resulting in a KIE of 1.5, 1.7 and 1.6 respectively. The ^{18}O – incorporation was determined by quenching aliquots (0.4 mL, 0.4 mmol) of the reaction with thioanisole (5 μL , 42.7 mmol) and determining the ratio of ^{16}O and ^{18}O – methylphenylsulfoxide by GC – MS, as previously described. ⁷⁷	209
Figure SIII.9. Comparison reactions between ^{18}O – labeled $\mathbf{3}^{\text{IV}}=\text{O}$ (generated from reaction of ^{16}O – labelled $\mathbf{3}^{\text{IV}}=\text{O}$ and 0.14 M H_2^{18}O , 1.0 mM) and H_2^{16}O or D_2^{16}O at 0 °C (0.42, 0.74 and 1.57 M). Bars indicate associated errors.....	209
Figure SIII.10. Experiments between ^{18}O – labeled $\mathbf{3}^{\text{IV}}=\text{O}$ (generated from reaction of ^{16}O – labelled $\mathbf{3}^{\text{IV}}=\text{O}$ and 0.14 M H_2^{18}O , 1.0 mM) and H_2^{16}O or D_2^{16}O at 22 °C (0.42 M of H_2O or D_2O) at 0 °C, resulting in a KIE of 1.8. The ^{18}O – incorporation was determined by quenching aliquots (0.4 mL, 0.4 mmol) of the reaction with thioanisole (5 μL , 42.7 mmol) and determining the ratio of ^{16}O and ^{18}O – methylphenylsulfoxide by GC – MS, as previously described. ⁷⁷	210

Figure SIII.11. Plot of E_{ox} vs $\log(k_x)$ from reactions of $1^{(IV)}=O$ (yellow circles) and $2^{(IV)}=O$ (red squares) with thioanisole substrates.....	211
Figure SIII.12. Final UV – vis spectra after reaction of $1^{(IV)}=O$ (left) and $2^{(IV)}=O$ upon addition of cumene, ethylbenzene and toluene.	212
Figure SIII.13. Plot of the pseudo – first – order rate constants, k_{obs} (min^{-1}) against substrate concentrations to determine second – order rate constants, k_2 and C – H kinetic isotope effect (KIE) value for the reaction of 1 mM of $1^{(IV)}=O$ (circles with solid line) and $2^{(IV)}=O$ (squares with dashed line) with toluene (green) and toluene – D_8 (red) in CH_3CN at 20 °C.....	212
Figure SIII.14. Eyring plot of $\ln(k/T)$ vs $1/T$ to obtain the thermodynamic parameters of reactions of $1^{(IV)}=O$ (top) and $2^{(IV)}=O$ (below) with thioanisole and alkylbenzylc substrates.	214
Figure SIII.15. Plot of the pseudo – first – order rate constants, k_{obs} (s^{-1}) against thioanisole concentrations to determine second – order rate constants, k_2 at different temperatures for complex $4^{(IV)}=O$	215
Figure SIII.16. Eyring plot of $\ln(k/T)$ vs $1/T$ to obtain the thermodynamic parameters of reactions of $4^{(IV)}=O$ with thioanisole and cumene substrates.....	215
Figure SIII.17. Top: (Blue line) UV – vis spectrum of $[Ru(bpy)_3]Cl_2$ in water (0.17 mM) in the presence of excess $Na_2S_2O_8$ (200 equiv); (Red line) spectrum obtained after 450nm light irradiation of previous solution in the oxidation to $[Ru^{III}(bpy)_3]$. Below: (Blue line) UV – vis spectrum of $1^{(III)}$ in $MeCN:H_2O$ 1:3 (0.4 mM); (Red line) spectrum obtained after addition of 10 equiv $Na_2S_2O_8$ (4 mM) in the oxidation of $1^{(III)}$ to $1^{(III)} - OH$	216
Figure SIII.18. Evolution of 715 nm feature of chemically generated $1^{(IV)}=O$ (0.4 mM, 0.02 mM $[Ru^{II}Cl_2(bpy)_3]$, 25°C) upon addition of 5 eq $^{MeO}PhSMe$ with irradiation at 447 nm (orange line) and without irradiation (green line).....	217
Figure SIII.19. Blue line: UV – vis spectrum of $1^{(III)}$ in $CH_3CN:H_2O$ 1:3. Yellow line: UV – vis spectrum obtained at the end of the reaction between chemically generated $1^{(IV)}=O$ and 5 equiv <i>para</i> – chloro – thioanisole in the presence of 5 mol% $[Ru^{II}Cl_2(bpy)_3]$ with 447nm – light irradiation at 298 K. Red – line: UV – vis spectrum obtained upon additon of 1 equiv ascorbic acid (with respect to iron) after reaction of chemically generated $1^{(IV)}=O$ and 5 equiv <i>para</i> – chloro – thioanisole in the presence of 5 mol% $[Ru^{II}Cl_2(bpy)_3]$ with 447nm – light irradiation at 298 K.	217
Figure SIII.20. ESI – MS spectrum obtained after reaction of chemically generated $1^{(IV)}=O$ with 5 equiv $^{Cl}PhSMe$ in the presence of 5 mol% $[Ru^{II}Cl_2(bpy)_3]$ with 450 nm – light irradiation at 298 K.....	218
Figure SIII.21. Plot $\log(P_X/P_H)$ vs. reduction potential of <i>p</i> – X – thioanisoles (E_{ox}) for competition experiments corresponding to the competitive reactions of $1^{(IV)}=O$ with thioanisole and <i>p</i> – X – thioanisoles in $CH_3CN:H_2O$ 1:3 in the presence of 5 mol% $[Ru^{II}(bpy)_3]Cl_2$ with 447 nm – light irradiation at 298 K. P_X corresponds to the amount of <i>para</i> – substituted phenylmethylsulfoxide obtained at the end of the reaction (determined by GC – FID or NMR). Competition experiments were run in the presence of 5 equiv thioanisole and 5 equiv <i>p</i> – X – thioanisole.....	218
Figure SIII.22. Transient kinetic trace observed at 470 nm after laser flash photolysis (532 nm) of deaerated solution of $[Ru^{II}(bpy)_3]^{2+}$ (0.07 mM) in $CH_3CN:H_2O$ (1:3) a) in the absence and b) in the presence of $1^{(IV)}=O$ (3.4 mM). Inset: $[Ru^{II}(bpy)_3]^{2+}$ time profile monitored at 470 nm in the presence of $1^{(IV)}=O$ (3.4 mM) over a period of 160 μs	219

Figure SIII.23. A) Transient kinetic traces monitored at 470 nm after laser flash photolysis (532 nm) of a deaerated CH ₃ CN:H ₂ O (1:3) solution of [Ru ^{II} (bpy) ₃] ²⁺ in the presence of 1^(IV)=O (3.4 mM) (black) or 1^(IV)=O (3.4 mM) and ^{MeO} PhSMe (3.4 mM) (red). B) Transient kinetic traces monitored at 550 nm after laser flash photolysis (532 nm) of a deaerated solution of [Ru ^{II} (bpy) ₃] ²⁺ in CH ₃ CN:H ₂ O (1:3) in the presence of 1^(IV)=O (3.4 mM) and ^{MeO} PhSMe (3.4 mM). Inset: transient absorption spectrum of a deaerated solution of [Ru ^{II} (bpy) ₃] ²⁺ in CH ₃ CN:H ₂ O (1:3) in the presence of 1^(IV)=O (3.4 mM) and ^{MeO} PhSMe recorded 2 μs after laser excitation (532 nm).	219
Figure SIV.1. (Top) UV – vis spectra of oxidation of 2^(II) to 2^(IV)=NTs in MeCN at 20°C, HR – MS spectrum of 2^(IV)=NTs prepared in CH ₃ CN exhibiting a base peak at m/z 275.09; inset show amplification of major peak for [Fe ^{IV} (NTs)(Me ₂ (CHPy ₂)tacn)] ²⁺ species. Proper simulation of the peaks requires inclusion of ≈50 % of [Fe ^{III} (NHTs)(L)] ²⁺ in the isotopic pattern corresponding to [Fe ^{IV} (NTs)(L)] ²⁺	221
Figure SIV.2. EPR spectra of isolated 1^(III) – NHTs/OTf (left) and 2^(III) – NHTs/OTf (right) at 2K.	224
Figure SIV.3. (Top) HR – MS of isolated 1^(III) – NHTs/OTf and 2^(III) – NHTs/OTf in CH ₃ CN. Below, CV spectra of species 1^(III) – NHTs/OTf and 2^(III) – NHTs/OTf in CH ₃ CN, small waves around 0.6 – 0.7 V are from [Fe ^{III} (OH)L]OTf ₂ formed from traces of water (L = MePy ₂ tacn or Me ₂ (CHPy ₂)tacn). (Medium) HR – MS of 1^(III) – NHTs/OTf and 2^(III) – NHTs/OTf , insets show [Fe ^{III} (NHTs)L] ²⁺ ions; the presence of minor peaks come from traces of [Fe ^{II} (CH ₃ CN)L]OTf ₂ and [Fe ^{III} (OH)L]OTf ₂ impurities due to adventitious water. (Below) Cyclic Voltammetry spectra of [Fe ^{II} (MeCN)(MePy ₂ tacn)]OTf ₂ (red line) and [Fe ^{II} (MeCN)(Me ₂ (CHPy ₂)tacn)]OTf ₂ (green line) in MeCN, 0.1mM of TBAPF ₆	225
Figure SIV.4. UV – vis spectra of isolated 1^(III) – NHTs/OTf and 2^(III) – NHTs/OTf in MeCN at 20 °C.	226
Figure SIV.5. ¹ H – NMR spectra of: (Top) [Fe ^{II} (MeCN)(MePy ₂ tacn)](OTf) ₂ , 1^(III) , in CD ₃ CN; (Below) reaction of 1^(IV)=NTs with ^{MeO} PhSMe in CD ₃ CN after 30 minutes time.....	226
Figure SIV.6. (Top left) Titration of 2^(III) – NHTs with ascorbic acid (1 equivalent) after reaction of 2^(IV)=NTs with MeOPhSMe in MeCN. (Top right) Titration of 2^(III) – NHTs to 2^(II) with 2 equivalents of ascorbic acid in MeCN. (Below) Titration of 2^(IV)=NTs to 2^(III) – NHTs with 1 equivalent of ascorbic acid in acetone.....	227
Figure SIV.7. (Top) Mass spectra of 1^(IV)=NTs reduced with: (top) one equivalent of ascorbic acid; (below) one equivalent of bis(1, 3 – dimethylbenzimidazolidin – 2 – ylidene).....	228
Figure SIV.8. Plot Eox vs log(k _x) in the reactions of 1^(IV)=NTs (green circles) and 2^(IV)=NTs (blue circles) with <i>p</i> – ^X PhSMe substrates.....	228
Figure SIV.9. (Top) UV – vis monitoring of the decay of 1^(IV)=NTs upon addition of 1 equivalent of [Ru ^{II} (bpy) ₃](PF ₆) ₂ in acetonitrile. (Below) HR – MS spectra of reaction mixture. Ions at m/z = 275.59, 700.14 and 550.18 evidence the reduction of 1^(IV)=NTs to 1^(III) – NHTs , despite only Ru ^{II} peaks (285.06 and 715.07) could be observed due to Ru ^{III} instability.	229
Figure SIV.10. (Top) UV – vis monitoring of the decay of 2^(IV)=NTs upon addition of 1 equivalent of [Ru ^{II} (bpy) ₃](PF ₆) ₂ in acetone. (Below) HR – MS spectrum of reaction mixture. Ions at m/z = 275.59, 700.14 and 550.18 evidence the reduction of 2^(IV)=NTs to 2^(III) – NHTs , despite only Ru ^{II} peaks (285.06 and 715.07) could be observed due to Ru ^{III} instability.....	230

Figure SIV.11. (Left) Rate dependence on [Fe] for the reaction of $1^{(IV)}=NTs$ with $MeOPhSMe$. (Right) $\log(k_{obs})$ vs $\log([1^{(IV)}=NTs])$ in the reaction of $1^{(IV)}=NTs$ with $MeOPhSMe$	231
Figure SIV.12. Dependence of k_{obs} on [Fe] in the reaction of $2^{(IV)}=NTs$ with $ClPhSMe$ (0.09 M) in MeCN.	231
Figure SIV.13. (Top) UV – vis monitoring reduction of $4^{(IV)}=NTs$ to $4^{(III)} – NHTs$ upon addition of one equivalent of ascorbic acid in MeCN. (Below) HR – MS spectrum after addition of 1 eq of ascorbic acid to $4^{(IV)}=NTs$. Ions at $m/z = 296.57$ and 592.13 belong to $[Fe^{III}(NHTs)(N4Py)]^{2+}$ and $[Fe^{III}(NTs)(N4Py)]^+$ respectively. Main ions $m/z = 220.06$ and 589.07 are due to the formation of $[Fe^{III}(OH)(N4Py)]^{2+}$ and $[Fe^{III}(OH)(OTf)(N4Py)]^{2+}$. Ions 211.56 and 572.07 belong to $[Fe^{II}(N4Py)]^{2+}$ and $[Fe^{II}(OTf)(N4Py)]^+$ ions. Ion at 240.07 is $[Fe^{IV}(O)(N4Py)]^{2+}$ formed from traces of water.....	232
Figure SV.1. Paramagnetic 1H -NMR spectrum of $1a^{(II)} – N_3$ (top) and $2a^{(II)} – N_3$ (below) in CD_3CN at 273 K.....	245
Figure SV.2. UV – vis spectra for complexes $1a^{(II)} – N_3$ (blue line) and $2a^{(II)} – N_3$ (orange line) in acetone at 298 K.....	245
Figure SV.3. Top; IR spectra of iron (II) azide $1a^{(II)} – N_3$ (left) and iron (II) azide $2a^{(II)} – N_3$ (right). Below; Raman spectra of $1a^{(II)} – N_3$ (left) and $2a^{(II)} – N_3$ (right); $\approx 2000\text{ cm}^{-1}$ features are typical for asymmetric stretching of $Fe – N_3$. ³²²	246
Figure SV.4. Top; IR spectra of iron (II) azide $1b^{(III)} – N_3$ (left) and iron (II) azide $2b^{(III)} – N_3$ (right). Below; Raman spectra of $1b^{(III)} – N_3$ (left) and $2b^{(III)} – N_3$ (right); $\approx 2000\text{ cm}^{-1}$ features are typical for asymmetric stretching of $Fe – N_3$ while $2200 – 2300\text{ cm}^{-1}$ features are typical for nitrile species. ^{322,374}	246
Figure SV.5. ESI – MS of complex $1a^{(II)} – N_3$ (left) and $2a^{(II)} – N_3$ (right), insets on the right side show the simulated peak for ion $[Fe^{II}(N_3)(L)]^+$. Peaks at $m/z = 190.5$ and 530.0 belong to $[Fe^{II}(L)]^{2+}$ and $[Fe^{II}(OTf)(L)]^+$ respectively. $m/z = 416.1$ corresponds to a minor impurity of $[Fe^{II}(Cl)(L)]^+$. (L) = $MePy_2tacn$ or $Me_2(CHPy_2)tacn$	247
Figure SV.6. Cyclic voltammetry of $1a^{(II)} – N_3$ (top) and $2a^{(II)} – N_3$ in acetone (below); $-20\text{ }^\circ\text{C}$ (1 mM Fe and 0.1 M TBAPF ₆ , values referenced vs. $Ag/AgNO_3$).	248
Figure SV.7. Cyclic voltammetry of $1a^{(II)} – N_3$ (blue) and $2a^{(II)} – N_3$ (red) in MeCN; $-20\text{ }^\circ\text{C}$ (1 mM Fe and 0.1 M TBAPF ₆ , values referenced vs. $Ag/AgNO_3$).....	249
Figure SV.8. Cyclic voltammeteries of complexes $1b^{(III)} – N_3$ in acetone (green) and acetonitrile (red) and $2b^{(III)} – N_3$ (blue) in acetonitrile at $-20\text{ }^\circ\text{C}$; 1 mM on iron and 0.2M $N(n – Bu)_4PF_6$ (values referenced vs. $Ag/AgNO_3$).....	249
Figure SV.9. Oxidation of $1a^{(II)} – N_3$ to $1b^{(III)} – N_3$ upon applying 0.5 V to the solution (acetone, $-20\text{ }^\circ\text{C}$, 0.2 mM, 0.2 M TBAPF ₆).....	250
Figure SV.10: Magnetic effective moment dependence on temperature for complex $1b^{(III)} – N_3$ (left) and $2b^{(III)} – N_3$ (right).....	250
Figure SV.11. (Top) UV – vis spectra for complexes $1b^{(III)} – N_3$ (blue line) and $2b^{(III)} – N_3$ (orange line) in acetone at 298 K. (Below) UV – vis spectra for complex $2b^{(III)} – N_3$ in acetone recorded at different temperatures.....	251
Figure SV.12. MS spectrum of $2b^{(III)} – N_3$ in acetone. The main ion peak $m/z = 211.58$ is the $[Fe^{III}(N_3)(Me_2(CHPy_2)tacn)]^{2+}$ ($2b^{(III)} – N_3$), peaks at $m/z = 423.17$ and 190.08 belong to	

[Fe ^{II} (N ₃)(Me ₂ (CHPy ₂)tacn)] ⁺ and [Fe ^{II} (Me ₂ (CHPy ₂)tacn)] ²⁺ respectively. The peak at m/z = 465.17 are attributed to aggregates of [Fe ^{III} (N ₃)(Me ₂ (CHPy ₂)tacn)] ⁺ with N ₃ ⁻ anions. Peaks at m/z = 199.08 and 197.58 belong to the [Fe ^{III} (OH)(Me ₂ (CHPy ₂)tacn)] ²⁺ and the in situ formation of [Fe ^V (N)(Me ₂ (CHPy ₂)tacn)] ²⁺ species, respectively.	252
Figure SV.13. Mössbauer spectra of ⁵⁷ Fe enriched samples of 1a^{II} – N ₃ (left row) and 2a^{II} – N ₃ (right row) in frozen acetone solution. Top spectra are samples before irradiation and below spectra are same samples after irradiation.	253
Figure SV.14. Photolysis of complex 1b^{III} – N ₃ (0.2 mM) and 2b^{III} – N ₃ (0.25 mM) with 530 nm LED in acetonitrile at 233 K.	254
Figure SV.15. SQUID measurement of solid complex 1^VΞN after 4.5 h photolysis at 77 K with a 470 nm LED in a beaker. Red line is the simulation of a mixture of 74 % of an S = 1/2 and a 26 % of S = 2 species.	255
Figure SV.16. Mössbauer spectra of solid sample containing putative 2^VΞN after 2.5 h photolysis at 77 K with a 470 nm LED lamp. Zero – field Mössbauer spectrum of solid sample containing putative 2^VΞN at 77 K. Obtained after 2.5 h of photolysis of a 2b^{III} – N ₃ sample at 77 K with a 470 nm (blue) LED. The Mössbauer spectrum was fitted with four Lorentzian doublets accounting for i) Iron (III) starting material (2b^{III} – N ₃ , 8%, in green), ferrous impurities ii) iron (II) HS (30%, in orange) and iii) iron (II) LS (26%, in yellow), and iv) the high – valent photo – product (2^VΞN , 36%, in blue).	255
Figure SV.17. Fe K pre – edge XANES region for compounds 1a^{II} – N ₃ , 1b^{III} – N ₃ and 1^VΞN highlighting the 1s→ 3d feature fit with a cumulative Gaussian lorentzian sum function having 0.75% Gaussian character.	256
Figure SV.18. Correlation between calculated and experimental Fe K pre – edge intensity averaged energies (left) and total intensities (right) 1a^{II} – N ₃ , 1b^{III} – N ₃ and 1^VΞN	256
Figure SV.19. Correlation between experimental Fe K pre – edges and calculated transitions including the difference density maps for: 1a^{II} – N ₃ , 1b^{III} – N ₃ and 1^VΞN . Transitions were shifted by 155.0 eV to match experiment.	257
Figure SV.20. (Top) Mössbauer spectra after decomposition of solid 1^VΞN at room temperature under anaerobic conditions. (Below) HR – MS analysis of melted sample after photolysis of 1b^{III} – N ₃ to 1^VΞN during online mass spectrometry studies; insets show the experimental and simulated ions 248.12 and 424.17, tentatively assigned to species [Fe ^{II} (COCH ₃)(MePy ₂ tacn)] ⁺ and [Fe ^{III} (COCH ₃)(CH ₃ COCH ₃)(MePy ₂ tacn)] ²⁺ suggesting that 1^VΞN could be reacting with acetone.	258
Figure SVI.1. ¹ H – NMR spectrum of the benzene derivative (500 MHz, CDCl ₃ , 20 °C).	263
Figure SVI.2. ¹ H – NMR spectrum of the toluene derivative (500 MHz, CDCl ₃ , 20 °C).	264
Figure SVI.3. Detail of the ¹ H – NMR spectrum of the toluene derivative (500 MHz, CDCl ₃ , 20 °C). Values in brackets are the normalised per number of C atoms (2 <i>ortho</i> , 2 <i>meta</i> and 1 <i>para</i>).	264
Figure SVI.4. ¹ H – NMR spectrum of the ethylbenzene derivative (500 MHz, CDCl ₃ , 20 °C). Values in brackets are the normalised per number of C atoms (2 <i>ortho</i> , 2 <i>meta</i> and 1 <i>para</i>).	265
Figure SVI.5. ¹ H – NMR spectrum of the isobutylbenzene derivative (500 MHz, CDCl ₃ , 20 °C). Values in brackets are the normalised per number of C atoms (2 <i>ortho</i> , 2 <i>meta</i> and 1 <i>para</i>).	265
Figure SVI.6. 2D – NOESY spectrum of the isobutylbenzene derivative (500 MHz, CDCl ₃ , 20 °C).	266

Figure SVI.7. ¹ H – NMR spectrum of the biphenyl derivative (500 MHz, CDCl ₃ , 20 °C). Values in brackets are the normalised per number of C atoms (2 <i>ortho</i> , 2 <i>meta</i> and 1 <i>para</i>).....	266
Figure SVI.8. 2D – NOESY spectrum of the biphenyl derivative (500 MHz, CDCl ₃ , 20 °C)	267
Figure SVI.9. ¹ H NMR spectrum of the cyclopropylbenzene derivative (500 MHz, CDCl ₃ , 20 °C). Values in brackets are the normalised per number of C atoms (2 <i>ortho</i> , 2 <i>meta</i> and 1 <i>para</i>).....	267
Figure SVI.10. ¹ H NMR spectrum of the anisole derivative (400 MHz, CDCl ₃ , 20 °C). O – Me functionalization product was assigned by comparison with commercially available ethyl phenoxyacetate.	268
Figure SVI.11. ¹ H NMR spectrum of the mesitylene derivative (500 MHz, CDCl ₃ , 20 °C).	268
Figure SVI.12. ¹ H NMR spectrum of the <i>p</i> – xylene derivative (400 MHz, CDCl ₃ , 20 °C).....	269
Figure SVI.13. ¹ H NMR spectrum of the <i>tert</i> – butylbenzene derivatives (400 MHz, CDCl ₃ , 20 °C). Values in brackets are the normalised per number of C atoms (2 <i>ortho</i> , 2 <i>meta</i> and 1 <i>para</i>).....	269
Figure SVI.14. 2D – NOESY spectrum of the <i>tert</i> – butylbenzene derivative (300 MHz, CDCl ₃ , 20 °C).	270
Figure SVI.15. ¹ H – NMR spectrum of the 1,3,5 – triethylbenzene derivative (400 MHz, CDCl ₃ , 20 °C).	270
Figure SVI.16. ¹ H NMR spectrum of the naphthalene derivatives (400 MHz, CDCl ₃ , 20 °C).	271
Figure SVI.17. 2D – NOESY spectrum of the naphthalene derivative (400 MHz, CDCl ₃ , 20 °C).	271
Figure SVI.18. ¹ H – NMR spectrum of the phenyl-cyclohexane derivatives (400 MHz, CDCl ₃ , 20 °C). Values in brackets are the normalised per number of C atoms (2 <i>ortho</i> , 2 <i>meta</i> and 1 <i>para</i>).	272
Figure SVI.19. 2D – NOESY spectrum of the cyclohexylbenzene derivative (400 MHz, CDCl ₃ , 20 °C).	272
Figure SVI.20. ¹ H NMR spectrum of the tetrahydronaphthalene derivatives (400 MHz, CDCl ₃ , 20 °C).	273
Figure SVI.21. 2D – NOESY spectrum of the tetrahydronaphthalene derivative (400 MHz, CDCl ₃ , 20 °C).	273

LIST OF SCHEMES

Scheme I.1. Molecular orbital diagrams of: (left) trigonal ligand field with degenerated orbitals that enables non – heme high – spin $\text{Fe}^{\text{IV}}=\text{O}$ species ($S = 2$); (middle) ligand field that leads to heme low – spin $\text{Fe}^{\text{IV}}=\text{O}$ species ($S=1$), (the porphirinato radical has a $S = 1/2$, giving place to a $S = 3/2$); (right) octahedral ligand field that leads to non – heme low – spin $\text{Fe}^{\text{IV}}=\text{O}$ species ($S=1$).....	9
Scheme I.2. Schematic mechanism for C – H hydroxylation by Cyt P450.	10
Scheme I.3. Schematic mechanism of taurine dioxygenase (TauD) and prolyl 4 – hydroxylase (P4H) in C – H oxidation reactivity.	11
Scheme I.4. Schematic mechanism of the pterin – dependent enzymes tyrosine hydroxylase (TyrH) and phenylalanine hydroxylase (PheH) in C – H oxidation reactivity.	11
Scheme I.5. Schematic mechanism of the halogenase enzymes in C – H halogenation reactivity.	12
Scheme I.6. Different strategies to synthesise iron – oxo complexes.	18
Scheme I.7. Reported syntheses and general reactivity of high – valent iron – imido species. L refers to the different non – heme ligands described in the text. Cz refers to the porphyrinic corrolazine macrocycle (<i>vide infra</i>).....	28
Scheme I.8. A) Photolytic reactivity of iron – azide complexes. (1) Homolytic cleavage of Fe – N and photoreduction of Fe centre; (2) Heterolytic cleavage of N – N and photooxidation of iron centre. B) Anthracene extrusion strategy to generate high – valent iron – nitrido species.....	37
Scheme I.9. Iron catalysed transformations of diazo compounds and the generally proposed metal mediated catalytic mechanism.	43
Scheme II.1. 1,4,7 – triazacyclononane ligands used in this work.	51
Scheme II.2. Schematic representation of the objectives of this work.	52
Scheme III.1. Schematic diagram for the preparation of iron (II) complexes 1^(II) and 2^(II) . S = solvent. ...	56
Scheme III.2. Chemical strategies to prepare 1^(IV)=O and 2^(IV)=O from its iron (II) precursors 1^(II) and 2^(II) , respectively.....	60
Scheme III.3. Equilibria for iron species in solution.	68
Scheme III.4. Proposed oxo – hydroxo tautomerism mechanisms for ^{18}O exchange in heme (top) and non – heme systems (below).	74
Scheme III.5. Common mechanism suggested for OAE with iron (IV) – oxo complexes studied.	78
Scheme III.6. General oxidation mechanism in OAT reactions for <i>p</i> – methylphenylthioethers performed by iron (IV) oxo complexes.	79
Scheme III.7. Proposed mechanism for oxidation HAT reactivity of alkylbenzenes with iron (IV) – oxo complexes.....	81
Scheme III.8. Possible products formed upon oxidation of a mixture of cumene and thioanisole with 1^(IV)=O depending of T.....	90
Scheme III.9. Chemical reactions taking place during the photocatalytic generation of 1^(IV)=O	92
Scheme III.10. Mechanistic pathways to explain the rate enhancement in the oxidation of sulfides by 1^(IV)=O under light irradiation.	95
Scheme III.11. Redox potentials of <i>p</i> – X – thioanisoles and $[\text{Ru}(\text{bpy})_3]^{2+/3+}$ (values vs SCE in CH_3CN). ²⁷⁹	96

Scheme IV.1. Chemical strategy for the generation of $1^{(IV)}=NTs$ and $2^{(IV)}=NTs$ from Fe^{II} precursors. S = MeCN, CF_3SO_3	105
Scheme IV.2. Iron mediated reaction of thioanisole with PhINTs.	117
Scheme V.1. Representative examples of non heme iron (V) and iron (VI) nitrido species reported in the literature. ^{215,314-317}	135
Scheme V.2. Schematic diagram of the preparation of the complexes. S = solvent.	137
Scheme V.3. Photolytic reactivity of iron – azide complexes. (1) Homolytic cleavage of Fe – N and photoreduction of Fe centre; (2) Heterolytic cleavage of N – N and photooxidation of iron centre.	145
Scheme VI.1. Arene functionalisation in the Buchner reaction.	157
Scheme VI.2. Proposed mechanism through Wheland – type intermediate for metal – catalysed functionalisation of benzene.	158
Scheme VI.3. Comparison of reaction of alkylbenzenes with diazoacetates in presence of different catalyst from previous work and this work.	162
Scheme VI.4. Comparison of reaction of anisole with diazoacetates in presence of different catalyst from previous work and this work.	163
Scheme VIII.1. Scheme of MePy ₂ tacn synthesis.	181
Scheme VIII.2. Scheme of Me ₂ (CHPy ₂)tacn synthesis.	184

LIST OF TABLES

Table I.1. Selection of iron proteins involved in biological oxidations of C – H bonds.	8
Table I.2. Structural and spectroscopic properties of selected high – valent iron – oxo species.	16
Table I.3. Rate constants for iron (IV) – oxo complexes with different substrates in HAT reactivity.	24
Table III.1. XAS data from reported pentadentate iron – oxo complexes.	65
Table III.2. Kinetic data and KIE values of OAE for tacn complexes 1^(IV)=O , 2^(IV)=O and 3^(IV)=O	77
Table III.3. k_2 values and $\log(K_X/K_H)$ and σ_{para} values for reaction of 1^(IV)=O and 2^(IV)=O with methylphenylthioethers.	80
Table III.4. Ferrocenium and iron (II) species recovered after adding one equivalent of ferrocene to the resulting solutions after $Fe^{IV}(O)$ consumption.	83
Table III.5. Product distribution of oxidation reactions of 1^(IV)=O and 2^(IV)=O with alkylbenzene substrates under N_2	84
Table III.6. Rate constants (k_2') obtained for alkylbenzenes oxidation. k_2 values were normalised by the number of H available on the substrate (2 for ethylbenzene and 3 for toluene) to obtain the corresponding k_2'	85
Table III.7. Rate constants obtained for H_8 – and D_8 – toluene.	87
Table III.8. Reported kinetic data for HAT reactivity with selected $Fe^{IV}(O)$ complexes.	87
Table III.9. Activation parameters obtained for methyl phenylthioethers oxidations with complexes 1^(IV)=O and 2^(IV)=O	88
Table III.10. Activation parameters obtained for alkylbenzenes oxidations with complexes 1^(IV)=O and 2^(IV)=O	88
Table III.11. Activation parameters obtained for substrate oxidations with $[Fe^{IV}(O)(N4Py)]^{2+}$ (4^(IV)=O).	91
Table III.12. Measured k_{obs} values corresponding to the decay rate of chemically generated 1^(IV)=O (0.4 mM in $CH_3CN:H_2O$ 1:3 in a N_2 atmosphere at 25°C) under different reaction conditions.	94
Table III.13. Measured k_{obs} values corresponding to the decay rate of chemically generated 2^(IV)=O (0.4 mM in $CH_3CN:H_2O$ 1:3 in a N_2 atmosphere at 25°C) under different reaction conditions.	98
Table IV.1. EXAFS data for complexes 1^(IV)=NTs and 2^(IV)=NTs	110
Table IV.2. Structural and spectroscopic properties of S = 1 high – valent tosylimido iron compounds.	112
Table IV.3. Spectroscopic data from isolated complexes 1^(III) – NHTs/OTf and 2^(III) – NHTs/OTf	114
Table IV.4. Measured second order rate constants for the reaction of 0.25 mM solutions of 1^(IV)=NTs and 2^(IV)=NTs with selected xPhSMe at 293 K.	125
Table V.1. Azide stretchings and Mössbauer parameters for the studied (top) and bibliography compounds (below).	143
Table V.2. Comparison of Fe – N bond distances and XAS energies.	149
Table VI.1. Catalytic results of iron (II) and manganese (II) complexes in the catalytic functionalisation of benzene.	160
Table VIII.1. Stability of cycloheptatriene A in benzene as solvent.	194
Table SIII.1. Crystallographic data and selected bond distances and angles of 1^(III)	199

Table SIII.2. Crystallographic data and selected bond distances and angles of 2^(IV)	200
Table SIII.3. EXAFS fitting parameters for 1^(IV)=O (k range = 2 – 15 Å ⁻¹ ; back transform range ~0.83 – 3.0 Å).....	204
Table SIII.4. Reported kinetic data for OAE between H ₂ ¹⁸ O and non – heme oxoiron (IV) complexes.....	210
Table SIII.5. Sulfoxide yields for 1^(IV)=O and 2^(IV)=O with thioanisole substrates.....	211
Table SIII.6. Product distribution of oxidation reactions of 1^(IV)=O and 2^(IV)=O with alkylbenzene substrates under O ₂	213
Table SIII.7. Sulfoxide yields for oxidation reactions of iron complexes with thioanisole:cumene mixtures (1:1).....	213
Table SIII.8. 4^(IV)=O rate constants obtained for thioanisole and cumene substrates.....	214
Table SIV.1. Crystal data and structure refinement for [Fe ^{III} (NHTs)(MePy ₂ tacn)](SbF ₆) ₂ (1^(III) – NHTs/SbF ₆) at 100 K.....	222
Table SIV.2. Selected bond lengths [Å] and angles [°] complex 1^(III) – NHTs/SbF ₆	223
Table SIV.3. Yield of sulfanylidene products (2.5 mM on Fe and 0.25 – 1.2 M on substrate), normalised according to the iron (IV) purity of sample measured by Mössbauer spectroscopy.....	225
Table SIV.4. XYZ coordinates of 1^(IV)=NTs and 2^(IV)=NTs	233
Table SV.1. Crystal data and structure refinement for [Fe ^{II} (N ₃)(MePy ₂ tacn)](OTf) (1a^(II) – N ₃) at 298K.....	235
Table SV.2. Selected bond lengths [Å] and angles [°] for [Fe ^{II} (N ₃)(MePy ₂ tacn)](OTf) (1a^(II) – N ₃) at 298K.....	236
Table SV.3. Selected crystal data and structure refinement for [Fe ^{II} (N ₃)(MePy ₂ tacn)](OTf) (1a^(II) – N ₃) at 200K.....	237
Table SV.4. Selected Bond lengths [Å] and angles [°] for [Fe ^{II} (N ₃)(MePy ₂ tacn)](OTf) (1a^(II) – N ₃) at 200K.....	238
Table SV.5. Crystal data and structure refinement for [Fe ^{II} (N ₃)(MePy ₂ tacn)](OTf) (1a^(II) – N ₃) at 100K.....	239
Table SV.6. Selected bond lengths [Å] and angles [°] for [Fe ^{II} (N ₃)(MePy ₂ tacn)](OTf) (1a^(II) – N ₃) at 100K.....	240
Table SV.7. Crystal data and structure refinement for [Fe ^{III} (N ₃)(MePy ₂ tacn)](PF ₆) ₂ (1b^(III) – N ₃) at 100 K.....	241
Table SV.8. Selected bond lengths [Å] and angles [°] for [Fe ^{III} (N ₃)(MePy ₂ tacn)](PF ₆) ₂ (1b^(III) – N ₃) at 100 K.....	242
Table SV.9. Crystal data and structure refinement for [Fe ^{II} (N ₃)Me ₂ (CHPy ₂)tacn](OTf) (2a^(II) – N ₃) at 100K.....	243
Table SV.10. Selected bond lengths [Å] and angles [°] for [Fe ^{II} (N ₃)Me ₂ (CHPy ₂)tacn](OTf) (2a^(II) – N ₃) at 100K.....	244
Table SV.11 Selected EXAFS fits for 1^(V)≡N . Fits carried out in r – space (Δk = 2 – 14 Å ⁻¹ ; Δr = 1 – 3 Å) with a Hanning window (dk 2), a k – weight = 3 and S ₀ = 0.9. Bond distances and disorder parameters (Δr _{eff} and σ ²) were allowed to float having initial values of 0.0 Å and 0.003 Å ² respectively, with a universal E ₀	

initially set to first inflection point of the rising edge and $\Delta E_0 = 0$ eV. (Fits highlighted in blue are the best models; values highlighted in red are either statistically or physically erroneous; σ^2 reported as $\times 10^3 \text{ \AA}^2$).

.....	256
Table SV.12. XYZ files of geometry optimized structures.....	259
Table SVI.1. Distribution of isomers for substituted benzenes as substrates (normalised values for the number of C available, 2 for <i>ortho</i> , 2 for <i>meta</i> and 1 for <i>para</i>).....	263

ACKNOWLEDGEMENTS

I want to thank the following people, who made this work possible:

- All the people who I shared lab with during my doctorate, in special my labmates from Huelva, and all the QBIS group members.
- Serveis Tècnics de Recerca from Universitat de Girona, specially Laura Gómez and Anna Costa for their help with mass spectrometry.
- Dr. Jean – Marc Latour and Dr. Martin Clémancey for all the collaborative effort in the tosylimido complexes study and their help with EPR and Mössbauer analysis.
- Dr. M^a del Mar Díaz and Prof. Pedro J. Pérez for a nice stay in CIQSO group in Huelva and the collaborative research in the iron and manganese C – C bond formation.
- Eckhard Bill, Thomas Weyhermüller, Bernd Mienert and Petra Höfer from Max Planck Institute for Chemical Energy Conversion for their help in the preparation of high – valent iron – nitrido species during my stay in Germany.
- Thanks to Vlad Martin Diaconescu for XAS measures and all the theoretical calculations.
- Financial support from European Research Council (ERC – 239910) and COST action CM1305 “Explicit Control Over Spin – states in Technology and Biochemistry (ECOSTBio)” (STSM reference, COST – STSM – CM1305 – 26587).

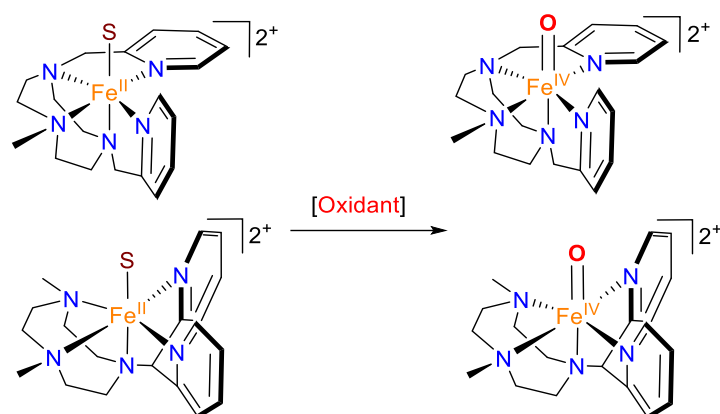
GRAPHICAL ABSTRACT

SUMMARY, RESUM AND RESUMEN (Page 1, 2 and 3)

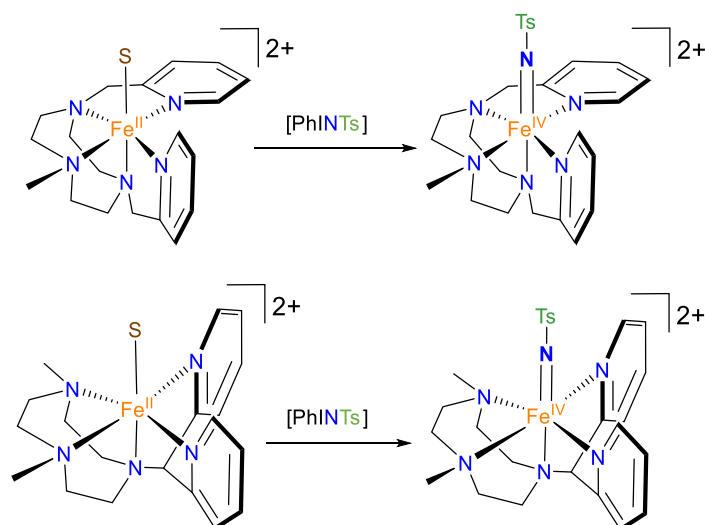
CHAPTER I. General Introduction (page 5)

CHAPTER II. Main Objectives (page 49)

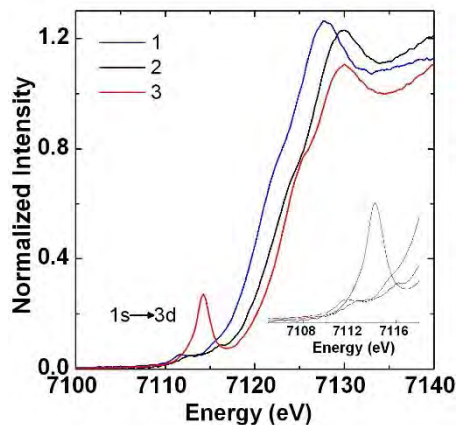
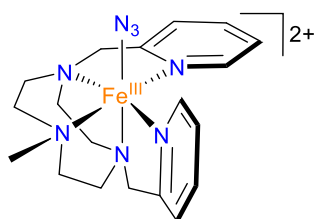
CHAPTER III. Synthesis, characterisation and reactivity of High – valent non – heme Iron (IV) – oxo species in TACN – based N₅ – pentadentate ligands. (page 53)



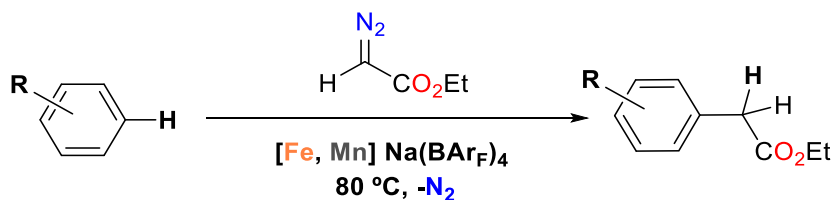
CHAPTER IV. Preparation, Spectroscopic Characterization and Reactivity of Iron (IV) Tosylimido Complexes with TACN – based N₅ – pentadentate Ligands (page 101)



CHAPTER V. Generation, Spectroscopic and Chemical Characterization of Octahedral Iron (V) – Nitrido Species at a neutral TACN – based pentadentate ligand platform (page 133)



CHAPTER VI. Fe and Mn for selective functionalization of C – H bonds of arenes by carbene insertion (page 155)



CHAPTER VII. General Conclusions (page 169)

CHAPTER VIII. Experimental Section (page 173)

ANNEX. Experimental section and Supplementary data (page 197)

REFERENCES. (page 275)

TABLE OF CONTENTS

SUMMARY	1
RESUM	2
RESUMEN	3
CHAPTER I. GENERAL INTRODUCTION	5
I.1. INTRODUCTION TO ENZYMATIC REACTIONS ON C – H BOND FUNCTIONALISATION.....	7
I.1.1. High – valent iron species characterised in biological systems	10
I.2. BIOINSPIRED MODEL COMPLEXES TO STUDY ENZYMES.....	14
I.2.1. Iron – oxo model complexes [Fe = O].....	14
I.2.2. Iron (V) – oxo species.....	26
I.2.3. High – valent iron – imido species [Fe = N – R].....	28
I.2.4. High – valent iron – nitrido species [Fe \equiv N].....	36
I.2.4.1. Pseudo – octahedral iron – nitrido species	37
I.2.4.2. Three – fold symmetric iron – nitrido species.....	40
I.2.5. Iron carbenes and C – C bond formation.....	41
CHAPTER II. MAIN OBJECTIVES	49
CHAPTER III. SYNTHESIS, CHARACTERISATION AND REACTIVITY OF HIGH – VALENT NON – HEME IRON (IV) – OXO SPECIES IN TACN – BASED N₅ – PENTADENTATE LIGANDS	53
III.1. GENERAL INSIGHT.....	55
III.2. RESULTS AND DISCUSSION.....	56
III.2.1. Syntheses and characterisation of [Fe ^{II} (MePy ₂ tacn)(CH ₃ CN)](CF ₃ SO ₃) ₂ (1^{II}) and [Fe ^{II} (Me ₂ (CHPy ₂)tacn)(CH ₃ CN)](CF ₃ SO ₃) ₂ (2^{II}).....	56
III.2.2. Synthesis and characterization of [Fe ^{IV} (O)(MePy ₂ tacn)](OTf) ₂ (1^{IV}=O) and [Fe ^{IV} (O)(Me ₂ (CHPy ₂)tacn)](OTf) ₂ (2^{IV}=O)	60
III.2.3. Electrochemical studies of 1^{IV}=O	66
III.2.4. Reactivity	74
III.2.4.1 Oxygen atom exchange reactivity	74
III.2.4.2. Reactivity of 1^{IV}=O and 2^{IV}=O with organic substrates	78
III.2.4.2.1. Reactivity of 1^{IV}=O and 2^{IV}=O in OAT reactions – Thioanisole oxidation	79
III.2.4.2.2. Reactivity of 1^{IV}=O and 2^{IV}=O in HAT – Alkylbenzene substrates	81
III.2.4.2.3. Comparative study of activation barriers in OAT and HAT.....	88
III.2.4.3. Photochemical enhanced reactivity towards sulphides oxidation.....	92
III.3. SUMMARY.....	99

CHAPTER IV. PREPARATION, SPECTROSCOPIC CHARACTERIZATION AND REACTIVITY OF IRON (IV) – TOSYLIMIDO COMPLEXES WITH TACN – BASED N5 – PENTADENTATE LIGANDS	101
IV.1. GENERAL INSIGHT	103
IV.2. RESULTS AND DISCUSSION.....	104
IV.2.1. Synthesis and characterization of $[\text{Fe}^{\text{IV}}(\text{NTs})(\text{MePy}_2\text{tacn})](\text{OTf})_2$ (1^{IV}=NTs) and $[\text{Fe}^{\text{IV}}(\text{NTs})(\text{Me}_2(\text{CHPy}_2)\text{tacn})](\text{OTf})_2$ (2^{IV}=NTs).....	104
IV.2.1.1. Spectroscopic characterization of 1^{IV}=NTs and 2^{IV}=NTs	104
IV.2.2. Synthesis and characterization of $[\text{Fe}^{\text{III}}(\text{NHTs})(\text{MePy}_2\text{tacn})](\text{X})_2$ (1^{III} – NHTs/X) and $[\text{Fe}^{\text{III}}(\text{NHTs})(\text{Me}_2(\text{CHPy}_2)\text{tacn})](\text{X})_2$ (2^{III} – NHTs/X).....	113
IV.2.3. Reactivity of 1^{IV}=NTs and 2^{IV}=NTs in formal N – atom transfer reactions	117
IV.2.3.1. Spectroscopic analysis of the reactions. Analysis of iron species formed after reaction with sulphides	117
IV.2.3.2. Direct preparation of $[\text{Fe}^{\text{III}}(\text{NHTs})(\text{L})]^{2+}$ by reaction of $\text{Fe}^{\text{IV}}(\text{NTs})$ with reducing agents.....	121
IV.2.3.3. Kinetic analysis of the reactions.....	124
IV.2.4. Extension to the previously described $[\text{Fe}^{\text{IV}}(\text{NTs})(\text{N4Py})]^{2+}$ system.....	126
IV.2.5. Reaction mechanism.....	128
IV.3. SUMMARY	131
CHAPTER V. GENERATION, SPECTROSCOPIC AND CHEMICAL CHARACTERIZATION OF OCTAHEDRAL IRON (V) – NITRIDO SPECIES AT A NEUTRAL TACN – BASED PENTADENTATE LIGAND PLATFORM	133
V.1. GENERAL INSIGHT	135
V.2. RESULTS AND DISCUSSION.....	137
V.2.1 Synthesis and characterization of $[\text{Fe}^{\text{II}}(\text{N}_3)(\text{MePy}_2\text{tacn})](\text{OTf})$ (1a^{II} – N₃) and $[\text{Fe}^{\text{II}}(\text{N}_3)(\text{Me}_2(\text{CHPy}_2)\text{tacn})](\text{OTf})$ (2a^{II} – N₃).....	137
V.2.2. Synthesis and characterization of $[\text{Fe}^{\text{III}}(\text{N}_3)(\text{MePy}_2\text{tacn})](\text{PF}_6)_2$ (1b^{III} – N₃) and $[\text{Fe}^{\text{III}}(\text{N}_3)(\text{Me}_2(\text{CHPy}_2)\text{tacn})](\text{PF}_6)_2$ (2b^{III} – N₃).....	140
V.2.3. Photolysis of Fe(II) – N ₃ species.....	145
V.2.4. Photolysis of Fe(III) – N ₃ species.....	145
V.2.4.1. Photolysis in solution.....	145
V.2.4.2. Photolysis of solid powder samples.....	146
V.2.5. DFT Calculations	149
V.2.6. Analysis of the formation and decay of 1^V≡N by gas evolution.....	150
V.3. SUMMARY.....	153
CHAPTER VI. Fe AND Mn FOR SELECTIVE FUNCTIONALIZATION OF C – H BONDS OF ARENES BY CARBENE INSERTION	155
VI.1. GENERAL INSIGHT	157

VI.2. RESULTS AND DISCUSSION.....	159
VI.2.1. Catalytic studies.....	159
VI.2.2. Mechanistic studies.....	163
VI.3. SUMMARY	167
CHAPTER VII. GENERAL CONCLUSIONS	169
CHAPTER VIII. EXPERIMENTAL SECTION	173
VIII.1. EXPERIMENTAL SECTION CHAPTER III.....	175
VIII.1.1. Instrumentation	175
VIII.1.2. Materials.....	176
VIII.1.3. Experimental procedures.....	176
VIII.2. EXPERIMENTAL SECTION CHAPTER IV.....	186
VIII.2.1. Instrumentation	186
VIII.2.2. Materials.....	186
VIII.2.3. Experimental procedures.....	186
VIII.3. EXPERIMENTAL SECTION CHAPTER V.....	189
VIII.3.1. Instrumentation	189
VIII.3.2. Materials.....	189
VIII.3.3. Experimental procedures.....	190
VIII.4. EXPERIMENTAL SECTION CHAPTER VI.....	193
VIII.4.1. Instrumentation	193
VIII.4.2. Materials.....	193
VIII.4.3. Experimental procedures.....	193
ANNEX.....	197
ANNEX CHAPTER III	199
ANNEX CHAPTER IV	221
ANNEX CHAPTER V	235
ANNEX CHAPTER VI.....	263
REFERENCES	277

SUMMARY

Selective C – H functionalisation is a challenging transformation but with a very high potential in organic synthesis. Hydrocarbon functionalisation is often associated to expensive metals and toxic reagents, generating high amounts of undesired by – products. In sharp contrast, a wide variety of enzymes perform the selective functionalisation of C – H bonds, using green reagents such as O₂ and H₂O₂. These enzymes are capable to oxygenate C – H bonds from a wide variety of substrates under mild conditions. Their active centres contain abundant transition metals such as iron, usually forming high – valent iron – oxo (IV or V) species. Indeed high – valent iron – oxo intermediates have been identified in a number of enzymes in their oxidative reactions. The study of such enzymes is desirable to understand how they work and to imitate their reactivity. A convenient way to study these intermediates is through the design and synthesis of bioinspired model complexes that could permit to generate high – valent artificial species capable of reproducing the enzymes reactivity. This doctoral dissertation is focused in the synthesis of non – heme iron (IV) and iron (V) species bearing 1,4,7 – triazacyclononane – based ligands with the aim to study their properties and reactivity.

In the first place we prepared and characterised two iron (IV) – oxo species and studied their reactivity towards prototypical substrates. In the oxygen atom transfer reactivity (OAT, two – electron process) to sulphur atoms and the hydroxylation of benzylic C – H bonds in the hydrogen atom transfer (HAT) reactivity. The reactivity of heme iron (IV) – oxo species towards C – H bonds is well known to take place through a hydrogen atom abstraction step, generating a C – centred radical and followed by a rebound step to hydroxylate the substrate. Nevertheless in non – heme bioinspired iron – oxo species the rebounding seems to not take place. In addition, the sulfoxidation reactivity of sulphides by the prepared iron (IV) – oxo species was studied under photocatalytic conditions, showing an enhancement of the oxidation rates.

Subsequently, we synthesised and characterised two novel iron (IV) – tosylimido species and studied their –NTs transfer properties towards sulphur atom groups. These species are isoelectronic with the iron (IV) – oxo species, suggesting that they may show a common reactivity. Nevertheless experimental data collected in this thesis shows that their reactivity is different from iron – oxo species and, for instance, reactivity with sulphides takes place through a one – electron step generating iron (III) species. A mechanism was proposed based on experimental data.

Nitrogen fixation by nitrogenase enzymes is postulated to occur through high – valent nitrido species but no evidence has been found to date. Artificial bioinspired iron (IV) and iron (V) – nitrido species are the only evidence that support this proposal, but few of them have been identified to date. Furthermore little information about its reactivity have been reported due to their high reactivity. Here we describe the generation of a new non – heme iron (V) – nitrido species, achieved through the photolytic cleavage of iron (III) – azido species. We successfully characterised this high – valent iron (V) species by a combination of experimental and theoretical techniques and studied its reactivity in the gas phase.

In the last place we describe the catalytic capacity of non – heme iron (II) complexes in the C – H functionalisation of arenes using the ethyl diazoacetate (EDA), a commercially available reagent. The system proved highly selective towards C – H (sp²) bonds with negligible amounts of by – products obtained. The mechanism was proposed to proceed through an iron – carbene species based on the experimental data.

RESUM

La funcionalització selectiva d'enllaços C – H és una tasca complicada però amb un gran potencial en la química orgànica sintètica. La funcionalització d'hidrocarburs generalment està relacionada amb metalls cars i reactius tòxics, generant grans quantitats de subproductes no desitjats. Contràriament, una àmplia varietat d'enzims que es troben en sistemes naturals duen a terme funcionalització selectiva d'enllaços C – H, utilitzant reactius innocuos com ara O_2 i H_2O_2 . Aquests enzims són capaços d'oxigenar enllaços C – H en una àmplia varietat de substrats en condicions suaus. Els seus centres actius contenen metalls abundants com ara el ferro, generalment com a espècies ferro – oxo en alts estats d'oxidació (IV o V). En efecte, intermedis ferro – oxo en alts estats d'oxidació s'han identificat en les reaccions d'oxidació de varis enzims. L'estudi d'aquests enzims és desitjable per entendre com funcionen i per imitar la seva reactivitat. Una forma pràctica d'estudiar aquests intermedis és mitjançant el disseny i la síntesis de complexes model bioinspirats, amb l'objectiu de generar espècies artificials en alt estat d'oxidació per intentar reproduir – ne la reactivitat. Aquesta tesis està enfocada en la síntesi d'espècies no hemo de ferro (IV) i ferro (V) que continguin lligands basats en 1,4,7 – triazaciclononà per estudiar les seves propietats i reactivitat.

En primer lloc hem preparat i caracteritzat dues espècies ferro (IV) – oxo i hem estudiat la seva reactivitat envers substrats típics. En reaccions de transferència d'àtom d'oxigen a àtoms de sofre (procés de dos electrons) i en la hidroxilació d'enllaços C – H benzílics en reaccions de transferència d'àtom d'hidrogen. La reactivitat d'espècies hemo de ferro (IV) – oxo en vers enllaços C – H es coneix que va a través d'un procés d'abstracció d'hidrogen, generant un radical en l'àtom de carboni i seguida d'un rebot donant lloc a la hidroxilació de l'enllaç C – H. Malgrat tot, en les espècies no hemo bioinspirades el rebot sembla no ocórrer. També hem estudiat els complexes ferro (IV) – oxo en les reaccions de sulfoxidació sota condicions fotocatalítiques, donant lloc a un augment de les velocitats d'oxidació.

Posteriorment hem sintetitzat i caracteritzat dos nous complexes de ferro (IV) – tosylimido i hem estudiat la seva capacitat en la transferència del grup –NTs a substrats sulfur. Aquestes espècies són isoelectròniques a les ferro (IV) – oxo, suggerint que poden exhibir una reactivitat anàloga. Malgrat tot les dades experimentals recollides en aquesta tesi indiquen que la seva reactivitat és diferent de les espècies ferro – oxo, per exemple la reactivitat amb substrats sulfur ocorre a través d'un procés d'un sol electró, generant espècies de ferro (III). En base a les dades experimentals hem proposat un mecanisme.

La fixació de nitrogen dels enzim nitrogenasa es postula que té lloc a través d'espècies ferro – nitrido en alt estat d'oxidació, tot i que a dia d'avui no existeix cap evidència directa. Les espècies bioinspirades artificials de ferro (IV) i ferro (V) – nitrido són la única evidència que suporta aquesta proposta, tot i que se n'han identificat molt poques a dia d'avui. A més, s'ha publicat poca informació sobre la seva reactivitat, ja que són especialment reactives. En aquest treball descrivim la preparació d'una nova espècie ferro (V) – nitrido, generada a través del trencament fotolític en espècies ferro (III) – azido. Hem caracteritzat aquesta nova espècie combinant tècniques experimentals i teòriques i hem estudiat la seva reactivitat en fase gas.

Per últim hem estudiat complexes no hemo de ferro (II) en la funcionalització catalítica de C – H en arens per formar enllaços C – C, mitjançant l'ús de diazoacetat d'etil, un reactiu comercial. El sistema ha demostrat ser altament selectiu cap a enllaços C – H (sp^2) generant quantitats negligibles de subproductes. En base a les dades experimentals hem proposat un mecanisme on proposem una espècie ferro – carbè.

RESUMEN

La funcionalización selectiva de enlaces C – H es una tarea complicada pero con un gran potencial en la química orgánica sintética. La funcionalización de hidrocarburos generalmente está relacionada con metales caros y reactivos tóxicos, generando grandes cantidades de subproductos no deseados. Contrariamente, una amplia variedad de enzimas que se encuentran en sistemas naturales llevan a cabo la funcionalización selectiva de enlaces C – H, utilizando reactivos inocuos como son O₂ y H₂O₂. Estas enzimas son capaces de oxigenar enlaces C – H en una amplia variedad de sustratos en condiciones suaves. Sus centros activos contienen metales abundantes como el hierro, generalmente como especies hierro – oxo en altos estados de oxidación (IV o V). De hecho, intermedios hierro – oxo en altos estados de oxidación se han identificado en reacciones de oxidación de varios enzimas. El estudio de estas enzimas es deseable para entender cómo funcionan y para imitar su reactividad. Una forma práctica de estudiar estos intermedios es mediante el diseño y síntesis de complejos modelo bioinspirados, con el objetivo de generar especies artificiales en alto estado de oxidación para intentar reproducir su reactividad. Esta tesis está enfocada en la síntesis de especies no hemo de hierro (IV) y hierro (V) que contengan ligandos basados en 1,4,7 - triazaciclono-nano para estudiar sus propiedades y reactividad.

En primer lugar hemos preparado y caracterizado dos especies hierro (IV) – oxo y hemos estudiado su reactividad hacia sustratos típicos. En reacciones de transferencia de átomo de oxígeno a átomos de azufre (proceso de dos electrones) y en la hidroxilación de enlaces C – H bencílicos en reacciones de transferencia de átomo de hidrógeno. La reactividad de especies hemo de hierro (IV) – oxo en enlaces C – H se conoce que va a través de un proceso de abstracción de hidrógeno, generando un radical en el carbono, seguida de un rebote dando lugar a la hidroxilación del enlace C – H. Sin embargo, en las especies bioinspiradas no hemo el rebote parece no ocurrir. También hemos estudiado los complejos hierro (IV) – oxo en las reacciones de sulfoxidación bajo condiciones fotocatalíticas, dando lugar a un aumento de las velocidades de oxidación.

Posteriormente hemos sintetizado y caracterizado dos nuevos complejos de hierro (IV) – tosylimido y hemos estudiado su capacidad en la transferencia del grupo –NTs a sustratos sulfuro. Estas especies son isoelectrónicas a las hierro (IV) – oxo, sugiriendo que deben exhibir una reactividad análoga. A pesar de todo, los datos experimentales recogidos en esta tesis indican que su reactividad es diferente de las especies hierro – oxo y la reactividad con sustratos sulfuro ocurre a través de un proceso de un solo electrón, generando especies de hierro (III). En base a los datos experimentales hemos propuesto un mecanismo.

La fijación de nitrógeno de los enzimas nitrogenasa se postula que tiene lugar a través de especies hierro – nitrado en alto estado de oxidación, aunque a día de hoy no existe ninguna evidencia directa. Las especies bioinspiradas artificiales de hierro (IV) y hierro (V) – nitrado son la única evidencia que soporta esta propuesta, aunque se han identificado muy pocas a día de hoy. Además, se ha publicado poca información sobre su reactividad, ya que son especialmente reactivas. En este trabajo describimos la preparación de una nueva especie hierro (V) – nitrado, generada a través de la rotura fotolítica en especies hierro (III) – azido. Hemos caracterizado esta nueva especie combinando técnicas experimentales y teóricas, además hemos estudiado su reactividad en fase gas.

Por último hemos estudiado complejos no hemo de hierro (II) en la funcionalización catalítica de C – H en arenas en la formación de enlaces C – C, mediante el uso de diazoacetato de etilo, un reactivo

comercial. El sistema ha demostrado ser altamente selectivo hacia enlaces C – H (sp^2) generando cantidades mínimas de subproductos. En base a los datos experimentales hemos propuesto un mecanismo donde proponemos una especie hierro – carbeno.

CHAPTER I

GENERAL INTRODUCTION

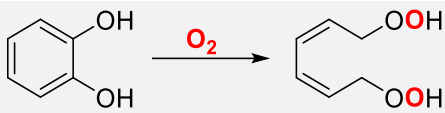
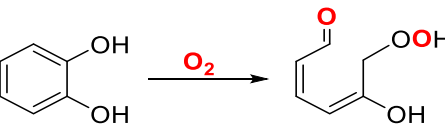
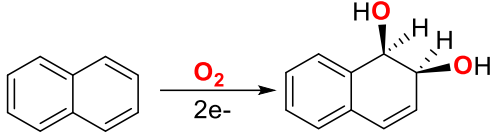
I.1. INTRODUCTION TO ENZYMATIC REACTIONS ON C – H BOND FUNCTIONALISATION

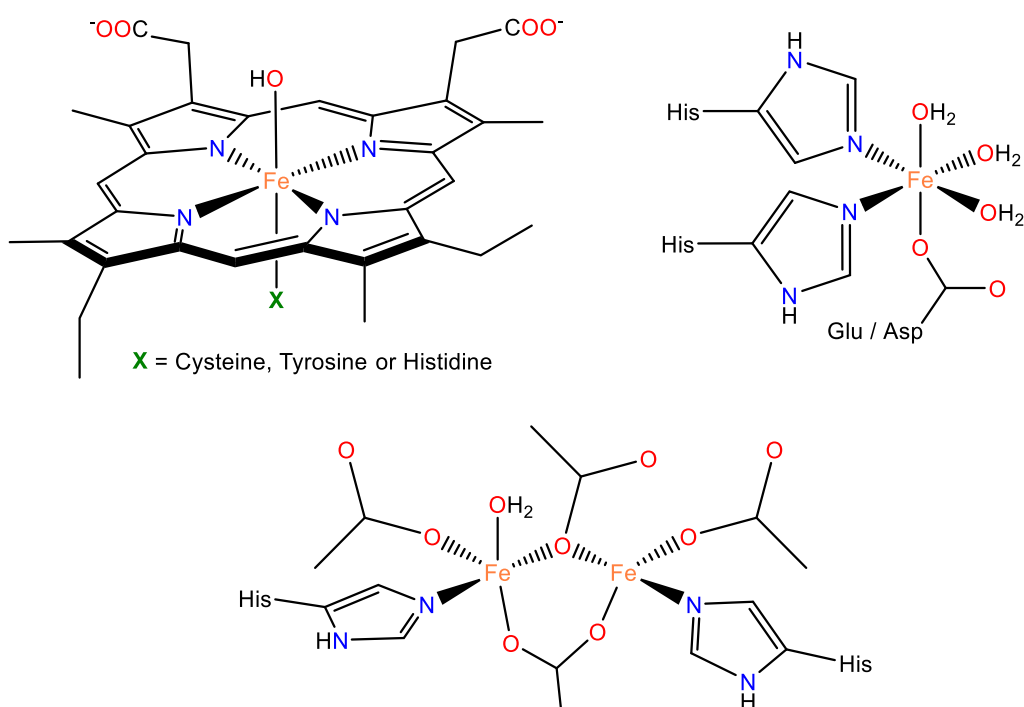
Selective functionalisation of C – H bonds remains one of the biggest challenges in organic chemical synthesis. The importance of C – H functionalisation lay in the ability of enable rapid synthesis of complex organic frameworks by avoiding the use of protective groups and enabling shorter synthetic strategies.¹⁻³ Indeed, wide range of strategies to functionalize C – H bonds have been reported, but they usually involve scarce and expensive metals such as palladium, rhodium or iridium.^{4,5} The functionalisation of C – H bonds is a challenging task due to the relative high strength of this bond, its low polarity, and its low energetic HOMO and high energetic LUMO, which translates into a low reactive and inert bond in comparison to other bonds. Among the different possibilities to functionalize a C – H bond, the transformation to C – O bonds represents an interesting and appealing reaction. A wide variety of metalloenzymes can make this challenging transformation by activating dioxygen and forming high – valent metal species that are highly electrophilic, and can break the C – H bond. These enzymes contain abundant transition metals such as iron, usually adopting high – valent iron – oxo (IV or V) species. The study of such enzymes is desirable to understand how they work and to imitate their reactivity.

Several high – valent iron species have been trapped in the active centre of many enzymes and, through spectroscopic techniques (*e.g.* Mössbauer, EXAFS, Raman Resonance), have been proved to be involved in oxidative enzymatic reactions, and identified as key intermediates in the oxidation reactivity of the respective enzymes.⁶⁻¹⁷ Iron participates mainly in the activation of the dioxygen molecule, and the insertion of oxygen atoms into inactivated C – H bonds, but iron also holds a key role in enzymes that participate in a diverse range of reactions such as halogenation, desaturation or epoxidation.^{7,17-19}

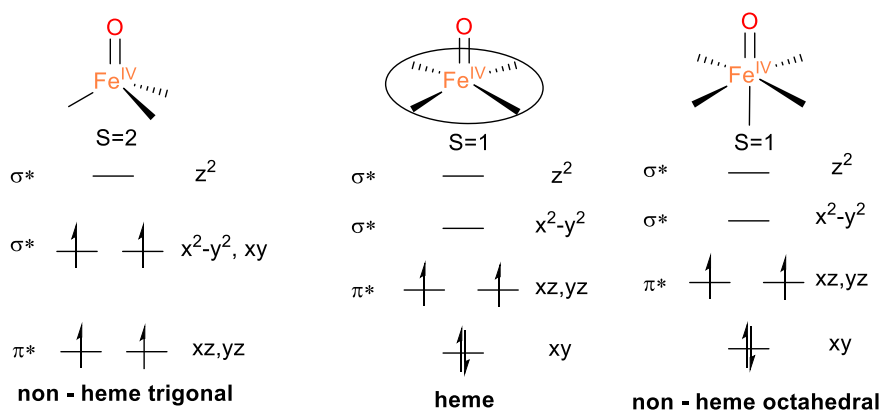
These enzymes can be classified in two groups: heme proteins (such as peroxidases or cytochrome P450) and non – heme metalloproteins (for example Rieske oxygenases or soluble Methano Monooxygenases). The coordination environment of the iron – oxo unit is different depending on the enzyme type. Three main types of active sites had been identified on these enzymatic systems (Figure I.1). The first case are the heme peroxidases, catalases and oxygenases which comprise mononuclear iron – protoporphyrin IX active sites coordinated to a cysteine, an histidine or a tyrosine residue.⁶ The second type, typical of many mononuclear non – heme iron enzymes such as Rieske oxygenases, is formed by mononuclear centres coordinated to two histidine groups and a carboxylate group (asparagine or glutamate residue) in a facial coordination, this coordination is known as the 2 – His – 1- carboxylate facial triad which leaves three available sites in the first coordination sphere of the iron centre, that serve to perform their reactivity.^{7,19,20} Finally, the third coordination type is present on systems like methane – monooxygenase and fatty acid desaturases, with an active centre conformed by a diiron nucleus coordinated to histidine and carboxylate groups.^{10,17,21,22}

Table I.1. Selection of iron proteins involved in biological oxidations of C – H bonds.

IRON PROTEIN	CATALYTIC REACTION
Heme proteins	
Cytochrome P450	$\text{C-H} / \text{C}=\text{C} \xrightarrow[2e^-, 2\text{H}^+]{\text{O}_2} \text{C-OH} / \text{C}=\text{C} + \text{H}_2\text{O}$
Mononuclear non – heme proteins	
<i>Iron (III) dioxygenases</i>	
Intradiol – cleaving catechol dioxygenases	
<i>Iron (II) dioxygenases with 2 – his – 1 – carboxylate facial triad motif</i>	
Extradiol – cleaving catechol dioxygenases	
α - Ketoglutarate dependent hydroxylases	$\text{RH} + \text{R}'\text{COCO}(\text{OH}) + \text{O}_2 \longrightarrow \text{ROH} + \text{R}'\text{CO}(\text{OH}) + \text{CO}_2$
Rieske oxygenases	
Dinuclear non – heme proteins	
Soluble methane – monooxygenases	$\text{CH}_4 + \text{O}_2 + 2\text{H}^+ + 2e^- \longrightarrow \text{CH}_3\text{OH} + \text{H}_2\text{O}$

**Figure I.1.** Structures of active centres of enzymatic reactions. (Top left) Cytochrome P450; (Top right) structure of Rieske oxygenases centre; (Below) intermediate Hred of soluble methane – monooxygenase (sMMO). His: histidine, Asp: asparagine, Glu: glutamic acid.

In addition to the coordination dissimilarities, studies of the active oxidants in both heme and non-heme oxygenases had revealed iron (IV) oxidation states with different spin states in the two cases. While heme enzymes show an $S = 1$ spin state^{12,23} for the iron centre, the non-heme enzymes have been shown to support a high-spin $S = 2$ state.^{7,8} This high-spin configuration is possibly due to the weak ligand field exerted by the combination of histidine and carboxylate ligands or the proposed trigonal bipyramidal coordination geometry²⁰ that leave $d(x^2-y^2)$ and $d(xy)$ orbitals nearly degenerated in energy (Scheme I.1).



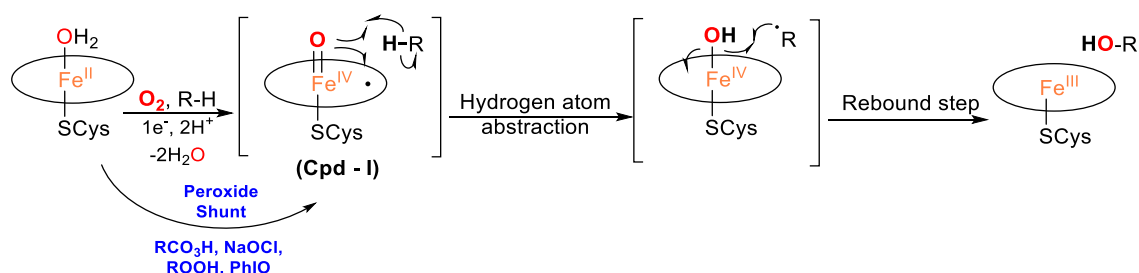
Scheme I.1. Molecular orbital diagrams of: (left) trigonal ligand field with degenerated orbitals that enables non-heme high-spin $\text{Fe}^{\text{IV}}=\text{O}$ species ($S = 2$); (middle) ligand field that leads to heme low-spin $\text{Fe}^{\text{IV}}=\text{O}$ species ($S=1$), (the porphyrinato radical has a $S = 1/2$, giving place to a $S_t = 3/2$); (right) octahedral ligand field that leads to non-heme low-spin $\text{Fe}^{\text{IV}}=\text{O}$ species ($S=1$). Extracted from ref. 24.

Despite the different spin state in high-valent iron (IV) – oxo intermediates of heme and non-heme enzymes the Fe – O distances (and Fe – O bond strengths) are comparable (1.64 – 1.68 Å). This similarity is expected by the electronic structure as is observed in the orbital diagram (*vide supra*). In both cases $[\text{Fe}=\text{O}] \pi^*$ antibonding orbitals $d(xz)$ and $d(yz)$ have the same number of electrons (two), and therefore the same iron – oxo destabilization is expected.

High-valent iron species have been spectroscopically characterised in both heme and non-heme enzymes as explained in the next section.

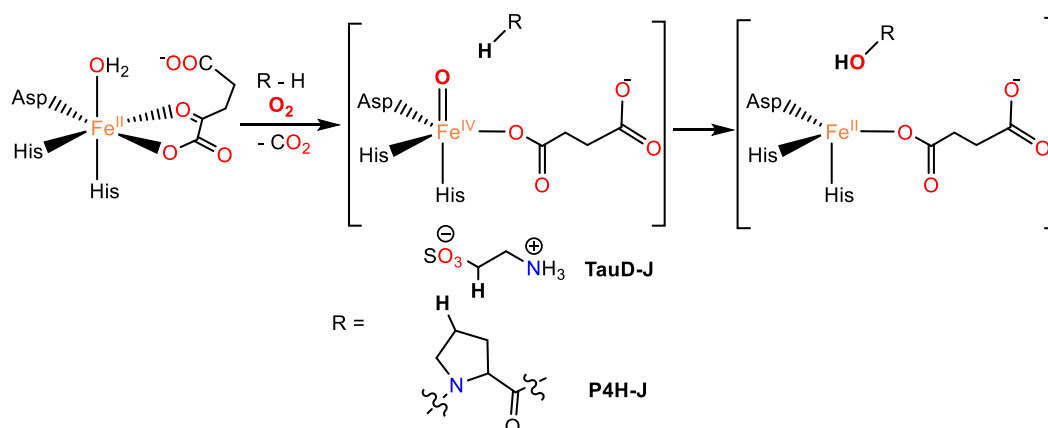
I.1.1. High – valent iron species characterised in biological systems

The most representative heme enzyme is the family of Cytochrome P450 monooxygenase enzymes (Cyt P450). Such enzymes can catalyse a number of C – H oxidations inserting one oxygen from O₂ into the substrate while generating a molecule of water from the two – electron reduction of the second oxygen.²⁵⁻²⁷ To perform these oxidations it is well known that they proceed through a high – valent iron species (Scheme I.2). Such high – valent species has been characterised as a low – spin (S = 1) iron (IV) centre which is coupled to an S = ½ radical on the porphyrin, to give a formal iron (V) – oxo intermediate. This intermediate is called the Compound – I and is the responsible to abstract a hydrogen atom from substrate, this step is characterized by a high kinetic isotope effect (KIE ≈ 5 – 12) values.²⁵ Cpd – I species have been identified in a number of heme enzymes by spectroscopic means, *e.g.* by Mössbauer spectroscopy ($\delta = 0.05 - 0.14$ mm/s; $\Delta E_Q = 0.90 - 1.33$ mm/s), EPR ($g_{\text{values}} = 1.60 - 3.32$) and Raman resonance ($\nu_{\text{Fe=O}} = 750 - 790$ cm⁻¹, $d_{\text{Fe=O}} = 1.64 - 1.67$ Å).^{11,15} Alternatively, the preparation of Compound – I can be performed using oxygen donors (*e.g.* peracids, NaOCl, PhIO) via the so called “peroxide shunt” which is used in catalysis.²⁸



Scheme I.2. Schematic mechanism for C – H hydroxylation by Cyt P450.

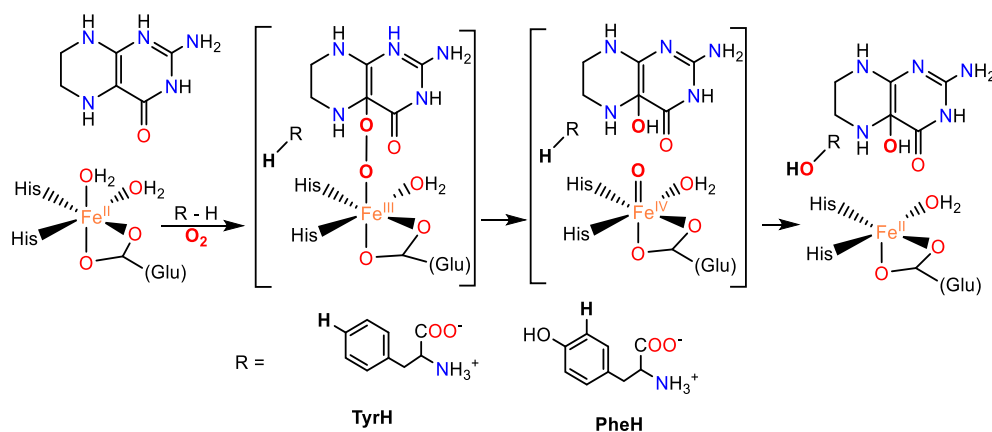
In 2003 Bollinger and Krebs reported the first conclusive spectroscopic evidence for an iron (IV) intermediate in a non – heme enzyme. It was detected in the taurine dioxygenase (TauD) that is a non – heme α – ketoglutarate – dependent enzyme, from a family of enzymes that activate dioxygen to catalyse the hydroxylation of substrates through the decarboxylation of the α – ketoglutarate co – substrate.²⁹ The high – valent species was assigned as a catalytically competent high – spin (S = 2) iron (IV) on the basis of kinetic (*e.g.* stopped – flow techniques) and Mössbauer experiments ($\delta = 0.31$ mm/s, $\Delta E_Q = -0.88$ mm/s). Reduction of high – valent intermediate by γ – irradiation at 77 K yielded a high – spin iron (III) species, further supporting the iron (IV) assignment.²⁹ The intermediate and its oxidative mechanism (Scheme I.3) were further studied by DFT calculations²⁰ and by deuteration of taurine substrate in the C₁ position, giving strong evidence for an hydrogen abstraction mechanism from a KIE ≈ 50.⁹ Moreover resonance Raman experiments in continuous – flow conditions revealed evidence for a Fe = O moiety, 821 cm⁻¹ band that shifted to 787 cm⁻¹ upon labelling with ¹⁸O.³⁰ Additionally, the length of Fe = O bond was established as 1.62 Å by extended X – ray absorption fine structure analysis (EXAFS).³¹



Scheme I.3. Schematic mechanism of taurine dioxygenase (TauD) and prolyl 4 – hydroxylase (P4H) in C – H oxidation reactivity.

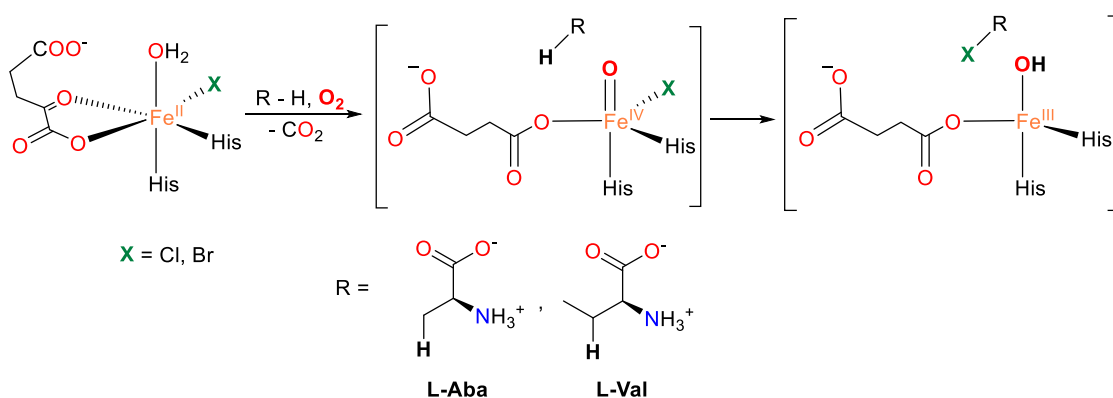
Subsequently, a few more iron (IV) intermediates were characterised in non – heme enzymes. In 2006 was characterised the active species in the enzyme prolyl 4 – hydroxylase (P4H), another example of a α – ketoglutarate – dependent enzyme. The intermediate P4H – J (Scheme I.3) was also assigned as a high – spin $S = 2$ iron (IV) species like TauD – J. Mössbauer spectroscopy revealed a doublet with $\delta = 0.30$ mm/s and $\Delta E_Q = -0.82$ mm/s, in high agreement with TauD – J results. Deuteration of substrate provided a KIE ≈ 60 , similarly to the behaviour observed on TauD – J.³²

In addition, two non – heme iron (IV) intermediates were identified in the pterin – dependent tyrosine hydroxylase (TyrH) and phenylalanine hydroxylase enzymes (PheH) (Scheme I.4). Pterin – dependent enzymes use tetrahydropterin as 2 – electron source to activate dioxygen and hydroxylate aminoacids. The active species of TyrH was characterised by Mössbauer ($\delta = 0.25$ mm/s and $\Delta E_Q = -1.27$ mm/s) as a high – spin species and further supported by γ – irradiation cryoreduction that yielded a high – spin Fe(III) complex.³³ Later on, the active species of the pterin – dependent phenylalanine hydroxylase (PheH) was also characterised as a high – spin (IV) species with $\delta = 0.28$ mm/s and $\Delta E_Q = 1.26$ mm/s.³⁴ These enzymes, TyrH and PheH, hydroxylate aromatic substrates and give KIE ≈ 0.9 , thus giving no information about a hydrogen abstraction step. However, PheH from the bacteria *Chromobacterium violaceum* is capable to hydroxylate the cyclohexylalanine substrate (KIE ≈ 15).³⁵



Scheme I.4. Schematic mechanism of the pterin – dependent enzymes tyrosine hydroxylase (TyrH) and phenylalanine hydroxylase (PheH) in C – H oxidation reactivity.

A particular group of α -ketoglutarate-dependent enzymes are the halogenases, these enzymes possess a halide (Cl or Br) in the substitution of a carboxylate ligand from asparagine or glutamate from the 2-His-1-carboxylate facial triad structure. These enzymes are capable to halogenate substrates instead of hydroxylating them. In the proposed mechanism the iron (IV) – oxo – halide intermediate abstracts a hydrogen atom from substrate generating a carbon-centred radical, subsequently the halide is introduced into the substrate in a rebound-like step, to finally obtain the halogenated product (Scheme I.5).^{36,37} Spectroscopic evidence for high-spin ($S = 2$) iron (IV) – oxo intermediates have been obtained for two halogenase enzymes: the CytC3 and the SyrB2. The former revealed by Mössbauer spectroscopy two rapidly equilibrating high-spin iron (IV) – oxo species with $\delta = 0.23$ mm/s, $\Delta E_Q = -0.81$ mm/s and 0.31 mm/s, $\Delta E_Q = -1.06$ mm/s in the bromination reaction of γ -methyl group from L-2-aminobutyric acid (L-Aba).³⁸ The same enzyme in the chlorination of L-Aba under same conditions revealed analogous intermediate species with $\delta = 0.22$ mm/s, $\Delta E_Q = 0.70$ mm/s and 0.30 mm/s, $\Delta E_Q = 1.09$ mm/s.³⁹ Such intermediates were found to decay at the same rate in the bromination of L-Aba, suggesting that they are related by a fast equilibrium. A Fe-Br distance of 2.43 Å and a short Fe-O distance ≈ 1.62 Å were obtained by EXAFS analysis in the intermediate responsible for the transfer of bromide. Furthermore, large KIE values were obtained in the chlorination reaction of L-Aba, revealing the implication of a hydrogen abstraction step in halogenase enzymes reactivity. For the second enzyme, SyrB2, a high-spin ($S = 2$) iron (IV) – oxo intermediate was also identified and characterised in the chlorination reaction of threonine (L-Thr) by Mössbauer spectroscopy ($\delta = 0.23$ mm/s, $\Delta E_Q = 0.76$ mm/s and 0.30 mm/s, $\Delta E_Q = 1.09$ mm/s), XANES ($E_{\text{edge}} = 7120.9$ eV for Fe(IV) intermediate, $\Delta E = 1.9$ eV vs initial Fe(II) consistent with a $2e^-$ oxidation) EXAFS (Fe-Cl = 2.35 Å, Fe-O = 1.64 Å) and DFT calculations. Similar Mössbauer parameters were obtained with Valine (L-Val) as substrate: $\delta = 0.24$ mm/s, $\Delta E_Q = 0.73$ mm/s and 0.29 mm/s, $\Delta E_Q = 1.09$ mm/s. Kinetic isotope effect in L-Thr chlorination ≈ 20 and ≈ 30 for L-Val chlorination confirmed a hydrogen abstraction step.⁴⁰ Previously, its crystal structure was resolved.⁴¹ Later on, SyrB2 was further characterised by Synchrotron-based nuclear resonance vibrational spectroscopy (NRVS) in combination with DFT calculations, a trigonal bipyramidal geometry was suggested on its basis. The bond distances calculated for SyrB2 with both Cl and Br (Fe-Cl = 2.30 Å, Fe-O = 1.66 Å and Fe-Br = 2.45 Å, Fe-O = 1.66 Å) correlate well with previous experimental ones obtained for either CytC3 and SyrB2.⁴²



Scheme I.5. Schematic mechanism of the halogenase enzymes in C-H halogenation reactivity.

In addition to the aforementioned direct spectroscopic data for iron (IV) intermediates, such species have been postulated for Rieske oxygenases on the basis of some indirect evidence, however iron (IV) have not been detected to date in these enzymes and it is not clear the real active species responsible for their oxidative reactivity. Rieske oxygenases are a wide family of mononuclear non – heme multicomponent enzymes (Figure I.2) and possess two parts: the first component is a 2 – His – 1 – carboxylate non – heme oxygenase centre, which possess an iron in high – spin responsible for the activation of O₂. The second part is a reductase centre, formed by an iron – sulfur cluster (Fe₂S₂), bonded to the oxygenase by an aspartate.^{43,44} This component delivers electrons to the oxygenase from NAD(P)H in a controlled manner, to achieve the catalytic behaviour. An example is naphthalene dioxygenase enzyme (NDO), capable to imitate the “peroxide shunt” observed in Cyt P450 by using H₂O₂ to oxidise the naphthalene substrate; in addition experiments with radical clock substrates revealed evidence for short – lived radical implication in the oxidation of norcarane by NDO enzyme, resembling the Cyt P450 rebound mechanism.⁴⁵ These data also suggests a common intermediate in the mechanism between both heme Cyt P450 and the non – heme Rieske oxygenases systems, pointing towards a possible high – valent iron – oxo intermediate. In addition, was observed incorporation of significant amounts of oxygen from H₂¹⁸O₂ to the oxidised product in the oxidation of naphthalene by this enzyme.⁴⁶ Furthermore in the oxidation of indane by the Rieske oxygenase toluene – monooxygenase (TM) revealed a ≈ 70 % of insertion of oxygen from H₂¹⁸O.⁴⁷ These results suggest that an iron species that would permit the exchange of oxygen should be involved, possibly a high – valent oxo intermediate.

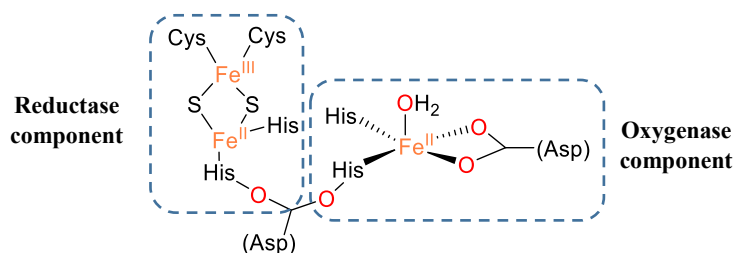


Figure I.2. Schematic representation of active centre of Rieske oxygenases; on the right oxygenase component showing 2 – His – 1 carboxylate facial triad and on the left the Fe₂S₂ reductase component.

Worth to mention is also the intermediate Q from the soluble methane – monooxygenase enzyme family (MMO) (Figure I.3). sMMO contains a diiron site in its active centre and performs the oxidation of light alkanes such as methane to methanol using O₂.^{21,48} Intermediate Q have been spectroscopically identified by different techniques as a diiron (IV) species with a diamond core structure with two oxo ligands bridging both metals, *e.g.* Mössbauer ($\delta = 0.17$ mm/s, $\Delta E_Q = 0.53$ mm/s) Raman resonance ($\nu = 690$ cm⁻¹, $\nu(^{18}\text{O}) = 654$ cm⁻¹, $\nu(^{16}\text{O}^{18}\text{O}) = 673$ cm⁻¹) and EXAFS spectroscopy ($d_{\text{Fe-O}} = 1.77$ Å).^{16,17,49}

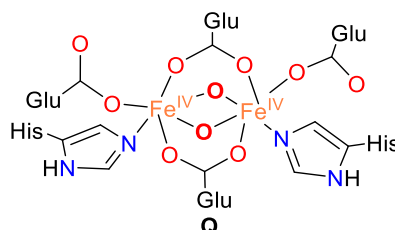


Figure I.3. Suggested structure for the spectroscopically characterised intermediate Q from MMO enzymes. Carboxylates may not be bridging between both iron atoms.¹⁷

I.2. BIOINSPIRED MODEL COMPLEXES TO STUDY ENZYMES

Natural metalloenzymes are notable for obvious reasons: they are capable of selectively performing challenging reactivities and often with high regio- and stereospecificities and, more important, under mild conditions and using green oxidants such as O₂. The generation of well-defined model compounds is important to investigate and understand the mechanism of such enzymatic reactions. Indeed the development of model systems is an excellent tool to study the mechanism of enzymatic reactions because the access to enzymes is often limited, high molecular weight proteins are usually very laborious to isolate and purify; thus in order to study the reactivity of such proteins is very useful the synthesis of bioinspired complexes. These bioinspired complexes consist in a metallic centre, iron in our scenario, and organic ligands coordinating to the metal to resemble the active centre of the metalloproteins. The objective is to imitate elements of the architecture of the iron first coordination sphere, to better understand the nature of the enzyme's active site and try to imitate its reactivity. Moreover, synthetic model systems offer some advantages in comparison to metalloenzymes. Bioinspired complexes are easily tuneable through modification of the organic ligands: changing electronic properties, steric effects, coordination geometry... leading to the design of synthetic species capable to expand the substrate scope, permitting the modulation of reactivity towards chemo-, regio- and stereoselective reactions.^{50,51} This is not only important to study the enzyme's reactivity and reproduce its activity but also to open new synthetic possibilities with potential interest in chemical synthesis.

In this regard, the chemistry of high-valent iron-oxo complexes have been widely studied with an interest in the syntheses of bioinspired model complexes capable to reproduce some of these iron enzymes' reactivity.⁵²⁻⁵⁶

I.2.1. Iron – oxo model complexes [Fe = O]

High valent iron-oxo complexes have been explored during the last 15 years with the aim to understand the chemistry of these species in enzymes.⁵⁷ Some of them are shown in Figures I.7 and I.10, and Table I.2 collects the structural and spectroscopic properties of some representative examples, as well as some enzyme intermediates. However, the reactivity of such bioinspired complexes is usually far from that seen on enzymes, with the former normally showing modest yields and selectivities in C-H bond functionalisation. Some authors have suggested that this is in part due to the fact that non-heme enzymes mainly have metal centres in high-spin (S = 2), while most of the prepared iron-oxo species remain in the low-spin state (S = 1). Both monomeric and dimeric iron-oxo species have been reported but this work focus on the first ones.

The first high-valent iron-oxo complex was synthesised in 1981 by Groves *et al.*⁵⁸ through the oxidation of porphyrinic [Fe^{III}(Cl)(TMP)] species with *m*-chloroperbenzoic acid in DCM:MeOH at -78 °C. This compound was the heme complex [Fe^{IV}=O(TMP·)]⁺ (Figure I.4) and was assigned to an iron (IV) – oxo porphyrin π-radical cation (d⁴) species with characteristic features of Cpd – I intermediate on UV-vis spectrum^{11,59} (broad Soret band at 405 nm and a Q-band at 674 nm). Electron paramagnetic resonance

(EPR) and Mössbauer studies had evidenced a ferromagnetic coupling between the Fe^{IV} ($S = 1$) centre and the porphyrin ($S = 1/2$) with a total spin of $S_t = 3/2$. EXAFS revealed a $\text{Fe} - \text{O}$ distance of 1.60 Å proving the $\text{Fe} = \text{O}$ double bond character and confirmed by vibrational Raman resonance (rRaman). The prepared complex was found to be a good oxidant in olefin epoxidation and in the hydroxylation of alkanes.^{59,60} Since then, many different heme iron (IV) – oxo complexes have been prepared with different groups in the porphyrin moiety, modifying the electronic properties and the steric demand of complex (Figure I.4), and studied to understand the chemical properties and reactivity of this group of high – valent iron species.⁵² Reactivity studies indicate that the electronic nature of porphyrin ligand controls the reactivity of these complexes and evidenced that the iron (IV) – oxo complexes with electronic deficient porphyrin ligands are better oxidants for organic substrates. Posterior studies had also revealed that the ligand located in *trans* position to the oxo atom influences dramatically the reactivity of these complexes.^{55,59-61} Theoretical and experimental studies show that, for porphyrinic ligands, rates for both HAT and OAT reactions increase when the electrodonating ability of the axial ligand is increased.⁶²

Iron (IV) – oxo porphyrin complexes were fully characterized but an iron – oxo characteristic band for the $\text{Fe}^{\text{IV}} = \text{O}$ moiety could not be identified by UV – vis spectrometry, as was masked by the strong absorptions of porphyrin ligands.

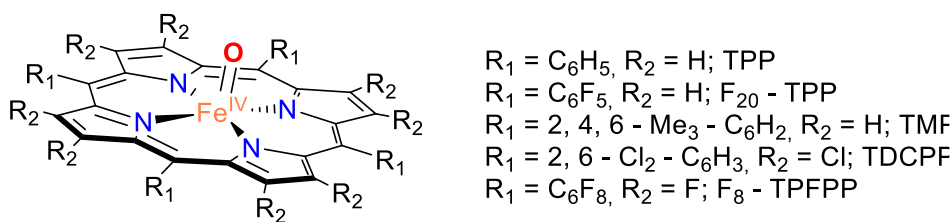


Figure I.4. Structure of $[\text{Fe}^{\text{IV}} = \text{O}(\text{TMP}\cdot)]^+$ and different porphyrin ligands from literature.

Table I.2. Structural and spectroscopic properties of selected high – valent iron – oxo species.

Species	λ_{\max} (ϵ ($M^{-1} \cdot cm^{-1}$))	Mössbauer spectroscopy		ν Fe – O (cm^{-1})	Fe – O bond (Å)	Ref.
		δ ($mm \cdot s^{-1}$)	ΔE_Q ($mm \cdot s^{-1}$)			
Heme systems (S = 1)						
P450 – I	690	0.11	0.90	-	-	15
[Fe ^{IV} (O)(TMP·) ⁺]	406(61300), 674 (7600)	0.08	1.62	828	1.64	63,64
P450 – II	-	0.14	2.06	-	1.82	14
Non – heme Fe^{IV} systems in low spin (S = 1)						
[Fe ^{IV} (O _{anti})(TMC)(NCMe)] ²⁺	824 (400)	0.17	1.24	834	1.646	65-69
[Fe ^{IV} (O _{anti})(O ₂ CCF ₃)(TMC)] ⁺	836 (250)	0.20	1.39	854	1.64	66-68
[Fe ^{IV} (O _{anti})(N ₃)(TMC)] ⁺	850 (130)	0.17	0.70	814	1.66	66
[Fe ^{IV} (O _{syn})(TMC)(NCMe)] ²⁺	815 (380)	0.16	1.55	856	1.625	70
[Fe ^{IV} (O)(cyclam – ac)] ⁺	676	0.01	1.37	-	-	71
[Fe ^{IV} (O)(TMC – Py)] ²⁺	834 (260)	0.18	1.08	826	1.667	72,73
[Fe ^{IV} (O)(TMCS)] ⁺	850 (230)	0.19	-0.22	-	1.70	66,74
[Fe ^{IV} (O)(TAML)] ²⁻	1435 (2500)	-0.19	3.95	-	1.69	75,76
[Fe ^{IV} (O)(Me ₂ Pytacn)(MeCN/H ₂ O)] ²⁺	750 (200)	0.05	0.73	-	-	77-79
^b [Fe ^{IV} (O)(Cl)(Me ₂ Pytacn)] ⁺	803	0.06	0.89	-	-	78
^b [Fe ^{IV} (O)(Br)(Me ₂ Pytacn)] ⁺	823	0.07	0.89	-	-	78
[Fe ^{IV} (O)(Me ₃ NTB)(MeCN)] ²⁺	770 (200)	0.02	1.53	-	-	80
[Fe ^{IV} (O)(N4Py)] ²⁺	695 (400)	-0.04	0.93	841	1.639	69,79,81-84
[Fe ^{IV} (O)(MePy ₂ tacn)] ²⁺	736 (310)	-0.01	0.93	-	1.63	79,85
[Fe ^{IV} (O)(Me ₂ (CHPy ₂)tacn)] ²⁺	740 (340)	-	-	839	1.63	83
[Fe ^{IV} (O)(Bn – TPEN)] ²⁺	740 (400)	0.01	0.87	835	1.67	68,78-82
Non – heme Fe^{IV} systems in high spin (S = 2)						
[(H ₂ O) ₅ Fe ^{IV} O] ²⁺	320 (500)	0.38	-0.33	-	-	86-89
TauD – J	318 (1550)	0.30	-0.90	821	1.62	20,29-31
P4H – J	320 (1500)	0.30	-0.82	-	-	32
[Fe ^{IV} (O)(TMG ₃ tren)] ²⁺	825 (250), 865 (260)	0.09	-0.29	843	1.661	90,91
[Fe ^{IV} (O)(H ₃ buea)] ⁻	808 (280)	0.02	0.43	798	1.680	92,93
[Fe ^{IV} (O)(tpa ^{Ph})] ⁻	~900	0.09	0.51	850	1.62	94
[Fe ^{IV} (O)(TMG ₂ dien)(MeCN)] ²⁺	805 (270)	0.08	0.58	807	1.65	
[Fe ^{IV} (O)(Cl)(TMG ₂ dien)] ⁺	827 (290)	0.12	-0.30	833	-	95
[Fe ^{IV} (O)(N ₃)(TMG ₂ dien)] ⁺	803 (290)	0.08	0.41	810	1.65	
[Fe ^{IV} (O)(TQA)(MeCN)] ²⁺	650 (300), 900 (75)	0.24	-1.05	838	-	96
[Fe ^{IV} (O)(Cl)(TQA)] ²⁺	625 (460), 875(110)	0.22	0.96	827	-	97
[Fe ^{IV} (O)(Br)(TQA)] ²⁺	625 (460), 875(110)	0.21	0.94	828	-	
^a MMOH intermediate Q	330 (7500), 430 (7500)	0.17	0.53	690	1.77	16,17,21
Non – heme Fe^V systems (S = 1/2)						
[Fe ^V (O)(TAML)] ⁻	445 (5400), 630 (4200)	-0.42	4.25	-	1.58	98,99
[Fe ^V (O)(bTAML)] ⁻	441 (4350), 613 (3420)	-0.44	4.27	-	-	100
[Fe ^V (O)(NC(O)CH ₃)(TMC)] ⁺	410 (4000), 780 (430)	0.10	-0.50	798	-	101
Non – heme Fe^{III} systems (S = 5/2)						
[Fe ^{III} (O)(H ₃ buea)] ²⁻	-	0.30	0.71	671	1.813	102,103
[(TMC)Fe ^{III} -O _{syn} -Sc ^{III} (OTf) ₄]	-	0.36	-1.02	-	1.754	104,105

^aDimeric active centre, included for comparison. ^bSpin not identified, inferred by comparison with related species.

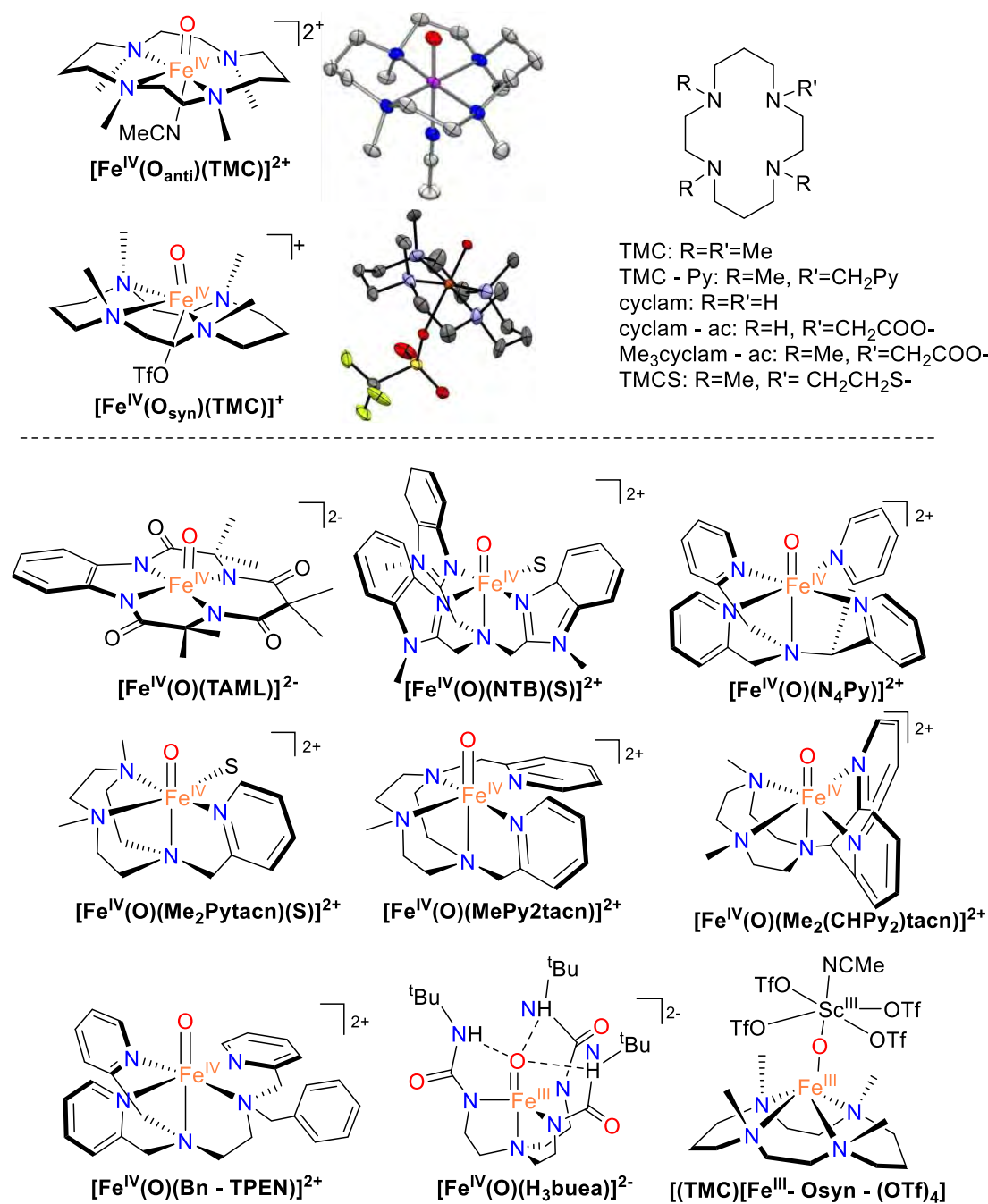


Figure I.5. (Top left) Structure and ORTEP plot of $[\text{Fe}^{\text{IV}}(\text{O}_{\text{anti}})(\text{TMC})(\text{MeCN})]^{2+}$ and $[\text{Fe}^{\text{IV}}(\text{O}_{\text{syn}})(\text{OTf})(\text{TMC})]^{+}$, extracted from ref. 65 and 70 (Top right) Structure of tetradentate N₄ – donor R₄ – cyclam family of ligands. Below structure of selected iron (IV) – oxo species in low spin and iron (III) – oxo.

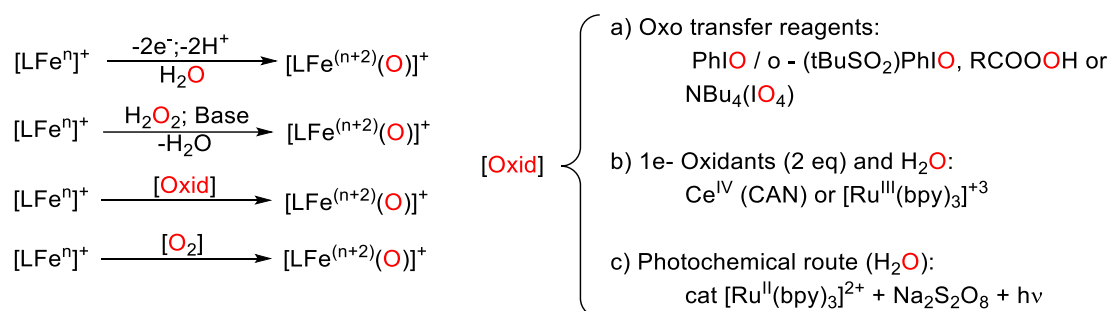
The first report of a non – heme $\text{Fe}^{\text{IV}} = \text{O}$ complex appeared in 2000,⁷¹ Grapperhaus *et al.* generated the terminal non heme iron (IV) – oxo species $[\text{Fe}^{\text{III}}(\text{cyclam} - \text{ac})(\text{CF}_3\text{SO}_3)]^{+}$ by ozonolysis (Figure I.5). The obtained compound had been characterized by Mössbauer as an iron (IV) – oxo species with $S = 1$ but its instability and low purity prevented further characterizations by other spectroscopic techniques.

Some years later, in 2003, Rohde *et al.*⁶⁵ reported the first X – ray crystal structure of a mononuclear $S = 1$ iron (IV) – oxo complex (Figure I.5), generated by reacting the $[\text{Fe}^{\text{II}}(\text{TMC})(\text{MeCN})]^{2+}$ complex with PhIO at room temperature in acetonitrile; this complex showed a Fe – O distance of 1.64 Å with a solvent

molecule in *trans* position to oxygen atom. This complex showed an *anti* configuration with the oxo moiety in *trans* position respect to the methyl groups. Alternatively, the complementary species in *syn* configuration has been prepared as well, by using the 2 – ^tBuSO₂ – C₆H₄IO oxidant or mediated by Lewis acids.^{106,107} The preparation of *syn* – [Fe^{IV}(O)(TMC)(MeCN)]²⁺ species was previously described by Prof. Fukuzumi and co – workers using scandium as Lewis acid.¹⁰⁴ It was assigned as Fe^{IV} – O – Sc³⁺ (Fe – O = 1.754 Å) although recently was reassigned to an iron (III) – oxo – scandium(III) species.¹⁰⁵

Since 2003 many complexes have been synthesised with a number of tetra– and pentadentate ligands, commonly bearing pyridine arms or amine nitrogen atom donors, all of them showing Fe – O bond distances comparable to the iron (IV) – oxo porphyrin intermediates. Only [Fe^{IV}(O)(Me₄cyS)]⁺ complex (Figure I.5) showed a larger Fe – O bond of 1.70Å. This complex is the model for the recently characterized Cpd – I intermediate in the catalytic cycle of Cyt P450.^{15,74} In general all these compounds have in common a near – infrared absorption band of moderate intensity in the UV – vis,¹⁰⁸ attributed to three of the five ligand – field transitions expected for an S = 1 Fe(IV) centre in C_{4v} symmetry.¹⁰⁹

Although different methods have been used to prepare bioinspired non – heme iron (IV) – oxo complexes, a general synthesis is carried out by oxidizing the iron (II) precursors with an oxygen atom transfer agent, such as a peracid or PhIO¹⁰⁸ (Scheme I.6). Alternative reported syntheses, although less common, are the use of electrochemical techniques or through photochemical oxidation in presence of an oxygen source, *e.g.* H₂O.^{83,85,110-112} A different approach is the use of H₂O₂ with a base, reported in the synthesis of [Fe^{IV}(O)(TMC)]²⁺ and [Fe^{IV}(O)(TMC – Py)]²⁺,¹¹³ resembling the heterolytic O – O cleavage step of the peroxoiron species in the O₂ activation in non – heme iron enzymes. Noteworthy are the synthesis of [Fe^{IV}(O)(TMC)]²⁺ and [Fe^{IV}(O)(TMC – Py)]²⁺ as the first examples using dioxygen as oxidant,^{72,114} these studies contribute to the understanding of the mechanism of O₂ activation by non – heme mononuclear enzymes, although no direct evidence was found of a peroxoiron species, thus consequently neither the postulated heterolytic evolution to an Fe^V(O)(OH) species or homolytic cleavage of O – O was found.



Scheme I.6. Different strategies to synthesise iron – oxo complexes.

Similarly, [Fe^{II}(N4Py)(S)]²⁺ and [Fe^{II}(Bn – TPEN)(S)]²⁺ (S = solvent) reacted with O₂ by adding protons and NADH as electron source to generate the respective iron (III) – hydroperoxo species, however no iron (IV) – oxo intermediate could be obtained.¹¹⁵ This behaviour contrasts with the mentioned [Fe^{II}(TMC)(MeCN)]²⁺ that, in similar conditions, yielded the iron (IV) species but was not possible to obtain the hydroperoxo intermediate; thus indicating a dependence on the supporting ligand of the formed species. The missing link between peroxoiron (III) and iron (IV) – oxo species was first reported by

Professor Que and co-workers in 2011, achieving in high yield the synthesis of the high-spin side-on intermediate η^2 -[Fe^{III}(OO)(TMC)]²⁺ with excess of H₂O₂. Upon addition of acid this species quantitatively evolved to the high-spin end-on η^1 -hydroperoxoiron (III) species [Fe^{III}(OOH)(TMC)]²⁺, which yielded fast the corresponding [Fe^{IV}(O)(TMC)]²⁺ complex in high amounts through a proton-assisted cleavage of the O-O bond (Figure I.6).¹¹⁶ Both peroxoiron (III) species were fully characterised by means of UV-vis, EPR, Mössbauer spectroscopy, EXAFS and Raman resonance. The formation of [Fe^{IV}(O)(TMC)]²⁺ species was suggested to proceed through heterolytic O-O cleavage, from a postulated transient iron (V)-oxo species that would be reduced in one e⁻ to obtain [Fe^{IV}(O)(TMC)]²⁺. This scenario was suggested on the basis that the rate of formation for the iron (IV)-oxo was dependent on the proton concentration, in addition DFT calculations previously suggested that an homolytic O-O cleavage was not energetically favoured.¹¹⁷ Moreover iron (V) species have been suggested in a number of catalytic studies of bioinspired iron (II) complexes and the fact that many of them give stereoselectivity would preclude the possibility of a •OH.¹¹⁸⁻¹²⁶

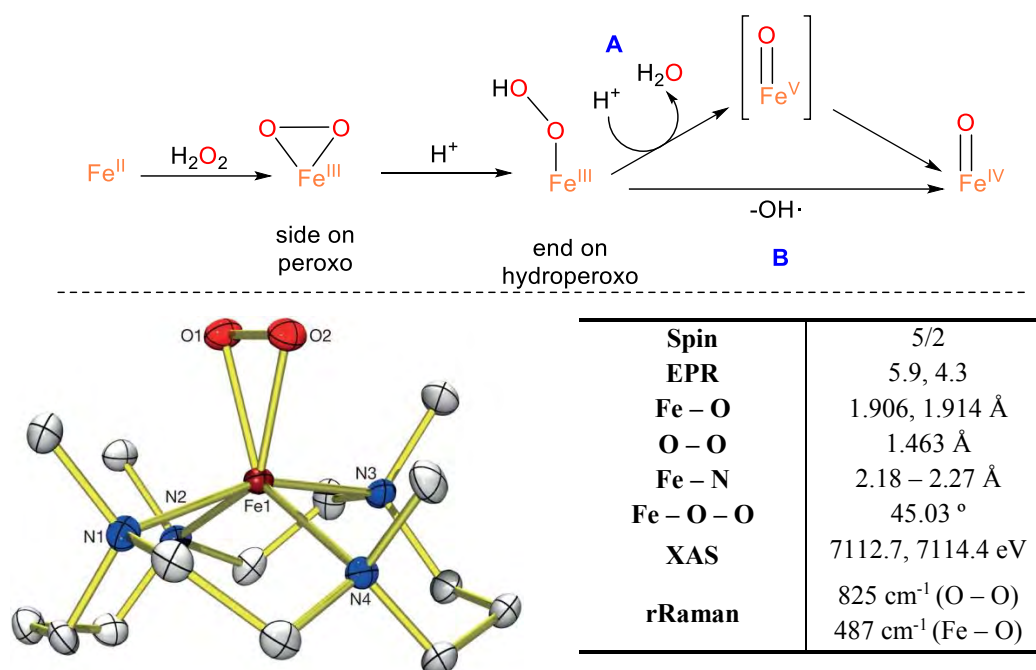


Figure I.6. (Top) synthetic pathway for η^2 -peroxo species in Fe-TMC system (A: proton-assisted heterolytic pathway; B: homolytic pathway). (Below) X-ray structure of η^2 -[Fe^{III}(OO)(TMC)]²⁺ extracted from ref. 127 (30% ellipsoid probability; Fe-O₁ = 1.906 Å, Fe-O₂ = 1.914 Å, O-O = 1.463 Å).

Subsequently, Cho *et al.* reported the crystal structure of η^2 -[Fe^{III}(OO)(TMC)]²⁺ prepared by using similar synthetic procedures (Figure I.6, below). That was the first example of a crystal structure from a side-on peroxoiron (III) in high-spin configuration.¹²⁷ In this report the same peroxo species were observed and iron (IV)-oxo species was suggested to be generated through an O-O homolytic cleavage due to the rate-independence with proton concentration of this step, but also on the basis that the same amounts of [Fe^{IV}(O)(TMC)]²⁺ were obtained in presence of substrates (that would quench the formation of a highly-reactive iron (V)-oxo species). Furthermore reactivity studies were performed with the three

species prepared, while the $[\text{Fe}^{\text{IV}}(\text{O})(\text{TMC})]^{2+}$ and $\eta^2 - [\text{Fe}^{\text{III}}(\text{OO})(\text{TMC})]^{2+}$ were found to be weak oxidants in the nucleophilic deformylation of aldehydes, $\eta^1 - [\text{Fe}^{\text{III}}(\text{OOH})(\text{TMC})]^{2+}$ proved to be more competent in the same reactivity. Moreover both $[\text{Fe}^{\text{IV}}(\text{O})(\text{TMC})]^{2+}$ and $\eta^1 - [\text{Fe}^{\text{III}}(\text{OOH})(\text{TMC})]^{2+}$ were found to be capable to perform electrophilic oxidation of weak C – H bonds, such as hydrogen abstraction from xanthene (75.5 kcal/mol) and 9, 10 – dihydroanthracene (77 kcal/mol) substrates. These works give relevant mechanistic information regarding to the activation of O_2 by non – heme enzymes.

Another example of O_2 activation system was reported by Borovik *et al.* using the trianionic ligand (H_3buea)³⁻.¹⁰² With this system was possible to achieve the synthesis of the sterically hindered species $[\text{Fe}^{\text{III}}(\text{O})(\text{H}_3\text{buea})]^{2-}$ and $[\text{Fe}^{\text{III}}(\text{OH})(\text{H}_3\text{buea})]^-$ by using O_2 as well as synthetic oxidants. Both species were found to possess sigma Fe – O bond character with interactions of the oxo moiety with H atoms from the ligand, and showing no oxo – transfer reactivity due to the constrained nature of the oxo moiety. The formation of the iron (III) species was suggested to occur through a transient iron (IV) – oxo species, although no direct evidence could be found. Later on, the $[\text{Fe}^{\text{IV}}(\text{O})(\text{H}_3\text{buea})]^-$ species could be finally detected, interestingly it was characterised as a high – spin ($S = 2$) iron – oxo species with a relatively long Fe – O bond of 1.68 Å. More importantly, was the first iron (IV) to be characterised by EPR spectroscopy (g values 8.19 and 4.06).⁹² This iron (IV) – oxo species could be prepared either from the Fe – O or the Fe – OH species through proton – coupled electron transfer processes (PCET).

Unlike its low – spin analogues, few high – spin ($S = 2$) complexes have been reported (Figure I.7), mainly in a trigonal bipyramidal configuration and have been characterised by means of spectroscopic techniques such as Mössbauer spectroscopy, XAS/EXAFS spectroscopy and FT – IR. Previously to the Borovik systems Pestovsky *et al.*^{86,89} had synthesised $[\text{Fe}^{\text{IV}}(\text{O})(\text{H}_2\text{O})_5]^{2+}$ using ozone in water and England *et al.*^{90,91} synthesised the $[\text{Fe}^{\text{IV}}(\text{O})(\text{TMG}_3\text{tren})]^{2+}$ using PhIO. These complexes show by Mössbauer spectroscopy a ground state of $S = 2$ similar to those iron – oxo (IV) intermediates observed in the non – heme oxygenases catalytic cycle (Table I.2), with a Fe – O distance of 1.66 Å in the case of the $[\text{Fe}^{\text{IV}}(\text{O})(\text{TMG}_3\text{tren})]^{2+}$. The high – spin ground state is attributed to their threefold symmetry with degenerated $d(xy)$ and $d(x^2-y^2)$ orbitals (Scheme I.1). Theoretical studies conclude that non – heme high – spin iron (IV) – oxo complexes should be better oxidants than the low – spin homologues.^{128,129} However $[\text{Fe}^{\text{IV}}(\text{O})(\text{TMG}_3\text{tren})]^{2+}$ was found to be a sluggish oxidant, with rates comparable to the $S = 1$ iron (IV) – oxo complexes, *e.g.* $[\text{Fe}^{\text{IV}}(\text{O})(\text{N}_4\text{Py})]^{2+}$ (Table I.3). Although showing remarkable selectivity towards small substrates, such as 1, 4 – cyclohexadiene (CHD) compared to 9, 10 – dihydroanthracene (DHA), most likely due to steric reasons ($k_2 = 1.2$ vs $0.09 \text{ M}^{-1}\text{s}^{-1}$). Proof of that, is the strategy followed to increase the TMG_3tren system reactivity, by the removal of a guanidyl arm to increase the access to the metal centre, giving place to the $[\text{Fe}^{\text{IV}}(\text{O})(\text{TMG}_2\text{dien})(\text{MeCN})]^{2+}$ (Figure I.7) complex with a symmetry between square – pyramidal and trigonal – bipyramidal.⁹⁵ Indeed the reactivity of this complex increased up to 15 – fold the rate of oxidation of CHD (18 vs $1.2 \text{ M}^{-1}\text{s}^{-1}$ at $-30 \text{ }^\circ\text{C}$) and >600 times the DHA oxidation rate (57 vs $0.09 \text{ M}^{-1}\text{s}^{-1}$ at $-30 \text{ }^\circ\text{C}$) compared to the $[\text{Fe}^{\text{IV}}(\text{O})(\text{TMG}_3\text{tren})]^{2+}$. This is the first direct evidence of an enhanced reactivity of an $S = 2$ non – heme high – spin iron (IV) – oxo system compared to the $S = 1$ examples, with 1 to 3 orders of magnitude faster compared to those. In the same report were characterised also the high – spin

species $[\text{Fe}^{\text{IV}}(\text{O})(\text{TMG}_2\text{dien})(\text{X})]^+$ ($\text{X} = \text{N}_3$ and Cl) with similar spectroscopic features, although no reactivity was tested.

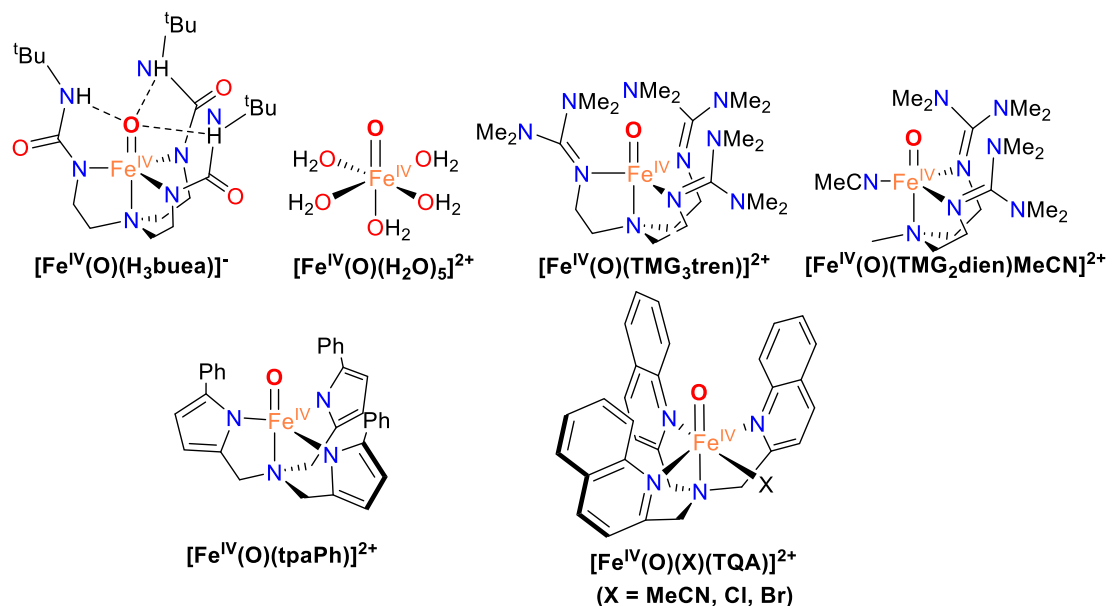


Figure I.7. High – spin ($S = 2$) iron (IV) – oxo complexes.

Chang and co – workers also reported the high – spin ($S = 2$) complex $[\text{Fe}^{\text{IV}}(\text{O})(\text{tpa}^{\text{Ph}})]^{2+}$ that was characterised by means of different techniques as well as EPR.⁹⁴ This complex was capable of performing intra – and intermolecular oxidation, although was found to be a sluggish oxidant due to the steric hindrance, thus reacting only with relatively small substrates such PMe_2Ph and CHD .

More recently Que and co – workers reported the synthesis of an electronic and functional model for TauD – J, the $[\text{Fe}^{\text{IV}}(\text{O})(\text{TQA})(\text{MeCN})]^{2+}$ species,⁹⁶ with a pseudo – octahedral geometry suggested by DFT calculations. It was characterised as a high – spin ($S = 2$) centre and showing the highest reactivity observed in the oxidation of cyclohexane ($k_2 = 0.37 \text{ M}^{-1}\text{s}^{-1}$ at -40°C), with a reactivity comparable to the TauD – J (13 s^{-1} in the oxidation of taurine at 5°C)⁹ and similar to that found for $[\text{Fe}^{\text{IV}}(\text{O})(\text{Me}_3\text{NTB})]^{2+}$ in the oxidation of cyclohexane ($k_2 = 0.23 \text{ M}^{-1}\text{s}^{-1}$ at -40°C).

Indirect evidence of higher reactivity for high – spin complexes was also reported, the $S = 1$ ground state $[\text{Fe}^{\text{IV}}(\text{O})(\text{Me}_3\text{NTB})(\text{CH}_3\text{CN})]$ complex⁸⁰ is the most reactive example in the literature of a non – heme $S = 1$ iron (IV) – oxo system, being capable to abstract an hydrogen atom from cyclohexane at -40°C and almost one order of magnitude faster than $[\text{Fe}^{\text{IV}}(\text{O})(\text{TMG}_2\text{dien})(\text{MeCN})]^{2+}$ in the oxidation of CHD and DHA .⁹⁵ Mössbauer studies revealed this compound as an $S = 1$ ground state oxoferryl complex, but DFT calculations showed that high – spin state is available, suggesting that a spin transfer may permit its high reactivity. Another indirect evidence comes from comparing complex $[\text{Fe}^{\text{IV}}(\text{O})(\text{TMC})(\text{X})]^{2+/+}$ ($\text{X} = \text{MeCN}$, $\cdot\text{Otf}$ or $\cdot\text{N}_3$) and $[\text{Fe}^{\text{IV}}(\text{O})(\text{TMCS})]^+$ reactivity in oxo transfer. Transfer ability decreased when the electrophilicity of $\text{Fe} = \text{O}$ moiety decreased, but when a more electrodonating *trans* axial ligand was inserted the rates of hydrogen abstraction increased.¹³⁰ This fact supports that the reactivity is modulated by the modification of the gap between triplet and quintet state, as it was showed by DFT. Very recently Andris *et al.* reported the reactivity comparison in the gas phase of two closely structurally related iron (IV) – oxo complexes $[\text{Fe}^{\text{IV}}(\text{O})(\text{NO}_3)(\text{Me}_2\text{Pytacn})]^{2+}$ in triplet and quintet state. For this system slightly higher

rates for quintet state were also found, questioning the notion that high – spin complexes are naturally more reactive than their low spin counterparts.¹³¹

Subsequently to the report of $[\text{Fe}^{\text{IV}}(\text{O})(\text{TQA})(\text{MeCN})]^{2+}$, Que and co – workers reported the synthesis of species $[\text{Fe}^{\text{IV}}(\text{O})(\text{X})(\text{TQA})]^{2+}$ ($\text{X} = \text{Cl}$ or Br), the only synthetic complexes in high – spin ($S = 2$) that reproduce the spectroscopic parameters of the $S = 2$ iron (IV) – oxo intermediates of the halogenase enzymes. Remarkably both complexes are capable of halogenate substrates such as cyclohexane and toluene.⁹⁷

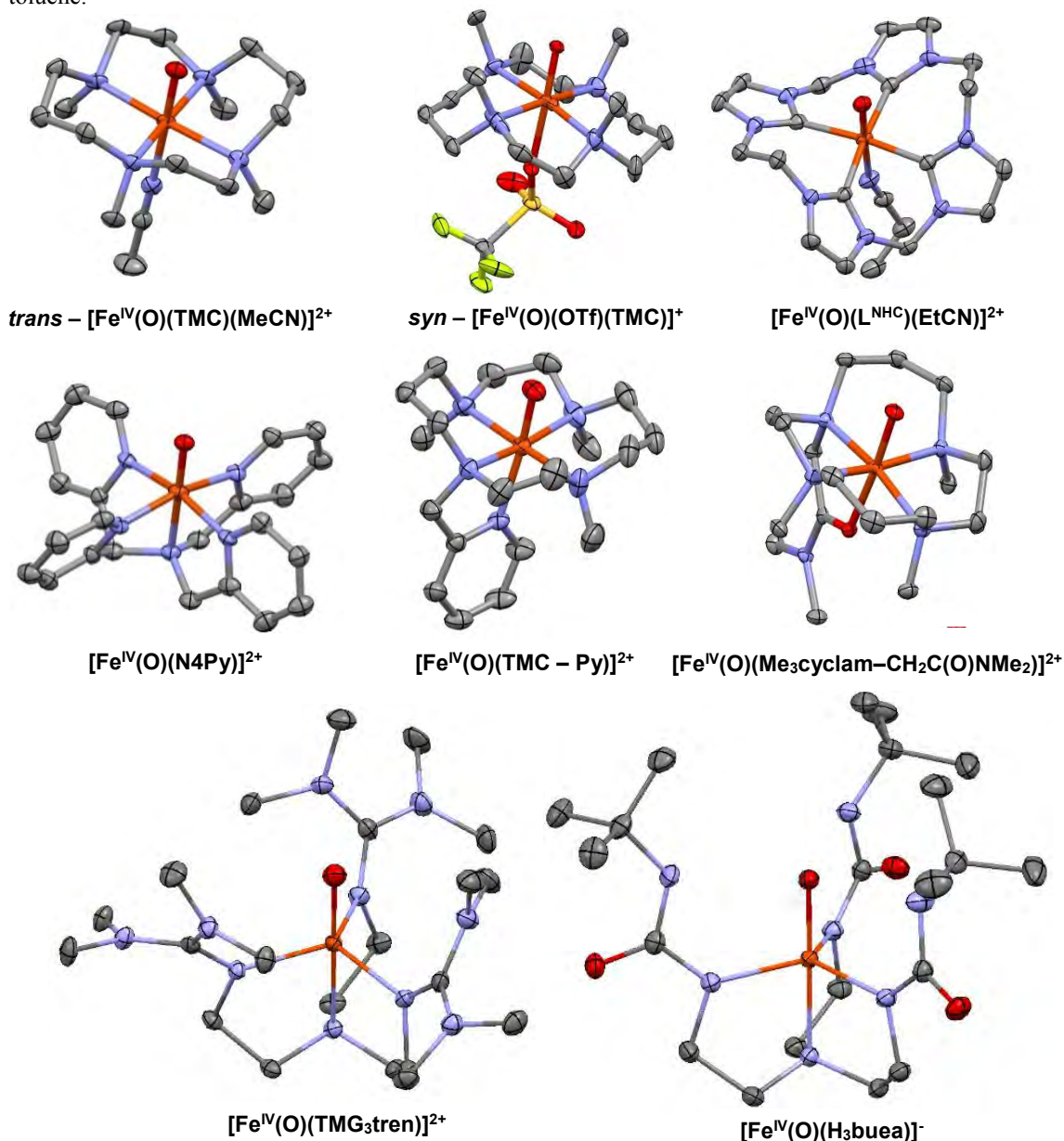


Figure I.8. ORTEP structures of crystallographically characterised non – heme iron (IV) – oxo complexes (50 % probability ellipsoids with counterions not shown for commodity).

During the last years many other high – valent iron – oxo complexes have been synthesised, with pyridine and amine chelators coordinating to the iron, with either tetra– or pentadentate ligands (Figure I.5 and I.7).^{53,55,57,108,132,133} Usually non – heme iron (IV) – oxo species are very reactive and show a very short lifetime in solution with readily decomposition towards its iron (III) – hydroxo species by inter – or intramolecular self – oxidation.^{77,91,94,134,135} A consequence of this metastable nature is that only a few number of crystallographic structures from high – valent iron (IV) species were reported: the two regioisomers of the tetradentate octahedral TMC species, *trans* – [Fe^{IV}(O)(TMC)(MeCN)]²⁺ and *syn* – [Fe^{IV}(O)(OTf)(TMC)]⁺,^{65,70} showing different disposition of methyls; the two high – spin square bipyramidal complexes [Fe^{IV}(O)(TMG₃tren)]²⁺⁹¹ and [Fe^{IV}(O)(H₃buea)]⁻;⁹² the three octahedral pentadentate complexes [Fe^{IV}(O)(N4Py)]²⁺,⁸² [Fe^{IV}(O)(TMC – Py)]²⁺⁷² and [Fe^{IV}(O)(Me₃cyclam – CH₂C(O)NMe₂)]²⁺,⁷³ the latter with an amide moiety coordinated to the iron in *trans* to the oxo; and the last crystal structure is the tetracarbene [Fe^{IV}(O)(L^{NHC})(EtCN)]²⁺¹³⁶, the first example of a tetracarbene iron (IV) – oxo (Figure I.8). Here are described some of them with a comparison of its spectroscopic data (Table I.2).

The reactivity of biomimetic iron (IV) – oxo complexes have been widely studied and it is well known that they can perform a number of oxidation reactions. Reactions like oxygen atom exchange with water; electron and hydride transfer; water oxidation; intermolecular oxygen atom transfer (OAT) to perform the oxidation of thioethers, phosphines or epoxidation of alkenes; even the defluorination hydroxylation of arenes. However, the most remarkable reactivity is the C – H bond oxidation through hydrogen atom abstraction (HAT), such as in the hydroxylation of aromatic and aliphatic substrates, in the cycloalkane aromatisation reactions or in the halogenation of C – H bonds.^{53,54,79-81,83,85,97,130,133,137-140} Table I.3 shows selected rate constants in the iron (IV) – oxo HAT reactivity with prototypical substrates for a comparative analysis. Although a direct comparison of reactivity between complexes is difficult due to the different experimental conditions used during experiments (*e.g.* temperature).

Table I.3. Rate constants for iron (IV) – oxo complexes with different substrates in HAT reactivity.

Complex	Substrate (BDE, Kcal·mol ⁻¹)	T (°C)	<i>k</i> ₂ (10 ⁻⁵ M ⁻¹ ·s ⁻¹)	Ref.	
^b [Fe ^{IV} (O)(TQA)(MeCN)] ²⁺	Cyclohexane (99)	-40	0.37	96	
[Fe ^{IV} (O)(Me ₃ NTB)(MeCN)] ²⁺			0.25	80	
[Fe ^{IV} (O)(Me ₂ Pytacn)(MeCN)] ²⁺		25	3.9·10 ⁻⁴	77	
[Fe ^{IV} (O)(Bn – TPEN)] ²⁺		25	4·10 ⁻⁴	81	
[Fe ^{IV} (O)(N4Py)] ²⁺			^c 6·10 ⁻⁵		
^b [Fe ^{IV} (O)(TQA)(MeCN)] ²⁺	Toluene (90)	-40	0.64	97	
^b [Fe ^{IV} (O)(Cl)(TQA)] ²⁺			0.05		
^b [Fe ^{IV} (O)(Br)(TQA)] ²⁺			0.07		
[Fe ^{IV} (O)(Me ₃ NTB)(MeCN)] ²⁺			0.47		80
[Fe ^{IV} (O)(Bn – TPEN)] ²⁺		25	8.9·10 ⁻³	81	
[Fe ^{IV} (O)(N4Py)] ²⁺			6.3·10 ⁻⁴		
[Fe ^{IV} (O)(Me ₃ NTB)(MeCN)] ²⁺	Ethylbenzene (87)	-40	1.5	80	
[Fe ^{IV} (O)(Bn – TPEN)] ²⁺		25	0.07	81	
[Fe ^{IV} (O)(N4Py)] ²⁺			4·10 ⁻³		
[Fe ^{IV} (O)(Me ₃ NTB)(MeCN)] ²⁺	Cyclohexadiene (78)	-40	940	80	
[Fe ^{IV} (O)(Bn – TPEN)] ²⁺			5.7		
[Fe ^{IV} (O)(TPA)(MeCN)] ²⁺			1.9		96
[Fe ^{IV} (O)(N4Py)] ²⁺			0.5		80
^b [Fe ^{IV} (O)(TMG ₃ tren)(MeCN)] ²⁺		-30	^a 1.2	90	
^b [Fe ^{IV} (O)(TMG ₂ dien)(MeCN)] ²⁺			18	95	
[Fe ^{IV} (O)(TMC)(MeCN)] ²⁺			0.02	90	
[Fe ^{IV} (O)(N4Py)] ²⁺		-15	1.3	77	
[Fe ^{IV} (O)(Me ₂ Pytacn)(MeCN)] ²⁺			4.2		
[Fe ^{IV} (O)(TMC)(MeCN)] ²⁺			0.12		130
[Fe ^{IV} (O)(Me ₃ NTB)(MeCN)] ²⁺	Dihydroanthracene (77)	-40	3100	80	
[Fe ^{IV} (O)(N4Py)] ²⁺			18	112	
^b [Fe ^{IV} (O)(TMG ₃ tren)(MeCN)] ²⁺		-30	^a 0.09	90	
[Fe ^{IV} (O)(TMC)(MeCN)] ²⁺			0.02	95	
^b [Fe ^{IV} (O)(TMG ₂ dien)(MeCN)] ²⁺			57		
[Fe ^{IV} (O)(N4Py)] ²⁺			2.8		112
[Fe ^{IV} (O)(Me ₂ Pytacn)(MeCN)] ²⁺			-15		5.7

^aThis reaction suffers from steric effects. ^bHigh – spin complex. ^cDerived from *k*_{obs} average. TPA = tris(2 – pyridylmethyl)amine.

Our group contributed to the field in the study of high – valent iron – oxo species based on the 1, 4, 7 – triazacyclononane (tacn) chelating ligand and the study of reactivity of such species. In 2011 Company *et al.* synthesised the low – spin $[\text{Fe}^{\text{IV}}(\text{O})(\text{Me}_2\text{Pytacn})(\text{S})]^{2+}$ ($\text{S} = \text{MeCN}$ or H_2O) with a remarkable stability ($t_{1/2} > 2$ h at 15°C) in comparison to the previously reported iron (IV) – oxo complexes bearing tetradentate ligands. This species was prepared by oxidation of iron (II) precursor with 2 eq. of peracetic acid and fully characterised by UV – vis, ^1H – NMR, Mössbauer spectroscopy, ESI – MS and DFT (Figure I.5, Table I.2). The decomposition species was identified as a dimeric iron (III) bearing an acetate and an oxo bridging ligands. $[\text{Fe}^{\text{IV}}(\text{O})(\text{Me}_2\text{Pytacn})(\text{S})]^{2+}$ was tested in the oxygen atom transfer (OAT) to thioanisole substrates (Hammett slope of $\rho = -1.5$) and in hydrogen atom abstraction (HAT) from substrates such as DHA, 2,3 – dimethyl – 2 – butene and cyclohexane. A plot of $\log(k_2)$ vs $\text{BDE}_{\text{C-H}}$ revealed a linear behaviour (slope ≈ -0.2) and DHA gave a $\text{KIE} = 27$, both suggesting a hydrogen abstraction step. Furthermore it was studied its capability in oxygen atom exchange with water ($\Delta\text{H}^\circ = 10.2 \pm 0.8$ kcal/mol, $\Delta\text{S}^\circ = -32 \pm 3$ cal/K·mol).⁷⁷ Prat *et al.* subsequently proved the implication of a high – valent iron (V) – oxohydroxo species in C – H oxidation and olefin epoxidation reactivity, mediated by $[\text{Fe}^{\text{II}}(\text{Me}_2\text{Pytacn})(\text{S})]^{2+}$ complex and using H_2O_2 as oxidant, as a biomimetic reaction of non – heme oxygenase enzymes. The $[\text{Fe}^{\text{V}}(\text{O})(\text{OH})(\text{Me}_2\text{Pytacn})]^{2+}$ intermediate was detected by variable temperature mass spectrometry and further identified by ^{18}O isotope labelling studies.¹⁴¹ Complex $[\text{Fe}^{\text{IV}}(\text{O})(\text{Me}_2\text{Pytacn})(\text{S})]^{2+}$ has a labile site *cis* to the oxo group, which constitutes a very common structural feature of non – heme iron oxygenases. Planas *et al.* synthesised the species $[\text{Fe}^{\text{IV}}(\text{O})(\text{X})(\text{Me}_2\text{Pytacn})]^+$ ($\text{X} = \text{Cl}$ and Br) as biomimetic models for mononuclear non – heme iron halogenase enzymes. These species were characterised by UV – vis, Mössbauer and $[\text{Fe}^{\text{IV}}(\text{O})(\text{Cl})(\text{Me}_2\text{Pytacn})]^+$ by high – resolution criospray mass spectrometry (CSI – MS). These complexes reacted with thioanisole substrate in OAT reactivity with modest rates (Hammett slope $\rho = -1.0$) and abstracted hydrogen atom from DHA, xanthene, 1, 4 – cyclohexadiene (CHD), fluorene, triphenylmethane and 2, 3 – dimethylbutane (DMB), showing a linear dependence of rate with $\text{BDE}_{\text{C-H}}$ (slope = 0.23) and a KIE of 26 for DHA. Remarkably, the new iron (IV) – oxo species showed enhanced reactivity towards HAT substrates, *e.g.* the rates for DHA were 2 – 3 times faster in comparison to the species without halogen ligand (2.22 (Cl) and 1.89 (Br) vs $0.81 \text{ M}^{-1}\text{s}^{-1}$). Unfortunately, $[\text{Fe}^{\text{IV}}(\text{O})(\text{X})(\text{Me}_2\text{Pytacn})]^+$ did not give halogenated products, an examination of Ph_3CH oxidation products and final iron species suggested that only rebounding of the oxo moiety occurred, giving the alcohol product in high yield.⁷⁸

Codolà *et al.* proved the involvement of high – valent species in the water oxidation process mediated by iron catalyst. In this regard, he showed that non – heme iron (IV) – oxo species were not able to oxidize water. However, when the iron (IV) – oxo complexes were exposed to CAN the oxidation of water was observed. Among the studied complexes are the $[\text{Fe}^{\text{IV}}(\text{O})(\text{Me}_2\text{Pytacn})(\text{S})]^{2+}$ family. Further studies were performed by introducing different electronwithdrawing groups into the pyridine ring and analysing its effect in this reactivity.^{139,142} The most active water oxidation catalysts were obtained with the α – $[\text{Fe}^{\text{IV}}(\text{O})(\text{mcp})(\text{H}_2\text{O})]^{2+}$ ($\text{mcp} = \text{N}$, N' – dimethyl – N' – bis(2 – pyridylmethyl) – cyclohexane – 1,2 – diamine) complex with >1000 TOF (h^{-1}) and 380 TON of O_2 produced. Some years later, the same authors identified by UV – vis, CSI – MS and Raman resonance an $\text{O}=\text{Fe}^{\text{IV}} - \text{O} - \text{Ce}^{\text{IV}}$ intermediate implicated in the oxidation of water. To date this species is the closest structural and functional model for the essential heterodimetallic $\text{Mn}^{\text{V}} - \text{O} - \text{Ca}^{\text{II}}$ centre involved in the water oxidation event in photosystem – II (PSII).¹⁴⁰

I.2.2. Iron (V) – oxo species

Iron (V) – oxo species have been postulated to be implicated in non – heme enzymatic oxidations, such as in the Rieske oxygenase enzymes, where an iron (III) – hydroperoxo intermediate is suggested to evolve through heterolytic O – O cleavage to an $\text{Fe}^{\text{V}}(\text{O})(\text{OH})$ species. However, direct characterisation of an iron (V) intermediate remains elusive in natural systems. Moreover, $\text{Fe}^{\text{III}}(\text{OOH})$ intermediates have been also suggested to be the responsible for the oxidation processes of these enzymes.^{19,43,143,144} Despite the fact that no direct evidence has been found of iron (V) species in natural systems, the use of model systems has allowed the trapping of some artificial biologically inspired non – heme iron (V) – oxo species (Figure I.9).

In 2007 Tiago de Oliveira *et al.*¹⁴⁵ reported the first synthesis of a $\text{Fe}^{\text{V}}=\text{O}$ complex using a tetra – amido macrocyclic ligand, TAML. This complex was synthesised from its Fe^{III} precursor with an excess of *m*CPBA at $-60\text{ }^{\circ}\text{C}$ and was fully characterised by UV – vis, EPR, Mössbauer ($\delta = -0.46\text{ mm/s}$, $\Delta E_{\text{Q}} = 4.25\text{ mm/s}$) and EXAFS studies. All this data was consistent with an $S = 1/2$ species, with a short Fe – O bond of 1.58 \AA consistent with an iron (V) – oxo moiety. Collins and co – workers as well as Nam and co – workers studied the reactivity of $[\text{Fe}^{\text{V}}(\text{O})(\text{TAML})]^{-}$ and proved the competence of iron (V) species to oxidise unactivated C – H bonds.^{99,146,147}

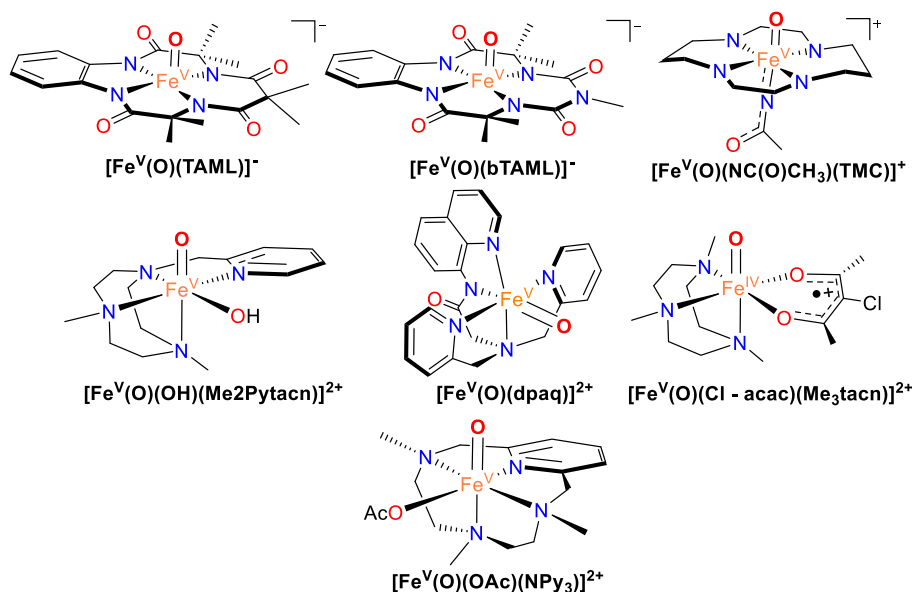


Figure I.9. Iron (V) – oxo species characterised in solution (Top) and detected by mass spectroscopy (Middle). (Below) Structure of oxo – acetate species $[\text{Fe}^{\text{V}}(\text{O})(\text{OAc})(\text{PyNMe}_3)]^{2+}$.

In many model systems $\text{Fe}^{\text{V}}(\text{O})(\text{OH})$ intermediates are postulated to be the active oxidant species,¹⁴⁸⁻¹⁵⁰ *e.g.* in the *cis* – dihydroxylation of C = C double bonds. This proposal is supported by the ^{18}O incorporation to substrate from H_2^{18}O , thereby excluding the possibility of a direct attack of the $\text{Fe}^{\text{III}} - \text{OOH}$ intermediate to the substrate. Furthermore, in our group has been suggested the $\text{Fe}^{\text{V}}(\text{O})(\text{OH})$ species implication on a water oxidation system.¹³⁹ But the existence of $\text{Fe}^{\text{V}}(\text{O})(\text{OH})$ species had been only indirectly proved. In 2007, the spectroscopically characterized $[\text{Fe}^{\text{V}}(\text{O})(\text{TAML})]^{-}$ was the first isolable non – heme iron (V) – oxo species that existed in literature; this was possibly consequence of its tetraanionic ligand.

Subsequent to the synthesis of $[\text{Fe}^{\text{V}}(\text{O})(\text{TAML})]^{-}$, Que and co – workers reported the iron (V) – oxo species $[\text{Fe}^{\text{V}}(\text{O})(\text{NC}(\text{O})\text{CH}_3)(\text{TMC})]^{+}$ following a different approach. This species was synthesised from its

$[\text{Fe}^{\text{IV}}(\text{O})(\text{TMC})(\text{MeCN})]^{2+}$ precursor by one – electron oxidation using a strong base in combination with $^t\text{BuOOH}$. The resulting compound was characterised by Mössbauer, EPR, UV – vis spectroscopy, DFT and Raman resonance.¹⁰¹ $[\text{Fe}^{\text{V}}(\text{O})(\text{NC}(\text{O})\text{CH}_3)(\text{TMC})]^{+}$ was reported in combination with its acid conjugate $[\text{Fe}^{\text{V}}(\text{O})(\text{NC}(\text{OH})\text{CH}_3)(\text{TMC})]^{2+}$ with $t_{1/2}$ of 60 and 30 min at $-44\text{ }^{\circ}\text{C}$, respectively.

Later on Gupta *et al.* synthesised an iron (V) – oxo species, $[\text{Fe}^{\text{V}}(\text{O})(\text{bTAML})]^{-}$, by introducing an N – Me group in the TAML ligand.¹⁰⁰ Remarkably this high – valent species was stable at room temperature and was capable to oxidise unactivated alkanes as strong as cyclohexane (99 kcal/mol), although with a reaction rate of one order of magnitude lower than the original $[\text{Fe}^{\text{V}}(\text{O})(\text{TAML})]^{-}$ ($2.3 \cdot 10^{-2}$ vs $0.25\text{ M}^{-1}\text{s}^{-1}$).⁹⁹

The existence of $\text{Fe}^{\text{V}}(\text{O})(\text{OH})$ intermediates in oxygenation reactions was doubtful until 2011, when Prat *et al.* reported direct evidence of an iron (V) – oxo species in a synthetic system, trapping by low temperature mass spectrometry the $[\text{Fe}^{\text{V}}(\text{O})(\text{OH})(\text{Me}_2\text{Pytacn})]^{2+}$ species.^{141,151} Since then few iron (V) – oxo species have been detected by mass spectrometry techniques. In 2012 Kodera and co – workers reported the $[\text{Fe}^{\text{V}}(\text{O})(\text{dpaq})]^{2+}$ species in the reaction of its iron (III) precursor with H_2O_2 , presumably formed upon O – O heterolytic cleavage from an iron (III) – hydroperoxo intermediate.¹⁵² This species was detected by cryospray ionisation mass spectrometry (CSI – MS) in the selective catalytic oxidation of alkane substrates. In 2014 Che and co – workers reported the reaction of $[\text{Fe}^{\text{III}}(\text{Cl})(\text{Cl} – \text{acac})(\text{Me}_3\text{tacn})]^{+}$ with oxone that resulted in a species attributable by mass spectrometry to an iron (V) – oxo species, which by DFT calculations was assigned to the cationic radical species $[\text{Fe}^{\text{IV}}(\text{O})(\text{Cl} – \text{acac})^{\bullet+}(\text{Me}_3\text{tacn})]^{2+}$, formally an iron (V) species.¹⁵³ This species was capable to hydroxylate at room temperature challenging substrates such as cyclohexane, light alkanes such as propane and ethane, as well as the epoxidation of alkenes. Moreover, an incorporation of 60 % of ^{18}O from H_2^{18}O into high – valent species and 32 % into cyclohexane substrate was shown. Previously, in 2010, Che and co – workers also proposed an iron (V) – oxo intermediate in the *cis* – dihydroxylation of alkenes by a complex with a Macrocyclic Tetraaza ligand, on the basis of ESI – MS, ^{18}O labelling studies and DFT calculations, although no spectroscopic evidence was found.¹⁵⁴

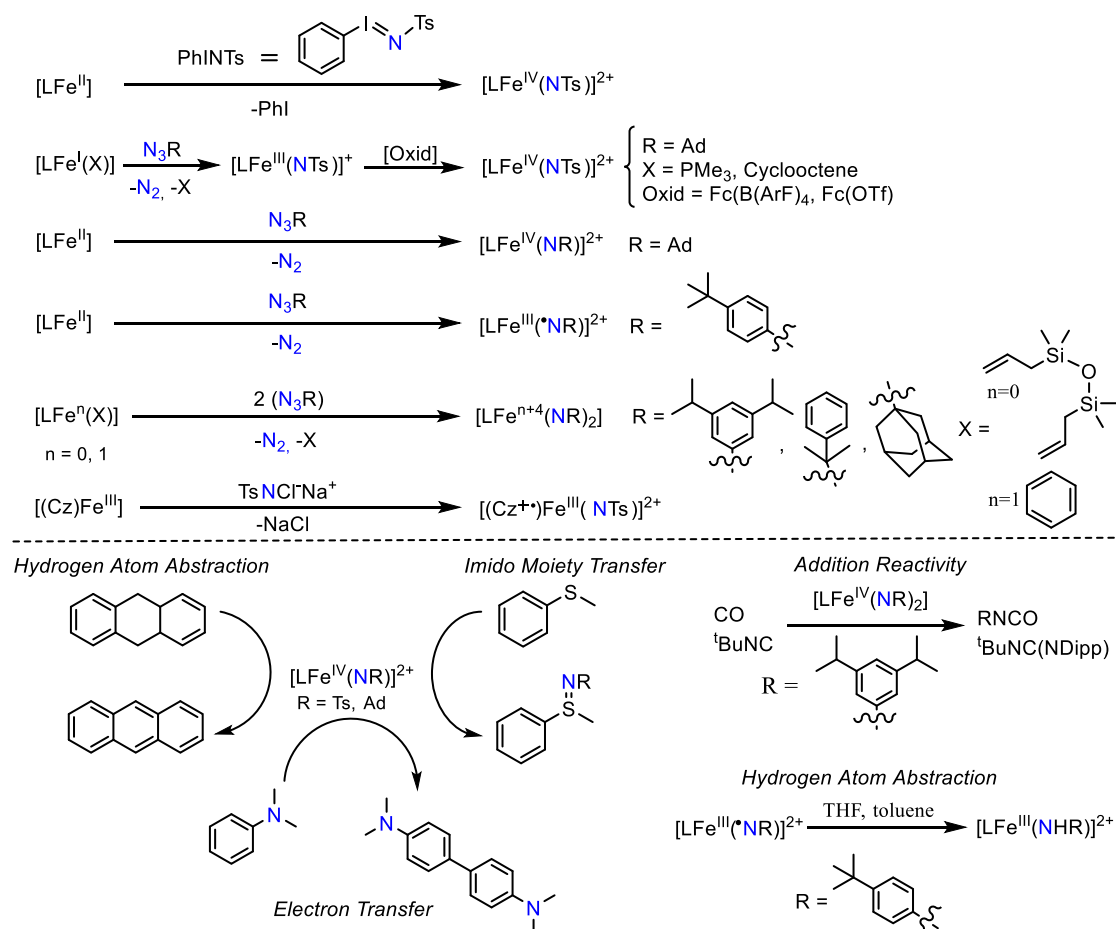
Recently spectroscopic evidence for an $\text{Fe}^{\text{V}}(\text{O})(\text{OAc})$ species was reported.¹¹⁹ Serrano *et al.* reported the stereospecific hydroxylation of unactivated alkanes and the hydroxyacetylation of olefins at low temperatures by a $\text{Fe}^{\text{V}}(\text{O})(\text{OAc})$ species. Remarkably, to the best of our knowledge this complex, $[\text{Fe}^{\text{V}}(\text{O})(\text{OAc})(\text{PyNMe}_3)]^{2+}$, is the most reactive high – valent species reported to date, with the highest rate for oxidation of cyclohexane ($2.5\text{ M}^{-1}\text{s}^{-1}$ at $-40\text{ }^{\circ}\text{C}$); one order of magnitude faster than the most reactive iron (IV) – oxo species and at least 4 orders of magnitude faster than the $[\text{Fe}^{\text{V}}(\text{O})(\text{TAML})]^{-}$ species. $[\text{Fe}^{\text{V}}(\text{O})(\text{OAc})(\text{PyNMe}_3)]^{2+}$ was characterised by UV – vis, EPR and mass spectroscopy.

Very recently, Borovik and co – workers reported the reaction of $[\text{Fe}^{\text{IV}}(\text{O})(\text{H}_3\text{buea})]^{-}$ with protons to generate a new structurally similar iron (IV) – oxo in a high – spin state. The protonation most likely takes place in one of the amido arms, rather than in the oxo moiety, as ascertained by XANES, EXAFS, Mössbauer and nuclear resonance vibrational spectroscopy (NRVS). The reaction of the new iron (IV) species was tested with one – electron oxidants, instead of observing the generation of an iron (V) – oxo species it was recovered the iron (IV) – oxo protonated species. To explain that behaviour a transient iron (V) – oxo species was suggested, although the only indirect evidences were the oxidative products obtained when the oxidation was performed in presence of phenols.⁹³

I.2.3. High – valent iron – imido species [Fe = N – R]

The capacity of bioinspired non – heme iron – oxo complexes to perform oxidative transformations with unactivated substrates has been widely studied.^{54,137,150,155} It is well – known that these species are capable to perform such an interesting and challenging chemistry as the abstraction and functionalisation of C – H bonds, even those as strong as in cyclohexane (BDE \approx 100 kcal/mol).^{80,81,96,97,99}

Related interesting compounds are the iron – imido species, which are analogues to iron – oxo complexes, *e.g.* the iron (IV) – imido species are isoelectronic to the iron (IV) – oxo complexes; thus it was hypothesized that the former should be capable to perform amination of C – H and C=C bonds and HAT reactions in analogy to the oxo transfer reactivity of iron (IV) – oxo species. However, it has been experimentally and theoretically demonstrated that there are differences in the electronic structures of the two type of species that it affects their relative reactivities, even when the comparison is done with complexes that share common ligand and coordination geometry (*e.g.* $[\text{Fe}^{\text{IV}}(\text{X})(\text{N4Py})]^{2+}$ X = O, NTs).^{156,157} Despite its interest, iron (IV) – imido species have been less studied than iron – oxo complexes. Recent studies reported its potential, showing the ability of heme and non – heme iron – imido compounds to transfer the –NR moiety to nucleophilic substrates, such as phosphines or sulphides, but also in the functionalisation of unactivated C – H bonds. Some reported high – valent iron – imido species are highlighted in the following lines and its synthesis and reactivity summarised in Scheme I.7.



Scheme I.7. Reported syntheses and general reactivity of high – valent iron – imido species. L refers to the different non – heme ligands described in the text. Cz refers to the porphyrinic corrolazine macrocycle (*vide infra*).

The first example of a C – H amination mediated by a Cyt P450 enzyme was published in 1985. Svastits *et al.* achieved the intramolecular C – H (sp^3) amination of a 2, 5 – diisopropylbenzene – N – sulphonyliminiodobenzene and also the intramolecular functionalisation of cyclohexane by using a tosylimido atom transfer agent (PhINTs).¹⁵⁸ Previously, analogous examples of bioinspired catalytic functionalisation were reported using $[Fe^{III}(TPP)(Cl)]$ as a model for Cyt P450 enzyme, leading to alkene and alkyl aminations.¹⁵⁹⁻¹⁶¹ More recently, in 2003, Que and co – workers suggested the involvement of an iron (IV) – tosylimido species in the reaction of the non – heme octahedral complex $[Fe^{II}(6 – PhTPA)(MeCN)]^{2+}$ with PhINTs. This species was capable to perform intramolecular C – H (sp^2) amination via insertion of the –NTs moiety into the *ortho* position of the phenyl arm on the ligand. By analogy with iron (IV) – oxo complexes an iron (IV) – tosylimido species was proposed.¹³⁴ Later on, Borovik and co – workers proposed the involvement of an iron (IV) – imido species in the generation of the crystallographically characterised iron (III) – tolylimido complex $[Fe^{III}(NHTol)(H_2O)]$, obtained by reaction of the corresponding iron (II) species and *p* – tolyl azide.¹⁶² Subsequently, Betley and co – workers reported the intramolecular benzylic C – H amination of an iron (II) dipyrromethene complex, by reaction of iron complex with different organic azides were obtained the corresponding aminated ligands. Intramolecular benzylic C – H bond amination was proved by ESI – MS and X – ray diffraction analysis. Despite of being suggested as reaction intermediates, no iron (IV) – imido species could be detected.¹⁶³ More recently, Latour *et al.* proposed a diiron (III,IV) – tosylimido species based on desorption electrospray ionisation mass spectrometry (DESI – MS) experiments and reactivity studies.¹⁶⁴ This high – valent dimeric species was highly reactive towards hydrogen atom abstraction and –NTs transfer to thioanisole substrates, thus its transient nature prevented further characterisation. Based on DFT studies the authors suggested an iron (III) – imido radical species.

In addition to these indirect evidences, few examples of isolated iron (IV) – imido species have been reported during last two decades (Figure I.10). All of them have been characterised in low spin configuration, X – ray structures have been obtained mainly in tetrahedral geometry due to its higher stability. The first of them was reported in 2000 by Verma *et al.* as the cubane cluster $[Fe^{III}Fe^{IV}(\mu^3 – N^tBu)_4(N^tBu)Cl_3]$ with a terminal N^tBu group. The imido cubane complex was prepared by a self – assembly reaction of $FeCl_3$ and $LiNH^tBu$. Surprisingly, even though it was obtained in very low yield (~1 – 2 %), good quality crystals were obtained, with a Fe – N bond of 1.635 Å in a linear fashion (Fe – N – C angle of 178.6°).¹⁶⁵

In 2006, Que and co – workers synthesised the first octahedral iron (IV) – tosylimido species, by reaction of $[Fe^{II}(N4Py)(MeCN)]^{2+}$ with the tosylimido transfer agent PhINTs. The corresponding iron (IV) – tosylimido species was obtained in high yield and a Fe – N_{imido} bond of 1.73 Å was determined by EXAFS spectroscopy. Its short lifetime ($t_{1/2} = 3$ h at room temperature) prevented obtaining crystalline material. This species was thoroughly characterised by K – edge XAS, Mössbauer, UV – vis, NMR and DFT calculations.¹⁶⁶ Some years later the reactivity of $[Fe^{IV}(NTs)(N4Py)]^{2+}$ was tested by de Visser *et al.* in the –NTs group transfer towards thioanisole and in the abstraction of H atom from benzylic and alkylaromatic substrates (*e.g.* benzyl alcohol and DHA). The –NTs transfer (sulfimidation) to *para* – substituted thioanisole substrates was experimentally found to be faster than the analogous sulfoxidation, while for HAT reactivity the opposite trend was found. Despite experimental results pointed towards one – electron

transfer mechanism in the sulfimination of thioanisole, de Visser and co-workers suggested that these reactions proceed *via* a two-electron mechanism. On the other hand, from DFT calculations it was argued that HAT proceeds through a two-step mechanism. Due to a high electron affinity of $[\text{Fe}^{\text{IV}}(\text{NTs})(\text{N4Py})]^{2+}$, this species would accept electrons from the substrate at a large distance to form $[\text{Fe}^{\text{III}}(\text{NTs})(\text{N4Py})]^+$. Being the latter responsible for a subsequent proton transfer reactivity. This $[\text{Fe}^{\text{III}}(\text{NTs})(\text{N4Py})]^+$ species would have a lower catalytic potential than $[\text{Fe}^{\text{IV}}(\text{O})(\text{N4Py})]^{2+}$ causing lower rates towards HAT reactivity for iron (IV) – tosylimido species in comparison to iron (IV) – oxo analogue.^{157,167} More recently Fukuzumi and co-workers studied the electron transfer capacity of this system in the dimerization of N, N – dimethylaniline. Experimental data revealed that $[\text{Fe}^{\text{IV}}(\text{NTs})(\text{N4Py})]^{2+}$ was more oxidant than the $[\text{Fe}^{\text{IV}}(\text{O})(\text{N4Py})]^{2+}$ species, thus easier to reduce to the iron (III) species. On the other hand the corresponding $[\text{Fe}^{\text{III}}(\text{NTs})(\text{N4Py})]^+$ was found to be less basic than the $[\text{Fe}^{\text{III}}(\text{O})(\text{N4Py})]^+$ analogue. In agreement with de Visser results.¹⁶⁸

In 2006 Peters and co-workers reported two tetrahedral species named as $[\text{Fe}^{\text{IV}}(\text{NAd})(\text{PhBPtBu}_2(\text{Pz}'))]^+$ (Figure I.10), supported by tridentate pyrazolyl/bis(phosphino)borate ligands and prepared by oxidation of the iron (III) – amido species with $\text{Fc}(\text{B}(\text{ArF})_4)$ at $-50\text{ }^\circ\text{C}$. In the case of $\text{R} = \text{H}$ ($t_{1/2} = 50\text{ min}$ at $-40\text{ }^\circ\text{C}$) only low quality crystals were obtained providing a $\text{Fe} - \text{N}_{\text{imido}}$ bond distance of 1.61 \AA and a $\text{Fe} - \text{N} - \text{Ad}$ of 173.7° , while for $\text{R} = \text{Me}$, with an enhanced stability, good quality crystals were obtained with a $\text{Fe} - \text{N}_{\text{imido}}$ bond distance of 1.634 \AA and a $\text{Fe} - \text{N} - \text{Ad}$ of 176.2° .¹⁶⁹

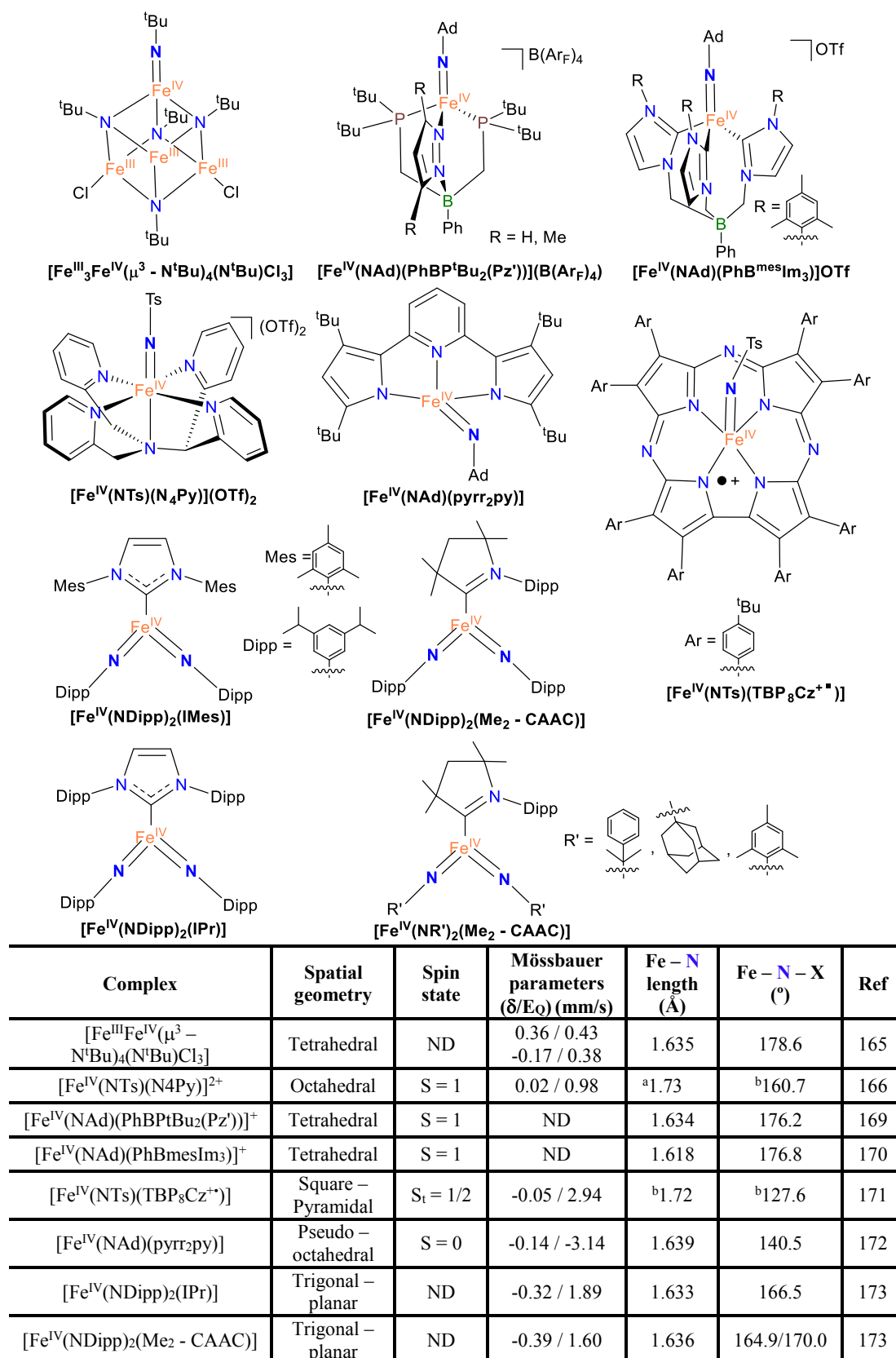


Figure I.10. Spectroscopically characterised iron (IV) – imido complexes with structural data. ND: Not determined, spectroscopic data suggest a low spin ($S = 1$) species. ^aValue from EXAFS. ^bValues from DFT calculations.

Some years later Smith and co-workers reported the synthesis of $[\text{Fe}^{\text{IV}}(\text{NAd})(\text{PhBmesIm}_3)]\text{OTf}$, supported by a tris(carbene)borate ligand and prepared by oxidation of the iron (III) precursor. The X-ray structure revealed a Fe – N bond of 1.618 Å and a Fe – N – C of 176.8°. This complex was a mild oxidant, very stable even at 100 °C and reacted at this temperature with 9, 10 – dihydroanthracene (DHA) in hydrogen abstraction. While the iron (III) and iron (IV) – imido species were stable, the corresponding Fe – N(H)Ad species was not stable and the reaction with DHA yielded the adamantyl amine product in 25 % yield.¹⁷⁰

In 2014 was reported the first X-ray structure for a pseudo – octahedral iron (IV) – imido complex.¹⁷² In contrast to the previous examples, $[\text{Fe}^{\text{IV}}(\text{NAd})(\text{pyrr}_2\text{py})]$ is tetracoordinated, bearing a tridentate dianionic bulky ligand with fourth coordination site occupied by the imido substituent. Square planar geometry is prevented by the *tert* – butyl groups on the ligand, leading to a geometry between trigonal pyramidal and *cis* – divacant octahedral. This steric effects are also translated into electronic differences, leading to an $S = 0$ species. The Fe – N_{imido} bond distance (1.639 Å) is comparable to the tetrahedral examples and significantly shorter than the octahedral iron (IV) – imido distance of 1.73 Å determined from EXAFS measurements by Que *et al.* The Fe – N – C angle is 140.5°, surprisingly is 35 – 38° lower than the other structurally characterised iron (IV) – imido species, similar deviations have also been observed in a series of iron – imido complexes synthesised by Chirik *et al.*¹⁷⁴

Deng and co-workers reported in 2014 the reaction of two iron (0) complexes with an arylazide to generate the trisubstituted bis(imido)iron (IV) derivatives $[\text{Fe}^{\text{IV}}(\text{NDipp})_2(\text{IMes})]$ and $[\text{Fe}^{\text{IV}}(\text{NDipp})_2(\text{Me}_2 - \text{CAAC})]$ with Fe – N_{imido} bond lengths of 1.633 and 1.636 Å, comparable to the previously reported tetrahedral iron (IV) – imido examples (1.62 – 1.64 Å). The Fe – N – C angles measure 164.9 and 170°.¹⁷³ More recently the authors reported four new bis(imido) iron (IV) species by modifying the substituent in the $\text{Me}_2 - \text{CAAC}$ ligand and the organic azide (Figure I.10). These four new species showed the same trigonal planar coordination geometry, with similar distances and Mössbauer parameters to the previously reported $[\text{Fe}^{\text{IV}}(\text{NDipp})_2(\text{IMes})]$ and $[\text{Fe}^{\text{IV}}(\text{NDipp})_2(\text{Me}_2 - \text{CAAC})]$, confirming its high – valent nature. Moreover the authors tested the reactivity of $[\text{Fe}^{\text{IV}}(\text{NDipp})_2(\text{IMes})]$, while it was unable to aminate toluene substrate at 100 °C, it was found that at this temperature one of the imido moieties abstracted a hydrogen from an ⁱPr on the other imido moiety. At room temperature $[\text{Fe}^{\text{IV}}(\text{NDipp})_2(\text{IMes})]$ was also capable to activate a Si – H bond from PhSiH_3 to obtain an iron species $[\text{Fe}^{\text{II}}(\text{NHDipp})(\text{NDippSiPhH}_2)(\text{IMes})]$. Furthermore the reaction of $[\text{Fe}^{\text{IV}}(\text{NDipp})_2(\text{IMes})]$ with CO or ^tBuNC at room temperature produced the addition products DippNCO and DippNCN^tBu. Moreover the reaction of $[\text{Fe}^{\text{IV}}(\text{NDipp})_2(\text{IMes})]$ with heterocumulenes (*i.e.* PhNCNPh or *p* – ⁱPr – $\text{C}_6\text{H}_4\text{NCO}$) lead to the formation of two new iron (IV) – monoimido species ($[\text{Fe}^{\text{IV}}(\text{NDipp})(\text{N}(\text{Dipp})\text{C}(\text{NPh})(=\text{NPh}))(\text{IMes})]$ and $[\text{Fe}^{\text{IV}}(\text{NDipp})(\text{N}(\text{Dipp})\text{C}(\text{O})\text{N}(\text{p} - \text{PrC}_6\text{H}_4))(\text{IMes})]$) through a $2\pi - 2\pi$ cycloaddition, the two species were characterised by Mössbauer, ¹H – NMR and magnetic susceptibility measurements, the former was also characterised by X – Ray diffraction spectroscopy.¹⁷⁵

Goldberg *et al.* reported the reaction of the square pyramidal heme complex $[\text{Fe}^{\text{III}}(\text{TBP}_8\text{Cz})]$ ($\text{TBP}_8\text{Cz} = \text{octakis}(4 - \text{tert} - \text{butylphenyl})\text{corrolazinato}$ ligand) with chloramine – T ($\text{TsNCl}^-\text{Na}^+$) to generate the species $[\text{Fe}^{\text{IV}}(\text{NTs})(\text{TBP}_8\text{Cz}^+)]$.¹⁷¹ Although this complex could be obtained as a solid in good purity, it readily decomposed and single crystals suitable for diffraction could not be obtained.

[Fe^{IV}(NTs)(TBP₈Cz⁺)] was characterised by UV – vis, DFT calculations, Mössbauer and EPR spectroscopy; revealing that this complex can be described as an iron (IV) – tosylimido complex (S = 1) with a radical localised in the corrolazine ligand as a π – cation radical (S = ½) with an antiferromagnetic coupling that gives S_{total} = 1/2. The –NTs transfer reactivity of this complex was tested with PPh₃ to generate the corresponding Ph₃P=NTs product. When crystals were grown from a reaction mixture of [Fe^{IV}(NTs)(TBP₈Cz⁺)] and PPh₃ was obtained the new species [Fe^{IV}(NPPH₃)(TBP₈Cz)] (characterised by X – ray diffraction), presumably through Ts group removal from hydrolysis of Ph₃P=NTs product. [Fe^{IV}(NTs)(TBP₈Cz⁺)] also showed sluggish reactivity towards styrene aziridination.

Very recently Maron and co – workers reported the synthesis of an octahedral iron (II) complex [Fe^{II}(B₂Pz₄Py)(THF)], bearing a dianionic tetrapodal pentadentate diborate ligand.¹⁷⁶ This iron (II) species when reacted with different organic azides yielded the corresponding low – spin iron (III) – amido complexes ([Fe^{III}(N(H)R)(B₂Pz₄Py)] (R = Adamantyl, *p* – ^tBu – C₆H₄ and *p* – ^tBu – C₆H₄ – SO₂) instead of the expected iron (IV) – imido species ([Fe^{IV}(NR)(B₂Pz₄Py)]). Although no iron (IV) could be identified, this system allowed the synthesis of an iron (III) – imido radical species [Fe^{III}(•NR)(B₂Pz₄Py)] (R = *p* – ^tBu – C₆H₄) upon reaction of the iron (II) precursor with corresponding azide, but only after removal of THF ligand and relatively weak C – H bonds from the media that could act as substrates. DFT calculations and Mössbauer spectroscopy revealed this system was best described as a low – spin iron (III) centre (d⁵, S = ½) bonded to an S = ½ imido radical species, giving an S = 1 species. As expected from its electronic configuration, this imido radical species reacts with THF and toluene (BDE = 89 kcal/mol) at room temperature in the abstraction of a hydrogen (k₂ = 1.60 · 10⁻³ M⁻¹s⁻¹) to yield the corresponding iron (III) – amido derivative ([Fe^{III}(N(H)^tBu)(B₂Pz₄Py)]. A KIE >300 was found by IR spectroscopy in the reaction with THF/THF – D₈.

In addition to the reported iron (III) and iron (IV) imido – species, to the best of our knowledge, exists one unique iron (V) – imido complex. This species is analogue to the iron (V) – oxo species (d³ configuration). The iron (V) species was characterised as a low – spin bis(imido)iron (V) supported by a bulky monodentate aryl ligand (Figure I.11), and was synthesised by reaction of the corresponding iron (I) species with two equivalents of adamantyl azide, via oxidative N₂ extrusion from the azide. It was remarkably stable and could be characterised by X – ray diffraction, magnetic susceptibility and DFT calculations. The iron atom has planar three – coordinate geometry with Fe – N distances of 1.642 and 1.619 Å, and Fe – N – C angles of 160.7 and 156.6 °. The bond distances are comparable to the ones found in the tetrahedral iron (IV) – imido species. The synthesised new species is assumed to be stable due to the metal is highly hindered, indeed when the iron (I) complex was reacted with the more steric demanding (2, 5 – mesityl)phenyl azide only one imido moiety could access to the metal, leading to an imido species (presumably iron (III)) that was capable to abstract one hydrogen from methyl on the mesitylene to generate a dimeric iron – amido species (Figure I.11, right).¹⁷⁷

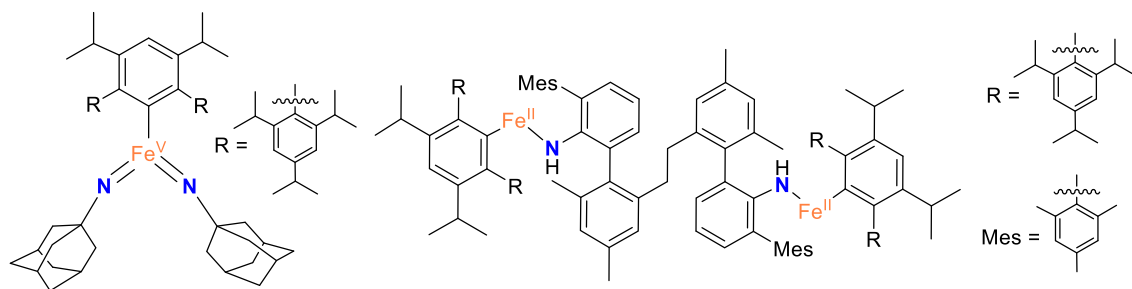


Figure I.11. (Left) Crystallographically characterised iron (V) – bis(imido) species; (right) dimeric species formed from reaction of iron (I) precursor with (2, 5 – mesityl)phenyl azide.

In addition to these structurally characterised iron (IV) – imido species, a number of iron catalysed C – N bond forming reactions have been described and usually suggested to be mediated by high – valent iron – imido species (Figure I.12). In this regard, in 2008 Che and co – workers reported the $[\text{Fe}^{\text{II}}(\text{Cl}_3\text{terpy})_2]^{2+}$ complex, capable of performing highly efficient catalytic C – H intermolecular aziridination of styrenes and terminal alkenes, as well as the intramolecular amination of benzylic C – H bonds at room temperature. ESI – MS analysis of the reaction of iron (II) species with an excess of PhINTs revealed the formation of an ion cluster attributable to an $[\text{Fe}^{\text{IV}}(\text{NTs})(\text{Cl}_3\text{terpy})_2]^{2+}$ species.¹⁷⁸ Some years later, Che and co – workers reported the catalytic amination of benzylic and alkylic aldehydes, mediated by iron salts and different N and P donor ligands, using PhINTs as oxidant at room temperature. Analogously to the previous work, ESI – MS analysis of a reaction mixture of FeCl_2 , terpy ligand and PhINTs revealed a cluster ion attributable to $[\text{Fe}^{\text{IV}}(\text{NTs})(\text{H}_3\text{terpy})_2]^{2+}$ species.¹⁷⁹

Subsequently Betley *et al.* reported the catalytic amination of different substrates by a dipyrromethene iron (II) species, $[\text{Fe}^{\text{II}}(\text{Cl})(\text{Ph}_3\text{Ph} - \text{pyac})]$, in combination with organic azides. The active species was assigned by Mössbauer, magnetic moment analysis and X – ray diffraction to a high – spin iron (III) ($S = 5/2$) centre coupled to an imido radical ($S = 1/2$). This species was capable to perform toluene amination, abstraction of a hydrogen from CHD, PMe_2Ph imination and styrene aziridination under mild conditions (r.t.).¹⁸⁰

In 2012 Paradine and White reported the intramolecular C – H amination of a wide variety of sulfamate esters by using $[\text{Fe}^{\text{III}}(\text{Pc})]\text{Cl}$ (Pc = phthalocyanine) as catalyst at room temperature. $\text{PhI}(\text{OPiv})_2$ was used as oxidant and a silver salt was required as additive to achieve optimal conditions. The system was capable to selectively perform aminative cyclisation of allylic substrates with good yields, over the aziridination of the styrenyl, trisubstituted or terminal allylic double bonds. Moreover the system showed selectivity towards the weaker C – H bonds (allylic > benzylic > 3° > 2° > 1°) and stereoretention in tertiary C – H centres, although scrambling was observed in the allylic amination reactions.¹⁸¹

In 2013 Betley and co – workers reported a system capable to aminate C – H bonds, catalysed by an iron (II) dipyrinato complex $[\text{Fe}^{\text{II}}(\text{Cl})(\text{Ad} - \text{pyac})]$. The reaction was used to synthesise N – heterocycles in good yields by intramolecular cyclisation of simple linear azides. This system was suitable for allylic, benzylic or alkylic (*i.e.* 3° , 2° and even 1°) C – H bond amination to generate pyrrolidines at 65°C . Although the formation of final products in catalytic amounts required the presence of an *in situ* protecting reagent, to overcome product inhibition of catalyst. The authors also studied competence of this methodology in the

synthesis of different ring sizes, being able to generate pyrrolidines, piperidines and azetidines working in stoichiometric conditions at room temperature. The active species was suggested to be an iron (III) – imido radical that would abstract a hydrogen from the C – H bond (supported by KIE studies) and followed by a radical rebounding to form the iron (III) with product bounded to the metal.¹⁸² Subsequently, the authors studied the ability of $[\text{Fe}^{\text{II}}(\text{Cl})(\text{Ad} - \text{pyac})]$ in the amination of different *para* substituted toluene substrates (46 – 60 % yields) and also in the aziridination of styrenes, achieving good yields (75 - 85 %) with different azides. On the other hand $[\text{Fe}^{\text{II}}(\text{Cl})(\text{tBu} - \text{pyac})]$ was capable to aminate allylic substrates, although higher temperatures or catalyst loading were required.¹⁸³

The same year, Che and co – workers reported the amination of a wide range of substrates catalysed by the $[\text{Fe}^{\text{II}}(\text{qpy})]^{2+}$ complex (qpy = quinquepyridine), and using $\text{PhI}(\text{OAc})_2$ or PhINTs as oxidants. This complex is the only non – heme example capable of selectively perform intermolecular amination of unactivated C – H (sp^3) bonds. Being capable to achieve high to good yields in intramolecular C – H (benzylic) amination of sulfamate esters, intermolecular amination of benzylic and allylic C – H (sp^3) (*i.e.* toluene, xanthene), intramolecular amination of natural products derivatised with sulfamate esters (steroids and terpenes), and cycloalkane amination (*i.e.* cyclohexane, adamantane). ESI – MS studies of a mixture of iron (II) complex and an excess of PhINTs revealed the presence of a cluster ion attributable to a $[\text{Fe}^{\text{IV}}(\text{NTs})(\text{qpy})]^{2+}$, but also a second cluster ion, only observable with an excess of PhINTs , that would match either a $[\text{Fe}^{\text{VI}}(\text{NTs})_2(\text{qpy})]^{2+}$ or $[\text{Fe}^{\text{II}}(\text{TsN}=\text{NTs})(\text{qpy})]^{2+}$ species, unfortunately no conclusive data could be obtained and the nature of that species remained ambiguous. Although an analogous species could not be found in the same experiments neither with $[\text{Fe}^{\text{II}}(\text{N4Py})(\text{MeCN})](\text{ClO}_4)_2$ nor $[\text{Fe}^{\text{II}}(\text{Cl}_3\text{terpy})_2](\text{ClO}_4)_2$, both of them unable to oxidise cyclic alkanes (*i.e.* cyclohexane).¹⁸⁴

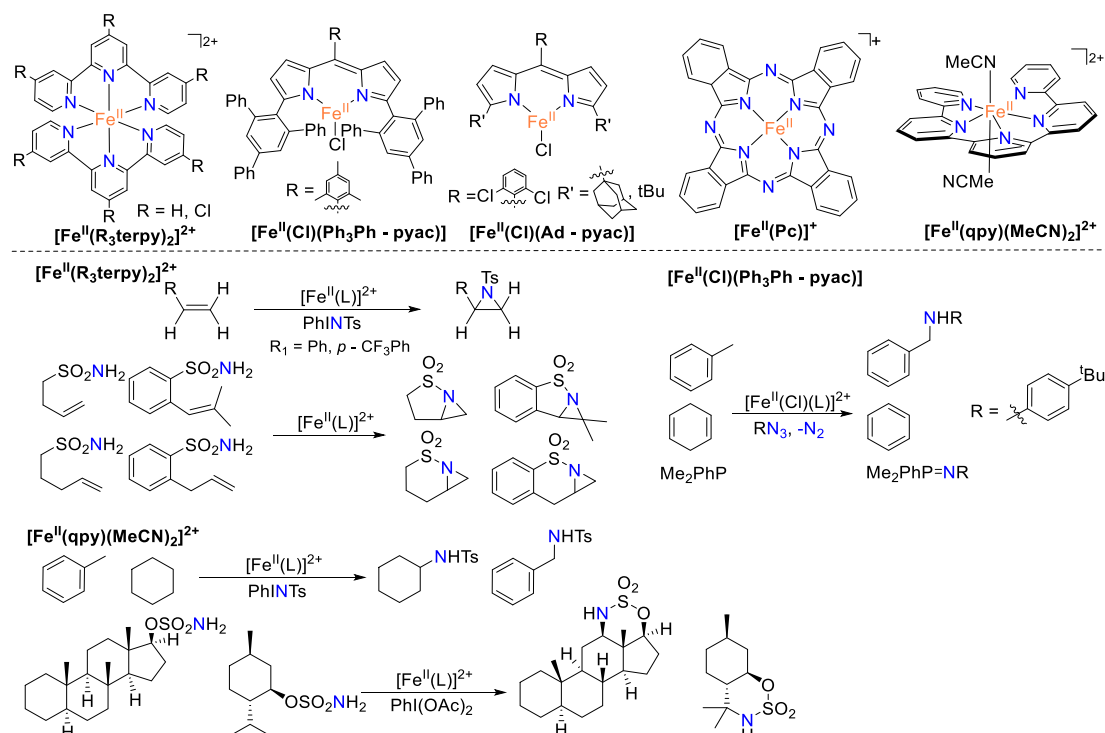


Figure I.12. Catalytically competent iron species involved in the formation of C – N bonds and representative reactions suggested to be mediated by high – valent iron – imido species.

I.2.4. High – valent iron – nitrido species [Fe \equiv N]

Iron – nitrido species have been postulated in the Haber – Bosch process¹⁸⁵ and also in the dinitrogen activation performed by nitrogenase enzymes. Haber – Bosch process is one of the most important industrial processes that sustains the production of ammonia and therefore the agriculture.¹⁸⁶ While nitrogenase enzymes are essential for life, as they are the responsible for the incorporation of inorganic nitrogen from the atmosphere to the biological cycle.¹⁸⁷ Although, there is no direct evidence of implication of high – valent iron species in N₂ fixation, it is known that FeMo nitrogenase possess a FeMo cofactor with a [Fe₇ – Mo – S₉] cluster.¹⁸⁸⁻¹⁹⁰ Despite the structural information, the mechanism of N₂ activation remains unclear, and the dinitrogen activation process is thought to occur at a single iron site in the FeMo cofactor.^{191,192} To shed light into these processes and to prove the involvement of high – valent iron – nitrido intermediates in the biological dinitrogen reduction, bioinorganic chemist have developed bioinspired compounds, involving high – valent iron – nitrido species. Well – described model compounds can provide insights into the mechanism of such enzymatic reactions and imitate the nitrogenase reactivity, such as in N₂ reduction to generate NH₃.

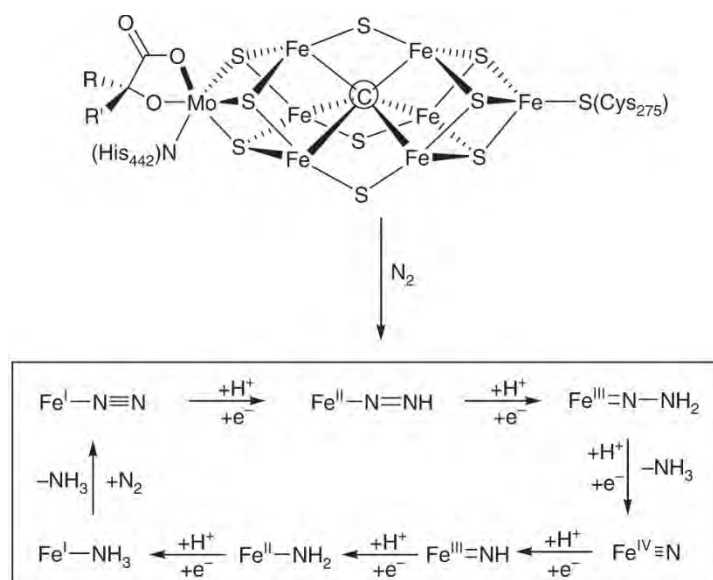
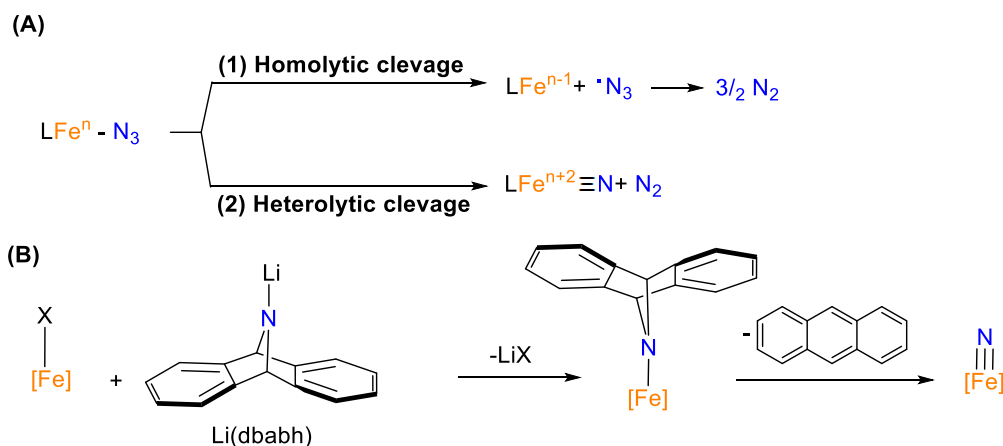


Figure I.13. Structure of the iron – molybdenum cofactor (FeMoco) of the nitrogenase enzyme with a central carbide atom and proposed intermediates in the N₂ activation process (figure extracted from ref. 55).

Due to its electronic configurations, iron (IV) – and iron (V) – imido (Fe = NR) species are analogue to the iron (IV) – and iron (V) – oxo (Fe = O) complexes. Also the iron – nitrene species (Fe \equiv N) are isoelectronic to the iron – oxo species and possess a nitrogen moiety with a -3 valence.

The first iron – nitrido examples were reported in 1989 by Wagner and Nakamoto. They synthesised the heme species [Fe^V(N)(OEP)], [Fe^V(N)(TPP)] and [Fe^V(N)(TMP)] (octaethyl – , tetraphenyl – and tetramesityl – porphyrinate anions) by laser photolysis of the corresponding [Fe^{III}(N₃)(L)] precursors at 30 K.¹⁹³ Characteristic stretching $\nu(\text{Fe} \equiv \text{N})$ were found at 876 cm⁻¹ (OEP, TPP) and 873 cm⁻¹ for TMP by Raman resonance, and confirmed by ⁵⁴Fe and ¹⁵N isotopic substitutions. No further spectroscopic characterisation could be performed but, by analogy to the isoelectronic manganese – oxo porphyrins, were tentatively assigned as high – spin species.

The first non-heme high-valent species was reported in 1999 and since then only few new examples have been prepared, usually due to their instability and high reactivity. The existing examples are scarce but exist in pseudo-tetrahedral and pseudo-octahedral symmetry as well as ranging from +4 to +6 oxidation states (Figure I.14).^{71,185-187} There are two main strategies to achieve the formation of high-valent nitrido species: A) Iron-azide photolysis and B) Anthracene extrusion from [Fe](dbabh) complexes. The irradiation of a metal-azide species may lead to two different scenarios (Scheme I.8): (1) Photoreduction of the metal centre through an homolytic cleavage of the Fe-N bond resulting in one electron reduction of the metal, and generation of an azide radical, which in turn reacts with a second azidyl radical, finally producing N₂ gas; or (2) heterolytic N-N cleavage resulting in a 2-electron oxidation of the metal centre with concomitant formation of N₂ gas.



Scheme I.8. A) Photolytic reactivity of iron-azide complexes. (1) Homolytic cleavage of Fe-N and photoreduction of Fe centre; (2) Heterolytic cleavage of N-N and photooxidation of iron centre. B) Anthracene extrusion strategy to generate high-valent iron-nitrido species.

I.2.4.1. Pseudo-octahedral iron-nitrido species

These high-valent species are highly unstable and, to the best of our knowledge only three examples are known, all of them prepared by photolysis of an iron-azide moiety with concomitant N₂ extrusion to give the photooxidised product.

In 1999 Wieghardt and co-workers reported the synthesis of the hexacoordinate *cis* and *trans* - [Fe^{III}(N₃)₂(cyclam)]⁺ in high and low spin configuration respectively. Interestingly, when these species were photolysed in solution at -35 °C in MeCN they yielded dimeric (Fe^{III} - N - Fe^V) species, presumably through a highly-reactive iron (V) decomposition pathway. Photolysis of initial high-spin *cis* - iron (III) - azido in frozen matrix led to the photoreduction by one-electron of the metal, forming the high-spin iron (II) via homolytic Fe-N cleavage. In contrast, when the low-spin *trans* isomer was irradiated at 4 or 77 K, a mixture of iron (II) species and iron (V) (54 % yield) was obtained. This new high-valent species was characterised as the high-spin [Fe^V(N)(N₃)(cyclam)]²⁺ by Mössbauer ($\delta = -0.04$ mm/s, $\Delta E_Q = -1.90$, 77 K) and EPR ($g \approx 4$ and 2).¹⁹⁴

In 2000, the same group reported the synthesis of a new hexacoordinate iron (V) - nitrido species, [Fe^V(N)(cyclam-ac)]⁺, through photolysis of the iron (III) - azide precursor.⁷¹ Irradiation of the iron (III) - azido species in solution at -35 °C yielded mainly the photoreduced iron (II) derivative and a minor

dimeric product $\text{Fe}^{\text{III}} - \text{N} - \text{Fe}^{\text{IV}}$ ($\approx 20\%$). In contrast, when $[\text{Fe}^{\text{III}}(\text{N}_3)(\text{cyclam} - \text{ac})]^+$ was irradiated in a frozen matrix, in MeCN at 77 K, the major product was found to be the $[\text{Fe}^{\text{V}}(\text{N})(\text{cyclam} - \text{ac})]^+$ (82 % yield), which was characterised by Mössbauer ($\delta = -0.04$ mm/s, $\Delta E_{\text{Q}} = -1.67$ mm/s) and EPR spectroscopies. Evidencing the dependence of product distribution on the supporting matrix. Surprisingly no photoreduced products were detected under frozen matrix with this system. The $[\text{Fe}^{\text{V}}(\text{N})(\text{cyclam} - \text{ac})]^+$ and the previously reported $[\text{Fe}^{\text{V}}(\text{N})(\text{N}_3)(\text{cyclam})]^+$ had initially been assigned as high – spin species, but this was proved to be erroneous some years later by Aliaga – Alcalde and co – workers.¹⁹⁵ Using a combination of theoretical and experimental techniques the ground state of $[\text{Fe}^{\text{V}}(\text{N})(\text{cyclam} - \text{ac})]^+$ was assigned to a d^3 system with an unusual nearly orbitally degenerated $S = \frac{1}{2}$ spin state. Furthermore this species was characterised by magnetic susceptibility measurements and XAS ($E_{\text{pre-edge}} = 7114.2$ eV; $E^{\circ} = 7124.1$ eV). Moreover EXAFS revealed a short Fe – N bond of 1.60 Å with a bond order of 2.5, in agreement with an oxidation state of +5.¹⁹⁵ Subsequently, Petrenko *et al.* established the $\nu(\text{Fe} - \text{N})$ at 864 cm^{-1} by Nuclear Resonance Vibrational Spectroscopy (NRVS) in combination with DFT calculations.¹⁹⁶

Comparing the Mössbauer isomer shifts from complexes $[\text{Fe}^{\text{V}}(\text{N})(\text{N}_3)(\text{cyclam})]^+$ and $[\text{Fe}^{\text{V}}(\text{N})(\text{cyclam} - \text{ac})]^+$ ($\delta = -0.04$ mm/s for both), with that of its iron (IV) – oxo analogues ($\delta = 0.01$ mm/s and $\delta = -0.04$ mm/s) but also with iron (V) – oxo species $[\text{Fe}^{\text{V}}(\text{O})(\text{TAML})]^-$ and $[\text{Fe}^{\text{V}}(\text{O})(\text{bTAML})]^-$ ($\delta = -0.46$ and -0.44 mm/s respectively) is evidenced a more positive trend for iron – nitrido species. This behaviour had been explained from the higher covalence of Fe – N bond compared to the Fe – O bond.¹⁹⁷

Interestingly, the methylated version of cyclam – acetate ligand gave the high – spin ($S = 5/2$) complex $[\text{Fe}^{\text{III}}(\text{N}_3)(\text{Me}_3\text{cyclam} - \text{ac})]^+$. This complex was found to be photolytically unable to follow the photooxidation pathway to yield iron (V), and instead under photolysis gave a photoreduced iron (II) species. In contrast to that, $[\text{Fe}^{\text{III}}(\text{N}_3)(\text{Me}_3\text{cyclam} - \text{ac})]^+$ could be electrochemically oxidised to the $[\text{Fe}^{\text{IV}}(\text{N}_3)(\text{Me}_3\text{cyclam} - \text{ac})]^{2+}$, which upon irradiation at 650 nm in a frozen matrix could be photooxidised to yield the iron (VI) – nitrido species (73 % yield). The new high – valent compound, $\text{Fe}^{\text{VI}}(\text{N})(\text{Me}_3\text{cyclam} - \text{ac})]^{2+}$, was characterised by Mössbauer spectroscopy ($\delta = -0.23$ mm/s, $\Delta E_{\text{Q}} = -1.59$ mm/s), XAS ($E_{\text{pre-edge}} = 7115.1$ eV; $E^{\circ} = 7125.0$ eV) and EXAFS (Fe – N bond of 1.57 Å).¹⁹⁸ The $\text{Fe}^{\text{VI}}(\text{N})(\text{Me}_3\text{cyclam} - \text{ac})]^{2+}$ was the first coordination complex Fe^{VI} species ever reported, and the only known to date. This iron (VI) species was stable only in frozen matrix, decomposing towards iron (III) upon warming. Only one additional example is known for an iron (VI), the ferrate anion $[\text{Fe}^{\text{VI}}\text{O}_4]^{2-}$, a powerful oxidant used in organic synthesis.¹⁹⁹

In 2007, Berry and co – workers reported the synthesis of three high – spin iron (III) – azide species based on the 1,4,7 – triazacyclononane framework (Figure I.14) with two carboxylate arms, giving the pentadentate complexes $[\text{Fe}^{\text{III}}(\text{N}_3)((\text{AcO})_2\text{tacnR})]$ ($\text{R} = \text{Bn}, ^i\text{Pr}, p - \text{MeO} - \text{PhCH}_2$). These iron (III) species could be reversibly oxidised to the respective iron (IV) – azide complexes by using electrochemical techniques ($E_{1/2} \approx 1.5 - 1.6$ V vs SCE) and $[\text{Fe}^{\text{III}}(\text{N}_3)((\text{AcO})_2\text{tacnR})]$ ($\text{R} = \text{Bn}$ and ^iPr) redox processes were monitored by UV – vis, IR and Mössbauer spectroscopy. Remarkably when $[\text{Fe}^{\text{III}}(\text{N}_3)((\text{AcO})_2\text{tacn}^i\text{Pr})]$ was photolysed either in MeCN solution or in frozen matrix (77 K) photoreduction products were obtained, with no oxidative reactivity.²⁰⁰ This behaviour, together with the fact that the high – spin *cis* – $[\text{Fe}^{\text{III}}(\text{N}_3)_2(\text{cyclam})]^+$ and $[\text{Fe}^{\text{III}}(\text{N}_3)(\text{Me}_3\text{cyclam} - \text{ac})]^+$ were neither capable to follow photooxidative

pathway, lead to the postulate that only low – spin iron (III) – azido species are capable to photolitically evolve to iron (V).

In terms of reactivity the pseudo – octahedral high – valent iron – nitrido species are highly reactive and only stable in frozen matrix, *e.g.* N – N coupling has been documented in the thermal decomposition of $[\text{Fe}^{\text{V}}(\text{N})(\text{cyclam} - \text{ac})]^+$ and $\text{trans} - [\text{Fe}^{\text{V}}(\text{N}_3)(\text{N})(\text{cyclam})]^+$.²⁰¹ This prevented reactivity studies for such compounds towards organic substrates. As exception, Vöhringer and co – workers studied the photo – induced generation of an $[\text{Fe}^{\text{V}}(\text{N})(\text{N}_3)(\text{cyclam})]^+$ species from the $[\text{Fe}^{\text{III}}(\text{N}_3)_2(\text{cyclam})]^+$ precursor complex at room temperature in liquid solution, and investigated its reactivity (microseconds scale time) with anionic nucleophiles and electrophiles (*e.g.* phosphines), through laser flash photolysis combined with time – resolved Fourier – transform infrared spectroscopy (TR – FTIR).²⁰²

Previously, Schwarz and co – workers had studied the formation of $[\text{Fe}^{\text{V}}(\text{N})(\text{cyclam} - \text{ac})]^+$ cation in gas phase and proved its capacity to perform hydrogen atom abstraction reactivity (HAT) and the self – oxidation decomposition of this high – valent species in gas phase.²⁰³ Later on, the same group reported a polydentate aminoligand capable to stabilize the high – valent $[\text{Fe}^{\text{V}}(\text{N})(\text{NN}_4)]^{2+}$ species in gas phase, through N – N cleavage with concomitant N_2 release from the low – spin iron (III) – azide. Furthermore they studied its reactivity towards methanol, olefins and alkanes, being capable to perform nitrogen atom transfer (NAT) to methanol and some olefins (*e.g.* butadiene, cyclohexene and cyclohexadienes) but not to ethylene, 1 – butene or butane.²⁰⁴

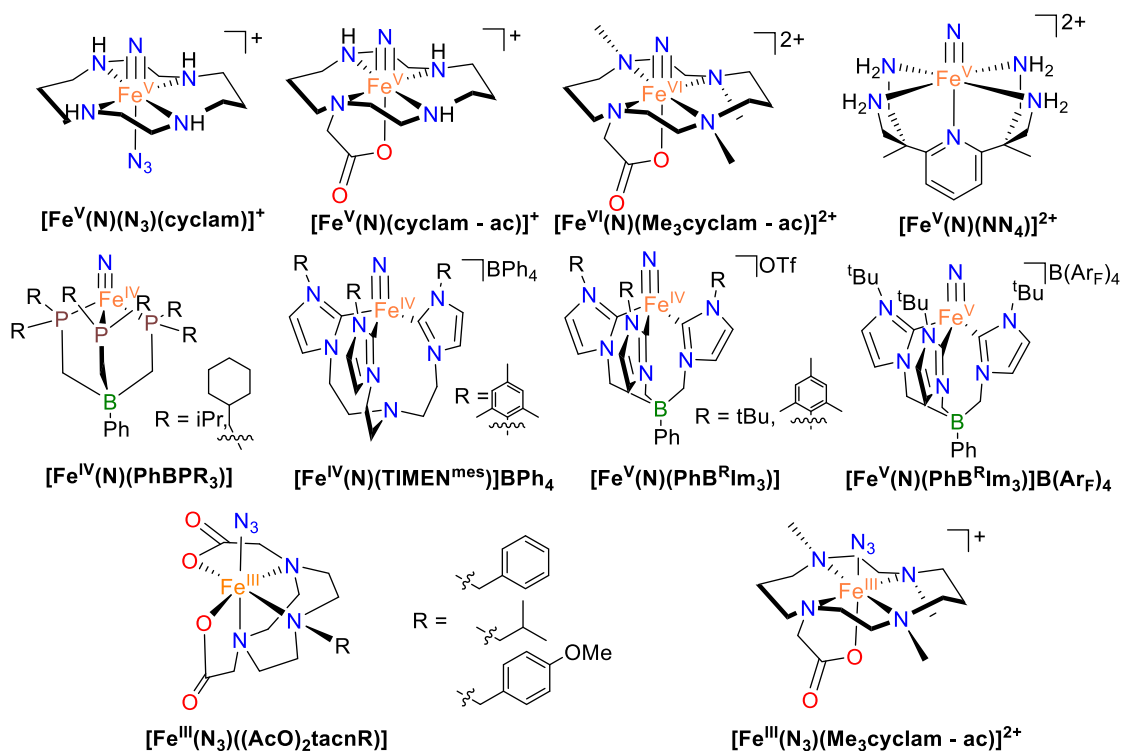


Figure I.14. First and second row, reported high – valent iron – nitrido species. Third row, high – spin iron (III) complexes prepared by Barry and co – workers²⁰⁰ and Wieghardt and co – workers.^{198,205}

I.2.4.2. Three – fold symmetric iron – nitrido species

This group of complexes englobes all the existing iron (IV) – nitrido species bearing tripodal ligands that confer them a three – fold symmetry, giving place to a pseudo – tetrahedral or trigonal pyramidal arrangement (Figure I.14, second row) that results in a $S = 0$ state for these complexes. Generally, this group of complexes show higher stabilities than the octahedral examples, allowing reactivity studies for some of them.

Peters and co – workers in 2004 reported the synthesis of tris(phosphino)borate complex $[\text{Fe}^{\text{IV}}(\text{N})(\text{PhBP}^i\text{Pr}_3)]$.²⁰⁶ The first terminal low – spin iron (IV) – nitrido complex, prepared by reaction at $-35\text{ }^\circ\text{C}$ of the $[\text{Fe}^{\text{II}}(\text{Cl})(\text{PhBP}^i\text{Pr}_3)]$ with $\text{Li}(\text{dbabh})$ ($\text{dbabh} = 2, 3: 5, 6$ – dibenzo – 7 – aza bicyclo[2.2.1]hepta – 2, 5 – diene) (Scheme I.8, path B). Upon warming up to room temperature, the system extruded anthracene and generated the high – valent iron species. $[\text{Fe}^{\text{IV}}(\text{N})(\text{PhBP}^i\text{Pr}_3)]$ was characterised by ^1H – , ^{31}P – and ^{15}N – NMR, UV – vis and IR spectroscopy (in solution) and was found to decompose to a dimeric $[(\text{Fe}^{\text{I}}(\text{PhBP}^i\text{Pr}_3))_2(\mu - \text{N}_2)]$ through a 6 – electron redox process. Later on, the analogous $[\text{Fe}^{\text{IV}}(\text{N})(\text{PhBPCH}_2\text{Cy}_3)]$ was reported, showing an interestingly higher stability due to the prevented dimerization decomposition by the bulkier ligand. Both $[\text{Fe}^{\text{IV}}(\text{N})(\text{PhBPR}_3)]$ ($\text{R} = ^i\text{Pr}$ and CH_2Cy) were characterised by Mössbauer, XAS and EXAFS spectroscopy. Mössbauer data ($\delta = -0.34\text{ mm/s}$, $\Delta E_{\text{Q}} = 6.01\text{ mm/s}$ for both) are much lower to that found for octahedral iron (V) – nitrido species and with higher quadrupole splitting. XAS showed intense features at $E_{\text{pre-edge}} = 7113.0$ and 7113.1 eV respectively, values $\approx 1\text{ eV}$ lower than those found for the iron (V) – nitrene octahedral species; the high intensity of these features indicate covalent Fe – N bond present in these complexes. EXAFS exposed short Fe – N bonds of $1.51 - 1.55\text{ \AA}$, even shorter than the Fe – N bond in the iron (VI) species reported (1.57 \AA).^{207,208} Addition of PPh_3 or PET_3 to $[\text{Fe}^{\text{IV}}(\text{N})(\text{PhBP}^i\text{Pr}_3)]$ generated the corresponding $S = 2$ iron (II) – phosphinimato species $[\text{Fe}(\text{N}=\text{PR}_3)(\text{PhBP}^i\text{Pr}_3)]$ (two electron transfer reactivity). Importantly, nitride ligand was a source of NH_3 (41 – 45 % yield) in the presence of 3 equivalents of protons ($[\text{LuH}][\text{BPh}_4]$) and electrons (CoCp_2), endorsing the believe for nitrido species to be involved in biological N_2 reduction.²⁰⁶

In 2008 Meyer and co – workers reported the first crystallographically characterised iron – nitrido species, the $[\text{Fe}^{\text{IV}}(\text{N})(\text{TIMEN}^{\text{mes}})]^+$. This system bore a tris(imidazolyl)carbene ligand with mesityl groups, was prepared by photolysis of the corresponding iron (II) – azide and was also characterised by FT – IR, DFT, ^1H – and ^{15}N – NMR and Mössbauer spectroscopy ($\delta = -0.27\text{ mm/s}$, $\Delta E_{\text{Q}} = 6.04\text{ mm/s}$) as an $S = 0$ iron (IV). The isomer shift differs a little from that of $[\text{Fe}^{\text{IV}}(\text{N})(\text{PhBPR}_3)]$, proposed to occur as consequence of a certain degree of ligand – to – metal (LMCT) back bonding from the π system from NHC ligand to the empty d orbitals from iron. This complex was stable at room temperature, due to the bulky mesitylene groups that prevented dimerization decomposition and allowed crystallographic characterisation, revealing a short Fe – N bond of 1.53 \AA and evidencing this complex was best described as a trigonal pyramidal system.²⁰⁹ The reaction of iron (IV) species with different oxidants in MeCN lead to the postulated formation of a highly – reactive transient iron (V) – nitrido that would attack an iron – carbene bond to insert the nitrido moiety into a Fe – C bond. The resulting iron (II) – imino species was characterised by ESI – MS and X – ray diffraction.²¹⁰

Subsequently Smith and co-workers combined the previous systems into the phenyl-tris(1-*tert*-butylimidazol-2-ylidene)borate ligand, (PhB(^tBuIm)₃). The pseudo-tetrahedral S = 0 [Fe^{IV}(N)(PhB(^tBuIm)₃)] was generated by photolysis of the iron(II)-azide species and characterised by ¹H- and ¹⁵N-NMR, UV-vis, Raman resonance and X-ray diffraction (Fe-N = 1.51 Å).²¹¹ This complex, unlike the previous borate system from Peters and co-workers, did not react with protons and electrons, although reacted with PPh₃, yielding the iron(II)-phosphiniminato species. Subsequently, the analogous complex [Fe^{IV}(N)(PhB(MesIm)₃)] was prepared by an analogous strategy and characterised by IR, ¹H- and ¹⁵N-NMR and X-ray diffraction (Fe-N = 1.50 Å). This complex shows remarkable reactivity, such as the N transfer to phosphines²¹² or cyclohexadienes²¹³ and, most remarkably, the synthesis of ammonia (74 % yield) from reaction with TEMPO-H.²¹⁴

The most remarkable of these species is the reaction of [Fe^{IV}(N)(PhB(^tBuIm)₃)] with Fc(B(Ar_F)₄) to generate the corresponding low-spin (S = ½) [Fe^V(N)(PhB(^tBuIm)₃)]⁺, the first isolated example of an iron(V)-nitrido complex. Moreover it was characterised by DFT, Mössbauer (δ = -0.45 mm/s, ΔE_Q = 4.78 mm/s), EPR (g = 2.29, 1.97) and X-ray diffraction (Fe-N bond 1.50 Å). Remarkably, this complex was capable to generate NH₃ in 90 % yield at -78 °C from the reaction with 15 equivalents of water and 3 equivalents of cobaltocene and Iron(II) was concomitantly recovered suggesting an uncommon 3 e⁻ reactivity.²¹⁵

1.2.5. Iron carbenes and C-C bond formation

High-valent iron-oxo and iron-imido species have been proved as highly reactive species, capable to perform the functionalisation of unactivated C-H bonds and generate new C-O and C-N bonds. Following the series, the next step is the formation of C-C bonds through analogous iron-carbene species. Actually exist a number of strategies and systems capable to functionalise C-H bonds, although usually imply the use of expensive metals such as rhodium, iridium or palladium.^{4,5} Nevertheless, iron is more attractive since it is much more abundant (cheap) and biocompatible compared to these other metals, as it is involved in a wide range of biological processes.^{144,216} An appealing strategy to synthesise new C-C bonds is through the generation of non-heteroatom-stabilised metal-carbene intermediates and this can be achieved by the use of diazo compounds (RR'C=N=N), specially diazoacetates. Such species are easily prepared from readily accessible precursors and can be induced to undergo a wide variety of chemical transformations under mild conditions. The transition-metal-catalysed transformations of diazo compounds are widely used in organic synthesis, mainly with expensive metals like rhodium, gold or silver. Although examples with copper and iron exist, the latter belong almost exclusively to heme systems.²¹⁷⁻²¹⁹ Moreover, the decomposition of diazo compounds by transition metal complexes is also convenient from an atom-economy perspective, since there are no by-products other than N₂ gas and sometimes the olefins generated from dimerization of diazo species. In the following lines will be briefly discussed some of the existing non-heteroatom iron-carbene systems and its application in the formation of new C-C bonds in combination with diazo compounds.

Mansuy and co-workers reported in 1977 the first iron-carbene that was isolated. By treatment of the heme [$\text{Fe}^{\text{II}}(\text{TPP})$] (TPP = tetraphenyl porphyrinato) with CCl_4 in presence of excess of a reducing agent (e.g. iron powder) was obtained the corresponding [$\text{Fe}^{\text{II}}(\text{CCl}_2)(\text{TPP})$] complex. This new species was assumed to be an iron (II) due to its similarity in the UV-vis to similar iron (II) heme species, but also due to its diamagnetic ^1H - and ^{13}C -NMR spectra and the need of a reducing agent to prepare it.²²⁰ In the same work, by using this method the authors could prepare a series of different [$\text{Fe}^{\text{II}}(\text{CX}_2)(\text{TPP})$] species ($\text{CX}_2 = \text{CBr}_2, \text{CBrCl}, \text{CF}_2, \text{C}(\text{Cl})\text{CO}_2\text{Et}$, etc). Later on, they reported the X-ray diffraction characterisation of [$\text{Fe}^{\text{II}}(\text{CCl}_2)(\text{TPP})(\text{H}_2\text{O})$] that confirmed the complex structure. The Fe-C bond was found to be 1.83 Å with a water molecule in *trans* position to the carbene.²²¹ That was the first structure for an iron-porphyrin carbene complex. Some years later, Suslick and co-workers reported the Mössbauer spectra for complex [$\text{Fe}^{\text{II}}(\text{CCl}_2)(\text{TPP})$], in contrast to the previous spectral data this technique showed values more typical for an iron (IV) species, $\delta = 0.10$ and $\Delta E_{\text{Q}} = 2.28$ mm/s.²²²

An alternative method to prepare iron-carbene species is through the decomposition of diazo compounds. With this methodology You and co-workers reported in 2002 the synthesis of the series [$\text{Fe}^{\text{II}}(\text{CPhR})(\text{F}_{20}-\text{TPP})$] ($\text{R} = \text{Ph}, \text{CO}_2\text{Et}, \text{CO}_2\text{CH}_2\text{CH}=\text{CH}_2$) and [$\text{Fe}^{\text{II}}(\text{CPh}_2)(\text{F}_{20}-\text{TPP})(\text{MeIm})$], prepared from the corresponding pentacoordinate iron (II) and the diazo compound.²²³ The crystal structure could be obtained for [$\text{Fe}^{\text{II}}(\text{CPh}_2)(\text{F}_{20}-\text{TPP})$] and [$\text{Fe}^{\text{II}}(\text{CPh}_2)(\text{F}_{20}-\text{TPP})(\text{MeIm})$] with Fe-C distances of 1.79 and 1.83 Å respectively, while the latter was similar to that found for [$\text{Fe}^{\text{II}}(\text{CCl}_2)(\text{TPP})(\text{H}_2\text{O})$] the first one was significantly shorter. It is worth to mention that [$\text{Fe}^{\text{II}}(\text{CCl}_2)(\text{TPP})(\text{H}_2\text{O})$] and [$\text{Fe}^{\text{II}}(\text{CPh}_2)(\text{F}_{20}-\text{TPP})(\text{MeIm})$] are hexacoordinate with a donor molecule in *trans* disposition to the carbene moiety, which possibly elongates the Fe-C bond. The four new iron-carbene species were assigned as iron (II) complexes, from similarity of the diamagnetic ^1H - and ^{13}C -NMR, UV-vis spectra and the X-ray distances with that of [$\text{Fe}^{\text{II}}(\text{CCl}_2)(\text{TPP})(\text{H}_2\text{O})$]. Interestingly, as previously observed for [$\text{Fe}^{\text{II}}(\text{CCl}_2)(\text{TPP})(\text{H}_2\text{O})$], the Mössbauer spectra revealed values that seemed surprisingly low for an iron (II) species ($\delta = 0.03$ and $\Delta E_{\text{Q}} = 2.34$ mm/s) and more typical for an iron (IV) species.²²³ All the reported iron-carbene species bearing a porphyrin ligand have been assigned as low-spin iron (II) species although there is an ongoing discussion about the oxidation state of the metal.²²⁴ As a general trend these species show diamagnetic ^{13}C -NMR spectra with deshielded C(carbene) with shifts 220–390 ppm, typical from iron (II) in low-spin, which contrast with Mössbauer data.^{220,223,225-227}

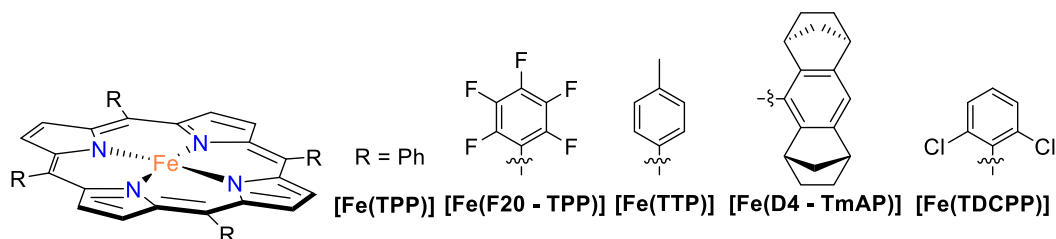
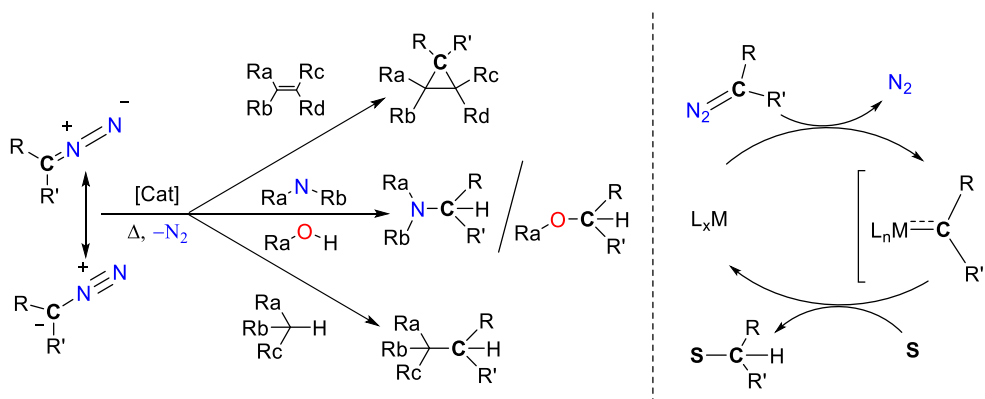


Figure I.15. Selected structures of reported iron porphyrin complexes used to prepare iron-carbene species.

These species show potential reactivity in the formation of C-C bonds. For example [$\text{Fe}^{\text{II}}(\text{CCl}_2)(\text{TPP})$] reacted with primary amines to generate the corresponding isonitrile complexes. Suslick and co-workers reported also the photoactivation of [$\text{Fe}^{\text{II}}(\text{CX}_2)(\text{TPP})$] species ($\text{CX}_2 = \text{CBr}_2, \text{CClF}$ and CCl_2) to generate the free carbenes, which reacted with alkenes such as styrene, cyclohexene, hexane and cyclooctene to generate

the cyclopropane products in good to excellent yields.²²⁸ On the other hand $[\text{Fe}^{\text{II}}(\text{C}(\text{Ph})\text{CO}_2\text{Et})(\text{F}_{20}-\text{TPP})]$ was capable to stoichiometrically cyclopropanate *p*-substituted styrenes at 60 °C, with no need of photoactivation. A Hammett plot revealed an electrophilic intermediate species with $\rho = -0.41$, slope comparable to the value obtained in the reaction with $[\text{Fe}^{\text{II}}(\text{TTP})]$ with *p*-substituted styrenes and EDA ($\rho = -0.68$), suggesting common related species.²²⁹ In contrast, $[\text{Fe}^{\text{II}}(\text{CPh}_2)(\text{F}_{20}-\text{TPP})]$ was not able to perform such reactivity, but was capable to catalytically cyclopropanate different styrenes with ethyl diazoacetate (EDA), with good yields and *trans:cis* selectivity up to $\approx 7:1$ ratio. Interestingly, when $[\text{Fe}^{\text{II}}(\text{CPh}_2)(\text{F}_{20}-\text{TPP})(\text{MeIm})]$ was reacted with excess of styrene at 80 °C it gave the cyclopropane product in 53 %, this change was rationalised by a *trans* effect of MeIm evidenced by the elongated Fe – C bond. More remarkably, complexes $[\text{Fe}^{\text{II}}(\text{CPh}_2)(\text{F}_{20}-\text{TPP})]$ and $[\text{Fe}^{\text{II}}(\text{C}(\text{Ph})\text{CO}_2\text{Et})(\text{F}_{20}-\text{TPP})]$ reacted with THF, cumene and cyclohexene to insert the CRR' moiety into the α C – H bond, the benzylic and allylic position, respectively. The yields obtained ranged from 15 – 88 % depending on substrate and conditions, these were the first examples of a carbene insertion into saturated C – H bonds.²²³

In addition to these stoichiometric reactivity with isolated iron – carbene species, the porphyrinic iron complexes have been widely studied in catalytic reactions, specially in the cyclopropanation of alkenes.^{218,230} These reactions are proposed to proceed through an iron – carbene species (Scheme I.9) based on the high selectivities observed and the formation of maleate/fumarate by – products and, more importantly, that some examples were observed by ESI – MS or ^1H – NMR spectroscopy.^{231,232} Some catalytic systems usually require the introduction of diazocompounds into the reaction mixture by slow addition over several minutes or hours to avoid undesired by – products (dimerization products of diazo compounds).



Scheme I.9. Iron catalyzed transformations of diazo compounds and the generally proposed metal mediated catalytic mechanism.

Iron porphyrin complexes are very active in the cyclopropanation of terminal olefins with diazo compounds and show high selectivity towards *trans* product. For example in 1995 Woo and co – workers reported the cyclopropanation of styrene with $[\text{Fe}^{\text{II}}(\text{TTP})]$ and EDA. The system achieved good diastereoselectivity and high turnover number at room temperature (*trans:cis* 8.8:1, 1300 TON) and was found to improve by lowering the temperature (*trans:cis* 29:1 at -78 °C). Donor solvents such as THF were found to improve the selectivity, although moderately. Furthermore the authors studied the catalytic capacity of the air stable $[\text{Fe}^{\text{III}}(\text{Cl})(\text{TTP})]$ complex in the cyclopropanation of styrene with EDA. As the iron (II) was the active species the initial catalyst had to be initially reduced by the EDA, but that required

higher temperatures (40 °C), having a negative effect in the selectivity. The addition of one – electron reducing agent (CoCp₂) into the reaction mixture at room temperature allowed reaching selectivities similar to that obtained with [Fe^{II}(TTP)] (8.7:1). The use of a more electron – deficient porphyrin [Fe^{III}(Cl)(F₂₀ – TPP)], more easily reduced by the EDA, allowed the cyclopropanation of alkenes at room temperature with high TON (4000) and good selectivities (3.3 – 6:1) without the need of reducing agents.²²⁹ Tagliatesta, in 2003, reported the cyclopropanation of styrene derivatives with the bulky porphyrin [Fe^{III}(Cl)(TDCPP)], EDA and cobaltocene at room temperature with high yields (up to 97%) and remarkable selectivity (*trans:cis* 78:1).²³³ In general electron – rich terminal alkenes are efficiently cyclopropanated with diazoacetates, in contrast to that 1, 2 – disubstituted alkenes did not react or gave low yields and maleate and fumarate were detected as products of the reactions.²²⁹ Alkene cyclopropanation can also take place using different diazoaryl compounds, such as in the cyclopropanation of styrene with [Fe^{II}(TTP)] and *p* – tolyldiazomethane (79 %, *trans:cis* 14:1) or the remarkably inverse selectivity found with mesityldiazomethane and styrene with this complex (*trans:cis* 1:2). Additionally the same system could functionalise *trans* – β – styrene with mesityldiazomethane (35 % yield), but not with EDA or trimethylsilyldiazomethane as diazo source.²³¹

In addition to the diazoacetate and diazoaryl compounds, diazo derivatives can be generated *in situ*, this strategy is quite useful for unstable or explosive reagents. For example Carreira and co – workers reported the diastereoselective cyclopropanation of styrenes with [Fe^{III}(Cl)(TPP)] through the *in situ* generation of the trifluorodiazomethane compound in aqueous media at room temperature.²³⁴ Later on, the same group reported the *in situ* generation of diazomethane to cyclopropanate terminal alkenes, in good to high yields (64 – 84 %) using [Fe^{III}(Cl)(TPP)] under mild conditions in aqueous media.²³⁵

The enantiomeric version of cyclopropanation reaction has also been studied, *e.g.* in 2006 Che and co – workers reported the reaction of [Fe^{III}(D4 – TmAP)] with styrenes and EDA, the reaction gave good yields (56 – 72 %) and was highly diastereospecific (*trans:cis* up to 23:1) and stereoselective for *trans* product (43 – 86 % *ee*). A Hammett study revealed a slope of $\rho = -0.57$ for the reaction with *p* – substituted styrenes, similarly to the observed slope for [Fe^{II}(TTP)]. Additionally an enhancement of selectivity towards *trans* product was observed upon addition of an axial ligand such as organic bases (*trans:cis* from 12:1 to 33:1), no effect was observed on *ee* for *trans* product. The detection of [Fe^{III}(CH(CO₂Et)(D4 – TmAP)(X)] (X = Py or MeIm) by ESI – MS studies allowed the proposal of a carbene complex as the active species.²³²

The iron – porphyrin species are also capable to catalyse other reactions through decomposition of diazo compounds. An example is the insertion of carbenoids into N – H bonds of aliphatic and aromatic amines in high yields with short reaction times.²¹⁸ For example Woo and co – workers reported the N – H insertion of EDA into piperidine, aniline and different primary and secondary amines catalysed by [Fe^{III}(Cl)(TPP)].²³⁶ The analogous reactivity with alcohols have been also reported.²³⁷

Furthermore, iron – porphyrin complexes are capable to cyclopropanate arenes in the so called Buchner reaction. Mbuvi and Woo reported the cyclopropanation of benzene with different *p* – substituted methyl phenyldiazoacetates and [Fe^{III}(Cl)(TPP)] (Figure I.16). The reaction gave two different product resulting from cyclopropanation: the norcaradiene product and the cycloheptatriene, the latter resulting from an

opening of the cyclopropane ring. The reaction products remained in a fast fluxional equilibria between both species even at $-60\text{ }^{\circ}\text{C}$, as evidenced by ^1H – NMR spectroscopy.²³⁸

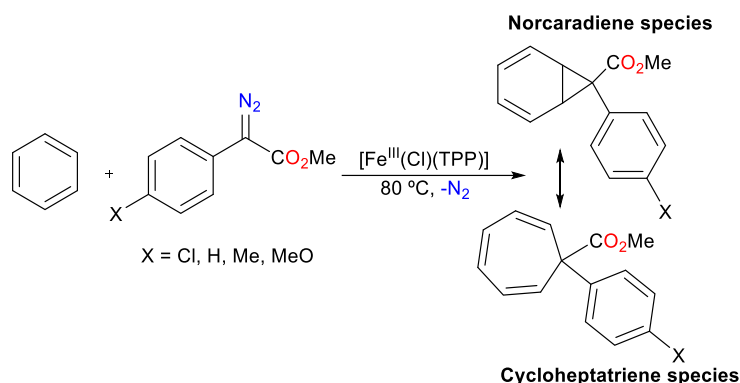


Figure I.16. Buchner reaction catalysed by $[\text{Fe}^{\text{III}}(\text{Cl})(\text{TPP})]$.

Apart from cyclopropanation and heteroatom insertion, reactions that are more important are the formation of C – C bonds through insertion into C – H bonds of alkanes. In this regard, iron – carbene species are capable to perform such an appealing reactivity. Che and co – workers studied the ability of $[\text{Fe}^{\text{II}}(\text{CPh}_2)(\text{F}_{20} - \text{TPP})]$ and $[\text{Fe}^{\text{II}}(\text{C}(\text{Ph})\text{CO}_2\text{Et})(\text{F}_{20} - \text{TPP})]$ in the stoichiometric insertion of CRR' moiety into the C – H bonds of THF (α position, activated C – H), benzylic position of cumene and allylic position of cyclohexene. The reactions worked at relatively mild conditions ($60 - 80\text{ }^{\circ}\text{C}$) with good yields from 15 – 88 % depending on substrate and reaction conditions, although needed long reaction times and did not react with cumene. Those were the first reported examples of a carbene insertion into saturated C – H bonds.²²³ Some years later Woo and co – workers reported the insertion of diazoacetates into C – H sp^3 bonds of alkyl substituted aromatic substrates with $[\text{Fe}^{\text{III}}(\text{Cl})(\text{TPP})]$ and $[\text{Fe}^{\text{III}}(\text{Cl})(\text{F}_{20} - \text{TPP})]$ (Figure I.17). Interestingly competition between benzylic sp^3 and aromatic sp^2 insertion was found with *p* – substituted toluenes and mesitylene substrates. With chlorobenzene substrate, mixtures of *o* and *p* functionalised products were obtained. Substrates with an oxygen atom, such as THF or anisole, revealed a competition between O – functionalisation and α C – H (THF) or C – H(sp^2) on anisole. The reactions proceeded with good to high yields. Remarkably the system was capable to insert with good yields the carbene moiety into cyclohexane (54 – 78 %) and also into tertiary C – H bonds of 2,2,4 – trimethylpentane (36 – 46 %), although involving long reaction times (up to 54 h) and the latter substrate with low regioselectivity. A competitive Hammett plot for the reaction of cyclohexane with *p* – substituted methyl 2 – phenyldiazoacetates revealed slopes of -1.11 and -0.82 for $[\text{Fe}^{\text{III}}(\text{Cl})(\text{TPP})]$ and $[\text{Fe}^{\text{III}}(\text{Cl})(\text{F}_{20} - \text{TPP})]$, evidencing the involvement of an electrophilic species in the rate determining step (RDS). Furthermore, the competitive reaction of 1:1 cyclohexane: D_{12} – cyclohexane with $[\text{Fe}^{\text{III}}(\text{Cl})(\text{TPP})]$ and (*p* – X – C_6H_4)(CO_2Et) $\text{C}=\text{N}_2$ (X = Me, MeO) gave KIEs of 1.97 and 1.96 respectively, indicative of a hydrogen atom abstraction during the reaction. The authors proposed that mechanism involved a concerted, nonsynchronous process.²³⁹

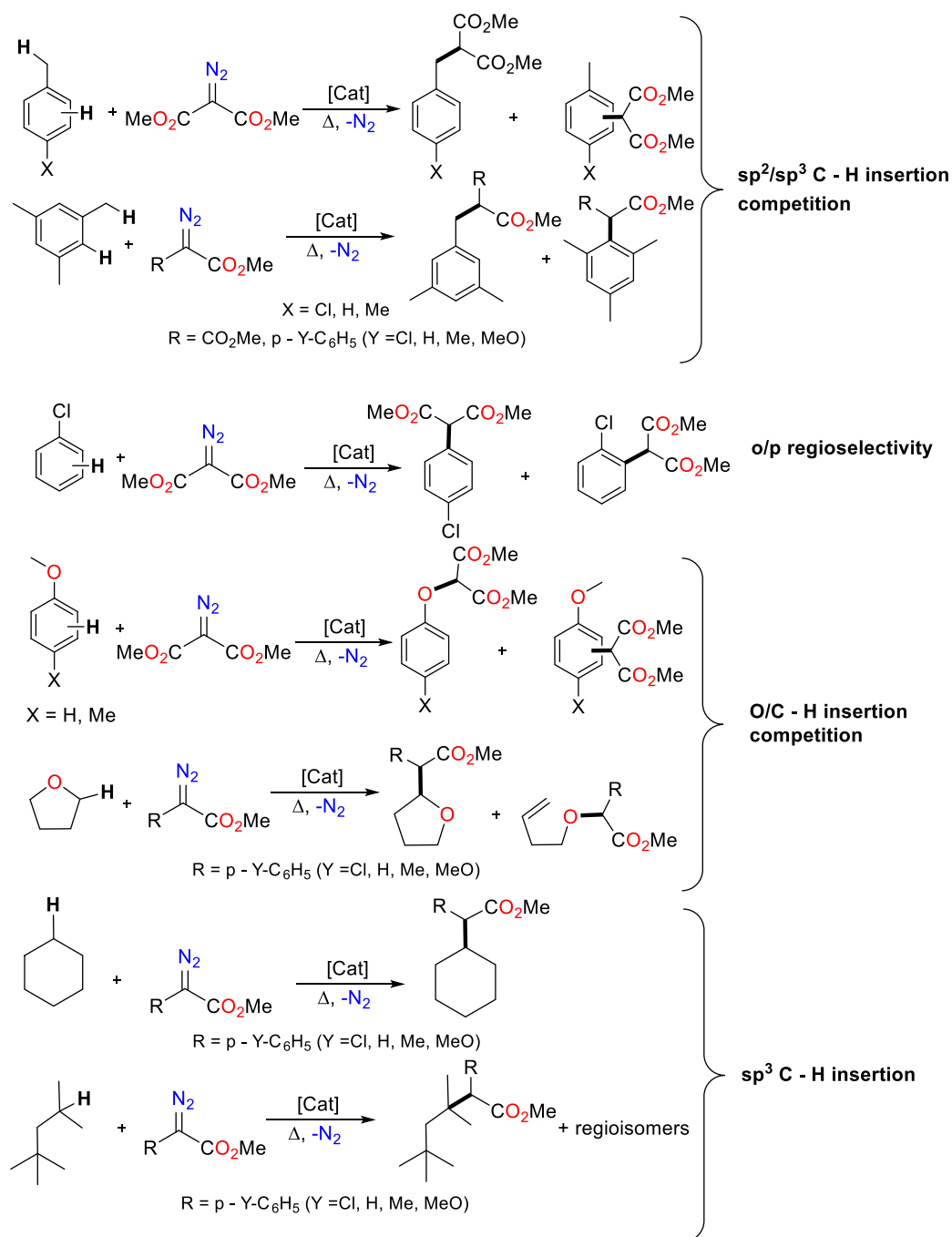


Figure I.17. C-H insertion reactivity of [Fe^{III}(Cl)(TPP)] and [Fe^{III}(Cl)(F₂₀-TPP)].

In contrast to the iron – porphyrin species, non – heme iron species have been far less studied and, to the best of our knowledge, only few examples exist in the formation of C – C bonds with diazo compounds, and almost exclusively in cyclopropanation of terminal olefins. Hossain reported in 1992 the first cyclopropanation catalysed by iron. Using the Lewis acid non – heme species [Fe^{II}(C₅H₅)(CO)₂(THF)]BF₄ achieved the cyclopropanation of styrene and α – methylstyrene with EDA in good yields (up to 71 %) under mild conditions (4 – 40 °C). Remarkably the reactions were highly selective towards the *cis* product (up to 90 %), a behaviour complementary to the observed for porphyrinic iron complexes.²⁴⁰ The authors successfully extended these reactions to *p* – methyl styrene, 2 – methoxypropene and ethyl vinyl ether although with lower selectivities; in contrast, cyclohexene and 2 – methyl – 2 – butene yielded only

dimerization by – products. The authors suggested an iron – carbene intermediate based on maleate/fumarate by – products and the high selectivity observed; despite the attempts to identify such species by variable temperature NMR spectroscopy failed.²⁴¹ Subsequently the same reactivity was reported with phenyldiazomethane to cyclopropanate alkenes with almost exclusively *cis* products. Remarkably, this system allowed the cyclopropanation of cyclopentene and 2 – methyl – 2 – butene, although with low yields (20 and 25 %). Again only indirect evidence was found for an iron – carbene species.²⁴²

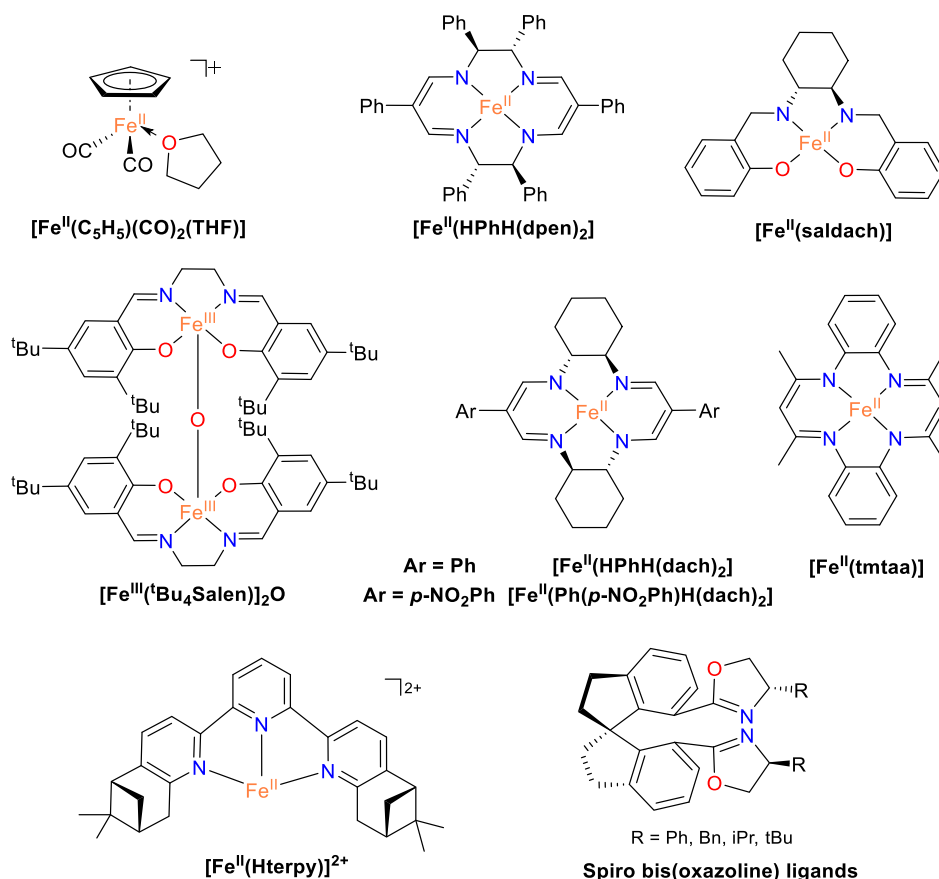


Figure I.18. Non – heme complexes and ligands used in the decomposition of diazoacetate compounds.

In 2001 Woo and co – workers reported the cyclopropanation of styrene using the species $[\text{Fe}^{\text{II}}(\text{L})]$ ($\text{L} = \text{saldach, tmtaa}$, Figure I.18). Using *p* – tolyldiazomethane both of them gave high amounts of olefin by – products and less than 20 % of cyclopropane products. The selectivity obtained were 2:1 and 4:1 towards *trans* product, much lower than the same reaction with $[\text{Fe}^{\text{II}}(\text{TPP})]$ (79 % yield 14:1) under same conditions. Using mesityl diazoacetate as carbene source, only $[\text{Fe}^{\text{II}}(\text{saldach})]$ reaction improved, with a 53 % of cyclopropanated product obtained.²³¹ In 2002 Woo and co – workers reported the cyclopropanation of styrenes with chiral complexes $[\text{Fe}^{\text{II}}(\text{L})]$ ($\text{L} = \text{HPhH}(\text{dach})_2, (p\text{-NO}_2)\text{PhH}(\text{dach})_2$ and $\text{HPhH}(\text{dpen})_2$, Figure I.18). These complexes were reacted with $\text{N}_2\text{C}(\text{H})\text{CO}_2\text{R}$ ($\text{R} = \text{Et, tBu}$ and menthyl), giving *trans* selectivity (*trans:cis* 3:1 – 15:1). The *ee* obtained for *trans* products were modest (19 – 55 %), except for $[\text{Fe}^{\text{II}}(\text{HPhH}(\text{dach})_2)]$ with $\text{N}_2\text{C}(\text{H})\text{CO}_2(\text{menthyl})$, giving a remarkable 95 % of yield with selectivity *trans:cis* = 13.3:1 and an *ee* of 79 % on *trans* product.²⁴³ Nguyen and Edulji reported a series of air – stable dimeric salen complexes, such as $[\text{Fe}^{\text{III}}(\text{tBu}_4\text{Salen})]_2\text{O}$ in the cyclopropanation of styrene with EDA. In general good yields were obtained but low selectivities were observed (*trans:cis* <3:1). The system was capable to

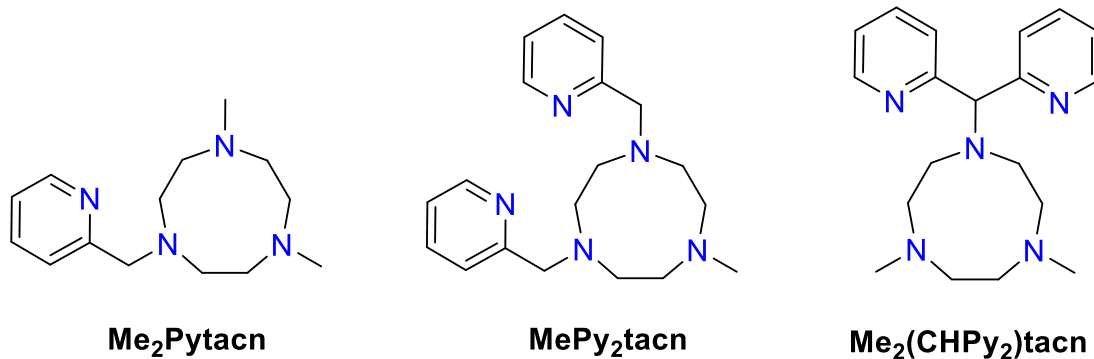
cyclopropanate a variety of mono – and disubstituted internal olefins and also unreactive internal alkenes, such as β – methylstyrene and ethylidenecyclohexane.^{244,245} Kwong and co – workers reported the cyclopropanation of styrene with EDA using chiral C₁ and C₂ terpyridine ligands. These complexes showed modest yields with low *trans* selectivity (*trans:cis* <3:1) and modest *ee*, being the better results obtained with [Fe^{II}(Cl₂)(Hterpy)], shown in Figure I.18 (78 % yield, *trans:cis* 3:1 and 65 % *ee* for *trans* and 67 % *ee* for *cis* products).²⁴⁶

To the best of our knowledge, the only example of C – C formation through C – H insertion catalysed by non – heme iron complexes was reported recently. Zhou and co – workers functionalised in high yields indoles with aryldiazoacetates, to obtain the insertion of the carbene moiety into the sp² C – H bond on the 5 – member ring. The reaction proceeded in high yields using Fe^{II}(ClO)₄ salt and tetramethylethylenediamine (TMEDA) as ligand (yields 72 – 95 %). Furthermore using a spiro bis(oxazoline) chiral ligand enantioselectivities up to 78 % were obtained.²⁴⁷ Despite not being a C – C formation, is worth to mention the application of these ligands in the highly efficient iron – catalysed insertion of diazoacetates into O – H bond of alcohols, showing high enantioselectivities. In comparison, other metals such as gold or rhodium gave much lower enantioselectivities²⁴⁸

CHAPTER II

MAIN OBJECTIVES

The focus of this thesis is the study of iron complexes in high oxidation states. The main objective is the synthesis and characterization of a family of complexes based on the 1,4,7 – triazacyclononane ligands (Scheme II.1) containing a metallic nucleus in a high oxidation state (IV or V) and characterise them to study their reactivity and oxidising power. The high basicity and robustness of N – donor ligands to use should permit the stabilisation of high – valent metal centre.



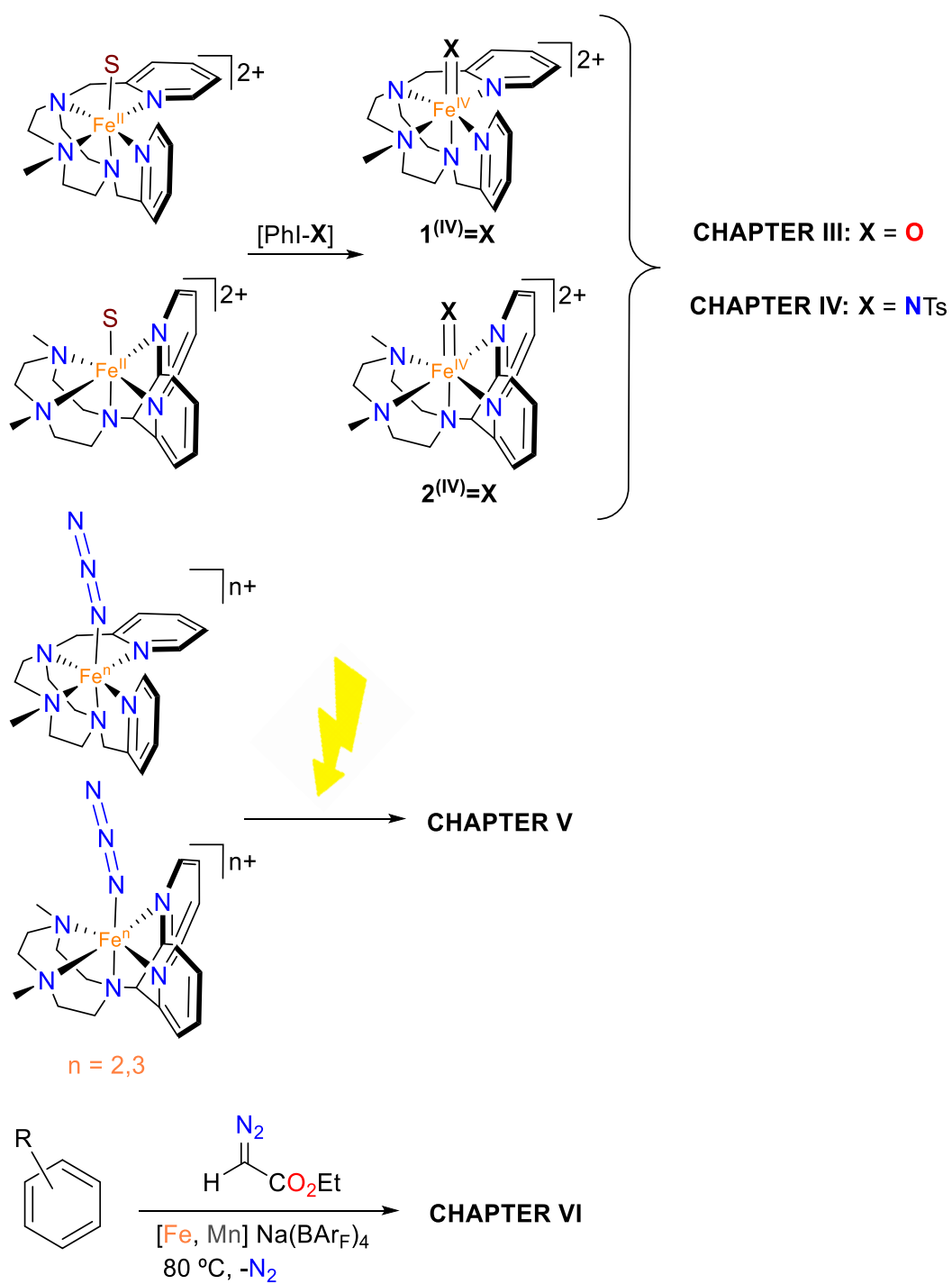
Scheme II.1. 1,4,7 – triazacyclononane ligands used in this work.

It is well – known that bioinspired complexes in high – oxidation states with terminal oxo ligands can react with a number of substrates to perform oxidation reactions through oxygen atom transfer (OAT) but also hydrogen atom transfer (HAT). Our goal is to study a family of non – heme iron (IV) – oxo complexes bearing pentadentate N – donor ligands capable to perform such reactions. In **Chapter III** we targeted the synthesis of species $1^{(IV)}=O$ and $2^{(IV)}=O$ and the study of their reactivity towards prototypical OAT and HAT substrates. In this chapter we also studied the mechanism of oxygen atom exchange (OAT) for iron (IV) – oxo species.

In contrast, high – valent iron – imido species have been far less studied in comparison to iron – oxo complexes. In **Chapter IV** we targeted the synthesis and study of the isoelectronic complexes $1^{(IV)}=NTs$ and $2^{(IV)}=NTs$ containing an imido (NR) ligand and the study of the reactivity for these species with sulphide substrates and its mechanism.

In addition, in **Chapter V** we pursue the synthesis of iron (IV) – and iron (V) – nitrido species through the photolysis of iron (II or III) – azido complexes. The irradiation of iron – azido complexes have to permit the N – N cleavage generating high – valent iron centres ($1^{(IV)}\equiv N$ and $2^{(V)}\equiv N$) supported by the neutral 1,4,7 – triazacyclononane N – donor macrocycle.

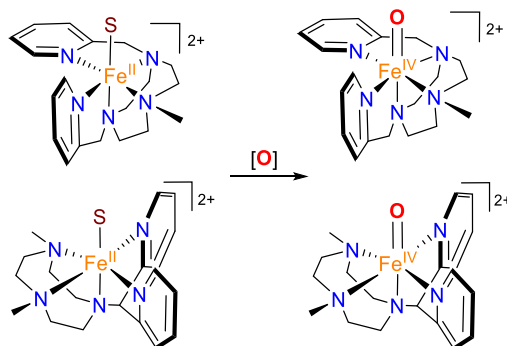
Unlike the oxo – and imidoiron species, to date no isoelectronic non – heme iron – carbene ($Fe = CR_2$) have been detected and characterised, only porphyrinic iron – carbene ($Fe = C$) species have been reported. Moreover, the reactivity studied is mainly in the cyclopropanation of alkenes with few exceptions. Studies related to non – heme iron – carbene complexes are very scarce and, again, almost exclusively in the cyclopropanation of alkenes. In this work, in **Chapter VI** we targeted the study of the C – H functionalisation of arenes through decomposition of commercially available ethyl diazoacetate, mediated by non – heme iron (II) and manganese (II) complexes bearing tetradentate 1,4,7 – triazacyclononane N – donor ligands. The aim is to generate new C – C bonds.



Scheme II.2. Schematic representation of the objectives of this work.

CHAPTER III

SYNTHESIS, CHARACTERISATION AND REACTIVITY OF HIGH – VALENT NON – HEME IRON (IV) – OXO SPECIES IN TACN – BASED N₅ – PENTADENTATE LIGANDS



Part of this chapter has been included in the following publications:

Triggering the Generation of an Iron (IV) – Oxo Compound and Its Reactivity toward Sulfides by Ru^{II} Photocatalysis. A. Company, G. Sabenya, M. González – Béjar, L. Gómez, M. Clémancey, G. Blondin, A.J. Jasniewski, M. Puri, W.R. Browne, J.M. Latour, L. Que Jr., M. Costas, J. Pérez – Prieto, J. Lloret – Fillol. *J. Am. Chem. Soc.* **2014**, 136, 4624 – 4633.

Oxygen Atom Exchange between H₂O and Non – Heme Oxoiron(IV) Complexes: Ligand Dependence and Mechanism. M. Puri, A. Company, G. Sabenya, M. Costas, L. Que Jr. *Inorg. Chem.* **2016**, 55, 5818 – 5827.

III.1. GENERAL INSIGHT

Selective functionalization of C – H bonds is a challenging transformation that has not yet been resolved in a satisfactory manner in the current synthetic chemistry. Among the different possibilities to functionalize a C – H bond, the hydroxylation represents an interesting and useful alternative. A wide variety of metalloenzymes can make these challenging transformations by activating dioxygen to form high – valent metal oxo species, responsible for attacking C-H bonds.^{18,19,249} These enzymes contain abundant transition metals such as iron, usually forming high – valent oxo – iron (IV) species.^{55,250}

Synthetic iron complexes in high oxidation states with terminal oxo ligands reproduce the active species in a number of non-heme iron dependent oxygenases, and are known to be capable of reacting with a wide variety of substrates to give place to oxygen atom transfer (OAT) and abstraction of a hydrogen atom (HAT) reactions.⁵⁴

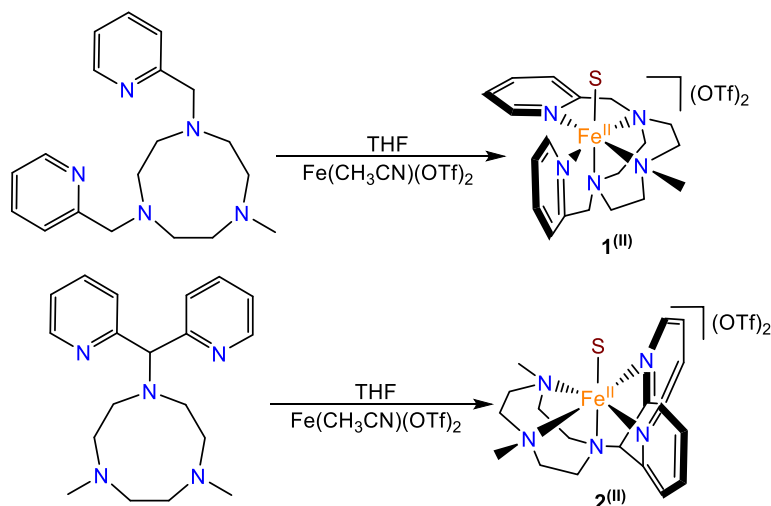
In this chapter we present the preparation and characterization two oxo – iron (IV) complexes $[\text{Fe}^{\text{IV}}(\text{O})(\text{MePy}_2\text{tacn})](\text{SO}_3\text{CF}_3)_2$ **1**^{(IV)=O} and $[\text{Fe}^{\text{IV}}(\text{O})(\text{Me}_2(\text{CHPy}_2)\text{tacn})](\text{SO}_3\text{CF}_3)_2$ **2**^{(IV)=O} containing pentadentate triazacyclononane based ligands, and their reactivity in typical examples of oxygen atom transfer (OAT) and hydrogen atom transfer (HAT) reactions. Thioanisole and alkylbenzenes are used as model substrates for the OAT and HAT reactions, respectively. A comparative analysis of kinetic and thermodynamic parameters of these reactions has been performed, as well as the characterization of the distribution of products that are formed. In addition, the oxygen atom exchange (OAE) was also studied and compared with a series of iron (IV) – oxo complexes with tetra – and pentadentate ligands. Kinetic and thermodynamic data was obtained as well as a mechanism has been proposed for this reactivity.

Finally, the photochemical preparation of **1**^{(IV)=O} was performed as well as we discovered a photoenhanced effect in the oxidation of thioanisole derivatives to their respective sulfoxides by **1**^{(IV)=O} and **2**^{(IV)=O} and assisted by the $[\text{Ru}^{\text{II}}(\text{bpy})_3]^{2+}$ as photosensitizer. Kinetic analysis of the oxidations as well as laser pulse excitation study of this reactivity allowed us to postulate a mechanism.

III.2. RESULTS AND DISCUSSION

III.2.1. Syntheses and characterisation of $[\text{Fe}^{\text{II}}(\text{MePy}_2\text{tacn})(\text{CH}_3\text{CN})](\text{CF}_3\text{SO}_3)_2$ ($\mathbf{1}^{\text{II}}$) and $[\text{Fe}^{\text{II}}(\text{Me}_2(\text{CHPy}_2)\text{tacn})(\text{CH}_3\text{CN})](\text{CF}_3\text{SO}_3)_2$ ($\mathbf{2}^{\text{II}}$)

The syntheses of the iron (II) complexes was carried out by adding a THF solution of $\text{Fe}^{\text{II}}(\text{SO}_3\text{CF}_3)_2(\text{CH}_3\text{CN})_2$ to a solution of the corresponding ligand in THF under heavy stirring for 2 – 3h. During this time, the solution turned turbid and dark red. The hexacoordinated complexes $[\text{Fe}^{\text{II}}(\text{MePy}_2\text{tacn})(\text{CH}_3\text{CN})](\text{CF}_3\text{SO}_3)_2$ ($\mathbf{1}^{\text{II}}$) and $[\text{Fe}^{\text{II}}(\text{Me}_2(\text{CHPy}_2)\text{tacn})(\text{CH}_3\text{CN})](\text{CF}_3\text{SO}_3)_2$ ($\mathbf{2}^{\text{II}}$) were isolated in 60 and 52 % yield, respectively, as a crystalline material by recrystallizing from CH_2Cl_2 – diethylether. Complexes $\mathbf{1}^{\text{II}}$ and $\mathbf{2}^{\text{II}}$ were characterized by UV – vis, $^1\text{H-NMR}$ spectroscopy, Electrospray Ionization – Mass Spectrometry (ESI – MS), X – ray diffraction and combustion analysis.



Scheme III.1. Schematic diagram for the preparation of iron (II) complexes $\mathbf{1}^{\text{II}}$ and $\mathbf{2}^{\text{II}}$. S = solvent.

UV – vis spectrum (Figure III.1) of $\mathbf{1}^{\text{II}}$ in acetonitrile shows a broad and intense band ($\epsilon = 6500 \text{ M}^{-1}\cdot\text{cm}^{-1}$) at 400 – 420 nm while $\mathbf{2}^{\text{II}}$ shows two intense bands ($\epsilon = 5000$ and $3800 \text{ M}^{-1}\cdot\text{cm}^{-1}$) at 459 and 390 nm, respectively in acetonitrile. These bands are attributed to metal – to – ligand charge transfer (MLCT) transitions from $d\pi(\text{Fe})$ to $\pi^*(\text{L})$.

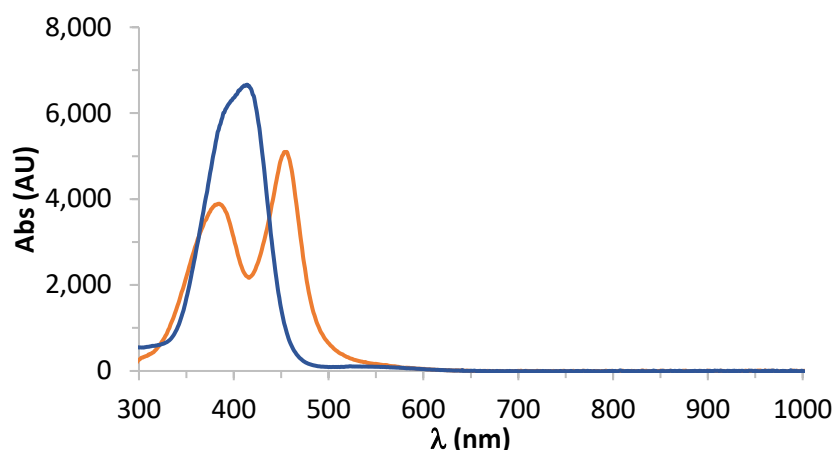


Figure III.1. UV – vis spectrum of **1**^(III) (blue) and **2**^(III) (orange) in acetonitrile.

Both complexes show a ¹H – NMR spectrum at 298 K in CD₃CN characteristic of diamagnetic molecules, typical for d⁶ Fe^{II} in the S = 0 low spin state. All signals are in the range from 0 to 10 ppm. In **1**^(III) the pyridine protons appear at 9.2 and 7.3 – 7.9 ppm as broad signals with integrations of 1 and 7 protons respectively. The fact that one proton of the pyridines appears downfield shifted with respect to the other aromatic protons is an indication that the pyridines have different orientation with respect to the Fe – CH₃CN axis (one parallel and the remainder in perpendicular dispositions). The downfield shift may indicate that the proton falls in close proximity and pointing towards the second aromatic ring, as observed in the single crystal X – Ray structure (vide infra). The four signals between 4 and 5.2 ppm, which integrate one proton each, are assigned to the CH₂Py protons, these four different signals also are in agreement with the expected different environment of the pyridines in the complex. The methyl group appears at 2.8 ppm and the rest of signals (2.8 – 3.6, 3.0 and 1.7 ppm) are assigned to the triazacyclononane macrocycle reflecting the low symmetry in the structure; there was a missing proton from the tacn macrocycle, which, based on COSY experiments (Figure SIII.1), was assigned under the solvent peak. Interestingly, multiplicity was not resolved at 298 K but when temperature was lowered to 273 K the multiplicity was observed and peaks become well resolved (Figure SIII.1); we attributed this to a fluxional equilibria of a pyridine at room temperature. In complex **2**^(III) the pentadentate ligand has the two pyridines bound to the same amine of the tacn leading to a more symmetrical complex (C_s symmetry), containing a plane of symmetry that passes through the N – CH vector and the iron centre. This is clearly reflected into the ¹H – NMR spectrum. Spectra is simpler and the protons of both pyridines appear as one set at 9.0 – 7.3 ppm. A singlet signal at 6.1 ppm is assigned to the proton at the benzylic position of the pyridines. The multiplet at 2.8 – 3.0 ppm belongs to the triazacyclononane protons and the singlet at 2.74 ppm are the two methyl groups.

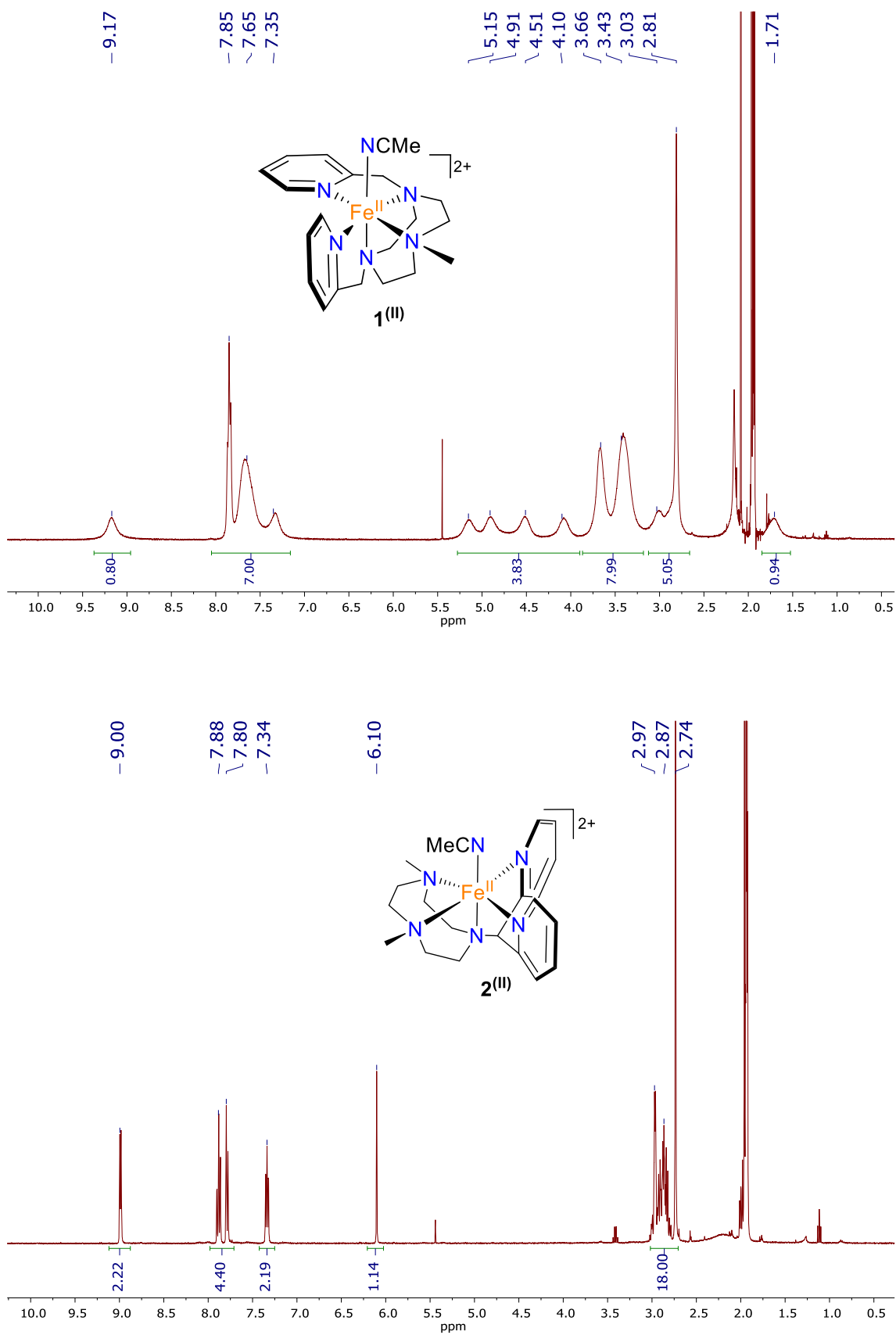


Figure III.2. ^1H – NMR spectroscopy of complex $1^{(\text{II})}$ (top) and $2^{(\text{II})}$ (below) in CD_3CN at 400 MHz at 298 K.

The ESI – MS spectrum shows peaks at $m/z = 190.5$ which belong to ions $[\text{Fe}^{\text{II}}(\text{L})]^{2+}$ and at $m/z = 530.2$ corresponding to $[\text{Fe}^{\text{II}}(\text{L})(\text{SO}_3\text{CF}_3)]^+$ confirming the nature of the synthesised complexes. In addition, elemental analyses are in agreement with the formation of compounds $\mathbf{1}^{\text{II}}$ and $\mathbf{2}^{\text{II}}$ and confirm the bulk purity of the complexes.

Solid state structures of $\mathbf{1}^{\text{II}}$ and $\mathbf{2}^{\text{II}}$ were established by single crystal X – Ray diffraction analysis. Figure III.3 shows the ORTEP diagrams of complexes and tables SIII.1 and SIII.2 gather selected bond lengths and angles for the crystallographically determined structures. Distances in both $\mathbf{1}^{\text{II}}$ and $\mathbf{2}^{\text{II}}$ are in the range typical for low spin complexes,²⁵⁰⁻²⁵⁶ with Fe – N(tacn) of 1.97 – 2.05 Å and the Fe – N(Py) of 1.97 – 1.99 Å. The Fe – N(Py) bonds are slightly shorter than the Fe – N(tacn) probably due to the π acceptor character of pyridine. The coordination geometry is distorted octahedral in both complexes, with five coordination sites occupied by the N atoms of the ligand and one acetonitrile molecule to complete the coordination environment, with a bond distance of 1.93 Å. In $\mathbf{1}^{\text{II}}$ the two pyridine ligands are located in *cis* relative position (in a facial manner) with the N1 – Fe1 – N5 angle of 95.67(8) ° and with the two pyridine rings disposed perpendicularly one respect to each other; this confirms our initial proposal made on the basis of ^1H – NMR spectroscopy. Complex $\mathbf{1}^{\text{II}}$ is formed of a mixture of both Δ and Λ isomers (Λ is shown in Figure III.3). In complex $\mathbf{2}^{\text{II}}$ the two pyridine ligands are located in *cis* and are parallel to the axis Fe – NCCCH₃ with the N1 – Fe1 – N2 angle of 84.58(9)°. This structure is in good agreement with the ^1H – NMR spectrum of this complex, with a plane bisecting the molecule.

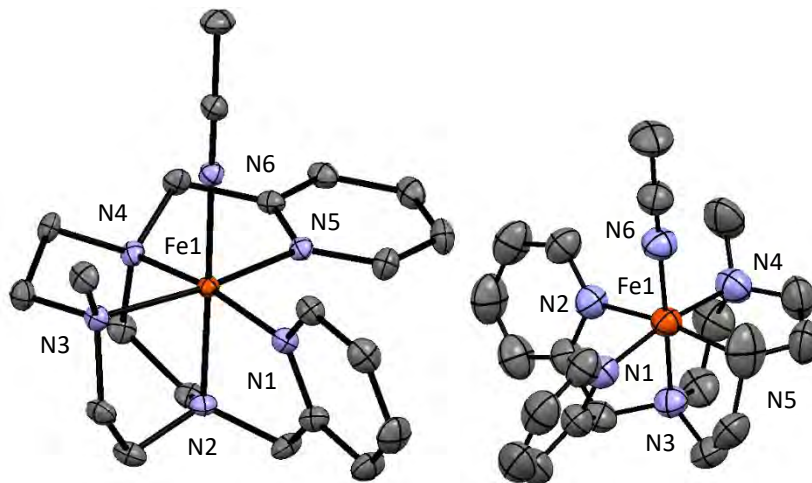
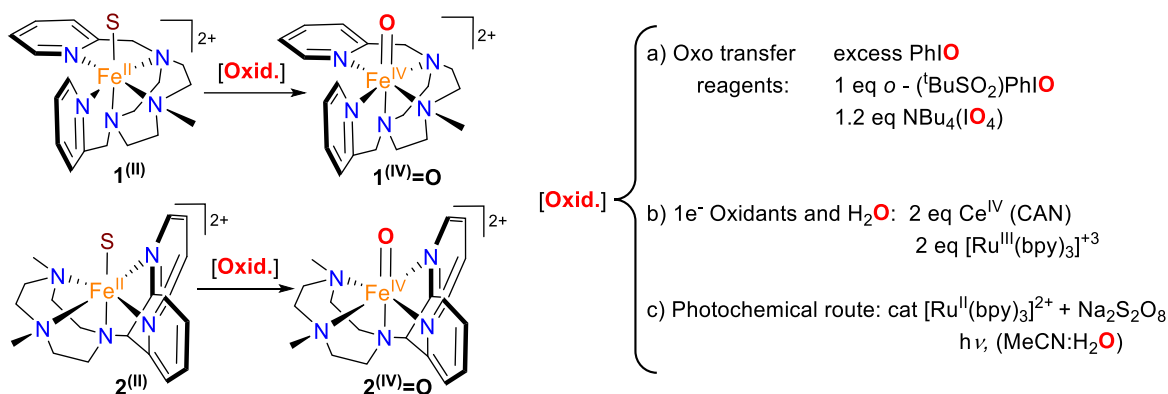


Figure III.3. Ortep representation at 50 % of probability of X – ray structure of $\mathbf{1}^{\text{II}}$ and $\mathbf{2}^{\text{II}}$, triflate anions and hydrogens are omitted for clarity.

III.2.2. Synthesis and characterization of $[\text{Fe}^{\text{IV}}(\text{O})(\text{MePy}_2\text{tacn})](\text{OTf})_2$ ($\mathbf{1}^{\text{IV}}=\text{O}$) and $[\text{Fe}^{\text{IV}}(\text{O})(\text{Me}_2(\text{CHPy}_2)\text{tacn})](\text{OTf})_2$ ($\mathbf{2}^{\text{IV}}=\text{O}$)

Mainly three different strategies are followed to synthesise iron – oxo species in high oxidation states by means of chemical oxidation, which are depicted in Scheme III.2: a) by using oxygen atom donors oxidants (such as iodosobenzene (PhIO) or periodates)⁶⁵, b) using water as oxygen source and oxidising the metal with strong single electron oxidants ($[\text{Ru}^{\text{III}}(\text{bpy})]^{3+}$, CAN (Cerium Ammonium Nitrate))²⁵⁷ and c) photochemically generating an oxidant (e.g. $[\text{Ru}^{\text{III}}(\text{bpy})]^{3+}$ from $[\text{Ru}^{\text{II}}(\text{bpy})]^{2+}$) and using a sacrificial acceptor of electrons (such as $\text{Na}_2\text{S}_2\text{O}_8$ or $[\text{Co}^{\text{III}}\text{Cl}(\text{NH}_3)_5]^{2+}$).¹¹⁰

We tested the synthesis of $\mathbf{1}^{\text{IV}}=\text{O}$ through different strategies (1.2 equiv of *n* – Bu_4NIO_4 in CH_3CN , CAN and $[\text{Ru}^{\text{II}}(\text{bpy})_3]^{2+} + \text{Na}_2\text{S}_2\text{O}_8$) and we performed the full characterisation using PhIO as oxidant in acetonitrile. The other methods yielded the same band in the UV – vis spectrometry proving that the same species were obtained (Figure SIII.2 in the annex).



Scheme III.2. Chemical strategies to prepare $\mathbf{1}^{\text{IV}}=\text{O}$ and $\mathbf{2}^{\text{IV}}=\text{O}$ from its iron (II) precursors $\mathbf{1}^{\text{II}}$ and $\mathbf{2}^{\text{II}}$, respectively.

The reaction of $\mathbf{1}^{\text{II}}$ and $\mathbf{2}^{\text{II}}$ with an excess of PhIO in acetonitrile at room temperature lead to the formation of the two iron – oxo compounds $[\text{Fe}^{\text{IV}}(\text{O})(\text{MePy}_2\text{tacn})](\text{OTf})_2$ $\mathbf{1}^{\text{IV}}=\text{O}$ and $[\text{Fe}^{\text{IV}}(\text{O})(\text{Me}_2(\text{CHPy}_2)\text{tacn})](\text{OTf})_2$ $\mathbf{2}^{\text{IV}}=\text{O}$, respectively. The initial yellow solutions quickly changed to pale – green colour when exposed to the oxidant. However, the formed compounds were relatively instable (estimated $t_{1/2}$ of 8 and 70 h at RT, respectively) and was not possible to isolate them as solids suitable for X – ray diffraction studies. Therefore, all analyses were done from freshly prepared solutions of the highly reactive complexes. Complexes $\mathbf{1}^{\text{IV}}=\text{O}$ and $\mathbf{2}^{\text{IV}}=\text{O}$ have been previously reported by our group and Que and co – workers.^{83,85} Notwithstanding, we completely characterised the species $\mathbf{1}^{\text{IV}}=\text{O}$ and $\mathbf{2}^{\text{IV}}=\text{O}$ to confirm its preparation. The iron – oxo (IV) complexes were characterised by ESI – MS, UV – vis, ^1H – NMR and $\mathbf{1}^{\text{IV}}=\text{O}$ was also analysed by voltamperometric techniques, Mössbauer and XAS spectroscopy.

The UV – vis spectra for $1^{(IV)=O}$ and $2^{(IV)=O}$ (Figure III.4) show a new band at 738 and 748 nm respectively with an excitation molar coefficient of 310 and 340 $M^{-1}\cdot cm^{-1}$ (extinction coefficients were corrected according to the purity of $1^{(IV)=O}$ determined by Mössbauer (see below) and the reported purity of $2^{(IV)=O}$ (82 and 85 % respectively). These bands are attributed to d – d transitions¹⁰⁹ and are characteristic from low spin ($S = 1$) $Fe^{IV}=O$ species.^{54,65,83}

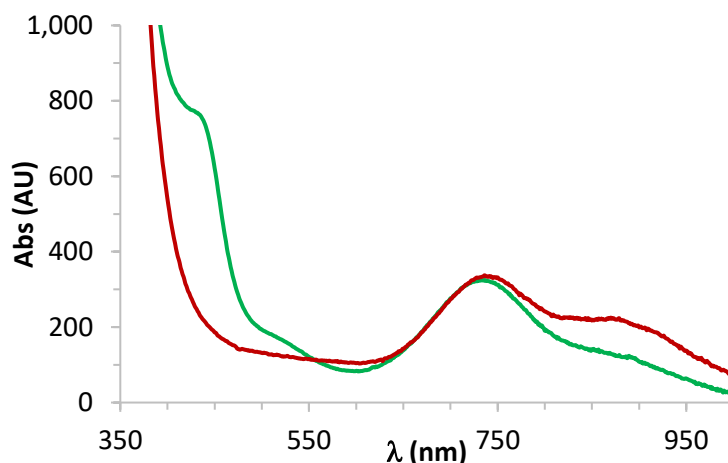


Figure III.4. UV – vis spectra of complexes $1^{(IV)=O}$ (green) and $2^{(IV)=O}$ (red) in acetonitrile prepared with PhIO as oxidant.

1H – NMR spectroscopy of complexes $1^{(IV)=O}$ and $2^{(IV)=O}$ in CD_3CN (Figure III.5) show paramagnetically shifted signals, as expected for its electronic configuration (d^4). Due to the paramagnetic nature of these compounds, the spectra show fast relaxing signals, translated into wide features that are difficult to analyse. Despite of this, the pyridine protons show sharp signals. These signals were assigned with the aid of bidimensional paramagnetic COSY experiments and by comparison to the related iron (IV) – oxo species $[Fe^{IV}(O)(N_4Py)]^{2+}$ (N_4Py , N,N – bis(2 – pyridylmethyl) – N – bis(2 – pyridyl)methylamine) and $[Fe^{IV}(O)(Bn – TPEN)]^{2+}$ ($Bn – TPEN$, N – benzyl – N,N',N' – tris(2 – pyridylmethyl) – 1, 2 – diaminoethane) depicted in Scheme III.5.⁸² The presence of wide signals in both $1^{(IV)=O}$ and $2^{(IV)=O}$ complexes in the high field region of the spectra, which were not observed in the related N_4Py and $Bn – TPEN$ complexes, suggest they belong to the triazacyclononane ring and possibly to the N – methyl groups.

As we know from X – ray diffraction the pyridines in complex $1^{(II)}$ show different orientations with respect to the $Fe – NCCH_3$ axis. Thus we speculate that the pyridines in $1^{(IV)=O}$ must have also different orientations with respect to the $Fe – O$ axis, with a pyridine lying perpendicular to the $Fe – O$ bond and the other lying parallel to this axis. Therefore, in $1^{(IV)=O}$ both pyridines should show a different shift pattern due to the different interaction with the d orbitals of iron, while in $2^{(IV)=O}$ both pyridines are expected to be parallel to that axis and symmetrically related thus giving a common pattern for the two rings. Indeed this is the behaviour that was observed. The 1H – NMR spectra obtained for $2^{(IV)=O}$ ranges from -55 to 35 ppm and reflects the C_2 symmetry of the complex. The bidimensional COSY spectrum, allowed the assignation of the pyridine hydrogens to the signals at 31.98 (β), 10.65 (γ) and -9.52 (β') ppm. The signal pattern ($H\beta$ downshifted, $H\beta'$ upshifted and $H\gamma$ centred) matches perfectly with that of $[Fe^{IV}(O)(N_4Py)]^{2+}$,

where all the pyridine rings are also parallel to the Fe – O axis.⁸² On the other hand, ¹H – NMR spectra for **1**^(IV)=O ranges from -90 to 50 ppm and is slightly more complex, consequence of its C₁ symmetry. The disposition of the pyridine rings in **1**^(II) (one parallel to the Fe – NCCH₃ axis and the other perpendicular) was maintained in **1**^(IV)=O, this was evidenced by the two sets of pyridine protons observed in the ¹H – NMR spectrum (Figure III.5). Bidimensional COSY experiments allowed the assignation of the two sets. First set (subset a, pyridine parallel to the Fe – O axis) follows the same trend observed in complexes **2**^(IV)=O and [Fe^{IV}(O)(N4Py)]²⁺ (β proton downshifted and β' signal upshifted, γ centred) and was assigned to 46.46 (β), 13.34 (γ) and -13.27 (β') ppm. The remainder pyridine (subset b, perpendicular to the Fe – O axis) shows a distinct pattern, with both β and β' proton signals upshifted; the same behaviour was observed on the previously reported [Fe^{IV}(O)(Bn – TPEN)]²⁺. The assignation of the signals from subset b was 11.23 (Hγ) and -1.36 (Hβ and Hβ') ppm. Apart from those signals, a considerable amount of iodobenzene from iodobenzene reduction was identified in the region 7 – 8 ppm.

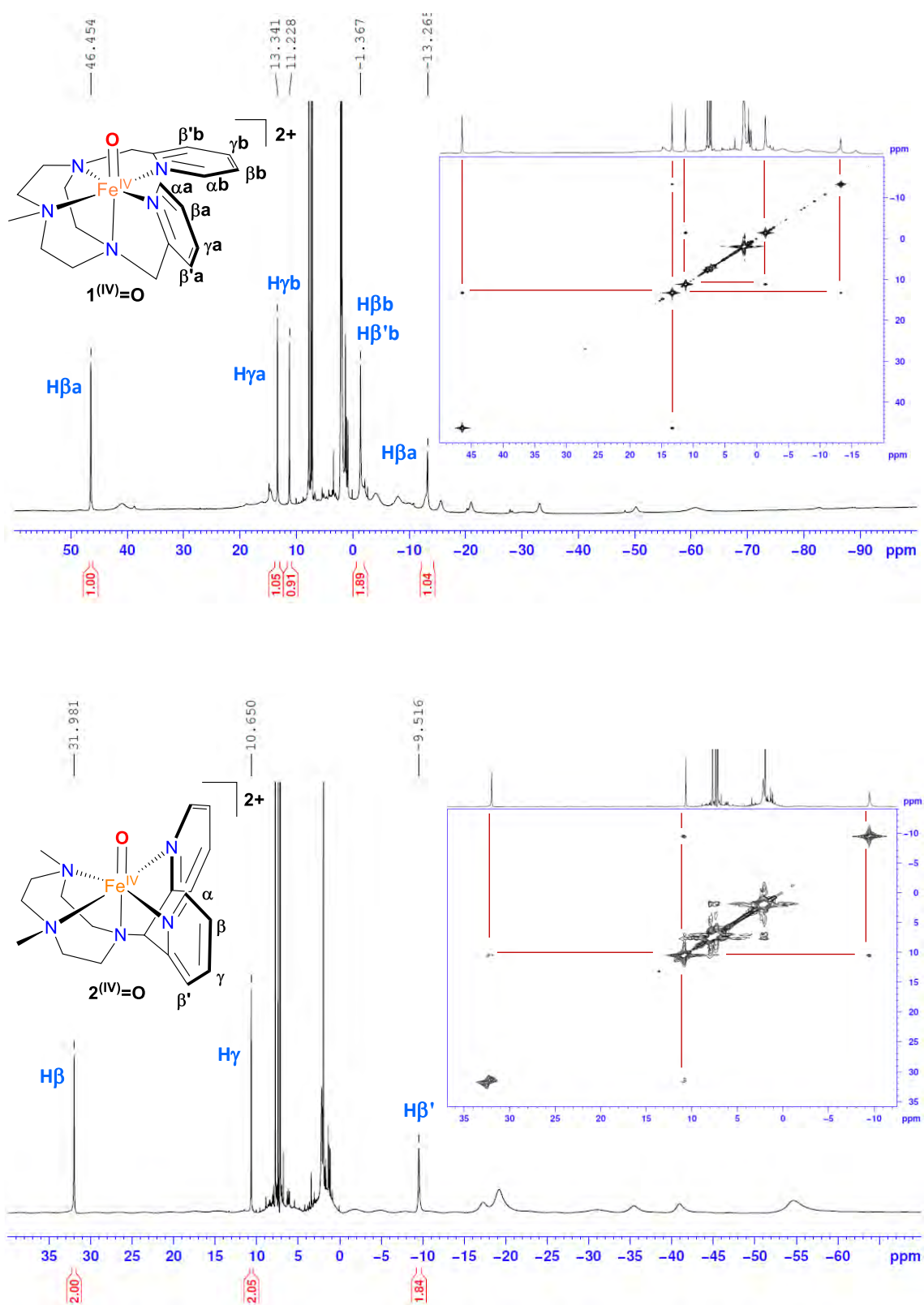


Figure III.5. ^1H -NMR and bidimensional COSY spectra of complex $1^{(\text{IV})}=\text{O}$ and $2^{(\text{IV})}=\text{O}$ in CD_3CN at 25°C .

In addition, the ESI – MS of $1^{(IV)=O}$ and $2^{(IV)=O}$ show a molecular peak at $m/z = 546.1$ which corresponds to the $[\text{Fe}^{IV}(\text{O})(\text{L})](\text{SO}_3\text{CF}_3)^+$ fragment (Figure III.6 and SIII.3). Isotope exchange ^{18}O experiments is a powerful experiment since allows determining the number of oxygen atoms from the complex that can be exchanged with water (usually the oxo moiety).^{258,259} Therefore, the addition of H_2^{18}O to the solution of $1^{(IV)=O}$ leads to a new peak in the ESI – MS at $m/z = 548.1$ which was assigned to $[\text{Fe}^{IV}(^{18}\text{O})(\text{MePy}_2\text{tacn})](\text{SO}_3\text{CF}_3)^+$. In both cases the simulated ESI – MS spectra correspond with the experimental one.

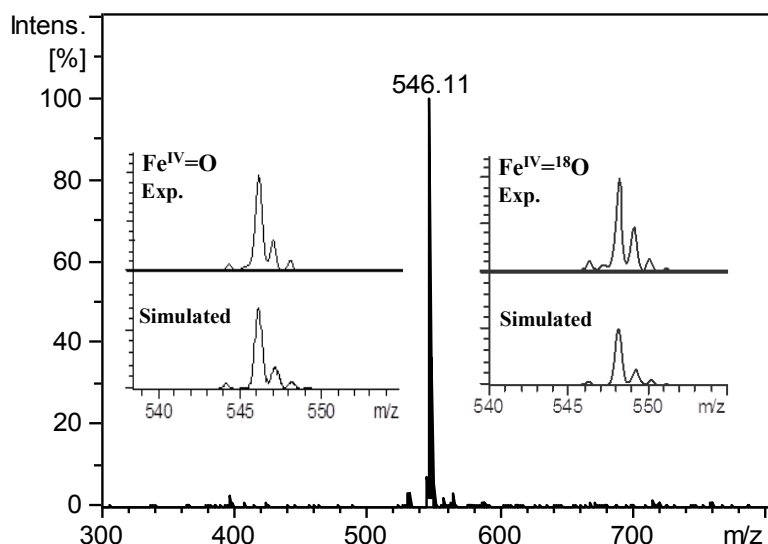
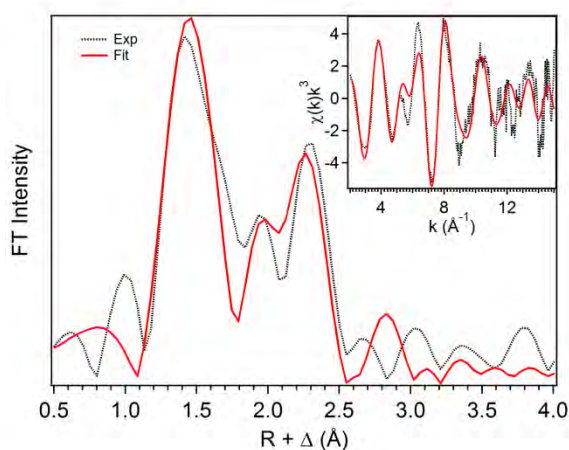


Figure III.6. ESI – MS spectra of complex $1^{(IV)=O}$ in acetonitrile.

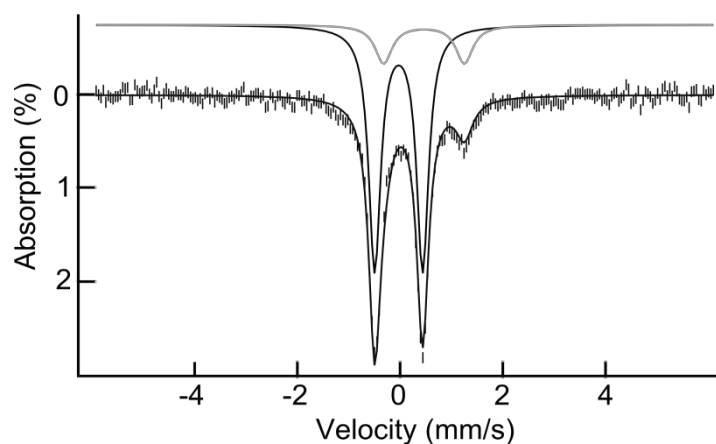
Complex $1^{(IV)=O}$ was further characterised by X – Ray Absorption Spectroscopy (XAS) (Figure III.7) and compared with the reported data from the related pentadentate complexes $2^{(IV)=O}$, $[\text{Fe}^{IV}(\text{O})(\text{N4Py})]^{2+}$ and $[\text{Fe}^{IV}(\text{O})(\text{Bn} - \text{TPEN})]^{2+}$.⁸³ The rising K – edge energy for $1^{(IV)=O}$ (7124.2 eV) was very similar to those reported for $2^{(IV)=O}$, N4Py and the Bn – TPEN complexes (7124.7, 7123.7 and 7124.2 respectively). Moreover the $1s \rightarrow 3d$ pre – edge energy fits perfectly within reported data (7114.1 vs 7114.1 – 7114.7). The area for this transition was 26, a bit lower than in N4Py and Bn – TPEN, thus indicating a less distorted environment compared to those. The EXAFS (X – Ray Absorption Fine Structure) data (Figure III.7) revealed a Fe – O distance of 1.63 Å, in concordance with literature values, and the coordination environment completed with a shell of N scatters of 2.00 Å from ligand (Table III.1).

Table III.1. XAS data from reported pentadentate iron – oxo complexes.

Complex	Area pre – edge	Energy pre – edge (eV)	Energy XAS edge (eV)	Fe = O bond (Å)	Ligand bonds (Å)
$1^{(IV)=O}$	26	7114.1	7124.2	1.63	5N @ 2.00
$2^{(IV)=O}$	24	7114.1	7124.7	1.64	4N @ 2.00
$^a[\text{Fe}^{IV}(\text{O})(\text{N4Py})]^{2+}$	31	7114.4	7124.0	1.67	4N @ 1.96
$^a[\text{Fe}^{IV}(\text{O})(\text{Bn} - \text{TPEN})]^{2+}$	29	7114.1	7123.7	1.63	4N @ 2.00

^aData from ref. 83

Figure III.7. Experimental EXAFS data (black line) and best fit (red line). Unfiltered data shown in the inset and corresponding Fourier transform of $1^{(IV)=O}$. k range = 2 – 15 \AA^{-1} ; back – transform range, \approx 0.83 – 3.0 \AA .

Furthermore, Mössbauer spectra of $1^{(IV)=O}$ revealed a superposition of two doublets. The major one constitutes the 82 % of the sample with $\delta = -0.01$ mm/s and $\Delta E_Q = 0.93$ mm/s, parameters that fall within the expected range for a $S = 1$ non – heme iron (IV) – oxo species.^{53,55} The minor doublet ($\delta = 0.48$ mm/s and $\Delta E_Q = 1.57$ mm/s) accounted for the remaining 18 % and was assigned to an oxo – bridged diferric compound presumably arising from decomposition of $1^{(IV)=O}$, as previously observed on analogous iron (IV) – oxo species, due to its metastable nature.^{77,260}


Figure III.8. Mössbauer spectrum of $1^{(IV)=O}$ recorded at 80 K with zero applied field. Hatched bars are the experimental data and the solid lines the contributions of $\text{Fe}^{IV}(\text{O})$ (black line) and dimeric decomposition (grey line).

All the characterization data together make us confident that the compounds formed under these conditions could be assigned to the $[\text{Fe}^{\text{IV}}(\text{O})(\text{MePy}_2\text{tacn})](\text{OTf})_2$ $\mathbf{1}^{\text{IV}}=\text{O}$ and $[\text{Fe}^{\text{IV}}(\text{O})(\text{Me}_2(\text{CHPy}_2)\text{tacn})](\text{OTf})_2$ $\mathbf{2}^{\text{IV}}=\text{O}$ with a similar arrangement as the respective iron (II) precursors.

III.2.3. Electrochemical studies of $\mathbf{1}^{\text{IV}}=\text{O}$

The corresponding oxidized iron (III) species $[\text{Fe}^{\text{III}}(\text{OH})(\text{MePy}_2\text{tacn})]^{2+}$ ($\mathbf{1}^{\text{III}} - \text{OH}$) was prepared by reacting $\mathbf{1}^{\text{III}}$ with H_2O_2 (2 eq) in acetonitrile and characterised by UV – vis (314 nm, $\epsilon = 2800 \text{ M}^{-1}\cdot\text{cm}^{-1}$; 343 nm, $\epsilon = 2600 \text{ M}^{-1}\cdot\text{cm}^{-1}$; shoulder 538 nm, $\epsilon = 140 \text{ M}^{-1}\cdot\text{cm}^{-1}$), EPR ($g_x = 2.24$, $g_y = 2.19$, $g_z = 1.92$) and Mössbauer ($\delta = 0.15 \text{ mm}\cdot\text{s}^{-1}$, $\Delta E_Q = -2.27 \text{ mm}\cdot\text{s}^{-1}$) Figures III.9, III.10 and III.11.

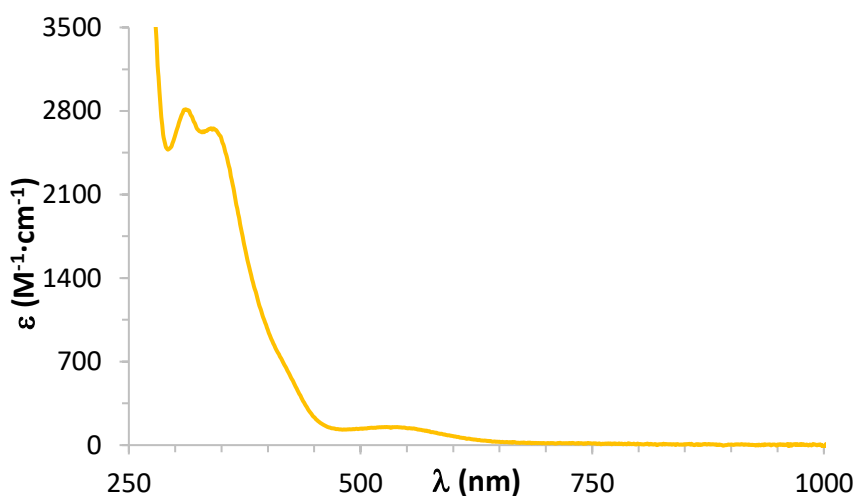


Figure III.9. UV – vis $\mathbf{1}^{\text{III}} - \text{OH}$ (0.4mM in MeCN) synthesised from $\mathbf{1}^{\text{III}}$ with 2 eq H_2O_2 .

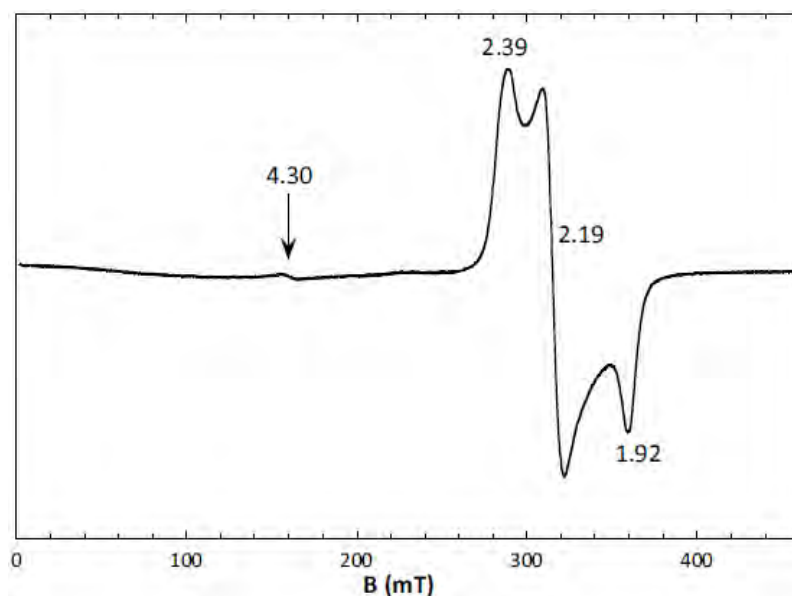
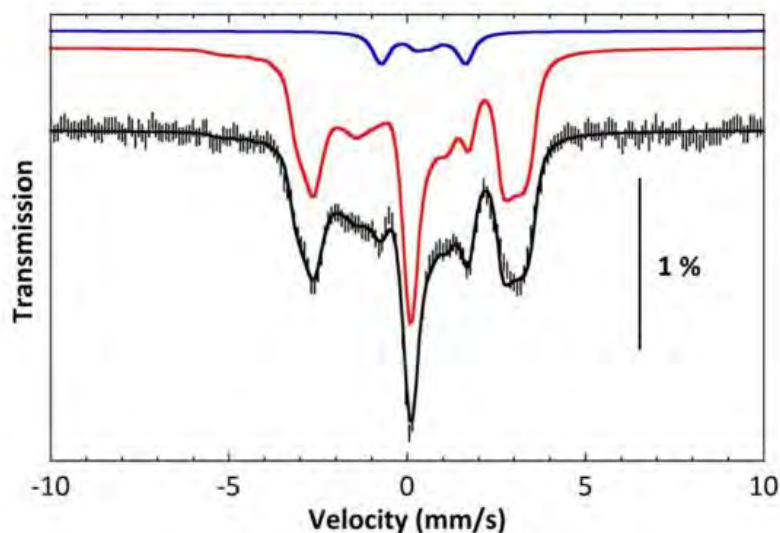


Figure III.10. EPR spectrum of $[\text{Fe}^{\text{III}}(\text{OH})(\text{MePy}_2\text{tacn})](\text{OTf})_2$ $\mathbf{1}^{\text{III}} - \text{OH}$ recorded at 5 K with the following parameters: microwave frequency = 9.6551 GHz, microwave power = 0.317 mW, receiver gain = $3.99 \cdot 10^3$, time constant = 40.96 ms, modulation frequency = 100 kHz, modulation amplitude = 0.5 mT. The g – values are indicated.



	S	$g_x/g_y/g_z$	δ ($\text{mm}\cdot\text{s}^{-1}$)	ΔE_Q ($\text{mm}\cdot\text{s}^{-1}$)	Γ ($\text{mm}\cdot\text{s}^{-1}$)	η	A_x (T)	A_y (T)	A_z (T)	%
Fe^{III}	1/2	2.39/2.19/1.92	0.19	-2.27	0.36	0.30	18.8	3.3	-43.2	92
Fe^{II}	0	-	0.44	-0.41	0.48	0	-	-	-	8

Figure III.11. Mössbauer spectrum of $[\text{Fe}^{\text{III}}(\text{OH})(\text{MePy}_2\text{tacn})](\text{OTf})_2 \mathbf{1}^{\text{(III)}} - \text{OH}$ recorded at 4.2 K under a magnetic field of 7 T applied parallel to the γ – rays. The spectrum was simulated under the assumption of slow relaxation by taking into account 92% of $S = 1/2$ species (red line) and 8% of $\mathbf{1}^{\text{(II)}}$ (blue line).

Alternatively, $[\text{Fe}^{\text{III}}(\text{OH})(\text{MePy}_2\text{tacn})]^{2+} (\mathbf{1}^{\text{(III)}} - \text{OH})$ and $[\text{Fe}^{\text{IV}}(\text{O})(\text{MePy}_2\text{tacn})]^{2+} (\mathbf{1}^{\text{(IV)}}=\text{O})$ were also electrochemically generated. Complex $\mathbf{1}^{\text{(II)}}$ was studied by cyclic voltammetry in acetonitrile to obtain the plot shown on Figure III.12, where the $\text{Fe}^{\text{II/III}} - \text{MeCN}$ couple was observed at $E_{1/2} = 0.84$ V vs SCE. Also a tiny wave at $E_{1/2} = 0.47$ V vs SCE was observed, belonging to the $\text{Fe}^{\text{II/III}} - \text{OH}_2/\text{OH}$ couple generated from traces of water (red line). When using completely anhydrous acetonitrile this wave disappeared confirming its nature (yellow line). When 5 % of water was added to the acetonitrile solution the scenario changed and two couples were observed (green line): the initial $\mathbf{1}^{\text{(II)}}$ was mainly in the $\text{Fe}^{\text{II}} - \text{MeCN}$ form so the oxidation wave was observed at $E_{p,A} = 0.84$ V, while the Fe^{III} is more oxophilic and after the oxidation, in the media conditions, it quickly exchanged the MeCN ligand for a hydroxyl, so the reduction wave observed was the $\text{Fe}^{\text{III/II}} - \text{OH}/\text{OH}_2$ ($E_{p,C} = 0.48$ V).

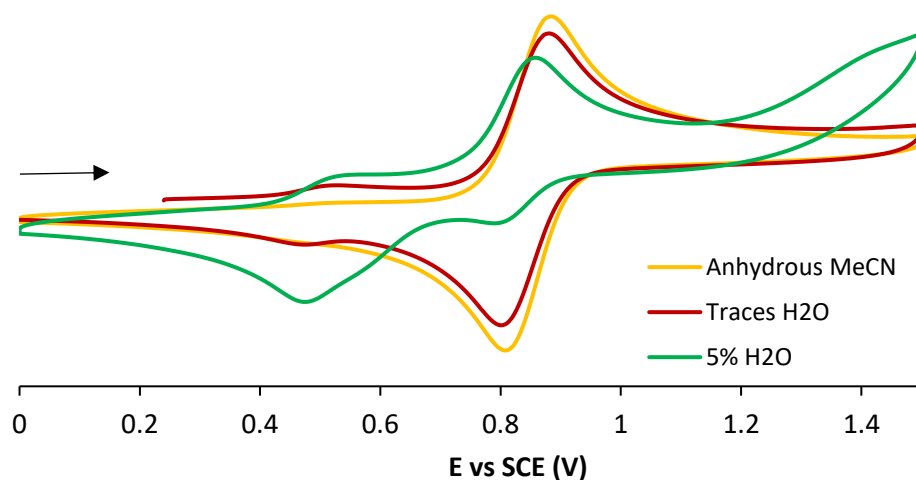
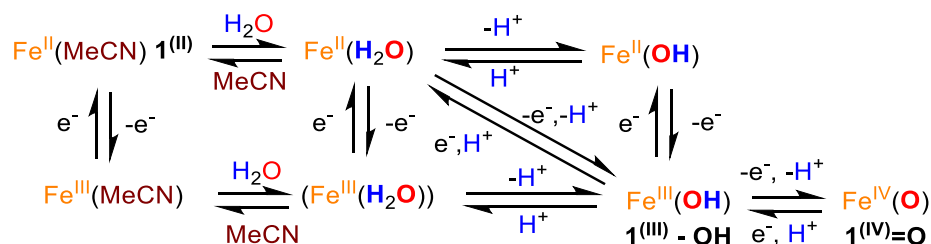


Figure III.12. Cyclic voltammetry of $1^{(II)}$. 1 mM in MeCN, 0.1 M TBAPF₆. Scanrate 0.1 V/s. GC working electrode, Pt counter electrode and SCE reference electrode.

Electrochemical studies revealed the presence of an equilibrium of species in the media depending on the oxidation state. This is not a simple scenario because there are many possible species (Scheme III.3) in solution in both oxidation states +2 and +3, such as $Fe^n(\text{MeCN})$, $Fe^n(\text{OH}_2)$ and $Fe^n(\text{OH})$ ($n = 2, 3$).

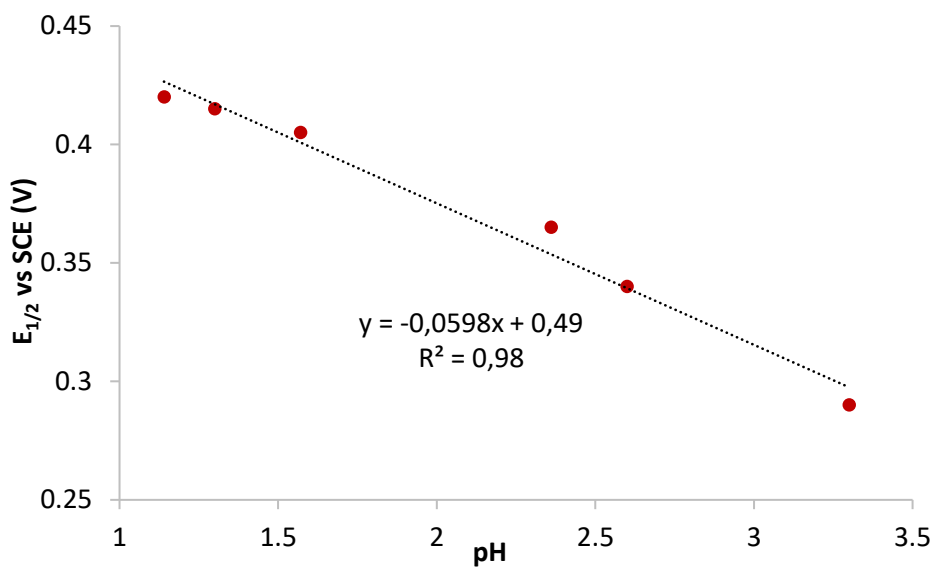


Scheme III.3. Equilibria for iron species in solution.

Further information was obtained by studying the system in water as solvent. The initial complex $1^{(II)}$ in solution showed two reversible waves at $E_{1/2} = -0.03$ and $E_{1/2} = 0.30$ V as observed in the Figure III.14 spectrum A, showing an equilibria of species $Fe^{II/III}(\text{MeCN})$ ($E_{1/2} = 0.30$ V) and $Fe^{II/III}(\text{OH}_2/\text{OH})$ ($E_{1/2} = -0.03$ V) in this solvent. The wave from $Fe^{II/III}(\text{MeCN})$ is located at higher potential due to the π – acceptor character of MeCN ligand. After some minutes in solution the $Fe^{II/III}(\text{MeCN})$ couple disappeared from the system, displaced by the high excess of water (Figure III.14 spectrum B) and the wave at $E_{1/2} = -0.03$ V from $Fe^{II/III}(\text{OH}_2/\text{OH})$ couple remained.

When triflic acid (HOTf) was added to the media, lowering the pH ≈ 3.3 , the $Fe^{II/III}(\text{OH}_2/\text{OH})$ wave was displaced to a higher potential ($E_{1/2} = 0.29$ V) (Figure III.14 spectra C). This shift is in agreement with the assignment of these bands as a proton – coupled electron – transfer step (PCET). Consistently with this interpretation, the couple shifted more with subsequent increases of the pH (Figure III.14 spectra C to G).

A Pourbaix plot (Figure III.13) was represented plotting the half – wave potential in front of the pH, revealing the dependence of $E_{1/2}$ with the pH and giving a slope of -0.0598. Which is quite close to the -0.059 (59 mV per pH unit) value expected for a PCET reaction,^{112,261} where one electron and one proton are delivered to the metal.



pH	$E_{1/2}$ vs SCE (V)
1.14	0.420
1.30	0.415
1.57	0.405
2.36	0.365
2.60	0.340
3.30	0.290

Figure III.13. Plot of $E_{1/2}$ vs pH of $\mathbf{1^{(IV)}}$ in H_2O (2mM, 0.1 M KNO_3 , scan rate = 100 mV/s).

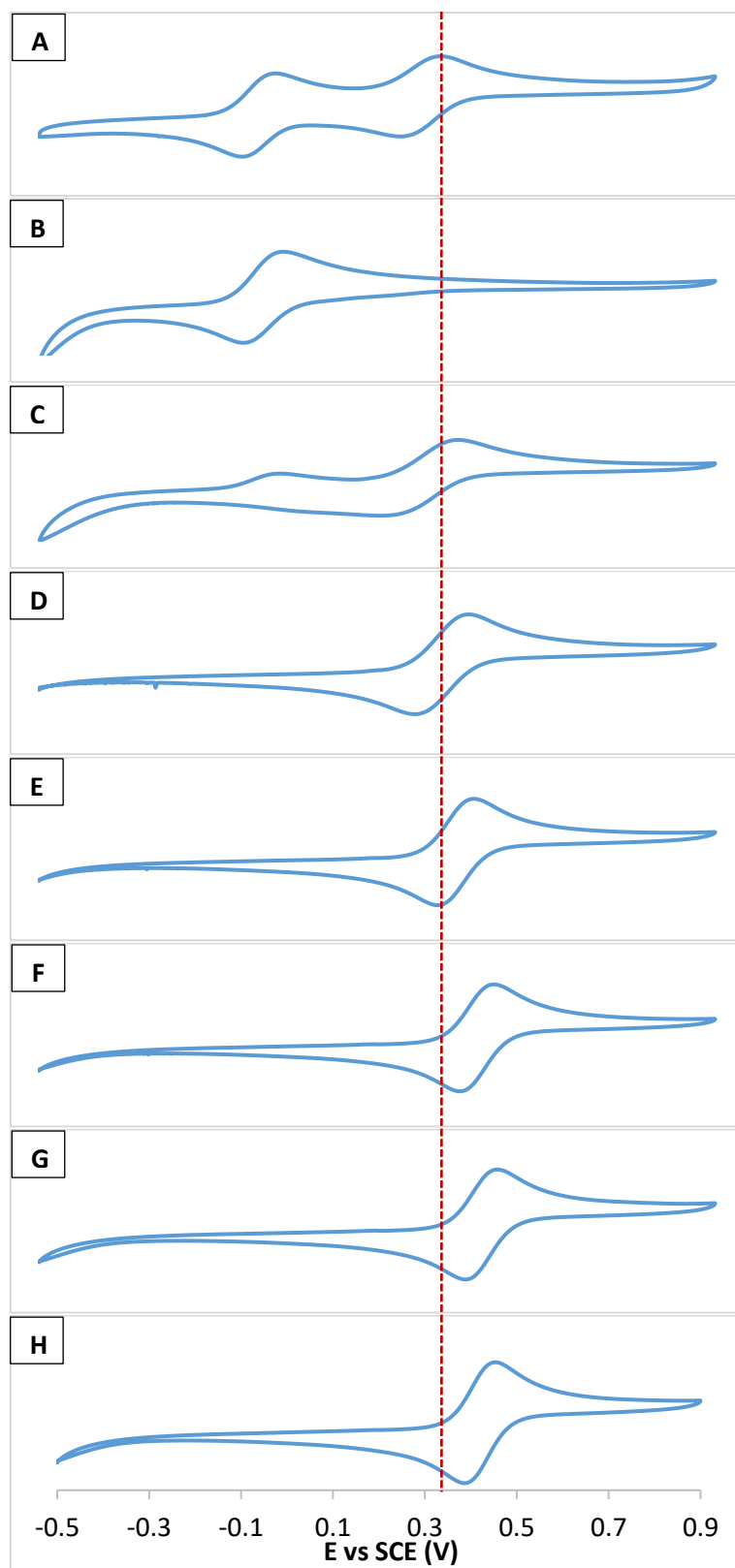
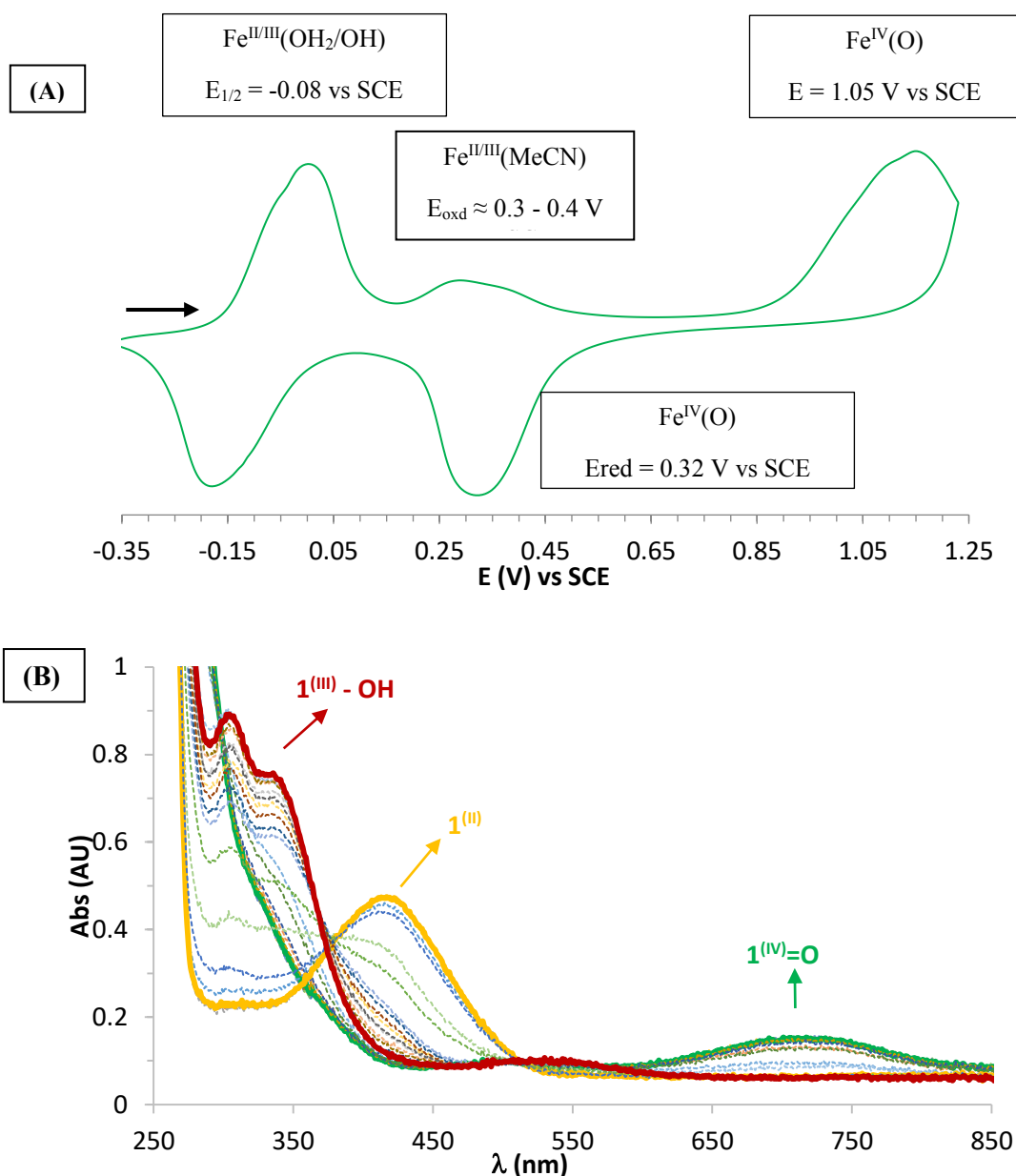


Figure III.14. Cyclic Voltammetry of $1^{(II)}$ in H_2O (2 mM, 0.1 M KNO_3 , scan rate = 100 mV/s). (A) Initial conditions. (B) CV initial conditions some minutes after preparation of the sample. (C) Addition of 1 μmol of HOTf (pH = 3.30). (D) Addition of 5 μmol of HOTf (pH = 2.60). (E) Addition of 10 μmol of HOTf (pH = 2.36). (F) Addition of 70 μmol of HOTf (pH = 1.57). (G) Addition of 130 μmol of HOTf (pH = 1.30). (H) Addition of 190 μmol of HOTf (pH = 1.14).

Furthermore bulk electrolytic oxidation of complex $1^{(III)}$ could be followed in a spectroelectrochemical OTTLE (optically transparent thin – layer electrode) cell. This cell allowed us to follow the oxidation and reduction of the iron species by both cyclic voltammetry and UV – vis spectroscopy at same time. The system uses a Pt minigrid as working electrode, a Pt auxiliary electrode and a pseudoreference electrode of Ag wire (Figure SIII.4).

We used the OTTLE system to follow the oxidation of $1^{(III)}$ in water. The initial iron (II) was oxidised to sequentially obtain the species $1^{(III)} - OH$ and $1^{(IV)}=O$ as ascertained by UV – vis spectroscopy changes. Below is shown the monitoring of the evolution in H_2O ($[Fe] = 14 \text{ mM}$, $0.1M \text{ KNO}_3$) when the potential was changed.



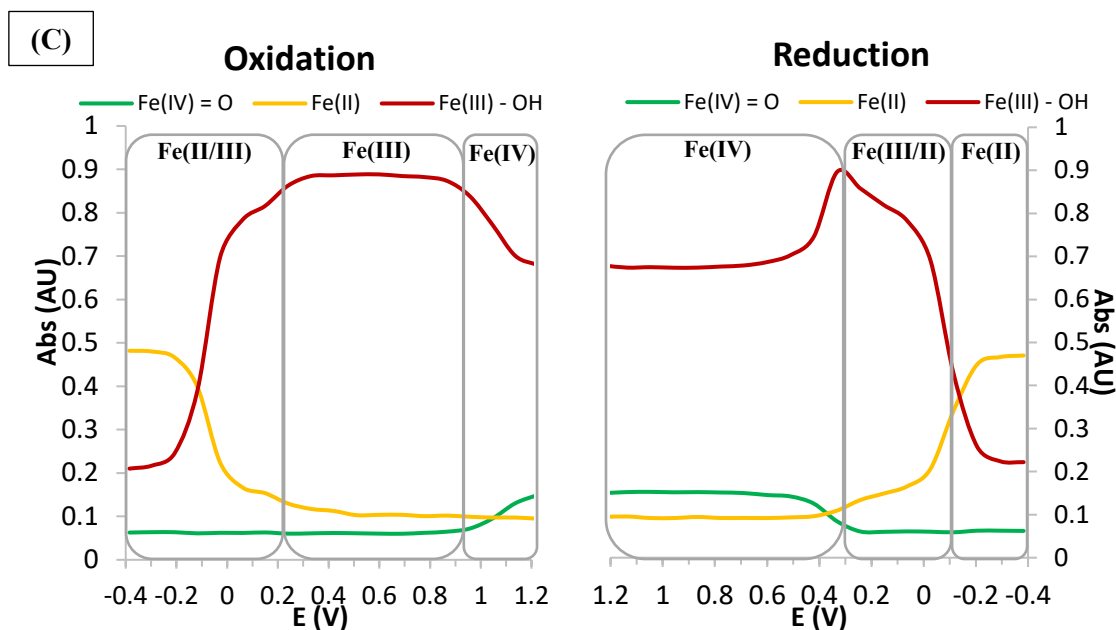


Figure III.15. Spectroelectrochemistry of complex $\mathbf{1}^{\text{III}}$ (14 mM in H_2O , 0.1 M KNO_3 , scan rate = 5 mV/s). (A) Cyclic voltammetry of $\mathbf{1}^{\text{III}}$ in H_2O . (B) UV – vis of the redox processes observed on the cyclic voltammetry spectrum. (C) Traces of the UV – vis evolution in front of the potential (Fe^{II} , Fe^{III} , and Fe^{IV} at 420 nm, 305 nm and 720 nm, respectively).

When the potential was increased, the iron (II) band ($\lambda = 420 \text{ nm}$) gradually disappeared to generate the iron (III) ($\lambda = 305 \text{ nm}$), as observed in the UV – vis (Figure III.15, B and C and SIII.6). This oxidation occurred in two steps, first at a potential between -0.2 and 0.1 V where the $\text{Fe}^{\text{II}}(\text{OH}_2)$ got oxidised to $\text{Fe}^{\text{III}}(\text{OH})$, at which point the UV the absorbance corresponding to Fe^{III} reaches a plateau. Then, the second oxidation step occurred between 0.1 and 0.3 V when the remaining Fe^{II} (in the $\text{Fe}^{\text{II}}(\text{MeCN})$ form) was oxidised and a small oxidation wave was observed in the CV. After the total oxidation to $\mathbf{1}^{\text{III}} - \text{OH}$, no changes took place until the potential reached 0.90 V, moment when the $\mathbf{1}^{\text{III}} - \text{OH}$ starts to be consumed to generate the iron (IV) – oxo complex $\mathbf{1}^{\text{IV}} = \text{O}$; the oxidation to $\mathbf{1}^{\text{IV}} = \text{O}$ was completed at 1.2 V. The estimated $E_{1/2} = 1.05 \text{ V}$ vs SCE is notably lower than the literature values (Figure III.16, $E_{1/2} = 1.23 - 1.63 \text{ V}$ vs SCE), reflecting the higher electron – donating behaviour of this ligand^{83,111} although this could be also due to the difference of conditions used (such as pH or solvent). The lower oxidation potential for $\mathbf{1}^{\text{IV}} = \text{O}$ compared to $\mathbf{2}^{\text{IV}} = \text{O}$ may be expected from comparison of $E_{1/2}$ for the $\text{Fe}^{\text{II/III}}(\text{MeCN})$ couple of $\mathbf{1}^{\text{III}}$ and $\mathbf{2}^{\text{III}}$ (Figure SIII.5, $\Delta E_{1/2} \approx -0.1 \text{ V}$). The oxidation and reduction of $\mathbf{1}^{\text{IV}} = \text{O}$ it appears as an irreversible electrochemical process and complex $\mathbf{1}^{\text{IV}} = \text{O}$ remained unchanged upon applying a reducing potential until 0.5 V, moment when $\mathbf{1}^{\text{IV}} = \text{O}$ starts to disappear to form back $\mathbf{1}^{\text{III}} - \text{OH}$. Noticeably the CV reveals that the reduction wave to $\text{Fe}^{\text{III}} - \text{OH}$ was as intense as the oxidation, indicating that $\mathbf{1}^{\text{IV}} = \text{O}$ remained unreacted, a fact that was also observed by UV – vis spectroscopy. The high stability of $\mathbf{1}^{\text{IV}} = \text{O}$ allowed to cycle between $\mathbf{1}^{\text{IV}} = \text{O}$ and $\mathbf{1}^{\text{III}} - \text{OH}$ several times with no loss of intensity. The reduction of $\mathbf{1}^{\text{IV}} = \text{O}$ to $\mathbf{1}^{\text{III}} - \text{OH}$ occurred at $E_{p,c} \approx 0.32 \text{ V}$, within the expected range. Professor Que and co – workers previously reported that the reduction of complex $[\text{Fe}^{\text{IV}}(\text{O})(\text{N4Py})]^{2+}$ is

highly dependent of the pH of the media ($E_{p,C} = -0.13 - 0.78$ V vs SCE, $[H^+] = 0.003 - 5$ M). This is expected from a PCET process, being easier the reduction at higher pH.¹¹²

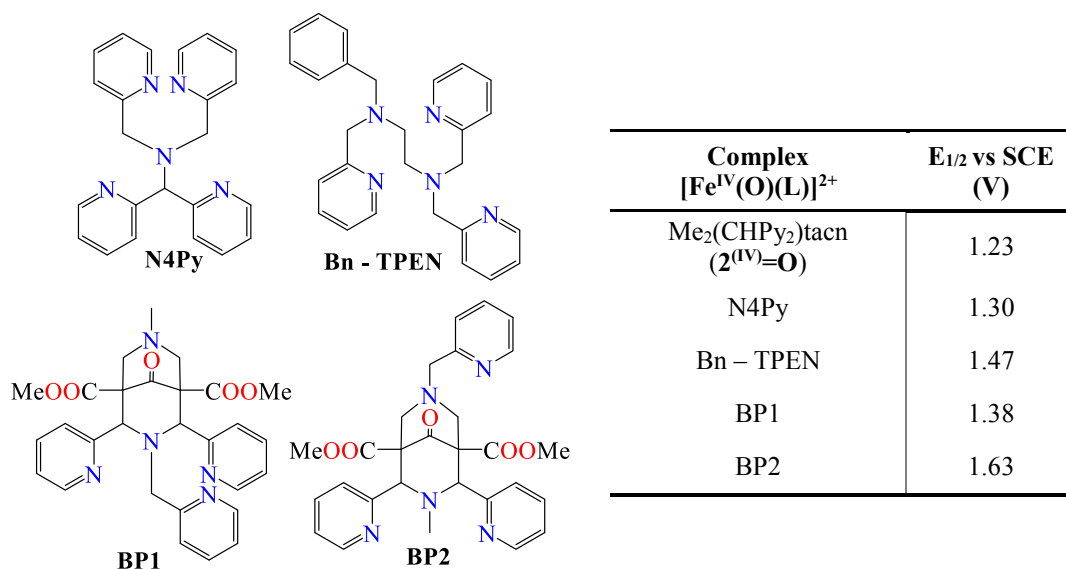


Figure III.16. $E_{1/2}$ of iron (IV) – oxo species in the literature.(ref. 83)

We also studied the redox behaviour of $1^{(II)}$ in MeCN:H₂O (1:3) following the same procedure as in H₂O, and a similar trend was observed (Figure SIII.7). Unexpectedly, there was a difference within the relative intensity of the waves for $Fe^{II/III}(MeCN)$ and $Fe^{II/III}(H_2O/OH)$ couples in the CV in favour of the former, meaning the equilibria is more displaced to the $Fe(MeCN)$ species when MeCN was introduced as co – solvent, in contrast to when only water was used. In this mixture of solvents (MeCN:H₂O, 1:3) both waves show similar intensities, while in H₂O the $Fe^{II/III}(MeCN)$ couple was almost inexistent; also in the UV – vis the step corresponding to the wave of $Fe^{II/III}(MeCN)$ (0 – 0.4 V) clearly increased in intensity, reflecting the higher amount of these species present in this conditions compared to the previous experiment (although a direct comparison may be affected by differences in the absorption coefficient, ϵ . Consequently, as there is more MeCN in solution the couple for $Fe^{II/III}(OH_2/OH)$ decreases in favour of $Fe^{II/III}(MeCN)$ couple, whose reduction half wave lies hidden under the reduction wave of the $Fe^{IV}(O)$. The potentials remained essentially the same in both media (Figure III.17).

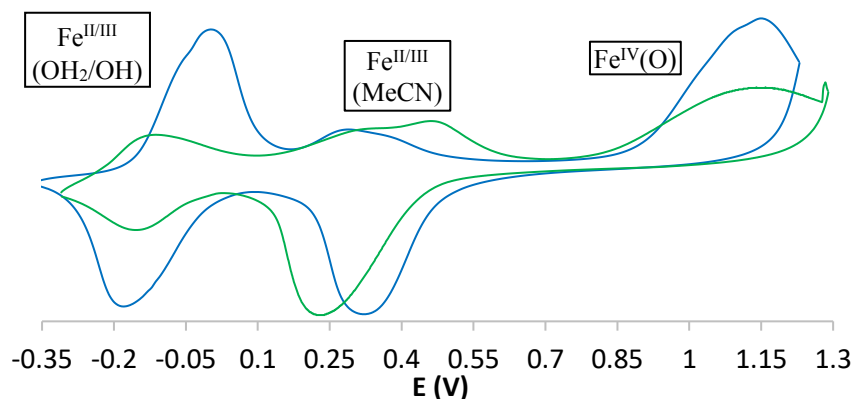


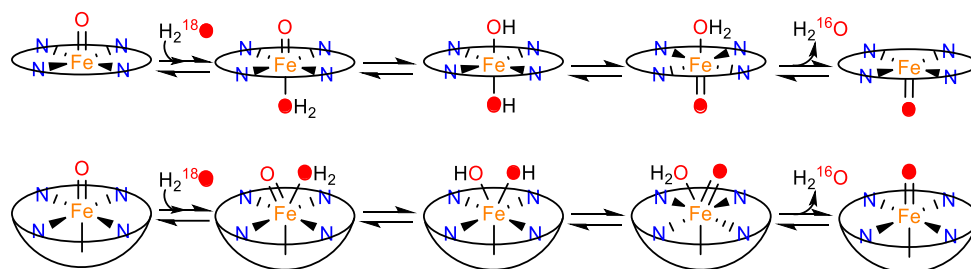
Figure III.17. Comparison of cyclic voltammetry spectra of complex $1^{(II)}$ (14 mM, 0.1 M KNO₃, scan rate = 5 mV/s) in H₂O (blue line) and MeCN:H₂O (1:3) (green line).

III.2.4. Reactivity

III.2.4.1 Oxygen atom exchange reactivity

Oxygen atom exchange (OAE) with H_2O molecules have been commonly used to indirectly identify highly reactive metal – oxo species, as intermediates in substrate oxidation reactions. This procedure has been proved very useful and widely used to establish the presence of metastable iron species, too reactive to trap or complicated to characterise.^{77,85,121,135,141,148,258,262-266} Usually an iron (II) or iron (III) species is reacted with an oxidant in presence of H_2^{18}O or an oxidant that already has ^{18}O , to form the ^{18}O – labelled iron – oxo species which subsequently transfers to the substrate. That way if the ^{18}O is incorporated into the substrate through an oxidation, the presence of an iron – oxo species is deduced.

This reactivity has been previously studied for both heme and non – heme systems and two different mechanisms were proposed (Scheme III.4). For heme systems an oxo – hydroxo tautomerism was proposed by Meunier and co – workers based on ^{18}O incorporation through epoxidation of carbamazepine substrate,²⁵⁸ where a water molecule binds *trans* to the oxo moiety to subsequently scramble the labelling through a *trans* – bis – hydroxo intermediate. While for non – heme complexes an analogous *cis* – bis – hydroxo intermediate was proposed by Seo *et al.*, because non heme complexes lack the symmetry plane present on porphyrin rings. Electrospray ionization mass spectrometry (ESI – MS) was used to give kinetic evidence by Seo *et al.* for OAE reactivity, as well as the activation parameters, for complexes $[\text{Fe}^{\text{IV}}(\text{O})(\text{L})]^{2+}$ (L = TMC and N4Py).²⁵⁹



Scheme III.4. Proposed oxo – hydroxo tautomerism mechanisms for ^{18}O exchange in heme (top) and non – heme systems (below).

More recently in our group we studied the OAE mechanism for tacn – based ligands in collaboration with Professor Lawrence Que’s group.⁷⁹

The oxygen exchange reactivity with H_2^{18}O was analysed for complexes $\mathbf{1}^{\text{IV}}=\text{O}$, $\mathbf{2}^{\text{IV}}=\text{O}$ and we revisited the tetradentate analogue $[\text{Fe}^{\text{IV}}(\text{O})(\text{Me}_2\text{Pytacn})(\text{MeCN})]^{2+}$ ($\mathbf{3}^{\text{IV}}=\text{O}$, Me_2Pytacn = 1 – (2’ – pyridylmethyl) – 4, 7 – di – methyl – 1, 4, 7 – triazacyclononane) previously studied in our group (Scheme III.5).⁷⁷ The oxygen atom exchange reactivity with water was compared with other well established oxoiron (IV) bearing tetra – and pentadentate macrocyclic and polipyridine ligands.

To study the rates of OAE, H_2^{18}O was added to solutions of the studied iron (IV) – oxo complexes and exchange reactions were monitored by electrospray mass spectrometry (monitoring the iron (IV) – oxo complex) or GC – MS (after transferring to a substrate) (see experimental section); the formation of the

$\text{Fe}^{\text{IV}}(^{18}\text{O})$ species were plotted vs time and adjusted to an exponential rise profile to obtain the observed exchange rates, k_{obs} (Figure III.18). The three ligands are based on the tacn platform with a difference in the number and disposition of pyridine rings, $\mathbf{1}^{\text{(IV)}}=\text{O}$ and $\mathbf{2}^{\text{(IV)}}=\text{O}$ have two picolyl arms attached to two different nitrogen atom on $\mathbf{1}^{\text{(IV)}}=\text{O}$ and in the same N on $\mathbf{2}^{\text{(IV)}}=\text{O}$ while $\mathbf{3}^{\text{(IV)}}=\text{O}$ has only one arm (Scheme III.5). Figure III.18 shows the different behaviour observed for each of them respect to the concentration of added H_2^{18}O .

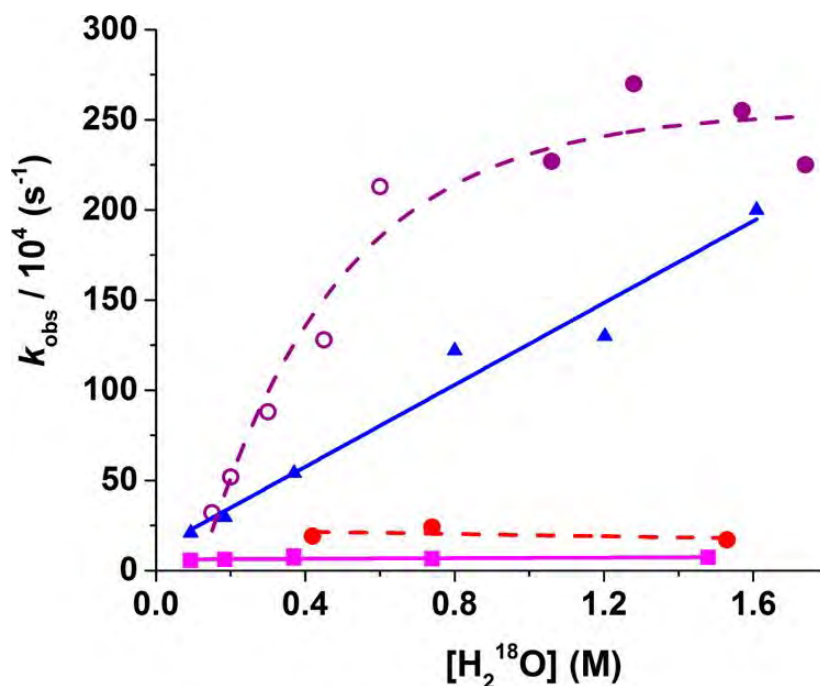


Figure III.18. Plot of H_2^{18}O concentration dependence for ^{18}O incorporation rate in $\mathbf{1}^{\text{(IV)}}=\text{O}$ (0.5 mM, filled blue triangles at 50 °C), $\mathbf{2}^{\text{(IV)}}=\text{O}$ (0.5 mM, filled pink squares at 50 °C) and $\mathbf{3}^{\text{(IV)}}=\text{O}$ (open and filled purple circles at 22 °C, filled red circles at 0 °C), in MeCN solution. Open purple circles are from ref 77.

A small difference in the syntheses of the iron – oxo complexes is present: $\mathbf{1}^{\text{(IV)}}=\text{O}$ and $\mathbf{2}^{\text{(IV)}}=\text{O}$ were generated with an excess of PhIO, while $\mathbf{3}^{\text{(IV)}}=\text{O}$ was prepared using peracetic acid as the oxidant as previously reported.⁷⁷ Exchange rates for ^{18}O label incorporation in $\mathbf{3}^{\text{(IV)}}=\text{O}$ showed a linear dependence on $[\text{H}_2^{18}\text{O}]$ at 22 °C, suggesting a bimolecular association of complex with water in the RDS. The analogue iron – oxo complexes of $\mathbf{3}^{\text{(IV)}}=\text{O}$ $[\text{Fe}^{\text{IV}}(\text{O})(\text{Me}_2\text{Pytacn})(\text{X})]^+$ with $\text{X} = \text{Cl}$ or Br did not exchange with $[\text{H}_2^{18}\text{O}]$ further supporting this mechanism.⁷⁸ In the current work the $[\text{H}_2^{18}\text{O}]$ range for water incorporation in $\mathbf{3}^{\text{(IV)}}=\text{O}$ was expanded up to $[\text{H}_2\text{O}] \approx 1.7$ M, finding that a gradual saturation occurred in incorporation rates until ≈ 0.6 M of labelled water addition. At higher $[\text{H}_2^{18}\text{O}]$ a saturation behaviour was reached. Moreover this saturation was found to be also temperature dependent, revealing that at 0 °C saturation was already achieved at low H_2^{18}O concentration (0.42 M, Figure III.18 and SIII.9). Surprisingly, complex $\mathbf{2}^{\text{(IV)}}=\text{O}$ showed exchange rates that are independent on water concentration at 50 °C, with a saturation behaviour observed from 0.1 to 1.5 M of $[\text{H}_2^{18}\text{O}]$, symptomatic of a possible difference in the RDS. This behaviour is in sharp contrast also with complex $\mathbf{1}^{\text{(IV)}}=\text{O}$, which exchange rates at 50 °C show a linear

dependence with $[\text{H}_2^{18}\text{O}]$, and with no saturation behaviour ($k_2 = 11 \cdot 10^{-3} \text{ M}^{-1}\text{s}^{-1}$), these data suggests that different RDS could exist for these complexes.

Furthermore KIE values corroborate these data, following the $^{18/16}\text{O}$ ratio evolution after addition of H_2O or D_2O to $\text{Fe}^{\text{IV}}(^{18}\text{O})$ solutions of $\mathbf{1}^{\text{IV}}=\mathbf{O}$, $\mathbf{2}^{\text{IV}}=\mathbf{O}$ and $\mathbf{3}^{\text{IV}}=\mathbf{O}$ revealed significant differences in reaction rates towards $\text{Fe}^{\text{IV}}(^{16}\text{O})$ formation. Complex $\mathbf{3}^{\text{IV}}=\mathbf{O}$ showed an almost invariable KIE value of 1.5 – 1.8 working in both the linear and the saturated regime at 22 and 0 °C respectively (Table III.2, Figures SIII.8 – SIII.10). In contrast to that, complex $\mathbf{2}^{\text{IV}}=\mathbf{O}$ showed a KIE = 5.7 suggesting a large degree of O – H/O – D cleavage during the RDS. A KIE of 1.3 was obtained for complex $\mathbf{1}^{\text{IV}}=\mathbf{O}$, in coherence with the differences already observed in the rate constants.

Moreover, the activation parameters for the OAE reactivity were also compared, revealing some differences between complexes. The previously reported activation parameters for $\mathbf{3}^{\text{IV}}=\mathbf{O}$ ($\Delta H^\ddagger = 10.2 \pm 0.8 \text{ kcal/mol}$ and $\Delta S^\ddagger = -32 \pm 3 \text{ cal/K}\cdot\text{mol}$)⁷⁷ were recalculated taking into account the two different regimes. Although the new results somehow differ from the previously reported values the conclusions are not changing. Combining the reported data with new values for the linear regimen a $\Delta H^\ddagger = 8.2 \pm 1.2 \text{ kcal/mol}$ and $\Delta S^\ddagger = -38.5 \pm 9.1 \text{ cal/K}\cdot\text{mol}$ were found, while in the saturated regime values of $\Delta H^\ddagger = 6.2 \pm 0.7 \text{ kcal/mol}$ and $\Delta S^\ddagger = -46.4 \pm 2.4 \text{ cal/K}\cdot\text{mol}$ were obtained. Interestingly, activation parameters obtained for both linear and saturated regimens (Figure III.19) are essentially the same within experimental error (following the KIE trend), thus revealing the possibility of a common mechanism in both regimes. Comparing this data with the activation parameters of $\mathbf{1}^{\text{IV}}=\mathbf{O}$ and $\mathbf{2}^{\text{IV}}=\mathbf{O}$ some differences were found (Table III.2), while ΔH^\ddagger for $\mathbf{2}^{\text{IV}}=\mathbf{O}$ ($5.3 \pm 0.3 \text{ kcal/mol}$) is close to the values obtained for $\mathbf{3}^{\text{IV}}=\mathbf{O}$, complex $\mathbf{1}^{\text{IV}}=\mathbf{O}$ shows a $\Delta H^\ddagger = 21.3 \text{ kcal/mol}$, which is 4 times that of $\mathbf{2}^{\text{IV}}=\mathbf{O}$. Moreover while ΔS^\ddagger on $\mathbf{2}^{\text{IV}}=\mathbf{O}$ and $\mathbf{3}^{\text{IV}}=\mathbf{O}$ is quite large and negative (from -38.5 to -52.6 $\text{cal/K}\cdot\text{mol}$), what was expected for an associative mechanism of iron complex with water, for complex $\mathbf{1}^{\text{IV}}=\mathbf{O}$ it is almost zero. These data could indicate that complex $\mathbf{1}^{\text{IV}}=\mathbf{O}$ could follow a pathway where a pyridine arm decoordinates to allow the binding of the water to the metal.

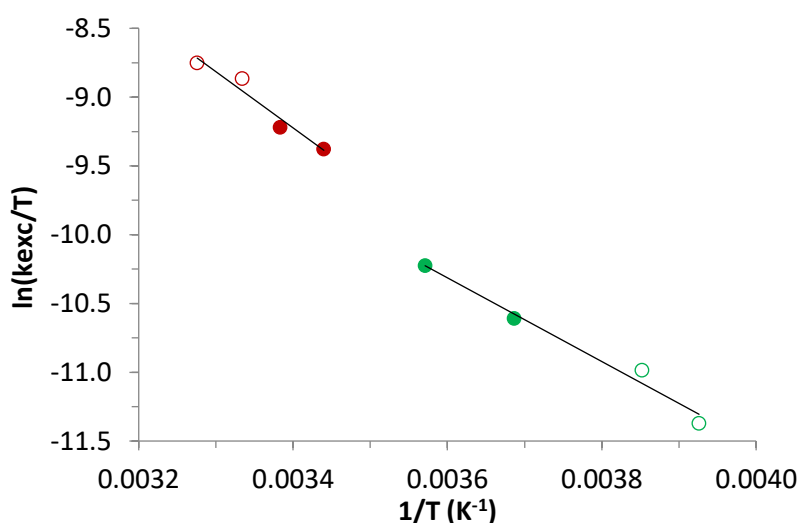


Figure III.19. Eyring plot for complex $\mathbf{3}^{\text{IV}}=\mathbf{O}$ linear regime (red circles) and saturated regime (green circles). Open circles are data from ref 77.

Table III.2. Kinetic data and KIE values of OAE for tacn complexes $1^{(IV)=O}$, $2^{(IV)=O}$ and $3^{(IV)=O}$.

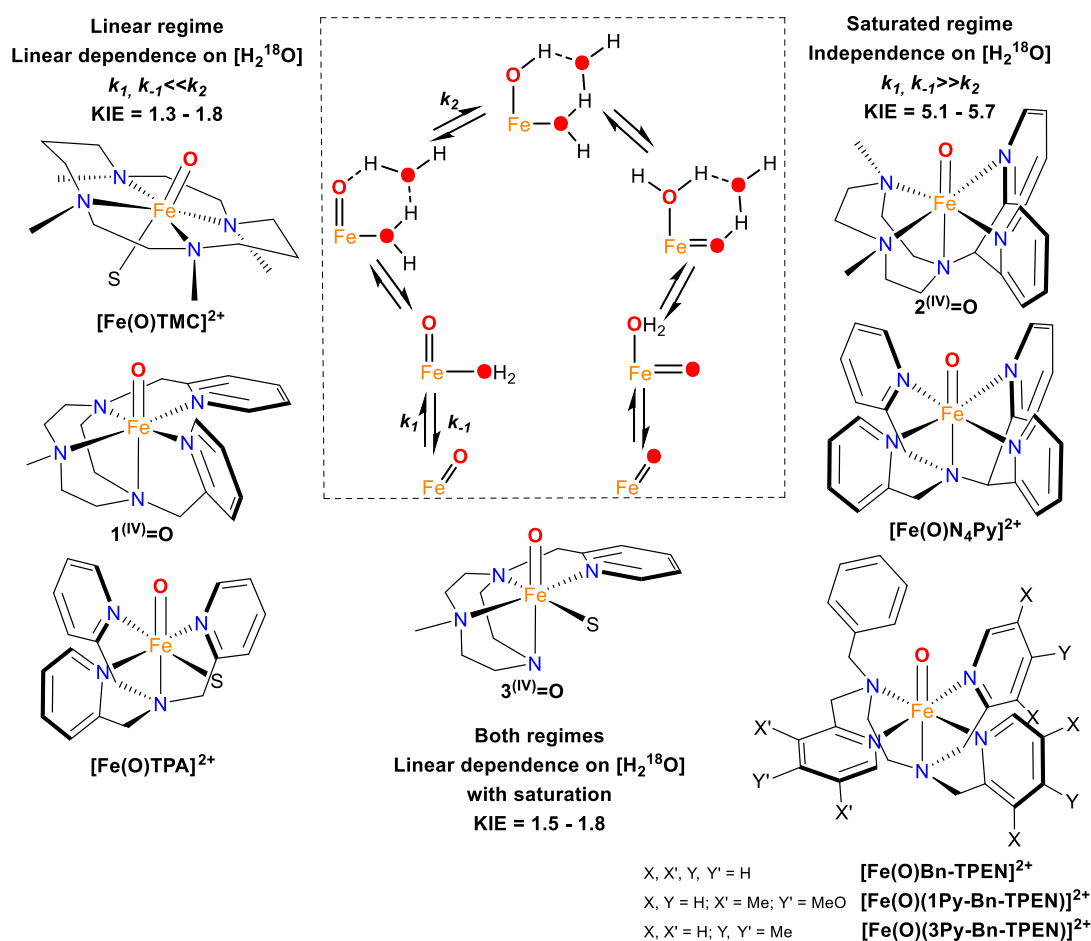
Complex	KIE (H ₂ O/D ₂ O)	[H ₂ O or D ₂ O] (M)	T (K)	ΔH^\ddagger (kcal/mol)	ΔS^\ddagger (cal/K·mol)	ΔG^\ddagger_{298} (kcal/mol)	[H ₂ O] regime
$1^{(IV)=O}^a$	1.3	0.37	303	21.3 ± 2.4	-2.4 ± 7.2	22.0	Linear
$2^{(IV)=O}^a$	5.7	0.37	318	5.3 ± 0.3	-52.6 ± 2.4	21.0	Saturation
$3^{(IV)=O}$	1.8	0.42	295	8.2 ± 1.2 ^b	-38.5 ± 9.1 ^b	19.6	Linear
	1.6	0.42	273				
	1.7	0.74	273	6.2 ± 0.7 ^c	-46.4 ± 2.4 ^c	20.1	Saturation
	1.5	1.57	273				

^aData from ref 79. ^bValues obtained between 310 and 295 K, data in combination with ref 77. ^cValues obtained between 258 and 284 K, data in combination with ref 77.

The obtained data was compared with a group of iron (IV) – oxo complexes containing tetra – and pentadentate ligands (Table SIII.4), to obtain a more general vision for reactivity of these species with water through OAE.⁷⁹ In general two main groups of complexes were found depending on its [H₂¹⁸O] dependence. First family comprises those complexes showing a linear dependence on water concentration thus suggesting a bimolecular RDS occurs, where H₂¹⁸O binds to the iron. The second family belongs to the complexes whose rates show independence from water concentration, in this group RDS would occur after an initial binding of water to the metal centre, and the determining step would be the abstraction of H atom or a possible tautomerization between oxo and aqua ligands. In this regard complexes [Fe^{IV}(O)(TMC)]²⁺, $1^{(IV)=O}$ and [Fe^{IV}(O)(TPA)]²⁺ were associated with the first family, showing linear dependence from [H₂¹⁸O] and relatively small KIEs (1.3 – 1.8). Complexes [Fe^{IV}(O)(N4Py)]²⁺, [Fe^{IV}(O)(Bn – TPEN)]²⁺, [Fe^{IV}(O)(1 – Py – Bn – TPEN)]²⁺, [Fe^{IV}(O)(3Py – Bn – TPEN)]²⁺ and $2^{(IV)=O}$ belong to the second family, showing rate independence from [H₂¹⁸O] and large KIEs associated (5.1 – 5.7). Interestingly $3^{(IV)=O}$ fits in both regimes, revealing a linear regimen at low [H₂¹⁸O] at 22 °C and saturation behaviour >0.6 M, indicating that a common mechanism for both families of complexes may take place.

In general, activation parameters are similar for all complexes including both families, with relatively small enthalpies ($\Delta H^\ddagger = 1.2$ to 10.3 kcal/mol) and large negative entropies ($\Delta S^\ddagger = -38.5$ to -59.8 J/K·mol) suggesting activation parameters imply a combination of steps in the mechanism. Only complex $1^{(IV)=O}$ differed from others with an almost zero entropy and a high enthalpy value, suggesting a unimolecular RDS, possibly a pyridine arm would dissociate to allow the coordination of water. Based on new results and the previously reported data⁷⁷ we proposed a mechanism common for all the studied complexes, shown in Scheme III.5. The depicted mechanism consists of several reversible steps, with an initial coordination of H₂¹⁸O to the metal and assisted by outer – sphere coordinated water molecules. The first family, containing the species [Fe^{IV}(O)(TMC)]²⁺, $1^{(IV)=O}$ and [Fe^{IV}(O)(TPA)]²⁺, would imply $k_{-1}, k_1 \ll k_2$ thus being the RDS the coordination of H₂¹⁸O to the metal and showing a linear dependence with [H₂¹⁸O] with relatively small KIEs (1.3 – 1.8). Regarding the second family (including species [Fe^{IV}(O)(N4Py)]²⁺, Bn – TPEN complexes, and $2^{(IV)=O}$), is suggested $k_{-1}, k_1 \gg k_2$ with a water binding pre – equilibrium and the

proton transfer becoming the RDS, thus making the reaction rate independent from $[\text{H}_2^{18}\text{O}]$ and giving higher KIE values (5.1 – 5.7). Complex $3^{(\text{IV})}=\text{O}$ remains as the connection between both families, fitting in both regimes depending on reaction conditions.



Scheme III.5. Common mechanism suggested for OAE with iron (IV) – oxo complexes studied.

III.2.4.2. Reactivity of $1^{(\text{IV})}=\text{O}$ and $2^{(\text{IV})}=\text{O}$ with organic substrates

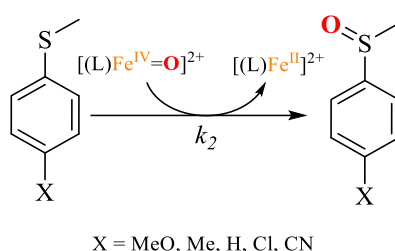
The oxidation capacity of $[\text{Fe}^{\text{IV}}(\text{O})(\text{MePy}_2\text{tacn})](\text{SO}_3\text{CF}_3)_2$, $1^{(\text{IV})}=\text{O}$, and $[\text{Fe}^{\text{IV}}(\text{O})(\text{Me}_2(\text{CHPy}_2)\text{tacn})](\text{SO}_3\text{CF}_3)_2$, $2^{(\text{IV})}=\text{O}$, complexes was studied towards typical substrates in HAT (Hydrogen Atom Transfer) and OAT (Oxygen Atom Transfer) reactions.

The kinetics of the reactions with sulphides (OAT) and alkylbenzenes (HAT) were explored using freshly prepared solutions of $1^{(\text{IV})}=\text{O}$ and $2^{(\text{IV})}=\text{O}$ (1 mM) in acetonitrile. OAT and HAT reactions were monitored by following the evolution over time of the absorbance from the low – energy bands corresponding to the iron (IV) species. The decay traces obtained by UV – vis spectroscopy were satisfactorily adjusted to first order exponential decay processes to obtain the values of the kinetic constants observed (k_{obs}), according to equation (1). The plot of k_{obs} vs. substrate concentration gives k_2 values as fit of the linear regression slope, which is the rate constant for a given reaction.

$$d[\text{Fe}^{\text{IV}}]/dt = k_{\text{obs}}[\text{Fe}^{\text{IV}}] \quad (1)$$

III.2.4.2.1. Reactivity of $1^{(IV)=O}$ and $2^{(IV)=O}$ in OAT reactions – Thioanisole oxidation

In first place reactions of $1^{(IV)=O}$ and $2^{(IV)=O}$ (1 mM) against different concentrations of thioanisole substrate (10 – 500 mM) were analysed at 20 °C. The observed reaction rates (k_{obs}) were found to be linearly dependent on sulphide concentration indicating that they are pseudo – first order rate constants with the expression $k_{obs} = k_2[\text{sulphide}]$. The respective second order rate constants (k_2) were then calculated from this fitting. Additionally, the k_2 values for $1^{(IV)=O}$ and $2^{(IV)=O}$ were determined for *para* substituted thioanisole substrates ($^X\text{PhSMe}$, X = MeO, Me, H, Cl and CN) to study the rate constant dependence as a function of the electronic demand of the substituent and are shown in Table III.3. A Hammett plot was also represented by plotting the k_2 against Hammett parameters (σ_p).



Scheme III.6. General oxidation mechanism in OAT reactions for *p* – methylphenylthioethers performed by iron (IV) oxo complexes.

An example of the decay of the $\text{Fe}^{IV}=\text{O}$ bands when adding 50 eq thioanisole at 20°C is shown in the following figure.

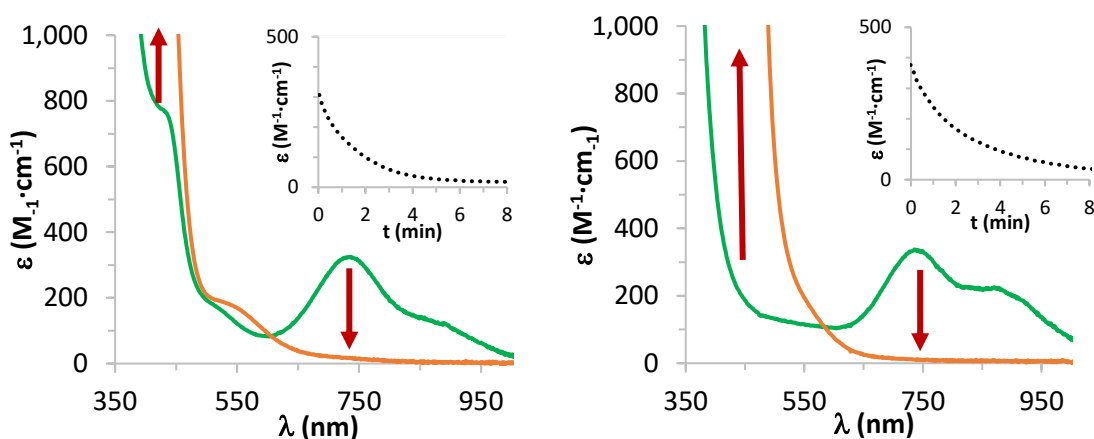


Figure III.20. UV – vis spectrum of the decay of complexes $1^{(IV)=O}$ (left) and $2^{(IV)=O}$ (right) upon addition of 50 eq of thioanisole at 20 °C, insets show the decay of 738 and 748 nm bands.

As could be observed, the characteristic bands at 738 and 748 nm disappeared upon addition of the thioanisole substrates, and the band corresponding to the Fe(II) (≈ 400 nm) species appears in a reaction that formally entails an oxygen atom transfer from the oxo – iron (IV) species to the substrate forming a sulfoxide product and an Fe(II) species.

To characterize the products obtained on the oxidation reactions, to the solution obtained from the oxidation of thioanisole substrates at RT was added one equivalent of biphenyl, the solution was filtered through silica to remove the metal complex and analysed by GC. The oxidations were carried out adding excess of thioanisole, consequently a large excess of corresponding substrates were observed in the GC. Peaks corresponding to biphenyl and sulfoxides were also observed and only traces of sulfone were found. It was also observed the iodobenzene peak (1 equivalent respect to Fe^{II}) which was formed on the reduction of iodobenzene during the formation of the oxoferryl complex.

Under this reaction conditions sulfoxides were obtained from good to excellent yields ranging from 65 to 94 % for complex **1**^(IV)=O and from 93 to 100 % for **2**^(IV)=O (Table SIII.5). These high yields confirm that only one equivalent of complex is needed to oxidize the substrates by OAT mechanism indicating Fe^{IV}=O evolves to form Fe^{II} complex.

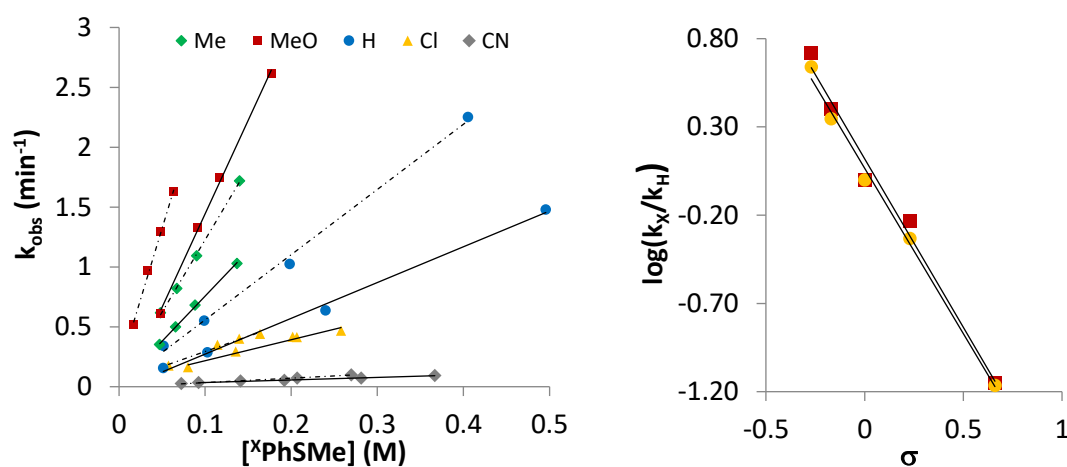


Figure III.21. (Left) Comparison plot of k_{obs} vs $[p - \text{XPhSMe}]$ concentration for complexes **1**^(IV)=O (solid lines) and **2**^(IV)=O (dashed lines). (Right) Hammett plot of **1**^(IV)=O (yellow circles) and **2**^(IV)=O (red squares).

Table III.3. k_2 values and $\log(K_X/K_H)$ and σ_{para} values for reaction of **1**^(IV)=O and **2**^(IV)=O with methylphenylthioethers.

Substituent in para	k_2 (M ⁻¹ ·s ⁻¹ , 10 ⁻³) complex 1 ^(IV) =O	k_2 (M ⁻¹ ·s ⁻¹ , 10 ⁻³) complex 2 ^(IV) =O	$\log(k_X/k_H)$	$\log(k_X/k_H)$	σ_{para}
CN	3.5 ± 0.1	6.2 ± 0.3	-1.15	-1.17	0.66
Cl	29 ± 3	42 ± 4	-0.23	-0.33	0.23
H	50 ± 2	91 ± 4	0.00	0.00	0.00
Me	126 ± 3	201 ± 4	0.40	0.34	-0.17
MeO	260 ± 9	400 ± 20	0.72	0.64	-0.27

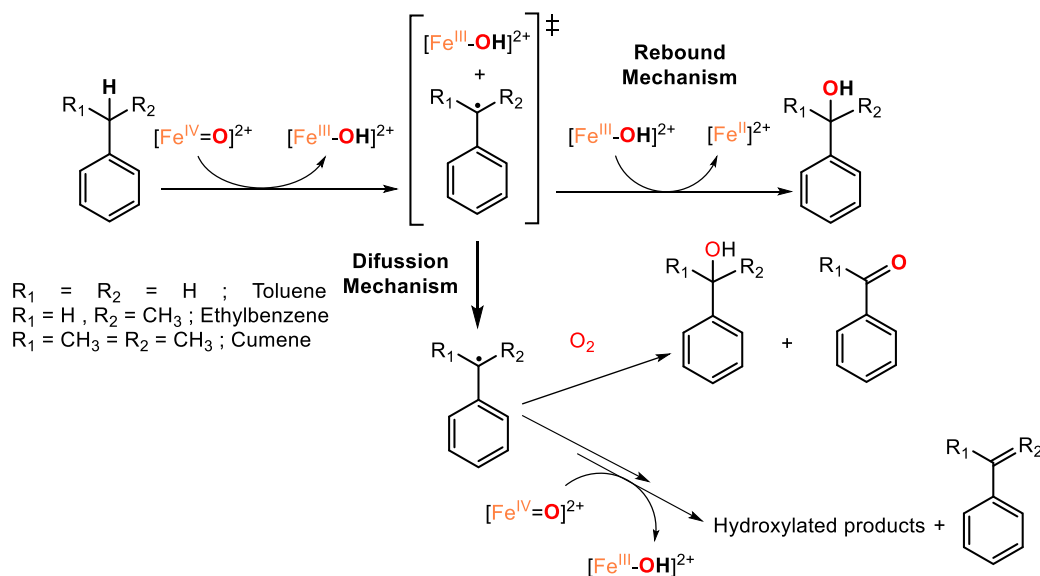
We obtained the rate constants, k_2 , of the studied reactions by Plotting k_{obs} vs the $p - \text{XPhSMe}$ concentration (X = MeO, Me, H, Cl and CN) (Figure III.21, left). As observed in Table III.3, in the oxo transfer reaction complex **2**^(IV)=O is faster than **1**^(IV)=O, being its rate constants about 1.4 to 1.9 times higher comparing with same substrates. As expected, the effect of the group at the para position of the thioanisole

modifies significantly the rate constants. Revealing a direct correlation between the electronic donating capacity of the group at the *p* – position of the benzene and the rate of the reaction. Being the more electron – withdrawing the substituent the slower the reaction. When the $\log(k_x/k_H)$ was represented against the σ_p values in a Hammett plot (Figure III.21, right), the correlation line shows linearity with a slope of $\rho = -1.91$ for $1^{(IV)=O}$ and -1.87 for $2^{(IV)=O}$. These data, together with the high amounts of sulfoxides obtained, indicate that $1^{(IV)=O}$ and $2^{(IV)=O}$ are highly electrophilic species. ρ values are consistent with the slopes reported in the literature, for example the oxo transfer to thioanisole substrates with $[\text{Fe}^{IV}(\text{O})(\text{X})(\text{Me}_2\text{Pytacn})]^{2+}$ (1 – (2' – pyridylmethyl) – 4,7 – dimethyl – 1,4,7 – triazacyclononane, X = MeCN, Cl, Br) from our group ($\rho = -1$ to -1.5)^{77,78} or the $\rho = -2.0$ obtained by Professor Nam with $[\text{Fe}^{IV}(\text{O})(\text{N4Py})]^{2+}$ species (N4Py = N, N – bis(2 – pyridylmethyl) – bis(2 – pyridyl)methylamine).²⁶⁷ On the other hand, the small slopes (-3.98 and -3.87) obtained by plotting $\log(k_x)$ vs the one – electron oxidation potential of *p* – X – thioanisoles (E°_{ox}) further suggests that the oxidation occurs via a direct oxygen – atom transfer process and not an initial electron transfer (ET) (Figure SIII.11).²⁶⁸

III.2.4.2.2. Reactivity of $1^{(IV)=O}$ and $2^{(IV)=O}$ in HAT – Alkylbenzene substrates

The oxidative capability of iron (IV) – oxo complexes $1^{(IV)=O}$ and $2^{(IV)=O}$ was also tested in HAT transformations. We studied as prototypical substrates cumene, ethylbenzene and toluene, a tertiary (CH), secondary (CH₂) and primary (CH₃) groups. Alkylbenzene rate constants at 20 °C have been calculated for its oxidation to the corresponding benzylic alcohols and we studied the products for these reactions. HAT reactions are much slower than those in OAT reactivity and consequently k_2 values are much smaller and higher substrate excess is needed (Table III.6).

The generally accepted mechanism for non – heme HAT reactivity is:



Scheme III.7. Proposed mechanism for oxidation HAT reactivity of alkylbenzenes with iron (IV) – oxo complexes.

It is known that high – valent heme oxoiron species perform alkane oxidations through a hydrogen abstraction – hydroxo rebounding radical mechanism. In the case of non – heme high – valent iron complexes it is assumed that these reactions go through the same mechanism,⁵⁴ where first the hydrogen atom is abstracted by the iron (IV) complex to form an iron (III) – hydroxo species. Subsequently, via a rebound – like step, the hydrogen is recovered by the substrate in form of a hydroxyl group to be oxidised. Rebound mechanism has been also established for ruthenium (IV) – oxo complexes.²⁶⁹ In contrast, recent evidence that the rebounding step of hydroxo moiety is not occurring with iron (IV) – oxo systems was reported by Professor Nam.²⁷⁰ Although the mechanism for such reactions is not completely clear and remains a controversial topic, leading to an ongoing debate whether a rebound mechanism or a dissociative pathway takes place.²⁴ As a general trend, with S = 1 non – heme iron (IV) – oxo species, low amounts of oxidised products are obtained, suggesting that no rebound step takes place. Contrasting results were reported by Maiti and co – workers, who claimed a rebound – like step in the oxidation of alkylbenzenes (*e.g.* cumene) using system $[\text{Fe}^{\text{IV}}(\text{O})\text{N4Py}^{\text{OMe,Me}}]$, suggesting different pathways after radical formation depending on substrate.²⁷¹ On the other hand, high kinetic isotope effects evidence that hydrogen abstraction takes place but, after this step the carbon – centred radical most likely escapes from metal vicinity diffusing to the media and reacting with adventitious water, dioxygen or another $\text{Fe}^{\text{IV}}=\text{O}$ species to generate the oxidised products through a dissociative mechanism.

In order to get insight into the oxidation mechanism of C – H bonds with iron complexes we studied the rate constants for the C – H abstraction of cumene, ethylbenzene and toluene. The values were obtained from the decay on UV – vis spectrum analysed with different substrate concentration at a Fe^{IV} fixed concentration (1 mM). Below is shown an example of the $\text{Fe}^{\text{IV}}=\text{O}$ consumption when adding 500 eq of cumene at 20°C.

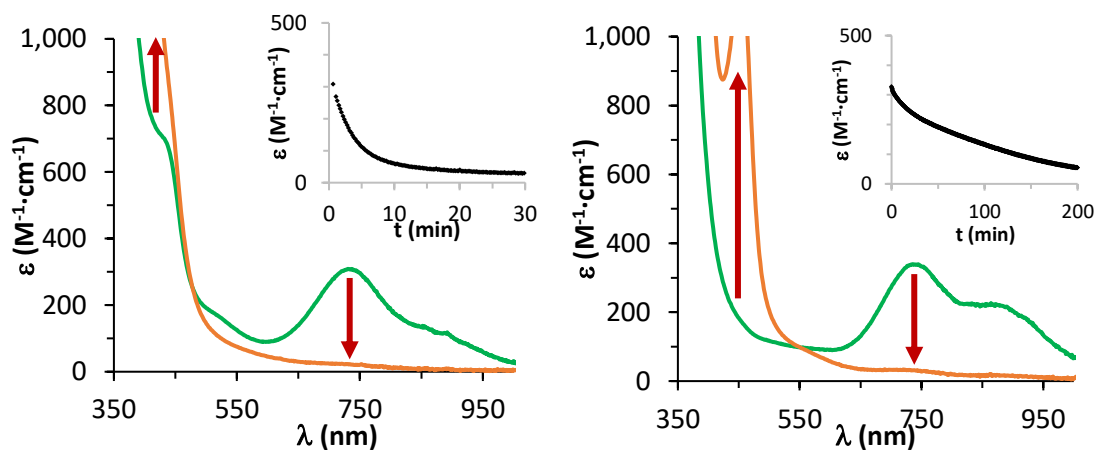


Figure III.22. UV – vis spectrum of the decay of complexes $1^{(\text{IV})}=\text{O}$ and $2^{(\text{IV})}=\text{O}$ upon addition of 500 eq. of cumene substrate were added at 20°C (insets show the traces of 738 and 748 nm features respectively).

As could be observed the characteristic bands at 738 and 748 nm gradually disappeared upon addition of the substrate (Figure III.22 and SIII.12). Unlike in the OAT reactions, $1^{(\text{III})}$ and $2^{(\text{III})}$ are not regenerated in these reactions, and mixtures were investigated to analyse whether iron (III) was formed. After reaction of $1^{(\text{IV})}=\text{O}$ and $2^{(\text{IV})}=\text{O}$ with alkylbenzylic substrates, the reaction mixtures were further analysed by UV – vis and reactivity with reducing agents.

When one equivalent of ferrocene (Fc) was added after the complete consumption of the iron (IV), the ferrocenium (Fc⁺) band appeared, indicating ferrocene was oxidised by one electron. The resulting solution allowed to quantify the amount of ferrocenium generated as well as the iron (II) (**1**^(II) or **2**^(II)) recovered. As shown on Table III.4 after reaction of **1**^{(IV)=O} and **2**^{(IV)=O} with alkylbenzenes the remaining iron species is basically iron (III) (75 – 100 % Fc⁺). Consequently, the oxidised products cannot be directly related to a rebounding of the hydroxo moiety on the basis that final iron species seem to remain iron (III). Since a rebound – like mechanism would yield iron (II) as the final iron species. On the other hand, we considered the possibility to generate Fe^{III} – OH from a comproportionation by the reaction of Fe^{II} and Fe^{IV}. Indeed Fe^{IV}(O) species decomposed after addition of Fe^{II} to generate Fe^{III}(OH), but we prove that this reaction only took place when additional water was added. This behaviour indicates that this scenario is disfavoured in our reaction conditions, since we work under anhydrous conditions.

Table III.4. Ferrocenium and iron (II) species recovered after adding one equivalent of ferrocene to the resulting solutions after Fe^{IV}(O) consumption.

Substrate	Complex 1 ^{(IV)=O}		Complex 2 ^{(IV)=O}	
	^a Fc ⁺ (Fe ^{III}) recovered respect to Fe	^b Fe(II) recovered	^a Fc ⁺ (Fe ^{III}) recovered respect to Fe	^b Fe(II) recovered
Cumene	91 %	73 %	38 %	78 %
Ethylbenzene	75 %	88 %	84 %	82 %
Toluene	100 %	96 %	93 %	70 %

^aDetermined based on the generation of the 615 nm band of Fc⁺ ($\epsilon = 400 \text{ M}^{-1} \cdot \text{cm}^{-1}$). ^bDetermined from Fe^{II} bands after Fc addition (415, $\epsilon = 8000 \text{ M}^{-1} \cdot \text{cm}^{-1}$ for **1**^(II) and 456, $\epsilon = 3220 \text{ M}^{-1} \cdot \text{cm}^{-1}$ for **2**^(II)).

This results are in concordance with the little amounts of oxidised products identified (Table III.5), supporting the lack of such rebounding. The products obtained (alcohol, ketone and desaturation alkene) resemble to the reactivity observed for the related *cis* – [Ru^{IV}(O)(bpy)₂(py)]²⁺ complex, recently re – examined by Dr. James Mayer, which proceeds through an hydrogen abstraction mechanism.²⁷² For complex **1**^{(IV)=O} and **2**^{(IV)=O} the transfer amounts of the oxo moiety to the substrate are quite scarce in general, thus suggesting rebounding is not occurring. Only in the case of cumene with complex **2**^{(IV)=O} the yield is significant ($\approx 40 \%$ of alcohol) and interestingly UV – vis spectrum suggests some recovery of **2**^(II) after oxidation ($\approx 25 \%$, Figure III.22 right). Such formation of Fe^{II} was not observed in complex **1**^{(IV)=O} and with **2**^{(IV)=O} was neither observed for EtPh, while in toluene was $<5 \%$ of the initial Fe (Figure SIII.12). However, oxidative products can be obtained from different pathways (Scheme III.7) and cannot be directly related to the iron (II) formation and a possible rebounding.

At this point we cannot be assured whether the oxygen comes from the iron – oxo/hydroxyl species or from other sources. Although, most likely, oxidised products are formed through a dissociative pathway.

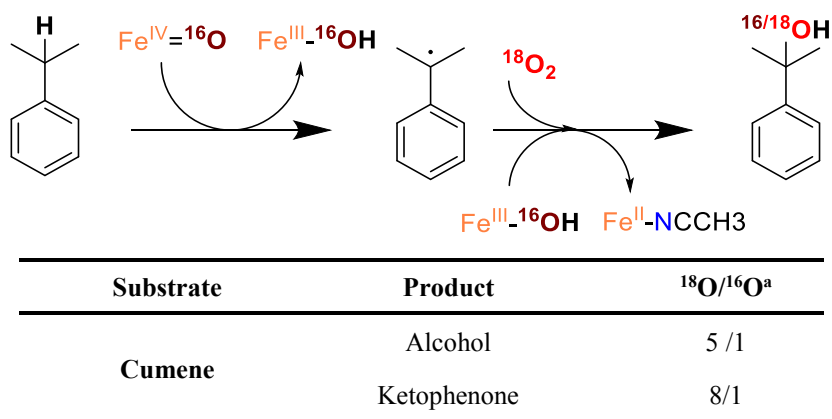
Table III.5. Product distribution of oxidation reactions of $1^{(IV)}=O$ and $2^{(IV)}=O$ with alkylbenzene substrates under N_2 .

Substrate	Product	Yield Complex $1^{(IV)}=O$ ^{a,b}	Yield Complex $2^{(IV)}=O$ ^{a,b}	Total eq. of oxidised products per atom of $1^{(IV)}=O / 2^{(IV)}=O$ ^c
Cumene	Alcohol	11.0 ± 3.7 %	37.6 ± 1.2 %	
	Ketone	1.2 ± 0.3 %	0.9 ± 0.2 %	0.36 / 1.07
	Alkene	4.5 ± 0.6 %	14.1 ± 3.5 %	
Ethylbenzene	Alcohol	4.4 ± 1.1 %	4.5 ± 1.0 %	
	Ketone	2.4 ± 1.2 %	2.6 ± 0.7 %	0.23 / 0.34
	Alkene	2.4 ± 1.2 %	7.1 ± 1.2 %	
Toluene	Alcohol	4.9 ± 3.7 %	3.9 ± 3.5 %	
	Aldehyde	8.8 ± 0.5 %	7.2 ± 1.8 %	0.45 / 0.37

^aYields were obtained by GC – FID with an external standard from an average of two replicates. ^bYields were corrected by Mössbauer purity ($1^{(IV)}=O$) and the reported purity ($2^{(IV)}=O$) of complexes.⁸³ ^cTotal yield calculated from the number of electrons required to generate each product, alcohol ($2e^-$), alkene ($2e^-$) and ketone/aldehyde ($4e^-$).

Comparing the data from the three substrates studied is observed that for the cumene, the alcohol produced is higher, this can be explained from longer living radicals than the other two substrates, that propitiates either higher rebounding or reacting with other species in solution, such as remaining $Fe^{IV}(O)$ or residual O_2 . Thus taking into account that $2 e^-$ are consumed to generate the alcohol or the alkene products, and $4 e^-$ to obtain the ketone or the aldehyde we can see only in the case of complex $2^{(IV)}=O$ with cumene substrate the oxidising power is transferred to the substrate. Despite this yield, it cannot be assumed a rebounding step taking into account data on Table III.4 and III.5. Moreover, in all cases very complex mixtures of different oxidation products are obtained. The improved oxidation of $2^{(IV)}=O$ with cumene it could be rationalised from a higher oxidation potential of $2^{(IV)}=O$ vs $1^{(IV)}=O$ ($\Delta E^{\circ}_{oxd} \approx 0.1 - 0.2$ V).^{83,85}

When the same reactions were performed under air, (Table SIII.6) the yields dramatically increased to values much higher than one equivalent per iron atom (up to 3 – 6 equivalents of alcohol). These data is in agreement with a dissociative mechanism, where the radicals generated after the hydrogen abstraction by the iron (IV) diffuse from the metal cage and react with oxygen from air and through self – oxidation pathway to generate the respective oxidation products. Furthermore, when to a reaction of $1^{(IV)}=O$ (1 mM) with cumene (1 M) under anaerobic conditions, was added $^{18}O_2$ (2 ml, in a 15 ml vial) and analysed by GC – MS. The resulting mixture revealed the ratios $^{18}O/^{16}O$ for the alcohol (78 % yield) and ketone (11 % yield) generated were 8/1 and 5/1 respectively. The observation of ^{18}O in the final substrate is in agreement with little to no rebounding mechanism under the studied conditions.



^aRatios are an average of three injections.

Figure III.23. Oxidation products ratio for reaction of $1^{(IV)}=O$ and cumene under anaerobic conditions with $^{18}O_2$.

The slope of plot k_{obs} vs [substrate] gives the rate constants, k_2 . Next figure shows the k_{obs} vs [substrate] plots and in the Table III.6 are shown k_2 values normalized by the number of equivalent hydrogen atoms from substrate (k_2'):

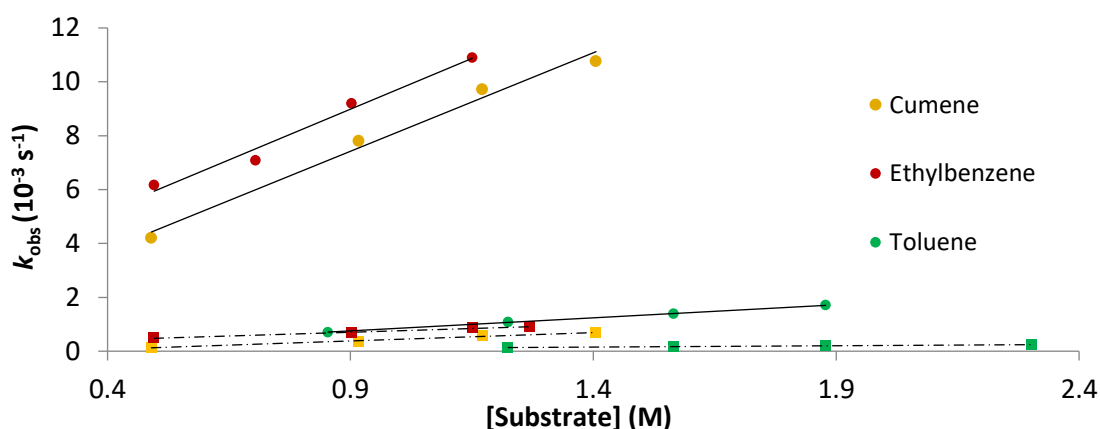


Figure III.24. Plot of the pseudo – first order rate constants, k_{obs} (s^{-1}), against substrate concentration to determine second – order rate constants, k_2 ($M^{-1}s^{-1}$), for the reaction of $1^{(IV)}=O$ and $2^{(IV)}=O$ with alkylbenzenes in CH_3CN at $25^\circ C$. Complex $1^{(IV)}=O$ are circles with solid line and $2^{(IV)}=O$ are squares with dashed line.

Table III.6. Rate constants (k_2') obtained for alkylbenzenes oxidation. k_2 values were normalised by the number of H available on the substrate (2 for ethylbenzene and 3 for toluene) to obtain the corresponding k_2' .

Substrate	k_2' ($M^{-1}\cdot s^{-1}$, 10^{-5})	k_2' ($M^{-1}\cdot s^{-1}$, 10^{-5})
	complex $1^{(IV)}=O$	complex $2^{(IV)}=O$
Toluene	32 ± 1	3.3 ± 0.5
Ethylbenzene	377 ± 40	29 ± 2
Cumene	731 ± 60	62 ± 3

As expected from bond dissociation energies, the oxidation of cumene is the fastest one, followed by ethylbenzene and toluene oxidation, which is the slower due to the stronger C – H bond. The results obtained are in good agreement with previously reported studies, being $1^{(IV)=O}$ comparable to, for example, the analogue $[Fe^{IV}(O)(N4Py)]^{2+}$ complex ($k_2 = 0.0038$ vs 0.0040 $M^{-1}s^{-1}$ in EtPh oxidation) but one order of magnitude slower for example than $[Fe^{IV}(O)(Bn - TPEN)]^{2+}$ ($k_2 = 0.0038$ vs 0.0690 $M^{-1}s^{-1}$ in EtPh oxidation).⁸¹ On the other hand, $2^{(IV)=O}$ was ten times slower than $1^{(IV)=O}$. Additionally, it was found a relationship of rate constants with the C – H bond strength, following a linear tendency, suggesting that all reactions operate under the same mechanism. The slope obtained from the plot of $\log(k_2')$ vs BDE_{C-H} of -0.25 obtained with complexes $1^{(IV)=O}$ and $2^{(IV)=O}$ is in concordance with values previously reported for HAT reactivity with related complexes such as $[Fe^{IV}(O)(Me_2Pytacn)]^{2+}$ ($3^{(IV)=O}$), $[Fe^{IV}(O)(N4Py)]^{2+}$ or $[Fe^{IV}(O)(Bn - TPEN)]^{2+}$.^{77,81} Such a correlation strongly suggests that reactions take place through an H – atom abstraction mechanism.

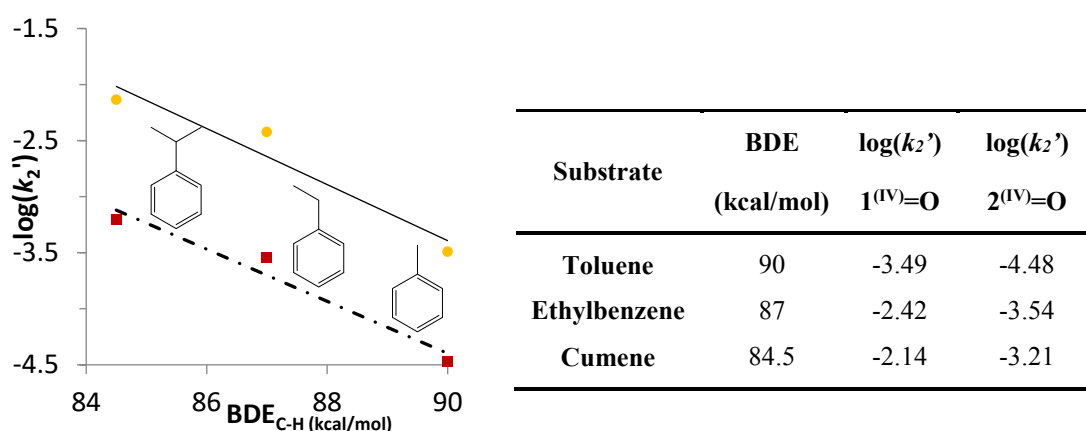


Figure III.25. Plot of $\log(k_2')$ vs BDE_{C-H} ($1^{(IV)=O}$ solid line with yellow circles; $2^{(IV)=O}$ dashed line with red squares). k_2 values were normalised by the number of H available on the substrate to obtain the corresponding k_2' (2 for ethylbenzene and 3 for toluene).

The reactivity with deuterated toluene was also studied with both $1^{(IV)=O}$ and $2^{(IV)=O}$ complexes to obtain the kinetic isotopic effect (KIE), Figure SIII.13 and Table III.7. From the oxidation of deuterated toluene can be noticed that the difference between rate constants for $1^{(IV)=O}$ is very large. For $1^{(IV)=O}$ a KIE of 32 was obtained, indicative of a non – classical KIE with a mechanism where tunnelling is heavily involved, and it is in good agreement with results published on previous works (Table III.8). Although k_D must be taken very carefully owing to the slowness of this reaction and the proximity of k_{obs} values to the self – decay rate ($k_{obs} = 3.6 - 6.8 \cdot 10^{-5} s^{-1}$ vs $k_{self-decay} = 2.5 \cdot 10^{-5} s^{-1}$). Although including the self – decay rate to calculate the KIE leads to a value of 40, thus not significantly changing our conclusion. Such a large KIE implies that C – H bond activation by $1^{(IV)=O}$ goes through a hydrogen atom abstraction mechanism.

On the other hand, complex $2^{(IV)=O}$ revealed a surprisingly small KIE with a ratio of 1.43. This result is in high contrast to that found for $1^{(IV)=O}$ and literature results obtained with iron (IV) – oxo species in HAT reactivity (up to 50), shown in Table III.8. Moreover the reactivity of this complex was previously reported in HAT reactivity with 9, 10 – dihydroanthracene (KIE \approx 32).⁸³ We conclude that, for complex $2^{(IV)=O}$ with toluene, we cannot be sure that we are measuring a hydrogen abstraction step despite the

kinetic data collected suggests it. Since reaction rate for this reaction is very slow, it is very likely that side – reactions are affecting the decay of the iron – oxo species.

Table III.7. Rate constants obtained for H_8 – and D_8 – toluene.

	Complex 1 ^{(IV)=O}	Complex 2 ^{(IV)=O}
k_H ($M^{-1}s^{-1}$, 10^{-5})	32 ± 1	3.3 ± 0.5
k_D ($M^{-1}s^{-1}$)	1.02 ± 0.06	2.3 ± 0.4
KIE 20°C	32	1.43

Table III.8. Reported kinetic data for HAT reactivity with selected Fe^{IV}(O) complexes.

Complex	Substrate	BDE _{C-H} (kcal/mol)	T (K)	k_2 ($M^{-1}s^{-1}$)	KIE	Reference
[Fe(O)(Me ₂ Pytacn)] ²⁺	DHA	77	258	5.7	27	Ref. 77
	D ₄ – DHA			0.21		
	AcrH ₂	86	258	86	4.7	
	AcrD ₂			18.3		
^a [Fe(O)(X)(Me ₂ Pytacn)] ²⁺ X = Cl / Br	DHA	77	243	0.042 / 0.038	25	Ref. 78
	D ₄ – DHA			0.0017 / 0.0015		
[Fe(O)(N4Py)] ²⁺	Ph – Et	87	298	0.0040	27	Ref. 81
	D ₁₀ – Ph – Et			0.00015		
	Ph – CH ₂ OH		273	0.0063	48	Ref. 273
	Ph – CH ₂ OD			0.00013		
[Fe(O)(Bn – TPEN)] ²⁺	Acr – H ₂	86	298	110	13.5	Ref. 274
	Acr – D ₂			8.15		
[Fe(O)(tpa)] ²⁺	Ph – Et	87	298	0.069	53	Ref. 81
	D ₁₀ – Ph – Et			0.0013		
[Fe(O)(bpd)] ²⁺	Ph – CH ₂ OH		233	0.022	58	Ref. 273
	Ph – CH ₂ OD			0.00038		
[Fe(O)(TQA)(CH ₃ CN)] ²⁺	Acr – H ₂	86	238	475.9	2.3	Ref. 275
	Acr – D ₂			209.1		
[Fe(O)(TQA)(CH ₃ CN)] ²⁺	Cumene	84.5	233	1	nd	Ref. 96,97
	Ethylbenzene	87	233	1.1	nd	
[Fe(O)(Cl)(TQA)] ²⁺	^b Toluene	90	233	0.21	25	
[Fe(O)(Br)(TQA)] ²⁺				0.017	nd	
[Fe(O)(MeCN)(TQA)] ²⁺	Cyclohexane	99.5	233	0.37	28	
Compound Q (sMMO)	Methane	104	277		> 50	Ref. 276
TauD	TauH ₂		278	13	37	Ref. 9
	TauD ₂			0.35		

^a k_{obs} were used to calculate KIE. ^bOxidation of D₈ – Toluene occurs at a comparable rate to the self – decay of complexes with X = Cl and Br. KIE for [Fe(O)(Br)(TQA)]²⁺ was obtained from brominated toluene ratio. nd: not determined.

^cDHA: 9, 10 – Dihydroanthracene; Acr: Acridine; Tau: 2 – aminoethane – 1 – sulfonic acid.

III.2.4.2.3. Comparative study of activation barriers in OAT and HAT

To gain further insight into the mechanism of complexes $1^{(IV)=O}$ and $2^{(IV)=O}$ in OAT and HAT reactivity we studied the thermodynamic parameters for the oxidation of methylphenylthioethers and alkylbenzenes. The ΔH^\ddagger , ΔS^\ddagger and ΔG^\ddagger can provide detailed information about the nature of the transition state. These parameters can be easily obtained from the Eyring equation:

$$\ln\left(\frac{k}{T}\right) = -\frac{\Delta H^\ddagger}{R} \cdot \frac{1}{T} + \ln\left(\frac{k_B}{h}\right) + \frac{\Delta S^\ddagger}{R}$$

$$k = k_{\text{obs}}/[S]$$

We calculated ΔH^\ddagger , ΔS^\ddagger and ΔG^\ddagger , k_{obs} for a selection of the studied substrates at different temperatures while maintaining constant all the remaining conditions.

The obtained k were plotted as $\ln(k/T)$ vs $1/T$ to obtain the thermodynamic parameters of the rate determining transition state. In the following tables are collected the activation parameters obtained for substrates and in the Figure SIII.14 are shown the data plotted.

Table III.9. Activation parameters obtained for methyl phenylthioethers oxidations with complexes $1^{(IV)=O}$ and $2^{(IV)=O}$.

Substrate	Complex $1^{(IV)=O}$			Complex $2^{(IV)=O}$		
	ΔH^\ddagger (kcal·mol ⁻¹)	ΔS^\ddagger (cal·K ⁻¹ ·mol ⁻¹)	ΔG^\ddagger_{298} (kcal·mol ⁻¹)	ΔH^\ddagger (kcal·mol ⁻¹)	ΔS^\ddagger (cal·K ⁻¹ ·mol ⁻¹)	ΔG^\ddagger_{298} (kcal·mol ⁻¹)
<i>p</i> - ^X PhSMe						
MeO	16.1 ± 0.1	-6.5 ± 0.3	18.1 ± 0.2	14.8 ± 1.0	14.2 ± 3.4	17.8 ± 2.0
H	19.1 ± 0.2	0.3 ± 0.5	19.0 ± 0.3	17.8 ± 0.3	2.9 ± 1.1	18.6 ± 0.7
CN	18.7 ± 1.3	-5.0 ± 4.5	20.2 ± 2.7	17.0 ± 0.6	-10.6 ± 2.1	20.2 ± 1.3

Table III.10. Activation parameters obtained for alkylbenzenes oxidations with complexes $1^{(IV)=O}$ and $2^{(IV)=O}$.

Substrate	Complex $1^{(IV)=O}$			Complex $2^{(IV)=O}$		
	ΔH^\ddagger (kcal·mol ⁻¹)	ΔS^\ddagger (cal·K ⁻¹ ·mol ⁻¹)	ΔG^\ddagger_{298} (kcal·mol ⁻¹)	ΔH^\ddagger (kcal·mol ⁻¹)	ΔS^\ddagger (cal·K ⁻¹ ·mol ⁻¹)	ΔG^\ddagger_{298} (kcal·mol ⁻¹)
Ph – CH – RR'						
Me, Me	8.6 ± 0,7	-38.9 ± 2.3	20.2 ± 1.3	12.8 ± 0.8	-30.0 ± 2.7	21.7 ± 1.6
H, Me	10.2 ± 0,2	-34.3 ± 0.6	20.4 ± 0.4	14.1 ± 0.9	-26.0 ± 3.0	21.9 ± 1.8
H, H	10.9 ± 0,8	-37.6 ± 2.5	22.0 ± 1.5	14.0 ± 0.8	-31.0 ± 2.6	23.3 ± 1.6

Obtained ΔG^\ddagger values revealed that the OAT and HAT energy barriers (OAT: 18 – 23 kcal·mol⁻¹; HAT: 20 – 23 kcal·mol⁻¹) are comparable. Activation barriers follow the electronrich nature of the substrates for the series of thioanisoles and the expected trend according to C – H bond strength in alkylbenzenes (cumene < ethylbenzene < toluene).

However, the analysis of ΔH^\ddagger and ΔS^\ddagger shows unexpected results. Surprisingly, the ΔH^\ddagger values for the C – H bond breakage are relatively small (from ≈ 9 to 14 Kcal/mol, Table III.10). But more surprisingly are smaller than the ΔH^\ddagger for the oxidation of the thioethers (from 15 to 19 Kcal/mol, Table III.9). The observed similar ΔG^\ddagger values for OAT and HAT can be explained by the fact that the OAT reactions present insignificant ΔS^\ddagger activation values. Although this is unexpected for a bimolecular reaction, it can be rationalize *via* formation of an adduct complex before the RDS that undergo the methyl phenylthioether oxidation. In the case of HAT reactions the value for ΔS^\ddagger is the expected for a bimolecular reaction and therefore the reaction is entropically controlled.

The obtained ΔH^\ddagger values suggest that the OAT rate constants should be significantly more affected by the temperature, whereas for the alkylbenzenes (HAT) the temperature should have a lower impact in the oxidation rate. Therefore, we could envision a selectivity control between OAT and HAT by simply temperature control. As result, lowering the temperature OAT mechanism may be shutdown, while keeping HAT mechanism operative (Figure III.25).

To test the idea we studied the OAT to methylphenylthioether versus the HAT reaction of alkylbenzylic substrates. From these data, we can theoretically find a temperature were the reactivity of the Fe^{IV}=O is shifted from the oxidation of methylphenylthioether (OAT reaction) to a C – H bond functionalisation (HAT reaction) implying a control of the oxidation selectivity for Fe^{IV}=O species by the temperature.

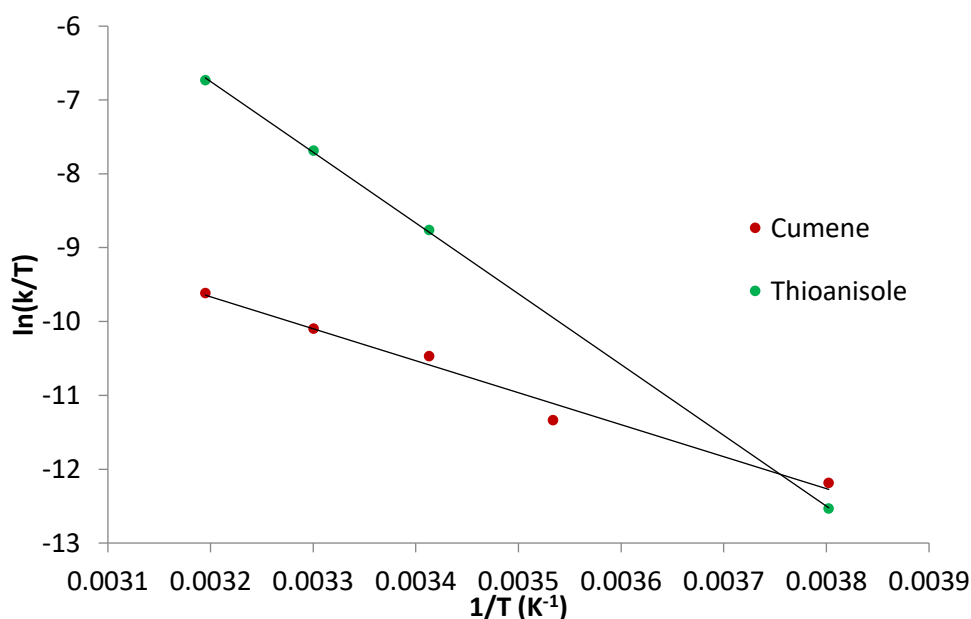
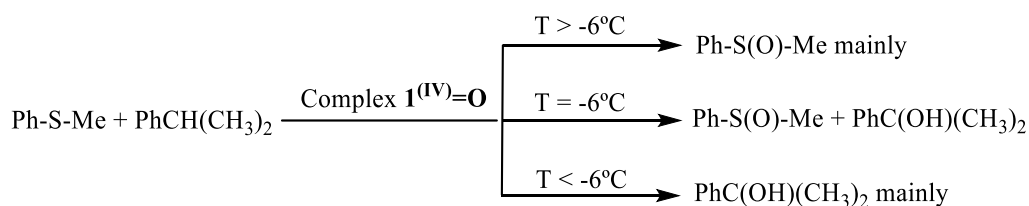


Figure III.26. Eyring plot for cumene and thioanisole on oxidation with complex 1^(IV)=O.

The plot shown at Figure III.26 is very illustrative. The cumene and thioanisole correlations have a very different slope because of their difference in enthalpy. As observed both lines end up crossing, and that occurs at an accessible temperature:

$$-4330.5 \cdot x + 4.2 = -9584.6 \cdot x + 23.9 \rightarrow x = \frac{19.7}{5254.1} = 0.00375 \rightarrow T = \frac{1}{x} = 267 \text{ K}$$

Experimental data predict that at $T = -6^\circ\text{C}$ both rate constants will have the same value, that means at a $T < -6^\circ\text{C}$ (267 K) HAT reactivity theoretically may be preferred, while above that T the reaction mainly would proceed through the OAT mechanism (Scheme III.8).



Scheme III.8. Possible products formed upon oxidation of a mixture of cumene and thioanisole with $\mathbf{1^{(IV)=O}}$ depending of T .

Unfortunately, under tested conditions (Table SIII.7), only small amounts of oxidation products were observed and a direct evidence for preferential reaction with the alkylbenzene substrate in front of thioanisole could not be obtained. The alcohol generated was too small to permit quantification. We could only ascertain that at -20°C a smaller quantity of methyl phenyl sulfoxide was generated when cumene was present into the reaction media (thioanisole: 91 %, -20°C ; cumene:thioanisole: 34 %, -20°C , Table SIII.7). These results suggest that the HAT reaction over the cumene may result in a radical that can evolve via multiple paths that difficult the analysis. Alternatively, could rationalize that radicals generated from HAT most likely interfere in the OAT reactivity (the same mixture yielded a 70 % of methyl phenylsulfoxide at 20°C). More efforts are needed in order to clarify this interesting reactivity.

Due to the remarkable results obtained we decided to study the well – known oxoferryl complex $[\text{Fe}^{\text{IV}}(\text{O})(\text{N4Py})]^{2+}$ ($\mathbf{4^{(IV)=O}}$) in comparison with our $\mathbf{1^{(IV)=O}}$ and $\mathbf{2^{(IV)=O}}$ complexes.

Analogously to $\mathbf{1^{(IV)=O}}$ and $\mathbf{2^{(IV)=O}}$, Eyring plot analysis has been performed for the oxoferryl $[\text{Fe}^{\text{IV}}(\text{O})(\text{N4Py})]^{2+}$ ($\mathbf{4^{(IV)=O}}$). This complex exhibits a NIR band at $\lambda = 695 \text{ nm}$ with $\epsilon = 400 \text{ M}^{-1}\text{cm}^{-1}$ that can be used to monitor the reaction with thioanisole. The observed reaction rates (k_{obs}) were found to be linearly dependent on sulphide concentration indicating that they are pseudo – first order rate constants with the expression $k_{\text{obs}} = k_2[\text{sulphide}]$. The respective second order rate constants (k_2) were then calculated from this fitting. k_2 data is shown in the annex (Figure SIII.15, Table SIII.8) and table below shows activation parameters obtained for N4Py complex:

Table III.11. Activation parameters obtained for substrate oxidations with $[\text{Fe}^{\text{IV}}(\text{O})(\text{N4Py})]^{2+}$ ($\mathbf{4}^{\text{IV}}=\text{O}$).

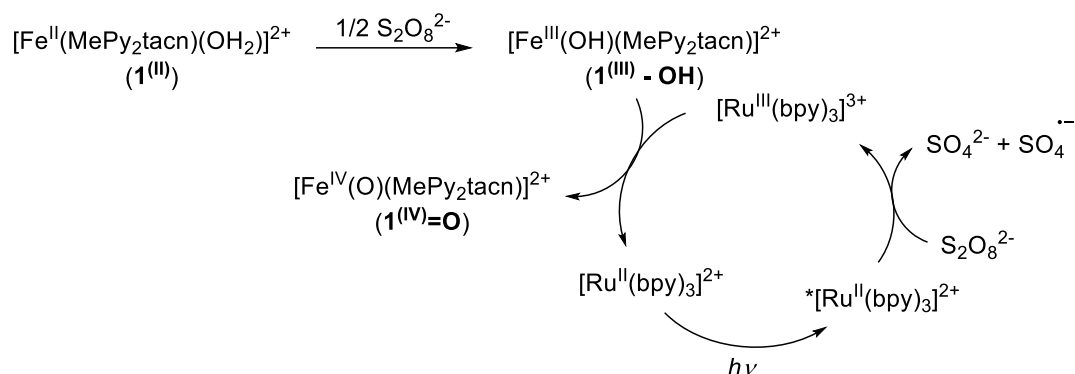
	OAT	HAT
	(H – Ph – SMe)	(Ph – CH – (CH ₃) ₂)
ΔH^\ddagger (Kcal·mol ⁻¹)	16.8	11.0
ΔS^\ddagger (cal·K ⁻¹ ·mol ⁻¹)	-3.1	-33.6
$\Delta\text{G}^\ddagger_{298}$ (Kcal·mol ⁻¹)	17.8	21.0

Similar reactivity patterns to $\mathbf{1}^{\text{IV}}=\text{O}$ and $\mathbf{2}^{\text{IV}}=\text{O}$ were found. As we can see from activation parameters the ΔG^\ddagger are close to the values found for $\mathbf{1}^{\text{IV}}=\text{O}$ and $\mathbf{2}^{\text{IV}}=\text{O}$ (e.g. 21.0 Kcal/mol vs 20.2 and 21.7 Kcal/mol for cumene, Tables III.10 and III.11). These data may not be an explanation for the higher oxidation of cumene in comparison to the other complexes ($\mathbf{4}^{\text{IV}}=\text{O}$, yields under N₂: 51 ± 5 % of alcohol, 11 ± 9 % of ketone and 7 ± 2 % of alkene, total yield 80 % if Fe^{II} is obtained). Interestingly, for this complex the crossing temperature of the Eyring lines is ≈ 60°C for thioanisole and cumene (Figure SIII.16), suggesting that below that temperature a mixture of both substrates would mainly yield the alcohol from cumene. As observed for complex $\mathbf{1}^{\text{IV}}=\text{O}$ we were not able to obtain an evidence for selective functionalization of C – H bond, moreover only a slight decrease of sulfoxide amount was detected on a competitive experiment with cumene (Table SIII.7).

As the three complexes studied present similar thermodynamic activation parameters and reactivity patterns, this could imply that this reactivity may be a general observation, however it has not been possible to find a complex that can perform satisfactorily the oxidation of a C – H bond in presence of a more reactive group such as a sulphur atom.

III.2.4.3. Photochemical enhanced reactivity towards sulphides oxidation

The reactivity of $\mathbf{1}^{(IV)=O}$ in the oxidation of sulphides under photochemical irradiation was studied.⁸⁵ As stated above, iron (IV) – oxo species can be generated through photooxidative pathway (Scheme III.2, route C). Using water as oxygen donor, a photosensitizer and a terminal acceptor of electrons promotes full generation of high – valent iron (IV) – oxo species upon irradiation. In this regard we were able to photochemically generate complex $\mathbf{1}^{(IV)=O}$, inspired by Prof. Fukuzumi's work, who used $[\text{Ru}^{\text{II}}(\text{bpy})_3]^{2+}$ in combination with $[\text{Co}^{\text{III}}\text{Cl}(\text{NH}_3)_5]^{2+}$ to photochemically generate the $[\text{Fe}^{\text{IV}}(\text{O})(\text{N4Py})]^{2+}$ complex in aqueous media.¹¹⁰



Scheme III.9. Chemical reactions taking place during the photocatalytic generation of $\mathbf{1}^{(IV)=O}$.

In Fukuzumi's work, under irradiation with a 450 nm lamp the photosensitizer $[\text{Ru}^{\text{II}}(\text{bpy})_3]^{2+}$ was oxidised to $[\text{Ru}^{\text{III}}(\text{bpy})_3]^{3+}$ by reaction with $[\text{Co}^{\text{III}}\text{Cl}(\text{NH}_3)_5]^{2+}$ via an electron – transfer mechanism. Subsequently, electron – transfer of two equivalents of the generated $[\text{Ru}^{\text{III}}(\text{bpy})_3]^{3+}$ oxidise the Fe^{II} species to $[\text{Fe}^{\text{IV}}(\text{O})(\text{N4Py})]^{2+}$, using H_2O as the oxygen source. Notwithstanding the system needed a 40 % of ruthenium photosensitizer to work.

In concordance to the proposed reactivity by Prof. Fukuzumi, in our system the oxidation of $\mathbf{1}^{(II)}$ proceeded through the mechanism depicted in Scheme III.9. Ru^{II} was excited to the $*[\text{Ru}^{\text{II}}]$ by irradiation, this excited species reacted by one electron – transfer with $\text{Na}_2\text{S}_2\text{O}_8$ to form the Ru^{III} (Figure SIII.17 top). On the other hand, initial Fe^{II} was oxidised as well by the final electron acceptor, $\text{Na}_2\text{S}_2\text{O}_8$, generating the respective $\text{Fe}^{\text{III}} - \text{OH}$ species (Figure SIII.17 below). Finally the Ru^{III} was capable to oxidise the iron (III) to the ultimate oxo species, coming the oxygen from H_2O (Figure SIII.2, top left). We tested the legitimacy of these reactions for $\mathbf{1}^{(IV)=O}$, proving the different steps of the mechanism. A difference in our procedure from that of Prof. Fukuzumi is the use of $\text{Na}_2\text{S}_2\text{O}_8$ as the sacrificial electron acceptor, moreover a remarkable improvement that we could achieve is the capability of using a catalytic amount of Ru (5 %) in contrast with the 40 % used by Prof. Fukuzumi and co – workers.

The photocatalytically generated species $\mathbf{1}^{(IV)=O}$ was also tested in the oxidation of sulfides. The addition of 5 eq of *p* – methoxythioanisole to a solution of $\mathbf{1}^{(IV)=O}$ (0.4 mM $\mathbf{1}^{(II)}$, 0.02 mM $[\text{Ru}^{\text{II}}(\text{bpy})_3]\text{Cl}_2$, 4 mM $\text{Na}_2\text{S}_2\text{O}_8$ in $\text{MeCN}:\text{H}_2\text{O}$ 1:3) lead to the decay of the 715 nm on the UV – vis band with a $k_{\text{obs}} = 1.5 \cdot 10^{-3} \text{ s}^{-1}$ (25 °C), obtained from an exponential decay fitting of the absorbance for that band. Remarkably when the same reaction was performed under irradiation the decay rate increased 150 times to a rate of $k_{\text{obs}} = 0.22 \text{ s}^{-1}$. These results are promising and deserve further investigation.

Furthermore, under the same conditions (0.4 mM $\mathbf{1}^{\text{II}}$, 0.02 mM $[\text{Ru}^{\text{II}}\text{Cl}_2(\text{bpy})_3]$, 4 mM $\text{Na}_2\text{S}_2\text{O}_8$ in $\text{MeCN}:\text{H}_2\text{O}$ 1:3), complex $\mathbf{1}^{\text{(IV)}=\text{O}}$ could be generated and subsequently recovered several times after reaction with $\text{Me}^{\text{O}}\text{PhSMe}$ substrate (Figure III.27). Complex $\mathbf{1}^{\text{(IV)}=\text{O}}$ was generated upon irradiation, after its formation, in the absence of light was added 1 eq of *p* – methoxythioanisole and $\mathbf{1}^{\text{(IV)}=\text{O}}$ immediately started to decay, when light was switched on again the decay of $\mathbf{1}^{\text{(IV)}=\text{O}}$ completed instantaneously. After consumption of $\text{Me}^{\text{O}}\text{PhSMe}$, complex $\mathbf{1}^{\text{(IV)}=\text{O}}$ was recovered again under irradiation, as observed from restoration of 715 nm band in the UV – vis spectrum. The iron (II) was reoxidised by the $\text{Na}_2\text{S}_2\text{O}_8$ excess or the Ru^{III} in solution, obtaining again $\mathbf{1}^{\text{(IV)}=\text{O}}$. The regeneration of $\mathbf{1}^{\text{(IV)}=\text{O}}$ was decreasing every cycle ($\approx 87\%$ recovery after first cycle) due to some partial decomposition associated to the irradiation. Also an increasing induction period was observed before $\mathbf{1}^{\text{(IV)}=\text{O}}$ started to recover after the substrate consumption, this was a consequence of the decomposition of $\mathbf{1}^{\text{(IV)}=\text{O}}$, an increasing excess of $\text{Me}^{\text{O}}\text{PhSMe}$ was added, which had to be consumed before $\mathbf{1}^{\text{(IV)}=\text{O}}$ could be regenerated.

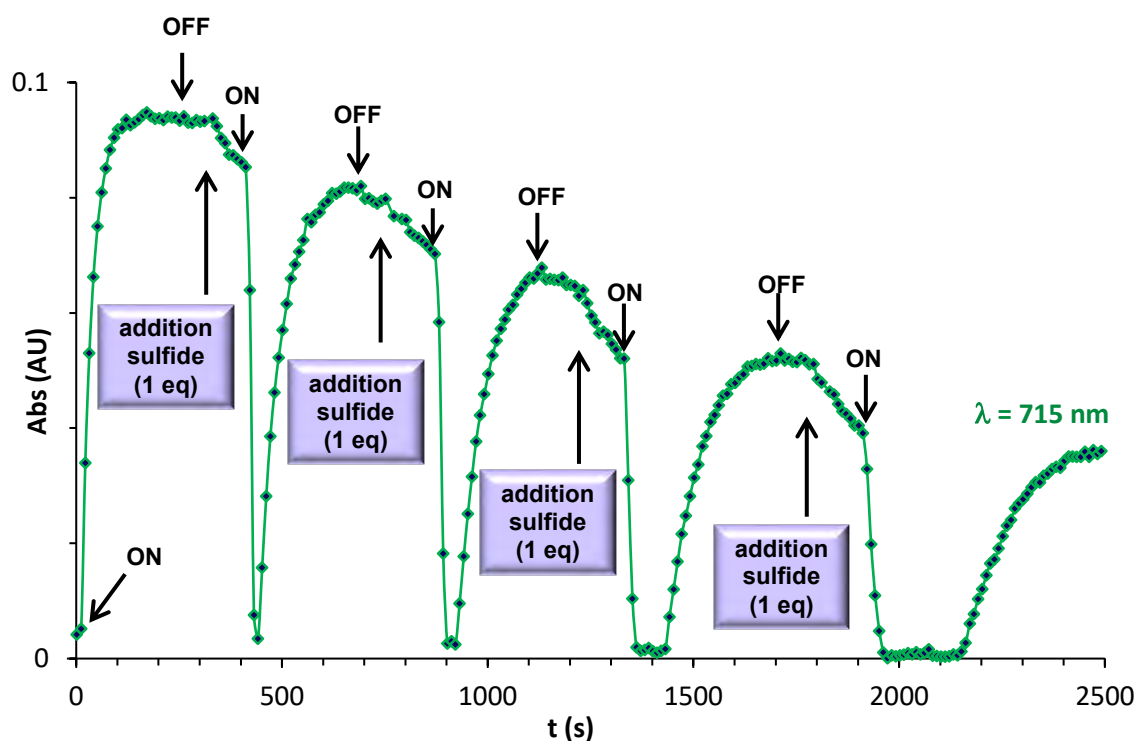


Figure III.27. Kinetic trace at 715 nm corresponding to the reaction mixture containing $\mathbf{1}^{\text{II}}$ (0.4 mM), 5 mol% $[\text{Ru}^{\text{II}}(\text{bpy})_3]\text{Cl}_2$ (0.02 mM) and $\text{Na}_2\text{S}_2\text{O}_8$ (4 mM, 10 equiv) under N_2 atmosphere at 25 °C. Labels on the figure indicate the initial (ON) and final (OFF) points of irradiation ($\lambda = 447 \pm 20 \text{ nm}$) as well as the addition of 1 equiv of $\text{Me}^{\text{O}}\text{PhSMe}$.

To simplify the study of this system and clarify the rate enhancement upon irradiation, we studied this reactivity with chemically generated $\mathbf{1}^{\text{(IV)}=\text{O}}$, prepared with an excess of PhIO. This allowed us the removal of $\text{Na}_2\text{S}_2\text{O}_8$ from the system and the associated noninnocent species generated from $\text{S}_2\text{O}_8^{2-}$.²⁷⁷ The study of the oxidative capacity of $\mathbf{1}^{\text{(IV)}=\text{O}}$ towards sulphide substrates was performed with following conditions: 0.4 mM $\mathbf{1}^{\text{(IV)}=\text{O}}$, 0.02 mM $[\text{Ru}^{\text{II}}(\text{bpy})_3]\text{Cl}_2$ in $\text{MeCN}:\text{H}_2\text{O}$ 1:3; and analyzed under different circumstances: with or without substrate, $[\text{Ru}^{\text{II}}(\text{bpy})_3]\text{Cl}_2$ and/or light. The results are shown in Table III.12.

Table III.12. Measured k_{obs} values corresponding to the decay rate of chemically generated $\mathbf{1}^{(\text{IV})}=\mathbf{O}$ (0.4 mM in $\text{CH}_3\text{CN}:\text{H}_2\text{O}$ 1:3 in a N_2 atmosphere at 25°C) under different reaction conditions.

Entry	$^{\text{X}}\text{PhSMe}$ (equiv) ^a	$[\text{Ru}^{\text{II}}(\text{bpy})_3]^{2+}$ (mol%) ^b	Light ^c	k_{obs} (10^{-4} s^{-1}) ^d X = MeO	k_{obs} (10^{-4} s^{-1}) ^d X = CN
1	5	-	No	11 ± 1	2 ± 0.1
2	5	-	Yes	12 ± 1	3 ± 1
3	5	5	No	12 ± 3	3 ± 2
4	5	5	Yes	76 ± 6	28 ± 1
5	-	5	No	3 ± 1	3 ± 1
6	-	5	Yes	22 ± 4	22 ± 4
7	-	-	No	0.9 ± 0.2	0.9 ± 0.2
8	-	-	Yes	4 ± 1	4 ± 1

^aAddition of 5 equiv *para*-X-phenylmethylsulfide ($^{\text{X}}\text{PhSMe}$, 2 mM) with respect to $\mathbf{1}^{(\text{IV})}=\mathbf{O}$ to the reaction mixture.

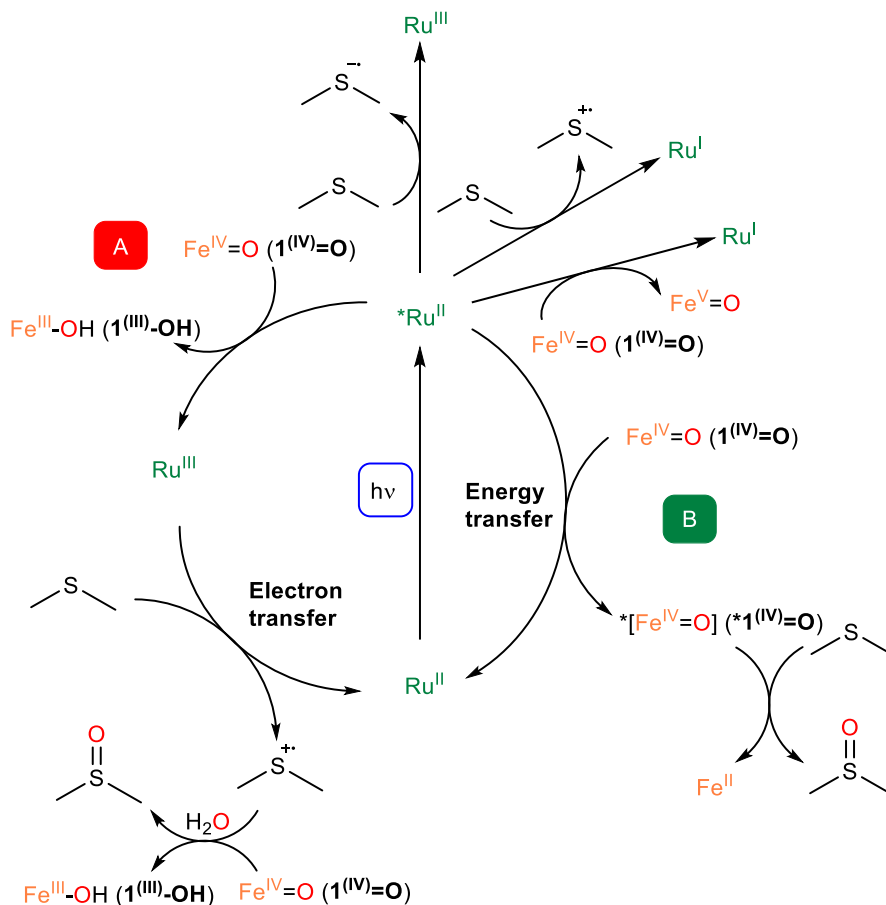
^bAddition of 5 mol% of $[\text{Ru}^{\text{II}}(\text{bpy})_3]\text{Cl}_2$ (0.02 mM) with respect to $\mathbf{1}^{(\text{IV})}=\mathbf{O}$ to the reaction mixture. ^cIrradiation at 447 nm. ^d k_{obs} values were obtained by fitting the decay of the absorbance at 715 nm over time to a single exponential function, results are from at least three replicates.

Comparing entries 1 and 2 the rate of reaction of $\mathbf{1}^{(\text{IV})}=\mathbf{O}$ with $^{\text{MeO}}\text{PhSMe}$, and in absence of Ru, was not affected by irradiation at 447 nm (11 vs $12 \cdot 10^{-4} \text{ s}^{-1}$ without and with irradiation). In contrast to that, when 5 % $[\text{Ru}^{\text{II}}(\text{bpy})_3]\text{Cl}_2$ was added to the system and without irradiation, no enhancement was observed; but upon irradiation a 7 – fold increase in the decay rate was observed (entries 3 and 4, Table III.12). Control experiments showed that in the absence of the sulfide, the decay of $\mathbf{1}^{(\text{IV})}=\mathbf{O}$ also occurred faster under irradiation in the presence of $[\text{Ru}^{\text{II}}(\text{bpy})_3]^{2+}$ (entries 5 and 6). The effect of light on the self – decay rate (without the sulfide or photosensitizer) is minor, although is significant (entries 7 and 8). From this set of experiments it is clear that the combination of $[\text{Ru}^{\text{II}}(\text{bpy})_3]^{2+}$ and irradiation was crucial for the enhanced oxidation rate of $^{\text{MeO}}\text{PhSMe}$ by $\mathbf{1}^{(\text{IV})}=\mathbf{O}$, what means $[\text{Ru}^{\text{II}}(\text{bpy})_3]^{2+}$ acts as a photosensitizer thus accelerating the process. A comparison plot of this acceleration is shown in Figure SIII.18.

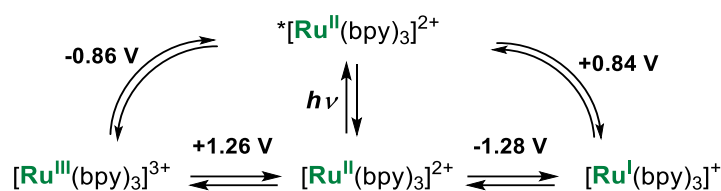
A series of *p*-substituted thioanisole substrates were also studied in the same reaction to gain further insight into the mechanism. In this regard we studied the oxidation of the $^{\text{X}}\text{PhSMe}$ (X = MeO, Me, H, Cl) with enhanced rates upon irradiation, and giving yields up to 40 % of respective sulfoxides. These yields are quite low in comparison to the amounts of sulfoxides obtained with $\mathbf{1}^{(\text{IV})}=\mathbf{O}$ in MeCN (Table SIII.5). Moreover the resulting iron species after oxidation was not iron (II), as expected from an oxidation of a sulphide with iron (IV) – oxo species. The lack of the 414 nm band at the end of the decay of $\mathbf{1}^{(\text{IV})}=\mathbf{O}$ revealed no $\mathbf{1}^{(\text{III})}$ was recovered after the oxidation, furthermore the addition of one equivalent of ascorbic acid (respect to the iron) regenerated the complex $\mathbf{1}^{(\text{III})}$ in 75 % (Figure SIII.19). In agreement with UV – vis spectrometry, the analysis of the final species by mass spectrometry revealed we had iron (III) – hydroxo

as proved by ions $m/z = 199.09$ and 547.11 , $[\text{Fe}^{\text{III}}(\text{OH})(\text{MePy}_2\text{tacn})]^{2+}$ and $([\text{Fe}^{\text{III}}(\text{OH})(\text{MePy}_2\text{tacn})]\text{OTf})^+$ respectively (Figure SIII.20).

Several different mechanisms can be proposed from the rich photochemistry and redox reactivity associated with $[\text{Ru}^{\text{II}}(\text{bpy})_3]^{2+}$ (Scheme III.10). Some of them can be initially ruled out, such as an electron transfer from $\mathbf{1}^{\text{(IV)}}=\text{O}$ to the $*[\text{Ru}^{\text{II}}(\text{bpy})_3]^{2+}$ ($E^*[\text{Ru}^{\text{II}}]/[\text{Ru}^{\text{I}}] = 0.84 \text{ V}$), due to the high redox potential needed to oxidise $\mathbf{1}^{\text{(IV)}}=\text{O}$ to the $\text{Fe}^{\text{V}}(\text{O})$ ($E > 1.5 \text{ V}$).²⁷⁸ Also an electron transfer from $^{\text{MeO}}\text{PhSMe}$ ($E_{\text{ox}} = 1.13 \text{ V}$) to the $*[\text{Ru}^{\text{II}}(\text{bpy})_3]^{2+}$ can also be excluded for same reason. Moreover taking into account the high negative potential for $*[\text{Ru}^{\text{II}}(\text{bpy})_3]^{2+}/[\text{Ru}^{\text{III}}(\text{bpy})_3]^{3+}$ couple also eliminates the possibility of an electron transfer from $*[\text{Ru}^{\text{II}}(\text{bpy})_3]^{2+}$ to the substrate. Thus, in our proposal, only two possible pathways remain: an electron transfer from $*[\text{Ru}^{\text{II}}(\text{bpy})_3]^{2+}$ to $\mathbf{1}^{\text{(IV)}}=\text{O}$, forming $[\text{Ru}^{\text{III}}(\text{bpy})_3]^{3+}$ which would react with substrate to generate the radical cation $^{\text{X}}\text{PhSMe}^{\bullet}$ (path A). That radical cation would react with another molecule of $\mathbf{1}^{\text{(IV)}}=\text{O}$ to generate the corresponding sulfoxides. The second possibility is the energy transfer from $*[\text{Ru}^{\text{II}}(\text{bpy})_3]^{2+}$ to $\mathbf{1}^{\text{(IV)}}=\text{O}$, to generate a highly reactive species $*\mathbf{1}^{\text{(IV)}}=\text{O}$ that oxidises the substrate (path B).



Scheme III.10. Mechanistic pathways to explain the rate enhancement in the oxidation of sulfides by $\mathbf{1}^{\text{(IV)}}=\text{O}$ under light irradiation.



Scheme III.11. Redox potentials of *p*-X-thioanisoles and $[\text{Ru}(\text{bpy})_3]^{2+/3+}$ (values vs SCE in CH_3CN).²⁷⁹

A Hammett plot was performed to obtain information of the RDS. The rates from reactions of $\mathbf{1}^{(\text{IV})}=\mathbf{O}$ with different *p*-X-PhSMe (X = MeO, Me, H, Cl) were studied under same conditions (0.4 mM $\mathbf{1}^{(\text{IV})}=\mathbf{O}$, 0.02 mM $[\text{Ru}^{\text{II}}\text{Cl}_2(\text{bpy})_3]$ in $\text{MeCN}:\text{H}_2\text{O}$ 1:3) and plotted against the σ_p values (Figure III.28, left). The slope ($\rho = -0.09$) indicates that rates are almost not influenced by the electronic properties of the substrates, thus not affecting the RDS of the process.²⁷³ In concordance to that, $[\text{Ru}^{\text{II}}(\text{bpy})_3]^{2+}$ remained unchanged as assessed by the intensity of its UV-vis band (450 nm), suggesting that the RDS occurred after transformation of the photosensitizer and before substrate was involved. Interestingly, in contrast to that Hammett plot, intermolecular competition experiments between mixtures of $^{\text{X}}\text{PhSMe}$ and $^{\text{H}}\text{PhSMe}$ gave a Hammett plot with a slope of $\rho = -2.5$, revealing that the substrate electronic properties have an effect on the product-determining step, but not affecting in the RDS.²⁸⁰ This slope of -2.5 is also in the range of that found in oxidative N-demethylation of amines performed by iron (IV)-oxo species ($\rho = -2.2$ to -3.3), proposed to proceed through an electron transfer coupled to a proton transfer mechanism.²⁸¹

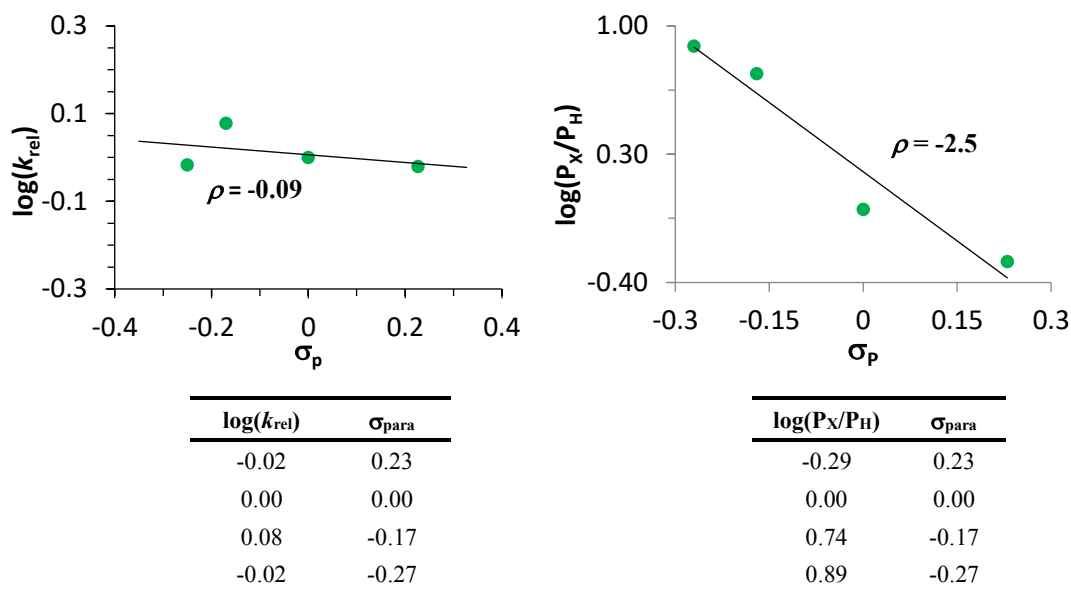


Figure III.28. (Left) Hammett plot representing $\log(k_{\text{rel}})$ against the Hammett parameter (σ_p) for the reaction of $\mathbf{1}^{(\text{IV})}=\mathbf{O}$ with *p*-X-thioanisole in $\text{CH}_3\text{CN}:\text{H}_2\text{O}$ 1:3 in the presence of 5 mol% $[\text{Ru}^{\text{II}}(\text{bpy})_3]\text{Cl}_2$ with 447 nm-light irradiation at 298 K. k_{rel} values were calculated by dividing k_{obs} of *p*-X-thioanisoles by k_{obs} of thioanisole obtained with 10 equiv. substrate. (Right) Hammett plot representing $\log(\text{P}_X/\text{P}_H)$ against the Hammett parameter (σ_p) for competition experiments corresponding to the simultaneous reaction of $\mathbf{1}^{(\text{IV})}=\mathbf{O}$ with thioanisole and *p*-X-thioanisole in $\text{CH}_3\text{CN}:\text{H}_2\text{O}$ 1:3 in the presence of 5 mol% $[\text{Ru}^{\text{II}}(\text{bpy})_3]\text{Cl}_2$ with 447 nm-light irradiation at 298 K. P_X corresponds to the amount of *p*-substituted phenylmethylsulfoxide obtained at the end of the reaction (determined by GC-FID or NMR). Competition experiments were run in the presence of 5 equiv thioanisole and 5 equiv *p*-X-thioanisole.

Comparing the ρ obtained from competition Hammett with those previously reported for OAT reactivity ($\rho = -1$ to -2)^{77,78,267} and contrasted with the reactions of $\mathbf{1}^{(IV)=O}$ and $\mathbf{2}^{(IV)=O}$ with thioanisole in MeCN ($\rho \approx -1.9$, with no photosensitizer nor irradiation, Figure III.21 right) slope is relatively more negative. Furthermore, when $\log(P_X/P_H)$ ratios were plotted in front of the $1 e^-$ potential of $^X\text{PhSMe}$ (E°_{ox}) the slope obtained was -5.0 (Figure SIII.21), a value that somehow falls halfway to that reported for OAT processes (from -2 to -3)^{77,78,267,268} and those published for electron transfer processes (from -8 to -10) by Prof. Nam.²⁶⁸ But this slope is close to those obtained in the oxidative N – demethylation of amines performed by iron (IV) – oxo species ($\rho = -3.3$ to -5.0).²⁸¹

In collaboration with Dr. Julia Pérez – Prieto's group nanosecond time – resolved spectroscopy (Nd:YAG, 532 nm, 10 ns pulse) was performed.⁸⁵ These experiments indicated that the iron species $\mathbf{1}^{(IV)=O}$ interacts with the $^*[\text{Ru}^{II}(\text{bpy})_3]^{2+}$ to generate a new species, $[\text{Ru}^{III}(\text{bpy})_3]^{3+}$ (Figure SIII.22). Indeed excitation of a solution of $^*[\text{Ru}^{II}(\text{bpy})_3]^{2+}$ and $\mathbf{1}^{(IV)=O}$ in presence of $^{\text{MeO}}\text{PhSMe}$ revealed the formation of $^{\text{MeO}}\text{PhSMe}^{+\bullet}$ (Figure SIII.23), obtained from the oxidation of the thioanisole by the in – situ generated Ru^{III} species. These data is in agreement with our proposal for an electron – transfer mechanism. Furthermore analysis of a mixture of $[\text{Ru}^{III}(\text{bpy})_3]^{3+}$, $\mathbf{1}^{(IV)=O}$ and $^{\text{MeO}}\text{PhSMe}$ indicated the instantaneous reaction of $\mathbf{1}^{(IV)=O}$ to generate the final sulfoxide product ($^{\text{MeO}}\text{PhS(O)Me}$) and the iron (III) – hydroxo complex.

The electron transfer mechanism explains the iron (III) obtained at the end of the reaction and also the low yields obtained for the sulfoxides generated ($\approx 40\%$). Although $^{\text{CN}}\text{PhSMe}$ has a high redox potential ($E_{\text{ox}} = 1.61$ V) in comparison to that of $[\text{Ru}^{III}(\text{bpy})_3]^{3+}$, thus is a substrate that lies in the limit of this mechanism; that would make the electron transfer process unlikely or very inefficient, as observed in the time – resolved absorption spectroscopic studies. Interestingly observing Table III.12 (entries 4 and 6) a slight rate photoenhancement was also observed for $^{\text{CN}}\text{PhSMe}$, furthermore the yield obtained for this reaction was $10 - 12\%$. These data, together with the fact that no efficient electron transfer was possible, led us to the proposal of an energy transfer mechanism; where the species $\mathbf{1}^{(IV)=O}$ is excited to an $S = 2$ species $^*\mathbf{1}^{(IV)=O}$ by $[\text{Ru}^{II}(\text{bpy})_3]^{2+}$. Although such species remained undetected, this light induced low spin/high spin transition is reasonable because this process was already reported for $d^4 - d^7$ metal complexes.²⁸²⁻²⁸⁴

Alternatively, the photoenhanced reactivity of $\mathbf{1}^{(IV)=O}$ towards sulfides could also be attributed to a change in the coordination mode of the ligand, such as a dissociation of one of the pyridyl arms triggered by 447 nm light irradiation. This possibility was evaluated by determining if acceleration in sulfide oxidation also occurred for $\mathbf{2}^{(IV)=O}$, with a highly rigid pentadentate ligand. In compound $\mathbf{2}^{(IV)=O}$ the two pyridine units are connected to a single carbon atom, making the pyridine dissociation very unlikely to occur. Although results should be taken carefully, because obviously complex $\mathbf{1}^{(IV)=O}$ and $\mathbf{2}^{(IV)=O}$ are not structurally and electronically the same. Interestingly, as with $\mathbf{1}^{(IV)=O}$ (Table III.12), a $10 - \text{fold}$ increase (11 vs. $130 \cdot 10^{-4} \text{ s}^{-1}$) in the reaction rate was observed upon irradiation of a solution containing $\mathbf{2}^{(IV)=O}$, $[\text{Ru}^{II}(\text{bpy})_3]^{2+}$, and $^{\text{MeO}}\text{PhSMe}$ (see Table III.13). This results suggests that a change in the coordination mode of the ligand triggered by light is unlikely, moreover results reveal that the proposed mechanism for $\mathbf{1}^{(IV)=O}$ is in agreement for $\mathbf{2}^{(IV)=O}$ also.

Table III.13. Measured k_{obs} values corresponding to the decay rate of chemically generated $2^{(\text{IV})}=\text{O}$ (0.4 mM in $\text{CH}_3\text{CN}:\text{H}_2\text{O}$ 1:3 in a N_2 atmosphere at 25°C) under different reaction conditions.

Entry	$^{\text{X}}\text{PhSMe}$ (equiv) ^a	$[\text{Ru}^{\text{II}}(\text{bpy})_3]^{2+}$ (mol%) ^b	Light ^c	k_{obs} (10^{-4} s^{-1}) ^d X = MeO	k_{obs} (10^{-4} s^{-1}) ^d X = CN
1	5	-	No	8.5 ± 0.7	0.96 ± 0.01
2	5	-	Yes	12.0 ± 0.1	3.00 ± 0.05
3	5	5	No	11 ± 2	0.83 ± 0.06
4	5	5	Yes	130 ± 7	90 ± 2
5	-	5	No	0.11 ± 0.05	0.11 ± 0.05
6	-	5	Yes	39 ± 3	39 ± 3
7	-	-	No	0.04 ± 0.01	0.04 ± 0.01
8	-	-	Yes	0.08 ± 0.01	0.08 ± 0.01

^aAddition of 5 equiv *para*-X-phenylmethylsulfide ($^{\text{X}}\text{PhSMe}$, 2 mM) with respect to $2^{(\text{IV})}=\text{O}$ in the reaction mixture.

^bAddition of 5 mol% $[\text{Ru}^{\text{II}}(\text{bpy})_3]\text{Cl}_2$ (0.02 mM) with respect to $2^{(\text{IV})}=\text{O}$ in the reaction mixture. ^cIrradiation at 447 nm.

^d k_{obs} values were obtained by fitting the decay of the absorbance at 725 nm over time to a single exponential function results are from at least three replicates.

III.3. SUMMARY

We found that complexes **1^(II)** and **2^(II)** react with different oxidants to form the high – valent iron (IV) – oxo complexes **1^{(IV)=O}** and **2^{(IV)=O}** through diverse strategies. These complexes have been generated and characterized as low – spin (S = 1) iron (IV) – oxo species by ¹H – NMR, UV – vis, ESI – MS and compound **1^{(IV)=O}** also by Cyclic Voltammetry, XAS and Mössbauer spectroscopy.

Complexes **1^{(IV)=O}** and **2^{(IV)=O}** are highly reactive against methylphenylthioethers and are able to transfer an O atom (OAT) that lead to the formation of methylphenylsulfoxides and Fe^{II}. Additionally, these complexes are capable also to react with C – H bonds (cumene, ethylbenzene and toluene), with slower rates, through a hydrogen abstraction step. A comparative analysis of kinetic parameters has been performed, as well as characterization studies of the products distribution for these transformations. Moreover, remarkably different activation parameters have been obtained for the OAT and HAT reactions.

Water exchange reactivity was also studied for complexes **1^{(IV)=O}**, **2^{(IV)=O}** and the analogous tetradentate **3^{(IV)=O}**. Results were compared with data obtained for a series of related iron (IV) – oxo complexes possessing either tetra – or pentadentate ligands, revealing a common mechanism for all of them and showing two different regimes with different KIE values and dependence on [H₂O].

Finally we demonstrated that [Ru^{II}(bpy)₃]²⁺ photoenhances the oxidation of **1^{(IV)=O}** and **2^{(IV)=O}** to generate the ^XPhS(O)Me products (X = MeO, Me, H, Cl). The data obtained supports that mechanism proceeds through an electron transfer from *[Ru^{II}(bpy)₃]²⁺ to the substrate to generate the sulphide radical cation, which is finally oxidised by the iron (IV) – oxo species. The ^{CN}PhSMe is unable to proceed through that mechanism due to its high 1 e⁻ oxidation potential. We proposed a possible energy transfer from *[Ru^{II}(bpy)₃]²⁺ to the iron (IV) – oxo species to presumably generate a low – lying highly reactive S = 2 oxoiron, although such species was not identified and further exploration is needed.

CHAPTER IV

**PREPARATION, SPECTROSCOPIC
CHARACTERIZATION AND REACTIVITY
OF IRON (IV) – TOSYLIMIDO COMPLEXES
WITH TACN – BASED
N5 – PENTADENTATE LIGANDS**

IV.1. GENERAL INSIGHT

The reaction of $[\text{Fe}^{\text{II}}(\text{CH}_3\text{CN})(\text{L})](\text{OTf})_2$, where L stands for pentadentate N – based aminopyridine ligands derived from triazacyclononane (**1^{III}**, L = MePy₂tacn = N – methyl – N, N – bis(2 – picolyl) – 1,4,7 – triazacyclononane, and **2^{III}**, L = Me₂(CHPy₂)tacn = 1 – (di(2 – pyridyl)methyl) – 4,7 – dimethyl – 1,4,7 – triazacyclononane) with PhINTs, (Ts = Tosyl) produces high – valent non – heme tosylimido complexes $[\text{Fe}^{\text{IV}}(\text{NTs})(\text{MePy}_2\text{tacn})](\text{OTf})_2$ (**1^{IV}=NTs**) and $[\text{Fe}^{\text{IV}}(\text{NTs})(\text{Me}_2(\text{CHPy}_2)\text{tacn})](\text{OTf})_2$ (**2^{IV}=NTs**). **1^{IV}=NTs** and **2^{IV}=NTs** are metastable complexes that have been spectroscopically characterized by UV – vis spectroscopy, ¹H – NMR, HR – MS, Raman Resonance, X – Ray absorption spectroscopy (XAS and EXAFS) and by DFT computational methods. **1^{IV}=NTs** and **2^{IV}=NTs** are isoelectronic analogues to the recently described iron (IV) – oxo complexes $[\text{Fe}^{\text{IV}}(\text{O})(\text{L})]^{2+}$ (L = MePy₂tacn and Me₂(CHPy₂)tacn). Nitrogen transfer competence of **1^{IV}=NTs** and **2^{IV}=NTs** has been investigated by studying their reactivity against thioanisole substrates. Reaction of **1^{IV}=NTs** and **2^{IV}=NTs** with different *p* – substituted thioanisole results in the transfer of the tosylimido moiety to the sulphur atom producing sulfanylidene products. Despite the reaction can be regarded as a formal analogue of the 2e⁻ oxidation oxo – transfer reactions mediated by the parent iron (IV) – oxo complexes, mechanistic studies in reactions of tosylimido transfer demonstrate that they are fundamentally distinct from a mechanistic perspective, entailing a single e⁻ transfer rate determining step. Reactions of **1^{IV}=NTs** and **2^{IV}=NTs** with thioanisole produce ferric complexes $[\text{Fe}^{\text{III}}(\text{NHTs})(\text{MePy}_2\text{tacn})](\text{OTf})_2$ (**1^{III} – NHTs**) and $[\text{Fe}^{\text{III}}(\text{NHTs})(\text{Me}_2(\text{CHPy}_2)\text{tacn})](\text{OTf})_2$ (**2^{III} – NHTs**) which have been characterized by EPR, Mössbauer, UV – vis spectroscopy and HR – MS. Hammett analyses suggest that the reactions occur via initial single electron transfer from thioanisole to the Fe^{IV}(NTs) moiety, followed by reaction of the radical cation with a second Fe^{IV}(NTs) moiety. A comparative analysis of kinetic parameters has been performed, as well as characterization studies of the reaction products.

IV.2. RESULTS AND DISCUSSION

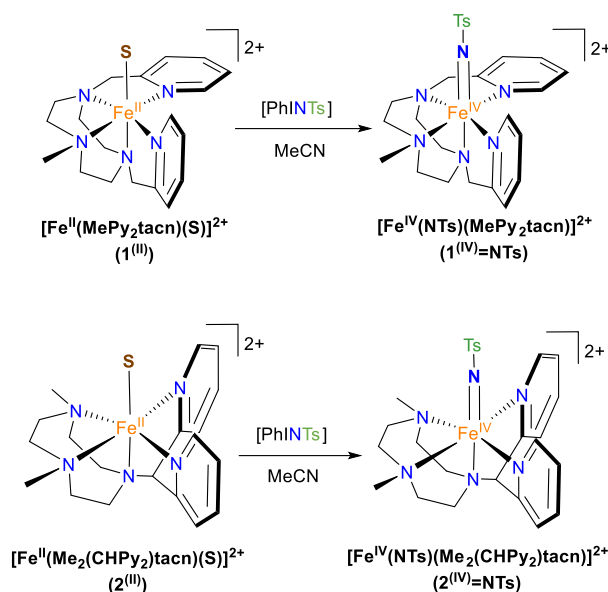
IV.2.1. Synthesis and characterization of $[\text{Fe}^{\text{IV}}(\text{NTs})(\text{MePy}_2\text{tacn})](\text{OTf})_2$ ($\mathbf{1}^{\text{IV}}=\text{NTs}$) and $[\text{Fe}^{\text{IV}}(\text{NTs})(\text{Me}_2(\text{CHPy}_2)\text{tacn})](\text{OTf})_2$ ($\mathbf{2}^{\text{IV}}=\text{NTs}$)

Ferrous complexes $[\text{Fe}^{\text{II}}(\text{CH}_3\text{CN})(\text{L})](\text{OTf})_2$ ($\mathbf{1}^{\text{II}}$, L = MePy₂tacn = N – methyl – N, N – bis(2 – picolyl) – 1,4,7 – triazacyclononane, and $\mathbf{2}^{\text{II}}$, L = Me₂(CHPy₂)tacn = 1 – (di(2 – pyridyl)methyl) – 4,7 – dimethyl – 1,4,7 – triazacyclononane) have been described in chapter III. Both complexes contain aminopyridine ligands based on a triazacyclononane moiety, providing a pentadentate donor set, leaving a sixth site available for an external labile ligand L6 (acetonitrile for $\mathbf{1}^{\text{II}}$ and $\mathbf{2}^{\text{II}}$). In $\mathbf{1}^{\text{II}}$, the two pyridine rings are in the same plane as the Fe – L6 axis, while in $\mathbf{2}^{\text{II}}$ one of the pyridines is parallel and a second one is perpendicular to this axis. Reaction of $[\text{Fe}^{\text{II}}(\text{MePy}_2\text{tacn})(\text{CH}_3\text{CN})](\text{OTf})_2$ $\mathbf{1}^{\text{II}}$ and $[\text{Fe}^{\text{II}}(\text{Me}_2(\text{CHPy}_2)\text{tacn})(\text{CH}_3\text{CN})](\text{OTf})_2$ $\mathbf{2}^{\text{II}}$ with 1.2 equiv of N – tosyliminobenzylidiodinane PhINTs in anhydrous CH₃CN at 25 °C produce $[\text{Fe}^{\text{IV}}(\text{NTs})(\text{MePy}_2\text{tacn})](\text{OTf})_2$ ($\mathbf{1}^{\text{IV}}=\text{NTs}$) and $[\text{Fe}^{\text{IV}}(\text{NTs})(\text{Me}_2(\text{CHPy}_2)\text{tacn})](\text{OTf})_2$ ($\mathbf{2}^{\text{IV}}=\text{NTs}$) (Scheme IV.1). The reaction could be conveniently monitored by UV – vis spectroscopy; reaction of $\mathbf{1}^{\text{II}}$ with PhINTs rapidly produces $\mathbf{1}^{\text{IV}}=\text{NTs}$, characterized by a low energy feature at $\lambda_{\text{max}} = 750$ nm and a prominent absorption at $\lambda_{\text{max}} = 455$ nm. Instead, reaction of $\mathbf{2}^{\text{II}}$ with PhINTs is slow, and formation of $\mathbf{2}^{\text{IV}}=\text{NTs}$ ($\lambda_{\text{max}} = 456$ and 740 nm) is mixed with its decay. However, use of acetone instead of acetonitrile leads to the fast formation of $\mathbf{2}^{\text{IV}}=\text{NTs}$, which can accumulate in good levels of purity (*vide infra*). Complexes $\mathbf{1}^{\text{IV}}=\text{NTs}$ and $\mathbf{2}^{\text{IV}}=\text{NTs}$ are metastable and decompose over time (complex $\mathbf{1}^{\text{IV}}=\text{NTs}$ $t_{1/2} \approx 40$ min. and few hours for complex $\mathbf{2}^{\text{IV}}=\text{NTs}$ at 20°C) to a mixture of iron (II) and iron (III) species (*vide infra*).

IV.2.1.1. Spectroscopic characterization of $\mathbf{1}^{\text{IV}}=\text{NTs}$ and $\mathbf{2}^{\text{IV}}=\text{NTs}$

Complexes $\mathbf{1}^{\text{IV}}=\text{NTs}$ and $\mathbf{2}^{\text{IV}}=\text{NTs}$ were characterized by Mössbauer spectroscopy using ⁵⁷Fe enriched samples. A frozen sample prepared after maximum accumulation of complex $\mathbf{1}^{\text{IV}}=\text{NTs}$ (followed by UV – vis spectroscopy) is shown in Figure IV.1. The spectrum recorded at 80 K under zero – applied magnetic field, is the superposition of three doublets. The major one corresponds to $\mathbf{1}^{\text{IV}}=\text{NTs}$ and constitutes the 87% of the total iron content (isomer shift $\delta = 0.05$ mm·s⁻¹, quadrupole splitting $\Delta E_Q = 1.09$ mm·s⁻¹), consistent with an iron (IV) centre in a low spin (S = 1) configuration.^{53,55} The rest of the sample corresponds to minor impurities assigned previously as dimeric ferric species. A frozen sample prepared after maximum accumulation of $\mathbf{2}^{\text{IV}}=\text{NTs}$ according to the UV – vis provides a more complex spectra, showing only 48% of high – valent iron (IV) species, with $\delta = 0.04$ mm·s⁻¹ and $\Delta E_Q = 0.74$ mm·s⁻¹ (see SI). However, when the same procedure was followed using acetone as solvent, the formation of $\mathbf{2}^{\text{IV}}=\text{NTs}$ was much faster and was obtained in higher purity (81%, $\delta = 0.06$ mm·s⁻¹, $\Delta E_Q = 0.73$ mm·s⁻¹). Obtained values are consistent with the previous structurally related reported species $[\text{Fe}^{\text{IV}}(\text{NTs})\text{N4Py}]^{2+}$ (N4Py, N,N – bis(2 – pyridylmethyl) – N – bis(2 – pyridyl)methylamine).¹⁶⁶ In $[\text{Fe}^{\text{IV}}(\text{NTs})\text{N4Py}]^{2+}$ Mössbauer spectrum consists of a doublet with a quadrupole splitting of 0.93 mm·s⁻¹ and an isomer shift of 0.02 mm·s⁻¹,

parameters that fall within the range of those previously reported for non – heme oxoiron (IV) complexes.^{53,55}



Scheme IV.1. Chemical strategy for the generation of $1^{\text{IV}}=\text{NTs}$ and $2^{\text{IV}}=\text{NTs}$ from Fe^{II} precursors. S = MeCN, CF_3SO_3 .

By taking into account the purities of the preparations of $1^{\text{IV}}=\text{NTs}$ and $2^{\text{IV}}=\text{NTs}$, established by Mossbauer spectroscopy, extinction coefficients for the features in the UV-Vis spectra of the two complexes could be derived. These are $\lambda_{\text{max}} = 455 \text{ nm}$ ($\epsilon = 4500 \text{ M}^{-1}\cdot\text{cm}^{-1}$) and 750 nm ($\epsilon = 200 \text{ M}^{-1}\text{ cm}^{-1}$) for $1^{\text{IV}}=\text{NTs}$, and $\lambda_{\text{max}} = 456 \text{ nm}$ ($\epsilon = 3600 \text{ M}^{-1}\cdot\text{cm}^{-1}$) and 740 nm , ($\epsilon = 170 \text{ M}^{-1}\text{ cm}^{-1}$) in the case of $2^{\text{IV}}=\text{NTs}$ in MeCN. In acetone $2^{\text{IV}}=\text{NTs}$ showed similar features at $\lambda_{\text{max}} = 455 \text{ nm}$ ($\epsilon = 4000 \text{ M}^{-1}\cdot\text{cm}^{-1}$) and 730 nm , ($\epsilon = 230 \text{ M}^{-1}\cdot\text{cm}^{-1}$). Of notice, the near – IR low absorption bands observed are characteristic of d – d bands of high – valent iron (IV) species with low spin (S=1) state.

High resolution mass spectra (HR – MS) of $1^{\text{IV}}=\text{NTs}$ and $2^{\text{IV}}=\text{NTs}$ in acetonitrile show a major peak at $m/z = 275.09$, with an isotopic pattern that corresponds to $[\text{Fe}^{\text{IV}}(\text{NTs})(\text{MePy}_2\text{tacn})]^{2+}$ and $[\text{Fe}^{\text{IV}}(\text{NTs})(\text{Me}_2(\text{CHPy}_2)\text{tacn})]^{2+}$ (Figure IV.1 and SIV.1). The spectra also show a lower intensity peak at $m/z = 699.13$, which corresponds to the $[[\text{Fe}^{\text{IV}}(\text{NTs})(\text{MePy}_2\text{tacn})](\text{OTf})]^+$ and $[[\text{Fe}^{\text{IV}}(\text{NTs})(\text{Me}_2(\text{CHPy}_2)\text{tacn})](\text{OTf})]^+$ cations. These peaks shifted in one unit, as expected upon formation of $1^{\text{IV}}=\text{NTs}$ and $2^{\text{IV}}=\text{NTs}$ with $\text{PhI}^{(15\text{N})}\text{Ts}$. Close inspection of these peaks reveal small contributions of the respective $[\text{Fe}^{\text{III}}(\text{HNTs})(\text{MePy}_2\text{tacn})]^{2+}$ species. Finally, a minor peak at $m/z = 550.18$ and its isotopic pattern evidence the presence of $[\text{Fe}^{\text{III}}(\text{NTs})(\text{L})]^+$ species.

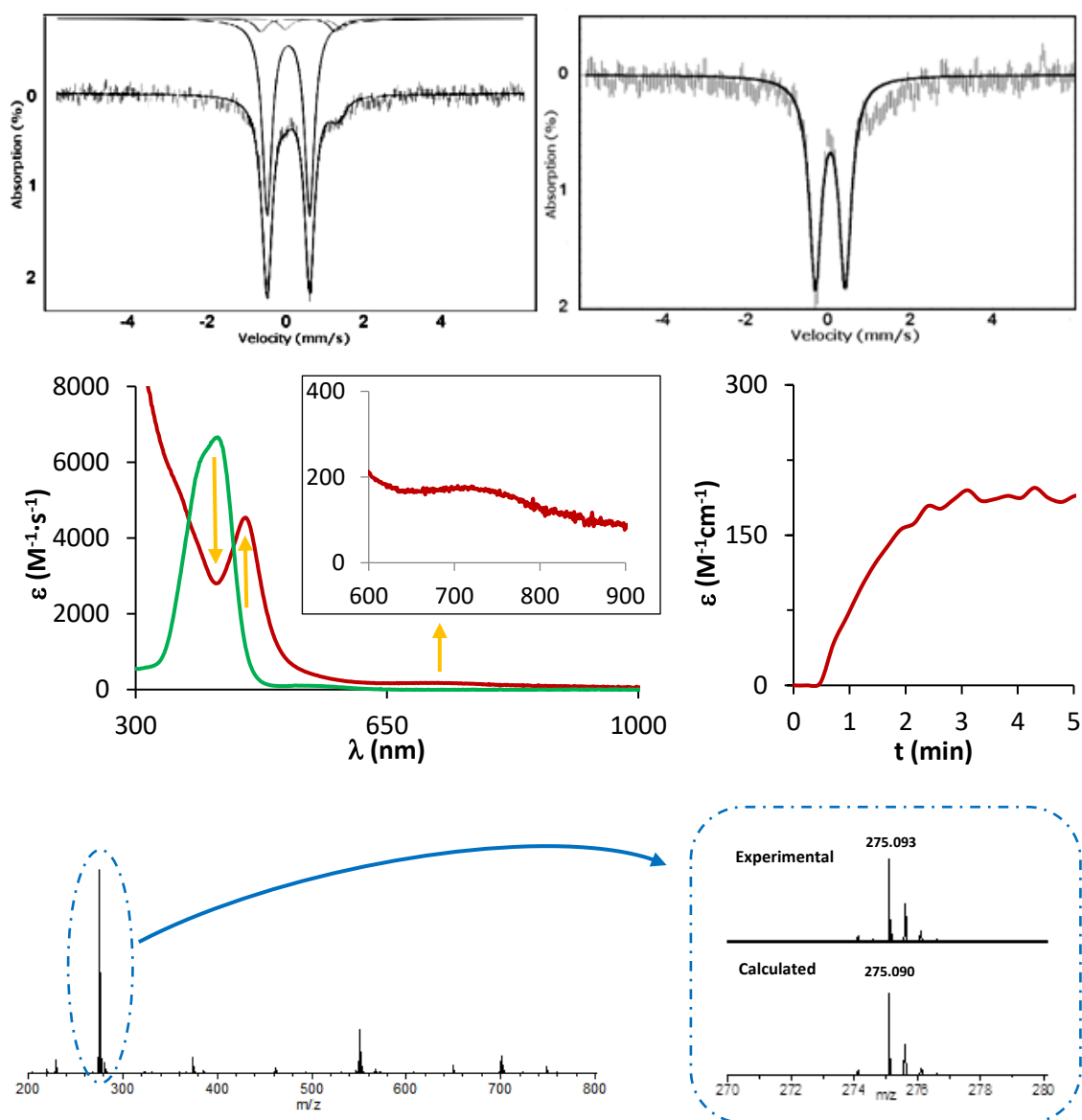


Figure IV.1. Top, Mössbauer spectrum of $1^{(IV)}=NTs$ (left) in acetonitrile recorded at 80K and Mössbauer spectrum of $2^{(IV)}=NTs$ (right) prepared in acetone and recorded at 80K. Experimental data are hatched bars and solid line represent the contributions of $1^{(IV)}=NTs$ and $2^{(IV)}=NTs$. Centre, UV – vis spectrum of oxidation of $1^{(II)}$ to $1^{(IV)}=NTs$ in CH_3CN and kinetic trace that shows the evolution of 750 nm feature. Below, HR – MS spectrum of $1^{(IV)}=NTs$ prepared in CH_3CN exhibiting a base peak at m/z 275.09; inset show amplification of major peak for $[Fe^{IV}(NTs)(MePy_2tacn)]^{2+}$ species. Proper simulation of the peak requires inclusion of $\approx 10\%$ of $[Fe^{III}(NHTs)(MePy_2tacn)]^{2+}$ in the isotopic pattern corresponding to $[Fe^{IV}(NTs)(MePy_2tacn)]^{2+}$.

The 1H – NMR spectrum of $1^{(IV)}=NTs$ and $2^{(IV)}=NTs$ in CD_3CN or D_6 – acetone show paramagnetically shifted signals between -75 and 50 ppm, being the signals of the pyridine moiety the most distinctive features (Figure IV.2). Full assignment of the spectra could not be accomplished because of the complications associated with the fast relaxation of paramagnetically affected signals, but signals corresponding to the pyridine rings could be identified by comparison with the spectra of the parent iron (IV) – oxo complexes, and also with that of $[Fe^{IV}(X)(N_4Py)]^{2+}$ ($X = O, NTs$) and $[Fe^{IV}(O)(Bn - TPEN)]^{2+}$.^{82,166} A remarkable observation is that when the solvent is not completely dry significant amounts

of iron (IV) – oxo species were identified, presumably obtained from PhINTs hydrolysis to PhIO, which then reacts with **1**^(III) and **2**^(III) to form the corresponding iron (IV) – oxo species previously reported^{77,83} and studied in Chapter III. The presence of the wide signals in both **1**^{(IV)=NTs} and **2**^{(IV)=NTs} complexes in the high – field region of the spectra, which are not present in the $[\text{Fe}^{\text{IV}}(\text{NTs})(\text{N4Py})]^{2+}$ spectrum, suggest they belong to the triazacyclononane ring and possibly to the methyl groups on the amines. The bidimensional COSY spectrum obtained for complex **2**^{(IV)=NTs}, allowed unequivocally the assignment of pyridine hydrogens to the signals at 20.87 (β), 9.70 (γ) and -6.56 (β') ppm. Of notice, the signal pattern closely resembles that of $[\text{Fe}^{\text{IV}}(\text{X})(\text{N}_4\text{Py})]^{2+}$ ($\text{X} = \text{O}, \text{NTs}$), where all the pyridine rings are also parallel to the Fe – N axis. On the other hand, **1**^{(IV)=NTs} presents a more complex spectrum, in accordance with its reduced symmetry. The two pyridine rings in this complex are one parallel and the other perpendicular to the Fe=N axis, and this is evidenced in the ¹H – NMR spectrum, and supported by COSY spectra, that show two sets of pyridine protons. The first set (subset a), is assigned to the pyridine parallel to the Fe – N axis, and show the same pattern observed for complex **2**^{(IV)=NTs} and the $[\text{Fe}^{\text{IV}}(\text{NTs})(\text{N4Py})]^{2+}$ complex, with β proton downshifted and β' signal upshifted; noticeably is, that the other set (subset b), which belongs to the pyridine perpendicular to that axis, shows a distinct pattern, with both β and β' proton signals upshifted, the same behaviour was also observed on the previously reported $[\text{Fe}^{\text{IV}}(\text{O})(\text{Bn} - \text{TPEN})]^{2+}$ (Bn – TPEN, N – benzyl – N,N',N' – tris(2 – pyridylmethyl) – 1, 2 – diaminoethane). With the bidimensional COSY spectra were assigned the signals of the pyridines: subset a (parallel to Fe – N axis) 41.04 (βa), 12.67 (γa) and -13.31 ($\beta'\text{a}$) ppm; subset b (perpendicular to Fe=N axis) -5.58 (βb), 6.02 (γb) and -6.93 ($\beta'\text{b}$) ppm. An important difference between the spectra of $[\text{Fe}^{\text{IV}}(\text{NTs})(\text{N}_4\text{Py})]^{2+}$ with that of **1**^{(IV)=NTs} and **2**^{(IV)=NTs}, is that the latter two complexes present prominent signals at 42.46 and 17.30 ppm for **1**^{(IV)=NTs}, and 44.59 and 16.72 ppm for **2**^{(IV)=NTs} that, on the basis of its relative integration, we speculate that they could belong to the Me group and the ring of the tosylimido moiety, although we couldn't obtain further evidence.

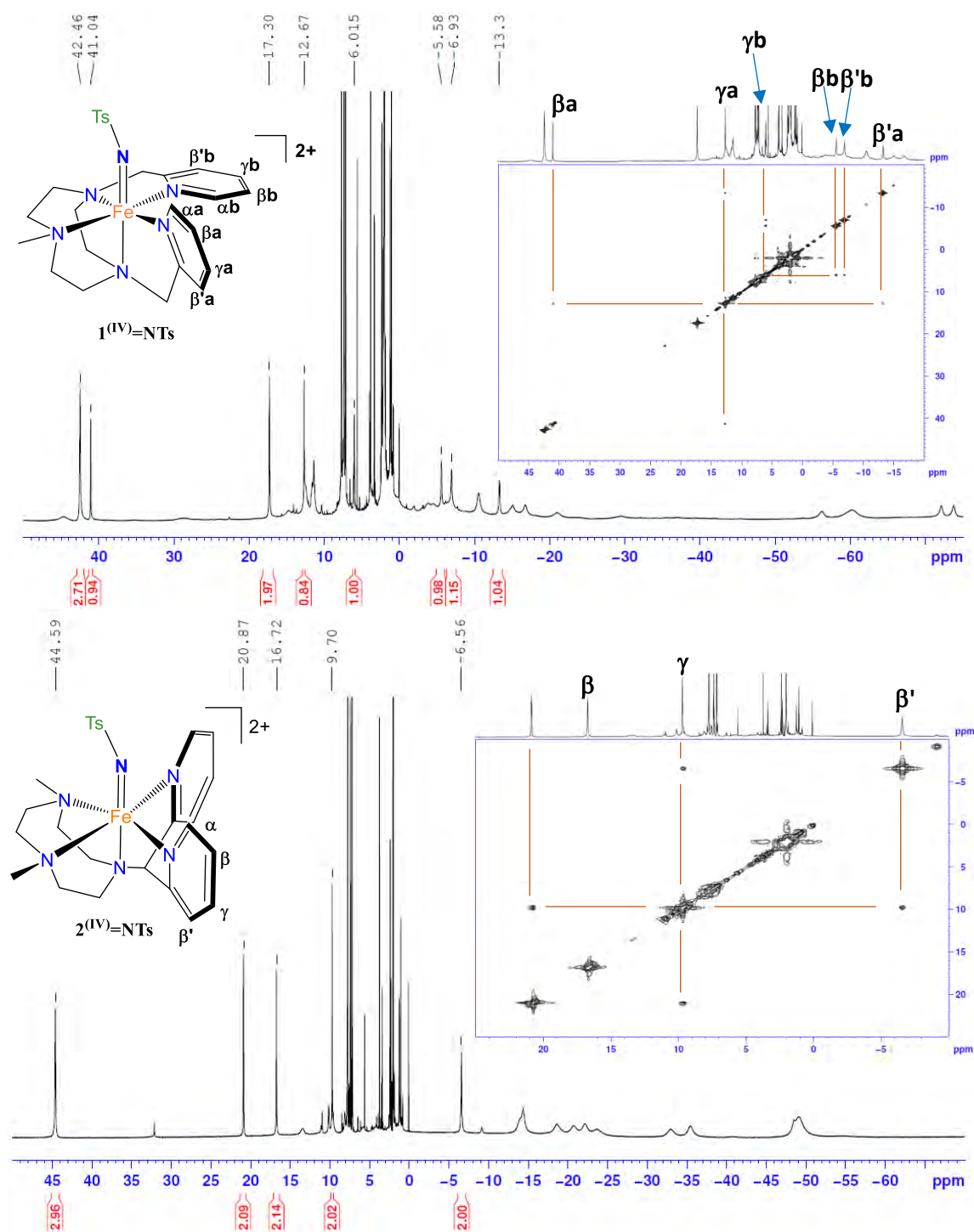


Figure IV.2. 1H -NMR and bidimensional COSY spectra of (top) complex $1^{(IV)}=NTs$ in D_6 - acetone at 0 °C and (below) $2^{(IV)}=NTs$ in D_6 acetone at 25 °C (small peaks at 32 and -9 ppm belong to <5% of $[Fe^{IV}(O)(Me_2(CHPy)_2)tacn]$). Spectra recorded in a 400 MHz spectrometer.

Complex $1^{(IV)}=NTs$ exhibited a resonance Raman enhanced broad feature at *ca.* 984 cm^{-1} when was excited at 488.0 nm, that can be assigned to the Fe=N stretching mode on the basis of the 24 cm^{-1} shift observed upon formation of $1^{(IV)}=NTs$ with $PhI^{15}NTs$. The $\nu(Fe=NTs)$ downshift from 984 cm^{-1} to 960 cm^{-1} was fully consistent with the 27 cm^{-1} shift expected for a diatomic Fe=NTs oscillator. The spectra also revealed several bands between 600 and 700 cm^{-1} which downshifted from 2 to 5 cm^{-1} upon ^{15}N

incorporation. (Figure IV.3). For compound $2^{(IV)}=NTs$ the Raman spectra shows a broader feature can be observed around 1016 cm^{-1} that shifts *ca.* 22 cm^{-1} upon formation of $2^{(IV)}=NTs$ with $PhI^{15}NTs$. Also consistent with the 27 cm^{-1} shift expected for a diatomic $Fe=NTs$ oscillator. The broad features may indicate that there is not only contribution only from Fe and N atoms. These vibrations are in agreement with values found for the analogue complexes $[Fe^{IV}(NTs)(N4Py)]^{2+}$ and $[Fe^{IV}(NTs)(Bn-TPEN)]^{2+}$, showing vibrations that shift from 998 to 975 cm^{-1} and 984 to 957 cm^{-1} respectively upon labelling with ^{15}N .²⁸⁵ Furthermore both reported complexes also show additional bands at $600 - 700\text{ cm}^{-1}$ that shift $2 - 5\text{ cm}^{-1}$ upon ^{15}N incorporation, which are tentatively assigned to aryl – N stretches on the basis of previous works reported for imidoiron (III) complexes.²⁸⁶

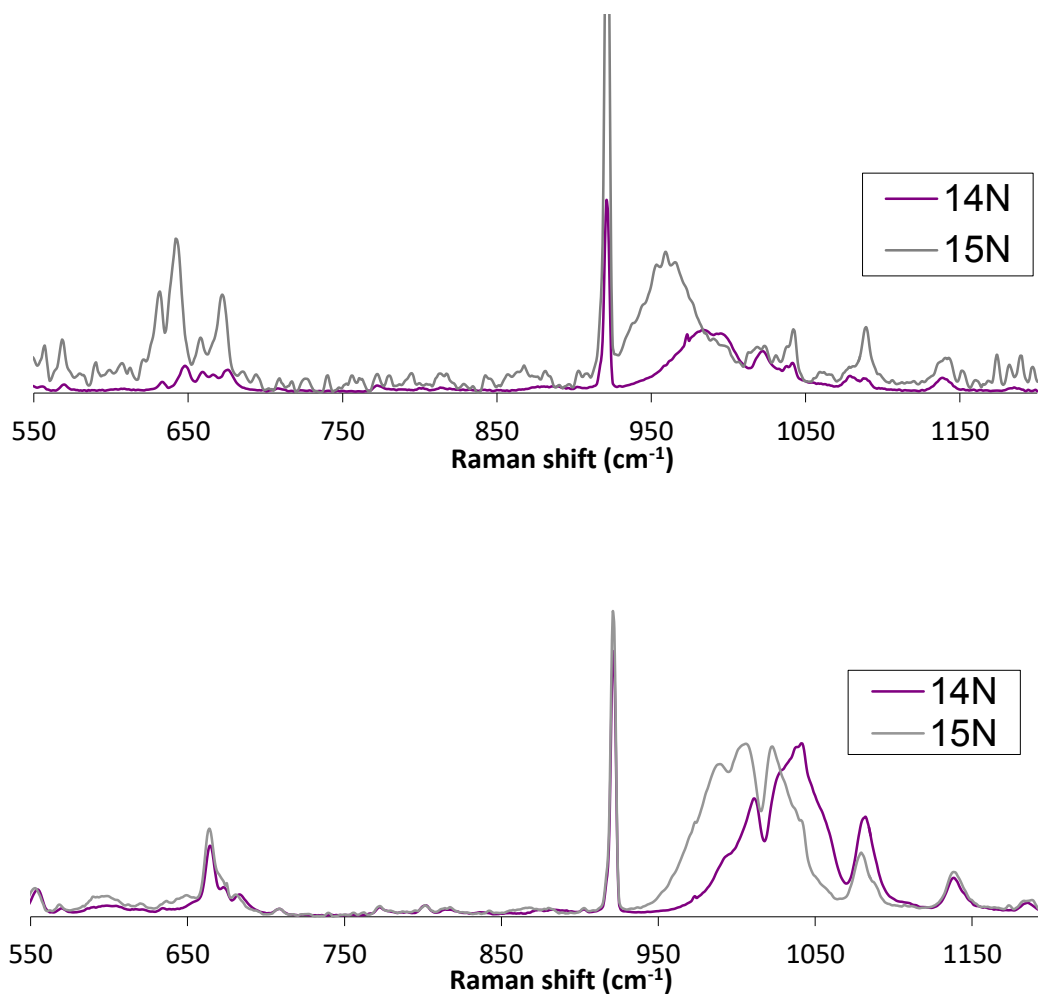


Figure IV.3. Enhanced Raman spectra for complex $1^{(IV)}=NTs$ (top) and $2^{(IV)}=NTs$ (below) upon excitation at 488 nm.

Unfortunately, to date no crystal structure could be obtained for complexes $1^{(IV)}=NTs$ and $2^{(IV)}=NTs$, and but their structure could be derived from XAFS analysis of frozen samples in acetone (Figure IV.4).

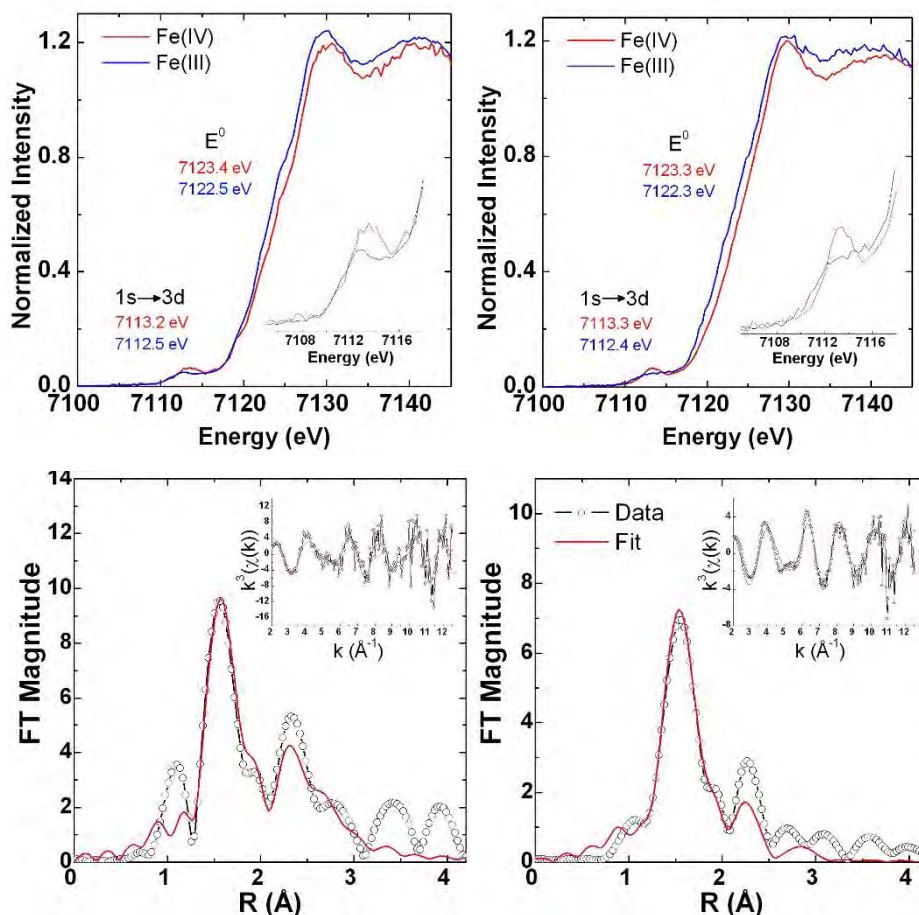


Figure IV.4. Iron K – edge X – ray absorption spectra of: top left, $1^{(IV)}=NTs$ (red) and $1^{(III)}=NHTs$ (blue); top right: $2^{(IV)}=NTs$ (red) and $2^{(III)}=NHTs$ (blue). Below, non – phase shift corrected Fourier transforms for $1^{(IV)}=NTs$ (left) and $2^{(IV)}=NTs$ (right) with insets showing the k – space data and fits. Experimental data are shown in black and fits in red.

Table IV.1. EXAFS data for complexes $1^{(IV)}=NTs$ and $2^{(IV)}=NTs$.

Complex $1^{(IV)}=NTs$				Complex $2^{(IV)}=NTs$			
Scatterer	r(Å)	s ² (x10 ³ Å ²)	%R	Scatterer	r(Å)	s ² (x10 ³ Å ²)	%R
1 N/O	1.73(2)			1 N/O	1.72(1)		
5 N/O	1.99(1)	2(1)	4.7	5 N/O	1.99(1)	4(1)	4.1
8 C	2.85(2)			1 C	2.55(5)		

Fe K – edge X – ray absorption spectroscopy (XAS) provides additional insight into the geometric and electronic structure of $1^{(IV)}=NTs$ and $2^{(IV)}=NTs$ (Figure IV.4). These complexes exhibit 1s→3d transitions centred around 7113.3 eV in the pre – edge region with intensities of 0.19 for $1^{(IV)}=NTs$ and 0.18 for $2^{(IV)}=NTs$. Accounting for the 0.8 eV difference in calibration, these values are in close agreement with the

structurally related octahedral $[\text{Fe}^{\text{IV}}(\text{NTs})\text{N4Py}]^{2+}$ complex (7113.9 eV) and similar to the iron (IV) – oxo analogues (7114.3 eV for $[\text{Fe}^{\text{IV}}(\text{O})(\text{N4Py})]^{2+}$ and 7114.1 for $[\text{Fe}^{\text{IV}}(\text{O})(\text{MePy}_2\text{tacn})]^{2+}$).^{84,85,166} Furthermore, the XANES region is consistent with a change of one oxidation state and is in agreement with the change from Fe(III) to Fe(IV) going from $\mathbf{1}^{\text{III}} - \text{NHTs}$ to $\mathbf{1}^{\text{IV}} = \text{NTs}$ or $\mathbf{2}^{\text{III}} - \text{NHTs}$ to $\mathbf{2}^{\text{IV}} = \text{NTs}$. Evidenced by a ~ 1 eV increase in the rising edge concomitant with a ~ 0.8 eV increase in the pre – edge energies. Moreover, EXAFS analysis data provide information of the iron coordination environments, and for complex $\mathbf{1}^{\text{IV}} = \text{NTs}$ and $\mathbf{2}^{\text{IV}} = \text{NTs}$ are consistent with a pseudo – octahedral geometry at the Fe centre having six Fe – N bonds, with one of them significantly shorter, having a length of 1.72 – 1.73 Å. Such a short distance is expected for a multiple Fe – N bond, the single scatterers at ~ 1.72 Å are thus attributed to the N atom of the NTs ligand. The obtained Fe – N bond distances are similar to that of $[\text{Fe}^{\text{IV}}(\text{NTs})(\text{N4Py})]^{2+}$ complex (1.73 Å),¹⁶⁶ but significantly longer than the ones found for its iron – oxo (IV) analogues (Fe – O = 1.63 Å).⁸⁵ The longer Fe = X could be rationalised on tosylimido species due to the electron – withdrawing character of the tosyl group, weakening the Fe = N bond, but also possibly due to its higher steric hindrance.

In addition, theoretical models were constructed for $\mathbf{1}^{\text{IV}} = \text{NTs}$ and $\mathbf{2}^{\text{IV}} = \text{NTs}$, and are found to be consistent with the experimental data (Figure IV.5). The Fe – N bond for both $\mathbf{1}^{\text{IV}} = \text{NTs}$ and $\mathbf{2}^{\text{IV}} = \text{NTs}$ is predicted at 1.74 Å, very close to that extracted from EXAFS analysis. Furthermore, calculated Mössbauer parameters are also in agreement with experimentally derived values (Table IV.2), suggesting that in addition to geometry the electronic structure is also well described by the theoretical models. It is important to highlight that similar to the Fe(III) analogues (*vide infra*) the quadrupole splitting for $\mathbf{1}^{\text{IV}} = \text{NTs}$ is larger than $\mathbf{2}^{\text{IV}} = \text{NTs}$, suggesting a more centro – symmetric environment for $\mathbf{2}^{\text{IV}} = \text{NTs}$. Qualitatively this is consistent with the pre – edge intensities from XAS analysis, where the intensity of $\mathbf{1}^{\text{IV}} = \text{NTs}$ is higher than $\mathbf{2}^{\text{IV}} = \text{NTs}$, consistent with a greater distortion from centro – symmetry in $\mathbf{1}^{\text{IV}} = \text{NTs}$. Indeed the first coordination sphere of the modelled Fe centre in $\mathbf{1}^{\text{IV}} = \text{NTs}$ shows a 0.25 Å root mean square deviation (RMSD) from octahedral symmetry while in $\mathbf{2}^{\text{IV}} = \text{NTs}$ this value is only 0.14 Å. Finally, the theoretical model predict similar intermediate spin $S = 1$ electronic configurations at the metal centre consistent with a $\delta(\text{Fed}_{xy})^2\pi^*(\text{Fed}_{xz,yz})^2\sigma^*(\text{Fed}_{x^2-y^2})^0\sigma^*(\text{Fed}_z)^0$ arrangement (Figure IV.5).

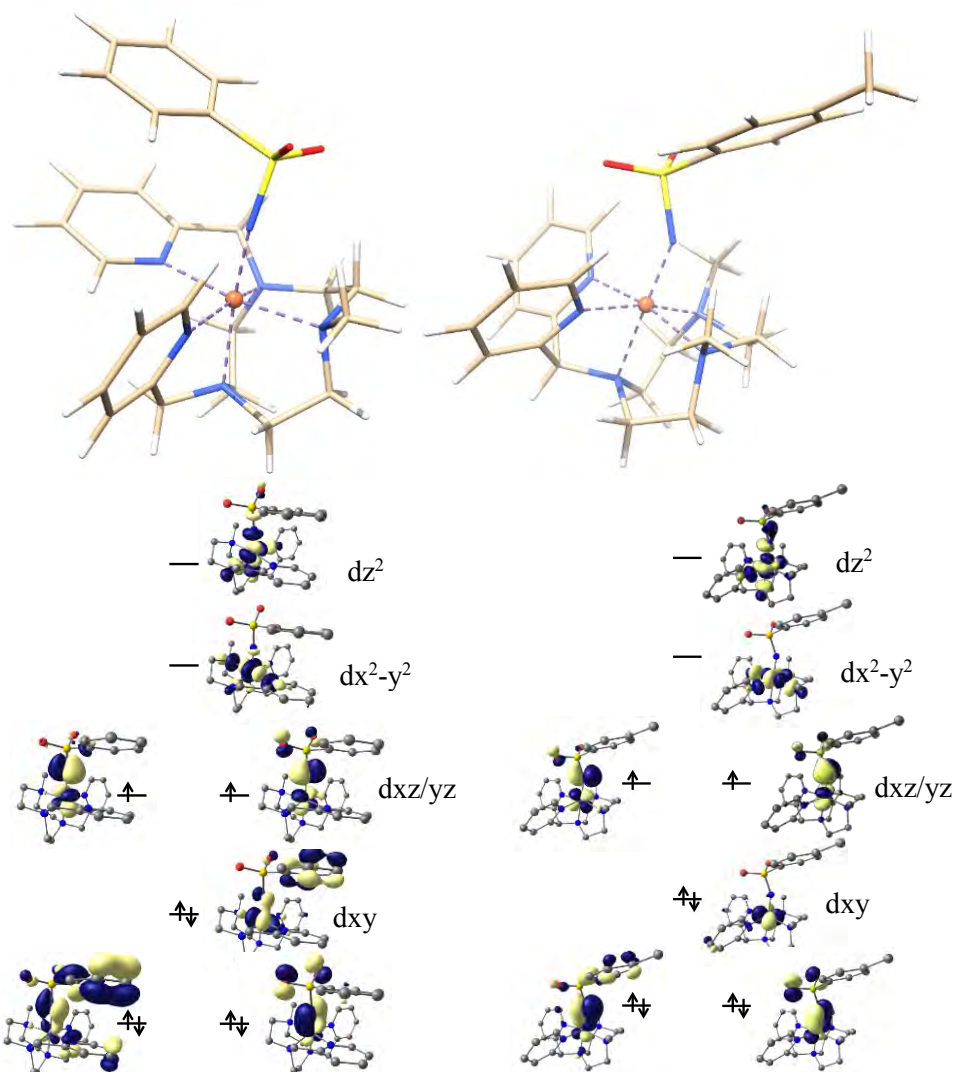


Figure IV.5. Computationally derived geometries and quasi – restricted orbitals (0.05 isovalue) showing the Fe d manifold for $1^{(IV)}=NTs$ (left) and $2^{(IV)}=NTs$ (right). (TPSSh/def2 – TZVP//TPSS/def2 – TZVP).

Table IV.2. Structural and spectroscopic properties of S = 1 high – valent tosylimido iron compounds.

Species		$1^{(IV)}=NTs$	$2^{(IV)}=NTs$	$2^{(IV)}=NTs^*$	${}^b[Fe^{IV}(NTs)(N4Py)]^{2+}$	${}^b[Fe^{IV}(NTs)(Bn - TPEN)]^{2+}$
^a Mössbauer Spectroscopy	δ (mm^{-1})	0.05 (0.02)	0.06 (0.02)	0.04 (0.02)	0.02	0.06
	ΔE_Q (mm^{-1})	1.09 (1.16)	0.73 (0.74)	0.74 (0.74)	0.98	0.99
Raman ν ^{14}N (^{15}N) (cm^{-1})		984 (960)	ND	1016 (994)	998 (975)	984 (957)
^a Fe – N distance XAS (Å)		1.73 (1.74)	1.72 (1.74)	ND	1.73	ND
EXAFS Data Eo ($E_{pre-edge}$) (eV)		7123.4 (7113.2)	7123.3 (7113.3)	ND	7123.8 (7113.9)	ND

^aDFT calculated values in parenthesis. Data from ref. ^{166,285}. $2^{(IV)}=NTs$: Data from complex prepared in acetone. $2^{(IV)}=NTs^*$: Data from complex prepared in MeCN. ND = Not determined.

To date only few iron (IV) – imido species have been prepared and structurally characterised (Figure IV.6). X – ray diffraction examples belong almost exclusively to the pseudo – tetrahedral geometry, with significantly shorter Fe=N bonds of 1.61 – 1.64 Å in comparison to octahedral systems.^{165,169,170,287,288} The aforementioned $[\text{Fe}^{\text{IV}}(\text{NTs})(\text{N}_4\text{Py})]^{2+}$ complex (Fe = N 1.73 Å from EXAFS data) is the only example structurally and electronically comparable to $1^{\text{(IV)}}=\text{NTs}$ and $2^{\text{(IV)}}=\text{NTs}$. Importantly, to the best of our knowledge, exists only one X – ray structure for a structurally comparable iron (IV) – imido complex, the $[\text{Fe}^{\text{IV}}(\text{NAd})(\text{pyrr}_2\text{py})]$, in a pseudo – octahedral – trigonal pyramidal geometry, retaining two free coordinative positions, and a short Fe = N bond distance of 1.64 Å.¹⁷²

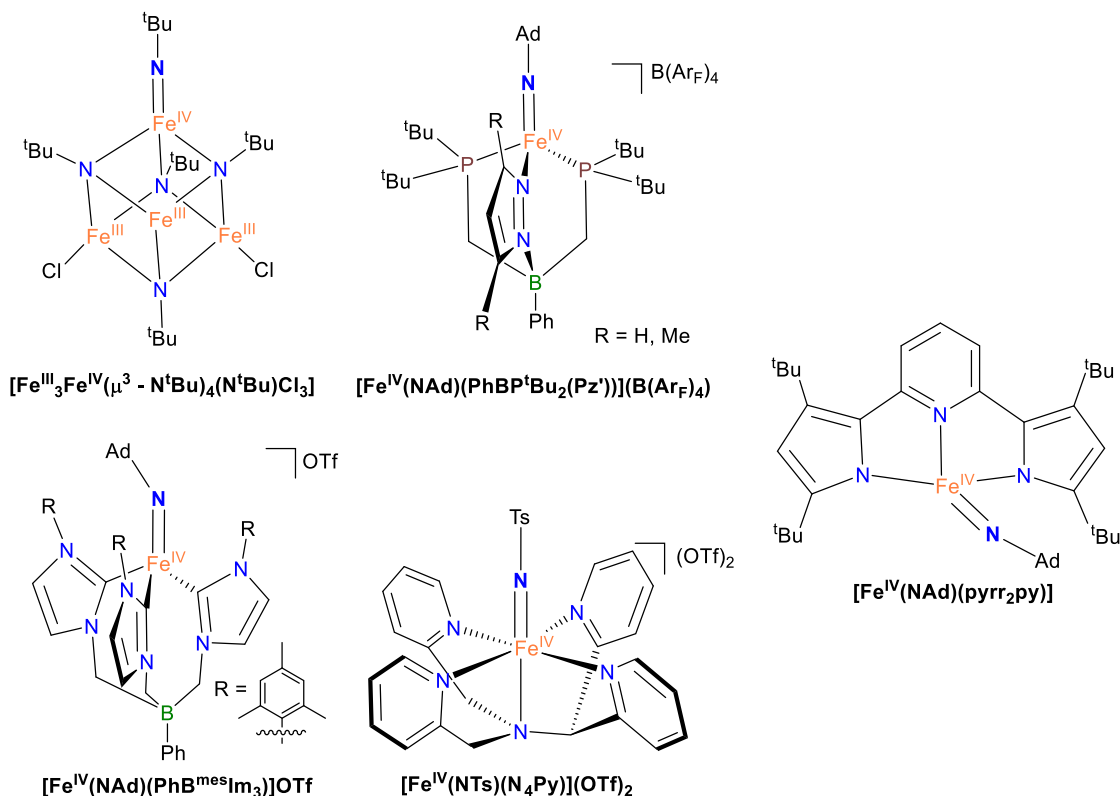


Figure IV.6. Selected structures of spectroscopically characterised iron (IV) – imido complexes. Ad = adamantane, $\text{B}(\text{Ar}_F)_4 = [\text{B}(3, 5 - (\text{CF}_3)_2\text{C}_6\text{H}_3)_4]^-$.^{165,166,169,170,172}

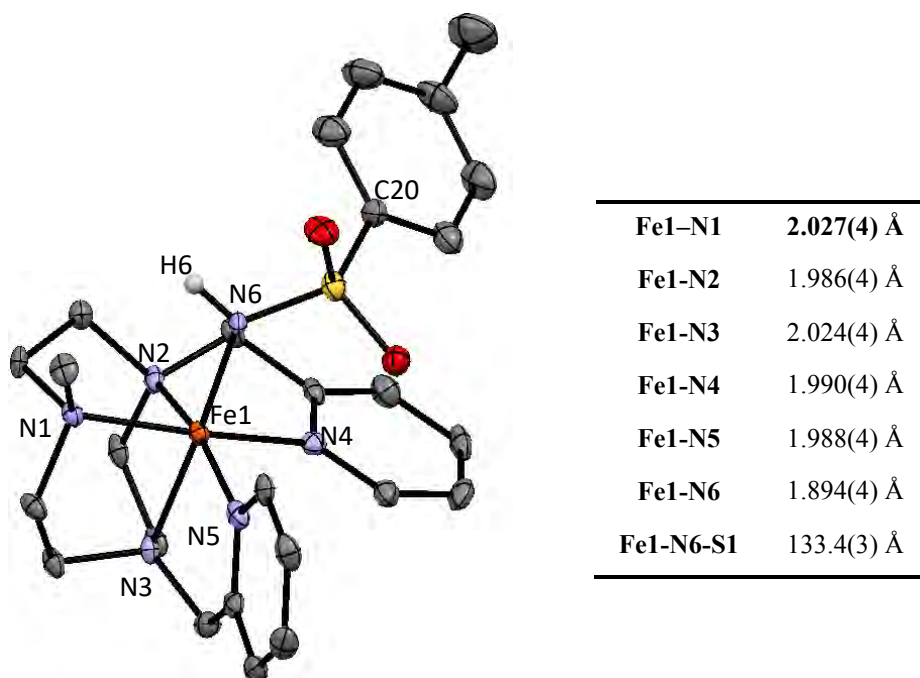
IV.2.2. Synthesis and characterization of $[\text{Fe}^{\text{III}}(\text{NHTs})(\text{MePy}_2\text{tacn})](\text{X})_2$ ($1^{\text{(III)}} - \text{NHTs}/\text{X}$) and $[\text{Fe}^{\text{III}}(\text{NHTs})(\text{Me}_2(\text{CHPy}_2)\text{tacn})](\text{X})_2$ ($2^{\text{(III)}} - \text{NHTs}/\text{X}$)

Our attempts to obtain single crystals of iron (IV) – tosylimido compounds $1^{\text{(IV)}}=\text{NTs}$ and $2^{\text{(IV)}}=\text{NTs}$ by slow diethyl ether diffusion to acetonitrile or acetone solutions of the compounds failed, providing instead the corresponding ferric complexes $[\text{Fe}^{\text{III}}(\text{NHTs})(\text{MePy}_2\text{tacn})](\text{OTf})_2$ ($1^{\text{(III)}} - \text{NHTs}/\text{OTf}$), and $[\text{Fe}^{\text{III}}(\text{NHTs})(\text{Me}_2(\text{CHPy}_2)\text{tacn})](\text{OTf})_2$ ($2^{\text{(III)}} - \text{NHTs}/\text{OTf}$) as crystalline materials. $1^{\text{(III)}} - \text{NHTs}/\text{OTf}$ and $2^{\text{(III)}} - \text{NHTs}/\text{OTf}$ were spectroscopically characterized. A collection of the spectroscopic data obtained for these two complexes is shown in Table IV.3.

Table IV.3. Spectroscopic data from isolated complexes $1^{(III)} - \text{NHTs/OTf}$ and $2^{(III)} - \text{NHTs/OTf}$.

	S	$g_x/g_y/g_z$	δ (mm.s^{-1})	ΔE_Q (mm.s^{-1})	Γ (mm.s^{-1})	η	A_x (T)	A_y (T)	A_z (T)	E_o ($E_{\text{pre-edge}}$) (eV)
$1^{(III)} - \text{NHTs}$	1/2	2.26/2.26/1.93	0.23	2.06	0.54	1.10	22	2	-47	7122.5 (7112.5)
$2^{(III)} - \text{NHTs}$	1/2	2.24/2.24/1.95	0.23	1.74	0.44	1.42	11	22	-30	7122.3 (7112.4)

Single crystals suitable for X – ray diffraction were obtained for the compound $1^{(III)} - \text{NHTs/SbF}_6$. An ORTEP diagram corresponding to the molecular structure of $1^{(III)} - \text{NHTs/SbF}_6$ is shown in Figure IV.7 and crystal data as well as selected bonds and angles in Tables S1 and S2. The complex contains an iron centre in a distorted octahedral geometry. Five coordination sites are occupied by nitrogen atoms from pentadentate ligand with Fe – N distances typical for iron (III) in low – spin (1.98 – 2.03 Å).^{256,289,290} The sixth site is occupied by the N atom of the hydrogen tosylimido moiety. The two pyridine rings are perpendicular one to each other, maintaining the structure of $1^{(III)}$, with one of them parallel to the Fe – N(H) axis. Fe – Py bonds are 1.990 and 1.988 Å and Fe – Nalkyl 2.024, 2.027 and 1.986 Å, Fe – Py bonds are slightly shorter likely to the π – acceptor character of pyridine. The Fe – N(H) distance is relatively short (1.89 Å) and denotes certain degree of π interaction. For comparison Fe – N(H) bond is 0.18 Å longer than Fe = N in $1^{(IV)} = \text{NTs}$, as expected from its lower π character.

**Figure IV.7.** Top, ORTEP structure of isolated ferric complex $1^{(III)} - \text{NHTs/SbF}_6$, 50% ellipsoid probability, counterions omitted for clarity.

Only few Fe^{III} – amido/imido species have been reported, and exclusively two of them in octahedral geometry (Figure IV.8). Chang and co – workers reported two high – spin ferric complexes bearing pentadentate aminopyridine ligands, the $[\text{Fe}^{III}(\text{NH} - \text{SO}_2\text{C}_6\text{H}_4\text{R})\text{TPA}_2^{\text{C}(\text{O})\text{NHtBu}}](\text{OTf})_2$ ($\text{TPA}_2^{\text{C}(\text{O})\text{NHtBu}} = 6,6'$

– (pyridine – 2 – ylmethylazanediy)bis(methylene)bis(N – tert – butylpicolinamide; R = CH₃, NO₂) with Fe – N(H) bonds 1.95 and 2.00 Å respectively.²⁹¹ Previously, Borovik and coworkers synthesised the high – spin [Fe^{III}(NHTol)(H₂)][–] complex with a Fe – NH bond of 1.97 Å.¹⁶² These Fe – N(H) bonds are longer than in **1**^(III) – NHTs/SbF₆ evidencing the difference in spin, although the former complexes are in a bipyramidal pentagonal symmetry and the latter in trigonal bipyramidal geometry. On the other hand, previously described pseudo – tetrahedral low spin iron (III) – imido complexes show much shorter distances than in **1**^(III) – NHTs/SbF₆ (1.62 – 1.66 Å).^{169,170,286} Very recently Spasyuk *et al.* reported the X – ray structures of the octahedral [Fe^{III}(NHR)(B₂Pz₄Py)] (R = C₆H₄C(CH₃)₃ or adamantane). The Fe – N(H) bond distances of 1.869 and 1.854 Å are in agreement with that of **1**^(III) – NHTs/SbF₆ and slightly shorter reflecting the electrowithdrawing character of tosyl group. Noticeably are also the differences in the angles, Fe – N(H) – S angle in **1**^(III) – NHTs/SbF₆ is 133.4 °, close to the 138.2 and 132.85 ° found for [Fe^{III}(NH – SO₂C₆H₄R)TPA₂^{C(O)NHtBu}](OTf)₂ (R = Me and NO₂ respectively) and also the 138.91 and 140.74 Å from [Fe^{III}(NHR)(B₂Pz₄Py)] (R = C₆H₄C(CH₃)₃ or adamantane). In contrast imido complexes [Fe^{III}(NAd)(PhBP^tBu₂(Pz')))] and [Fe^{III}(NAd)(PhB^{mes}Im₃)] show angles almost linear of 172.1 and 177.0 ° respectively, as a consequence of not having the hydrogen in the N.

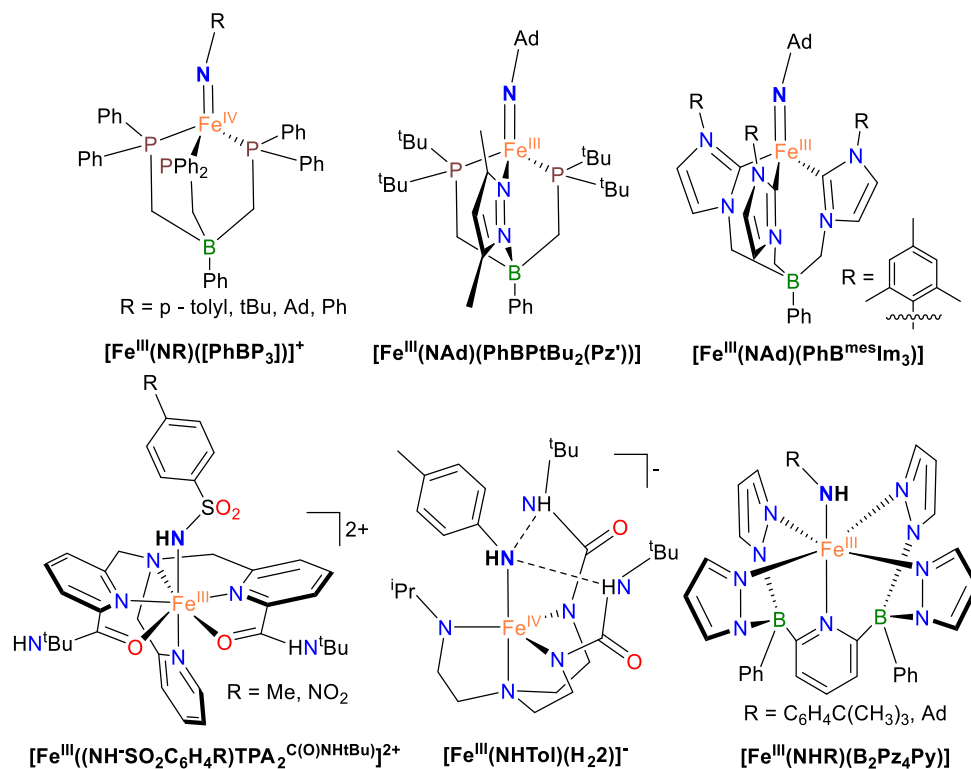


Figure IV.8. Structures of reported iron (III) – amido/imido complexes. Ad = adamantane

EPR of **1**^(III) – NHTs/OTf at 2 K (Figure SIV.2) show axial spectra with two similar species with mean values $g_{eff,\perp} = 2.23$ and $g_{eff,\parallel} = 1.93$, indicative of S = 1/2 systems characteristic of low spin ferric centres. On the other hand **2**^(III) – NHTs/OTf shows a signal attributed to low – spin Fe^{III} complex of axial symmetry with $g_{eff,\perp} = 2.21$ and $g_{eff,\parallel} = 1.95$. In both samples a minor high – spin signal is observed. This is further supported by a Mossbauer study that evidence an asymmetric doublet with $\delta = 0.23$ mm·s^{–1} for both complexes and $\Delta E_Q = 2.06$ and 1.74 mm·s^{–1} respectively (Figure IV.9). When recorded at 4.2 K, spectra

under an applied field of 7 T show these species are iron (III) in low spin. Mössbauer spectroscopy revealed $\approx 90\%$ purity on iron (III) in both samples.

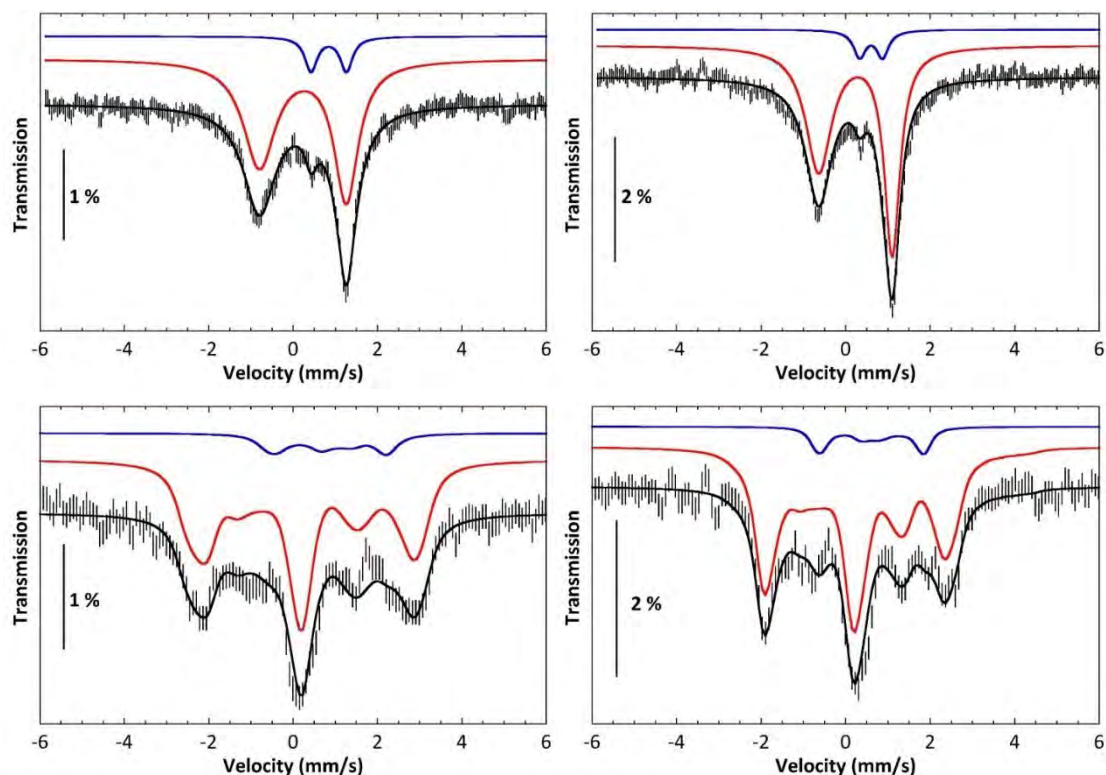


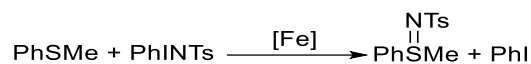
Figure IV.9. Spectroscopic data of isolated $\mathbf{1}^{(III)} - \text{NHTs/OTf}$ (left) and $\mathbf{2}^{(III)} - \text{NHTs/OTf}$ (right). (Top) Zero Field Mössbauer spectra at 80 K. (Below) Mössbauer spectra at 4.2 K and 7T.

The HR – MS (Figure SIV.3) spectra of solutions of $\mathbf{1}^{(III)} - \text{NHTs/OTf}$ and $\mathbf{2}^{(III)} - \text{NHTs/OTf}$ revealed, for both complexes, two major peaks at $m/z = 275.59$ and 700.13 that are assigned to corresponding to $[\text{Fe}^{III}(\text{NHTs})\text{L}]^{2+}$ and $[\text{Fe}^{III}(\text{NHTs})\text{L}(\text{OTf})]^{+}$ ions on the basis of the mass and isotopic patterns. The complexes are hydrolytically very sensitive and peaks at $m/z = 199.08$ and 547.12 that could be assigned to $[\text{Fe}^{III}(\text{OH})\text{L}]^{2+}$ and $[\text{Fe}^{III}(\text{OH})\text{L}(\text{OTf})]^{+}$ ions, respectively, are also observed.

Cyclic voltammetry (CV) in Figure SIV.3. showed for both compounds waves corresponding to a chemically non reversible one – electron oxidation/reduction process at with $E_{1/2} = 0.34\text{V}$ and $E_{1/2} = 0.47\text{V}$ vs SCE respectively, which is assigned to the Fe(III)/Fe(II) redox couple of $\mathbf{1}^{(III)} - \text{NHTs/OTf}$ and $\mathbf{2}^{(III)} - \text{NHTs/OTf}$. After reduction, an anodic scan shows a second one – electron reversible process at $E_{1/2} = 0.86\text{V}$ and 0.90 vs SCE for $\mathbf{1}^{(III)} - \text{NHTs/OTf}$ and $\mathbf{2}^{(III)} - \text{NHTs/OTf}$, respectively. This second wave can be assigned to the reversible oxidation of $[\text{Fe}^{II}(\text{MeCN})(\text{MePy}_2\text{tacn})]^{2+}$, $\mathbf{1}^{(II)}$ and $[\text{Fe}^{II}(\text{MeCN})(\text{Me}_2(\text{CHPy}_2)\text{tacn})]^{2+}$ $\mathbf{2}^{(II)}$ (Figure SIV.3), and are formed only after reduction and subsequent solvolysis of $\mathbf{1}^{(III)} - \text{NHTs/OTf}$ and $\mathbf{2}^{(III)} - \text{NHTs/OTf}$ species, respectively. The anionic character of the tosylimido moiety is presumably the most important reason for the substantial cathodic shift of $\mathbf{1}^{(III)} - \text{NHTs/OTf}$ and $\mathbf{2}^{(III)} - \text{NHTs/OTf}$ with respect to $\mathbf{1}^{(II)}$ and $\mathbf{2}^{(II)}$ that contain the neutral π – acceptor acetonitrile bound molecule. UV – vis spectrometry in MeCN of $\mathbf{1}^{(III)} - \text{NHTs/OTf}$ and $\mathbf{2}^{(III)} - \text{NHTs/OTf}$ revealed features at 468 ($\epsilon = 2400\text{ M}^{-1}\text{cm}^{-1}$) and 472 nm ($\epsilon = 1750\text{ M}^{-1}\text{cm}^{-1}$) respectively (Figure SIV.4).

IV.2.3. Reactivity of $1^{(IV)}=NTs$ and $2^{(IV)}=NTs$ in formal N – atom transfer reactions

Tosylimido – iron (IV) complexes $1^{(IV)}=NTs$ and $2^{(IV)}=NTs$, were freshly prepared *in situ* in acetonitrile at 20 °C by reaction of the starting Fe(II) complexes with 1.2 equiv of PhINTs), and rapidly (5 – 15 min) reacted with thioanisole substrates. Reaction was ascertained by the bleaching of their characteristic low – energy bands in the visible spectra of the complexes (*vide infra*). 1H – NMR analyses at the end of the reactions show formation of sulfanylidene products with yields of ~0.6 and ~0.5 equiv (Table SIV.3) per mol of $1^{(IV)}=NTs$ and $2^{(IV)}=NTs$, respectively. Alternatively, when excess of PhINTs (*e.g.* 5 eq.) are used to generate the iron (IV) species, $1^{(IV)}=NTs$ and $2^{(IV)}=NTs$ show catalytic behaviour; $1^{(IV)}=NTs$ reacts with MeO^PhSMe and HPhSMe to provide 1.35 and 2.1 eq of the corresponding sulfanylidene product. In analogous conditions, $2^{(IV)}=NTs$ provides 3.5 eq and 2.9 eq of the corresponding sulfanylidene products. Blank experiments under analogous conditions and in the absence of iron generate ≈ 0.1 eq of product. Thus, we conclude that $1^{(IV)}=NTs$ and $2^{(IV)}=NTs$ are competent N atom transfer agents, and that they show catalytic behaviour, despite quite modest.



Scheme IV.2. Iron mediated reaction of thioanisole with PhINTs.

IV.2.3.1. Spectroscopic analysis of the reactions. Analysis of iron species formed after reaction with sulphides

When different *para* substituted thioanisole substrates, X^PhSMe ($X = MeO, Me, H, Cl$), were added to fresh solutions of $1^{(IV)}=NTs$ and $2^{(IV)}=NTs$ at 293 K, a reaction with two phases is really apparent from the time dependent changes observed in the UV – Vis spectra. In a first phase, the characteristic low energy features at 750 and 740 nm of the respective visible spectra rapidly decrease in intensity (*e.g.* 5 – 15 min for MeO^PhSMe). Simultaneously a red shifting was observed of the initial iron (IV) – tosylimido bands at 455 and 456 nm towards 470 and 465 nm, respectively (Figure IV.10). Importantly, upon complete consumption of the initial iron (IV) at the end of this phase, as ascertained by the bleaching of the band at ~700 nm, the spectra that result do not match to that of the corresponding Fe(II) complexes $1^{(II)}$ and $2^{(II)}$, as may have been initially expected from considering that reactions entail a transfer of the tosylimido moiety to the sulphides. At this point, the spectra that results are the same irrespective of the nature of the *para* substituted thioanisole substrate employed, but reaction rates are sensitive to the concentration and nature of the sulphide, reactions being faster as the sulphide is more electron rich, and slower as electron – poorer sulphides were employed. A second and slower phase (hours) follows and entails formation of $1^{(II)}$ and $2^{(II)}$, which show characteristic UV – Vis spectra. This second process is independent of the nature and concentration of the substrate.

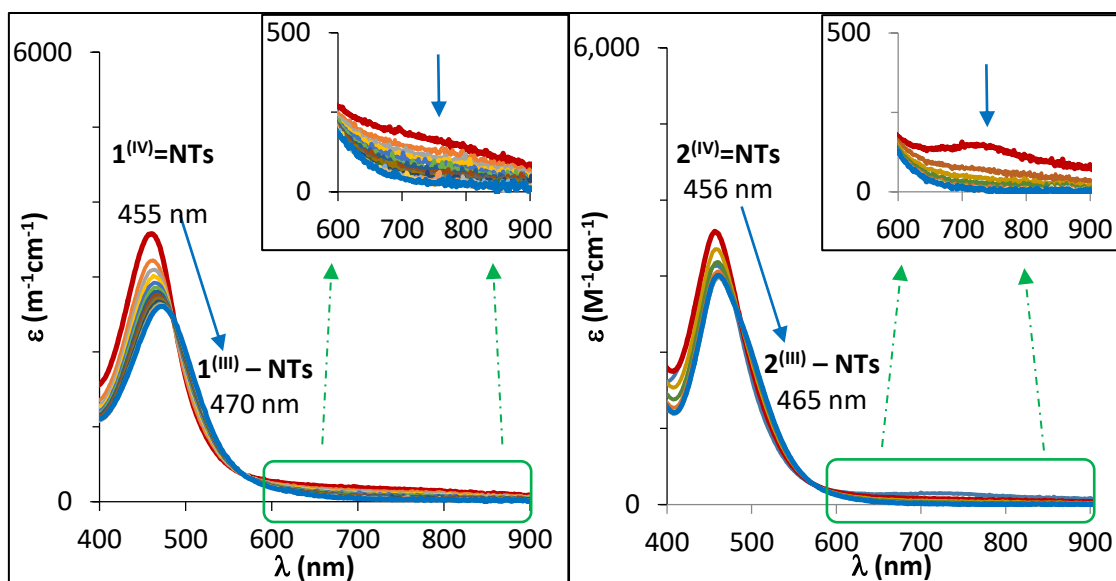


Figure IV.10. UV – vis spectra corresponding to the reaction of $1^{(IV)}=NTs$ and $2^{(IV)}=NTs$ upon addition of an excess of p - $MeOPhSMe$ (reaction at 20 °C with 100 and 50 eq of substrate added respectively, $[Fe] = 0.25$ mM in MeCN). Spectra correspond to the first rapid phase of the reaction.

To identify the new iron species formed in the first phase, the reaction of $1^{(IV)}=NTs$ with $MeOPhSMe$ was monitored by HR – MS (Figure IV.11). To a 0.25 mM solution of $1^{(IV)}=NTs$ was added an excess of $MeOPhSMe$ (100 eq, 25 mM). Peaks corresponding to $1^{(IV)}=NTs$ ($m/z = 275.090$) completely disappeared within 10 – 15 minutes upon $MeOPhSMe$ addition, in agreement with UV – vis spectroscopy, and in the same time course the sulfanylidene product $MeOPhS(NTs)Me$ started to form between 5 and 10 minutes of reaction. Consumption of the initial $[Fe^{IV}(NTs)(MePy_2tacn)]^{+2}$ ($m/z = 275.090$) resulted in the apparition of cluster ions at $m/z = 550.18$ and 275.59 that could be assigned to $[Fe^{III}(NTs)(MePy_2tacn)]^+$ and $[Fe^{III}(NHTs)(MePy_2tacn)]^{+2}$ species. At the same time was observed the generation of ions attributable to iron (II) ($m/z = 190.08$) and iron (II) aggregates with molecules of the sulfanylidene ($MeOPhS(NTs)Me$) product (e.g. $m/z = 352.11$ and 513.64). A tiny peak corresponding to unreacted PhINTs was also observed ($m/z = 373.97$). When the same experiment was performed with $2^{(IV)}=NTs$, the corresponding ions at $m/z = 275.09$ were rapidly consumed after 5 minutes, and sulfanylidene $MeOPhS(NTs)Me$ started to form almost instantaneously after substrate addition. Analogously to $1^{(IV)}=NTs$, the consumption of the initial $[Fe^{IV}(NTs)(MePy_2tacn)]^{+2}$ ($m/z = 275.090$) results in the fast formation of cluster ions at $m/z = 550.18$ and 275.59 that could be assigned to $[Fe^{III}(NTs)(Me_2(CHPy_2)tacn)]^+$ and $[Fe^{III}(NHTs)(Me_2(CHPy_2)tacn)]^{+2}$ species; furthermore an ion peak attributable to aggregates of $[Fe^{III}(NHTs)(MePy_2tacn)]^{+2}$ with two sulfanylidene molecules was also observed ($m/z = 598.66$). Iron (II) generation was also observed ($m/z = 190.58$) as well as aggregates of iron (II) with molecules of the sulfanylidene ($MeOPhS(NTs)Me$) product ($m/z = 352.11$).

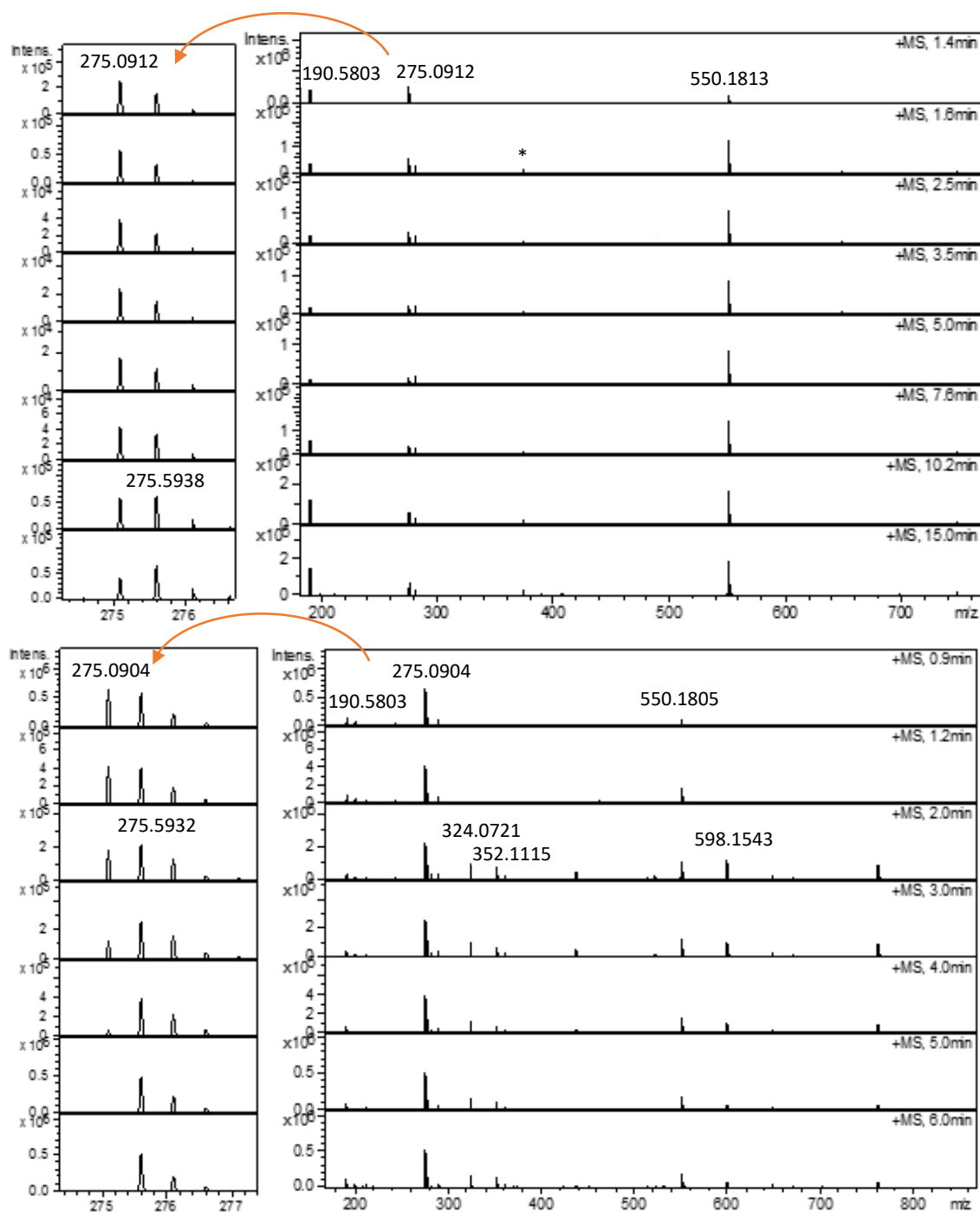


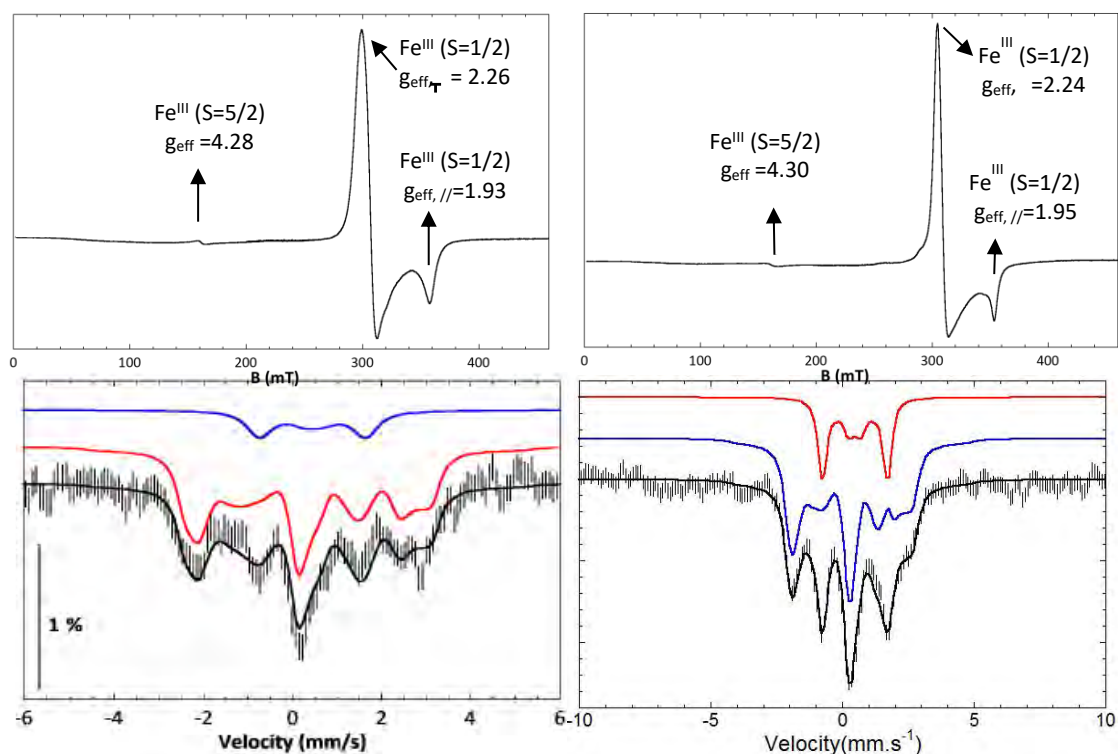
Figure IV.11. HR – MS monitoring of evolution of 0.25 mM solutions of $1^{(IV)}=NTs$ (top) and $2^{(IV)}=NTs$ (below) in MeCN upon addition of 100 and 50 eq of $p\text{-MeOPhSMe}$, respectively. Insets on the left show expanded region for iron (III) – tosylimido/tosylamido species. $m/z = 275.09$ ($[Fe^{IV}(NTs)L]^{2+}$), $m/z = 275.59$ ($[Fe^{III}(NHTs)L]^+$), $m/z = 550.18$ ($[Fe^{III}(NTs)L]^{2+}$). *Traces of unreacted PhINTs.

The reaction of $1^{(IV)}=NTs$ with $MeOPhSMe$ was also followed by means of 1H – NMR spectroscopy (Figure SIV.5), a 12 mM solution of $1^{(IV)}=NTs$ in CD_3CN was prepared and 100 equivalents of $MeOPhSMe$ were added. Within initial 5 minutes the paramagnetically shifted signals of $1^{(IV)}=NTs$ totally disappeared and the sulfanylidene product was formed. After that, within 30 minutes no further evolution was observed on the diamagnetic zone, thus no formation of $1^{(III)}$ was observed. This is in contrast to UV – vis and HR –

MS experiments results, taking into account all the spectroscopic data collected we speculate that the big excess of substrate masks the small amount of iron (II) that is generated. Neither sulfoxide nor sulfone by-products were detected in the reaction crude.

Frozen samples were prepared immediately following the first rapid phase of decay of $\mathbf{1}^{(IV)}=\mathbf{NTs}$ and $\mathbf{2}^{(IV)}=\mathbf{NTs}$ upon reaction with $^{57}\text{Fe}^{0}\text{PhSMe}$ addition, and analysed by Mössbauer and EPR spectroscopy. As shown in Figure IV.12, EPR samples confirmed that the formed species contain mononuclear iron (III) species. EPR of the decay of $\mathbf{1}^{(IV)}=\mathbf{NTs}$ shows a minor high-spin Fe^{III} system ($S = 5/2$) EPR active species, and the major EPR active species is a low-spin Fe^{III} complex ($S = 1/2$) of axial symmetry with $g_{\text{eff},\perp} = 2.26$ and $g_{\text{eff},\parallel} = 1.93$. Similar results were found following the decay of $\mathbf{2}^{(IV)}=\mathbf{NTs}$; the major EPR active species is a low-spin Fe^{III} complex ($S = 1/2$) of axial symmetry with $g_{\text{eff},\perp} = 2.24$ and $g_{\text{eff},\parallel} = 1.95$, and the spectra also show a minor EPR active species corresponding to a high-spin Fe^{III} system ($S = 5/2$). Mössbauer spectroscopy (Figure IV.12) of the same samples revealed the presence of two iron species with a rough relative ratios of $\text{Fe(II)} : \text{Fe(III)}$ of 1:5 for the decay of $\mathbf{1}^{(IV)}=\mathbf{NTs}$ and 1:3 for $\mathbf{2}^{(IV)}=\mathbf{NTs}$, indicating 1.16 and 1.19 e^- were consumed respectively. According to sulfanylidene yields (Table SIV.3) complex $\mathbf{1}^{(IV)}=\mathbf{NTs}$ (57% yield) inverted 1.14 e^- in $^{57}\text{Fe}^{0}\text{PhSMe}$ substrate while for complex $\mathbf{2}^{(IV)}=\mathbf{NTs}$ (48 % yield) 0.96 e^- were incorporated on substrate; for complex $\mathbf{1}^{(IV)}=\mathbf{NTs}$ Mössbauer data and product yield matches perfectly, complex $\mathbf{2}^{(IV)}=\mathbf{NTs}$ shows a small difference, possibly attributable to some decomposition of $\mathbf{2}^{(IV)}=\mathbf{NTs}$. In both cases, the Mössbauer parameters of the major species ($\delta = 0.25$ and $0.25 \text{ mm}^{-1} \text{ s}^{-1}$ and $\Delta E_{\text{Q}} = -1.8$ and $-1.7 \text{ mm}^{-1} \text{ s}^{-1}$) are consistent with a low spin ($S = 1/2$) ferric centre, in good agreement with the EPR analysis.

In conclusion, ferric species formed after reaction of $\mathbf{1}^{(IV)}=\mathbf{NTs}$ and $\mathbf{2}^{(IV)}=\mathbf{NTs}$ with the sulphide can be identified as $\mathbf{1}^{(\text{III})}=\mathbf{NHTs}$ and $\mathbf{2}^{(\text{III})}=\mathbf{NHTs}$, respectively on the basis of the excellent agreement with the EPR and Mössbauer parameters of the independently prepared complexes. On the other hand, the parameters of the minor component reproduce well those of $\mathbf{1}^{(\text{II})}$ and $\mathbf{2}^{(\text{II})}$, respectively. The sum of the spectroscopic data suggests that transfer of the tosylimido moiety to the sulphide does not correspond to a $2e^- \text{ N}$ -transfer where the Fe(IV) centre becomes reduced to Fe(II) , but instead, mainly Fe(III) species are formed as reaction intermediates.



Complex	S	$g_x/g_y/g_z$	δ ($\text{mm}\cdot\text{s}^{-1}$)	ΔE_Q ($\text{mm}\cdot\text{s}^{-1}$)	Γ ($\text{mm}\cdot\text{s}^{-1}$)	η	A_x (T)	A_y (T)	A_z (T)	%
Complex 1^(IV)NTs										
Fe^{III}	1/2	2.26/2.26/1.93	0.25	-1.8	0.38	0.66	-46	2	4	86
Fe^{II}	0		0.45	0.45	0.6	1				14
Complex 2^(IV)NTs										
Fe^{III}	1/2	2.24/2.24/1.95	0.25	-1.7	0.42	0.66	-40.5	-3.8	2.1	73
Fe^{II}	0		0.47	0.55	0.3	0				23

Figure IV.12. Spectroscopic properties of iron(III) – tosylamido compounds resulting from reaction of $1^{(IV)}=NTs$ and $2^{(IV)}=NTs$ with p - $MeOPhSMe$. Mössbauer spectra of $1^{(III)}-NHTs$ (left) and $2^{(III)}-NHTs$ (right) formed after reaction of respective iron (IV) species with $MeOPhSMe$.

IV.2.3.2. Direct preparation of $[Fe^{III}(NHTs)(L)]^{2+}$ by reaction of $Fe^{IV}(NTs)$ with reducing agents

The spectroscopic data of $1^{(III)}-NHTs$ and $2^{(III)}-NHTs$, revealed that the intermediate species formed (470 nm and 465 nm band on the UV – vis) upon addition of XPhSMe to $1^{(IV)}=NTs$ and $2^{(IV)}=NTs$, are not, as expected, iron (II) species but mainly iron (III) species. The analysis by HR – MS of these intermediate species formed from reaction of $1^{(IV)}=NTs$ and $2^{(IV)}=NTs$ with $MeOPhSMe$ confirms our proposal and show a mixture of $[Fe^{III}(NTs)(L)]^+$ ($m/z = 550.18$) and $[Fe^{III}(NHTs)(L)]^+$ ($m/z = 275.59$) ions, being the latter the more intense one.

Further support for the proposal that the initial reaction of $[Fe^{IV}(NTs)(L)]$ species $1^{(IV)}=NTs$ and $2^{(IV)}=NTs$ with thioanisole generates the ferric species $[Fe^{III}(NHTs)(L)]^{2+}$ was gained by preparing species

$\mathbf{1}^{(III)} - \mathbf{NHTs}$ and $\mathbf{1}^{(III)} - \mathbf{NHTs}$ by reaction with ascorbic acid, a reducing agent. Upon reaction of $\mathbf{1}^{(IV)} = \mathbf{NTs}$ with 1 eq of ascorbic acid, the initial iron(IV) bands in the UV – vis spectrum gradually disappeared, evolving to a novel species, with a band centred at 470 nm (Figure IV.13 top). The reduction process exhibit clean isosbestic points and the band obtained was the same to those formed upon reactivity of $\mathbf{1}^{(IV)} = \mathbf{NTs}$ with $^X\text{PhSMe}$ substrates. The titration of the species $\mathbf{1}^{(IV)} = \mathbf{NTs}$ with ascorbic acid also allowed us to determine the purity of $\mathbf{1}^{(IV)} = \mathbf{NTs}$ as 88%, a result which is in high agreement with Mössbauer characterization (87% purity). This process was then followed by the successive reduction to the iron (II) species $\mathbf{1}^{(II)}$, completed after the addition of a 2nd equivalent of the reducing agent. Alternatively, when $\mathbf{1}^{(III)} - \mathbf{NTs}$ was generated upon addition of 100 eq of $p - \text{MeOPhSMe}$ to $\mathbf{1}^{(IV)} = \mathbf{NTs}$, upon addition of one equivalent of ascorbic acid the iron (II) compound $\mathbf{1}^{(II)}$ was recovered.

The same results were observed for compound $\mathbf{2}^{(IV)} = \mathbf{NTs}$ (Figure SIV.6) either employing acetone or MeCN as solvents. The formation of $\mathbf{2}^{(III)} - \mathbf{NHTs}$ was achieved upon titration of $\mathbf{2}^{(IV)} = \mathbf{NTs}$ in MeCN with one equivalent of ascorbic acid, revealing an initial purity of the iron (IV) of ca. 40 % (48 % by Mössbauer spectroscopy); $\mathbf{2}^{(IV)} = \mathbf{NTs}$ was consecutively reduced by addition of a 2nd equivalent of ascorbic acid to fully recover $\mathbf{2}^{(II)}$. Analogously, $\mathbf{2}^{(III)} - \mathbf{NHTs}$ could be generated in acetone following the same procedure (83 % yield of iron (IV) by titration vs. 81 % by Mössbauer). Species $\mathbf{2}^{(III)} - \mathbf{NHTs}$ obtained after reaction of $\mathbf{2}^{(IV)} = \mathbf{NTs}$ with 50 eq. of $p - \text{MeOPhSMe}$ in MeCN was also reduced to $\mathbf{2}^{(II)}$ in quantitative yield, by addition of one equivalent of ascorbic acid.

Moreover, the solution resulting from the reaction of $\mathbf{1}^{(IV)} = \mathbf{NTs}$ with one equivalent of ascorbic acid was analysed by HR – MS. The main iron (III) species was $[\text{Fe}^{III}(\text{NHTs})(\text{MePy}_2\text{tacn})]^+$ ($m/z = 275.59$) while the peak for $[\text{Fe}^{III}(\text{NTs})(\text{MePy}_2\text{tacn})]^+$ was nearly inexistent (Figure SIV.7, top). This contrasts with the HR – MS spectra of the reaction mixture obtained after the reaction of $\mathbf{1}^{(IV)} = \mathbf{NTs}$ with $p - \text{MeOPhSMe}$, which showed the two peaks. Presumably, this may be because the reducing agent used, ascorbic acid, is an electron donor as well a proton donor. Employing alternative single e^- reducing agents (*e.g.* ferrocene or bis(1,3 – dimethylbenzimidazolidin – 2 – ylidene), provide reaction mixtures where the relative intensity of the $[\text{Fe}^{III}(\text{NTs})(\text{MePy}_2\text{tacn})]^+$ ion increase a bit, with respect to that of $[\text{Fe}^{III}(\text{NHTs})(\text{MePy}_2\text{tacn})]^{2+}$, although the later still remains the most intense peak for iron (III) species in the spectra (Figure SIV.7, below). These results suggests that $[\text{Fe}^{III}(\text{NTs})(\text{MePy}_2\text{tacn})]^+$ is highly basic and easily protonates in the reaction media, in agreement with previous studies of iron (III) – imido species.^{157,170,176} Alternatively, decay of $[\text{Fe}^{IV}(\text{NTs})(\text{MePy}_2\text{tacn})]^{2+}$ involves hydrogen atom abstraction from a weak C – H bond forming $[\text{Fe}^{III}(\text{NHTs})(\text{MePy}_2\text{tacn})]^{2+}$. Tests to try to identify the source of hydrogens by deuterating benzylic positions of the ligand, using CD_3CN or reacting $^{\text{CD}_3}\text{OPhSCD}_3$ with $\mathbf{1}^{(IV)} = \mathbf{NTs}$ gave no deuterated $[\text{Fe}^{III}(\text{NHTs})(\text{MePy}_2\text{tacn})]^{2+}$, precluding identification of the hydrogen/deuterium source. Moreover, our attempts to obtain the species $[\text{Fe}^{III}(\text{NTs})(\text{MePy}_2\text{tacn})]^+$ failed, so we conclude that protons most likely originate from adventitious water.

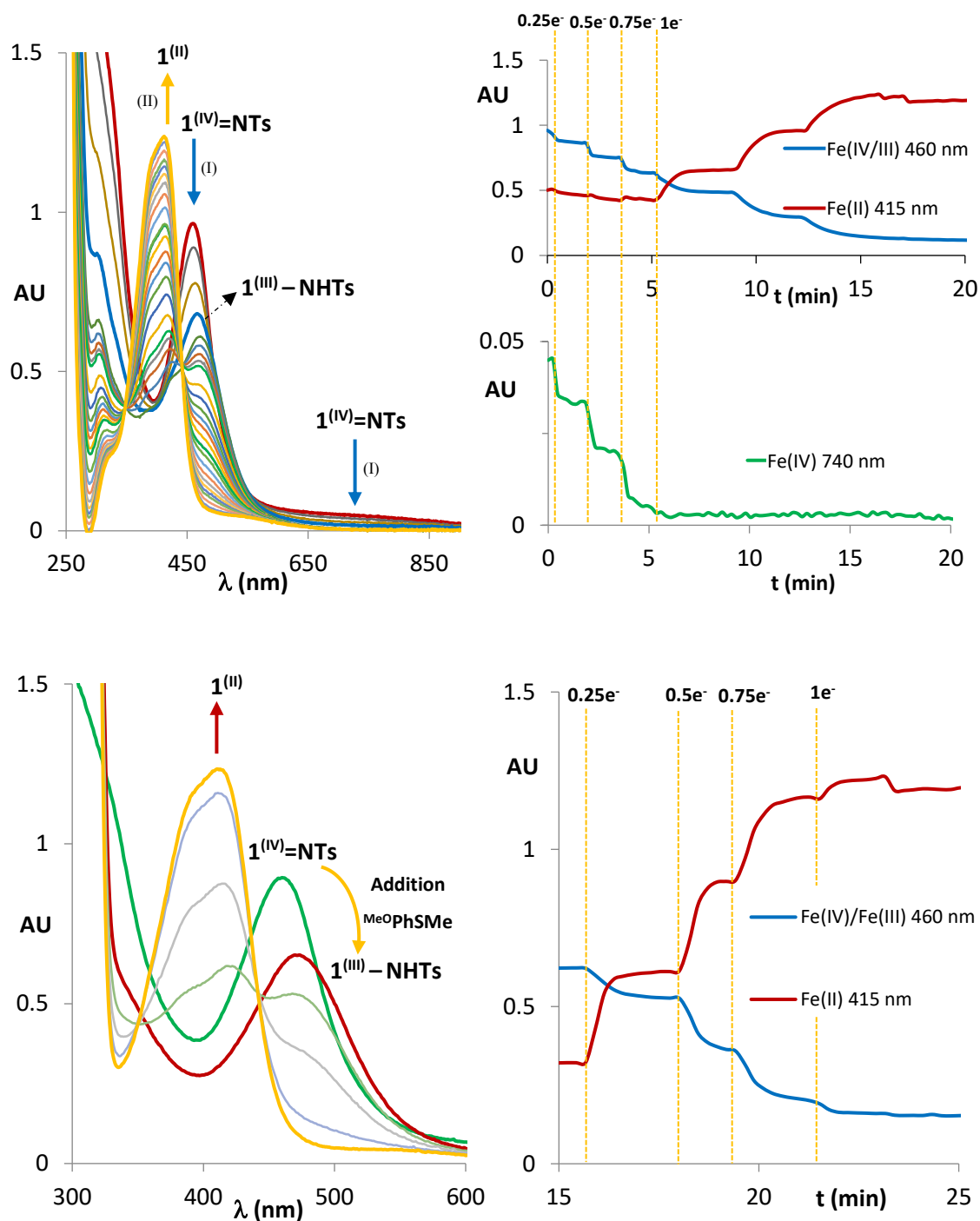


Figure IV.13. (Top) Titration of $1^{(IV)}=NTs$ with ascorbic acid, initial iron (IV) is successively reduced to iron (III), $1^{(III)}-NHTs$, and iron (II), $1^{(II)}$. (Below) Titration of $1^{(III)}-NHTs$ with ascorbic acid after reaction of $1^{(IV)}=NTs$ with $MeOPhSMe$.

IV.2.3.3. Kinetic analysis of the reactions

The kinetics of the reactions with sulphides were explored using freshly prepared solutions of $1^{(IV)}=NTs$ and $2^{(IV)}=NTs$ (0.25 – 4 mM) in acetonitrile. Reactions were monitored by following the evolution over time of the absorbance of the low – energy bands corresponding to the iron (IV) species (Figure IV.14). Data was satisfactorily adjusted to first order decay processes according to equation (1)

$$d[Fe^{IV}]/dt = k_{obs}[Fe^{IV}] \quad (1)$$

The respective pseudo – first order rate constants (k_{obs}) were then calculated from this fitting. Reaction rates were interrogated with respect to substrate and Fe^{IV} concentration.

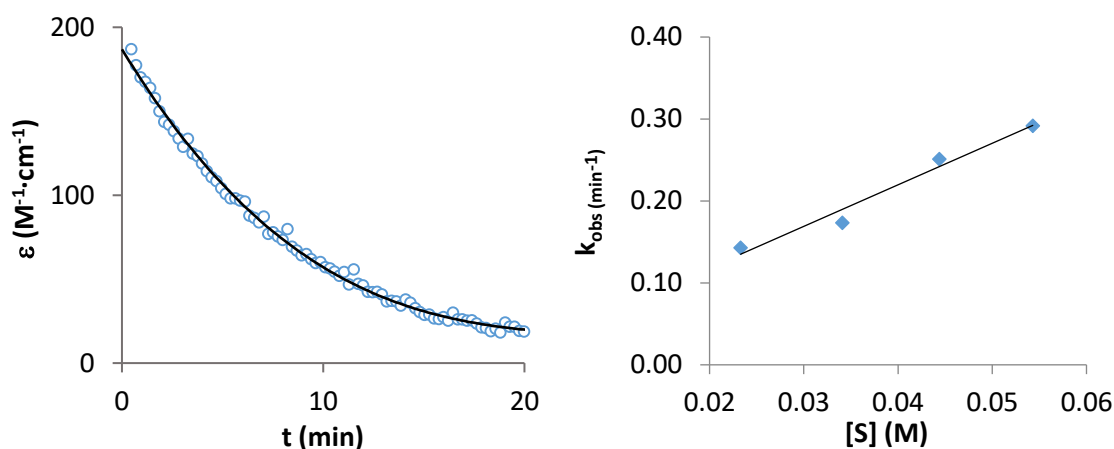


Figure IV.14. (Left) Decay profile of $1^{(IV)}=NTs$ (750 nm feature) upon addition of 100 eq of $MeOPhSMe$. (Right) Rate dependence on substrate concentration.

In the first place, reactions of $1^{(IV)}=NTs$ and $2^{(IV)}=NTs$ (0.25 mM) against different concentrations of thioanisole substrate (30 – 220 mM) were analysed. Observed reaction rates (k_{obs}) were found to be linearly dependent on sulphide concentration indicating that they are pseudo – first order rate constants with the expression $k_{obs} = k_2[\text{sulphide}]$. The respective second order rate constants (k_2) were then calculated from this fitting. The k_2 values for $1^{(IV)}=NTs$ and $2^{(IV)}=NTs$ were determined for *para* substituted thioanisole substrates ($XPhSMe$, X = MeO, Me, H, Cl) and are shown in Table IV.4. A Hammett plot was represented by plotting the k_2 against Hammett parameters (σ_p). The obtained plots (Figure IV.15) show linearity with a slope of $\rho = -3.12$ and $\rho = -3.89$ for $1^{(IV)}=NTs$ and $2^{(IV)}=NTs$ respectively. These are relatively low values compared to those published for OAT reactivity examples with iron (IV) – oxo compounds, which range between $\rho = -1$ – -2 .^{77,78,267,268} Most significantly, these slopes indicate that the electronic properties of the substrate have a very significant influence in the rate – determining step, and suggest that O and N atom transfer reactions occur via fundamentally different mechanisms. Moreover, when k_2 values were plotted against the oxidation potentials of corresponding thioanisole substrates, a linear plot was obtained with slopes of -5.9 and -7.8 for $1^{(IV)}=NTs$ and $2^{(IV)}=NTs$ respectively (Figure SIV.8). For comparison, for OAT with iron (IV) – oxo processes those values range between -2 and -3 . In fact, determined values are somewhat closer to those reported for electron transfer processes.²⁶⁸

An electron transfer process between our iron (IV) complexes and thioanisole substrates ($E^{\circ}_{\text{oxd}} = 1.13 - 1.37 \text{ V}$) seems also possible, taking into account complex $\mathbf{1}^{\text{(IV)}}=\text{NTs}$ and $\mathbf{2}^{\text{(IV)}}=\text{NTs}$ are capable to react with $[\text{Ru}^{\text{II}}(\text{bpy})_3]^{2+}$ ($E_{1/2} = 1.26 \text{ vs SCE}$)²⁷⁹ to generate $\mathbf{1}^{\text{(III)}} - \text{NHTs}$ and $\mathbf{2}^{\text{(III)}} - \text{NHTs}$ (Figure SIV.9 and SIV.10).

Table IV.4. Measured second order rate constants for the reaction of 0.25 mM solutions of $\mathbf{1}^{\text{(IV)}}=\text{NTs}$ and $\mathbf{2}^{\text{(IV)}}=\text{NTs}$ with selected $^x\text{PhSMe}$ at 293 K.

$^x\text{PhSMe}$ \ Complex	$k_2 [\mathbf{1}^{\text{(IV)}}=\text{NTs}]$ (10^{-3}) ($\text{M}^{-1}\cdot\text{s}^{-1}$)	$k_2 [\mathbf{2}^{\text{(IV)}}=\text{NTs}]$ (10^{-3}) ($\text{M}^{-1}\cdot\text{s}^{-1}$)	$^a k_2 [\text{Fe}^{\text{IV}}(\text{NTs})(\text{N4Py})]^{2+}$ (10^{-3}) ($\text{M}^{-1}\cdot\text{s}^{-1}$)
CH₃O	77.4 ± 10.0	207.4 ± 14.0	118
CH₃	20.3 ± 2.7	49.3 ± 1.0	83
H	11.8 ± 2.0	7.9 ± 0.8	50
Cl	1.6 ± 0.3	2.2 ± 0.5	44

^aData from reference 157, 1mM solutions at 273 K.

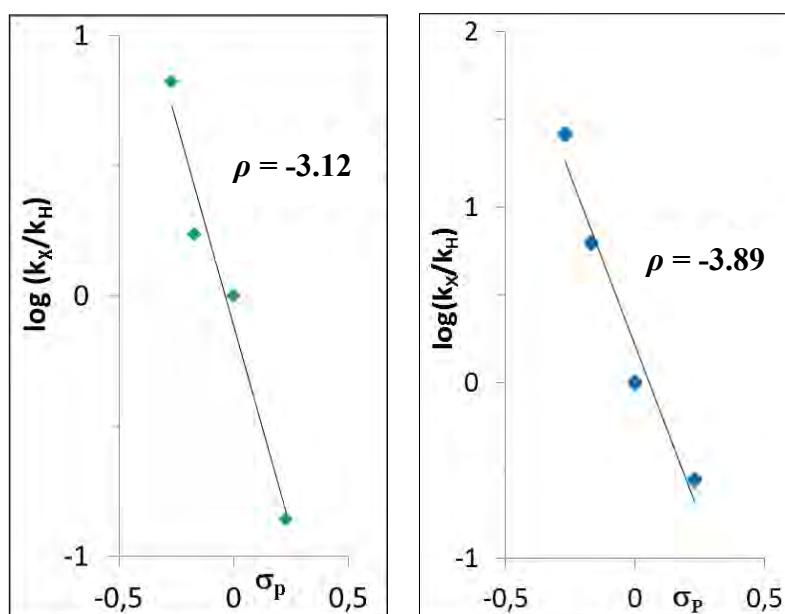


Figure IV.15. Hammett plot representing $\log(k_x/k_H)$ against Hammett parameter (σ_p) for the reaction of $\mathbf{1}^{\text{(IV)}}=\text{NTs}$ (left) and $\mathbf{2}^{\text{(IV)}}=\text{NTs}$ (right) with $p - X - \text{thioanisoles}$ in acetonitrile at 293 K. k_x values correspond to the second order rate constants obtained by measuring k_{obs} values at different $p - X - \text{thioanisole}$ concentrations.

The dependence of observed reactions rates with respect to iron (IV) concentration ($[\mathbf{1}^{\text{(IV)}}=\text{NTs}]$ and $[\mathbf{2}^{\text{(IV)}}=\text{NTs}]$) was then determined. The observed reaction rate (k_{obs}) for the reaction of $\mathbf{1}^{\text{(IV)}}=\text{NTs}$ with MeO^xPhSMe is linearly dependent on $[\mathbf{1}^{\text{(IV)}}=\text{NTs}]$ (0.2 – 2 mM), suggesting a second order dependence on $[\mathbf{1}^{\text{(IV)}}=\text{NTs}]$ (Figure SIV.11). This was supported by a plot of $\log k_{\text{obs}}$ vs $\log[\mathbf{1}^{\text{(IV)}}=\text{NTs}]$ that yielded a linear correlation with a slope of 1.16. The second order in $[\mathbf{1}^{\text{(IV)}}=\text{NTs}]$ translates in a rate law with the expression $d[\mathbf{1}^{\text{(IV)}}=\text{NTs}]/dt = k[\mathbf{1}^{\text{(IV)}}=\text{NTs}]^2[\text{sulphide}]$, which can be converted into expression (1) by considering $k_{\text{obs}} \sim k[\mathbf{1}^{\text{(IV)}}=\text{NTs}][\text{sulphide}]$. This rate law strongly suggests the implication of a second iron (IV) molecule in

the rate – determining step for the reaction of $1^{(IV)}=NTs$ with sulphides. In contrast, k_{obs} values for the reaction of $2^{(IV)}=NTs$ (0.2 – 0.8 mM) against $^{Cl}PhSMe$ are independent of $[2^{(IV)}=NTs]$ (Figure SIV.12), suggesting that the rate determining step involves a bimolecular reaction of $[2^{(IV)}=NTs]$ with the sulphide substrate.

IV.2.4. Extension to the previously described $[Fe^{IV}(NTs)(N4Py)]^{2+}$ system

The exploration of the mechanism of tosylimido transfer determined for $1^{(IV)}=NTs$ and $2^{(IV)}=NTs$ can be extended to the previously described and structurally related compound $[Fe^{IV}(NTs)(N4Py)]^{2+}$ $4^{(IV)}=NTs$. This compound was initially reported in 2006 by Que *et al.* and constitutes the only example of an octahedral non – heme tosylimido – iron (IV) complex.¹⁶⁶ More recently, it has been described that $4^{(IV)}=NTs$ reacts with thioanisole substrate to yield the sulfanylidene product $PhS(NTs)Me$ in 85% and $[Fe^{II}(N4Py)]^{2+}$ ($4^{(II)}$) at 273 K.^{157,167} The reaction was initially considered to be a single $2e^-$ step process where the $-NTs$ moiety is transferred to the sulphide and the $Fe(IV)$ is reduced to $Fe(II)$. Despite, a Hammett analysis of the second – order rate constants obtained from reaction of 1 mM solutions of $4^{(IV)}=NTs$ with different $p - XPhSMe$ at 273 K showed a slope value of $\rho = -3.36$, suggestive of a rate determining SET mechanism. Despite of that, the authors finally concluded from computational studies that the reaction of $4^{(IV)}=NTs$ towards heteroatom transfer reactions entailed a rate determining step dominated by a $(-NTs)^{2-}$ group transfer to the sulphur, instead of proceeding through an electron transfer step.¹⁵⁷

The analysis of the reactivity of $4^{(IV)}=NTs$ against sulphides provides some hints that a similar mechanism to that observed for $1^{(IV)}=NTs$ and $2^{(IV)}=NTs$ may apply. Most significantly, the Hammett parameter previously reported for $4^{(IV)}=NTs$ ($\rho = -3.36$) is in close agreement with the ones we obtained with $1^{(IV)}=NTs$ ($\rho = -3.12$) and $2^{(IV)}=NTs$ ($\rho = -3.89$), strongly pointing up towards a SET rate determining step. This prompted us to reinvestigate the reaction. We observed that $4^{(IV)}=NTs$ shows different behaviours depending on the reaction conditions. As is shown in Figure IV.16, at 293 K, when 100 equivalents of $^{MeO}PhSMe$ respect to the complex are added to a 0.25 mM fresh solution of $4^{(IV)}=NTs$ the corresponding iron (II) species, $4^{(II)}$ is very rapidly formed, reproducing the original observations.¹⁶⁷ In contrast to that, when the amount of $^{MeO}PhSMe$ is reduced to 40 – 10 equiv. monitoring the reaction by UV – vis spectroscopy reveals the formation of a transient species exhibiting a new band at 456 nm, which disappears in the course of few minutes to form $4^{(II)}$. This spectrum formed after the initial rapid reaction between $4^{(IV)}=NTs$ and $^{MeO}PhSMe$ can be reproduced by reacting $4^{(IV)}=NTs$ with one equivalent of ascorbic acid, suggesting that the 456 nm band corresponds to a $Fe(III)$ species $4^{(III)} - NHTs$ (Figure SIV.13, titration of $4^{(IV)}=NTs$ with ascorbic acid (2 eq.) indicates a purity on $4^{(IV)}=NTs$ of 92 %). In agreement with this interpretation, HR – MS spectrum of the reaction mixture prepared by reacting $4^{(IV)}=NTs$ with one equivalent of ascorbic acid shows peaks at $m/z = 296.57$ and 592.13 with similar intensities, which can be assigned to $[Fe^{III}(NHTs)(N4Py)]^{2+}$ and $[Fe^{III}(NTs)(N4Py)]^+$ ions (Figure SIV.13).

Furthermore, we studied the effect of temperature in this reaction (Figure IV.16). At 273K, reaction of $4^{(IV)}=NTs$ with $^{MeO}PhSMe$ (10 equiv.) is substantially slowed down and the iron (III) species $4^{(III)} - NHTs$

was obtained after few minutes. Under these conditions $1^{(III)}-NHTs$ converts to the iron (II) species $4^{(II)}$ slowly, in the course of several hours.

The same reactivity was reproduced when $4^{(IV)}=NTs$ was reacted at a larger concentration (0.5 mM) at 273 K. By adding 40 equivalents of the thioanisole ($^{MeO}PhSMe$) to $4^{(IV)}=NTs$, iron (II) species $4^{(II)}$ was obtained almost instantaneously along with 88% of sulfanylidene product. Instead, using 10 equivalents of substrate leads to the formation of the iron (III) species $4^{(III)}-NHTs$ in less than 2 minutes, which rapidly evolves to $4^{(II)}$; interestingly the yield of sulfanylidene product was only 58% with these conditions, resembling to the behaviour observed with $1^{(IV)}=NTs$ and $2^{(IV)}=NTs$ in the same reactivity.

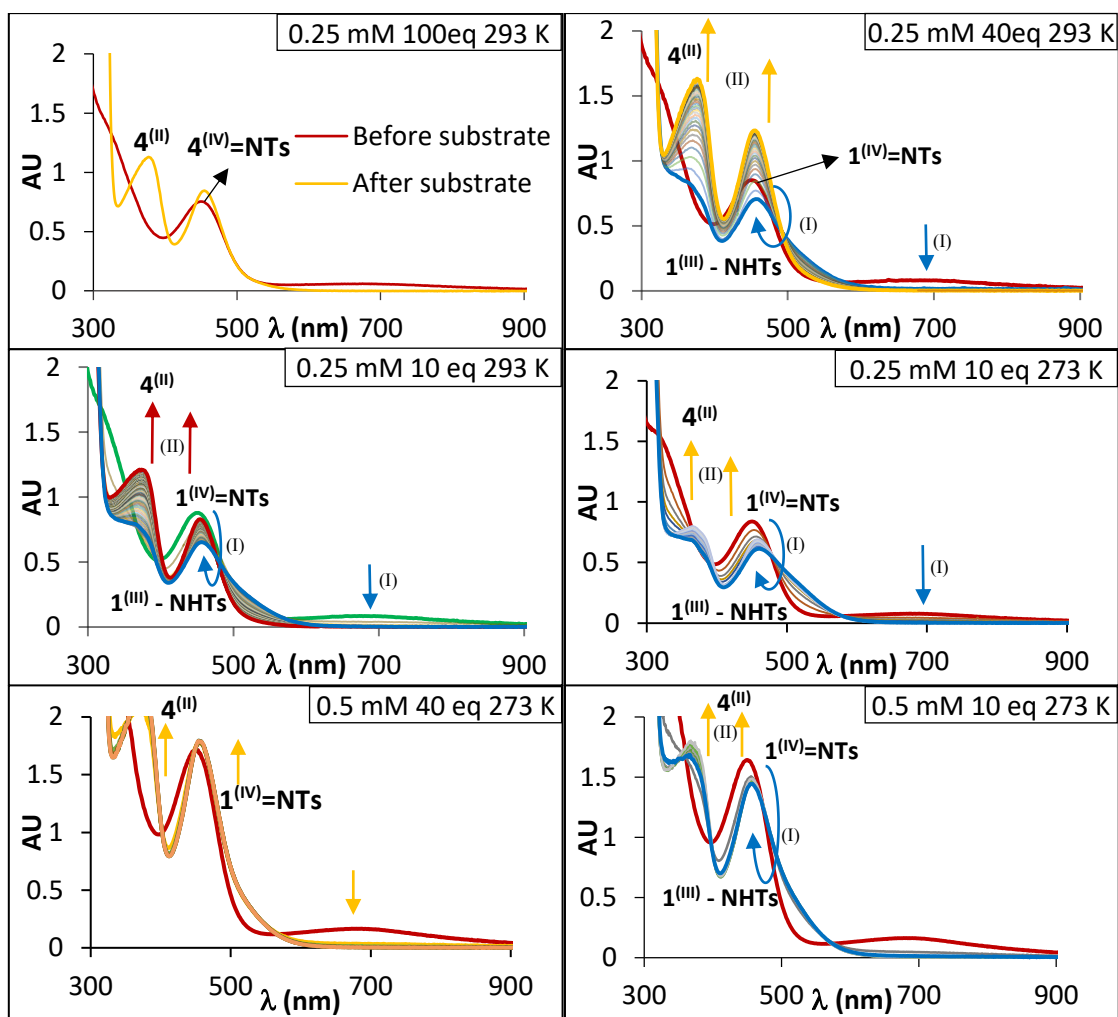


Figure IV.16. UV – vis monitoring for reactivity of $[Fe^{IV}(NTs)N_4Py]^{2+}$ ($4^{(IV)}=NTs$) with $^{MeO}PhSMe$ at different temperature and complex and substrate conditions.

The sum of these experimental observations indicate that $4^{(IV)}=NTs$ follows analogous single electron path to those observed for $1^{(IV)}=NTs$ and $2^{(IV)}=NTs$, entailing formation of short living Fe(III) reaction intermediates, but these paths may be disguised under specific reaction conditions.

IV.2.5. Reaction mechanism

With all data in hand the following mechanism is proposed (Figure IV.17). Reaction of the $\text{Fe}^{\text{IV}}\text{NTs}$ complex with $p-X$ -thioanisole substrate entails a reversible ET from the sulphide to the $\text{Fe}^{\text{IV}}\text{NTs}$ complex to form the corresponding iron (III) – tosylimido species and the sulfur cation radical. This reaction accounts for the large ρ values extracted from the Hammett correlations. The oxidation potential of the $\text{Fe}^{\text{IV}}\text{NTs}/\text{Fe}^{\text{III}}\text{NTs}$ couple could not be determined by CV but we observe that $\mathbf{1}^{(\text{IV})}=\text{NTs}$ and $\mathbf{2}^{(\text{IV})}=\text{NTs}$ react with $[\text{Ru}^{\text{II}}(\text{bpy})_3]^{2+}$ to give the corresponding $[\text{Fe}^{\text{III}}(\text{NHTs})(\text{L})]^{2+}$ species (Figure SIV.9 and SIV.10), setting a lower limit value of 1.26 V vs SCE for this process.²⁷⁹ Considering that the $E_{1/2}$ for the $1e^-$ oxidation of thioanisole substrates range from 1.13 to 1.37 V, it can be concluded that the Fe^{IV} potential is close to those values. When this reaction is rate determining, a bimolecular rate law of the form $d[\text{Fe}^{\text{IV}}\text{NTs}]/dt = k_{\text{obs}}[\text{Fe}^{\text{IV}}\text{NTs}][\text{S}]$ is observed, and this is the case for $\mathbf{2}^{(\text{IV})}=\text{NTs}$ and $\mathbf{4}^{(\text{IV})}=\text{NTs}$. On the other hand, if the reaction reaches equilibrium a different scenario may open leading to a path rate law with a bimolecular dependence on $[\text{Fe}^{\text{IV}}\text{NTs}]$ (*vide infra*). Following the initial ET, the sulphide radical cation can follow two different paths; (a) it can react with the incipient $\text{Fe}^{\text{III}}\text{NTs}$ complex, in a rebound – like manner, producing Fe^{II} and the corresponding sulfanylidene product. This would result in a formal $2e^-$ NTs transfer from the $\text{Fe}^{\text{IV}}\text{NTs}$ complex to the sulphide. (b) Alternatively, the sulphide radical can react with a second $\text{Fe}^{\text{IV}}\text{NTs}$ complex, producing Fe^{III} and the sulfanylidene product. In this process the sulphide will consume two $\text{Fe}^{\text{IV}}\text{NTs}$ units, leaving a $\text{Fe}^{\text{III}}\text{NTs}$ complex and a Fe^{III} complex, which sixth ligand could not be unambiguously elucidated. Branching between the two possible paths is dependent in the relative reactivity of the sulphide cation radical against $\text{Fe}^{\text{III}}\text{NTs}$ vs. $\text{Fe}^{\text{IV}}\text{NTs}$, and on the relative amount of the latter two iron species. Under conditions of large concentration of substrate, $\text{Fe}^{\text{IV}}\text{NTs}$ is very rapidly depleted in favour of $\text{Fe}^{\text{III}}\text{NTs}$ by the initial $1e^-$ reduction by the sulphide substrate. Consequently, reaction with $\text{Fe}^{\text{III}}\text{NTs}$ is dominant and Fe^{II} is obtained. Under conditions of small amount of substrate, the ratio $\text{Fe}^{\text{III}}\text{NTs}/\text{Fe}^{\text{IV}}\text{NTs}$ is small, and reaction of the sulphide cation radical with a second $\text{Fe}(\text{IV})$ moiety dominates. The second step would imply a competition between two different pathways. The first pathway is favoured for $[\text{Fe}^{\text{IV}}(\text{NTs})(\text{N4Py})]^{2+}$, $\mathbf{4}^{(\text{IV})}=\text{NTs}$, and involves the fast transfer of the tosylimido moiety to the radical, recovering the iron (II) metal complex and the corresponding sulfanylidene complex in high yield. As we have proven, in the case of $\mathbf{1}^{(\text{IV})}=\text{NTs}$ and $\mathbf{2}^{(\text{IV})}=\text{NTs}$ the rebounding step is unfavourable, and the radical sulphur is attacked by a second iron (IV) molecule to form iron (III) and sulfanylidene in ca. 50% yield. The second order dependence on $[\mathbf{1}^{(\text{IV})}=\text{NTs}]$ can also be accommodated to this mechanistic scheme by assuming that for this complex, ET reaction from the sulphide to $[\mathbf{1}^{(\text{IV})}=\text{NTs}]$ reaches equilibrium, so in this case reaction of the sulphide cation radical with a second molecule of $[\mathbf{1}^{(\text{IV})}=\text{NTs}]$ is rate determining.

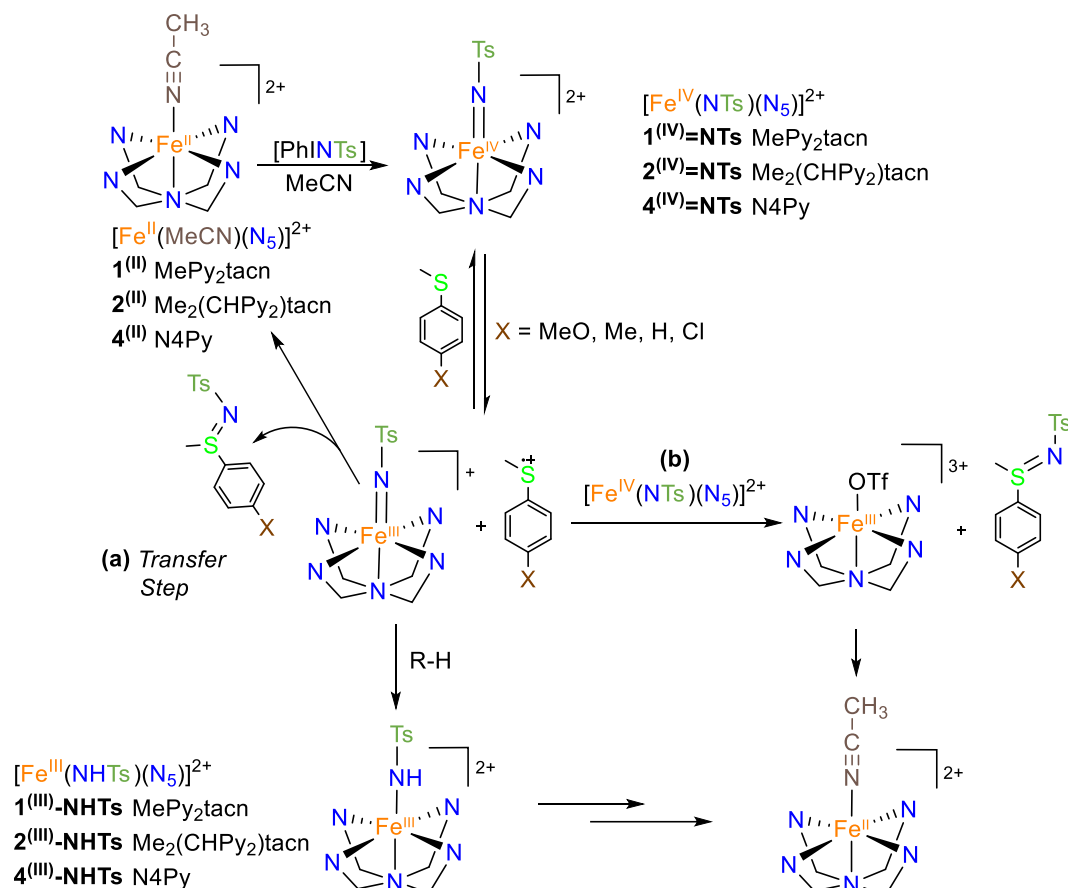


Figure IV.17. Mechanism proposal for the reactions of iron (IV) – tosylimido complexes with thioanisole substrates.

To further investigate the proposed mechanism and the second order on $[\mathbf{1}^{\text{(IV)}}=\text{NTs}]$ we performed the oxidation of ^{MeO}PhSMe at different initial concentrations of complex $\mathbf{1}^{\text{(IV)}}=\text{NTs}$ (0.25 – 2 mM) and at a fixed ^{MeO}PhSMe concentration (24 mM). Under these conditions, ^{MeO}PhSMe substrate was added to freshly prepared solutions of $\mathbf{1}^{\text{(IV)}}=\text{NTs}$, to obtain the species $\mathbf{1}^{\text{(III)}}-\text{NHTs}$, and the analysis of final solutions revealed the formation of different Fe^{III}/Fe^{II} ratios. After complete consumption of $\mathbf{1}^{\text{(IV)}}=\text{NTs}$ the amount of iron (III) formed was analysed by titration with ascorbic acid (*vide infra*). Interestingly, the amount of iron (III) generated was linearly dependent on $[\mathbf{1}^{\text{(IV)}}=\text{NTs}]$, being the more concentrated solution the one that gave higher amount of iron (III).

$[\mathbf{1}^{\text{(IV)}}=\text{NTs}]$ (mM)	^a Fe ^{III}	^b Fe ^{II}
0.24	82	18
0.45	84	16
1.04	92	8
2.08	98	2

^aCalculated from titration with ascorbic acid.

^bCalculated by subtraction from Fe^{III} amount.

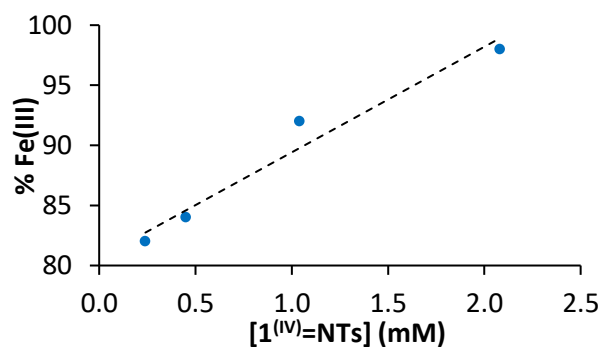


Figure IV.18. Plot of iron (III) formed depending on $[\mathbf{1}^{\text{(IV)}}=\text{NTs}]$.

Furthermore, the amount of sulfanylidene product was analysed at different concentrations of $\mathbf{1}^{(IV)=NTs}$ and variations on sulfanylidene yields were also found. When reaction of $\mathbf{1}^{(IV)=NTs}$ with $p - \text{MeO}PhSMe$ (260 mM) was interrogated at different concentrations of complex (0.4 – 3 mM) the yield of sulfanylidene increased with $[\mathbf{1}^{(IV)=NTs}]$, revealing a linear trend ranging from 23 to 57 % yield under the studied conditions (Figure IV.19). These data together suggest that the iron (II) could be formed in a parallel reaction (possibly decomposition of $\mathbf{1}^{(IV)=NTs}$), competing with the sulfimidation reaction of substrate that generates iron (III). If the iron (II) was obtained from a transfer of the $-NTs$ moiety to the $\text{MeO}PhSMe$ substrate, the yield of sulfanylidene would increase at lower iron concentrations, as one molecule of $\mathbf{1}^{(IV)=NTs}$ would be necessary to form the product (two – electron step), instead of the two molecules of $\mathbf{1}^{(IV)=NTs}$ needed if iron (III) is formed. On the contrary when same procedure was performed with complex $\mathbf{2}^{(IV)=NTs}$, reacting this species (0.5 – 2 mM) with $p - \text{MeO}PhSMe$ (0.14 mM) sulfanylidene yields remained *ca.* 50 % respect to the initial $\mathbf{2}^{(IV)=NTs}$.

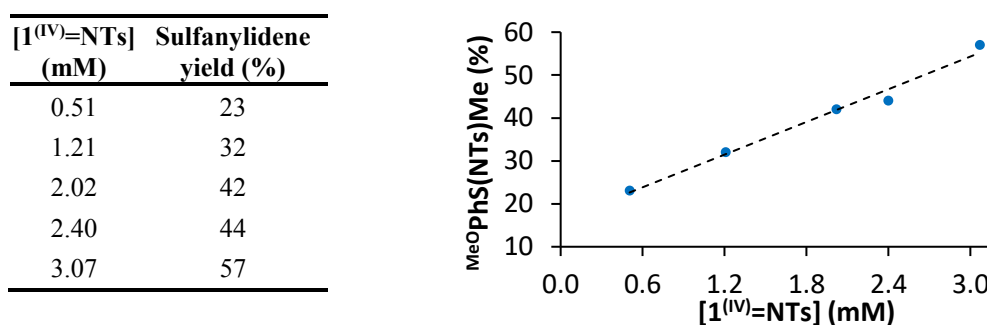


Figure IV.19. Sulfanylidene product ($\text{MeO}PhS(NTs)Me$) vs. $[\mathbf{1}^{(IV)=NTs}]$.

IV.3. SUMMARY

We have synthesised the two novel iron (IV) – tosylimido species $\mathbf{1}^{(IV)=NTs}$ and $\mathbf{2}^{(IV)=NTs}$ bearing structurally related non – heme pentadentate aminopyridine ligands, based on tacn platform. These new species have been fully characterised by means of UV – vis, HR – MS, 1H – NMR, DFT calculations, Mössbauer and X – ray absorption spectra (XANES and EXAFS). These complexes are metastable and decay fast towards iron (II) and iron (III) mixtures. Attempts to obtain crystalline material afforded the corresponding low – spin Fe^{III} – NHTs, $\mathbf{1}^{(III)} – NHTs/OTf$ and $\mathbf{2}^{(III)} – NHTs/OTf$, fully characterised by cyclic voltammetries, UV – vis, HR – MS, EPR and Mössbauer spectroscopy. We have investigated reactivity of $\mathbf{1}^{(IV)=NTs}$ and $\mathbf{2}^{(IV)=NTs}$ towards thioanisole substrates to understand the transfer of the tosylimido moiety to the sulphur atom. A comparative analysis of kinetic parameters has been performed, as well as characterization studies of the reaction products by 1H – NMR. Hammett plot analysis as well as monitoring the reactions of $\mathbf{1}^{(IV)=NTs}$ and $\mathbf{2}^{(IV)=NTs}$ with $^{MeO}PhSMe$ by 1H – NMR, EPR and Mössbauer proved that reactions with sulphides follow a single e^- transfer (SET) process to generate the corresponding Fe^{III} – NHTs species. This behaviour contrasts with that found for iron (IV) – oxo species with same substrates. The corresponding Fe^{III} – NHTs species have been fully characterised by means of UV – vis, HR – MS, EPR and Mössbauer spectroscopy. Reactivity of the previously reported $[Fe^{IV}(NTs)(N4Py)]^{2+}$ ($\mathbf{4}^{(IV)=NTs}$) with thioanisole substrates have been reinvestigated and we have concluded that all three iron (IV) – tosylimido complexes proceed through a common mechanism.

CHAPTER V

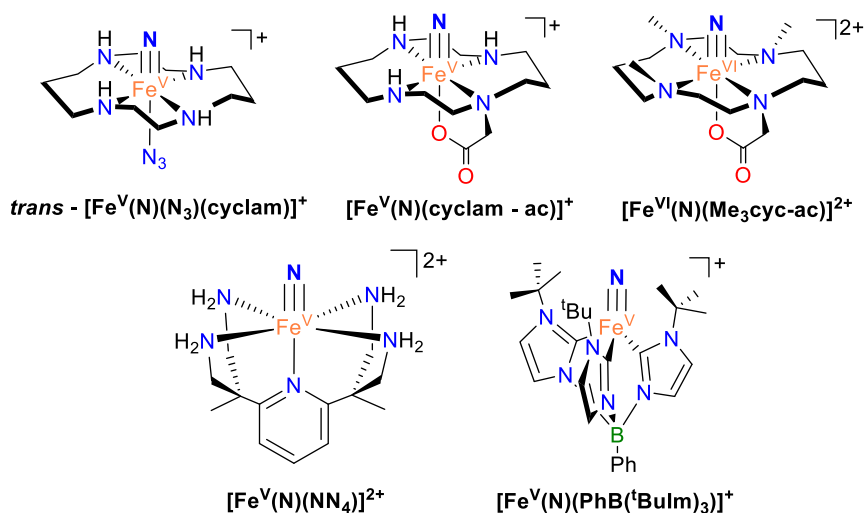
GENERATION, SPECTROSCOPIC AND CHEMICAL CHARACTERIZATION OF OCTAHEDRAL IRON (V) – NITRIDO SPECIES AT A NEUTRAL TACN – BASED PENTADENTATE LIGAND PLATFORM

Part of this chapter was submitted and is currently under revision:

Generation, spectroscopic and chemical characterization of an octahedral iron (V) – nitrido species with a neutral ligand platform. Sabenya, Gerard; Lazaro, Laura; Gamba, Ilaria; Martin – Diaconescu, Vlad; Andris, Erik; Weyhermuller, Thomas; Neese, Frank; Roithova, Jana; Bill, Eckhard; Lloret – Fillol, Julio; Costas, Miquel.

V.1. GENERAL INSIGHT

High – valent iron compounds are very reactive species implicated in a number of reactions of interest in biology, chemical synthesis and technology.^{60,137,292-296} For instance, high – valent iron – oxo species engage in a number of challenging oxidation reactions such as C – H hydroxylation²⁹⁷⁻²⁹⁹ and water oxidation,³⁰⁰⁻³⁰² and high – valent nitride and related species have been considered as possible intermediates in iron mediated dinitrogen – reduction to ammonia.^{303,304} One of the mechanisms proposed for this process is the release of ammonia and the generation of an $\text{Fe}^{\text{IV}}\equiv\text{N}$ intermediate, which takes place at a single iron site on the FeMo cofactor at a nitrogenase enzyme.^{189,305,306} The nitride ligand is regarded as particularly suitable for stabilizing high oxidation states because of its negative charge, and its powerful σ and π donor abilities. Nevertheless, preparation and characterization of high – valent iron – nitride species in a non porphyrinic environment remains a challenge in synthetic inorganic chemistry, and their reactivity is of high interest.^{287,294,307-309} Tetrahedral iron (IV) nitride species can be made relatively stable with the use of bulky ligands and their reactivity has been explored in some detail.^{207,209,213,310-313} Nitride transfer to styrene,³¹³ isocyanides³¹² and triarylphosphines²¹² has been documented. In addition, reaction with cyclohexadienes has been shown to proceed via cycloaddition and hydrogen – abstraction.²¹³ Peters and Smith have independently showed intermolecular reaction between two iron (IV) nitride complexes leading to $\text{Fe}^{\text{I}} - \text{NN} - \text{Fe}^{\text{I}}$ dimeric species.^{207,310} Some of these complexes also reacted with water protons and electrons to afford quantitative amounts of ammonia.²¹⁴



Scheme V.1. Representative examples of non heme iron (V) and iron (VI) nitrido species reported in the literature.^{215,314-317}

On the other hand, high – valent iron (V) and iron (VI) – nitrido species remain rare and are of high interest because the high oxidation state presumes that these species must be extraordinarily reactive. Pioneering examples of the preparation of iron (V) nitrido species in octahedral environments were described by Wieghardt *et al*, via photolysis of the corresponding ferric – azide precursors in a frozen matrix.^{314,315} The same authors also described preparation of iron (VI) nitrido species from photolysis of the iron (IV) – azide complex.³¹⁶ The use of the frozen matrix proved crucial for the successful preparation of these species. Attempts to prepare analogous complexes with anionic triazacyclononane based

pentadentate ligands resulted instead in the generation of ferrous complexes via homolytic cleavage of the Fe – N_{azide} bond.³¹⁸ Most remarkably, The groups of Smith and Meyer have recently described the preparation and structural characterization of an iron (V) nitride species with a sterically encumbered tris – carbene ligand that enforces a distorted tetrahedral geometry.²¹⁵

With the single exception of the later, iron (V) – nitride species can only be prepared in frozen solutions at cryogenic temperatures, and their reactivity remains poorly explored. Most interesting, the Fe^V nitride species described by Smith and Meyer has been shown to react with water to produce ammonia.²¹⁵ N – N coupling has been also documented in the thermal decomposition of [Fe^V(N)(cyclam – ac)]⁺ and *trans* – [Fe^V(N₃)(N)(cyclam)]⁺.^{201,310} Formation of the later by N₂ extrusion from the ferric azide precursor, and its reaction with triphenylphosphine has been monitored by real time FT – IR.²⁰² Gas phase has also been proven a convenient tool to generate and study the chemistry of such reactive species,^{203,317} although ligand degradation appears to be a competing or even a dominating path in some of the previous studies.²⁰³

Overall, these precedents evidence that examples of high – valent iron – nitride species remain scarce. Their high reactivity makes them very interesting but at the same time hampers their preparation and the study of their reactivity. With these considerations in mind, we targeted the synthesis, and characterization of novel octahedral iron (V) – nitride species, and the investigation of their reactivity.

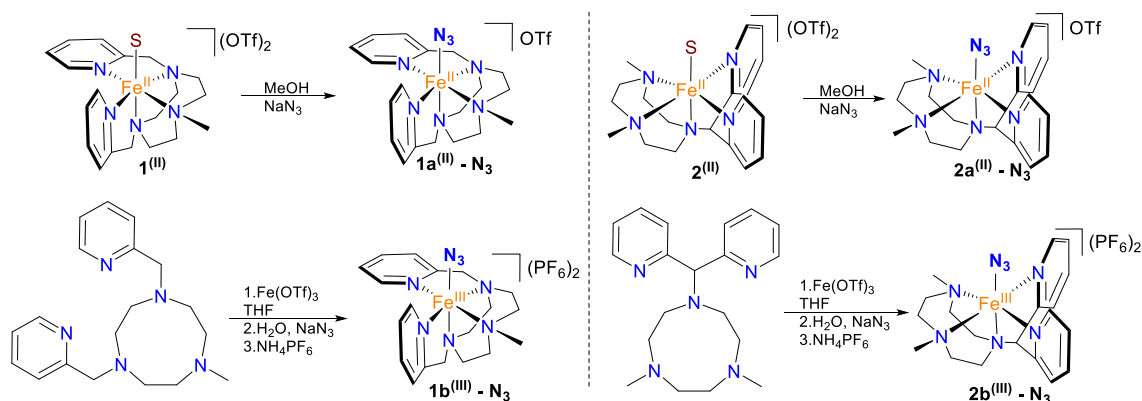
In this work we describe the generation and spectroscopic and chemical characterization of a Fe^V(N) species. Towards this end, we describe the synthesis of two new iron (II) – azide complexes [Fe^{II}(N₃)(MePy₂tacn)]OTf (**1a**^{II} – N₃, MePy₂tacn = N – methyl – N, N – bis(2– picolyl) – 1, 4, 7 – triazacyclononane), and [Fe^{II}(N₃)(Me₂(CHPy₂)tacn)]OTf (**2a**^{II} – N₃, Me₂(CHPy₂)tacn = 1 – (di(2 – pyridyl)methyl) – 4,7 – dimethyl – 1, 4, 7 – triazacyclononane), and two iron (III) – azide [Fe^{III}(N₃)(MePy₂tacn)](PF₆)₂ (**1b**^{III} – N₃) and [Fe^{III}(N₃)(Me₂(CHPy₂)tacn)](PF₆)₂ (**2b**^{III} – N₃), shown in Scheme V.2. The complexes have been characterized by means of ¹H – RMN, FT – IR, MS, UV – vis, Mössbauer spectroscopy, Raman Resonance and EPR. Solid state structure of **1a**^{II} – N₃, **2b**^{III} – N₃ and **1b**^{III} – N₃ have been determined by X – ray diffraction analysis.

Photolysis of iron – azide complexes **1a**^{II} – N₃, **2a**^{II} – N₃, **1b**^{III} – N₃, and **2b**^{III} – N₃ has been studied with the aim to generate the corresponding high – valent species [Feⁿ⁺²(N)(MePy₂tacn)]⁽ⁿ⁻¹⁾⁺ and [Feⁿ⁺²(N)(Me₂(CHPy₂)tacn)]⁽ⁿ⁻¹⁾⁺. Iron (II) – azido compounds could not be photolytically converted into the corresponding iron (IV) derivatives; instead we found that **1b**^{III} – N₃ constitutes a suitable platform to photolytically yield the corresponding high – valent iron (V) species [Fe^V(N)(MePy₂tacn)]²⁺ (**1**^V≡N) which has been spectroscopically characterized by a combination of spectroscopic methods (Mössbauer spectroscopy, magnetic susceptibility, EPR, and X – ray absorption spectroscopy (XANES and EXAFS)) and DFT computational analysis. **1**^V≡N is only stable at very low temperatures in frozen solution. Octahedral Fe^V species with a neutral ligand framework have been only generated previously in the gas phase ([Fe^V(N)(NN₄)]²⁺), and proved to be highly reactive, rapidly reacting with external molecules and also with the ligand.^{203,204} Moreover **1**^V≡N constitutes the first octahedral example of such species, containing a neutral ligand framework, to be spectroscopically characterized.

V.2. RESULTS AND DISCUSSION

V.2.1 Synthesis and characterization of $[\text{Fe}^{\text{II}}(\text{N}_3)(\text{MePy}_2\text{tacn})](\text{OTf})$ ($1\text{a}^{\text{II}} - \text{N}_3$) and $[\text{Fe}^{\text{II}}(\text{N}_3)(\text{Me}_2(\text{CHPy}_2)\text{tacn})](\text{OTf})$ ($2\text{a}^{\text{II}} - \text{N}_3$)

Ferrous – azide compounds $[\text{Fe}^{\text{II}}(\text{N}_3)(\text{MePy}_2\text{tacn})](\text{OTf})$ ($1\text{a}^{\text{II}} - \text{N}_3$) and $[\text{Fe}^{\text{II}}(\text{N}_3)(\text{Me}_2(\text{CHPy}_2)\text{tacn})](\text{OTf})$ ($2\text{a}^{\text{II}} - \text{N}_3$) (Scheme V.2) were prepared, under nitrogen atmosphere and protected from light, by stirring overnight the corresponding $[\text{Fe}^{\text{II}}(\text{MeCN})\text{L}](\text{OTf})_2$ L = MePy_2tacn and $\text{Me}_2(\text{CHPy}_2)\text{tacn}$ precursors (1^{II} and 2^{II}) in anhydrous methanol with an excess (10 eq.) of sodium azide. After crystallization, $1\text{a}^{\text{II}} - \text{N}_3$ and $2\text{a}^{\text{II}} - \text{N}_3$ were obtained in 75 % and 78 % yield, and were spectroscopically characterised by means of Mössbauer, ^1H – NMR, FT – IR, UV – vis, Resonance Raman and magnetic susceptibility measurements.



Scheme V.2. Schematic diagram of the preparation of the complexes. S = solvent.

Solid – state structures of the iron (II) – azide complexes $1\text{a}^{\text{II}} - \text{N}_3$ and $2\text{a}^{\text{II}} - \text{N}_3$ were established by X – Ray diffraction analysis. Figure V.1 shows the ORTEP diagrams of the cationic parts of the complexes. Table from Figure V.1 and tables in the annex collect the crystallographic data and selected bond lengths and angles for the crystallographically determined structures. These complexes show iron centres in a distorted octahedral coordination geometry with five coordination sites occupied by the N atoms of the ligand and one azide anion to complete the coordination environment. In complex $1\text{a}^{\text{II}} - \text{N}_3$ one of the pyridine ligands is coplanar with the Fe – N_3 axis, while the second one is perpendicular to this axis. The azide and the pyridine ligands are *trans* to N atoms of the TACN macrocycle. X – ray diffraction analysis of $1\text{a}^{\text{II}} - \text{N}_3$ was collected at 298 K, 200 K and 100 K in order to ascertain structural changes as a response to a change in spin state (*vide infra*). All Fe – N bond lengths show a shortening when lowering the temperature (from $\approx 2.15 - 2.27$ Å at 298 K to $\approx 1.95 - 2.05$ Å at 100 K), suggesting a spin transition; noticeably is the elongation of the N – N bond on the azide moiety upon changing from the high – spin to the low – spin state (from 2.015 to 2.069 Å). The Fe – N(6) – N(7) (azide) angle is also sensitive to spin and oxidation state of the iron centre (Figure V.1). Upon lowering the temperature from 298 to 100K, the Fe – N(6) – N(7) angle in $1\text{a}^{\text{II}} - \text{N}_3$ decreases from 132.6 to 126.9°. Comparing $1\text{a}^{\text{II}} - \text{N}_3$ and $2\text{a}^{\text{II}} - \text{N}_3$ azide bonds Fe – N(6) bond are almost the same in both Fe(II) complexes, in contrast N(6) – N(7) bond on $2\text{a}^{\text{II}} - \text{N}_3$ is much shorter with respect to $1\text{a}^{\text{II}} - \text{N}_3$ at 100K (1.184 Å vs 1.080 Å), effect of the different spin state. In complex $2\text{a}^{\text{II}} - \text{N}_3$ the two pyridine rings are coplanar with the Fe – N_3 vector and almost

perpendicular to each other ($N1 - Fe1 - N2$ angle is 81.28°). This symmetrical structure is in agreement with the relative simplicity of its $^1H - NMR$ spectrum.

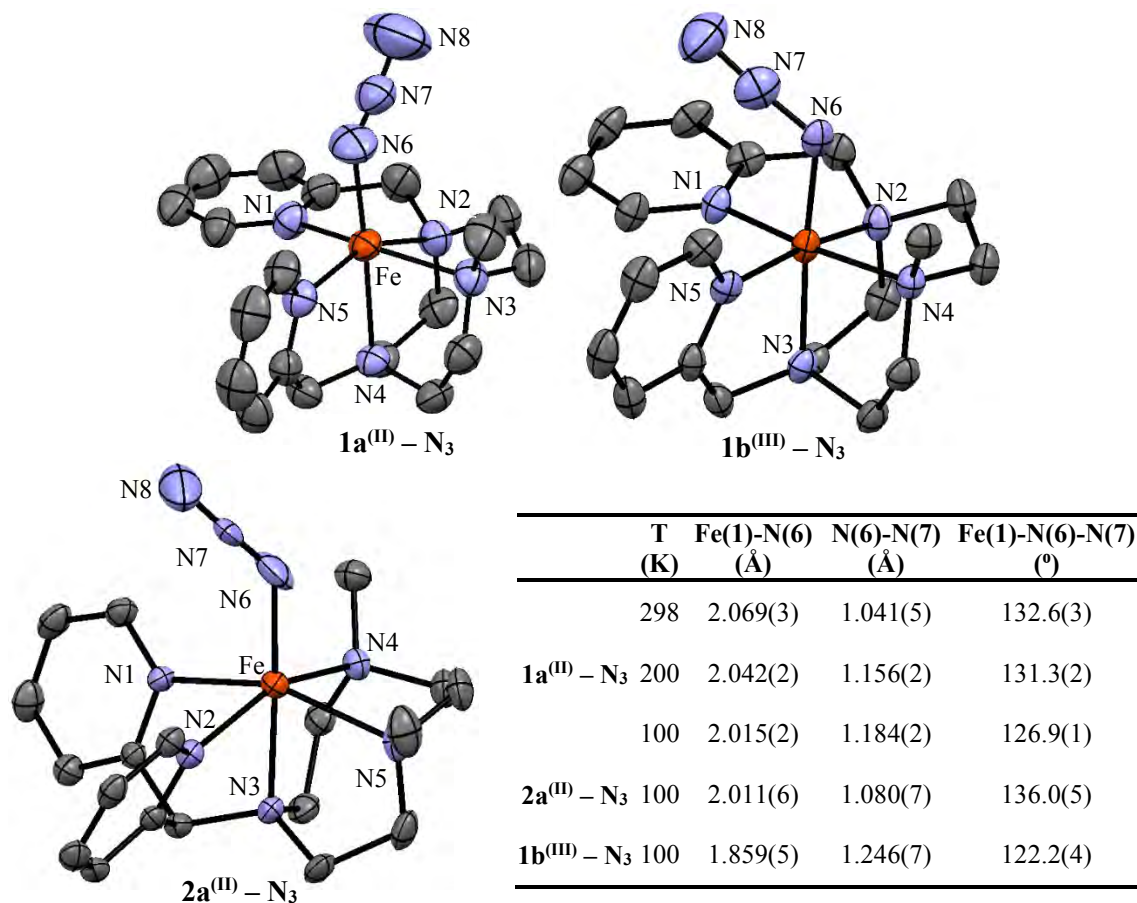


Figure V.1. (Top left) ORTEP representation on 50% of probability of the X-ray diffraction analysis of **1a^(II) - N₃** at 298 K (Top right), **1b^(III) - N₃** (Top right) and **2a^(II) - N₃** (Below left) at 100 K. Protons, hexafluorophosphate (PF_6^-) and trifluoromethanesulfonate ($CF_3SO_3^-$) anions were omitted for clarity. Table shows selected bond distances and angles for these compounds.

Mössbauer spectroscopy was performed using solid ^{57}Fe enriched samples, Figure V.2. The spectrum of **1a^(II) - N₃** recorded at 80K under zero-applied magnetic field, is the superposition of two doublets. The major one constitutes the 94% of the total iron content (isomer shift $\delta = 0.49 \text{ mm}\cdot\text{s}^{-1}$, quadrupole splitting $\Delta E_Q = 0.46 \text{ mm}\cdot\text{s}^{-1}$), consistent with an iron (II) centre in a low-spin ($S = 0$) state. The rest of the sample corresponds to minor iron (II) species in a high spin state ($S = 2$, isomer shift $\delta = 1.04 \text{ mm}\cdot\text{s}^{-1}$ and quadrupole splitting $\Delta E_Q = 3.08 \text{ mm}\cdot\text{s}^{-1}$). When the same sample was analysed at 297 K, only one high-spin iron (II) species was observed with an isomer shift $\delta = 0.88 \text{ mm}\cdot\text{s}^{-1}$ and quadrupole splitting $\Delta E_Q = 2.49 \text{ mm}\cdot\text{s}^{-1}$, evidencing a spin transition behaviour. SQUID measurements support this interpretation; at 80 K a μ_{eff} of *ca.* 1.2 MB was determined, and the effective magnetic moment remains approx. constant from 10 to 100K. This value is consistent with the presence of a diamagnetic low spin Fe(II) centre in an octahedral environment. The small deviation from the theoretical diamagnetic value indicates incomplete spin transition and the presence of small amounts of the high-spin paramagnetic species. Increasing the temperature over 100 K results in an increase of μ_{eff} until approx. 250 K, where the value saturates at ~ 5

MB. At 290 K $\mathbf{1a^{(II)}} - \mathbf{N_3}$ shows a $\mu_{\text{eff}} = 5.0 \mu\text{B}$ in agreement with a high – spin $S = 2$ Fe(II) complex. For species $\mathbf{2a^{(II)}} - \mathbf{N_3}$ the Mössbauer spectrum recorded at 80 K under zero – applied magnetic field shows only one doublet, with an isomer shift $\delta = 1.03 \text{ mm} \cdot \text{s}^{-1}$ and a quadrupole splitting $\Delta E_Q = 2.65 \text{ mm} \cdot \text{s}^{-1}$, typical of high – spin iron (II) species. These observations suggest that MePy₂tacn exerts a strongest ligand field than Me₂(CHPy₂)tacn.

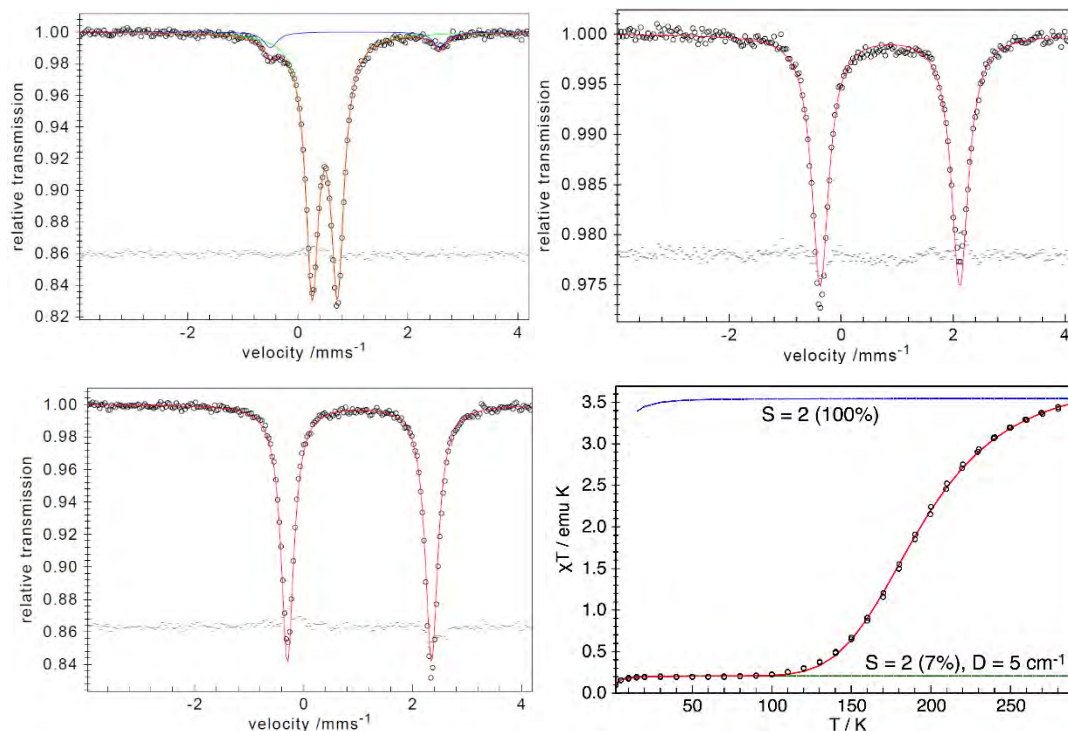


Figure V.2. Zero – field Mössbauer spectra of $\mathbf{1a^{(II)}} - \mathbf{N_3}$ recorded at 80 K (top left) and 297 K (top right). The green and blue lines are Lorentzian doublets accounting for low – spin (LS) and high – spin (HS) components with parameters given in the text; the red line in the top left spectrum is the superposition of the subspectra. The asymmetry of the top right spectrum results from a difference in line widths, not relative intensities, which presumably reflects a slight heterogeneity of iron (II) sites in the powder sample at room temperature. Below left spectrum shows Mössbauer data of $\mathbf{2a^{(II)}} - \mathbf{N_3}$ at 80 K under zero – applied magnetic field. Temperature dependence of the magnetic susceptibility of $\mathbf{1a^{(II)}} - \mathbf{N_3}$ (χT vs. T). Experimental data (open circles) are corrected for underlying diamagnetism. The blue and green line represent spin Hamiltonian simulations for the iron(II) high – spin species (HS) with $S = 2$, $D = 5 \text{ cm}^{-1}$, $g = 2.1$ and with ca. 100% abundance found above 295 K and ca. 7% abundance below 100 K. The red line is a simulation of an incomplete $S = 0$ to $S = 2$ phase transition, obtained with Sorai’s domain model^{319,320} for which the high – spin fraction is given by $x = 0.07 + 1/(1 + \exp[(n\Delta H/R) - (1/T - 1/T_c)])$. There T_c is the transition temperature, $T_c = 194 \text{ K}$, and $n\Delta H$ is an enthalpy term, $n\Delta H = 917 \text{ cm}^{-1}$ for a domain size n , which determines the width of the transition.

The ^1H – NMR spectra of ferrous azide species $\mathbf{1a^{(II)}} - \mathbf{N_3}$ and $\mathbf{2a^{(II)}} - \mathbf{N_3}$ in acetonitrile – D_3 at 0 °C show paramagnetic patterns (Figure SV.1), ranging between 220 and –60 ppm in the case of the $\mathbf{1a^{(II)}} - \mathbf{N_3}$, and from 150 to 0 ppm in the case of the $\mathbf{2a^{(II)}} - \mathbf{N_3}$; consistent with iron (II) centres in a high – spin state. The large spectral window, strongly suggests that the azide ligand remains bound in acetonitrile solution, since the corresponding acetonitrile – bound complexes $\mathbf{1^{(II)}}$ and $\mathbf{2^{(II)}}$ are diamagnetic. Complex $\mathbf{2a^{(II)}} - \mathbf{N_3}$ shows a simpler spectra than $\mathbf{1a^{(II)}} - \mathbf{N_3}$, as expected from its symmetrical structure. Since $\mathbf{1a^{(II)}} - \mathbf{N_3}$ is C_1 symmetric, all protons (except for the $\text{N} - \text{CH}_3$) are non – equivalent, and this translates into a very complex

spectrum. Full assignment of $\mathbf{1a^{(II)}} - \mathbf{N_3}$ and $\mathbf{2a^{(II)}} - \mathbf{N_3}$ could not be made, however, the sharper signals could be assigned to the protons of pyridines, on the basis of their relative integration, and comparison with the patterns described for related complexes described in the literature.

FT – IR spectra of $\mathbf{1a^{(II)}} - \mathbf{N_3}$ and $\mathbf{2a^{(II)}} - \mathbf{N_3}$ show a characteristic single intense peak (Figure SV.3) at 2055 and 2063 cm^{-1} respectively, typical wavenumbers of N – N asymmetric stretching for azides coordinated to iron, and in the expected range for ferrous – azide complexes.^{321,322} In contrast to the infrared spectra, Raman resonance showed no characteristic feature for the azido moiety, only in complex $\mathbf{2a^{(II)}} - \mathbf{N_3}$ was observed a tiny feature around 2000 cm^{-1} (Figure SV.3).

The ESI – MS experiments of the $\text{Fe}^{\text{II}}(\text{N}_3)$ complexes showed the prominent peaks at m/z ratios of 423.1 and 190.5 corresponding to $[\text{Fe}^{\text{II}}(\text{N}_3)(\text{L})]^+$ and $[\text{Fe}^{\text{II}}(\text{L})]^{2+}$ ($\text{L} = \text{MePy}_2\text{tacn}$ or $\text{Me}_2(\text{CHPy}_2)\text{tacn}$), respectively (Figure SV.5) and no peaks that could be attributed to putative $\text{Fe}^{\text{IV}}=\text{N}$ ions could be observed.

Cyclic voltammeteries were performed for complexes $\mathbf{1a^{(II)}} - \mathbf{N_3}$ and $\mathbf{2a^{(II)}} - \mathbf{N_3}$ in acetone and acetonitrile solution at -20°C . Figure SV.6 and SV.7 show the obtained data. In both solvents $\mathbf{1a^{(II)}} - \mathbf{N_3}$ and $\mathbf{2a^{(II)}} - \mathbf{N_3}$ exhibit a reversible wave attributed to the $\text{Fe}^{\text{II}}(\text{N}_3)/\text{Fe}^{\text{III}}(\text{N}_3)$ couple at $E_{1/2} = -0.03$ V and 0.07 V vs Ag/AgNO_3 respectively in acetone ($E_{1/2} = -0.02$ V and $E_{1/2} = 0.06$ V vs Ag/AgNO_3 in acetonitrile). For comparison, the related $[\text{Fe}^{\text{III}}(\text{N}_3)(\text{AcO}_2\text{tacnR})]$ complexes show $\text{Fe}^{\text{II/III}}$ couples at lower $E_{1/2}$ potentials ≈ -0.38 V vs Ag/AgNO_3 , as expected from their negatively charged carboxylate ligands.²⁰⁰ In acetonitrile solution small additional waves at 0.59 and 0.64 V were observed for $\mathbf{1a^{(II)}} - \mathbf{N_3}$ and $\mathbf{2a^{(II)}} - \mathbf{N_3}$, identified as the respective $\text{Fe}^{\text{II/III}}(\text{MeCN})$ couples. Higher potentials were scanned for both complexes to investigate the possibility of reaching the Fe^{IV} oxidation state. Both complexes exhibited an irreversible oxidation wave at 1.5 – 1.6 V which is assigned to the irreversible oxidation of uncoordinated azide, yielding the azide radical which would rapidly decompose with formation of N_2 . Reaching higher potentials produced an unidentified reduction wave around 0.5 – 0.6 V attributed to some decomposition of $\mathbf{1a^{(II)}} - \mathbf{N_3}$ and $\mathbf{2a^{(II)}} - \mathbf{N_3}$. To rule out that high valent iron (IV) species could be generated via an electrochemically slow oxidation, spectroelectrochemical oxidation studies were performed at -20°C . For instance, to a 0.2 mM solution of $\mathbf{1a^{(II)}} - \mathbf{N_3}$ in acetone and 0.2 M of TBAPF_6 was applied a potential of 0.5 V to achieve the oxidation to $\mathbf{1b^{(III)}} - \mathbf{N_3}$. UV – Vis monitoring of the process shows that $\mathbf{1a^{(II)}} - \mathbf{N_3}$ slowly disappeared to generate $\mathbf{1b^{(III)}} - \mathbf{N_3}$, and the spectra showed two isosbestic points, indicative of a clean and quantitative oxidation (Figure SV.9). Upon applying a higher potential (1.7 – 1.8 V) no more changes were observed on the UV – vis, ruling out the formation of Fe^{IV} species.

V.2.2. Synthesis and characterization of $[\text{Fe}^{\text{III}}(\text{N}_3)(\text{MePy}_2\text{tacn})](\text{PF}_6)_2$ ($\mathbf{1b^{(III)}} - \mathbf{N_3}$) and $[\text{Fe}^{\text{III}}(\text{N}_3)(\text{Me}_2(\text{CHPy}_2)\text{tacn})](\text{PF}_6)_2$ ($\mathbf{2b^{(III)}} - \mathbf{N_3}$)

Ferric species $[\text{Fe}^{\text{III}}(\text{N}_3)(\text{MePy}_2\text{tacn})](\text{PF}_6)_2$ ($\mathbf{1b^{(III)}} - \mathbf{N_3}$) and $[\text{Fe}^{\text{III}}(\text{N}_3)(\text{Me}_2(\text{CHPy}_2)\text{tacn})](\text{PF}_6)_2$ ($\mathbf{2b^{(III)}} - \mathbf{N_3}$) were prepared by reacting equimolar amounts of iron (III) triflate and the corresponding ligand in THF under anaerobic conditions. The resulting reddish solutions were evaporated under vacuum, and the resulting solids were dried and solved in water, followed by addition of an excess of NaN_3 . After several hours of stirring, a saturated NaPF_6 or NH_4PF_6 solution was added and stirred for some hours. The resulting

purplish solid that precipitated was filtered and recrystallized in acetone with diethyl ether diffusion. The resulting ferric azide species $[\text{Fe}^{\text{III}}(\text{N}_3)(\text{MePy}_2\text{tacn})](\text{PF}_6)_2$ (**1b**^{III} – N₃) and $[\text{Fe}^{\text{III}}(\text{N}_3)(\text{Me}_2(\text{CHPy}_2)\text{tacn})](\text{PF}_6)_2$ (**2b**^{III} – N₃) were obtained in 56 and 53 % yield and are ¹H – NMR silent. The iron (III) species were characterised by Mössbauer, UV – vis, FT – IR, Raman, EPR, magnetic susceptibility and mass spectrometry. The solid state structure of **1b**^{III} – N₃ could be determined by single crystal X – ray diffraction analysis.

The structure of **1b**^{III} – N₃ is very similar to that of **1a**^{III} – N₃, and only relevant differences will be discussed. As expected, the length of the Fe – N(6) bond is around 0.15 Å shorter on the Fe^{III} complex than in the corresponding ferrous complex $[\text{Fe}^{\text{II}}(\text{N}_3)(\text{MePy}_2\text{tacn})](\text{CF}_3\text{SO}_3)$, (**1a**^{II} – N₃), consequence of the major electronic demand of the metal. Noticeable is also the elongation of the N(6) – N(7) bond of the azide in the Fe^{III} complex in comparison with **1a**^{II} – N₃, consistent with the energy of stretching vibrations observed by FT – IR spectroscopy (vide infra). Such elongation is quite interesting since it may suggest that the bond could be activated towards breakage under photolytic conditions.

Mössbauer spectra of **1b**^{III} – N₃ under zero – applied magnetic field at 80K shows a single doublet with an isomer shift $\delta = 0.21 \text{ mm}\cdot\text{s}^{-1}$ and quadrupole splitting $\Delta E_Q = 2.13 \text{ mm}\cdot\text{s}^{-1}$ characteristic from low spin ($S = \frac{1}{2}$) iron (III) species (Figure V.3 top left). Consistently the EPR spectrum of **1b**^{III} – N₃ in frozen acetone solution at 10 K (Figure V.3 below left) is characteristic of a low spin Fe^{III} complex ($S = 1/2$) with rhombic symmetry with $g_z = 2.57$, $g_y = 2.28$ and $g_x = 1.84$. The effective moment dependence on temperature for **1b**^{III} – N₃ was also studied (Figure SV.10). An effective magnetic moment of 1.5 – 1.8 μB was found from 10 to 300K, consistent with an $S = \frac{1}{2}$ Fe^{III} complex. This is further supported by theoretical calculations of Mössbauer parameters that within error³²³ correlate well with experimental values (Table V.1; $\delta_{\text{error}}: 0.1 \text{ mm/s}$ $\Delta E_{Q\text{error}}: 0.3 \text{ mm/s}$, although quadrupole splitting errors $> 0.5 \text{ mm/s}$ have previously been reported).³²⁴

In contrast, pure samples of compound **2b**^{III} – N₃ could not be prepared, and the iron (III) – azido species **2b**^{III} – N₃ was only present in 50 % purity (Figure V.3 top right). The spectra of a sample of complex **2b**^{III} – N₃ is a mixture of three doublets, one of them with isomer shift $\delta = 0.22 \text{ mm}\cdot\text{s}^{-1}$ and a quadrupole splitting $\Delta E_Q = 1.83 \text{ mm}\cdot\text{s}^{-1}$ assigned to iron (III) species in low – spin. The remaining 50% (21 % and 29 %), belong to two doublets with isomer shift $\delta = 0.51$ and $1.02 \text{ mm}\cdot\text{s}^{-1}$ and quadrupole splitting $\Delta E_Q = 0.71$ and $2.63 \text{ mm}\cdot\text{s}^{-1}$, respectively. These spectral features can be associated to the low – spin $[\text{Fe}^{\text{II}}(\text{MeCN})\text{Me}_2(\text{CHPy}_2)\text{tacn}](\text{PF}_6)_2$ (**2**^{II}) and the high – spin species $[\text{Fe}^{\text{II}}(\text{N}_3)\text{Me}_2(\text{CHPy}_2)\text{tacn}](\text{PF}_6)_2$ (**2a**^{II} – N₃). The first one comes most likely from the decomposition of **2b**^{III} – N₃ through a reductive homolytic cleavage of the ferric – azido moiety, and shows Mössbauer parameters that are in good agreement with those of similar iron (II) complexes.^{85,194} Complex **2b**^{III} – N₃ was also characterised by electron paramagnetic spectroscopy (EPR) showing a spectrum characteristic of a low – spin Fe^{III} complex ($S = 1/2$) with rhombic symmetry with $g_z = 2.46$, $g_y = 2.25$ and $g_x = 1.90$, similar to that of **1b**^{III} – N₃ (Fe^{II} impurities remained silent in the EPR). **2b**^{III} – N₃ shows a μ_{eff} that ranges from 1.6 to 2 μB between 10 and 300 K, remaining in the range for an $S = 1/2$ iron (III) complex.

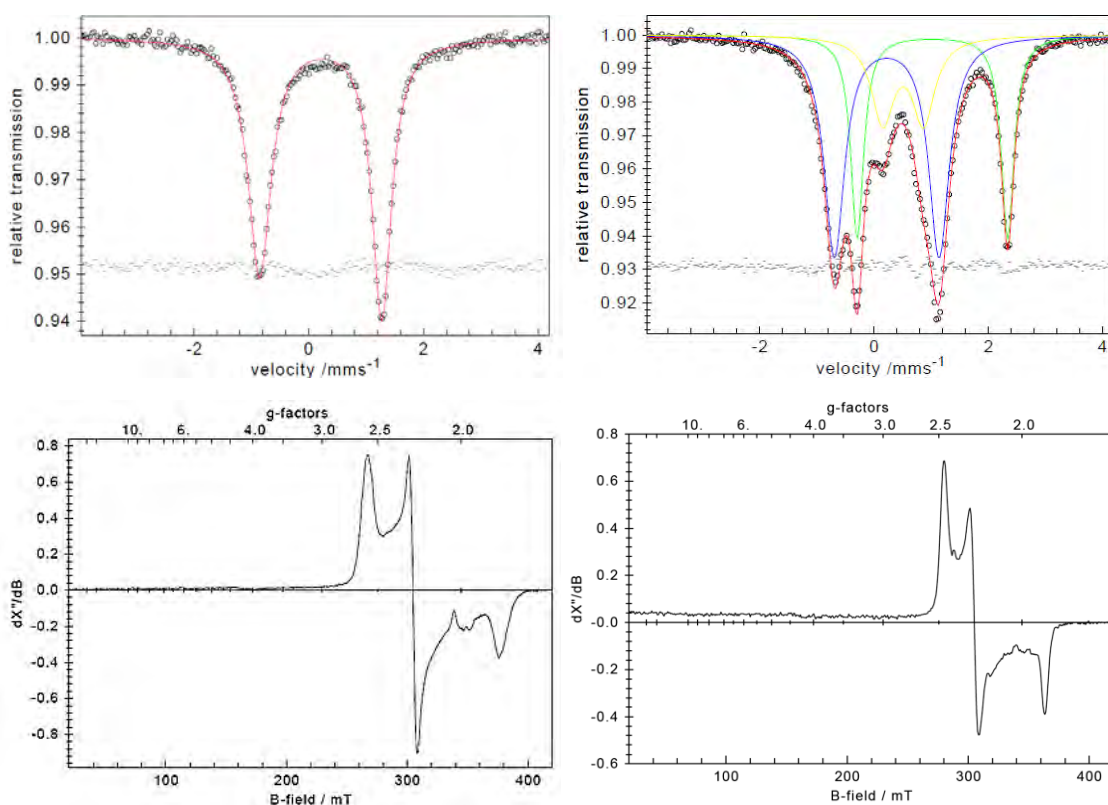


Figure V.3. Zero – field Mössbauer spectra of **1b**^(III) – N₃ (Top left) and **2b**^(III) – N₃ (Top right) at 80 K. Below EPR spectra of **1b**^(III) – N₃ (Below left) and **2b**^(III) – N₃ (Below right) in a frozen acetone solution at 10 K. The Mössbauer spectrum for **2b**^(III) – N₃ was fitted with three Lorentzian doublets accounting for i) Iron (III) LS (**2b**^(III) – N₃, 50%, in blue) and ferrous impurities ii) Iron (II) HS **2a**^(II) – N₃ (29%, in green), and iii) Iron (II) LS [Fe^{II}(MeCN)Me₂(CHPy₂)tacn](PF₆)₂ (21%, in yellow).

The resonance Raman spectrum of complex **1b**^(III) – N₃ exhibits a weak signal at 2026 cm⁻¹, assigned to the asymmetric stretching of the coordinated azide. On the other hand, the FT – IR spectra is very informative (Figure SV.4), a single peak is present at 2019 cm⁻¹, a value which is characteristic of the azide stretching vibration on similar Fe^{III} – N₃ compounds (Table V.1).³²² Moreover, when **1b**^(III) – N₃ was prepared using ¹⁵N terminally labelled sodium azide, its IR spectrum exhibited two features at 2021 and 1998 cm⁻¹ equal in intensity, assigned to the N – N stretching mode. The $\nu(\text{N} - \text{N})$ downshift from 2021 cm⁻¹ to 1998 cm⁻¹ ($\Delta\nu = 23 \text{ cm}^{-1}$) is lower than the expected 33 cm⁻¹ shift for a diatomic N – N oscillator. This indicates the observed features are not only reflecting the stretching from the N – N bond but possibly a contribution of the rest of the azide moiety or the iron centre in the observed vibrations. In the case of **2b**^(III) – N₃ a 2021 cm⁻¹ stretching band was obtained in the FT – IR but no vibration of the azide ligand could be identified on the resonance Raman spectrum. Instead, a 2264 cm⁻¹ vibration signal was observed. This value is characteristic from coordinated nitrile molecules.³²² Resonance Raman is in agreement with Mössbauer analysis, supporting the assignment of an impurity to [Fe^{II}(CH₃CN)(Me₂(CHPy₂)tacn)(OTf)₂ (**2**^(II)).

Comparing the different values of azide N – N stretching, summarized on Table V.1, it can be seen that the energy of the N – N stretching mode is sensitive to the oxidation state of the iron centre. The N – N stretching frequency values (ν) are lower in the Fe^{III} complex, thus reflecting a weaker bond, in agreement with the less electro – donating capacity of the metal centre in comparison to the iron (II).³²¹

Table V.1. Azide stretchings and Mössbauer parameters for the studied (top) and bibliography compounds (below).

Compound	ν (cm^{-1})	Spin State	Fe – N distance (Å)	N – N distance (Å)	δ (DFT) ($\text{mm}\cdot\text{s}^{-1}$)	ΔE_Q (DFT) ($\text{mm}\cdot\text{s}^{-1}$)
NaN ₃	2120	---	---	---	---	---
[Fe ^{II} (N ₃)(MePy ₂ tacn)]OTf (1a ^{II} – N ₃)	2055	0 2	2.015 2.069	1.184 1.042	0.49(0.37) 0.88(0.81)	0.46(-0.54) 2.49(3.02)
[Fe ^{II} (N ₃)(Me ₂ (CHPy ₂)tacn)]OTf (2a ^{II} – N ₃)	2063	2	2.011	1.080	1.03	2.65
[Fe ^{III} (N ₃)(MePy ₂ tacn)](PF ₆) ₂ (1b ^{III} – N ₃)	2019	1/2	1.859	1.246	0.21(0.16)	2.13(-1.94)
^a [Fe ^{III} (N ₃)(Me ₂ (CHPy ₂)tacn)](PF ₆) ₂ (2b ^{III} – N ₃)	2021	1/2	ND	ND	0.22	1.83
[Fe ^{III} (¹⁵ NN ₂)(MePy ₂ tacn)](PF ₆) ₂ (1b ^{III} – ¹⁵ N ₃)	2021 1998	ND	ND	ND	ND	ND
^b [Fe ^{III} (N ₃)(cyclam – ac)](PF ₆)	2051	1/2	1.931	1.209	0.27	2.53
^c <i>cis</i> - [Fe ^{III} (N ₃) ₂ (cyclam)](ClO ₄)	2078 2047	5/2	1.976 1.970	1.194 1.210	0.46	0.29
^c <i>trans</i> - [Fe ^{III} (N ₃) ₂ (cyclam)](ClO ₄)	2044	1/2	1.937	1.180	0.29	2.26
^d [Fe ^{III} (N ₃)(Ac ₂ tacnCH ₂ C ₆ H ₄ OMe)]	2064	5/2	---	---	0.56	0.47
^d [Fe ^{III} (N ₃)(Ac ₂ tacn ⁱ Pr)]	2066	5/2	1.981	---	0.46	0.82
^d [Fe ^{III} (N ₃)(Ac ₂ tacnCH ₂ C ₆ H ₅)]	2066	5/2	1.975	---	0.46	0.61
^c <i>trans</i> - [Fe ^{II} (N ₃) ₂ (cyclam)](ClO ₄)	---	0	---	---	0.55	0.72
^c <i>cis</i> - [Fe ^{II} (N ₃) ₂ (cyclam)](ClO ₄)	---	2	---	---	1.11	2.84

ND: Not determined. ^aComponent from the mixture that was attributed to Fe^{III}(N₃). ^bref 71. ^cref 194. ^dref 200.

Complex **1b**^{III} – N₃ was also analysed by mass spectrometry (Figure V.4 top). The spectrum shows a main peak at $m/z = 211.58$ with an isotopic pattern indicative of a [Fe^{III}(N₃)(MePy₂tacn)]²⁺ ion. Interestingly, the spectra showed two additional peaks at $m/z = 190.58$ and 197.58 that can be assigned to [Fe^{II}(MePy₂tacn)]²⁺ (**1**^{II}) and [Fe^V(N)(MePy₂tacn)]²⁺ (**1**^V≡N) ions, respectively. MS/MS analysis shows that they both proceed from fragmentation of the $m/z = 211.58$ ion, indicating that they originated from the cleavage of Fe – N and N – N bonds of the azide complex, respectively. These observations evidence the possibility to cleave the N – N bond to gain access to high – valent iron species.

High resolution mass spectrometry of complex [Fe^{III}(¹⁵N₃)(MePy₂tacn)](PF₆)₂ (**1b**^{III} – ¹⁵N₃) (Figure V.4 below) confirmed the assignment of the ions observed on **1**^V≡N. The same distribution that was observed on **1b**^{III} – N₃ was found also on **1b**^{III} – ¹⁵N₃, therefore, the formation of [Fe^{II}(MePy₂tacn)]²⁺ and [Fe^V(N)(MePy₂tacn)]²⁺ was observed as well. As the azide anion is labelled in one of the two terminal positions, both the [Fe^V(¹⁴N)(MePy₂tacn)]²⁺ and [Fe^V(¹⁵N)(MePy₂tacn)]²⁺ were observed in a 1:1 ratio for each of these ions ($m/z = 197.58$ and 198.08), which are formed from N – N cleavage on the [Fe^{III}(N₂=¹⁵N)(MePy₂tacn)]²⁺ and [Fe^{III}(¹⁵N=N₂)(MePy₂tacn)]²⁺ respectively.

Analogously, complex **2b**^{III} – N₃ shows a similar spectra with same peaks found in **1b**^{III} – N₃, but as was observed in the Mössbauer and Raman spectroscopy, peaks arising from contamination with species **2**^{II} (Figure SV.12) were also present in important amounts.

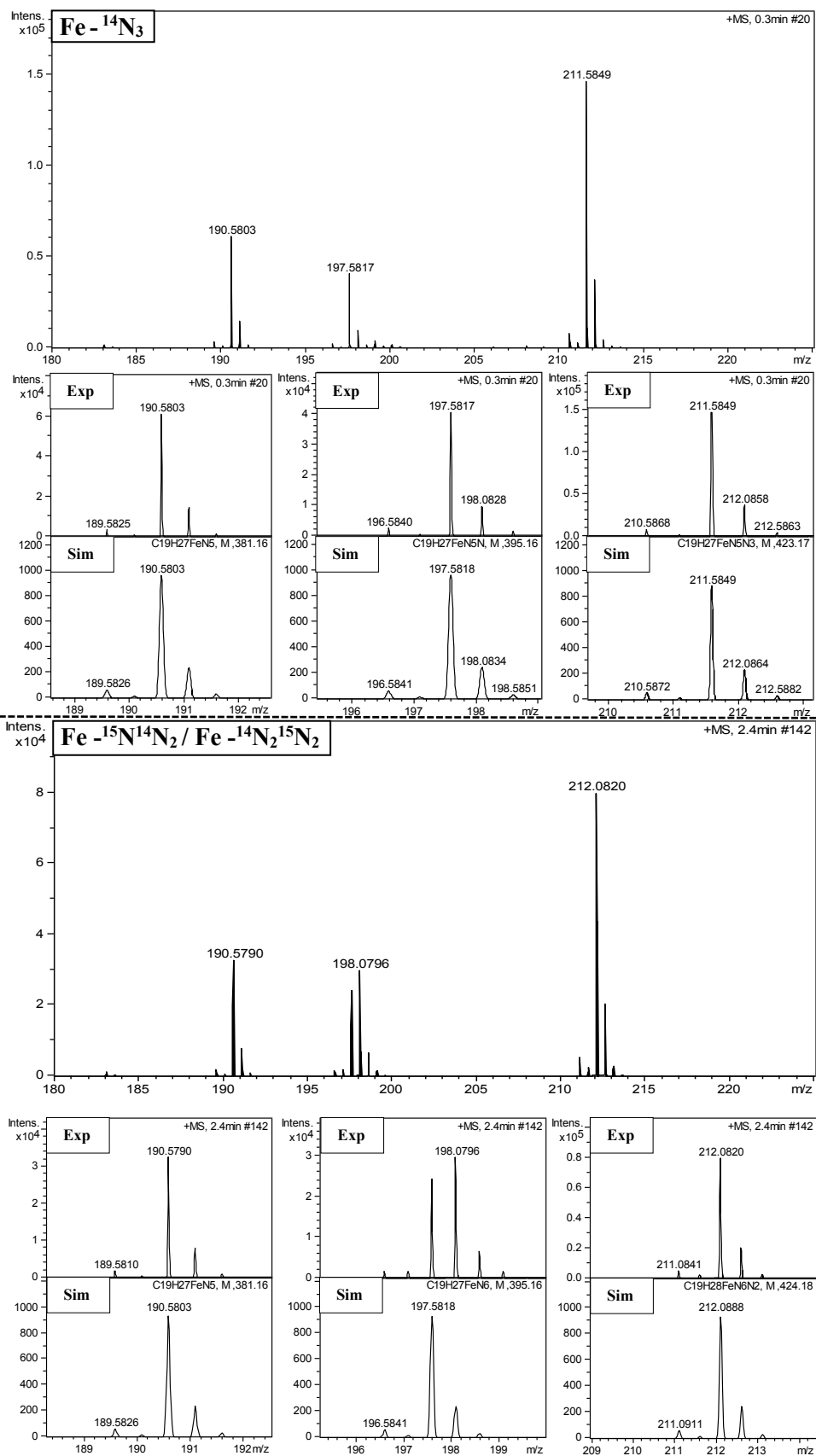
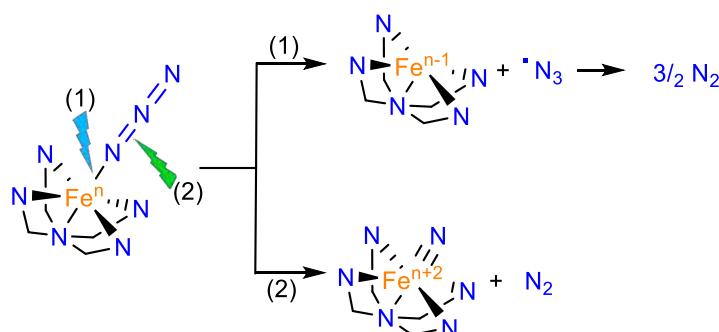


Figure V.4. (Top) High resolution mass spectra of **1b**^(III) – N₃ in acetone, insets are ions for Fe^{II}(L), Fe^{III}(N₃)(L) and Fe^V(N)(L), with simulated peaks. (Below) High resolution mass spectra of **1b**^(III) – ¹⁵N₃ in acetone, below are shown simulated ions of [Fe^{II}(L)]²⁺, [Fe^{III}(^{14/15}N₃)(L)]²⁺ and [Fe^V(N)(L)]²⁺ / [Fe^V(¹⁵N)(L)]²⁺ species. L = MePy₂tacn.

V.2.3. Photolysis of Fe(II) – N₃ species

Considering precedent studies which showed that high – valent nitrido – iron species can be prepared by photolysis of iron (II) – azide precursors,^{209,211,214} we irradiated solutions of the iron (II) – azido complexes **1a**^(II) – N₃ and **2a**^(II) – N₃ in acetone with a 470 nm lamp, to investigate if high – valent iron (IV) – nitrido species could be generated. The irradiation of a metal – azide species may lead to two different scenarios (Scheme V.3): (1) Photoreduction of the metal centre through an homolytic cleavage of the Fe – N bond resulting in one electron reduction of the metal, and generation of an azide radical, which in turn reacts with a second azidyl radical, finally producing N₂ gas; or (2) heterolytic N – N cleavage resulting in a 2 – electron oxidation of the metal centre with concomitant formation of N₂ gas.



Scheme V.3. Photolytic reactivity of iron – azide complexes. (1) Homolytic cleavage of Fe – N and photoreduction of Fe centre; (2) Heterolytic cleavage of N – N and photooxidation of iron centre.

Unfortunately, **1a**^(II) – N₃ and **2a**^(II) – N₃ proved unreactive upon irradiation with a 470 nm (blue) and also with 530 nm (green) LED light, either at -80 °C or at room temperature. Moreover analogous experiments were performed with frozen samples of both complexes using blue and green LED lamps and photolysing with a Rayonet Photochemical Reactor (RPR – 100) equipped with 350 or 253 nm tubes. Mössbauer analysis revealed that none of those experiments evolved to any feature attributable to high – valent iron species (See SI, Figure SV.13).

V.2.4. Photolysis of Fe(III) – N₃ species

V.2.4.1. Photolysis in solution

When solutions of **1b**^(III) – N₃ and **2b**^(III) – N₃ in acetonitrile were photolysed at 233 K with blue or green LED lamps (470 or 530 nm) during few minutes (15 – 20 min), formation of **1**^(III) and **2**^(III) occur, as revealed by UV – Vis spectroscopy. Monitoring of the reactions by UV – Vis spectroscopy revealed that the process occurs with isobestic points, thus reflecting a clean photoreduction (see example of **1b**^(III) – N₃ on Figure SV.14) without significant accumulation of other species. Such behaviour has been reported also for analogous iron (III) complexes with cyclam ligands^{71,194} and led us to think that formation of the iron (V) compounds may require a frozen matrix, presumably to prevent fast decomposition of the highly reactive species.

V.2.4.2. Photolysis of solid powder samples

Solid samples of $\mathbf{1b}^{(III)} - \text{N}_3$ were suspended in a liquid nitrogen bath (77 K) and under stirring were photolysed using a 470 nm LED lamp. After 4.5 h of illumination the initial purple color had turned to brown – orange, and aliquots of the product were analyzed by complementary Mössbauer, EPR and SQUID measurements. The zero – field Mössbauer spectrum depicted in Figure V.5 left, revealed total consumption of the initial iron(III) – azide complex $\mathbf{1b}^{(III)} - \text{N}_3$ (compare with Figure V.3 left), and generation of two new species attributable to 26 % of low – spin iron (II) ($\delta = 0.38 \text{ mm} \cdot \text{s}^{-1}$, $\Delta E_Q = 0.67 \text{ mm} \cdot \text{s}^{-1}$) and 74 % of a new component ($\mathbf{1}^{(V)}\equiv\text{N}$). This latter subspectrum is broad and asymmetric, as expected for half – integer spin with intermediate spin relaxation, but an approximate fit with an asymmetric quadrupole doublet revealed a remarkably low isomer shift of approximately $\delta = -0.01 \text{ mm} \cdot \text{s}^{-1}$ and moderately large quadrupole splitting of *ca.* $\Delta E_Q = 1.02 \text{ mm} \cdot \text{s}^{-1}$. By comparison with the iron (V) complexes $[\text{Fe}^{\text{V}}(\text{N})(\text{N}_3)(\text{cyclam})]^+$ and $[\text{Fe}^{\text{V}}(\text{N})(\text{cyclam} - \text{ac})]^+$ ($\delta = -0.04$ and $-0.01 \text{ mm} \cdot \text{s}^{-1}$, $\Delta E_Q = 1.90$ and $1.58 \text{ mm} \cdot \text{s}^{-1}$, respectively),^{201,314,315} this major subspectrum of the photolyzed sample can be assigned, in particular due to its low isomer shift, to a high – valent nitrido iron (V) complex ($\mathbf{1}^{(V)}\equiv\text{N}$) with spin $S = 1/2$.

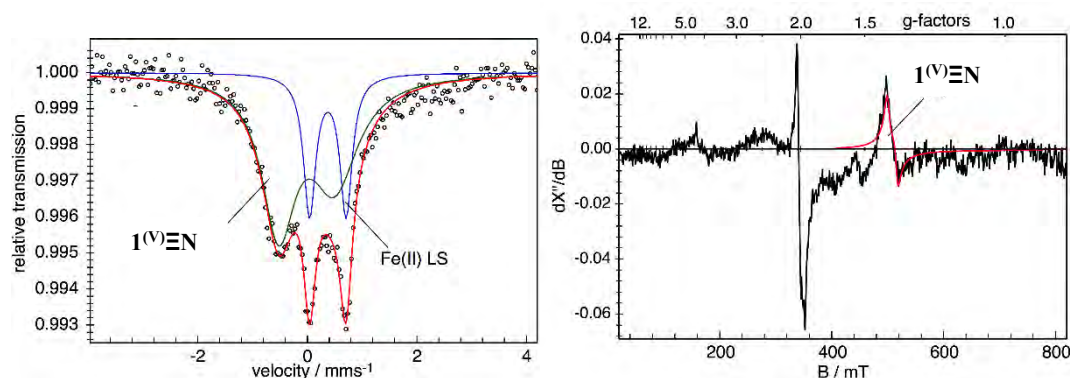


Figure V.5. (Left) Zero – field Mössbauer spectrum of solid complex $\mathbf{1b}^{(III)} - \text{N}_3$ after 4.5 h photolysis at 77 K with a 470 nm (blue) LED, and (Right) EPR spectrum recorded at 10 K ($T = 10 \text{ K}$, frequency 9.6459 GHz, power 0.2 mW, modulation 0.75 mT / 100 kHz). The EPR derivative amplitudes are given in arbitrary units, consistent with those of Figure V.3. The green and blue lines in left spectrum are Lorentzian doublets accounting for a new low – spin iron (II) species (Fe(II) LS) and the high – valent photo – product ($\mathbf{1}^{(V)}\equiv\text{N}$); the red is the superposition of the subspectra. The extended asymmetry of the subspectrum from ($\mathbf{1}^{(V)}\equiv\text{N}$) presumably results from intermediate spin relaxation. The red line in EPR spectrum is a simulation with $g_1 = 1.38$ and $g_2 = 1.33$, $g_3 = 1$ (fixed) and Lorentzian line of the widths $= 56 \cdot 10^{-4} \text{ cm}^{-1}$ for the g_{\perp} directions, and fixed $1000 \cdot 10^{-4} \text{ cm}^{-1}$ for g_{\parallel} , respectively.

EPR spectra of photolysed samples of $\mathbf{1b}^{(III)} - \text{N}_3$ in frozen acetone (Figure V.5, right), confirmed that no iron (III) remains in the sample. Moreover the spectra shows a sharp signal with isotropic symmetry at $g = 2.0$, assigned to the azide radical generated from homolytic photodecomposition of the $\text{Fe}^{\text{III}} - \text{N}_3$ unit. In addition, a broad signal at $g \approx 1.35$ was observed. Additional EPR studies were performed by irradiating with 530 nm light a solid sample of $\mathbf{1b}^{(III)} - \text{N}_3$ inside a sealed EPR tube and under vacuum. Following this procedure the broad signal at $g \approx 1.35$ appears better defined, so we can tentatively attribute it to the new species $\mathbf{1}^{(V)}\equiv\text{N}$, although $\mathbf{1b}^{(III)} - \text{N}_3$ was not completely consumed in these conditions due to the inhomogeneity of the sample (Figure V.6 right). To the best of our knowledge, EPR data from iron (V)

species exists only for the pseudo tetrahedral $[\text{Fe}^{\text{V}}(\text{N})(^t\text{BuIm}_3\text{BPh})]^+$ ($S = 1/2$, $g_{\perp} = 1.971$, $g_{\parallel} = 2.299$).²¹⁵ And more recently Krahe and coworkers reported the EPR spectra for $[\text{Fe}^{\text{V}}(\text{N})(\text{cyclam} - \text{ac})]^+$ ($g_1 = 1.036$, $g_2 = 1.629$ and $g_3 = 1.746$) and $[\text{Fe}^{\text{V}}(\text{N})(\text{N}_3)(\text{cyclam})]^+$ ($g_1 = 0.985$, $g_2 = 1.626$ and $g_3 = 1.748$).³²⁵ The broad signal obtained by irradiation of $\mathbf{1}^{\text{(V)}\equiv\text{N}}$ ($g \approx 1.35$) falls within the observed range of cyclam species.

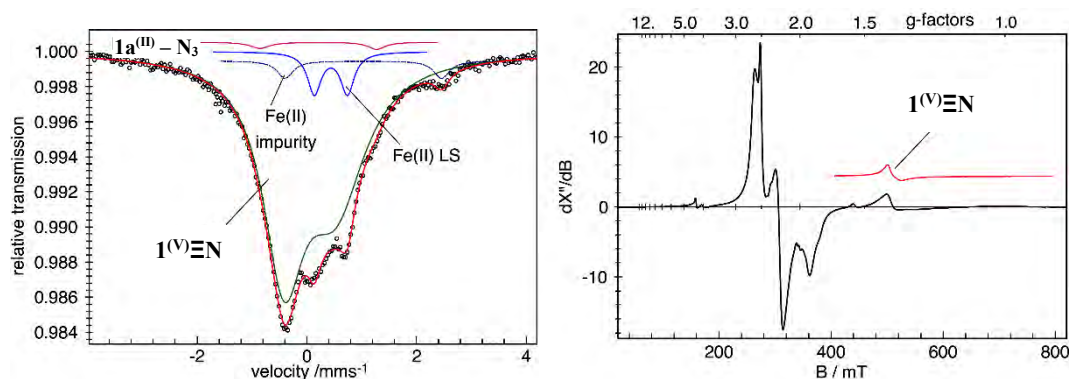


Figure V.6. (Left) Zero – field Mössbauer spectrum of solid complex $\mathbf{1b}^{\text{(III)}} - \text{N}_3$ after 5 h photolysis at 77 K with a 530 nm (green) LED, and (Right) EPR spectrum of a similar sample photolysed in a sealed EPR tube under vacuum ($T = 10$ K, frequency 9.6468 GHz, power 0.2 mW, modulation 0.75 mT / 100 kHz). The EPR derivative amplitudes are given in arbitrary units, consistent with those of Figures V.3 and V.4. The Mössbauer spectrum was fitted with four Lorentzian doublets accounting for i) Iron (III) starting material ($\mathbf{1b}^{\text{(III)}} - \text{N}_3$, 1%, in pink), ii) ferrous impurity, iron (II) HS (4%, in dark blue), and the photoproducts iii) Iron (II) LS (6%, in blue), and iv) the high – valent photo – product ($\mathbf{1}^{\text{(V)}\equiv\text{N}}$, 89%, in green). The red line in EPR spectrum is a simulation with g values $g_1 = 1.37$ and $g_2 = 1.33$, $g_3 = 1$ (fixed) and Lorentzian line of the widths 56 , 149 , and $1000 \cdot 10^{-4} \text{ cm}^{-1}$.

Magnetic susceptibility experiments are consistent with a sample constituted by 25 % of iron(II) with $S = 0$, and the remaining 75 % of $\mathbf{1}^{\text{(V)}\equiv\text{N}}$ with $S = 1/2$ (see Figure SV.15); The effective magnetic moment approaches 0.9 MB as the temperature approaches 0 K, and at higher temperature the effective magnetic moment is close to 1.4 MB. All these data together indicate that a complete photolysis of the initial iron (III) – azide complex takes place to generate a 25 % of iron (II), presumably through an homolytic cleavage of the Fe – N bond. Moreover, what is more important, the low spin iron (III) – azido would be capable to evolve to a high – valent iron (V) species ($\mathbf{1}^{\text{(V)}\equiv\text{N}}$) through heterolytic cleavage of the N – N bond (as was first suggested by mass spectrometry).

Alternatively, samples of complex $\mathbf{2b}^{\text{(III)}} - \text{N}_3$ were photolysed with a 470 nm LED following the same procedure as in $\mathbf{1b}^{\text{(III)}} - \text{N}_3$. After 2.5 hours a brownish mixture resulted and a Mössbauer analysis of this sample revealed only 8 % of initial iron (III) remained unphotolysed (Figure SV.16). Remarkably, 36 % of the sample was a new species with isomer shift $\delta = 0.00 \text{ mm} \cdot \text{s}^{-1}$ and a quadrupole splitting $\Delta E_{\text{Q}} = 1.18 \text{ mm} \cdot \text{s}^{-1}$, assigned to a possible iron (V) species ($\mathbf{2}^{\text{(V)}\equiv\text{N}}$) by similarity of its Mössbauer parameters with $\mathbf{1}^{\text{(V)}\equiv\text{N}}$. The remainders were assigned to the initial iron (II) species. Considering only 50 % of starting material was iron (III) then can be estimated that 86 % of the photolysed iron (III) was converted into iron (V).

Furthermore we tested by Mössbauer the wavelength – dependence of the photolytic reactivity of $\mathbf{1b}^{\text{(III)}} - \text{N}_3$, by irradiating with a 530 nm lamp. When a solid sample of $\mathbf{1b}^{\text{(III)}} - \text{N}_3$ was photolysed for 5 hours

suspended on liquid nitrogen, the initial purple solid changed to brown colour. Mössbauer analysis, showed in Figure V.6 left, indicated that only a 1 % of initial Fe^{III} remained unphotolysed. Residual iron (II) impurities (3 % of the initial sample) remained unchanged during irradiation. The remainder species, generated from photolysis, were identified as a low spin iron (II) species (4 %, isomer shift $\delta = 0.39 \text{ mm}\cdot\text{s}^{-1}$, quadrupole splitting $\Delta E_Q = 0.70 \text{ mm}\cdot\text{s}^{-1}$) and a 78 % of species **1**^(V) \equiv N, previously assigned to low spin ($S = \frac{1}{2}$) iron (V) species (isomer shift $\delta = 0.00 \text{ mm}\cdot\text{s}^{-1}$ and quadrupole splitting $\Delta E_Q = 0.86 \text{ mm}\cdot\text{s}^{-1}$). Taking into account only the purity of the initial iron (III) in the sample, it could be concluded that a 95 % conversion of **1b**^(III) – N₃ towards the iron (V) species, **1**^(V) \equiv N is achieved; revealing an effect of the wavelength on the photolysis pathway.

The series was also characterised by Fe K – edge X – ray absorption spectroscopy (XAS), summarised in Table V.2, providing further insight into their electronic and geometric structure (Figure V.7 and Figure SV.17). The rising edge spectra (Figure V.7 left) for **1a**^(II) – N₃, **1b**^(III) – N₃ and **1**^(V) \equiv N are consistent with a sequential increase in the metal oxidation state. Compound **1a**^(II) – N₃ with a rising edge energy of 7120.6 eV, has a small pre – edge feature attributed to $1s \rightarrow 3d$ dipole forbidden transitions at $\sim 7111.6 \text{ eV}$ with an intensity of ~ 0.045 normalized units. This is consistent with a low spin octahedral Fe(II) centre having dipole forbidden pre – edge transitions to the e_g set of orbitals.³²⁶ A low spin pseudo – octahedral Fe(II) centre for **1a**^(II) – N₃ agrees both with the magnetic susceptibility studies and the corresponding crystal structure that show **1a**^(II) – N₃ as being low spin below 100 K. Compound **1b**^(III) – N₃ on the other hand experiences a shift in its rising edge to 7122.7 eV concomitant with a 1 eV shift in its pre – edge intensity weighted average energy. The pre – edge of **1b**^(III) – N₃ can be fit with two low intensity peaks at 7111.9 eV and 7113.2 eV similar to previously reported low spin six coordinate Fe(III) complexes. Lastly, **1**^(V) \equiv N was generated by irradiating a 4 mM frozen solution of **1b**^(III) – N₃ in acetone for 5 h at 77 K during which the colour progressively changed from purple to orange. Compound **1**^(V) \equiv N has a rising edge at 7123.8 eV with a very intense pre – edge at 7114.2 eV and a shoulder at 7112.4 eV giving an intensity weighted average pre – edge of 7113.9 eV. Such a profile correlates with the previously reported values for the XAS spectra of the related $[\text{Fe}^{\text{V}}(\text{N})(\text{cyclam} - \text{ac})]^+$ complex having a rising edge of $\sim 7124.1 \text{ eV}$ and a pre-edge energy of 7114.2 eV.¹⁹⁵ Furthermore the pre – edge energy of **1**^(V) \equiv N is below that of $[\text{Fe}^{\text{VI}}(\text{N})(\text{Me}_3\text{cyclam} - \text{ac})]^+$ (7115.1 eV) strongly pointing to the formation of an Fe(V) centre.^{195,198} To obtain insight into the coordination structure of **1**^(V) \equiv N, EXAFS analysis was carried out. A picture emerges of a six coordinate metal centre consisting of N/O scattering atoms having a short 1.64 Å Fe – N/O bond. Presumably, this corresponds to the short Fe – nitride bond that causes a tetragonal distortion of the octahedral geometry and facilitates p – d mixing through a strong metal – ligand covalent interaction resulting in a very intense pre – edge.^{195,327} Previous researchers have reported similar Fe – nitride bond lengths of 1.61 Å for the $[\text{Fe}^{\text{V}}(\text{N})(\text{cyclam} - \text{ac})]^+$ complex and 1.57 Å for $[\text{Fe}^{\text{VI}}(\text{N})(\text{Me}_3\text{cyclam} - \text{ac})]^+$.^{195,198} Comparing these values to the related $[\text{Fe}^{\text{V}}(\text{N})(\text{tBuIm}_3\text{BPh})]^+$ complex, with an Fe – N bond of 1.502(2) Å, we have a sensibly longer bond. This can be rationalised by the fact that **1**^(V) \equiv N is a hexacoordinate complex and the former is a tetradentate complex in pseudo – tetrahedral geometry, which translates to a shorter Fe – N bond for a lower coordination number.²¹⁵

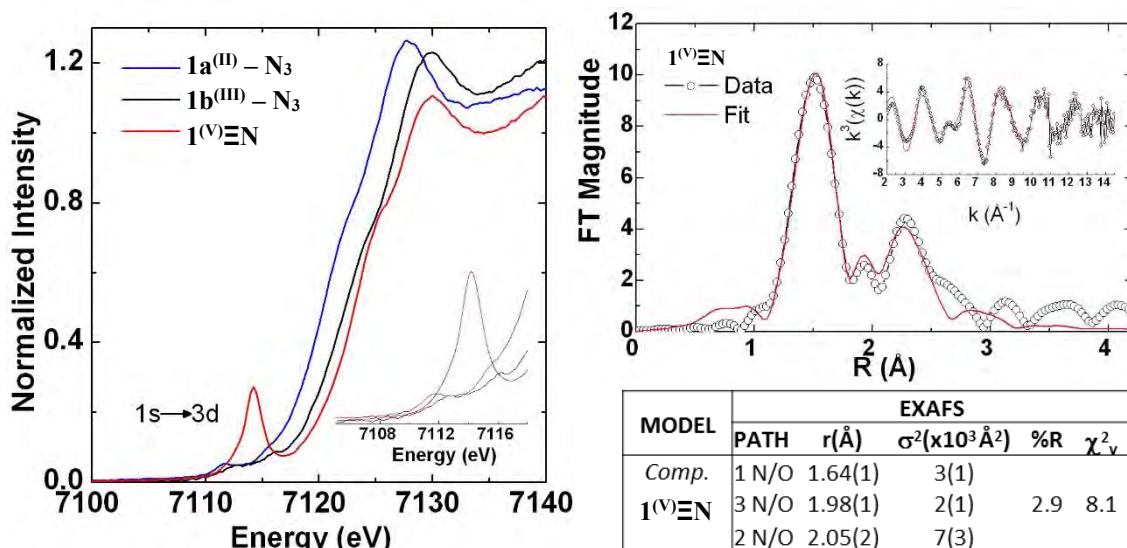


Figure V.7. (Left) Iron K – edge X – ray absorption spectra of **1a^(III) – N₃** (blue), **1b^(III) – N₃** (black) and **1^(V)EN** (red). The inset is an expansion of the pre – edge region. (Right) Fourier transformed EXAFS spectra of **1^(V)EN** (inset: k³-weighted unfiltered EXAFS spectra (Data: black circles; Fits: red line)).

Table V.2. Comparison of Fe – N bond distances and XAS energies.

Complex	Fe – N distance XAS (DFT) (Å)	EXAFS Data	
		E ^o (eV)	E _{pre – edge} (eV)
<i>Fe^{II}(N₃)(MePy₂tacn)](PF₆) (1a^(III) – N₃)</i>	1.99*(2.02)	7120.6	7111.6
[Fe^{III}(N₃)(MePy₂tacn)](PF₆)₂ (1b^(III) – N₃)	1.86*(1.90)	7122.1	7112.7
[Fe^V(N)(MePy₂tacn)](PF₆)₂ (1^(V)EN)	1.64 (1.60)	7123.8	7113.9
^a [Fe^{III}(N₃)(cyclam – ac)]⁺	1.94	7123.0	7112.4
^a [Fe^V(N)(cyclam – ac)]⁺	1.61 (1.60)	7124.1	7114.2
^b [Fe^{VI}(N)(Me₃cyclam – ac)]²⁺	1.57 (1.53)	7125.0	7115.1

*Values from X – ray diffraction. ^aData from reference 195. ^bData from reference 198.

V.2.5. DFT Calculations

To help build a molecular orbital picture for **1^(V)EN**, theoretical calculations for the series were carried out. A low spin $S = 1/2$ Fe(V) centre for **1^(V)EN** is found to better match experimental data having a calculated Fe – nitride bond of 1.60 Å, matching the experimentally determined distance of 1.64 Å. A high spin $S = 3/2$ Fe(V) centre on the other hand is predicted to have a bond length of 1.76 Å well outside the resolution limit of the EXAFS data (0.1 Å). Also the calculated Mössbauer quadrupole splitting ΔE_Q = of -1.7 mm·s⁻¹ ($\delta = -0.17$) for an $S = 1/2$ Fe(V) centre, qualitatively is more consistent with the experimental value of ~1.03 mm·s⁻¹ than the -4.31 mm·s⁻¹ ($\delta = 0.01$) value calculated for an $S = 3/2$ system. Lastly the XAS pre – edges for the series were also calculated and found to correlate well to experiment (Annex Figure SV.18). Difference density maps for the transitions highlight that for **1^(V)EN** the intense feature at 7114.2

eV arises from excitations to the d_{z^2} set of orbitals which have a σ^* antibonding interaction with the nitride p_z orbital (Annex Figure SV.19). As this is a σ – type interaction p – d mixing is more favoured ($\sim 2.7\%$ p – character) than for transitions to π^* (1.5% p – character) orbitals or transitions to non – bonding orbitals ($\sim 0.5\%$ p – character) the latter forming the shoulder observed at 7112.4 eV.³²⁶ Therefore an orbital picture emerges for $\mathbf{1}^{(V)}\Xi\text{N}$ consistent with a low spin Fe(V) centre. Using the notation $\Gamma(X)^n$ where Γ is the bonding nature, X is the predominant character of the orbital, and n its occupation number,³²⁸ $\mathbf{1}^{(V)}\Xi\text{N}$ is best described as having a $\sigma(\text{N}p_z)^2\delta(\text{Fe}d_{xy})^2\pi^*(\text{Fe}d_{xz,yz})^1\sigma^*(\text{Fe}d_{x^2-y^2})^0\sigma^*(\text{Fe}d_{z^2})^0$ electronic arrangement (Figure V.8). Furthermore the singly occupied π^* $\text{Fe}d_{xz/yz}$ shows a strong covalent Fe – N interaction having a 43.3% Fe – character with 42.8% - N character similar to other highly covalent $[\text{FeX}]^{+n}$ cores (X = N, O) with the Fe – N bond order best described as 2.5.^{195,197}

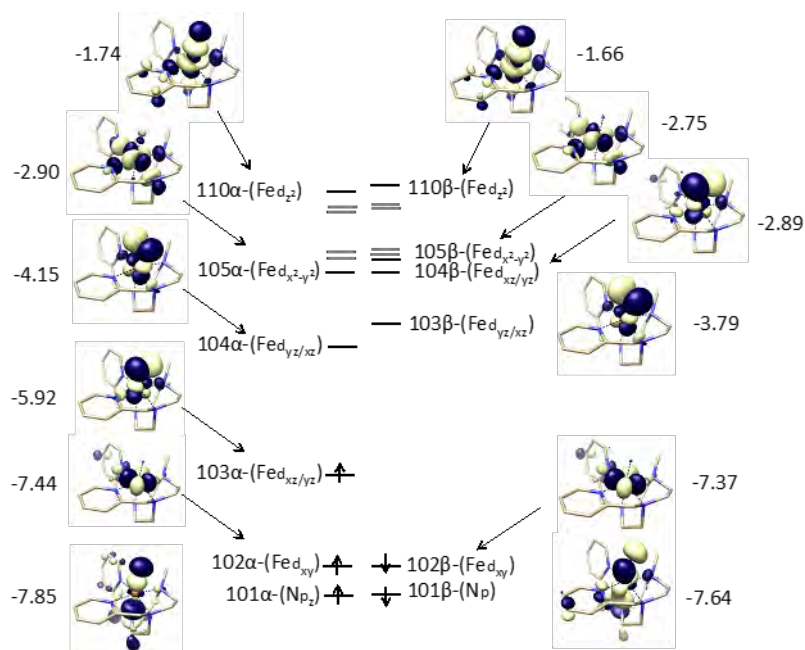


Figure V.8. Molecular orbital picture for compound $\mathbf{1}^{(V)}\Xi\text{N}$.

V.2.6. Analysis of the formation and decay of $\mathbf{1}^{(V)}\Xi\text{N}$ by gas evolution

A mass spectrometry online system (EI – MS) was used to analyse the gas evolution during formation and decay of $\mathbf{1}^{(V)}\Xi\text{N}$. First, a frozen solution of $\mathbf{1b}^{(III)} - ^{15}\text{N}_3$ was analysed during photolysis. It was reasoned that this procedure should result in the production of N_2 gas, and that the use of isotopically labelled azide ligands may provide information about the mechanism (Figure V.9). The photolysis of $\mathbf{1b}^{(III)} - \text{N}_3$ was performed on a 4 mM acetone solution (1 ml) under Ar at 77 K. The solution turned from purple to orange during the irradiation process. Despite of the change in colour, no N_2 evolution could be detected while it was being irradiated, presumably because the gas remains trapped inside the frozen solution. So the analysis of the N_2 formed was performed by melting the sample very slowly (for 3 h) after 3.5 h of photolysis with green LED (530 nm).

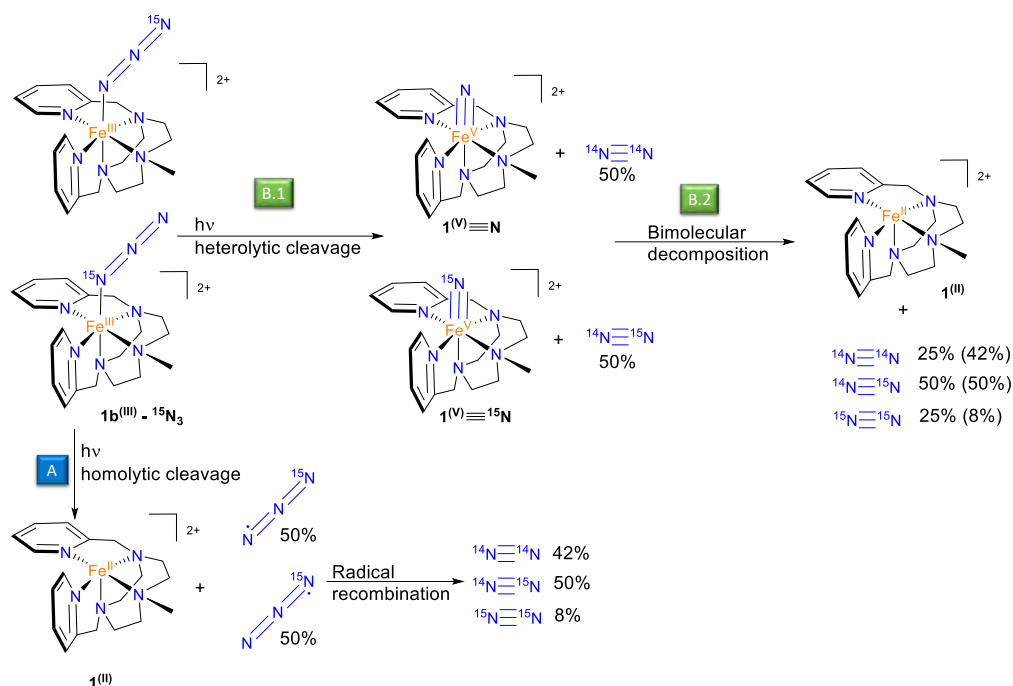


Figure V.9. Reactivity of $1b^{(III)} - N_3$ upon irradiation, percentages are the N_2 amounts generated after photolysis (percentage in parentheses are the combination of B.1 and B.2).

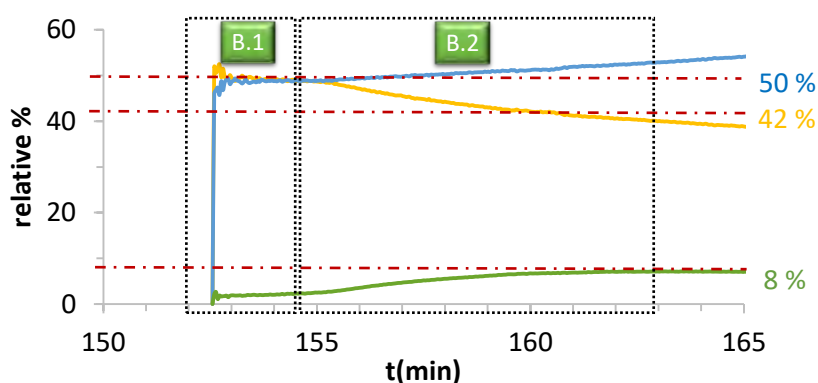


Figure V.10: Evolution of the relative composition of the nitrogen gas isotopes ($^{14}N - ^{14}N$ yellow line, $^{14}N - ^{15}N$ blue line and $^{15}N - ^{15}N$ green line) green line at the headspace of a solution of complex $1^{(V)}\equiv N$, generated by irradiation of a solution of $1b^{(III)} - N_3$ (4 mM) in acetone solution at 530 nm LED for 3.5 hours under Ar at 77 K while slowly melting.

After 2.5 h of slowly melting the sample under no irradiation N_2 was released. Importantly only $^{14}N^{14}N$ and $^{14}N^{15}N$ were detected, and more significantly showing a ratio 1:1, which was maintained for a short period of time (*ca.* 5 min.). The ratio of 1:1 and the total absence of $^{15}N^{15}N$ clearly reflects the step B.1, the photooxidation of the iron (III) ($1b^{(III)} - N_3$) to iron (V) ($1^{(V)}\equiv N$).

Following this first phase, that lasts for 5 minutes, the $^{14}N^{14}N$: $^{14}N^{15}N$ ratio start to differ from 1:1, in favour of the later. Moreover at the same time $^{15}N^{15}N$ was detected. This change suggests a bimolecular decomposition of $1^{(V)}\equiv N$ (step B.2). For a short period of 6 – 8 minutes the proportion between $^{14}N^{14}N$: $^{14}N^{15}N$: $^{15}N^{15}N$ gases stayed close to theoretical ratio of 42:50:8 (Figure V.10). Interestingly this ratio is the one expected for a scenario where the gas that emerge from the heterolytic cleavage of the N –

N bond in $\mathbf{1b^{(III)}} - \text{N}_3$ and the bimolecular decomposition of $\mathbf{1^{(V)}\equiv N}$ are combined. Of interest, Bill, Neese *et al.* recently studied the decomposition of $[\text{Fe}^{\text{V}}(\text{N})(\text{cyclam} - \text{ac})]^+$ and $[\text{Fe}^{\text{V}}(\text{N})(\text{N}_3)(\text{cyclam})]^+$. The study of the gases released after photolysis and subsequently decomposition was performed by EI – MS and revealed ratios of $^{14}\text{N}^{14}\text{N}:^{14}\text{N}:^{15}\text{N}:^{15}\text{N}^{15}\text{N}$ of $\approx 74:22:4$ and $\approx 82:15:3$, respectively. Those amounts of $^{14}\text{N}^{15}\text{N}$ and $^{15}\text{N}^{15}\text{N}$ are lower than the expected (42:50:8), most likely due to atmospheric N_2 contamination. Despite of that, this study provides clear evidence of the extrusion of $^{15}\text{N}^{15}\text{N}$ from a bimolecular decay pathway contributing to N_2 evolution, as the only source can be the decomposition pathway of $\text{Fe}^{\text{V}}(\text{N})$ species.²⁰¹

The fact that, in our reaction, the ratios do not remain constant over time is indicative that the iron (V) species is not only decomposing through a bimolecular pathway, but instead additional non identified paths must be occurring. This is not surprising if we take into account that $\mathbf{1^{(V)}\equiv N}$ is expected to be a very electrophilic and reactive species, thus most likely capable of reacting with solvent or the ligand. Alternative decomposition is also suggested by the detection of ions attributable to CN^- moiety (mass of 26 and 27), which appears simultaneously with $^{15}\text{N}^{15}\text{N}$ gas release, presumably when $\mathbf{1^{(V)}\equiv N}$ acquires some mobility upon the melting of the frozen solution.

Alternatively, when the sample that was previously photolysed with blue LED (Figure V.5), containing a 26% low spin Fe(II) and 74% $S = 1/2$ Fe(V), was left to warm up to room temperature under anaerobic conditions, a mixture of iron (II) and iron (III) was obtained (Figure SV.20 top). The mixture somehow evolved to a combination of 72 % of a new low spin iron(III) compound (isomer shift $\delta = 0.30 \text{ mm}\cdot\text{s}^{-1}$, quadrupole splitting $\Delta E_{\text{Q}} = 1.41 \text{ mm}\cdot\text{s}^{-1}$) and two iron (II) components, the first one (21 %) in the high – spin state, and the second one 7 % in low spin (isomer shift $\delta = 1.29$ and $0.57 \text{ mm}\cdot\text{s}^{-1}$, quadrupole splitting $\Delta E_{\text{Q}} = 2.33$ and $0.77 \text{ mm}\cdot\text{s}^{-1}$ respectively). Thus suggesting a 2 – electron reactivity, instead of the clean decay to iron (II) (3e- reaction) upon N_2 generation previously observed by Dr. Eckhard and co – workers.²⁰¹

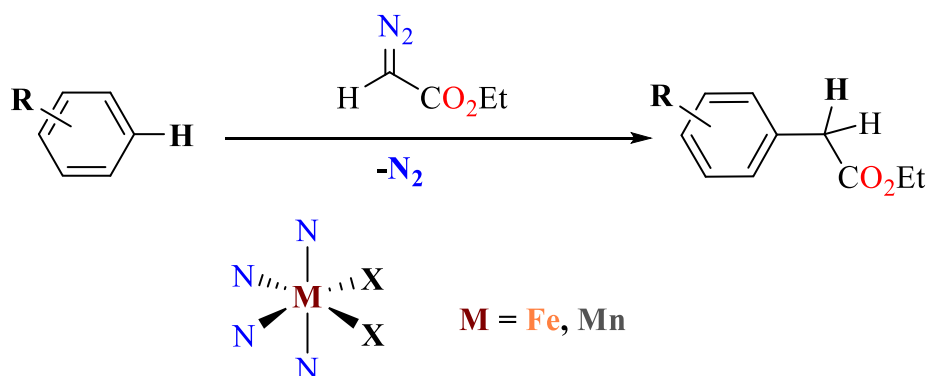
Finally, after monitoring of gases, HR – MS was performed in melted solution samples (Figure SV.20), confirming the conclusions of the Mössbauer analysis. The decomposition mixture was composed mainly by $[\text{Fe}^{\text{III}}(\text{OH})(\text{MePy}_2\text{tacn})]^{2+}$ ($m/z = 199.08$) and a small amount of unreacted $\mathbf{1b^{(III)}} - \text{N}_3$. A small peak corresponding to the Fe^{V} species was also observed, presumably resulting from the cleavage of the residual $\mathbf{1b^{(III)}} - \text{N}_3$.

V.3. SUMMARY

Octahedral iron – azide complexes $\mathbf{1a^{(II)}} - \mathbf{N_3}$, $\mathbf{2a^{(II)}} - \mathbf{N_3}$, $\mathbf{1b^{(III)}} - \mathbf{N_3}$ and $\mathbf{2b^{(III)}} - \mathbf{N_3}$ bearing neutral pentadentate aminopyridine ligands based on the macrocycle triazacyclononane have been synthesised and studied as potential precursors of high – valent iron – nitride species. $\mathbf{1a^{(II)}} - \mathbf{N_3}$ exhibits a temperature dependent spin transition phenomena. Photolysis of iron (II) species $\mathbf{1a^{(II)}} - \mathbf{N_3}$ and $\mathbf{2a^{(II)}} - \mathbf{N_3}$ does not result in photooxidative cleavage of the N – N bond on the azide moiety. In contrast to that, $\mathbf{1b^{(III)}} - \mathbf{N_3}$ extrudes $\mathbf{N_2}$ to generate the high – valent iron (V) – nitrene species $\mathbf{1^{(V)}\equiv N}$ in the gas phase and also upon photolysis in a frozen matrix or powder at 77 K. Analysis of the $\mathbf{N_2}$ gas mixtures generated upon photolysis of $\mathbf{1b^{(III)}} - \mathbf{N_3}$ by MS – online techniques give further evidence of an heterolytic $\mathbf{N_2}$ extrusion. Iron (V) nitrene species $\mathbf{1^{(V)}\equiv N}$, generated by photolysis of $\mathbf{1b^{(III)}} - \mathbf{N_3}$ was studied in detail by Mössbauer spectroscopy, EPR, SQUID, XAS and EXAFS, and identified as a low spin ($S = 1/2$) iron (V) – nitrido species. XAS and EXAFS analysis confirmed the existence of a very short Fe – N bond in high concordance with previously reported high – valent iron (V) species. These species are highly reactive and rapidly decompose upon warming, preventing the study of its reactivity in solution. MS – online techniques provide evidence that decomposition of $\mathbf{1^{(V)}\equiv N}$ involve N – N formation.

CHAPTER VI

Fe AND Mn FOR SELECTIVE FUNCTIONALIZATION OF C – H BONDS OF ARENES BY CARBENE INSERTION



Part of this chapter has been included in the following publication:

Iron and Manganese Catalysts for the Selective Functionalization of Arene C(sp²) – H Bonds by Carbene Insertion. A. Conde,[‡] G. Sabenya,[‡] M. Rodríguez,[‡] V. Postils, J.M. Luis, M. Mar Díaz – Requejo, M. Costas, P. J. Pérez. *Angew. Chem.Int. Ed.* **2016**, 55, 6530 – 6534.

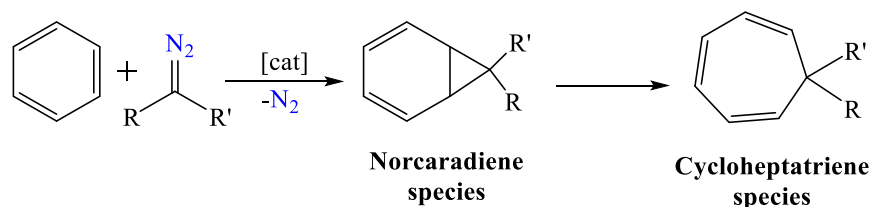
[‡]Authors contributed equally to this work.

VI.1. GENERAL INSIGHT

The selective formation of C – C bonds from unactivated C – H bonds is desirable to simplify the syntheses of complex molecules. There are several strategies to functionalise C – H bonds⁴ and among them the use of diazo compounds to generate electrophilic carbenes is appealing due to its versatility and atom economy, generating only N₂ as by – products.²¹⁷ The use of iron catalysts to decompose diazo compounds to functionalise substrates is convenient because of its biocompatibility and availability.^{144,216}

The metal – mediated carbene transfer from diazo compounds have been widely studied with different metals, such as rhodium, gold and silver, with substrates that include olefins, alcohols, amines or alkanes, even methane.^{217,329-331} On the other hand, iron have been mainly used in the cyclopropanation of alkenes and almost exclusively with porphyrinic complexes.^{218,230} Non– heme examples have been scarcely studied and almost exclusively in the cyclopropanation of alkenes. The only exceptions are the C – H (sp²) insertion into indoles with aryldiazoacetates, recently reported, using iron salts and tetraethylenediamine (TEDA) as ligand, or spiro bis(oxazoline) ligands to obtain chiral products.²⁴⁷

In contrast, the C – H functionalisation of arenes have been much less studied. One example is the called Buchner reaction (Scheme VI.1), in the reaction of benzenes with diazocompounds mediated by metals (*e.g.* gold, copper, silver and iron). This reaction results in the formal addition of the carbene into a double bond from the benzene ring to generate the norcaradiene product. This species can open to form the cycloheptatriene ring, product of the expansion of benzene substrate. The latter species is usually an undesired by – product and is generally obtained in important amounts.^{238,332-334}

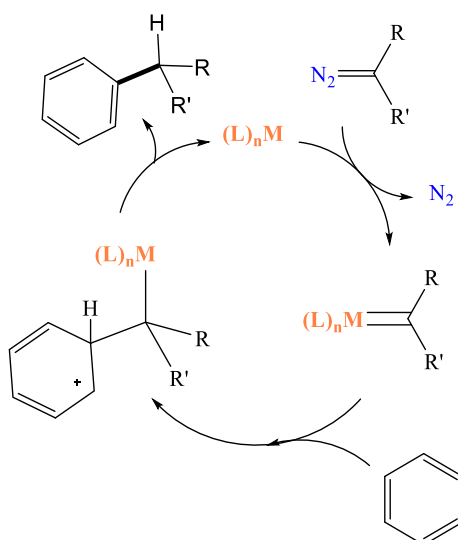


Scheme VI.1. Arene functionalisation in the Buchner reaction.

The formal insertion of diazocompounds into C – H bonds of cyclohexane and benzene have been also reported with other metals, such as rhodium, silver or gold. Schechter and Livant reported examples using Rh₂(OAc)₄ and Rh₂(O₂CCF₃)₄.^{335,336} The term insertion is used in the sense that carbene moiety have been formally inserted in the C – H bond, despite this designation does not imply the mechanism proceeds through an insertion. The group of Professor Pedro Pérez reported in 2005 the use of the commercially available ethyl diazoacetate (EDA) in the insertion into C – H (sp²) of benzene and toluene using the gold catalyst [Au(Cl)(IPr)] (IPr = 1,3 – bis(diisopropylphenyl)imidazole – 2 – ylidene) and Na(BAr_F)₄ as halide scavenger. These reactions gave good yields with low catalyst loadings but mixtures of insertion and expansion (≈ 3:1) were obtained, as well as different regioisomers in toluene. Remarkably this system gave no by – products from EDA dimerization (namely diethyl fumarate and maleate).³³⁷ Later on, the same group expanded this reactivity with different nitrogen heterocyclic carbene (NHC) ligands and using different diazoacetate compounds (*e.g.* N₂CR(CO₂Et) R = Me, CF₃, SiMe₃). The system proved selective towards C – H (sp²) bonds and not reacting towards C – H (sp³), furthermore the ratio insertion:addition

products was improved in some reactions (e.g. toluene with $\text{N}_2\text{CSiMe}_3(\text{CO}_2\text{Et})$). Interestingly the isobutyl benzene product was obtained in good yields, this substrate has special interest as a possible precursor of the ibuprofen molecule. Despite the good results the reaction showed no regioselectivity and gave mixtures of *ortho*, *meta* and *para* isomers.³³⁸ In general the mechanism have been proposed to proceed through a metal – carbene species upon reaction of the metal with the diazo compound, responsible for the C – H functionalisation. Very recently DFT studies of the mechanism of diazoacetate insertion into the benzene ring and mediated by gold catalysts have been reported. Zhang and co – workers proposed the mechanism of C – H (sp^2) insertion into phenol to proceed through an enolate intermediate, with a 1,3 – H shift.³³⁹ Pérez and co – workers subsequently suggested a similar mechanism for $\text{M}(\text{IPr})$ systems ($\text{M} = \text{Ag}, \text{Au}$ and Cu).³⁴⁰ The previously accepted mechanism was generally assumed to proceed through a Wheland intermediate with a 1,2 – H shift by analogy with rhodium systems (Scheme VI.2).^{335,340,341}

In a collaborative effort with Professor Pedro's group, in this work we have studied the functionalisation of unactivated aryl C – H (sp^2) bonds using EDA and catalysed by non – heme iron (II) and manganese (II) complexes. The reactions are selective towards C – H (sp^2) bonds with no C – H (sp^3) functionalisation. Importantly, no malonate or fumarate by – products were observed and moreover, high selectivity towards insertion was obtained.



Scheme VI.2. Proposed mechanism through Wheland – type intermediate for metal – catalysed functionalisation of benzene.

VI.2. RESULTS AND DISCUSSION

Motivated by the interesting results obtained with gold, previously reported by Professor Pedro Pérez, we decided to study, in collaboration with his group, the reaction of non – heme iron (II) and manganese (II) complexes in the decomposition of the commercially available ethyl diazoacetate (EDA) to functionalise benzene. To the best of our knowledge is the first time that a non – heme iron complex has been reported in C – H (sp²) functionalisation of benzene, furthermore non – heme manganese complexes have never been reported in the decomposition of diazocompounds to functionalise C – H bonds.

VI.2.1. Catalytic studies

A series of iron (II) and manganese (II) complexes bearing non – heme neutral macrocyclic ligands were tested in the decomposition of EDA in neat benzene. The reactions were performed at 80 °C because at lower temperatures poor reactivity was observed, in addition two equivalents of Na(BArF)₄ (sodium tetrakis(bis – 3,5 – trifluoromethylphenyl)borate) were needed as halide and triflate scavenger for the reaction to proceed. In this regard we studied the activity of a series of robust and basic, tetra – and pentadentate N – donor ligands that have been used previously in the stabilisation of high oxidation state species (Figure VI.1 and Table VI.1). Importantly, a blank experiment revealed that Na(BArF)₄ did not yield any reactivity in the absence of metal. Surprisingly blank experiments with M(OTf)₂ (M = Fe and Mn), FeCl₂ and Na(BArF)₄ in neat benzene showed high conversions but low selectivity towards insertion product (entries 13 – 15). Initial screening revealed promising results obtaining a high level of EDA consumption with the tetradentate 1,4,7 – triazacyclononane ligand with both Fe^{II} and Mn^{II} (entries 6 and 7). While all catalysts studied gave good to excellent conversions in the consumption of EDA to functionalise the benzene, only [M^{II}(OTf)₂(Me₂Pytacn)] (M = Fe, **3^{II}**, and Mn, **3Mn^{II}**) gave high selectivity towards insertion products (I >85 %). We tested also the effect of counterions by using [Fe^{II}Cl₂(Me₂Pytacn)] (**3^{II}Cl**) as catalyst, and interestingly it was found that the complex gave inverse selectivity, providing only 15 % of insertion product. Further optimisation revealed that the amount of counterion scavenger had a positive effect on the yield, giving the best results with addition of 8 equivalents of Na(BArF)₄. For instance, EDA conversion slightly increases from using 2 to 8 equivalents of this salt in presence of **3^{II}** and **3Mn^{II}**, which also translated into a selectivity increase from 85 to 97 % (entries 7 and 8 vs. 11 and 12), being insertion almost the only product. The addition of only one equivalent of this salt did not perform the reaction, remaining most of the EDA unreacted. These observations may indicate that the EDA activation require two vacant sites in the metal to take place, the high amounts of Na(BArF)₄ required to get high selectivity suggest that exists an equilibria of species between [M(OTf)₂(L)] \leftrightarrow [M(OTf)(L)](BArF)₄ \leftrightarrow [M(L)](BArF)₄₂, (L = Me₂Pytacn) and the latter is the responsible for the ring – insertion product. Moreover, when the reaction of benzene with EDA was performed using [Fe^{II}(OTf)(MePy₂tacn)](OTf) (**1^{II}**) as catalyst it gave no functionalisation of benzene, further supporting our assumptions. Additional salts (e.g. NaPF₆, NaBF₄ or NaBPh₄) were tested but only Na(BArF)₄ propitiated the full consumption of EDA.

To the best of our knowledge, such degree of selectivity (>97 %) into the insertion product is unprecedented in the literature for the reaction of benzene and EDA. As mentioned above, the highest values of selectivity toward the insertion product has been described with gold – based catalysts as 75%.

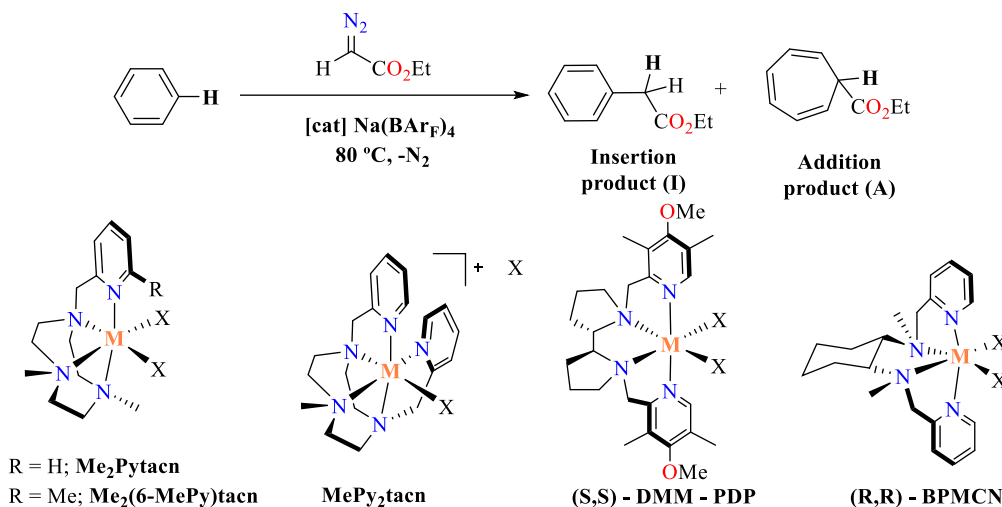


Figure VI.1. (Top) Metal – catalysed reaction of benzene with EDA and complexes used in this work (X = OTf, Cl).

Table VI.1. Catalytic results of iron (II) and manganese (II) complexes in the catalytic functionalisation of benzene.

Entry	Complex	Na(BArF) ₄ equivalents	Conversion (%) ^b	Insertion: Addition ratio ^c
1	[Fe ^{II} Cl ₂ (DMM – PDP)]	2	79	25:75
2	[Fe ^{II} (OTf) ₂ (DMM – PDP)]	2	74	20:80
3	[Mn ^{II} (OTf) ₂ (DMM – PDP)]	2	99	29:71
4	[Fe ^{II} (OTf) ₂ (BPMCN)]	2	41 ^d	66:34
5	[Mn ^{II} (OTf) ₂ (BPMCN)]	2	93 ^d	36:64
6	[Fe ^{II} Cl ₂ (Me ₂ Pytacn)] 3^(II)Cl	2	67	15:85
7	[Fe ^{II} (OTf) ₂ (Me ₂ Pytacn)] 3^(II)	2	95	85:15
8	[Mn ^{II} (OTf) ₂ (Me ₂ Pytacn)] 3Mn^(II)	2	98	89:11
9	[Fe ^{II} (OTf) ₂ (Me ₂ (6-MePy)tacn)]	2	63	21:79
10	[Mn ^{II} (OTf) ₂ (Me ₂ (6-MePy)tacn)]	2	42 ^d	27:73
11	[Fe ^{II} (OTf) ₂ (Me ₂ Pytacn)] 3^(II)	8	99	97:3
12	[Mn ^{II} (OTf) ₂ (Me ₂ Pytacn)] 3Mn^(II)	8	99	98:2
13	[Fe ^{II} Cl ₂]	2	93	33:67
14	[Fe ^{II} (OTf) ₂ (MeCN) ₂]	2	91	32:68
15	[Mn ^{II} (OTf) ₂]	2	85 ^d	51:49

^aReactions carried out at 80 °C with 0.005 mmol of catalyst, n equiv of NaBAr₄F and 20 equiv of ethyl diazoacetate in 3 mL of neat benzene. Reaction time: 12 h. ^bInitial EDA converted into insertion and addition products, the remaining were assigned to dimer by – products and ethyl – glycolate from adventitious water. Determined by GC. ^cDetermined by ¹H – NMR. ^dEDA not completely consumed after 12 h.

In addition to the high selectivity found using **3^(II)** and **3Mn^(II)**, importantly diethyl fumarate and maleate by – products, formed from carbene dimerization, were only detected in negligible amounts (<1 %).

The substrate scope of this reactivity was further studied with **3^(II)** in the C – H functionalisation with different alkylbenzenes (Figure VI.2). Reactions were performed in a 10 – fold scale (1 mmol EDA) and

reaction products were isolated (*e.g.* benzene insertion product was isolated in 87 % yield). In all cases was observed exclusive functionalisation of C – H (sp^2) bonds and generally in good yields. Albeit in some cases, when substrate was not completely anhydrous, it was observed some ethyl glycolate from adventitious water. High selectivity towards insertion and absence of dimerization by – products were maintained, although when possible, products were obtained as a mixture of *ortho*, *meta* and *para* isomers. The isomer ratios were calculated by NMR and identified in NOESY experiments on the basis of the number of NOE signals (see Annex). A closer look to monoalkylated benzene (toluene, ethylbenzene, isobutylbenzene and *tert* – butyl benzene) revealed a preference towards *o* and *p* positions, as expected from their directing properties, with some preference towards *para* isomer due to steric effects. Between them, only a higher effect on the regioselectivity was observed for the latter, leading to an increase on the *para* isomer due to the higher steric hindrance in the *ortho* position in this substrate. Cyclohexylbenzene showed the same behaviour, giving a mixture of regioisomers similar to the monoalkyl benzenes.

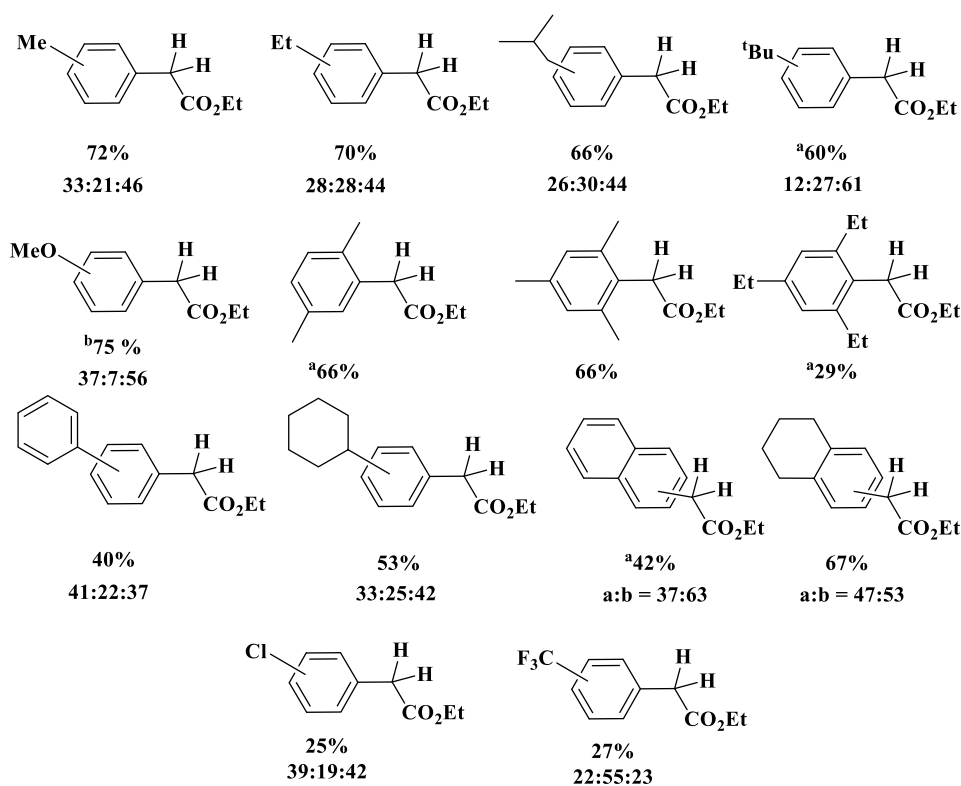
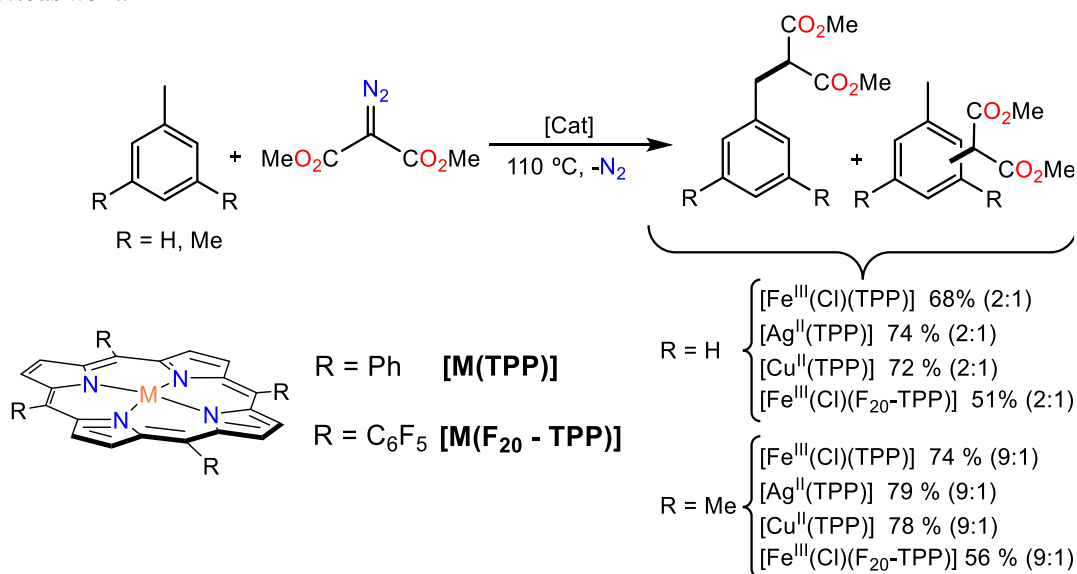


Figure VI.2. Substrate scope for reaction of arenes with EDA and **3**^(II) (8 eq. of Na(BArF)₄). Yields were isolated and isomer ratios were determined by ¹H – NMR and are normalised by the number of positions available (2 *ortho*, 2 *meta* and 1 *para*). ^aWork performed by Mònica Rodriguez. ^bCombined yield of C – H and C – O functionalisation, see text for details.

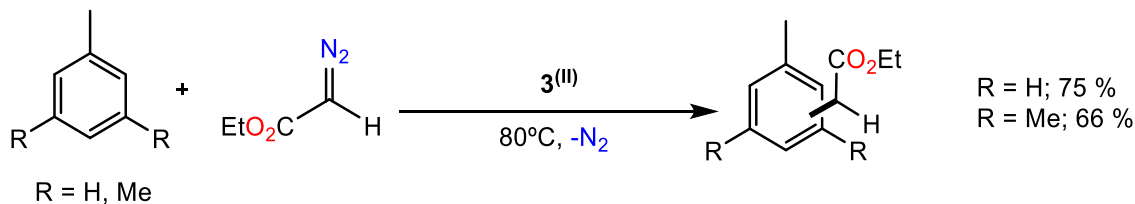
The functionalisation of polyalkylbenzenes such as *p* – xylene, mesitylene and 1,3,5 – triethylbenzene remained selective, with no C – H(sp^3) functionalisation. Trisubstituted substrates (mesitylene and 1,3,5 – triethylbenzene) are of special interest since they give an orthogonal reactivity than that observed in arene borylation using iridium catalysts. Iridium gives the C – H(sp^3) borylation, moreover 1,3,5 – triethylbenzene was not possible to functionalise with Ir and required a Pt catalyst at temperatures up to 140 °C.³⁴² Thus the 1,3,5 – triethylbenzene functionalisation, despite the modest yield, is a promising result. The exclusive

functionalisation of C – H (sp^2) also contrasts with the work reported by Mbuvi and Woo, where they observed C – H (sp^3) functionalisation as main products with toluene and mesitylene as substrates (Scheme VI.3). In addition to that, porphyrinic systems required higher temperatures (110 °C) and much longer times (32 – 72 h).²³⁹

Previous work:



This work:



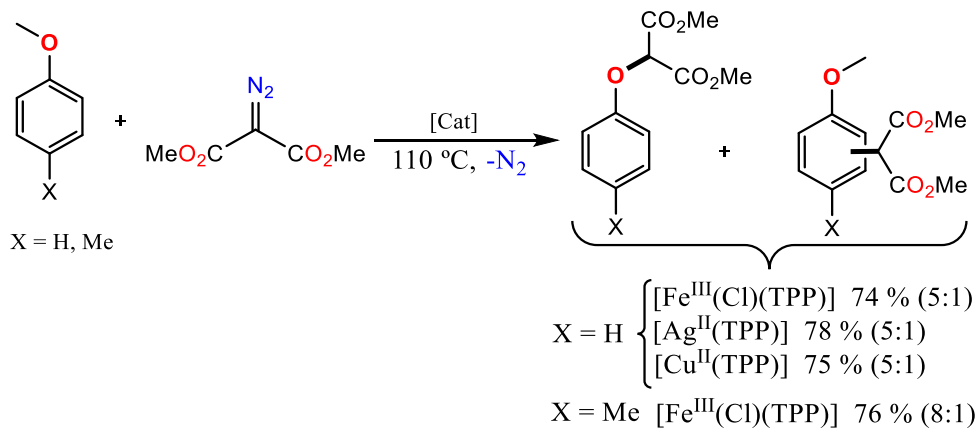
Scheme VI.3. Comparison of reaction of alkylbenzenes with diazoacetates in presence of different catalyst from previous work and this work.

The system also proved competent towards functionalisation of other polycyclic substrates, such as biphenyl, 1,2,3,4 – tetrahydronaphthalene and naphthalene, always with C – H (sp^2) selectivity and regioisomer mixtures. Naphthalene insertion is also noticeable since it is a substrate that tends to give cyclopropanation products, not observed in this work.³⁴³

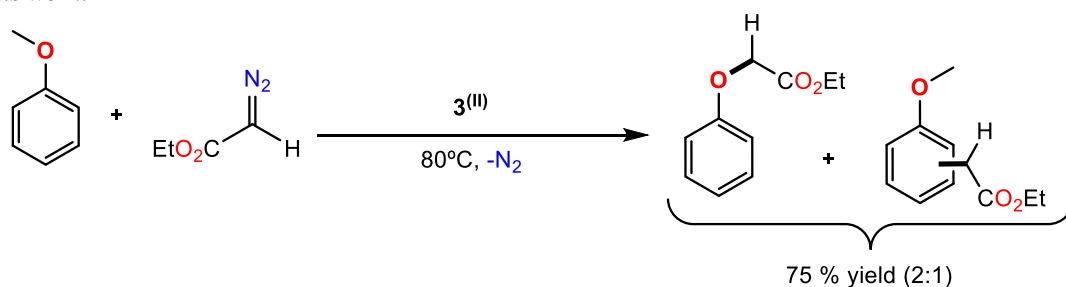
The functionalisation of anisole gave almost no *meta* product, as expected from the strong *o*, *p* activating nature of methoxy group. However anisole substrate gave a mixture of O – Me and C – H activation products with a rough ratio 2:1. In addition to these products a <5 % of expansion was detected but no fumarate or maleate. The observation of O functionalisation is in agreement with previous results reported by Mbuvi and Woo in the functionalisation of anisole and *p* – tolylanisole with dimethyl diazomalonate, catalysed by [Fe^{III}(Cl)(TPP)] and [M^I(TPP)] (M = Ag, Cu) (Scheme VI.4). In all cases the yields were comparable to previous results (74 – 78 % vs. 75 % of combined products). Interestingly, in our case the

chemoselectivity improved, as in porphyrinic complexes the ratio O – Me:C – H functionalisation was 5:1 with anisole and 8:1 in the case of *p* – tolylanisole (Scheme VI.4).²³⁹

Previous work:



This work:



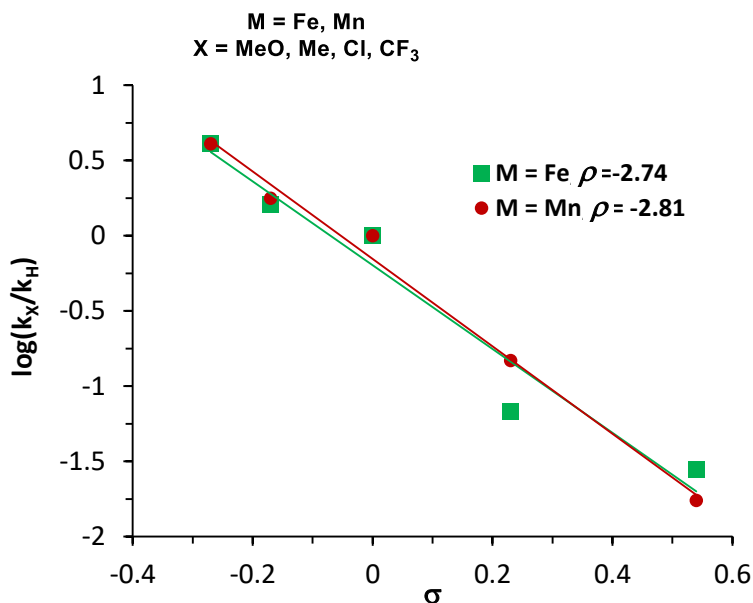
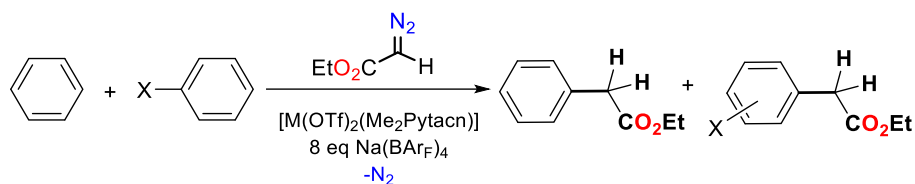
Scheme VI.4. Comparison of reaction of anisole with diazoacetates in presence of different catalyst from previous work and this work.

When unactivated arene substrates bearing electron – withdrawing groups were analysed the yields dramatically decreased. Chlorobenzene products were isolated as a mixture of the three regioisomers in 27 % yield (38 % yield by GC) with a rough ratio 39:19:42. Trifluoromethylbenzene gave a mixture of the three regioisomers in 23 % yield with ratio 25:62:13. In both substrates were obtained a combined yield of *ca.* 5 % of expansion and dimers as by – products.

VI.2.2. Mechanistic studies

To gain further insight into the details of these reactions we performed mechanistic studies. In this regard we performed competition experiments between equimolar amounts of benzene and substituted benzenes with different electronic properties (anisole, toluene, chlorobenzene and trifluorotoluene). A Hammett plot ($\log(k_X/k_H)$ vs. σ) for complexes $[M^I(OTf)_2(Me_2Pytacn)]$ ($M = Fe, Mn$) gave slopes of -2.74 and -2.81 respectively (Figure VI.3). These slopes clearly indicate that an electrophilic intermediate is involved in the rate determining step (RDS). Reactivity of diazocompounds with metallic complexes is usually associated with metalcarbene species, for example in the work of Woo *et al.*²³⁹ Our Hammett

slopes are in agreement with those obtained in this work, slopes of -1.11 and -0.82 were obtained for $[\text{Fe}^{\text{III}}(\text{Cl})(\text{TPP})]$ and $[\text{Fe}^{\text{III}}(\text{Cl})(\text{F}_{20} - \text{TPP})]$ in the functionalisation of cyclohexane with $\text{N}_2\text{C}(\text{X} - \text{C}_6\text{H}_5)\text{CO}_2\text{Me}$. In addition Hammett plot of the isolated metallocarbene $[\text{Fe}^{\text{III}}(\text{C}(\text{Ph})\text{CO}_2\text{Et})(\text{F}_{20} - \text{TPP})]$ in the competitive stoichiometric (1:1) cyclopropanation of *p*-substituted styrenes gave a slope of $\rho = -0.41$.



X - Ph	3^{III}			3Mn^{III}		
	k_X/k_H	σ	$\log(k_X/k_H)$	k_X/k_H	σ	$\log(k_X/k_H)$
MeO	4.07	-0.27	0.61	4.03	-0.27	0.61
Me	1.64	-0.17	0.21	1.77	-0.17	0.25
H	1.00	0	0.00	1.00	0	0.00
Cl	0.07	0.23	-1.17	0.15	0.23	-0.83
CF_3	0.03	0.54	-1.55	0.02	0.54	-1.76

Figure VI.3. Hammett plot from competition experiments for functionalisation of benzene with EDA and $[\text{M}(\text{OTf})_2(\text{Me}_2\text{Pytacn})]$ complexes. k_X/k_H = ratio of insertion products on benzene and X - C_6H_5 (X = MeO, Me, Cl and CF_3), calculated by GC.

We measured the kinetic isotopic effect (KIE) performing the functionalisation of equimolar mixtures of benzene and deuterated benzene. When 3^{III} was used as catalyst a KIE of 0.95 ± 0.01 was obtained while for 3Mn^{III} a KIE of 0.80 ± 0.02 was obtained. These values are in agreement with a change in the C - H bond hybridisation from sp^2 to sp^3 .

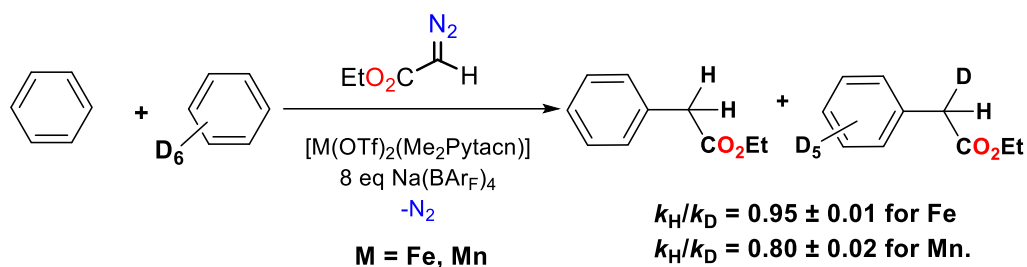


Figure VI.4. Competitive experiments for functionalisation of benzene and deuterated benzene with EDA and $[\text{M}(\text{OTf})_2(\text{Me}_2\text{Pytacn})]$ complexes. $k_{\text{H}}/k_{\text{D}}$ = ratio of insertion products on benzene and deuterated benzene, calculated by GC.

In addition we tested the functionalisation of cyclopropylbenzene as substrate to check whether a carbon – centred radical was implicated in the reaction. It is expected that, if a radical species was involved in the reactivity, the cyclopropyl ring would open at least to a certain extent. At the end of the reaction of **3^{III}** with cyclopropylbenzene we could not identify any product derived from cyclopropane ring opening, thus we rationalise that no long – living substrate carbon – radical species is involved in our reactivity (Figure VI.5).

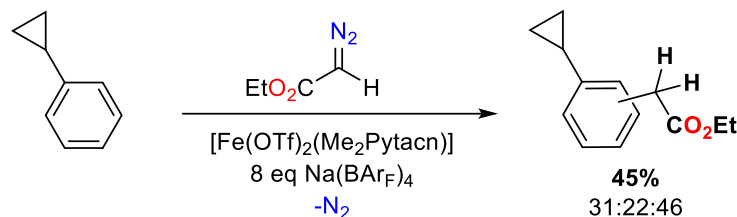


Figure VI.5. Functionalisation of cyclopropylbenzene with EDA and **3^{III}**. Ratio of isomers normalised to the number of carbons available (2 *ortho*, 2 *meta* and 1 *para*).

Taking into consideration all the experimental information we proposed a plausible mechanism. This mechanism has to take into account the relative selectivity of *ortho*, *meta* and *para* isomers obtained: generally activating alkyl groups and especially the methoxy act as *ortho* and *para* directing groups; on the other hand CF_3 acts as a strong *meta* directing group as a highly deactivating substituent. This trend resembles an electrophilic aromatic substitution. Also mechanism has to take into account the necessity of two labile positions on the complex, as the removal of only one counteranion or a pentadentate ligand does not allow the reaction to occur. Furthermore Hammett plot indicates that a highly electrophilic metal – carbene intermediate is involved on reactivity. KIE studies indicate that a change on C – H bond hybridisation from sp^2 to sp^3 takes place. Considering these observations we propose the following mechanism (Figure VI.6).

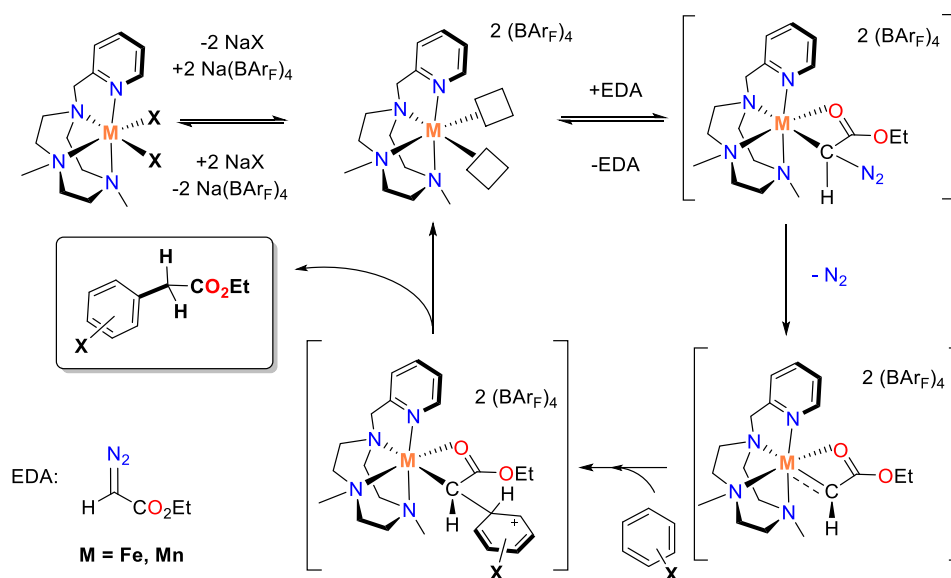


Figure VI.6. Proposed mechanism for arene functionalisation with EDA catalysed by non-heme iron and manganese complexes. The oxidation state for these species is not easily defined due to the highly covalent character of the bonds.

On first place, according to the lack of reactivity observed with **1**^(II) and using only one equivalent of $\text{Na}(\text{BArF}_4)$ we propose the formation of the divacant – site dicationic species; we propose an equilibria on the basis of high amount of $\text{Na}(\text{BArF}_4)$ needed. Subsequently it reacts with EDA to extrude N_2 and generate a metalcarbene species, such species is plausible since is in agreement with Hammett plot ($\rho = -2.74$ and -2.81), furthermore these species have been identified and isolated with metals such as rhodium, gold, cobalt or even iron, some of them very recently.^{223,344,345} Different coordination manners and metal oxidation states can be proposed for the metalcarbene but at this point we are not able to distinguish between them, here we depict one of them as illustrative structure. The coordination of the carbonyl oxygen is necessary in order to explain the need of two vacant sites. The postulated metalcarbene species would react with arene substrates in an outer sphere mechanism generating a Wheland – type intermediate in agreement with product distributions and inverse KIE results. This final intermediate is in agreement also with previous proposal with rhodium from Tran and co-workers, involving a 1, 2 – hydrogen shift.³⁴¹ Finally product would be liberated and initial catalyst recovered to close the catalytic cycle. DFT calculations are ongoing to evaluate the mechanism and the high chemo – and regioselectivities observed.

VI.3. SUMMARY

To conclude, we developed a novel non – heme iron and manganese system based on the 1,4,7 – triazacyclononane macrocycle, capable to functionalise C – H arene bonds. New C – C bonds are generated through the decomposition of ethyl diazoacetate (EDA) in the reaction with benzene rings. Products are obtained in good yields and with high selectivity towards C – H (sp^2), furthermore dimer by – products such as diethyl fumarate or maleate were not obtained, albeit ethyl glycolate from adventitious water was observed when conditions were not completely anhydrous. Despite the high chemoselectivity, the system is not regioselective, and shows some drawbacks that prevent it to be synthetically feasible at the moment. In this regard requires high substrate excess, high $Na(BArF)_4$ amounts and high temperatures (80 °C). The system is under investigation to improve it. Nevertheless is the first time this reactivity is performed with iron and manganese, moreover are obtained none or very low amounts of cycloheptatriene by – products, unlike analogous reactivity with rhodium or gold systems that give important amounts of ring – expansion product. On the other hand the system proved limited reactivity towards substrates with electron – poor rings, as chloro – and trifluorotoluene.

Isomer ratios, kinetic isotopic effect and competitive experiments suggest the mechanism proceed through an electrophilic aromatic substitution with a metallocarbene electrophilic species involved. On the basis of experimental and literature data we have proposed the catalytic mechanism.

CHAPTER VII

GENERAL CONCLUSIONS

In **Chapter III** we synthesised two iron (IV) – oxo complexes ($\mathbf{1}^{(IV)=O}$ and $\mathbf{2}^{(IV)=O}$) bearing pentadentate aminopyridine triazacyclonane – based ligands, and characterised them as low – spin ($S = 1$) by means of ^1H – NMR, UV – vis, ESI – MS and compound $\mathbf{1}^{(IV)=O}$ also by Cyclic Voltammetry, XAS and Mössbauer spectroscopy. These complexes were found to be highly reactive in the sulfoxidation of thioethers (OAT reactivity) as well as found capable, with slower rates, to abstract benzylic hydrogen atoms from cumene, ethylbenzene and toluene; despite giving low amounts of oxidised products, typical from a diffusion mechanism. A comparative analysis of kinetic parameters has been performed, as well as characterization studies of products distribution for these transformations. Moreover, remarkably different activation parameters have been obtained for the OAT and HAT reactions.

Oxygen atom exchange (OAE) capacity for $\mathbf{1}^{(IV)=O}$, $\mathbf{2}^{(IV)=O}$ and the previously reported tetradentate complex $\mathbf{3}^{(IV)=O}$ was tested and compared to a series of analogous iron (IV) – oxo complexes bearing either tetra – and pentadentate macrocyclic ligands. Activation parameters and a common mechanism with two different regimes, involving different KIE values and water concentration dependence, were determined for all of them.

Photoenhanced sulfoxidation of thioanisole substrates was studied for $\mathbf{1}^{(IV)=O}$ and $\mathbf{2}^{(IV)=O}$ in combination with $[\text{Ru}^{\text{II}}(\text{bpy})_3]^{2+}$. A mechanism supported by the data obtained was proposed, where an electron transfer from $*[\text{Ru}^{\text{II}}(\text{bpy})_3]^{2+}$ to the substrate takes place to generate the sulphide radical cation, which is finally oxidised by the iron (IV) – oxo species.

In **Chapter IV** we describe the synthesis and characterisation of two novel low – spin ($S = 1$) iron (IV) – tosylimido species ($\mathbf{1}^{(IV)=\text{NTs}}$ and $\mathbf{2}^{(IV)=\text{NTs}}$), characterised by UV – vis, HR – MS, ^1H – NMR, DFT calculations, Mössbauer spectroscopy and X – ray absorption spectra (XANES and EXAFS). These species readily decomposed giving iron (II) and iron (III) mixtures in acetonitrile. Low – spin $\text{Fe}^{\text{III}} – \text{NHTs}$, $\mathbf{1}^{(\text{III})} – \text{NHTs}$ and $\mathbf{2}^{(\text{III})} – \text{NHTs}$ were obtained when crystalline material was obtained from $\mathbf{1}^{(IV)=\text{NTs}}$ and $\mathbf{2}^{(IV)=\text{NTs}}$, these complexes were fully characterised by cyclic voltammetry, UV – vis, HR – MS, EPR and Mössbauer spectroscopy. $\mathbf{1}^{(IV)=\text{NTs}}$ and $\mathbf{2}^{(IV)=\text{NTs}}$ are highly reactive and upon addition of thioanisole substrates generate the corresponding sulfanylidene products. Reactivity comparative analysis of kinetic parameters has been performed, as well as characterization studies of the reaction products by ^1H – NMR. Interestingly, Hammett plot analysis as well as monitoring the reactions of $\mathbf{1}^{(IV)=\text{NTs}}$ and $\mathbf{2}^{(IV)=\text{NTs}}$ with MeO^iPhSMe by ^1H – NMR, EPR and Mössbauer evidenced that reactions with sulphides proceed through a single electron transfer (SET) process to generate the corresponding $\text{Fe}^{\text{III}} – \text{NHTs}$ species. This behaviour is in high contrast with that found for iron (IV) – oxo species with same substrates, that follow a two – electron oxo – transfer step. Previously reported $[\text{Fe}^{\text{IV}}(\text{NTs})(\text{N4Py})]^{2+}$ was re – examined in the same reactivity and the obtained results suggested that all complexes follow a common mechanism.

In **Chapter V** we synthesised the iron (II) – azido and iron (III) – azido complexes bearing the pentadentate aminopyridine neutral ligands MePy_2tacn and $\text{Me}_2(\text{CHPy}_2)\text{tacn}$. The prepared complexes were fully characterised by ^1H – NMR, FT – IR, mass spectrometry, UV – vis, Mössbauer spectroscopy, Raman Resonance and EPR; and some of them were structurally determined by X – ray diffraction analysis. Among the iron (II) – azido species, complex $\mathbf{1a} – \text{N}_3$ showed a spin – transition behaviour as evidenced by SQUID measurements and X – ray structures, while $\mathbf{2a} – \text{N}_3$ is high – spin at room temperature. On the other hand, both iron (III) – azido species are low – spin. The prepared complexes were photolytically

studied to generate the corresponding high – valent iron – nitrido species $[\text{Fe}^{n+2}(\text{N})(\text{L})]$, $\text{L} = \text{MePy}_2\text{tacn}$, $\text{Me}_2(\text{CHPy}_2)\text{tacn}$. While the iron (II) – azido species were photolytically inactive, the iron (III) – azido complexes were found competent to generate and stabilize the iron (V) – nitrido species in solid state, or in frozen solution upon N_2 extrusion. The new species $[\text{Fe}^{\text{V}}(\text{N})(\text{MePy}_2\text{tacn})]$ ($\mathbf{1}^{\text{V}}\equiv\text{N}$) was spectroscopically characterized by Mössbauer spectroscopy, magnetic susceptibility, EPR, X – ray absorption spectroscopy (XANES and EXAFS) and DFT computational analysis. $\mathbf{1}^{\text{V}}\equiv\text{N}$ was found to be only stable at very low temperatures in frozen solution, thus its reactivity was studied in the gas phase. Octahedral Fe^{V} species with a neutral ligand framework have been only generated previously in the gas phase by Schwarz and co – workers, and proved to be highly reactive, rapidly reacting with external molecules and also with the ligand. Therefore, to the best of our knowledge, $\mathbf{1}^{\text{V}}\equiv\text{N}$ constitutes the first octahedral example of such species that was both spectroscopically characterized and was studied its reactivity.

In **Chapter VI** we studied the C – H (sp^2) functionalization of benzene through the decomposition of the commercially available ethyl diazoacetate, mediated by non – heme iron (II) and manganese (II) complexes bearing N – donor tetradentate ligands. The best results were obtained with $[\text{Fe}^{\text{II}}(\text{OTf})_2(\text{Me}_2\text{Pytacn})]$ ($\mathbf{3}^{\text{II}}$). This complex exclusively yielded the so called insertion product and showed high chemoselectivity towards C – H (sp^2), functionalising a number of aryl substrates, with no C – H (sp^3) functionalisation detected. Furthermore, dimer by – products such as diethyl fumarate or maleate were not obtained. These results are unprecedented with first row metals such as iron and manganese, moreover the high selectivity towards insertion contrasts with that of rhodium or gold systems that give important amounts of ring – expansion product. Nonetheless several drawbacks such as high amounts of $\text{Na}(\text{BAr}_\text{F})_4$, high temperature or substrate excess needed, as well as the low regioselectivity, currently prevent the synthetically applicability of this methodology.

On the basis on experimental data (*e.g.* KIE values and regioisomer ratios) a mechanism was proposed through an electrophilic aromatic substitution with an electrophilic metallocarbene species involved.

CHAPTER VIII

EXPERIMENTAL SECTION

VIII.1. EXPERIMENTAL SECTION CHAPTER III

VIII.1.1. Instrumentation

FT – IR spectrum were taken in a Mattson – Galaxy Satellite FT – IR spectrophotometer containing a MKII Golden Gate Single Reflection ATR System. Elemental analyses were conducted in a Carlo Erba Instrument, Mod. CHNS 1108. UV – vis spectroscopy was performed on a Cary 50 Scan (Varian) UV – vis spectrophotometer or on an Agilent 8453 diode array spectrophotometer with 1 cm quartz cells. Cyclic voltammetry was recorded using a CH Instruments CHI600D at room temperature. A cryostat from Unisoku Scientific Instruments was used for the temperature control. Electrospray ionization mass spectrometry (ESI – MS) experiments were performed on a Bruker Daltonics Esquire 3000 Spectrometer. Elemental analyses were conducted in a Carlo Erba Instrument, Mod. CHNS 1108. Crystals of **1**^(II) and **2**^(II) were used for low temperature (100(2) K) X – ray structure determination. The measurement was carried out on a BRUKER SMART APEX CCD diffractometer using graphite – monochromated Mo K α radiation ($\lambda = 0.71073 \text{ \AA}$) from an X – Ray Tube. The measurements were made in the range 2.11 to 28.64° for θ . Full – sphere data collection was carried out with ω and ϕ scans. A total of 45423 reflections were collected of which 14395 [R(int) = 0.0750] were unique. Programs used: data collection, Smart version 5.631 (Bruker AXS 1997 – 02); data reduction, Saint + version 6.36A (Bruker AXS 2001); absorption correction, SADABS version 2.10 (Bruker AXS 2001). Structure solution and refinement was done using SHELXTL Version 6.14 (Bruker AXS 2000 – 2003). The structure was solved by direct methods and refined by full – matrix least – squares methods on F^2 . The non – hydrogen atoms were refined anisotropically. The H – atoms were placed in geometrically optimized positions and forced to ride on the atom to which they are attached. Laser flash photolysis experiments were carried out with the second harmonic (532 nm) of a Q – switched Nd:YAG laser (Spectra Physics QuantaRay (Indi); pulse width ca. 9 ns and 15 mJ pulse⁻¹). The signal from the monochromator/photomultiplier detection system was captured by a Tektronix TDS640A digitizer and transferred to a PC computer that controlled the experiment and provided suitable processing and data storage capabilities. ¹H and ¹³C NMR spectra were recorded on a Bruker Avance 400 MHz spectrometer as solutions at 25°C and referenced to residual solvent peaks. GC product analyses were performed on an Agilent 7820A gas chromatograph equipped with a HP – 5 capillary column 30mx0.32mmx0.25 μ m and a flame ionization detector. ⁵⁷Fe Mössbauer experiments were performed at 80 K on a zero – field Mössbauer spectrometer equipped with a Janis SVT – 400 cryostat as already described.³⁴⁶ Analysis of the data was performed with the program WMOSS (WEB Research, Edina, MN, USA). Fe K – edge X – ray absorption spectra were collected on beamline 9 – 3 of the Stanford Synchrotron Radiation Lightsource (SSRL) at the SLAC National Accelerator Laboratory with a SPEAR storage ring current of ~450 mA at a power of 3.0 GeV. The incoming X – rays were unfocused using a Si(220) double crystal monochromator, which was detuned to 40% of the maximal flux to attenuate harmonic X – rays. Four (4) scans were collected from 6882 eV to 8000 eV at a temperature (10 K) that was controlled by an Oxford Instruments CF1208 continuous flow liquid helium cryostat. Harmonic rejection was achieved by a 9 keV cutoff filter. Data were obtained as fluorescence excitation spectra with a 100 – element solid – state Ge detector array (Canberra). In fluorescence mode, photon scattering “noise”

was reduced using a 3 μm Mn filter and a Soller slit. An iron foil was placed in the beam pathway prior to I_0 and scanned concomitantly for an energy calibration, with the first inflection point of the edge assigned to 7112.0 eV. Photoreduction was monitored by scanning the same spot on the sample twice and comparing the first derivative peaks associated with the edge energy during collection, but none was observed in the present study. The detector channels from the scans were examined, calibrated, averaged, and processed for EXAFS analysis using EXAFSPAK to extract $\chi(k)$. Theoretical phase and amplitude parameters for a given absorber – scatterer pair were calculated using FEFF 8.40 and were utilized by the “opt” program of the EXAFSPAK package during curve fitting. Parameters for $\mathbf{1}^{\text{IV}}=\mathbf{O}$ were calculated using similar coordinates of the available crystal structure of the corresponding Fe^{II} complex ($\mathbf{1}^{\text{II}}$). In all analyses, the coordination number of a given shell was a fixed parameter and was varied iteratively in integer steps, while the bond lengths (R) and mean – square deviation (σ^2) were allowed to freely float. The amplitude reduction factor S_0 was fixed at 0.9, while the edge – shift parameter E_0 was allowed to float as a single value for all shells. Thus, in any given fit, the number of floating parameters was typically equal to (2 x num shells) + 1. Pre – edge analysis was performed on data normalized in the “process” program of the EXAFSPAK package, and pre – edge features were fit between 7108 eV to 7118 eV using the *Fityk* program with pseudo – Voigt functions composed of 50:50 Gaussian/Lorentzian functions.

VIII.1.2. Materials

Reagents were purchased from commercial sources and used as received, without any further purification. H_2^{18}O (98% ^{18}O – enriched) was received from ICON Isotopes (USA). Cerium Ammonium Nitrate (CAN) >99.99% trace metals basis and $n\text{Bu}_4\text{IO}_4$ were purchased from Sigma – Aldrich and used without further purification. Compounds methyl *p* – tolyl sulfide, 4 – chlorothioanisole and formaldehyde were purchased from Fluorochem, Alfa Aesar and Scharlab respectively, while the rest of the compounds were purchased from Sigma – Aldrich. Alkylbenzene substrates were filtered in basic alumina before doing oxidation reactions. Solvents were purchased from SDS and Scharlab, purified and dried by passing through an activated alumina purification system (MBraun SPS – 800) and stored in an anaerobic glovebox under N_2 . Preparation of 1,4 – bis(2 – pyridylmethyl) – 1,4,7 – triazacyclononane,³⁴⁷ $\text{Me}_2(\text{CHPy}_2)\text{tacn}$ ³⁴⁸ and $[\text{Fe}^{\text{IV}}(\text{O})(\text{Me}_2(\text{CHPy}_2)\text{tacn})]^{2+}$ ($\mathbf{1}^{\text{IV}}=\mathbf{O}$)⁸³ were carried out as previously described. Water (18.2 $\text{M}\Omega\cdot\text{cm}$) was purified with a Milli – Q Millipore Gradient AIS system. Iodosylbenzene (PhIO) was synthesized according to reported procedures.³⁴⁹

VIII.1.3. Experimental procedures

$[\text{Fe}^{\text{II}}(\text{MePy}_2\text{tacn})(\text{CH}_3\text{CN})](\text{SO}_3\text{CF}_3)_2$ ($\mathbf{1}^{\text{II}}$). Synthesis of this complex was carried under N_2 . 200mg (0.46 mmols) of $\text{Fe}(\text{CH}_3\text{CN})(\text{SO}_3\text{CF}_3)_2$ were solved in 1ml of THF and added to a vial with 150mg (0.46 mmols) of MePy_2Tacn solved in the minimum of THF. After 3h stirring was stopped and the solid was separated from the dark red solution and dried under vacuum. Once dried, solid was solved in CH_2Cl_2 with

some drops of CH₃CN, filtered with celite and precipitated with ether diffusion. The complex crystallized as big dark red crystals (0.18 mmols, 60 %).

ESI – MS (m/z experimental (calculated)): [M-(CH₃CN)-(SO₃CF₃)]⁺ = 530.2 (530.1), [M-(CH₃CN)-2(SO₃CF₃)]²⁺ = 190.5 (190.6). ¹H – NMR (CD₃CN, 400 MHz, 273 K) δ, ppm: 8.90 (d, 1H, PyH), 7.94 – 7.18 (m, 7H, PyH), 4.72 (d, 1H, CH₂ – Py), 4.56 (m, 2H, CH₂ – Py), 4.06 (d, 1H, CH₂ – Py), 3.38 – 2.94 (m, 9H, N – CH₂), 2.59 – 2.56 (m, 4H, N – CH₂ and N – CH₃), 1.60 (m, 1H, N – CH₂).

[Fe^{II}(Me₂(CHPy₂)tacn)(CH₃CN)](SO₃CF₃)₂ (2^{II}). In an anaerobic glovebox, a solution of Fe(SO₃CF₃)₂ (134 mg, 0.31 mmols) in anhydrous THF (1 mL) was added dropwise to a vigorously stirred solution of Me₂(CHPy₂)tacn (100 mg, 0.31 mmols) in THF (1 mL). After a few seconds the solution became cloudy and a red – brown precipitate appeared. After stirring for 1 hour the solution was filtered off and the resultant solid was dried under vacuum. This solid was dissolved in CH₂Cl₂ and filtered through Celite. Slow diethyl ether diffusion over the resultant solution afforded, in a few days, 115 mg of red – brown crystals (0.16 mmols, 52 %).

ESI – MS (m/z experimental (calculated)): [M-(CH₃CN)-(SO₃CF₃)]⁺ = 530.0 (530.1), [M-(CH₃CN)-2(SO₃CF₃)]²⁺ = 190.4 (190.6). ¹H – NMR (CD₃CN, 400 MHz, 298 K) δ, ppm: 9.00 (d, 2H, PyH_α), 7.80 – 7.88 (m, 4H, PyH_γ and PyH_β'), 7.34 (m, 2H, PyH_β), 6.10 (s, 1H, CH – Py₂), 2.74 – 2.97 (m, 18H, N – CH₂ and N – CH₃).

[Fe^{IV}(O)(MePy₂tacn)](SO₃CF₃)₂ (1^{IV}=O). In an anaerobic glove box 7.28mg (1·10⁻² mmols) of [Fe^{II}(MePy₂tacn)(CH₃CN)](SO₃CF₃)₂ (1^{II}) were solved in 1 ml of CH₃CN and 200 μl of this solution were added to a PhIO suspension (8.8mgr, 2·10⁻¹ mmols) in 1.8ml of CH₃CN. Solution was stirred for 10 minutes and the pale green resulting solution was filtered with a disk filter. Fe^{IV} complex was prepared in situ and obtained in solution due to its instability and because decomposes when it is tried to isolate, until date no crystal data have been obtained.

ESI – MS (m/z experimental (calculated)): [M-(SO₃CF₃)]⁺ = 546.1 (546.1), [M-2(SO₃CF₃)]²⁺ = 198.5 (198.6). ¹H – NMR (CD₃CN, 400 MHz, 300 K) δ, ppm: 46.45 (s, 1H, PyH_{βa}), 13.34 (s, 1H, PyH_{γa}), 11.22 (s, 1H, PyH_{γb}), -1.37 (s, 1H, PyH_{βb} and PyH_{β'b}), -13.27 (s, 1H, PyH_{βa}).

[Fe^{IV}(O)(Me₂(CHPy₂)tacn)](SO₃CF₃)₂ (2^{IV}=O). This complex was prepared following analogous procedure as [Fe^{IV}(O)(MePy₂tacn)](SO₃CF₃)₂ (1^{IV}=O). In an anaerobic glove box 7.28 mg (1·10⁻² mmols) of [Fe^{II}(Me₂(CHPy₂)tacn)(CH₃CN)](SO₃CF₃)₂ (2^{II}) were solved in 1ml of CH₃CN and 200 μl of this solution were added to a PhIO suspension (8.8 mgr, 2·10⁻¹ mmols) in 1.8ml of CH₃CN. Solution was stirred for 5 minutes and the greenish solution was filtered with a disk filter. Fe^{IV} complex was prepared in situ and obtained in solution due to its instability and because decomposes when it's tried to isolate, until date no crystal data have been obtained.

ESI – MS (*m/z* experimental (calculated)): [M-(SO₃CF₃)]⁺ = 546.1 (546.1), [M-2(SO₃CF₃)]²⁺=198.5 (198.6). ¹H – NMR (CD₃CN, 400 MHz, 300 K) δ, ppm: 31.98 (s, 2H, PyHβ), 10.65 (s, 2H, PyHγ), -9.52 (s, 2H, PyHγ).

Reactivity studies of Fe^{IV} complexes in HAT/OAT. The oxidation capacity of **1^{(IV)=O}** and **2^{(IV)=O}** complex has been studied with typically substrates that gives HAT (Hydrogen Atom Transfer) and OAT (Oxygen Atom Transfer) reactions.

In all reactions done with complex **1^{(IV)=O}** and **2^{(IV)=O}** were synthesized as described above. The OAT and HAT reactions had been studied by following the decay of the Fe^{IV} oxocomplexes bands at 738 and 748 nm assuming that the disappearing of complex **1^{(IV)=O}** and **2^{(IV)=O}** is due to the oxidation of the substrate.

The points obtained by UV – vis spectroscopy were adjusted to a first order exponential decay regression to obtain the *k*_{obs} values. The plot of *k*_{obs} vs. substrate concentration gives *k*₂ values as the slope of the linear regression fits, which is the rate constant of oxidation. On HAT reactivity *k*₂ values were divided by the number of equivalent hydrogen atoms that can react, to obtain the *k*₂'.

Comparative studies of activation barriers. For the oxoferryl complexes **1^{(IV)=O}**, **2^{(IV)=O}** and **4^{(IV)=O}** have been developed thermodynamic studies to determine Δ*H*[‡], Δ*S*[‡] and Δ*G*[‡] on the oxidation reactions for the studied substrates.

In all reactions done complexes were synthesized as described. **4^{(IV)=O}** was prepared using 2 eq. of PhIO as previously reported.⁸¹ The OAT and HAT activation parameters had been studied by following the decay of the iron (IV) – oxo complexes band at 738 nm for **1^{(IV)=O}**, the 748 nm band for **2^{(IV)=O}** and the 695 nm band for **4^{(IV)=O}**, assuming that the disappearing of complexes is due to the oxidation of the substrate.

To calculate rate constants the decay on UV – vis spectrum oxidation reactions are performed at various temperatures and with a fixed substrate concentration and a constant Fe^{IV} concentration.

Then results are plotted as ln(*k*/T) vs 1/T and thermodynamic parameters of transition state can be readily obtained with Eyring equation:

$$\ln\left(\frac{k}{T}\right) = -\frac{\Delta H^{\ddagger}}{R} \cdot \frac{1}{T} + \ln\left(\frac{k_B}{h}\right) + \frac{\Delta S^{\ddagger}}{R}$$

$$k = k_{\text{obs}}/[S]$$

Preparation of $[\text{Fe}^{\text{IV}}(\text{O})(\text{Me}_2\text{Pytacn})(\text{MeCN})](\text{OTf})_2$ ($\mathbf{3}^{\text{IV}}=\text{O}$). Synthesis of $\mathbf{3}^{\text{IV}}=\text{O}$ was adapted from Company *et al.*⁷⁷ A 1 mM solution of $[\text{Fe}^{\text{IV}}(\text{O})(\text{Me}_2\text{Pytacn})(\text{MeCN})](\text{OTf})_2$ was prepared under anaerobic conditions by dissolving 3.6 mg $[\text{Fe}^{\text{II}}(\text{Me}_2\text{Pytacn})(\text{OTf})_2]$ (6 μmol) in 6 mL of anhydrous CH_3CN . 15 μL of H_2O (0.8 μmol) were added to this solution, which was stirred for 5 min at 0 °C. $\text{CH}_3\text{CO}_3\text{H}$ (12 μmol , 150 μL of an 8 mM CH_3CN solution) was then added at 0 °C and the solution was stirred for 1 h.

ESI – MS Studies – H_2^{18}O concentration dependence. The procedure for monitoring the kinetics of OAE between $[\text{Fe}^{\text{IV}}(^{16}\text{O})(\text{L})]^{2+}$ and H_2^{18}O by ESI – MS has been adapted from Tagore *et al* and Seo *et al.*^{350,351}

1 mM solution of $[\text{Fe}^{\text{IV}}(^{16}\text{O})(\text{L})]^{2+}$ was generated using an excess of PhIO, as detailed above. A stock solution of 1.11 M H_2^{18}O was then prepared by dissolving H_2^{18}O (40 μL) in CH_3CN (2.0 mL). To begin the reaction, a vial with $\text{Fe}^{\text{IV}}(\text{O})$ solution was placed in a temperature – controlled bath set at the desired temperature. The desired amount of H_2^{18}O from stock solution was then added and the reaction progress for oxygen atom exchange was monitored by ESI – MS mass spectrometer using a spray chamber voltage of 4000 V and a gas carrier temperature of 200 °C.

Alternatively, injection of the reaction mixtures into the ESI – MS was accomplished by inserting a capillary tube through the rubber – septum capping each of the vials. The capillary tube was then inserted into the ESI – MS outlet and the other end of the capillary tube was submerged into the acetonitrile solution containing the $[\text{Fe}^{\text{IV}}(^{16}\text{O})(\text{L})]^{2+}$ complex and H_2^{18}O . A syringe of air was then used to slightly pressurize the vial, causing the solution to transfer through the capillary tube into the ESI – MS.

OAE rates for complex $\mathbf{3}^{\text{IV}}=\text{O}$ could not be determined by ESI – MS, because it decomposes during the time required for full exchange to take place. Instead, exchange rates were measured by the following alternative method. Specific amounts of H_2^{18}O were added to a solution of $\mathbf{3}^{\text{IV}}=\text{O}$ (prepared as detailed above) at 0 °C. At specific times, 0.4 mL aliquots were taken and reacted with 5 μL of thioanisole (43 μmol) to generate the respective sulfoxide products. The amounts of ^{16}O – and ^{18}O – sulfoxide were determined by GC – MS and plotted versus time to obtain the corresponding k_{obs} values.

ESI – MS Studies – KIE determination. Upon formation of a 1 mM solution of $[\text{Fe}^{\text{IV}}(^{18}\text{O})(\text{L})]^{2+}$, the solution was split into two vials (1.5 mL each), labeled H and D. Two separate stock solutions of 1.85 M H_2^{16}O and 1.85 M D_2^{16}O were then prepared by dissolving H_2^{16}O (100 μL) and D_2^{16}O (100 μL) in CH_3CN (3.0 mL). To begin the reaction, the vials H and D were placed in a temperature – controlled bath. The H_2^{16}O stock solution was then added to vial H (1.5 mL corresponding to 50 μL of H_2^{16}O) and the D_2^{16}O stock solution was added to vial D (1.5 mL corresponding to 50 μL of D_2^{16}O) and the reaction progress in each vial was monitored by ESI – MS.

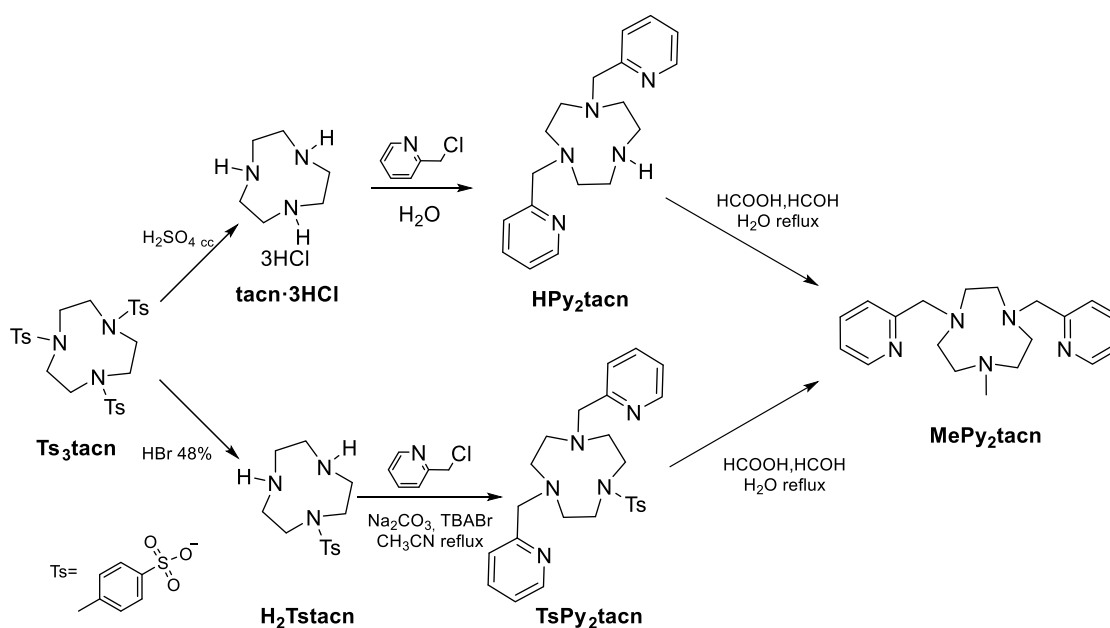
For complex $\mathbf{3}^{\text{IV}}=\text{O}$, a different procedure was followed. In a representative case, a 1 mM solution of $[\text{Fe}(^{18}\text{O})(\text{Me}_2\text{Pytacn})(\text{MeCN})](\text{OTf})_2$ was prepared as described above but with H_2^{18}O instead of H_2^{16}O . At this point the fraction of ^{18}O – labeled $\mathbf{3}^{\text{IV}}=\text{O}$ complex was determined to be *ca.* 80 %. After 1 h, either

H₂¹⁶O or D₂¹⁶O was added to the solution (150 μL, 8.3 mmol) and kept at 0 °C; at this point water concentration was 1.32 M. At specific times, 0.4 mL aliquots were taken and reacted with 5 μL of thioanisole (43 μmol) to generate the respective sulfoxide products. The amounts of ¹⁶O – and ¹⁸O – labeled sulfoxide were calculated by GC – MS and plotted versus time to obtain the corresponding *k*_{obs} and KIE.

Preparation of [Fe^{IV}(O)(MePy₂tacn)]²⁺ (1^(IV)=O) under photocatalytic conditions. In an anaerobic glovebox, a solution of 1^(II) (0.72 mg, 1·10⁻³ mmol) in CH₃CN (625 μL) was placed in a UV – vis cuvette. Addition of 5 mol% [Ru(bpy)₃]Cl₂ (0.05 μmol, 100 μL of a 0.5 mM solution in deaerated water), 10 equiv Na₂S₂O₈ (10 μmol, 100 μL of a 100 mM solution in deaerated water) and deaerated water (1.6 mL) afforded the initial reaction mixture (solvent ratio CH₃CN:H₂O 1:3, 0.4 mM in 1^(II)). Irradiation at 447 nm caused immediate changes in the UV – vis spectrum that led to the formation of 1^(IV)=O as evidenced by the appearance of its characteristic band at 715 nm (see Figure SIII.2).

Kinetic Studies under photocatalytic conditions. The required amount of 1^(IV)=O (625 μL of a 1.6 mM solution of 1^(IV)=O in CH₃CN obtained by direct oxidation of 1^(II) with PhIO) was diluted in deaerated Milli – Q water (1.67 mL). Then, the desired quantity of photosensitizer (dissolved in CH₃CN:H₂O 1:3) and/or sulfide (^XPhSMe, dissolved in CH₃CN) was added. Finally, the appropriate amounts of CH₃CN and H₂O were added to reach a CH₃CN:H₂O ratio of 1:3 and an initial concentration of 1^(IV)=O of 0.4 mM. The progress of the reaction was monitored by UV – vis spectroscopy at 25°C. Analogous procedure was followed with 2^(IV)=O.

Identification and quantification of sulfoxides under photocatalytic conditions. Reaction of 1^(IV)=O with sulfides (^XPhSMe) caused a decay of its characteristic absorption band (λ_{max} = 715 nm). After full decay of this band, an internal standard was added to the solution (trimethoxybenzene or biphenyl) and the amount of formed sulfoxide was quantified by ¹H – NMR spectroscopy or gas chromatography.

Syntheses of 1 – methyl – 4, 7 – bis(pyridyl – 2 – methyl) – 1, 4, 7 – triazacyclononane, MePy₂tacnScheme VIII.1. Scheme of MePy₂tacn synthesis.

1, 4, 7 – triazacyclononane trihydrochloride, tacn·3HCl. 1, 4, 7 – triazacyclononane trihydrochloride is synthesised refluxing 1, 4, 7 – tritosyl – 1,4,7 – triazacyclononane (14.59 gr) in H₂SO₄ (25 ml) for 30 minutes at 170°C. The reaction mixture is added to a 120 ml of cold ethanol and 180ml of diethylether are added dropwise. The solution is stored at fridge overnight. The white – beige solid is vacuum – filtered, solved in 60 ml of distilled water and refluxed 30 minutes at 120°C. The solid impurities are removed by filtration and the solvent is removed under reduced pressure. A brown solid appears and 11 ml of HCl cc and 65 ml of absolute ethanol are added, filtered and washed with ethanol and diethylether. 4.76gr (81%) of a beige solid are obtained.

¹H – NMR (CDCl₃, 400MHz, 300 K) δ, ppm: 1.57(s, 12H, N – CH₂).

Anal. Calcd for C₆H₁₅·3HCl·H₂SO₄ (MW = 311.51 g/mol): C, 21.41; H, 5.99; N, 12.48%. Found: C, 21.56; H, 5.60; N, 12.45%.

1, 4 – bis(2 – pyridylmethyl) – 1, 4, 7 – triazacyclononane, HPy₂tacn. In a 100mL flask tacn·6HCl (1 g, 2.87 mmols), 2 – Pycolyl chloride hydrochloride (0.94g, 5.74 mmols), and water (30 ml) were mixed and stirred to achieve a complete dissolution. Then NaOH 2M was added to set pH to 9. The resulting red solution was stirred for 3 days at room temperature and then, NaOH 2M was added again to readjust the pH to 9. The mixture was stirred for another 3 days. After that the reaction was quenched by the addition of NaOH 2 M to pH 13. The solution was extracted with CH₂Cl₂ (3 x 60 ml). The combined organic layers were then dried over anhydrous MgSO₄, filtered and the solvent was removed under reduced pressure. The resulting crude red mixture was purified by basic alumina column chromatography (AcOEt:MeOH, 90:10 with 1 % of NH₃) to provide 0.344 g (1.105 mmols, 39%) of the desired product.

^1H -NMR (CDCl_3 , 300 MHz, 300 K) δ , ppm: 8.53 (d, 2H, PyH α), 7.61 (dt, 2H, PyH γ), 7.44 (d, 2H, PyH β), 7.15 (m, 2H, H β'), 3.88 (s, 4H, CH $_2$ -Py), 2.81 – 2.73 (m, 8H, N-CH $_2$), 2.66 (s, 4H, N-CH $_2$).

1 – methyl – 4, 7 – bis(pyridyl – 2 – methyl) – 1, 4, 7 – triazacyclononane, MePy $_2$ tacn. 1, 4 – bis(2 – pyridylmethyl) – 1, 4, 7 – triazacyclononane (0.34 g, 1.09 mmols) was solved in formaldehyde 37 % (3 ml), 98% formic acid (3 ml) and water (2.5 ml) and the resulting yellow solution was refluxed for 30 hours. After cooling to room temperature, 3 mL HCl cc were added and the mixture was left stirring for 10 minutes. The solvent was removed under vacuum and a small amount of water (10 ml) was added to the resulting residue. The solution was brought to pH = 14 by the addition of NaOH 4 M. After stirring 20 min at room temperature the aqueous layer was further extracted with 3 x 50 ml CH $_2$ Cl $_2$. The combined organic layers were dried over anhydrous MgSO $_4$ and the solvent was removed under reduced pressure. The resulting residue was treated with n – hexane (75 ml) and stirred for 12 hours. The mixture was filtered and the solvent from de yellow filtrates was removed under reduced pressure to yield 0.162 g of a yellow – orange oil (0.50 mmols, 46%).

^1H -NMR (CDCl_3 , 300 MHz, 300 K) δ , ppm: 8.50 (d, 2H, PyH α), 7.64 (dt, 2H, PyH γ), 7.49 (d, 2H, PyH β), 7.10 (dd, 2H, PyH β'), 3.82 (s, 4H, CH $_2$ -Py), 2.90 – 2.82 (m, 8H, N-CH $_2$), 2.74 (s, 4H, N-CH $_2$), 2.34 (s, 3H, CH $_3$).

Alternative synthesis of 1 – methyl – 4, 7 – bis(pyridyl – 2 – methyl) – 1, 4, 7 – triazacyclononane, MePy $_2$ tacn

1 – (*p* – toluensulfonyl) – 1, 4, 7 – triazacyclononane, TsH $_2$ tacn. Ts $_3$ tacn (24.6 g, 41.6 mmol) and phenol (35.2 g, 374 mmol) were mixed in 500 mL flask. A solution of HBr in acetic acid (33 %, 380 ml) was added with extreme care as an important evolution of HBr $_{(g)}$ takes place. The mixture was gently heated with stirring to 90 °C which caused the complete dissolution of all the starting reagents giving rise to the formation of a dark solution. A colorless precipitate of 1 – (*p* – toluensulfonyl) – 1, 4, 7 – triazacyclononane-2HBr appeared within 2 – 4 h. After heating for 36 h, the mixture was cooled to room temperature and filtered. The solid was washed with diethyl ether (125 ml) and then dissolved in aqueous NaOH 1 M (320 ml). The resultant pink aqueous mixture was then extracted with CH $_2$ Cl $_2$ (3 x 190 ml) the organic layer was dried with anhydrous MgSO $_4$, filtered and evaporated under reduced pressure. Drying the resultant oil under vacuum afforded 9.88 g the pure product (36.9 mmol, 84 %). ^1H -NMR (CDCl_3 , 400 MHz, 300K) δ , ppm: 7.70 (d, 2H, ArH), 7.34 (d, 2H, ArH), 3.23 – 3.18 (m, 4H, TsN-CH $_2$), 3.12 – 3.09 (m, 4H, CH $_2$ -NH), 2.90 (s, 4H, N-CH $_2$), 2.44 (s, 3H, Ar-CH $_3$), 1.85 (s, 2H, NH).

1, 4 – di(picoly) – 7 – (p – toluenesulfonyl) – 1, 4, 7 – triazacyclononane (TsPy₂tacn). To 2 – picolyl chloride hydrochloride (4.05 g, 24.8 mmol), Tstacn (3.5 g, 12.4 mmol) Na₂CO₃ (5.3 g) and tetrabutylammonium bromide (185 mg) in a 100 ml flask was added anhydrous acetonitrile (120 ml) under N₂. The resulting mixture was heated at reflux (90 °C) under N₂ for 24 h. After cooling to room temperature, the resulting orange mixture was filtered and the filter cake was washed with CH₂Cl₂. The combined filtrates were evaporated under reduce pressure and NaOH (2 M, 150 ml) was added to the resulting residue, the solution was extracted with CH₂Cl₂ (5 x 100 ml). The combined organic layers were dried over MgSO₄ and the solvent was removed under reduced pressure. 5.90 g of dark brown oil appeared which were used directly for the next reaction.

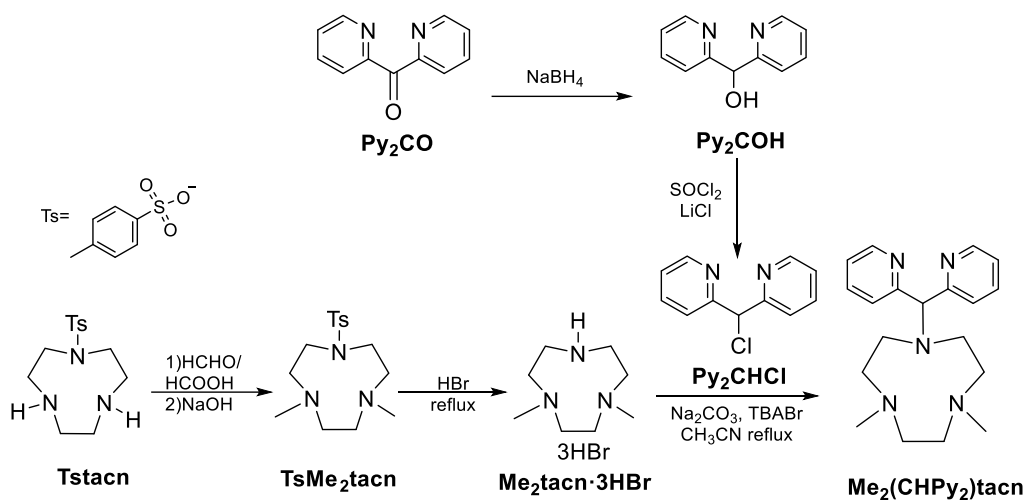
Alternatively, in a different synthetic batch, on 1 g scale reaction, the resulting residue was treated with n – hexane (100 ml) and stirred for 12 h to get a white solid which was filtered off and dried under vacuum. 1.34 g of the desired product (2.88 mmols, 82%) were obtained.

¹H – NMR (CDCl₃, 300 MHz, 300 K): δ = 8.50 (d, J = 4.8 Hz, 2H; PyH), 7.66 – 7.60 (m, 4H; TsH and PyH), 7.47 (d, 2H; TsH), 7.26 (d, 2H; PyH), 7.15 – 7.11 (m, 2H; PyH), 3.86 (s, 4H; CH₂ – Py), 3.22 (m, 4H; N – CH₂), 3.12 (m, 4H; N – CH₂), 2.79 (s, 4H; N – CH₂), 2.40 ppm (s, 3H; N – CH₃).

1, 4 – di(picoly) – 1, 4, 7 – triazacyclononane (HPy₂tacn). To the dark brown oil (5.9 g) was added 60 ml of H₂SO₄ cc and refluxed for 30 min at 160 – 170 °C (30 min exactly with bath already at 160 – 170 °C). The solution was cooled at RT and carefully poured to 120 ml of cold EtOH. Et₂O was added dropwise (180 ml) to precipitate the ligand as solid. The solution was left overnight in the fridge and filtered. The brown pale solid is extracted with 100 ml NaOH 2 M and DCM (4 x 100 ml). The combined organic layers were dried over anhydrous MgSO₄ and the solvent was removed under reduced pressure. The resulting yellowish oil was solved in minimum EtOH and precipitated by adding HBr/CH₃COOEt dropwise and then filtered.

¹H – NMR (CDCl₃, 300 MHz, 300 K) δ, ppm: 8.53 (d, J= 4.5 Hz, 2H, PyH_α), 7.61 (dt, J= 7.8 Hz, 2H, PyH_γ), 7.44 (d, J= 7.8 Hz, 2H, PyH_β), 7.15 (m, 2H, H_β'), 3.88 (s, 4H, CH₂ – Py), 2.81-2.73 (m, 8H, N – CH₂), 2.66 (s, 4H, N – CH₂).

Synthesys of 1 – (di(2 – pyridyl)methyl) – 4, 7 – dimethyl – 1, 4, 7 – triazacyclononane, Me₂(CHPy₂)tacn



Scheme VIII.2. Scheme of Me₂(CHPy₂)tacn synthesis.

Di(2 – pyridyl)methanol. Py₂COH. To a solution of di(2 – pyridyl)ketone (5 gr, 27.1 mmol) in methanol (50 mL) was slowly added NaBH₄ (27.1 mmol) at 0 °C. After all the NaBH₄ was added, the ice bath was removed and stirring continued overnight. Removal of the solvent under reduced pressure was followed by addition of water (20 mL) and the mixture was acidified with 2 M HCl and stirred for 10 min. The clear solution was made alkaline with dilute ammonia and extracted with CH₂Cl₂ (3x50 mL). The combined CH₂Cl₂ layers were dried (Na₂SO₄) and the solvent evaporated to give di(2 – pyridyl)methanol (4.6 g, 0.25 mol, 92 %) as a yellow oil, which was used without further purification.

¹H – NMR (CDCl₃) δ, ppm: 5.88 (s, 2H, CH and OH), 7.11 – 7.19 (m, 2H, PyH), 7.47 – 7.67 (m, 4H, PyH), 8.50 – 8.54 (m, 2H, PyH).

Di(2 – pyridyl)methyl chloride. Py₂CHCl. A 100 mL flame dried round bottom flask was charged with 7.8 g of LiCl (185 mmol) absolutely dried and 2 g of Di(2 – pyridyl)methanol (10.7 mmol). About 50 ml of THF was added under N₂ to obtain a pale yellow solution. Then, NEt₃ (3.7 mL, 25.6 mmol) was added carefully and stirring always under N₂. After that, the mixture was cooled to 0 °C. Finally, MeSO₂Cl (2 mL, 26 mmol) was added dropwise at 0 °C. The stirring continued for 2 hours at the same temperature and then for 1 day at room temperature. The reaction was quenched by the addition of H₂O (15 ml) and neutralized using NaHCO₃. The resulting solution was extracted 3 x 60 ml CH₂Cl₂. The combined organic layers were then washed with a saturated NaCl solution. The red organic phase was then dried over MgSO₄, filtered and the solvent removed under vacuum. The crude mixture was purified by column chromatography (AcOEt) to provide 1.3 g (6.35 mmol, 59 %) of the desired product.

¹H-NMR (CDCl₃, 400 MHz, 300K) δ, ppm: 6.20 (s, 1H), 7.14 - 7.20 (m, 2H), 7.60 - 7.73 (m, 4H), 8.51 - 8.54 (m, 2H).

1, 4 – dimethyl – 7 – (*p*-toluenesulfonyl) – 1, 4, 7 – triazacyclononane, TsMe₂tacn. Ts – tacn (8.5 g, 30 mmols) was dissolved in 37 % formaldehyde (25 mL) and 98% formic acid (25 mL) and the resulting Orange solution was refluxed for 24 h. After cooling to room temperature, 10 mL HCl cc were added and the mixture was left stirring for 10 min. The solvent was removed under vacuum and a small amount of water (10 mL) was added to the resulting residue. The solution was brought to pH > 14 by addition of NaOH 4 M. This caused the slow formation of a white precipitate corresponding to the desired product. After stirring for 20 h at room temperature, filtration of the mixture gave a white precipitate which was dissolved in 50 mL CH₂Cl₂ giving a pale yellow solution which was treated with 50 mL NaOH 4 M. The aqueous layer was further extracted with 2 x 50 ml CH₂Cl₂. The combined organic layers were dried over anhydrous MgSO₄ and the solvent was removed under reduced pressure to yield 8.3 g of a crystalline white solid (27 mmols, 90 %).

¹H – NMR (CDCl₃, 300 MHz, 300K) δ, ppm: 7.67 (d, 2H, ArH), 7.30 (d, 2H, ArH), 3.27 – 3.23 (m, 4H, N – CH₂), 2.92 – 2.88 (m, 4H, N – CH₂), 2.69 (s, 4H, N – CH₂), 2.42 (s, 3H, Ar – CH₃), 2.39 (s, 6H, N – CH₃).

1, 4 – dimethyl – 1, 4, 7 – triazacyclononane trihydrobromide, Me₂tacn·3HBr. Me₂tacnmt (8.6 g, 27 mmols) was dissolved in 48 % HBr (86 mL) and refluxed for 48h. After cooling at room temperature, the solvent of the black crude mixture was removed under reduced pressure. Addition of acetone (100 mL) and stirring for 3 hours afforded a fine pale precipitate which was filtered off and washed with acetone. The resulting pale grey solid was dissolved with boiling water (75 mL) and filtered. The solvent from the yellow filtrates was removed under reduced pressure and the resulting residue was treated with absolute ethanol (100 mL). A fine pale yellow precipitated appeared which was filtered off and dried under vacuum to yield 5.3 g of the desired product (13 mmols, 49%).

¹H – NMR (D₂O, 300 MHz, 300K) δ, ppm: 3.49 – 3.42 (m, 4H, N – CH₂), 3.33 – 3.30 (m, 4H, N – CH₂), 3.22 (s, 4H, N – CH₂), 2.80 (s, 6H, N – CH₃).

1 – (di(2 – pyridyl)methyl) – 4, 7 – dimethyl – 1, 4, 7 – triazacyclononane, Me₂(CHPy₂)tacn. Di(2 – pyridyl)methyl chloride, 1, 4 – dimethyl – 1, 4, 7 – triazacyclononane trihydrochloride were mixed in anhydrous acetonitrile. Na₂CO₃ and tetrabutylammonium bromide, TBABr, were added directly as solids and the resulting mixture was heated at reflux under N₂ for 20 hours. After cooling to room temperature, the resulting yellow mixture was filtered and washed with CH₂Cl₂. The combined filtrates were evaporated under reduced pressure. To the resulting residue, 1 M NaOH was added and the mixture was extracted with CH₂Cl₂. The combined organic layers are pushed together and solvent was removed under reduced pressure. The resulting residue was treated with *n* – hexane and stirred for 12 hours. The mixture was filtered and the solvent was removed under reduced pressure to yield the ligand as a yellow oil.

¹H – NMR(CDCl₃, 200MHz, 300 K) δ,ppm: 8.47(d, 2H, PyH_α), 7.57(m,4H, PyH_γ and PyH_β), 7.06(dt, 2H, PyH_{β'}), 5.11(s, 1H, Py₂CH), 2.81(m, 4H, CH₂), 2.79(s, 4H, CH₂), 2.63(m, 4H, CH₂), 2.28(s, 6H, CH₃).

VIII.2. EXPERIMENTAL SECTION CHAPTER IV

VIII.2.1. Instrumentation

UV – VIS – NIR spectra were recorded on a Cary 50 diode array spectrophotometer (190 – 1100 nm range) in 1 cm quartz cells. A cryostat from Unisoku Scientific Instruments was used for the temperature control. Electrospray ionization mass spectrometry (ESI – MS) experiments were performed on a Bruker Daltonics Esquire 3000 Spectrometer or on a high – resolution mass spectrometer Bruker microTOF QII (Q – TOF) with a quadrupole analyser. ^1H and ^{13}C NMR spectra were recorded on a Bruker Avance 400 MHz spectrometer as solutions at 25°C and referenced to residual solvent peaks. ^{57}Fe Mössbauer experiments were performed at 80 K on a zero – field Mössbauer spectrometer equipped with a Janis SVT – 400 cryostat as already described.³⁴⁶ Analysis of the data was performed with the program WMOSS (WEB Research, Edina, MN, USA).

VIII.2.2. Materials

Reagents were purchased from commercial sources and used as received, without any further purification. Compounds methyl *p* – tolyl sulfide, 4 – chlorothioanisole and formaldehyde were purchased from Fluorochem, Alfa Aesar and Scharlab respectively, while the rest of the compounds were purchased from Sigma – Aldrich. Solvents were purchased from SDS and Scharlab, purified and dried by passing through an activated alumina purification system (MBraun SPS – 800) and stored in an anaerobic glovebox under N_2 .

VIII.2.3. Experimental procedures

Syntheses of $[\text{Fe}^{\text{II}}(\text{CH}_3\text{CN})(\text{MePy}_2\text{tacn})](\text{OTf})_2$ ($\mathbf{1}^{\text{II}}$) and $[\text{Fe}^{\text{II}}(\text{CH}_3\text{CN})(\text{Me}_2(\text{CHPy}_2)\text{tacn})](\text{OTf})_2$ ($\mathbf{2}^{\text{II}}$). The syntheses of $\mathbf{1}^{\text{II}}$ and $\mathbf{2}^{\text{II}}$ were performed as previously reported and described on experimental section from Chapter III.^{85,352}

Preparation of $[\text{Fe}^{\text{IV}}(\text{NTs})(\text{MePy}_2\text{tacn})]^{2+}$ ($\mathbf{1}^{\text{IV}}=\text{NTs}$) with PhINTs. In an anaerobic glovebox, $\mathbf{1}^{\text{IV}}=\text{NTs}$ (1.8 mg, $2.5 \cdot 10^{-3}$ mmol) and PhINTs (1.12 mg, $3 \cdot 10^{-3}$ mmol) were mixed in CH_3CN (1 mL). The resulting solution was vigorously stirred 1 – 2 minutes. Removal of unreacted PhINTs was achieved by filtration, which afforded a golden solution of compound $\mathbf{1}^{\text{IV}}=\text{NTs}$. The yield of the reaction was estimated according to the amount of Fe^{IV} determined by Mössbauer spectroscopy by preparation of a 50% ^{57}Fe enriched sample of compound $\mathbf{1}^{\text{IV}}=\text{NTs}$. Yield: 87 %. ^1H – NMR (CD_3CN , 400 MHz, 300 K) δ , ppm: 41.04 (s, Py $\mathbf{H}\beta\mathbf{a}$), 12.67 (s, Py $\mathbf{H}\gamma\mathbf{a}$), -13.31 (s, Py $\mathbf{H}\beta'\mathbf{a}$), 6.02 (s, 1H, Py $\mathbf{H}\gamma\mathbf{b}$), -5.58 (s, 1H, Py $\mathbf{H}\beta\mathbf{b}$) and -6.93 (s, 1H, Py $\mathbf{H}\beta'\mathbf{b}$). ESI – MS (m/z): $[\text{M}-2\text{CF}_3\text{SO}_3]^+ = 275.09$ (100%), $[\text{M}-\text{CF}_3\text{SO}_3]^{2+} = 699.13$ (6%). UV-Vis (CH_3CN): $\lambda_{\text{max}} = 455$ nm, $\varepsilon = 4000 \text{ M}^{-1}\text{cm}^{-1}$, $\lambda = 750$ nm, $\varepsilon = 200 \text{ M}^{-1}\text{cm}^{-1}$.

Preparation of $[\text{Fe}^{\text{IV}}(\text{NTs})(\text{Me}_2(\text{CHPy}_2)\text{tacn})]^{2+}$ ($2^{\text{IV}}=\text{NTs}$) with PhINTs. In an anaerobic glovebox, 2^{II} (1.8 mg, $2.5 \cdot 10^{-3}$ mmol) and PhINTs (1.12 mg, $3 \cdot 10^{-3}$ mmol) were mixed in CH_3CN (1 mL). The resulting solution was vigorously stirred until total formation of $2^{\text{IV}}=\text{NTs}$. Removal of unreacted PhINTs was achieved by filtration, which afforded a golden – orange solution of compound $4^{\text{IV}}=\text{NTs}$. The yield of the reaction was estimated according to the amount of Fe^{IV} determined by Mössbauer spectroscopy by preparation of a 50% ^{57}Fe enriched sample of compound $2^{\text{IV}}=\text{NTs}$. Yield: 48 %. (The same procedure in acetone gave 81 % yield of $2^{\text{IV}}=\text{NTs}$). ^1H – NMR (CD_3CN , 400 MHz, 300 K) δ , ppm: 20.87 (s, $\text{PyH}\beta$), 9.70 (s, $\text{PyH}\gamma$), -6.56 (s, $\text{PyH}\beta'$). ESI – MS (m/z): $[\text{M}-2\text{CF}_3\text{SO}_3]^+ = 275.09$ (100%), $[\text{M}-\text{CF}_3\text{SO}_3]^{2+} = 699.13$ (2%). UV-Vis (CH_3CN): $\lambda_{\text{max}} = 456$ nm, $\epsilon = 3600$ $\text{M}^{-1}\text{cm}^{-1}$, $\lambda = 740$ nm, $\epsilon = 170$ $\text{M}^{-1}\text{cm}^{-1}$.

Preparation of $[\text{Fe}^{\text{IV}}(\text{NTs})(\text{N4Py})]^{2+}$ ($4^{\text{IV}}=\text{NTs}$) with PhINTs. The synthesis of $4^{\text{IV}}=\text{NTs}$ was performed as previously reported.¹⁶⁶

Kinetic Studies. The required amount of $1^{\text{IV}}=\text{NTs}$ or $2^{\text{IV}}=\text{NTs}$ (200 μL of a 2.5 mM solution of $1^{\text{IV}}=\text{NTs}$ or $2^{\text{IV}}=\text{NTs}$ in CH_3CN obtained by direct oxidation of 1^{II} and 2^{II} with PhINTs) was diluted in CH_3CN to obtain the desired final concentration of $1^{\text{IV}}=\text{NTs}$ or $2^{\text{IV}}=\text{NTs}$. Then, the desired quantity of thioanisole ($^X\text{PhSMe}$, dissolved in CH_3CN) was added. The progress of the reaction was monitored by UV – vis spectroscopy at 293 K.

Identification and quantification of sulfanylidene. Reaction of $1^{\text{IV}}=\text{NTs}$ or $2^{\text{IV}}=\text{NTs}$ with sulphides ($^X\text{PhSMe}$) caused a decay of its characteristic absorption bands ($\lambda_{\text{max}} = 455/456$ and $750/740$ nm). After full decay of this band, an internal standard was added to the solution (trimethoxybenzene) and the amount of formed sulfanylidene was quantified by ^1H – NMR spectroscopy by comparison with real products. All quantifications had been done with 5 mg ($7 \cdot 10^{-3}$ mmol) of $1^{\text{IV}}=\text{NTs}$ and $2^{\text{IV}}=\text{NTs}$ and PhINTs (3.12 mg, $8.3 \cdot 10^{-3}$ mmol) in 2 ml of acetone. Blank experiments without iron revealed ≈ 0.1 eq of sulfanylidene products.

XAS data collection and processing. Samples for X – ray absorption measurements were prepared as 4 mM solutions in acetone loaded in sample holders and stored at liquid nitrogen temperatures until run.. XAS data on compounds $1^{\text{IV}}=\text{NTs}$, $1^{\text{III}} - \text{NHTs}$, and $2^{\text{III}} - \text{NHTs}$ was collected at the ESRF synchrotron, Spline beamline, under anaerobic conditions at 90 K using a liquid nitrogen cryostat a 13 element detector and a Si(111) double crystal monochromator.. Compound $2^{\text{IV}}=\text{NTs}$, on the other hand was run at 25 K using a liquid helium cryostat from the SAMBA beamline at SOLEIL synchrotron, equipped with a Si (220) double crystal monochromator and a 35 – element Ge detector.

Data processing was carried out with the Athena software package.³⁵³ A linear pre – edge together with a quadratic post – edge function were used for baseline subtraction and normalization of the edge jump to 1. Energy calibration was carried out using the first inflection point of Fe foil set as 7111.2 eV. The

AUTOBK algorithm was used to extract EXAFS with E0 set as the first inflection point of the rising edge, together with an R_{bkg} of 1 and a spline with a k – range of 1 to 14.5 \AA^{-1} . EXAFS analysis was carried out with Artemis, employing the Iffefit engine and FEFF6 code.^{354,355} The k^3 – weighted data was fit in R – space between 1 and 3 \AA , with a k – range of 2 – 12.5 \AA , and a Kaiser – Bessel window with a dk of 2. Fits were carried out with a global S_0^2 of 0.9 as well as a global ΔE_0 . Scattering paths were fit in terms of ΔR_{eff} and σ^2 , and the goodness of fit was the R_{factor} (%R) and reduced χ^2 (χ^2_{v}) were minimized as previously described.^{356,357}

Theoretical calculations. Theoretical calculations were carried out with the ORCA software package.³⁵⁸ Geometry optimizations were carried out using a TPSS functional with a def2 – TZVP as well as a def2 – TZVP/J auxiliary basis set on all atoms.^{359,360} Subsequent single point calculations to explore the electronic structure and calculate the XAS spectra used the TPSSh functional with an expanded CP(PPP) basis set³⁶¹ on the iron and a def2 – TZVP basis set on the remaining atoms. The above calculations employed a dense integration grid (ORCA Grid 5 = Lebedev 434 points) along with the Grimme and coworkers DFT – D3BJ dispersion correction.^{362,363} In addition solvent effects were included using a conductor like screening model (COSMO) using acetone as solvent.³⁶⁴ Mössbauer parameters were also calculated, but in order to allow comparison with previously calibrated approaches the TPSSh functional was employed together with the CP(PPP) basis set on the iron, TZVP basis set on the remaining atoms and a COSMO model simulating an aqueous solution environment.³²³

VIII.3. EXPERIMENTAL SECTION CHAPTER V

VIII.3.1. Instrumentation

FT – IR spectrum were taken in a Mattson – Galaxy Satellite FT – IR spectrophotometer containing a MKII Golden Gate Single Reflection ATR System. Elemental analyses were conducted in a Carlo Erba Instrument, Mod. CHNS 1108. UV – vis spectroscopy was performed on a Cary 50 Scan (Varian) UV – vis spectrophotometer or on an Agilent 8453 diode array spectrophotometer with 1 cm quartz cells. A cryostat from Unisoku Scientific Instruments was used for the temperature control. Cyclic voltammetry and coulometry were recorded using an EG&G potentiostat/galvanostat model 273A with acetonitrile or acetone solutions of samples containing 0.1 M $[N(n - Bu)_4]PF_6$ as supporting electrolyte. Electrospray ionization mass spectrometry (ESI – MS) experiments were performed on a Bruker Daltonics Esquire 3000 Spectrometer. Elemental analyses were conducted in a Carlo Erba Instrument, Mod. CHNS 1108. X – ray structure determination was carried out on a BRUKER SMART APEX CCD diffractometer using graphite – monochromated Mo $K\alpha$ radiation ($\lambda = 0.71073 \text{ \AA}$) from an X – Ray Tube. The measurements were made in the range 2.11 to 28.64° for θ . Full – sphere data collection was carried out with ω and ϕ scans. Programs used: data collection, Smart version 5.631 (Bruker AXS 1997 – 02); data reduction, Saint + version 6.36A (Bruker AXS 2001); absorption correction, SADABS version 2.10 (Bruker AXS 2001). Structure solution and refinement was done using SHELXTL Version 6.14 (Bruker AXS 2000 – 2003). The structure was solved by direct methods and refined by full – matrix least – squares methods on F^2 . The non – hydrogen atoms were refined anisotropically. The H – atoms were placed in geometrically optimized positions and forced to ride on the atom to which they are attached. Laser flash photolysis experiments were carried out with the second harmonic (532 nm) of a Q – switched Nd:YAG laser (Spectra Physics QuantaRay (Indi); pulse width ca. 9 ns and 15 mJ pulse⁻¹). The signal from the monochromator/photomultiplier detection system was captured by a Tektronix TDS640A digitizer and transferred to a PC computer that controlled the experiment and provided suitable processing and data storage capabilities. 1H and ^{13}C – NMR spectra were recorded on a Bruker Avance 400 MHz spectrometer as solutions at $25^\circ C$ and referenced to residual solvent peaks

VIII.3.2. Materials

Reagents were purchased from commercial sources and used as received, without any further purification. Compounds iron (III) trifluoromethanesulfonate, ammonium hexafluorophosphate and sodium azide (^{14}N – and ^{15}N – terminal) were purchased from Sigma – Aldrich. Solvents were purchased from SDS and Scharlab, purified and dried by passing through an activated alumina purification system (MBraun SPS – 800) and stored in an anaerobic glovebox under N_2 .

VIII.3.3. Experimental procedures

$[\text{Fe}^{\text{II}}(\text{MeCN})(\text{L})](\text{CF}_3\text{SO}_3)_2$ (L = MePy₂tacn (**1^{II}**) and Me₂(CHPy₂)tacn (**2^{II}**)) complexes were prepared as previously described.^{85,352} Synthesis of both complexes are described in experimental section from chapter III.

[Fe^{II}(N₃)(MePy₂tacn)]OTf (1a^{II} – N₃). 50.2mg (0.074 mmol) of $[\text{Fe}^{\text{II}}(\text{MePy}_2\text{tacn})(\text{MeCN})](\text{OTf})_2$ and 47.9mg (0.74 mmol) of NaN₃ were dissolved in MeOH, under N₂ atmosphere, and stirred overnight protected from light. The resulting orange solution was dried and the obtained orange solid was dissolved in the minimum CH₂Cl₂, filtered with Celite and precipitated under diethyl ether diffusion protected from light to provide 31.7mg (0.055 mmol, 75% of yield) of orange needles.

Elemental Analysis (calculated C₁₉H₂₇N₅FeN₃(CF₃SO₃): C, 41.70; N, 18.87; H, 4.45 (C, 41.97; N, 19.58; H, 4.75). ESI – MS (m/z experimental (calculated)): [M-(N₃)]⁺=530.1 (530.1), [M-(SO₃CF₃)]⁺=423.1, [M-(N₃)-(SO₃CF₃)]²⁺=190.5 (190.6). IR (Fe – N – N): 2055 cm⁻¹

[Fe^{III}(N₃)(MePy₂tacn)](PF₆)₂ (1b^{III} – N₃). 108 mg (0.33 mmol) of MePy₂tacn was dissolved with minimum THF. To the solution was added, under energetic stirring, 150 mg of Fe^{III}(OTf)₃ (0.32 mmol) suspended in minimum THF; the solution rapidly turned reddish and a dark oil precipitated. The stirring continued for 2 hours. The solution was removed and the oil was dried to become a solid. 1 ml of degassed water was added followed by 210 mg (3.2 mmol) of NaN₃, the solution readily turned reddish and was stirred preserved from light for 2 hours. Then, 1 ml of saturated NH₄PF₆ solved in degassed water was added and a purple solid precipitated. The mixture was stirred for 1 - 2 h protected from light. The precipitate was filtered and dried to afford 116 mg of solid (0.16 mmol, 56 % of yield). The residue was dissolved in acetone, filtered with Celite and recrystallized with diethyl ether diffusion at low temperature to provide dark purple crystals.

The same procedure was followed using Na(¹⁵NN₂) to obtain $[\text{Fe}^{\text{III}}(^{15}\text{NN}_2)(\text{MePy}_2\text{tacn})](\text{PF}_6)_2$.

Elemental Analysis (calculated C₁₉H₂₇N₅FeN₃(PF₆)₂): C, 32.41; N, 15.34; H, 3.72 (C, 32.0; N, 15.71; H, 3.82). HR – MS (m/z experimental (calculated)): [M-(PF₆)]⁺ = 197.5817 (197.5818), [M-(N₃)-(PF₆)]⁺ = 190.5803 (190.5803), [M-(N₂)-(PF₆)]²⁺ = 211.5849 (211.5849).

IR (Fe – N – N): 2019 cm⁻¹ IR (Fe – ¹⁵N = N = N / Fe – N = N = N): 1998 / 2021 cm⁻¹

[Fe^{II}(N₃)(Me₂(CHPy₂)tacn)]OTf (2a^{II} – N₃). This compound was synthesized in analogous manner as $[\text{Fe}^{\text{II}}(\text{N}_3)(\text{MePy}_2\text{tacn})]\text{OTf}$ **1a^{II} – N₃**: 71mg of **2^{II}** as the starting complex provided 46.6mg (0.082 mmol, 78%) of orange – reddish needles after recrystallization in CH₂Cl₂/Et₂O protected from light.

Elemental Analysis (calculated C₁₉H₂₇N₅FeN₃(CF₃SO₃): C, 42.06; N, 19.19; H, 4.77 (C, 41.97; N, 19.58; H, 4.75). ESI – MS (m/z experimental (calculated)): [M-(N₃)]⁺=530.0 (530.1), [M-(SO₃CF₃)]⁺=423.1, [M-(N₃)-(SO₃CF₃)]²⁺=190.5 (190.6). IR (Fe – N – N): 2063 cm⁻¹

[Fe^{III}(N₃)(Me₂(CHPy₂)tacn)](PF₆)₂ (2b^{III} – N₃). This compound was synthesized in analogous manner as [Fe^{III}(N₃)(MePy₂tacn)](PF₆)₂ 1b^{III} – N₃: using 150 mg of Fe^{III}(OTf)₃ (0.32 mmol) and 108 mg (0.33 mmol) of the starting ligand provided 110 mg (0.11 mmol, 53 %) of orange – reddish crystalline material after recrystallization in acetone/Et₂O protected from light.

HR – MS (m/z experimental (calculated)): [M-(PF₆)]⁺ = 197.5816 (197.5818), [M-(N₃)-(PF₆)]⁺ = 190.5803 (190.5803), [M-(N₂)-(PF₆)]²⁺ = 211.5828 (211.5849). IR (Fe – N – N): 2021 cm⁻¹

Photolysis experiments. Solid powder samples (*ca.* 50 mg) of 1b^{III} – N₃ (or 2b^{III} – N₃) were suspended in an open liquid nitrogen bath and photolysed under strong stirring at 77 K, using a 470 or a 530 nm LED lamp. After 4.5 – 5 h of illumination, product sample (1^VΞN or 2^VΞN) was kept at 77 K and moved to the appropriate holder for Mössbauer, EPR and SQUID measurements.

Mössbauer Spectroscopy. Mössbauer spectra were recorded on a conventional spectrometer with alternating constant acceleration of the γ – source (⁵⁷Co/Rh, 1.8 GBq), which was kept at room temperature. The minimum experimental line width was 0.24 mm/s (full width at half – height). The sample temperature was maintained constant in an Oxford Instruments Variox cryostat. Isomer shifts are quoted relative to iron metal at 300 K.

EPR Spectroscopy. X – band EPR derivative spectra were recorded on a Bruker ELEXSYS E500 spectrometer equipped with the Bruker dual – mode cavity (ER4116DM) and a helium flow cryostat (Oxford Instruments ESR 900). Microwave frequencies were calibrated with a Hewlett – Packard frequency counter (HP5352B), and the field control was calibrated with a Bruker NMR field probe (ER035M). The powder spectra were simulated with the program esimX_gfit (by E.B.) using effective g values and anisotropic line widths (Lorentzian line shapes were used).

XAS data collection and processing. Samples for X – ray absorption measurements were prepared as 4 mM solutions in acetone loaded in sample holders and stored at liquid nitrogen temperatures until run. Compound 1^VΞN was generated by loading a solution of 1b^{III} – N₃ in a sample holder and photolysing the sample in a liquid nitrogen bath using a 570 nm (green) light for 5 hours. XAS data on compounds 1a^{III} – N₃ and 1b^{III} – N₃ was collected at the SOLEIL synchrotron, SAMBA beamline, under anaerobic conditions at 25 K using a liquid helium cryostat. The SAMBA beamline is also equipped with a Si (220) double crystal monochromator and a Canberra 35 – element Ge detector. Compound 1^VΞN, on the other hand was run at 80 K using a liquid helium cryostat from the DIAMOND beamline B18 equipped with a Si (111) double crystal monochromator and an 8 – element Ge detector.

Data processing was carried out with the Athena software package.³⁵³ A linear pre – edge followed by a quadratic post – edge function were used for baseline subtraction and normalization of the edge jump to 1. Energy calibration was performed using the first inflection point of Fe foil taken as 7111.2 eV. EXAFS were extracted using the AUTOBK algorithm with E0 taken as the first inflection point of the rising edge, having an R_{bkg} of 1 and a spline with a k – range of 1 to 15 Å⁻¹. EXAFS analysis was carried out with Artemis, employing the Iffefit engine and FEFF6 code.^{354,355} The k³ – weighted data was fit in R – space

between 1 and 3 Å, having a k – range of 2 – 14 Å⁻¹, and a Hannings window with a dk of 2. Fits were carried out with a global S_0^2 of 0.9 as well as a global ΔE_0 . Scattering paths were fit in terms of ΔR_{eff} and σ^2 , and the goodness of fit was the R_{factor} (%R) and reduced χ^2 (χ^2_{ν}) were minimized as previously described.^{356,357}

Theoretical calculations. Theoretical calculations were carried out with the ORCA software package.³⁵⁸ Geometry optimizations were carried out using a TPSS functional with a def2 – TZVP as well as a def2 – TZVP/J auxiliary basis set on all atoms.^{359,360} Subsequent single point calculations to explore the electronic structure and calculate the XAS spectra employed the TPSSh functional with an expanded CP(PPP) basis set³⁶¹ on the iron and a def2 – TZVP basis set on the remaining atoms. The above calculations employed a dense integration grid (ORCA Grid 5 = Lebedev 434 points) along with the Grimme and coworkers DFT – D3BJ dispersion correction.^{362,363} In addition solvent effects were included using a conductor like screening model (COSMO) using acetone as solvent.³⁶⁴ XAS spectra was calculated using the TD – DFT method employing the Tamm – Dancoff approximation.^{365,366} Mössbauer parameters were also calculated, but in order to allow comparison with previously calibrated approaches the TPSSh functional was employed together with the CP(PPP) basis set on the iron, TZVP basis set on the remaining atoms and a COSMO model simulating an aqueous solution environment.³²³

VIII.4. EXPERIMENTAL SECTION CHAPTER VI

VIII.4.1. Instrumentation

^1H – NMR spectra were recorded on Bruker Avance 400 MHz, or Agilent 500 DD2 spectrometers as solutions at 298 K and referenced to residual solvent peaks. GC product analyses were performed on Agilent 7820A, Varian 3800 and 3900 chromatographs equipped with 60 m x 0.25 mm x 1.00 μm (MS detector) and ZB – 1MS 30 m x 0.25 mm x 0.25 μm (FID detector) columns.

VIII.4.2. Materials

All air – and moisture – sensitive manipulations were carried out with standard Schlenck techniques under nitrogen atmosphere or in a glovebox. All solvents and reagents were purchased from commercial sources in anhydrous packages and used without any further purification; except for ethylbenzene, isobutylbenzene and mesitylene which were filtered through basic alumina and degassed with freeze – pump techniques. The iron – and manganese complexes^{85,251,266,367,368} and the sodium tetrakis(3,5 – bis(trifluoromethyl)phenyl)borate salt ($\text{Na}(\text{BAr}_\text{F})_4$)³⁶⁹ were synthesised and purified according to previously reported methods.

VIII.4.3. Experimental procedures

Catalyst screening experiments. Catalyst screening was performed mixing 0.005 mmol of catalyst, 0.01 – 0.04 mmol of ($\text{Na}(\text{BAr}_\text{F})_4$) (2 – 8 eq.) and 3 mL of benzene as the solvent. The solution was stirred at room temperature for 20 min and then 0.1 mmol of ethyl diazoacetate was added and heated for 12 h at 80 °C. After that reaction time the mixtures were analysed by GC and ^1H – NMR spectroscopy.

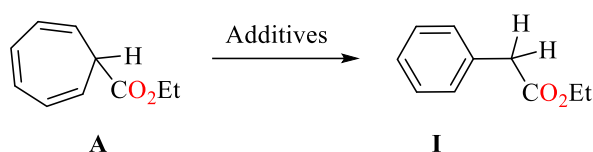
Product isolation procedure. Catalytic experiments were performed following the previous procedure, and the final mixture was directly purified with a silica gel column using hexane and ethyl acetate as eluents; isolated oils were weighted providing isolated yields. Evidence of purity was given by NMR spectroscopy (see below).

Mass balance experiments. Following the above procedure, 0.05 mmol (30.1 mg) of **3^(III)** and 0.4 mmol of NaBAr_F (356 mg) were stirred for 20 min in 30 mL of substrate (for mesitylene, a mixture of 7 mL (50 mmol) of substrate in 23 mL of DCM mixture was used; for biphenyl 7.8 gr (50 mmol) of substrate were dissolved in 30 mL of dichloromethane). Ethyl diazoacetate was then added and the mixture heated at 80 °C for 14 h. After cooling, 5 mL of acetonitrile were added and a 5 mL aliquot was taken. 1,3,5 – Trimethoxybenzene was added as standard, the catalyst was removed with a flash silica gel column and the sample was analysed by ^1H – NMR spectroscopy to assess mass balance. In all cases >95% of the initial

EDA was quantified as a mixture of the product, some ethyl glycolate resulting from adventitious water (insertion of carbene into O – H bond) and, in some cases, unreacted EDA (< 10%).

Stability of ethyl cyclohepta – 2, 4, 6 – trienecarboxylate under reaction conditions and additives.

Two decades ago, McKervery and co-workers described³⁷⁰ that the rhodium – catalysed reaction of diazoketones and benzenes provided cycloheptatrienes that upon addition of triflic acid rearranged into the corresponding benzyl ketones. Thus, it might occur that some of the transformations shown in Table VI.1 in the manuscript might be sensible to the presence of traces of triflic acid produced from hydrolysis of triflate ligand or any other acidic traces.



A series of experiments have been carried out to validate the stability of the addition product, *i. e.*, the cycloheptatriene **A** under the reaction conditions, since it has been previously reported that it can be converted into the alkylated benzene **I** in the presence of acid.

Table VIII.1. Stability of cycloheptatriene **A** in benzene as solvent.

Entry	Additives	% I
1	Na(BAr _F) ₄	No reaction
2	NaOTf	No reaction
3	Fe(OTf) ₂	No reaction
4	HOTf	Full conversion
5	3 ^(III)	No reaction
6	3 ^(III) + NaBar ^F ₄ (8 equiv)	No reaction
7	3 ^(III) Cl + NaOTf (8 equiv)	No reaction
8	3Mn ^(II)	No reaction

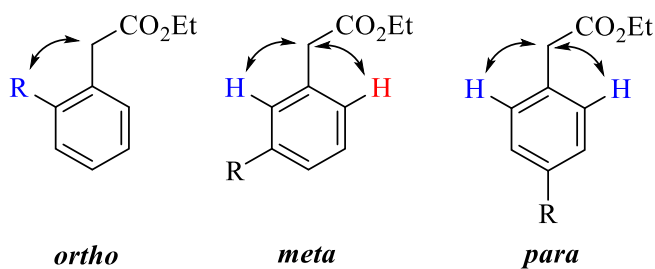
Table VIII.1 shows the different reactants and additives added to solutions of previously prepared and isolated cycloheptatriene **A**. The reactions were carried out at 80 °C in 3 mL of benzene during 12 h. After that reaction time the mixtures were analysed by ¹H – NMR spectroscopy. In none of the cases the conversion of **A** to the insertion product **I** was observed. *Only when commercial triflic acid (5 equiv.) was added a neat conversion of cycloheptatriene A into the alkyl-benzene I was observed.*

Competition experiments and Hammett plot. Following the already described procedure, 3 ml of equimolar mixtures of benzene and the corresponding substituted benzene (0.15: 0.15 mmol) were stirred for 20 min with 0.005 mmol of the catalyst and 0.04 mmol of Na(BAr_F)₄ (35.6 mg). After that time 0.1 mmol of ethyl diazoacetate were added and the mixture was heated for 12 h at 80 °C. The reaction mixtures were then analysed by GC, providing the ratio of the insertion products shown below.

KIE experiments. An equimolar mixture of benzene and deuterated benzene (0.17:0.17 mmol) was stirred for 20 min with 0.005 mmol of catalyst and 0.04 mmol of $\text{Na}(\text{BAr}_F)_4$ (35.6 mg). After that time 0.1 mmol of ethyl diazoacetate were added and the mixture was heated for 12 hours at 80 °C, before being analysed by GC – MS to obtain the relative ratio of products.

Cyclopropylbenzene as reactant. Cyclopropylbenzene reaction was performed mixing 0.05 mmol of catalyst, 0.4 mmol of $\text{Na}(\text{BAr}_F)_4$ (356 mg) and a mixture of 9 mL of DCM and 5.3 mL of cyclopropylbenzene. The solution was stirred for 20 min and then 0.84 mmol of ethyl diazoacetate was added and heated for 12 h at 80 °C. After that reaction time the reaction mixture was analysed by NMR showing no products derived from cyclopropyl – ring opening. Purification with a silica gel column using hexane and ethyl acetate as eluents gave a mixture of the three isomers of the alkylated benzene (see next section).

NMR identification of products and isomers. Products are commercially available or have been previously described.^{338,343} For the sake of completeness, the ^1H – NMR spectra of the isolated products are shown below. The identification of the *ortho*, *meta* and *para* isomers has been carried out on the basis of NOESY experiments. Thus, the *ortho* derivatives show NOE of the $\text{CH}_2\text{CO}_2\text{Et}$ nuclei with the benzylic C – H nuclei of the substituent (or the aromatic C-H bond of the second Ph ring in the case of biphenyl). *Meta*– and *para*– isomers are identified in the NOESY experiment on the basis of the number of NOE signals. Due to the lack of symmetry, the former provides two signals whereas the latter gives just one. Once assigned, integration of the $\text{CH}_2\text{CO}_2\text{Et}$ or any other relevant resonance (*i. e.*, the Me group in the toluene derivatives) provided the relative *o:m:p* ratio.



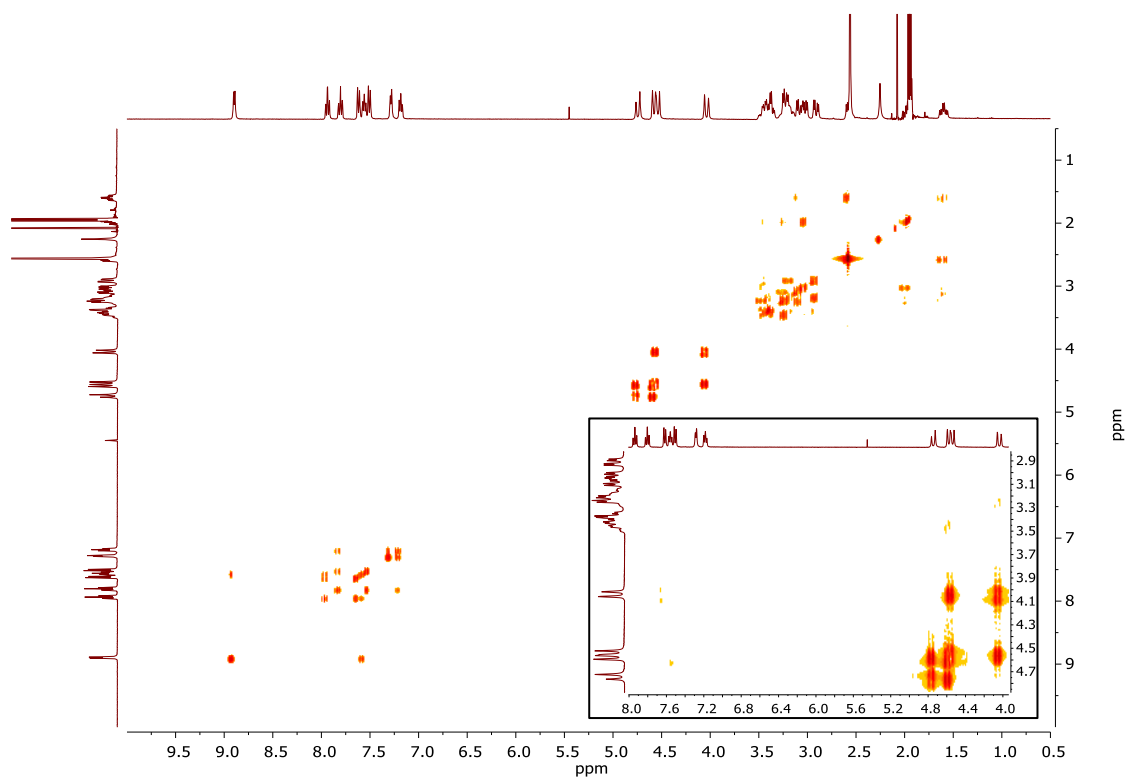
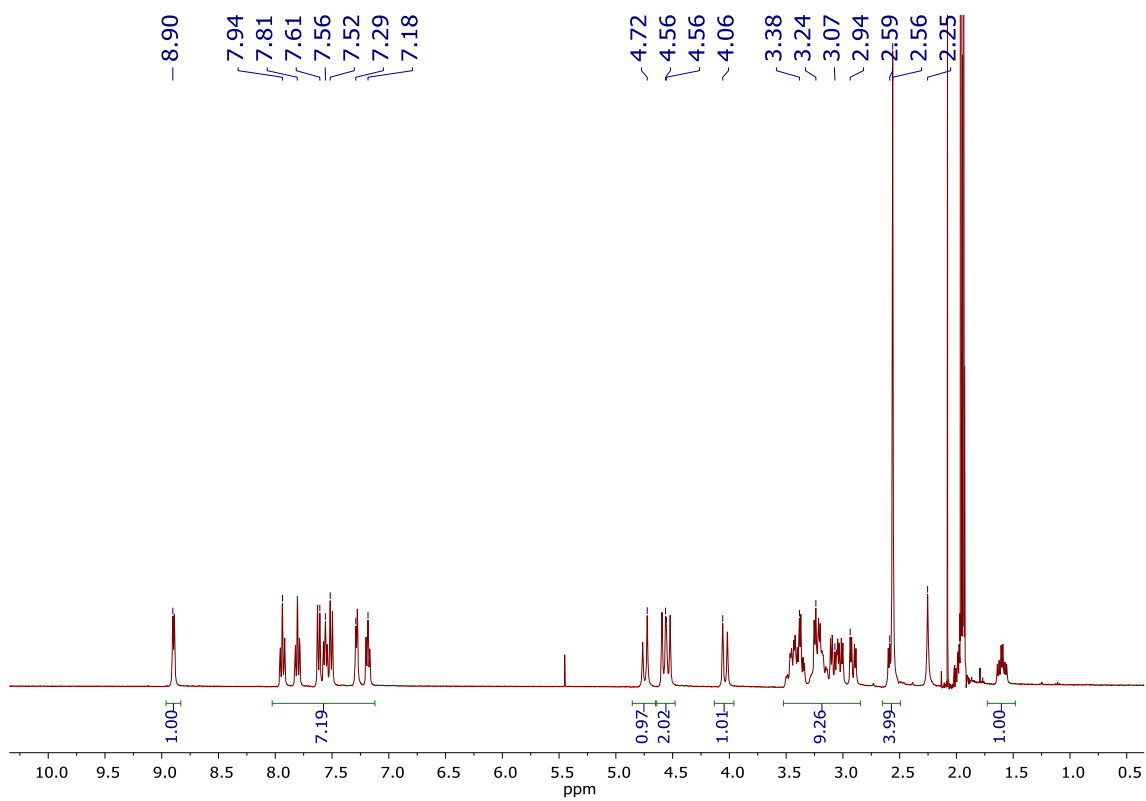
ANNEX

ANNEX CHAPTER III**Table SIII.1.** Crystallographic data and selected bond distances and angles of **1^(III)**.

Empirical formula	C ₂₁ H ₃₀ FeN ₆ ,2(CF ₃ O ₃ S)		
Molar weight	720.49		
Temperature, K	100(2)		
λ , Å	0.71073		
Crystal system	Triclinic		
Space group	P-1		
a, Å	11.183(5)		
b, Å	16.059(8)		
c, Å	17.358(9)		
α , °	70.642(8)		
β , °	88.410(9)		
γ , °	86.803(9)		
V, Å ³	2936.33		
Z	4		
R1	4.78		
wR2	0.1227		
<hr/>			
Fe(1)-N(6)	1.929(2)	N(6)-Fe(1)-N(1)	95.72(9)
Fe(1)-N(1)	1.970(2)	N(6)-Fe(1)-N(5)	87.80(8)
Fe(1)-N(5)	1.988(2)	N(1)-Fe(1)-N(5)	95.67(8)
Fe(1)-N(2)	1.992(2)	N(6)-Fe(1)-N(2)	177.80(8)
Fe(1)-N(4)	1.994(2)	N(1)-Fe(1)-N(2)	83.20(9)
Fe(1)-N(3)	2.047(2)	N(5)-Fe(1)-N(2)	94.21(8)
		N(6)-Fe(1)-N(4)	95.27(9)
		N(1)-Fe(1)-N(4)	168.88(8)
		N(5)-Fe(1)-N(4)	83.04(8)
		N(2)-Fe(1)-N(4)	85.87(9)
		N(6)-Fe(1)-N(3)	92.58(8)
		N(1)-Fe(1)-N(3)	95.59(8)
		N(5)-Fe(1)-N(3)	168.64(8)
		N(2)-Fe(1)-N(3)	85.63(8)
		N(4)-Fe(1)-N(3)	85.61(8)

Table SIII.2. Crystallographic data and selected bond distances and angles of **2^(III)**.

Empirical formula	C ₂₃ H ₃₀ FeN ₆ ,2(CF ₃ O ₃ S)		
Molar weight	720.49		
Temperature, K	300(2)		
λ , Å	0.71073		
Crystal system	Monoclinic		
Space group	P21/n		
a, Å	13.2032(13)		
b, Å	18.3757(18)		
c, Å	13.5861(14)		
α , °	90		
β , °	113.5861(14)		
γ , °	90		
V, Å ³	3031.4(5)		
Z	4		
R1	5.81		
wR2	0.1702		
<hr/>			
Fe(1)-N(6)	1.932(2)	N(6)-Fe(1)-N(3)	178.62(10)
Fe(1)-N(3)	1.967(2)	N(6)-Fe(1)-N(1)	95.47(10)
Fe(1)-N(1)	1.977(2)	N(3)-Fe(1)-N(1)	83.41(9)
Fe(1)-N(2)	1.978(2)	N(6)-Fe(1)-N(2)	95.57(10)
Fe(1)-N(4)	2.041(2)	N(1)-Fe(1)-N(2)	84.58(9)
Fe(1)-N(5)	2.051(2)	N(3)-Fe(1)-N(4)	85.42(10)
		N(1)-Fe(1)-N(4)	168.83(10)
		N(2)-Fe(1)-N(4)	94.18(10)
		N(6)-Fe(1)-N(5)	95.28(10)
		N(1)-Fe(1)-N(5)	94.17(10)
		N(2)-Fe(1)-N(5)	169.15(10)
		N(4)-Fe(1)-N(5)	84.96(11)
		N(3)-Fe(1)-N(2)	83.52(9)
		N(6)-Fe(1)-N(4)	95.70(10)
		N(3)-Fe(1)-N(5)	85.62(10)



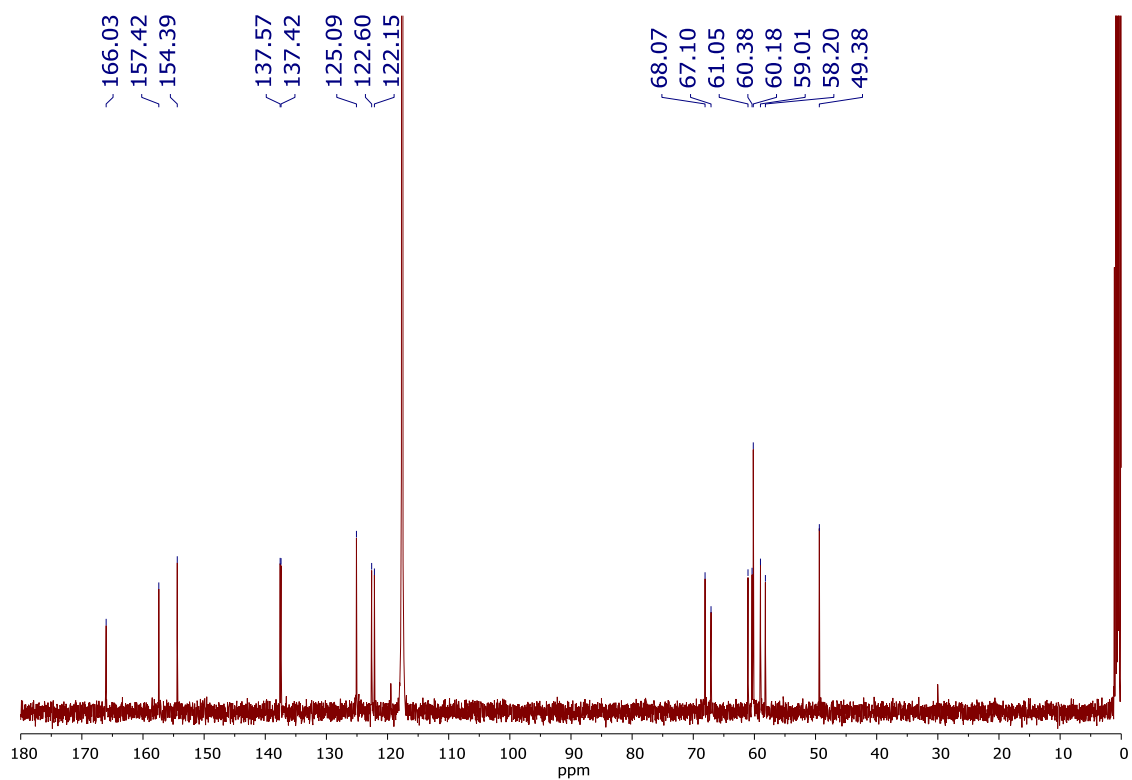


Figure SIII.1. ^1H – NMR, bidimensional COSY and ^{13}C – NMR spectra of **1^(II)** in CD_3CN at 273 K.

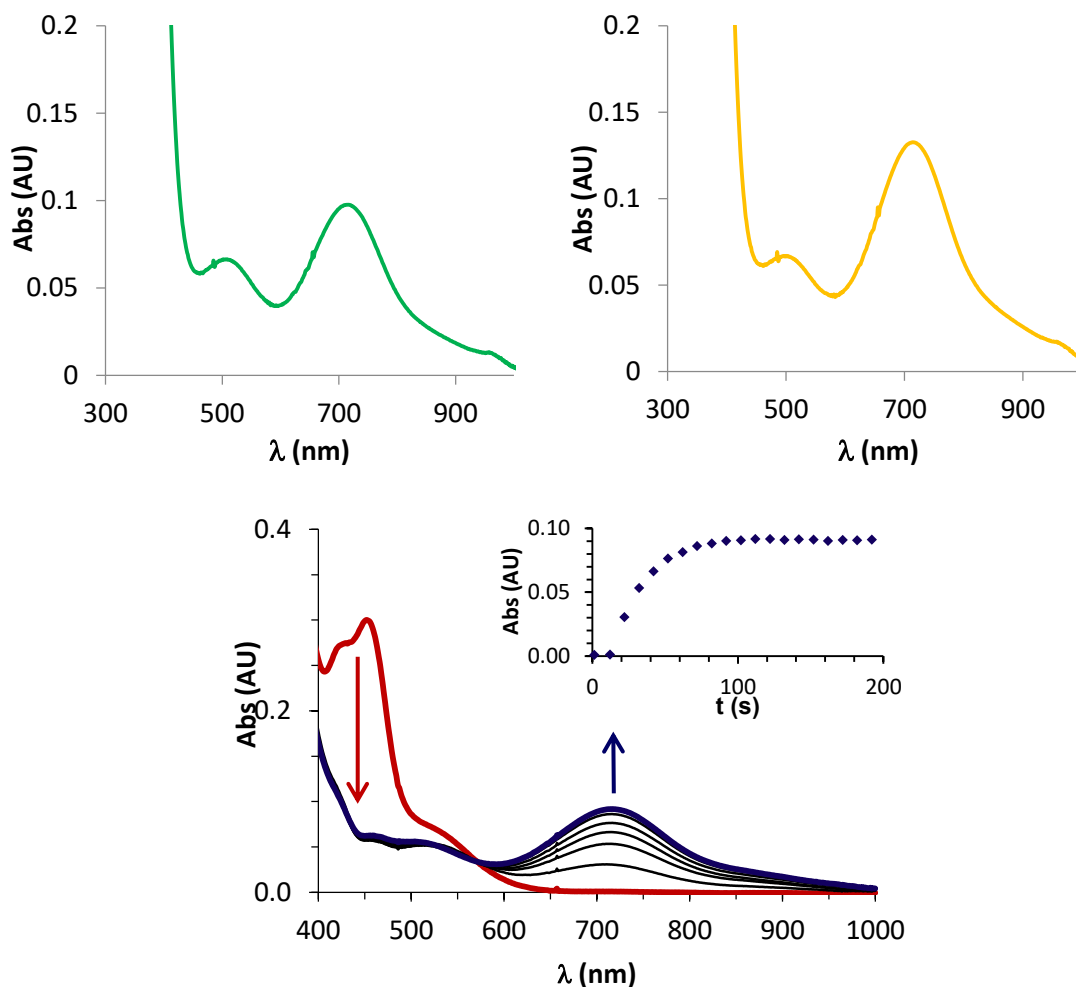


Figure SIII.2. Top left: UV – vis spectrum of $\mathbf{1}^{(IV)=O}$ obtained upon reaction of $\mathbf{1}^{(II)}$ (0.4 mM) with 2 equiv $[\text{Ru}^{III}(\text{bpy})_3](\text{PF}_6)_3$ in water. Top right: UV – vis spectrum of $\mathbf{1}^{(IV)=O}$ obtained after reaction of $\mathbf{1}^{(II)}$ (0.4 mM) with 15 equiv ceric ammonium nitrate (CAN) in $\text{CH}_3\text{CN}:\text{H}_2\text{O}$ 1:3. Below: UV – vis evolution of photochemical oxidation of $\mathbf{1}^{(II)}$ (0.4 mM in $\text{MeCN}:\text{H}_2\text{O}$ (1:3), 0.02 mM of $[\text{RuCl}_2(\text{bpy})_3]$ and 4 mM $\text{Na}_2\text{S}_2\text{O}_8$) to generate $\mathbf{1}^{(IV)=O}$ upon irradiation (447 nm). Inset shows the kinetic trace of 715 nm. The lack of 414 nm band of initial $\mathbf{1}^{(II)}$ is due to its previous oxidation to $\mathbf{1}^{(III)} - \text{OH}$ upon addition of $\text{Na}_2\text{S}_2\text{O}_8$ before irradiating. Immediate consumption of band at 450 nm after starting irradiation indicates the fast oxidation of Ru^{II} to Ru^{III} . Complex $\mathbf{1}^{(IV)=O}$ was not formed in absence of $\text{Na}_2\text{S}_2\text{O}_8$ or $[\text{Ru}^{II}\text{Cl}_2(\text{bpy})_3]$. It was observed a solvatochromic effect when water was added to $\mathbf{1}^{(IV)=O}$, for example in a mixture 1:3 $\text{MeCN}:\text{H}_2\text{O}$ the 738 nm band (in MeCN) blue – shifted about 20 nm, to obtain a feature with a maximum at 715 nm with no significant change in the absorption coefficient. Such behaviour was also observed in related complexes such as $\mathbf{2}^{(IV)=O}$ or $[\text{Fe}^{IV}(\text{O})(\text{N4Py})]^{2+}$.

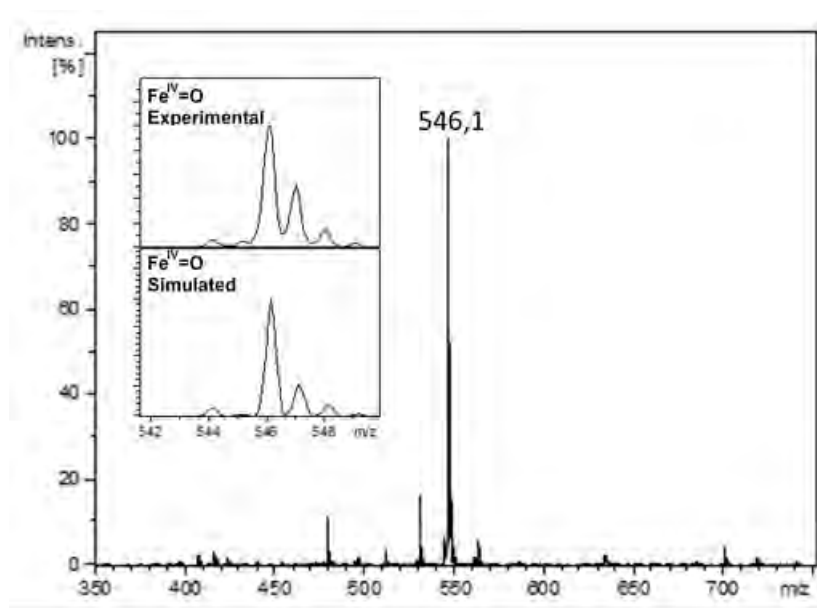


Figure SIII.3. ESI – MS spectrum of complex $2^{(IV)}=O$ in MeCN prepared with excess of PhIO.

Table SIII.3. EXAFS fitting parameters for $1^{(IV)}=O$ (k range = 2 – 15 \AA^{-1} ; back transform range ~ 0.83 – 3.0 \AA).

Fit	Fe – N			Fe – O			Fe \cdots C			Fe \cdots C			GOF		
	N	R (\AA)	σ^2 (10^{-3})	N	R (\AA)	σ^2 (10^{-3})	N	R (\AA)	σ^2 (10^{-3})	N	R (\AA)	σ^2 (10^{-3})	E_0	F	F'
1	6	2.01	7.01										-6.91	556	650
2	5	2.01	5.78										-6.16	538	639
3	3	2.02	4.53										-5.22	545	643
4	5	2.02	6.31	1	1.63	3.43							-3.72	476	601
5	4	2.02	4.95	1	1.63	3.09							-2.98	506	619
6	5	2.01	6.42	1	1.63	3.22	2	2.85	2.93				-4.93	386	541
7	5	2.02	4.95	1	1.63	3.25	4	2.86	5.17				-5.35	343	511
8	5	2.00	6.57	1	1.63	3.28	6	2.86	6.94				-5.68	325	467
9	5	2.00	6.62	1	1.63	3.30	8	2.86	8.62				-6.03	321	493
10	5	2.00	6.64	1	1.63	3.66	6	2.83	2.37	2	2.97	-1.50	-6.28	281	462
11	5	2.00	6.68	1	1.63	3.58	6	2.82	2.25	4	2.96	0.95	-6.16	291	470
12	5	2.00	6.74	1	1.63	3.60	6	2.81	2.30	5	2.95	2.02	-6.34	301	477
13	5	2.00	6.71	1	1.63	3.52	6	2.81	2.3	6	2.95	2.87	-6.26	310	486
14	5	1.99	6.80	1	1.63	3.52	6	2.80	2.82	8	2.94	5.10	-6.51	335	504

Scale Factor $S_0^2 = 0.9$. GOF = Goodness – of – fit calculated as $F = \sqrt{\sum k^6 (\chi_{\text{exp}} - \chi_{\text{calc}})^2}$

$$F' = \sqrt{\sum k^6 (\chi_{\text{exp}} - \chi_{\text{calc}})^2 / \sum k^6 \chi_{\text{exp}}^2}$$

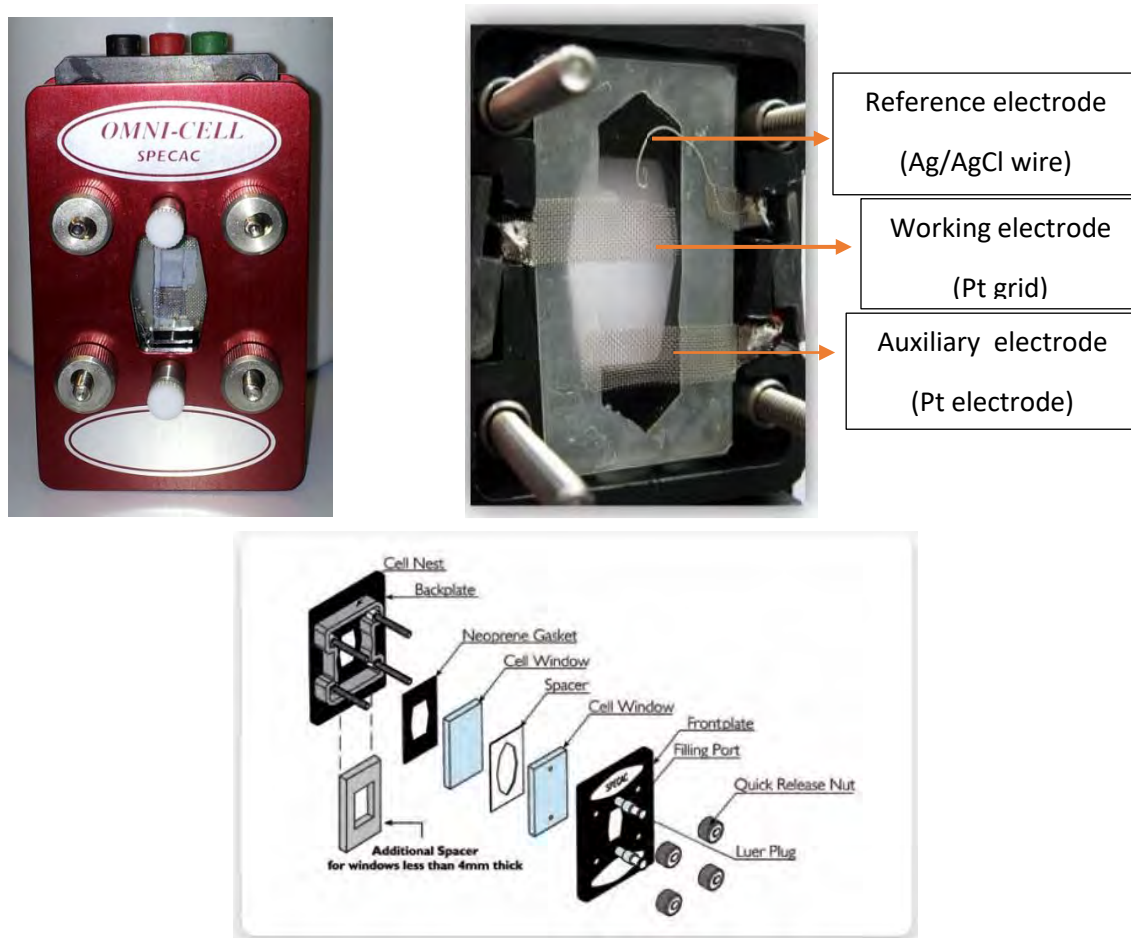


Figure SIII.4. OTTLE cell system used for spectrochemical measurements. See ref 371 and <https://www.reading.ac.uk/chemistry/research/chem-spectroelectrochemistry.aspx>.

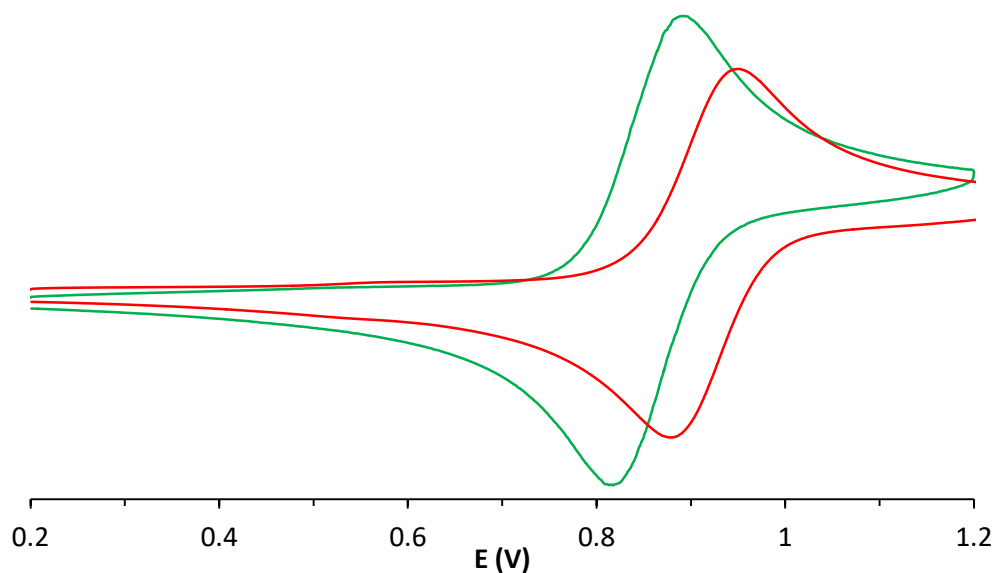


Figure SIII.5. Cyclic Voltammometry spectra of $1^{(II)}$ (green line) and $2^{(II)}$ (red line) in MeCN, 0.1 mM of TBAPF₆.

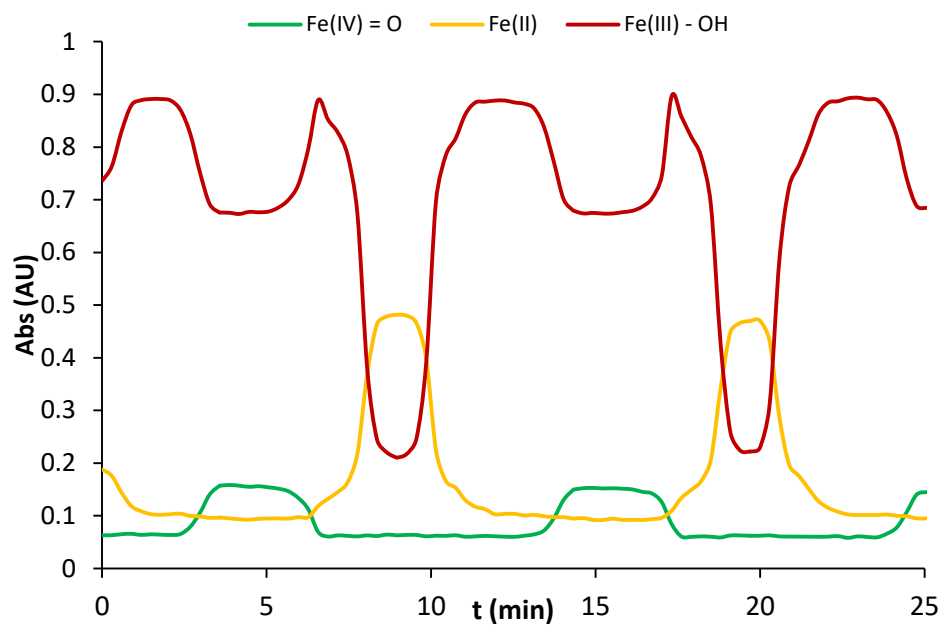


Figure SIII.6. UV – vis traces of redox processes of $1^{(III)}$ (14 mM in H_2O , 0.1 M KNO_3 , scanrate = 5 mV/s) followed by spectroelectrochemistry. Fe(II) was monitored at 423 nm, Fe(III) at 305 nm and Fe(IV) at 715 nm.

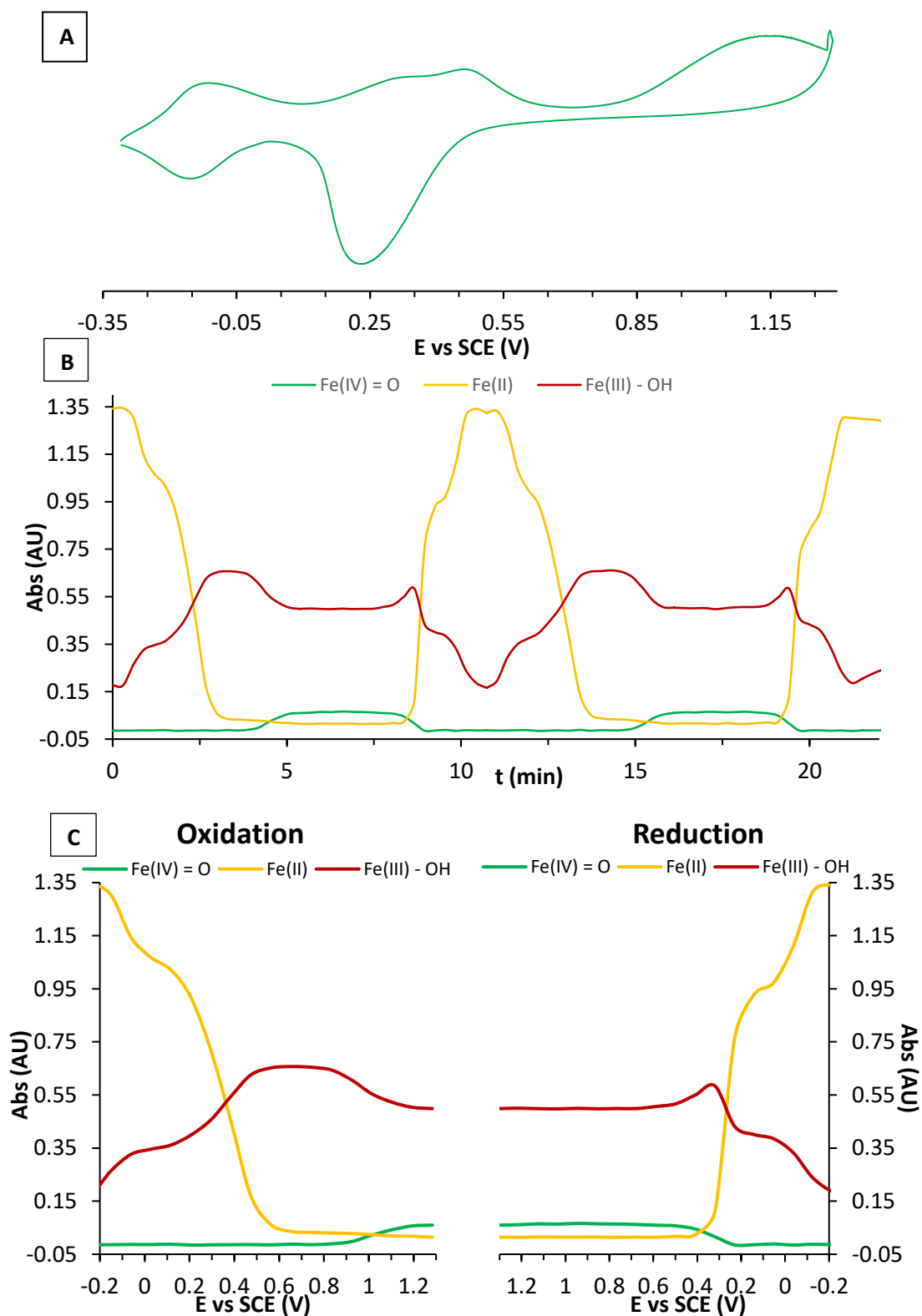
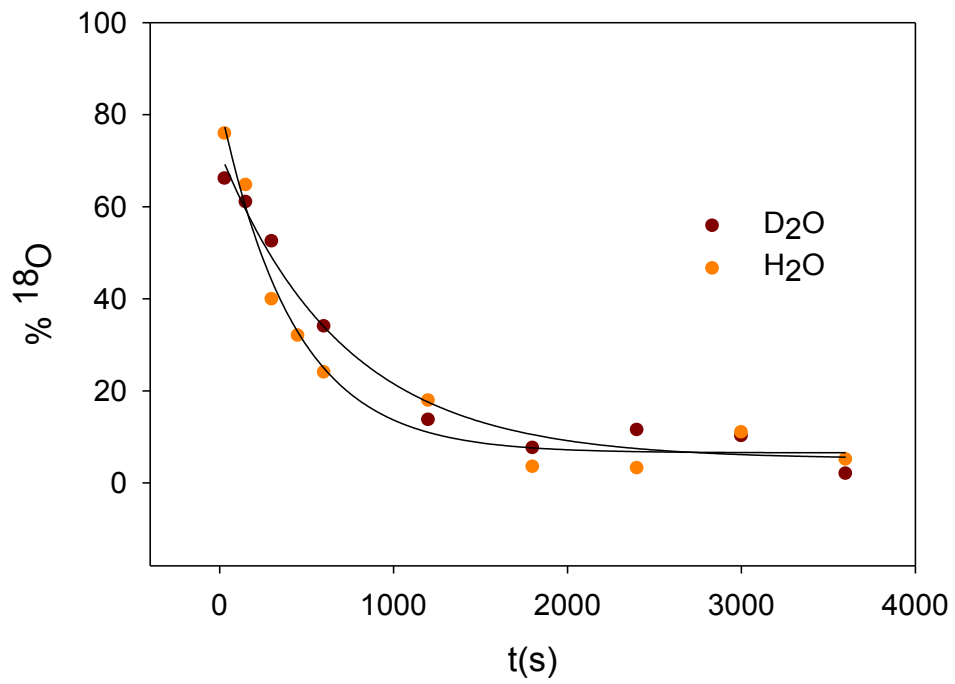
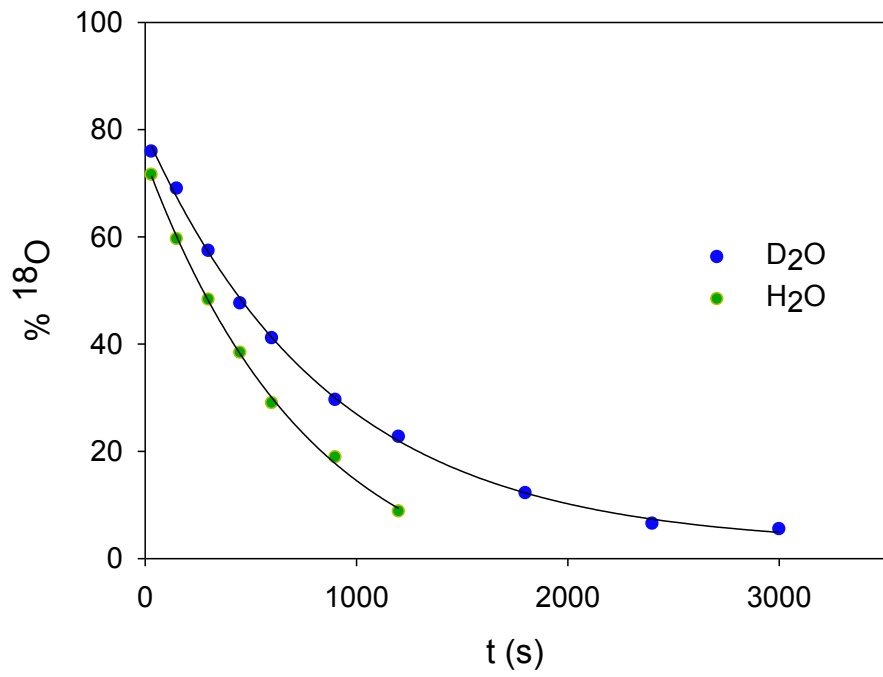


Figure SIII.7. Spectroelectrochemistry of complex $1^{(III)}$ (14 mM in MeCN:H₂O (1:3), 0.1 M KNO₃, scanrate = 5 mV/s). (A) Cyclic voltammetry of $1^{(III)}$. (B) Evolution of the UV – vis in front of the potential. (C) UV – vis traces for the oxidation and reduction processes observed vs potential. Fe(II) was monitored at 420 nm, Fe(III) at 310 nm and Fe(IV) at 720 nm.



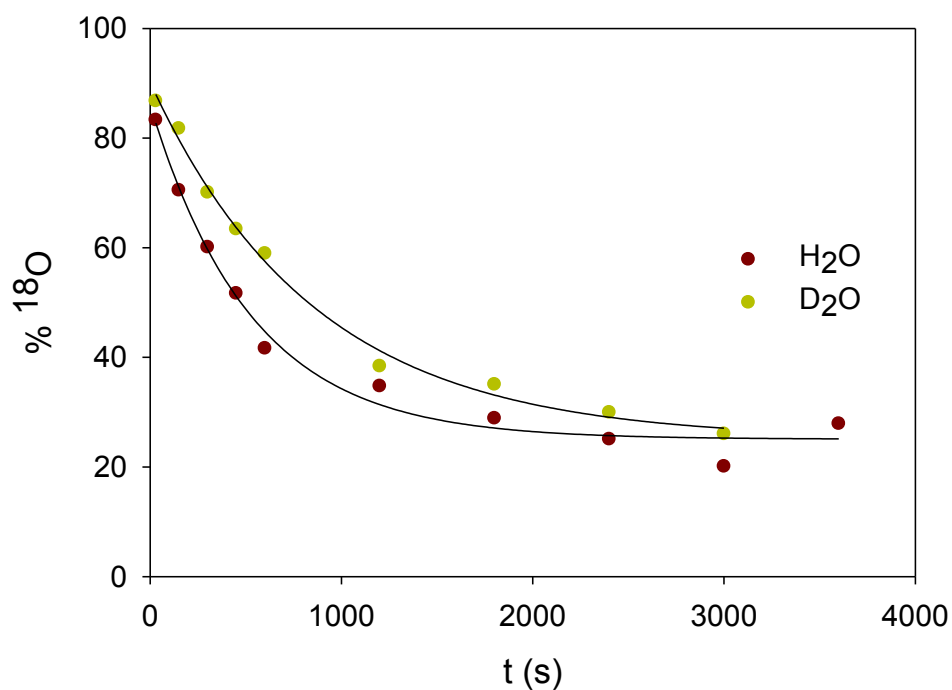


Figure SIII.8. Experiments between ^{18}O – labeled $3^{(\text{IV})}=\text{O}$ (generated from reaction of ^{16}O – labelled $3^{(\text{IV})}=\text{O}$ and 0.14 M H_2^{18}O , 1.0 mM) and H_2^{16}O or D_2^{16}O at 0 °C (Top 1.57 M, Center 0.74 M and Below 0.42 M of H_2O or D_2O) at 0 °C, resulting in a KIE of 1.5, 1.7 and 1.6 respectively. The ^{18}O – incorporation was determined by quenching aliquots (0.4 mL, 0.4 mmol) of the reaction with thioanisole (5 μL , 42.7 mmol) and determining the ratio of ^{16}O and ^{18}O – methylphenylsulfoxide by GC – MS, as previously described.⁷⁷

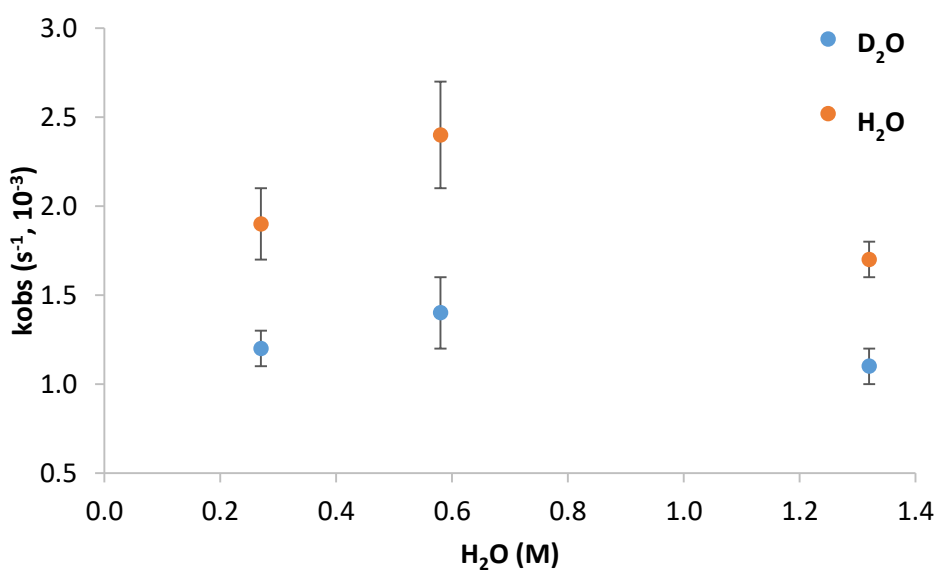


Figure SIII.9. Comparison reactions between ^{18}O – labeled $3^{(\text{IV})}=\text{O}$ (generated from reaction of ^{16}O – labelled $3^{(\text{IV})}=\text{O}$ and 0.14 M H_2^{18}O , 1.0 mM) and H_2^{16}O or D_2^{16}O at 0 °C (0.42, 0.74 and 1.57 M). Bars indicate associated errors.

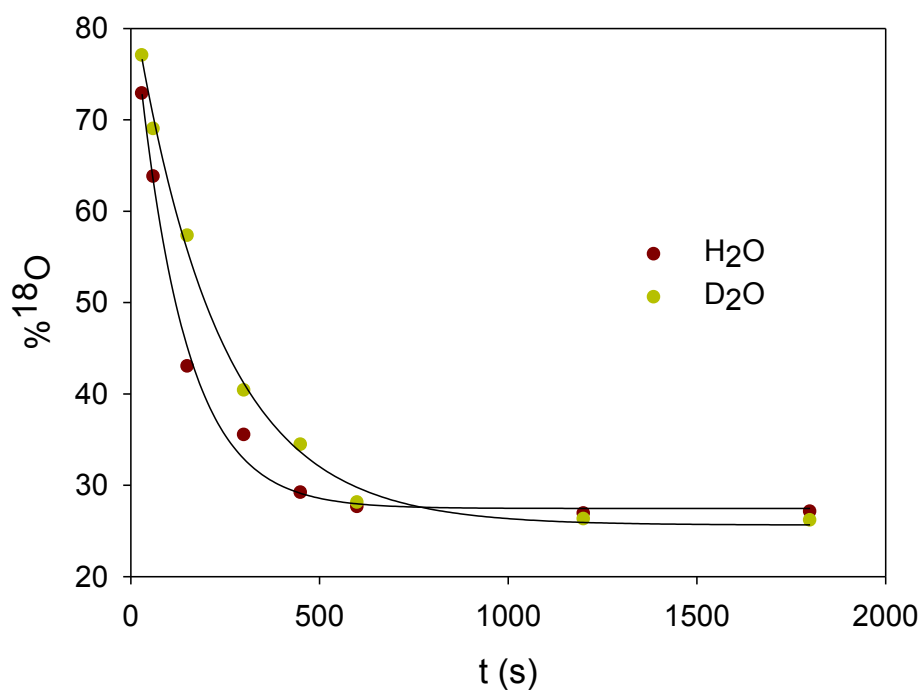


Figure SIII.10. Experiments between ¹⁸O – labeled **3^(IV)=O** (generated from reaction of ¹⁶O – labelled **3^(IV)=O** and 0.14 M H₂¹⁸O, 1.0 mM) and H₂¹⁶O or D₂¹⁶O at 22 °C (0.42 M of H₂O or D₂O) at 0 °C, resulting in a KIE of 1.8. The ¹⁸O – incorporation was determined by quenching aliquots (0.4 mL, 0.4 mmol) of the reaction with thioanisole (5 μL, 42.7 mmol) and determining the ratio of ¹⁶O and ¹⁸O – methylphenylsulfoxide by GC – MS, as previously described.⁷⁷

Table SIII.4. Reported kinetic data for OAE between H₂¹⁸O and non – heme oxoiron (IV) complexes.⁷⁹

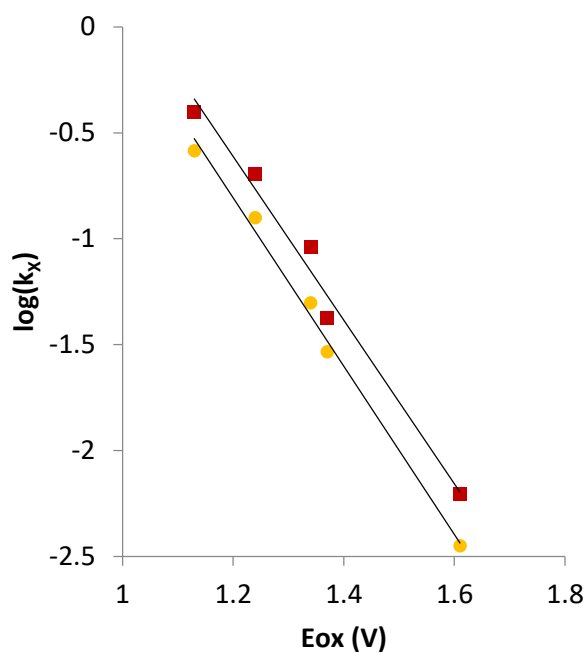
Complex [Fe(O)(L)] ²⁺	ΔH^\ddagger (kcal/mol)	ΔS^\ddagger (cal/K·mol)	ΔG^\ddagger_{298} (kcal/mol)
^a TMC	4.1 ± 0.7	-57.4 ± 8.1	21.0
N4Py	10.3 ± 2.4	-38.2 ± 7.9	22.0
Bn – TPEN	1.2 ± 0.3	-59.8 ± 2.4	18.9
1Py – Bn – TPEN	2.9 ± 0.7	-57.4 ± 2.6	19.6
2Py – Bn – TPEN	4.8 ± 1.2	-50.2 ± 4.5	19.6

^aData from ref. 259.

Table SIII.5. Sulfoxide yields for $1^{(IV)=O}$ and $2^{(IV)=O}$ with thioanisole substrates.

X	$1^{(IV)=O}$	$2^{(IV)=O}$
	Sulfoxide yield ^a	Sulfoxide yield ^a
CH ₃ O	94 ± 6%	99 ± 1%
CH ₃	92 ± 3%	100 ± 2%
H	84 ± 7%	99 ± 1%
Cl	93 ± 5%	99 ± 2%
CN	65 ± 1%	93 ± 5%

^aYields were obtained by GC – FID with an external standard from an average of two replicates and corrected by Mössbauer purity or the reported purity of complex.⁸³

**Figure SIII.11.** Plot of E_{ox} vs log(k_x) from reactions of $1^{(IV)=O}$ (yellow circles) and $2^{(IV)=O}$ (red squares) with thioanisole substrates.

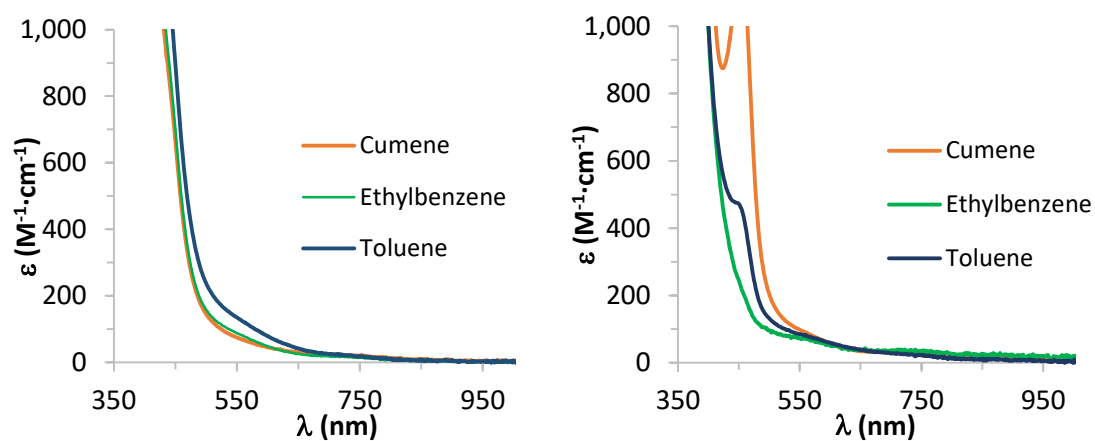


Figure SIII.12. Final UV – vis spectra after reaction of $1^{(IV)}=O$ (left) and $2^{(IV)}=O$ upon addition of cumene, ethylbenzene and toluene.

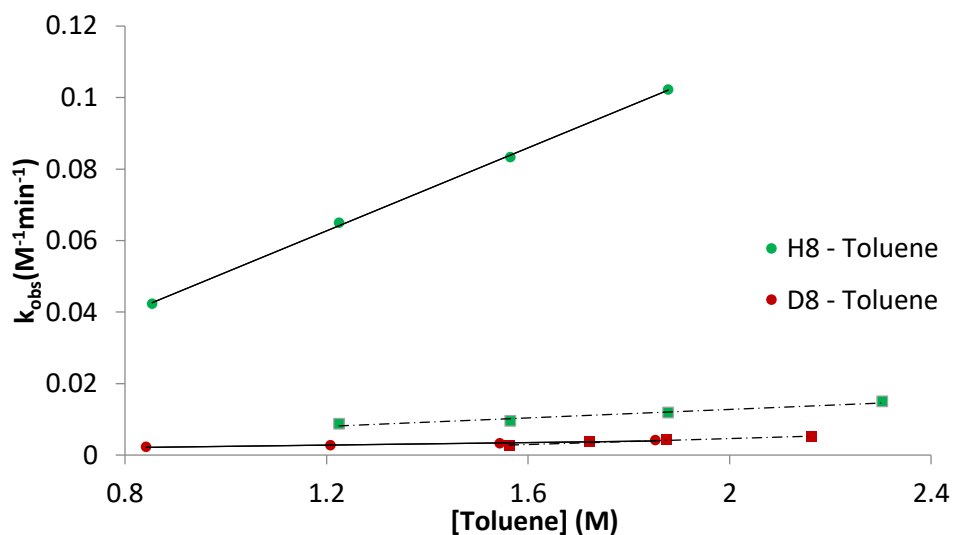


Figure SIII.13. Plot of the pseudo – first – order rate constants, k_{obs} (min^{-1}) against substrate concentrations to determine second – order rate constants, k_2 and C – H kinetic isotope effect (KIE) value for the reaction of 1 mM of $1^{(IV)}=O$ (circles with solid line) and $2^{(IV)}=O$ (squares with dashed line) with toluene (green) and toluene – D_8 (red) in CH_3CN at 20 °C.

Table SIII.6. Product distribution of oxidation reactions of $1^{(IV)=O}$ and $2^{(IV)=O}$ with alkylbenzene substrates under O_2 .

Substrate	Product	Complex $1^{(IV)=O}$ ^{a,b} Yield under O_2	Complex $2^{(IV)=O}$ ^{a,b} Yield under O_2	Total equivalents of oxidised products per unit of $1^{(IV)=O} / 2^{(IV)=O}$ ^c
Cumene	Alcohol	295 %	627 %	8.8 / 18.8
	Ketone	65,5 %	137 %	
	Alkene	12.4 %	38.8 %	
Ethylbenzene	Alcohol	53.2 %	68.8 %	4.3 / 4.9
	Ketone	78.2 %	86.6 %	
	Alkene	3.6 %	3.2 %	
Toluene	Alcohol	8.8 %	8.7 %	2.7 / 1.7
	Aldehyde	63.4 %	38.9 %	

^aYields were obtained by GC – FID with an external standard. ^bYields were corrected by Mössbauer purity ($1^{(IV)=O}$) and the reported purity ($2^{(IV)=O}$) of complexes. ^cTotal yield calculated from the number of electrons required to generate each product, alcohol ($2e^-$), alkene ($2e^-$) and ketone/aldehyde ($4e^-$).

Table SIII.7. Sulfoxide yields for oxidation reactions of iron complexes with thioanisole:cumene mixtures (1:1).

Substrate	T(°C)	Yield sulfoxide	
		$1^{(IV)=O}$	$4^{(IV)=O}$
Thioanisole	-20	^a 91 ± 1	^c 97 ± 4
Cumene	20	^a 70 ± 3	^d 87 ± 2
Thioanisole (1:1)	-20	^a 34 ± 2	-
1 – phenyl – 1 propanol yield			
Cumene	20	^b 11 ± 4	^e 51 ± 5

Yields calculated by GC from two replicates using an external standard. ^aExperiments done with 500 equivalents of each substrate. ^bExperiments done with 2500 equivalents of substrate. ^cExperiments done with 200 equivalents of substrate. ^dExperiments done with 100 equivalents of each substrate, alkene and ketophenone were also observed. ^eExperiments done with 100 equivalents of substrate.

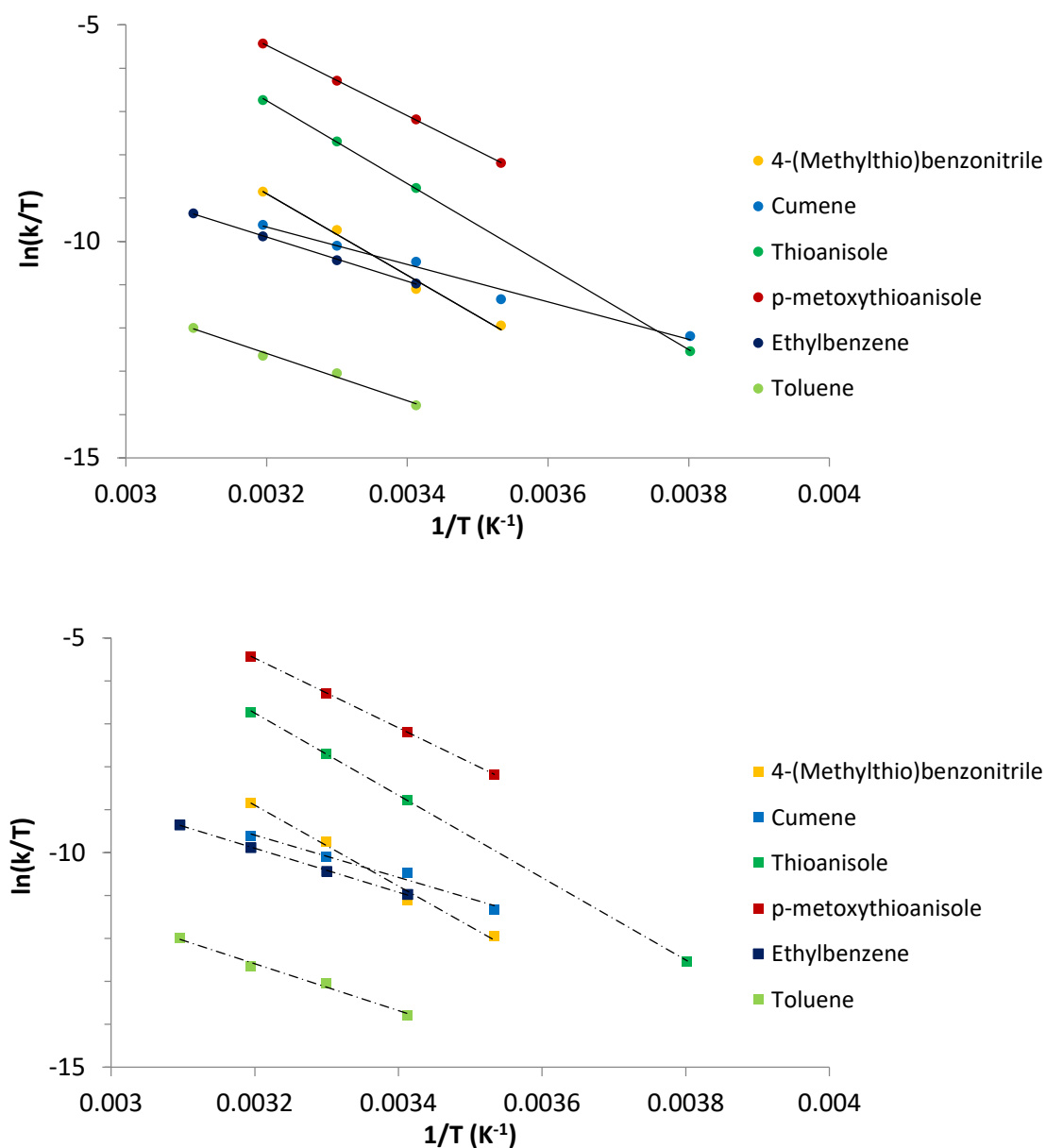


Figure SIII.14. Eyring plot of $\ln(k/T)$ vs $1/T$ to obtain the thermodynamic parameters of reactions of $1^{(IV)}=O$ (top) and $2^{(IV)}=O$ (below) with thioanisole and alkylbenzylic substrates.

Table SIII.8. $4^{(IV)}=O$ rate constants obtained for thioanisole and cumene substrates.

T (°C)	k_2 thioanisole ($M^{-1}s^{-1}$)	T (°C)	k_{obs} cumene (s^{-1}) ^a
40	2.42	35	0.0050
25	0.46	25	0.0025
0	0.098	15	0.0013
-20	0.002	0	0.0043

^a[cumene] = 0.78 M. k_2 (cumene, 25 °C) = 0.0025(2) $M^{-1}s^{-1}$.

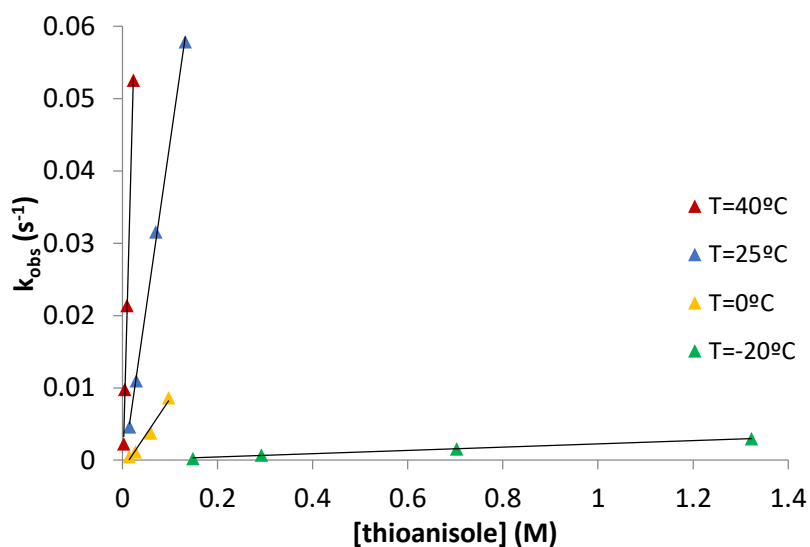


Figure SIII.15. Plot of the pseudo – first – order rate constants, k_{obs} (s⁻¹) against thioanisole concentrations to determine second – order rate constants, k_2 at different temperatures for complex $4^{(\text{IV})}=\text{O}$.

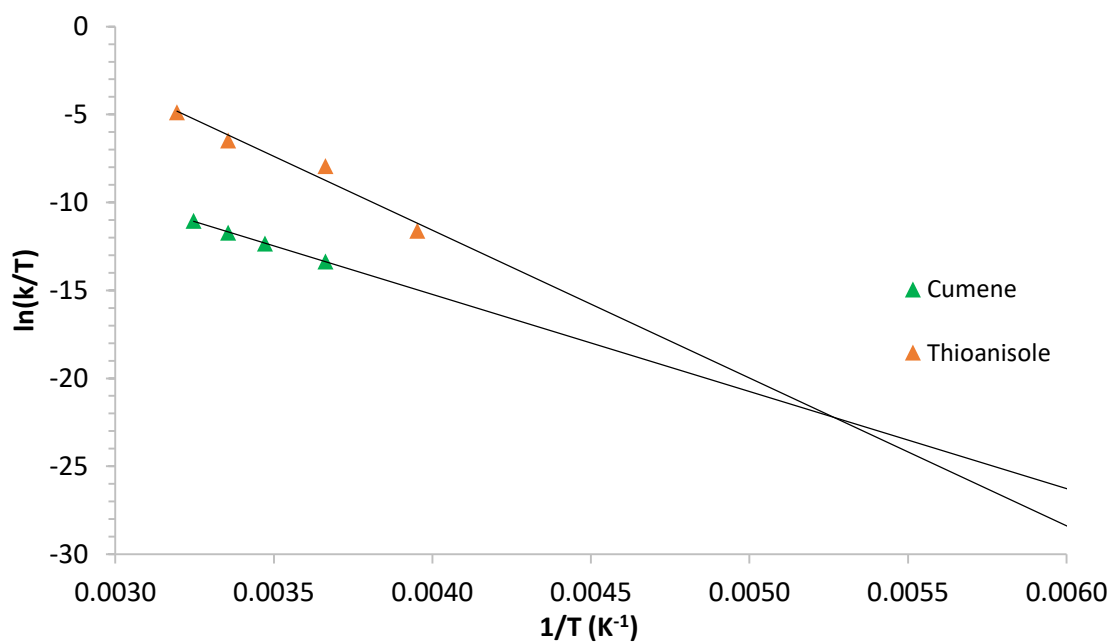


Figure SIII.16. Eyring plot of $\ln(k/T)$ vs $1/T$ to obtain the thermodynamic parameters of reactions of $4^{(\text{IV})}=\text{O}$ with thioanisole and cumene substrates.

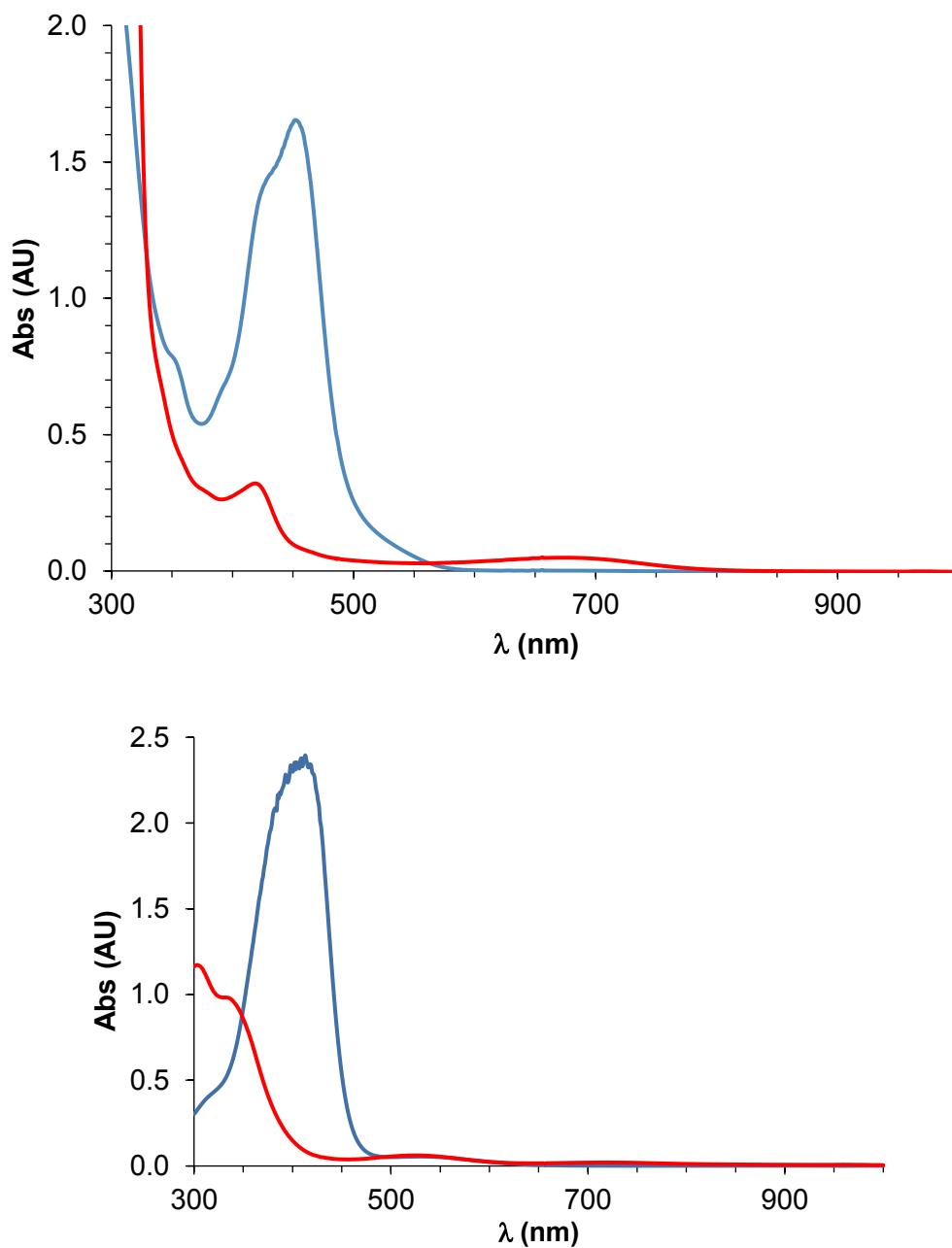


Figure SIII.17. Top: (Blue line) UV – vis spectrum of $[\text{Ru}(\text{bpy})_3]\text{Cl}_2$ in water (0.17 mM) in the presence of excess $\text{Na}_2\text{S}_2\text{O}_8$ (200 equiv); (Red line) spectrum obtained after 450nm light irradiation of previous solution in the oxidation to $[\text{Ru}^{\text{III}}(\text{bpy})_3]$. Below: (Blue line) UV – vis spectrum of $\mathbf{1}^{\text{(II)}}$ in MeCN:H₂O 1:3 (0.4 mM); (Red line) spectrum obtained after addition of 10 equiv $\text{Na}_2\text{S}_2\text{O}_8$ (4 mM) in the oxidation of $\mathbf{1}^{\text{(II)}}$ to $\mathbf{1}^{\text{(III)}} - \text{OH}$.

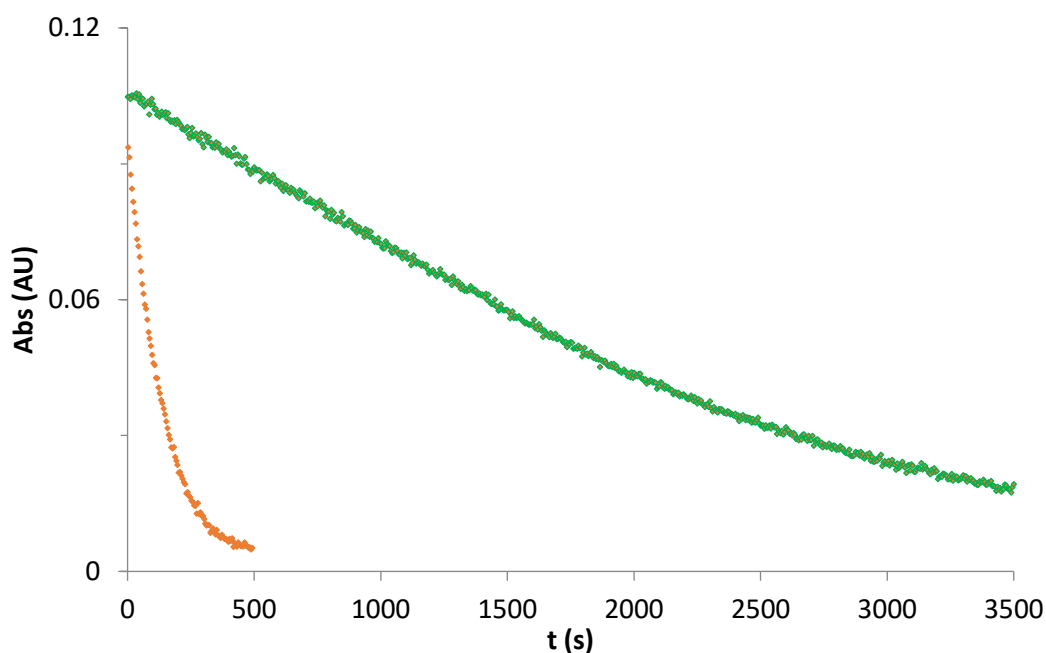


Figure SIII.18. Evolution of 715 nm feature of chemically generated $1^{(IV)}=O$ (0.4 mM, 0.02 mM $[Ru^{II}Cl_2(bpy)_3]$, 25°C) upon addition of 5 eq $^{MeO}PhSMe$ with irradiation at 447 nm (orange line) and without irradiation (green line).

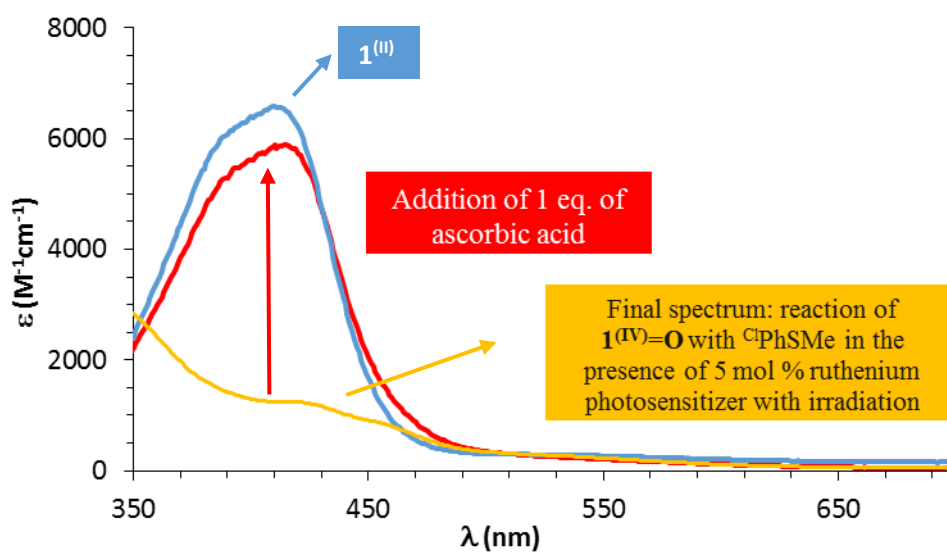


Figure SIII.19. Blue line: UV – vis spectrum of $1^{(III)}$ in $CH_3CN:H_2O$ 1:3. Yellow line: UV – vis spectrum obtained at the end of the reaction between chemically generated $1^{(IV)}=O$ and 5 equiv *para* – chloro – thioanisole in the presence of 5 mol% $[Ru^{II}Cl_2(bpy)_3]$ with 447nm – light irradiation at 298 K. Red – line: UV – vis spectrum obtained upon addition of 1 equiv ascorbic acid (with respect to iron) after reaction of chemically generated $1^{(IV)}=O$ and 5 equiv *para* – chloro – thioanisole in the presence of 5 mol% $[Ru^{II}Cl_2(bpy)_3]$ with 447nm – light irradiation at 298 K.

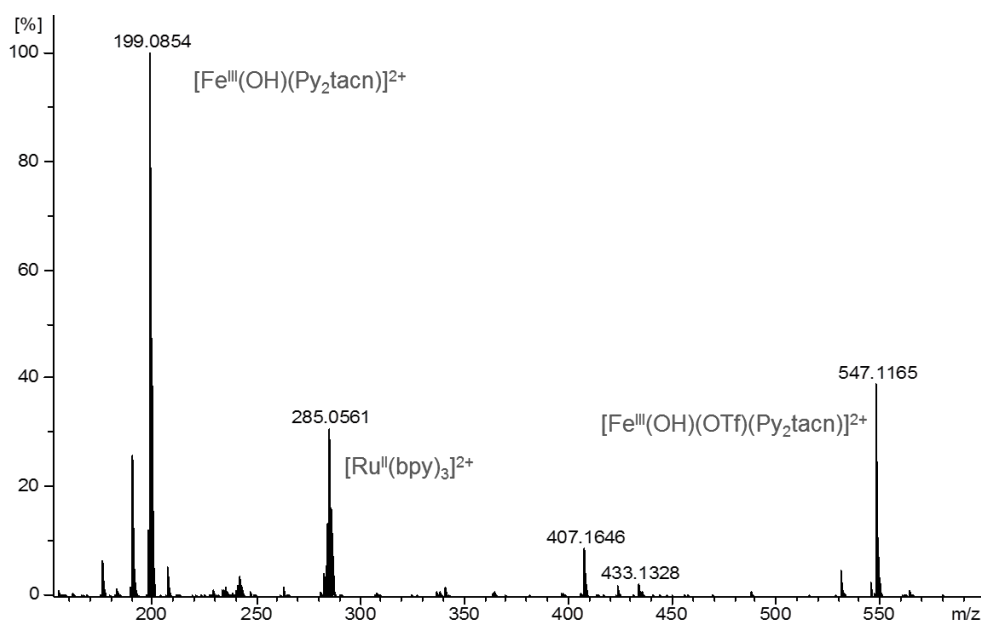


Figure SIII.20. ESI – MS spectrum obtained after reaction of chemically generated $1^{(IV)}=O$ with 5 equiv $ClPhSMe$ in the presence of 5 mol% $[Ru^{II}Cl_2(bpy)_3]$ with 450 nm – light irradiation at 298 K.

$p - XMeOPhSMe$	E_{ox} (V)
MeO	1.13
Me	1.24
H	1.34
Cl	1.37
CN	1.61

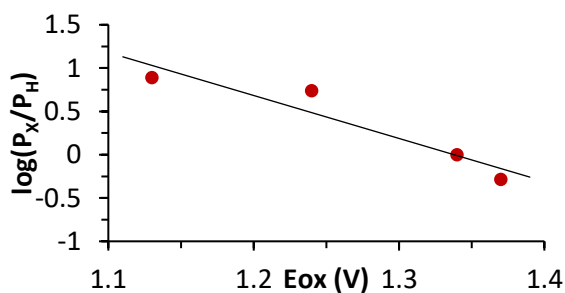


Figure SIII.21. Plot $\log(P_X/P_H)$ vs. reduction potential of $p - X -$ thioanisoles (E_{ox}) for competition experiments corresponding to the competitive reactions of $1^{(IV)}=O$ with thioanisole and $p - X -$ thioanisoles in $CH_3CN:H_2O$ 1:3 in the presence of 5 mol% $[Ru^{II}(bpy)_3]Cl_2$ with 447 nm – light irradiation at 298 K. P_X corresponds to the amount of *para* – substituted phenylmethylsulfoxide obtained at the end of the reaction (determined by GC – FID or NMR). Competition experiments were run in the presence of 5 equiv thioanisole and 5 equiv $p - X -$ thioanisole.

Photophysical experiments

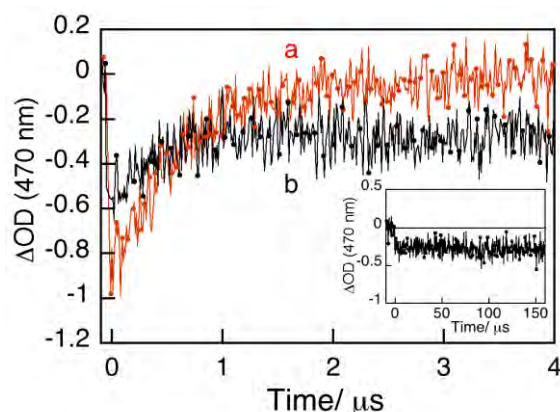


Figure SIII.22. Transient kinetic trace observed at 470 nm after laser flash photolysis (532 nm) of deaerated solution of $[\text{Ru}^{\text{II}}(\text{bpy})_3]^{2+}$ (0.07 mM) in $\text{CH}_3\text{CN}:\text{H}_2\text{O}$ (1:3) a) in the absence and b) in the presence of $\mathbf{1}^{(\text{IV})}=\mathbf{O}$ (3.4 mM). Inset: $[\text{Ru}^{\text{II}}(\text{bpy})_3]^{2+}$ time profile monitored at 470 nm in the presence of $\mathbf{1}^{(\text{IV})}=\mathbf{O}$ (3.4 mM) over a period of 160 μs .

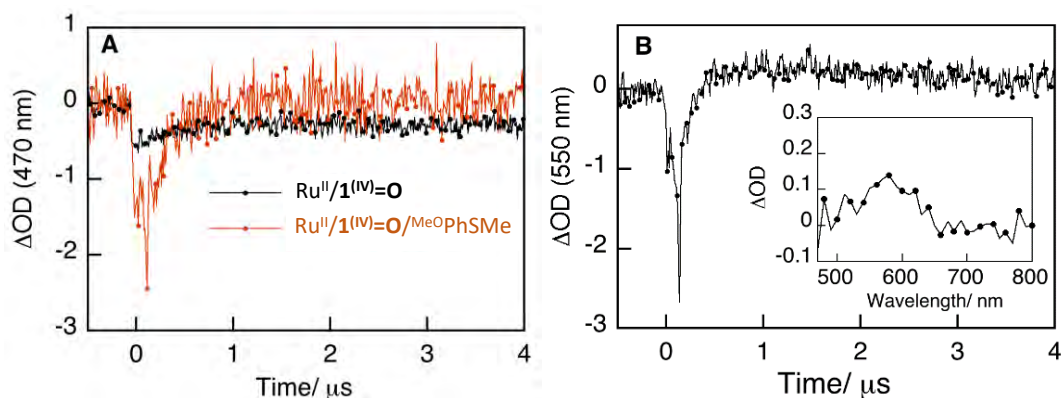


Figure SIII.23. A) Transient kinetic traces monitored at 470 nm after laser flash photolysis (532 nm) of a deaerated $\text{CH}_3\text{CN}:\text{H}_2\text{O}$ (1:3) solution of $[\text{Ru}^{\text{II}}(\text{bpy})_3]^{2+}$ in the presence of $\mathbf{1}^{(\text{IV})}=\mathbf{O}$ (3.4 mM) (black) or $\mathbf{1}^{(\text{IV})}=\mathbf{O}$ (3.4 mM) and $\text{Me}^{\text{O}}\text{PhSMe}$ (3.4 mM) (red). B) Transient kinetic traces monitored at 550 nm after laser flash photolysis (532 nm) of a deaerated solution of $[\text{Ru}^{\text{II}}(\text{bpy})_3]^{2+}$ in $\text{CH}_3\text{CN}:\text{H}_2\text{O}$ (1:3) in the presence of $\mathbf{1}^{(\text{IV})}=\mathbf{O}$ (3.4 mM) and $\text{Me}^{\text{O}}\text{PhSMe}$ (3.4 mM). Inset: transient absorption spectrum of a deaerated solution of $[\text{Ru}^{\text{II}}(\text{bpy})_3]^{2+}$ in $\text{CH}_3\text{CN}:\text{H}_2\text{O}$ (1:3) in the presence of $\mathbf{1}^{(\text{IV})}=\mathbf{O}$ (3.4 mM) and $\text{Me}^{\text{O}}\text{PhSMe}$ recorded 2 μs after laser excitation (532 nm).

Pulsed excitation at 532 nm (15 mJ/pulse) of deaerated $\text{CH}_3\text{CN}:\text{H}_2\text{O}$ (1:3) solutions of $[\text{Ru}^{\text{II}}(\text{bpy})_3]^{2+}$ (0.07 mM, absorbance 0.06 at 532 nm) led to the disappearance of the $[\text{Ru}^{\text{II}}]$ as evidenced by the strong bleaching near 470 nm. This was accompanied by the formation of $^*[\text{Ru}^{\text{II}}(\text{bpy})_3]^{2+}$ ($^3\text{MLCT}$ state) which exhibits characteristic absorption bands below 400 nm and an emission centered at ca. 620 nm, with a lifetime, τ , of 920 ns.⁸⁵ As expected, the bleaching at ca. 470 nm recovered fully in less than 3 μs (Figure S24 curve a), which is associated with the full recovery of $[\text{Ru}^{\text{II}}(\text{bpy})_3]^{2+}$. Comparatively, the same experiment in the presence of increasing amounts of $\mathbf{1}^{(\text{IV})}=\mathbf{O}$ showed that $\mathbf{1}^{(\text{IV})}=\mathbf{O}$ quenched the emission of $^*[\text{Ru}^{\text{II}}(\text{bpy})_3]^{2+}$ at 620 nm with a rate constant, k_q , of $5.7 \times 10^8 \text{ M}^{-1} \text{ s}^{-1}$. This is indicative of an interaction

between $^*[\text{Ru}^{\text{II}}(\text{bpy})_3]^{2+}$ and $\mathbf{1}^{(\text{IV})}=\mathbf{O}$. However, under these conditions $^*[\text{Ru}^{\text{II}}(\text{bpy})_3]^{2+}$ did not completely revert back to the starting $[\text{Ru}^{\text{II}}(\text{bpy})_3]^{2+}$ compound, *i.e.* its characteristic absorption at 470 nm was not fully recovered. This prolonged bleaching (no changes were detected even after 150 μs of the laser pulse) (inset in Figure S24 curve b) is in accordance with the formation of a new long – lived species with an absorbance in this region lower than that of $[\text{Ru}^{\text{II}}(\text{bpy})_3]^{2+}$. This new species could be $[\text{Ru}^{\text{III}}(\text{bpy})_3]^{3+}$, whose absorption at 470 nm is only 4% of that of $[\text{Ru}^{\text{II}}(\text{bpy})_3]^{2+}$. Interestingly, the 470 nm band was completely recovered when the $[\text{Ru}^{\text{II}}(\text{bpy})_3]^{2+}/\mathbf{1}^{(\text{IV})}=\mathbf{O}$ mixture was excited in the presence of $^{\text{MeO}}\text{PhSMe}$ (3.4 mM) (Figure S25 A). In this case, formation of a species with an absorption band centered at 580 nm was detected (Figure S25 B inset). This species can be assigned to a radical cation $^{\text{MeO}}\text{PhSMe}^{\bullet+}$.^{372,373}

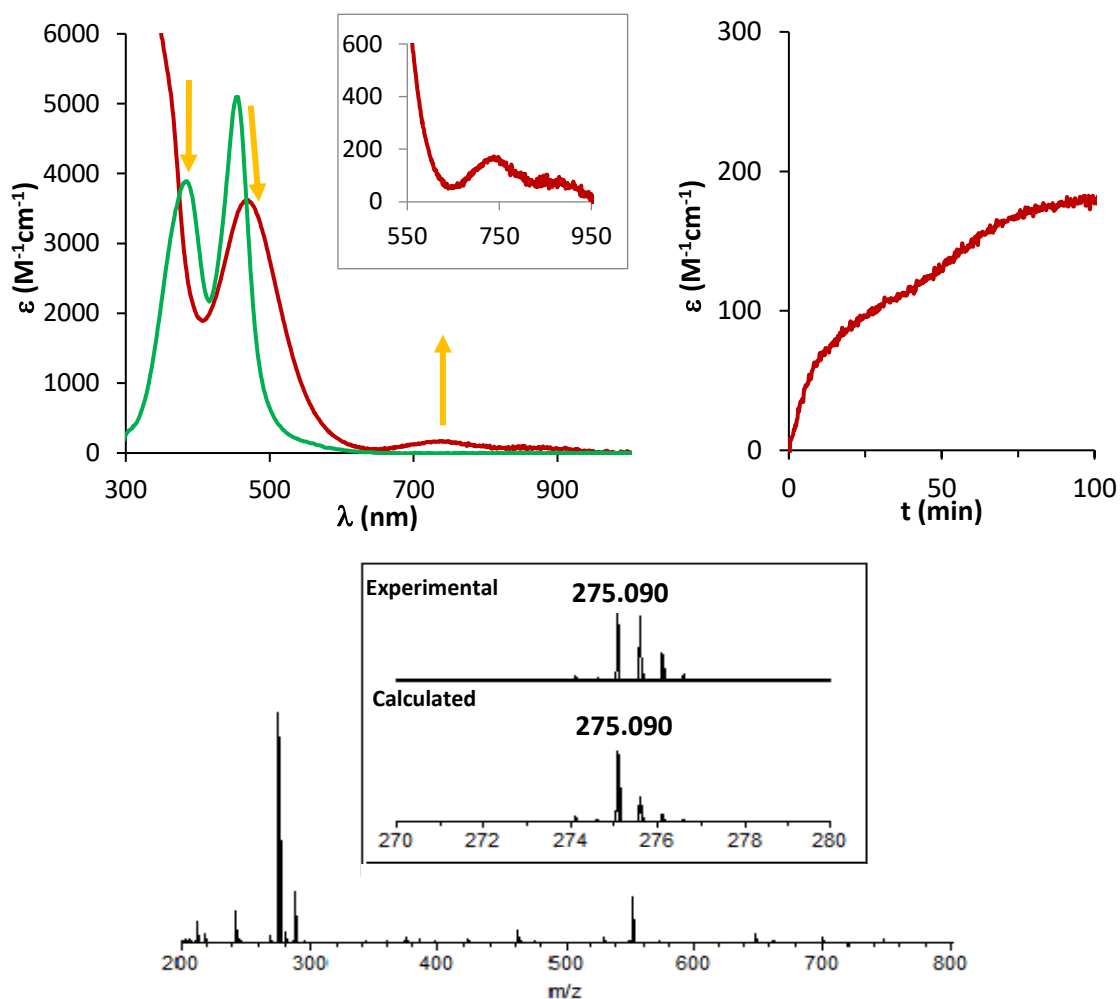
ANNEX CHAPTER IV

Figure SIV.1. (Top) UV – vis spectra of oxidation of $2^{(III)}$ to $2^{(IV)}=NTs$ in MeCN at 20°C, HR – MS spectrum of $2^{(IV)}=NTs$ prepared in CH_3CN exhibiting a base peak at m/z 275.09; inset show amplification of major peak for $[Fe^{IV}(NTs)(Me_2CHPy_2)tacn)]^{2+}$ species. Proper simulation of the peaks requires inclusion of $\approx 50\%$ of $[Fe^{III}(NHTs)(L)]^{2+}$ in the isotopic pattern corresponding to $[Fe^{IV}(NTs)(L)]^{2+}$.

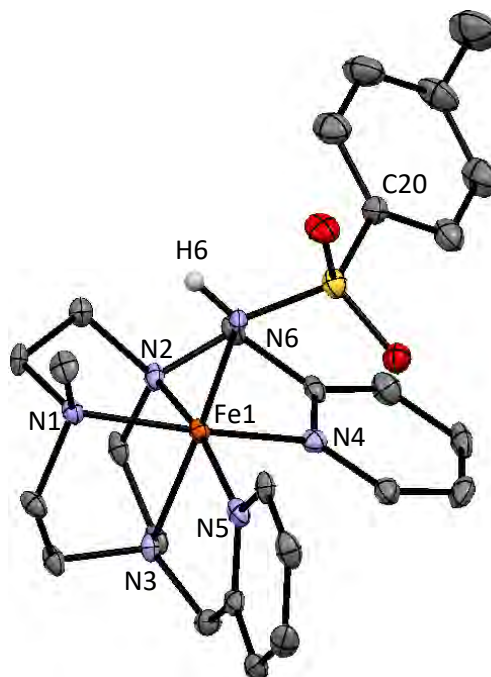


Table SIV.1. Crystal data and structure refinement for $[\text{Fe}^{\text{III}}(\text{NHTs})(\text{MePy}_2\text{tacn})](\text{SbF}_6)_2$ ($\mathbf{1}^{\text{III}} - \text{NHTs/SbF}_6$) at 100 K.

Empirical formula	C ₃₆ H ₅₇ F ₁₂ Fe N ₆ O ₅ S Sb ₂	
Formula weight	1213.28	
Temperature	100(2) K	
Wavelength	0.71073 Å	
Crystal system	Monoclinic	
Space group	P2(1)/c	
Unit cell dimensions	a = 8.5051(16)Å	α = 90°.
	b = 38.523(6)Å	β = 100.466(6)°.
	c = 14.211(2)Å	γ = 90°.
Volume	4578.8(13) Å ³	
Z	4	
Final R indices [I > 2σ(I)]	R1 = 0.0489, wR2 = 0.0915	
R indices (all data)	R1 = 0.0781, wR2 = 0.1015	

Table SIV.2. Selected bond lengths [Å] and angles [°] complex **1^(III)** – **NHTs/SbF₆**.

Fe1-N6	1.894(4)
Fe1-N2	1.986(4)
Fe1-N5	1.988(4)
Fe1-N4	1.990(4)
Fe1-N3	2.024(4)
Fe1-N1	2.027(4)
N6-S1	1.593(4)
<hr/>	
N6-Fe1-N2	95.43(17)
N6-Fe1-N5	98.01(18)
N2-Fe1-N5	166.39(17)
N6-Fe1-N4	90.65(17)
N2-Fe1-N4	82.81(17)
N5-Fe1-N4	94.89(17)
N6-Fe1-N3	176.46(17)
N2-Fe1-N3	84.71(16)
N5-Fe1-N3	82.01(17)
N4-Fe1-N3	92.88(16)
N6-Fe1-N1	91.05(17)
N2-Fe1-N1	86.53(17)
N5-Fe1-N1	95.32(17)
N4-Fe1-N1	169.32(18)
N3-Fe1-N1	85.42(16)
S1-N6-Fe1	133.4(3)
N6-S1-C20	107.7(3)
N1-C1-C2	111.2(4)

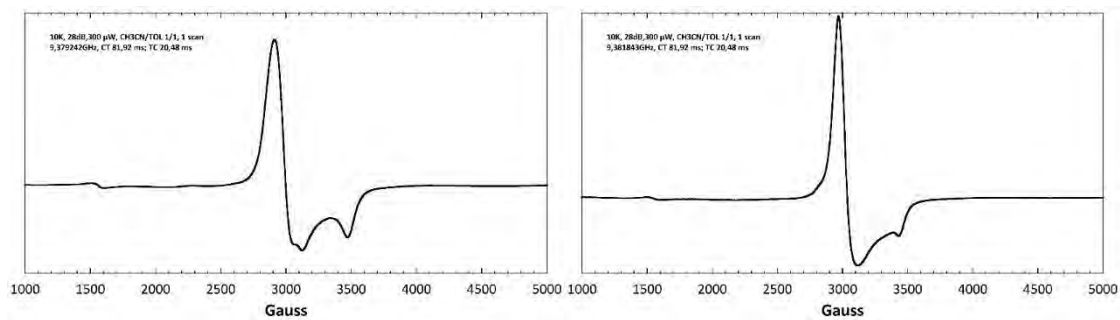
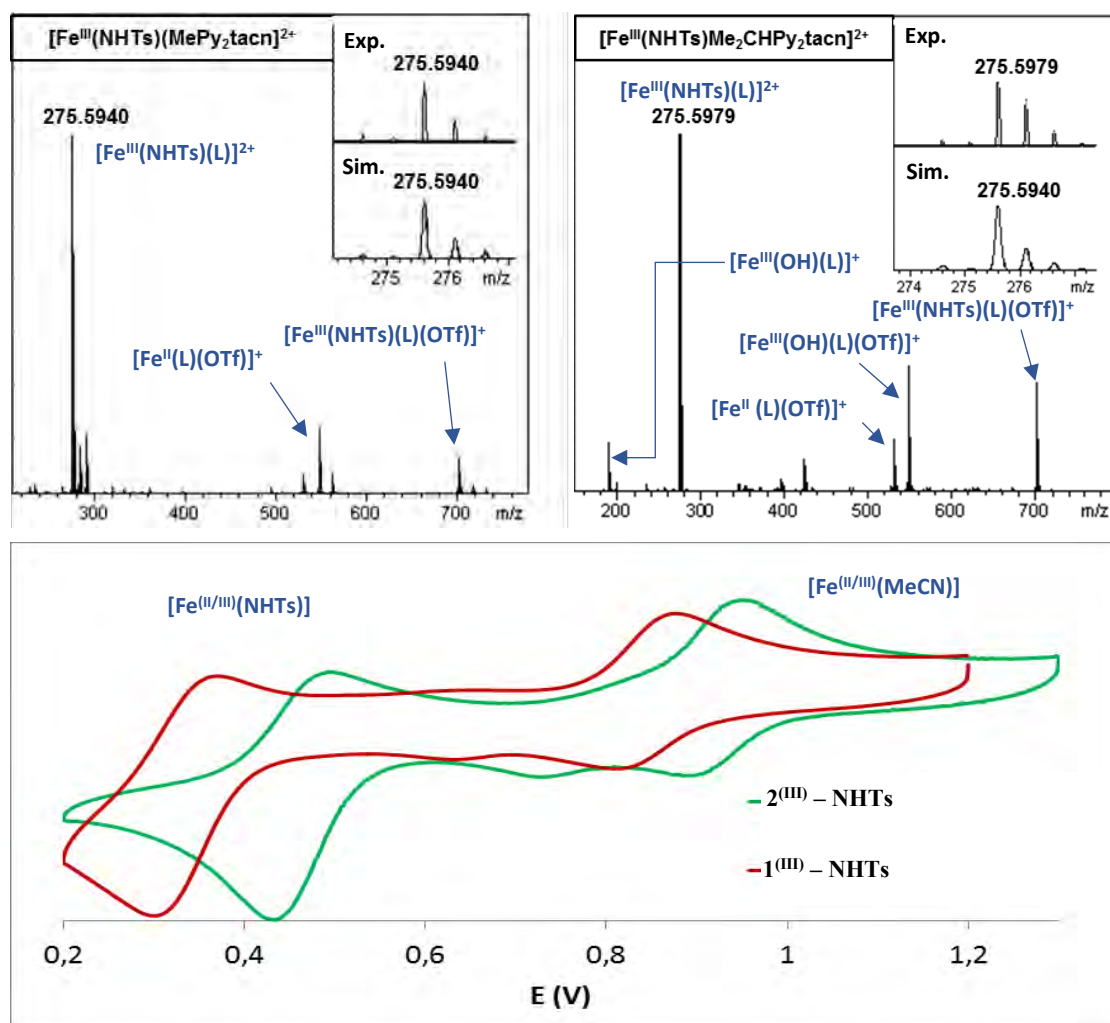


Figure SIV.2. EPR spectra of isolated $1^{(III)} - \text{NHTs/OTf}$ (left) and $2^{(III)} - \text{NHTs/OTf}$ (right) at 2K.



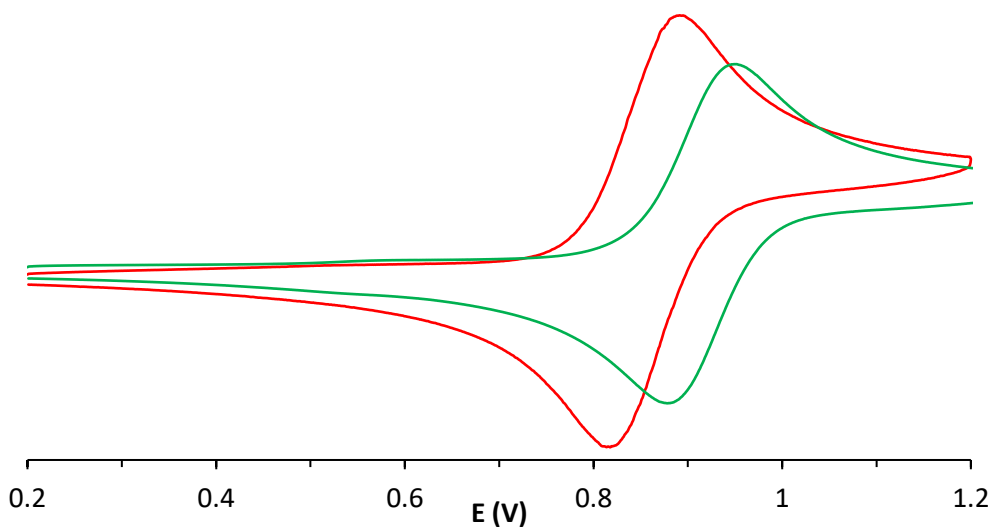


Figure SIV.3. (Top) HR – MS of isolated $1^{(III)} - \text{NHTs}/\text{OTf}$ and $2^{(III)} - \text{NHTs}/\text{OTf}$ in CH_3CN . Below, CV spectra of species $1^{(III)} - \text{NHTs}/\text{OTf}$ and $2^{(III)} - \text{NHTs}/\text{OTf}$ in CH_3CN , small waves around 0.6 – 0.7 V are from $[\text{Fe}^{III}(\text{OH})\text{L}]\text{OTf}_2$ formed from traces of water ($\text{L} = \text{MePy}_2\text{tacn}$ or $\text{Me}_2(\text{CHPy}_2)\text{tacn}$). (Medium) HR – MS of $1^{(III)} - \text{NHTs}/\text{OTf}$ and $2^{(III)} - \text{NHTs}/\text{OTf}$, insets show $[\text{Fe}^{III}(\text{NHTs})\text{L}]^{2+}$ ions; the presence of minor peaks come from traces of $[\text{Fe}^{II}(\text{CH}_3\text{CN})\text{L}]\text{OTf}_2$ and $[\text{Fe}^{III}(\text{OH})\text{L}]\text{OTf}_2$ impurities due to adventitious water. (Below) Cyclic Voltammetry spectra of $[\text{Fe}^{II}(\text{MeCN})(\text{MePy}_2\text{tacn})]\text{OTf}_2$ (red line) and $[\text{Fe}^{II}(\text{MeCN})(\text{Me}_2(\text{CHPy}_2)\text{tacn})]\text{OTf}_2$ (green line) in MeCN , 0.1mM of TBAPF_6 .

Table SIV.3. Yield of sulfanylidene products (2.5 mM on Fe and 0.25 – 1.2 M on substrate), normalised according to the iron (IV) purity of sample measured by Mössbauer spectroscopy.

Complex	$^X\text{PhS}(\text{NTs})\text{Me}$ Yields (%)		
	$[\text{Fe}^{IV}(\text{NTs})(\text{MePy}_2\text{tacn})]^{2+}$ $1^{(IV)=\text{NTs}}$	$[\text{Fe}^{IV}(\text{NTs})(\text{Me}_2(\text{CHPy}_2)\text{tacn})]^{2+}$ $2^{(IV)=\text{NTs}}$	
Solvent	Acetonitrile	Acetone	Acetonitrile
X			
MeO	57	42	48
Me	46	43	44
H	49	53	33
Cl	44	43	29

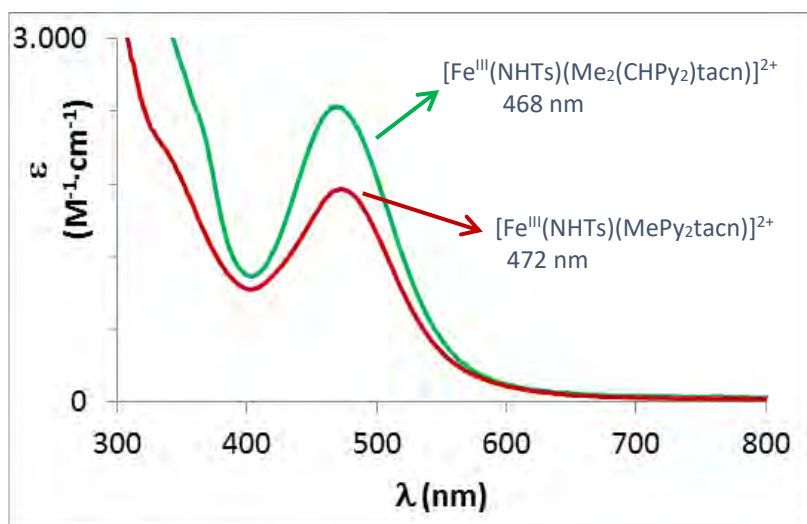


Figure SIV.4. UV – vis spectra of isolated $1^{(III)}$ – NHTs/OTf and $2^{(III)}$ – NHTs/OTf in MeCN at 20 °C.

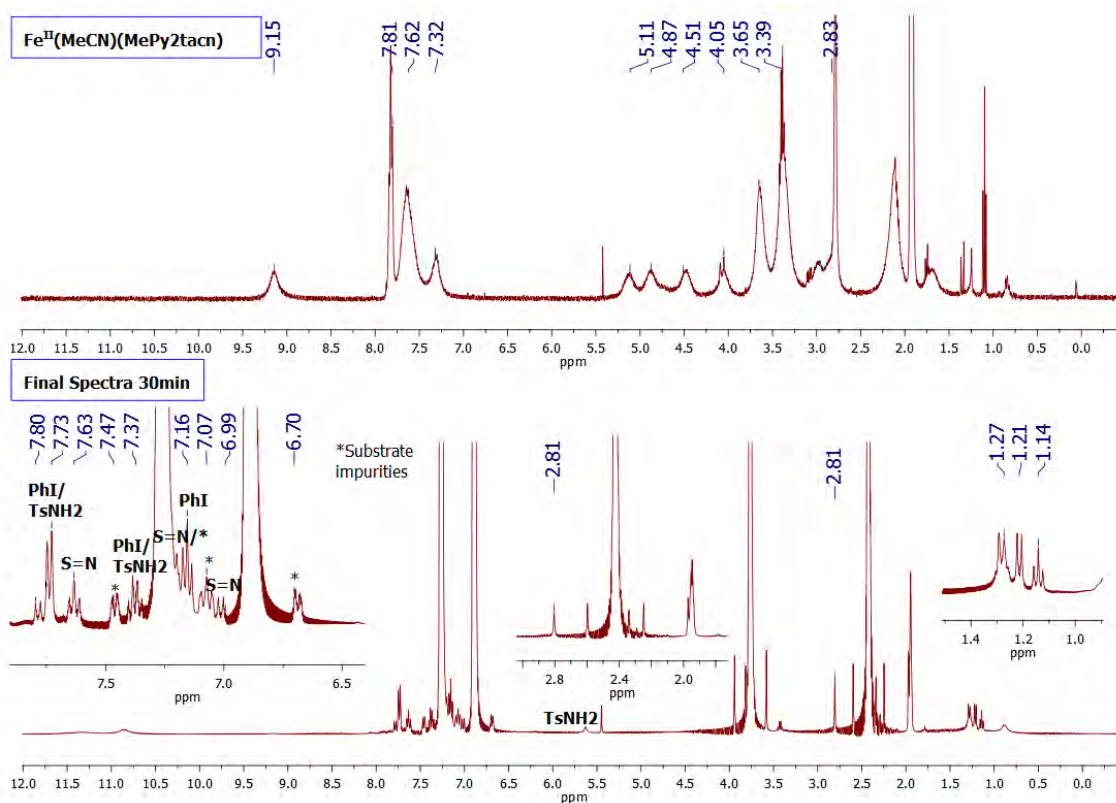


Figure SIV.5. ^1H – NMR spectra of: (Top) $[\text{Fe}^{II}(\text{MeCN})(\text{MePy}_2\text{tacn})](\text{OTf})_2$, $1^{(III)}$, in CD_3CN ; (Below) reaction of $1^{(IV)}=\text{NTs}$ with $^{\text{MeO}}\text{PhSMe}$ in CD_3CN after 30 minutes time.

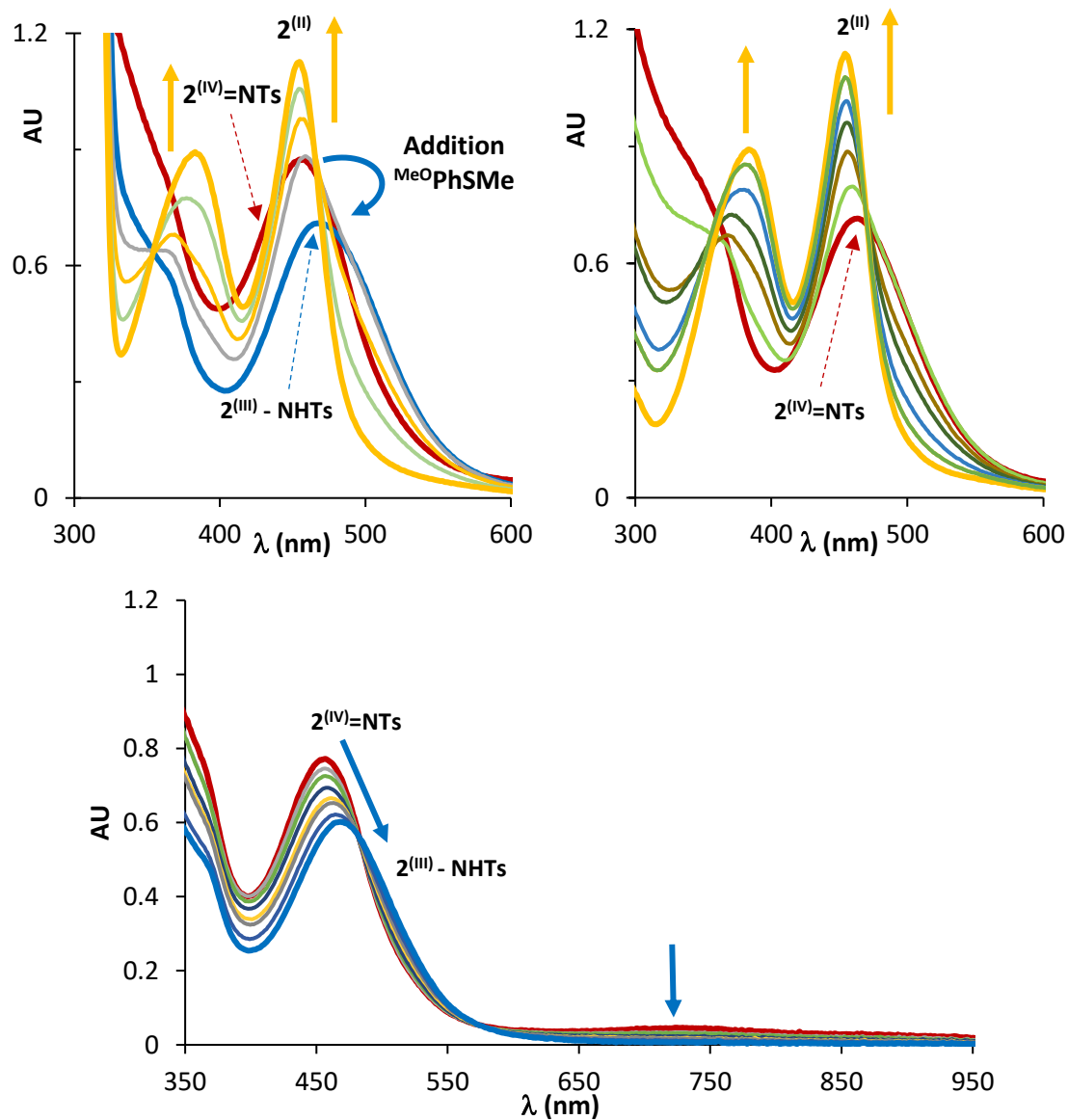


Figure SIV.6. (Top left) Titration of $2^{(III)}\text{-NHTs}$ with ascorbic acid (1 equivalent) after reaction of $2^{(IV)}\text{=NTs}$ with MeOPhSMe in MeCN. (Top right) Titration of $2^{(III)}\text{-NHTs}$ to $2^{(II)}$ with 2 equivalents of ascorbic acid in MeCN. (Below) Titration of $2^{(IV)}\text{=NTs}$ to $2^{(III)}\text{-NHTs}$ with 1 equivalent of ascorbic acid in acetone.

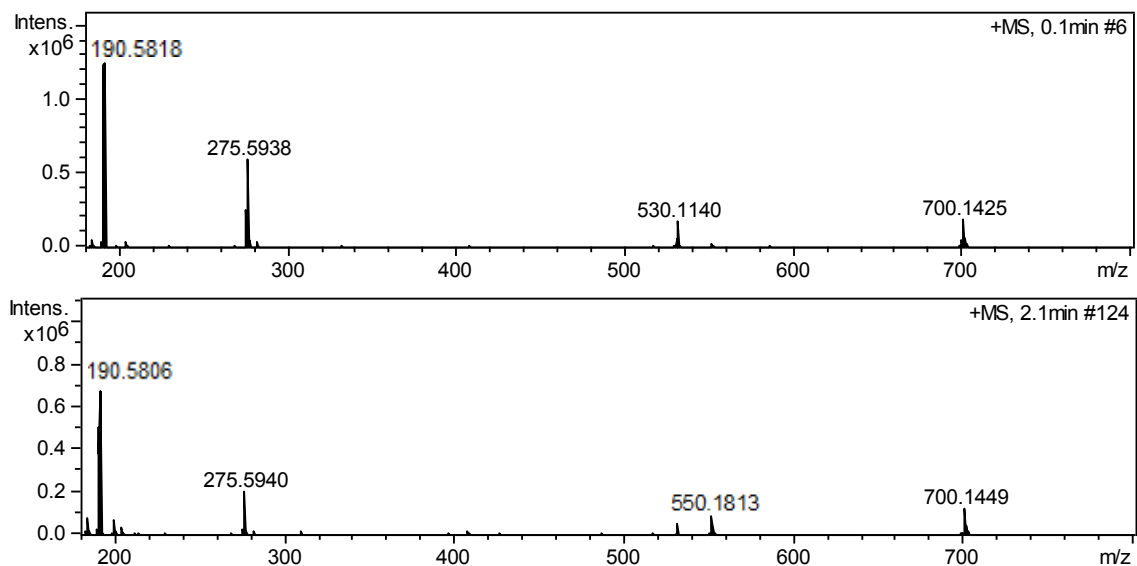


Figure SIV.7. (Top) Mass spectra of $1^{(IV)}=NTs$ reduced with: (top) one equivalent of ascorbic acid; (below) one equivalent of bis(1,3 – dimethylbenzimidazolidin – 2 – ylidene).

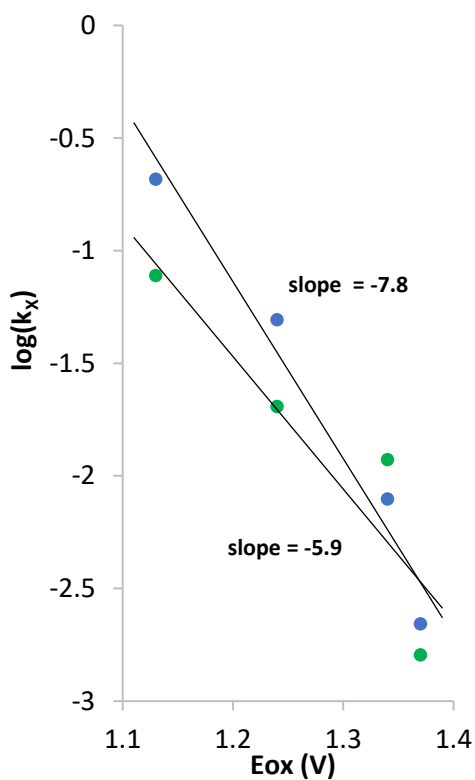


Figure SIV.8. Plot E_{ox} vs $\log(k_x)$ in the reactions of $1^{(IV)}=NTs$ (green circles) and $2^{(IV)}=NTs$ (blue circles) with p – XPhSMe substrates.

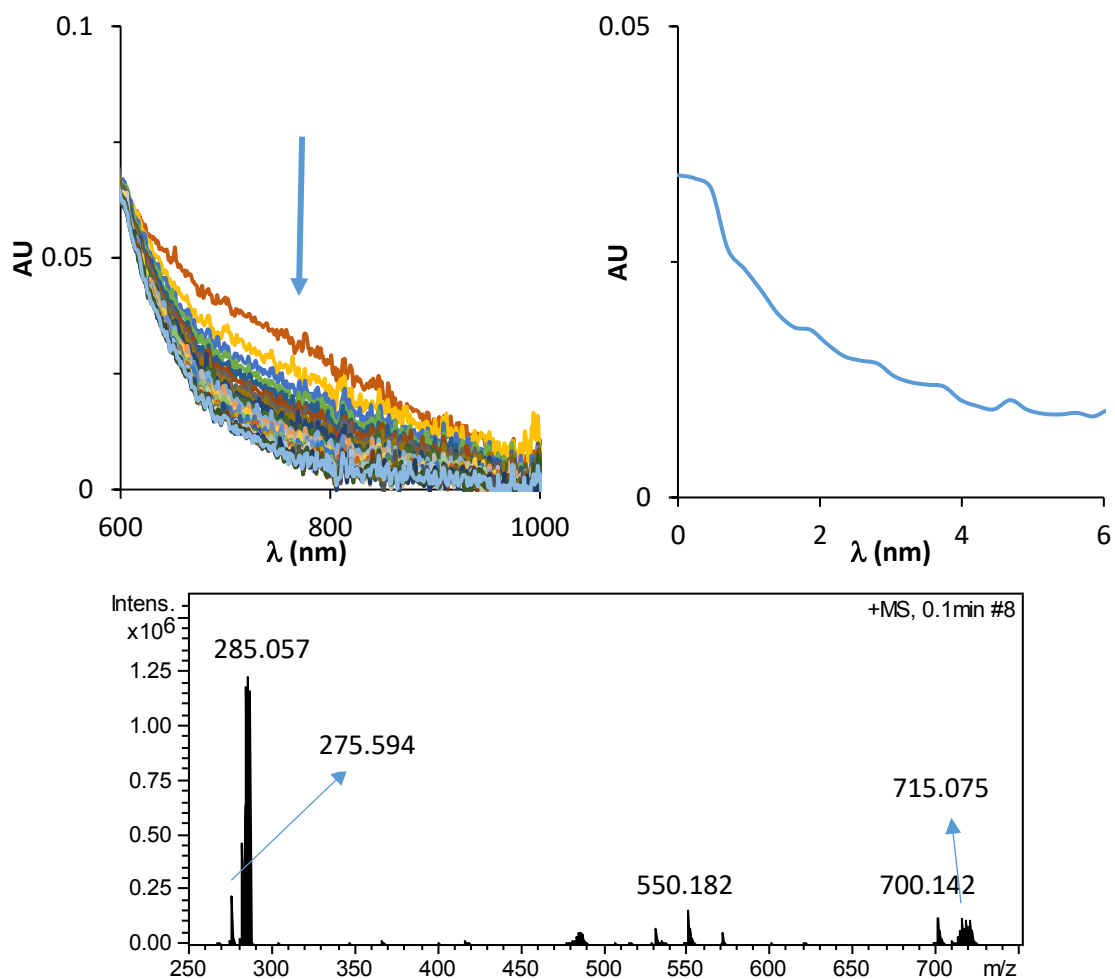


Figure SIV.9. (Top) UV – vis monitoring of the decay of $\mathbf{1}^{(IV)}=NTs$ upon addition of 1 equivalent of $[Ru^{II}(bpy)_3](PF_6)_2$ in acetonitrile. (Below) HR – MS spectra of reaction mixture. Ions at $m/z = 275.59$, 700.14 and 550.18 evidence the reduction of $\mathbf{1}^{(IV)}=NTs$ to $\mathbf{1}^{(III)}-NHTs$, despite only Ru^{II} peaks (285.06 and 715.07) could be observed due to Ru^{III} instability.

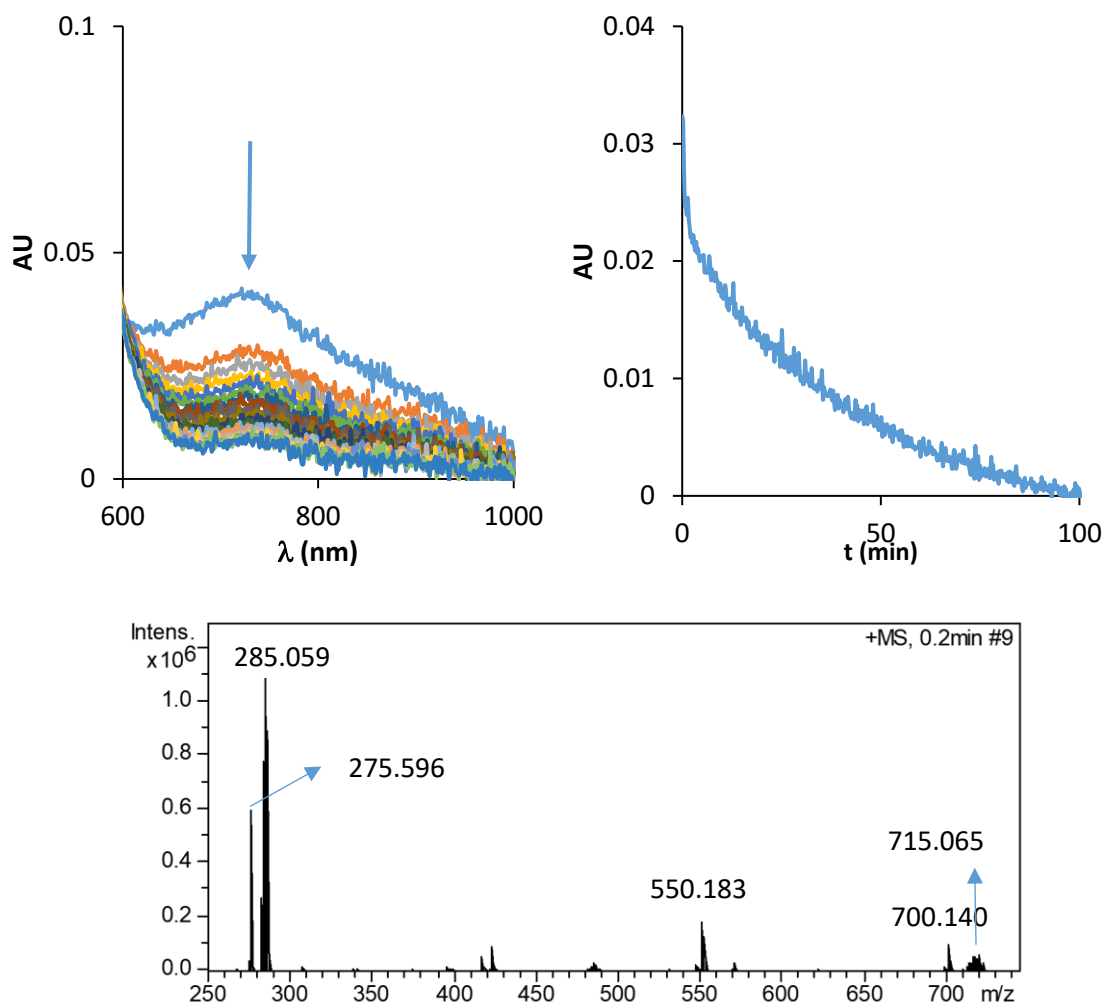


Figure SIV.10. (Top) UV – vis monitoring of the decay of $2^{(IV)}$ =NTs upon addition of 1 equivalent of $[\text{Ru}^{\text{II}}(\text{bpy})_3](\text{PF}_6)_2$ in acetone. (Below) HR – MS spectrum of reaction mixture. Ions at $m/z = 275.59$, 700.14 and 550.18 evidence the reduction of $2^{(IV)}$ =NTs to $2^{(III)}$ – NHTs, despite only Ru^{II} peaks (285.06 and 715.07) could be observed due to Ru^{III} instability.

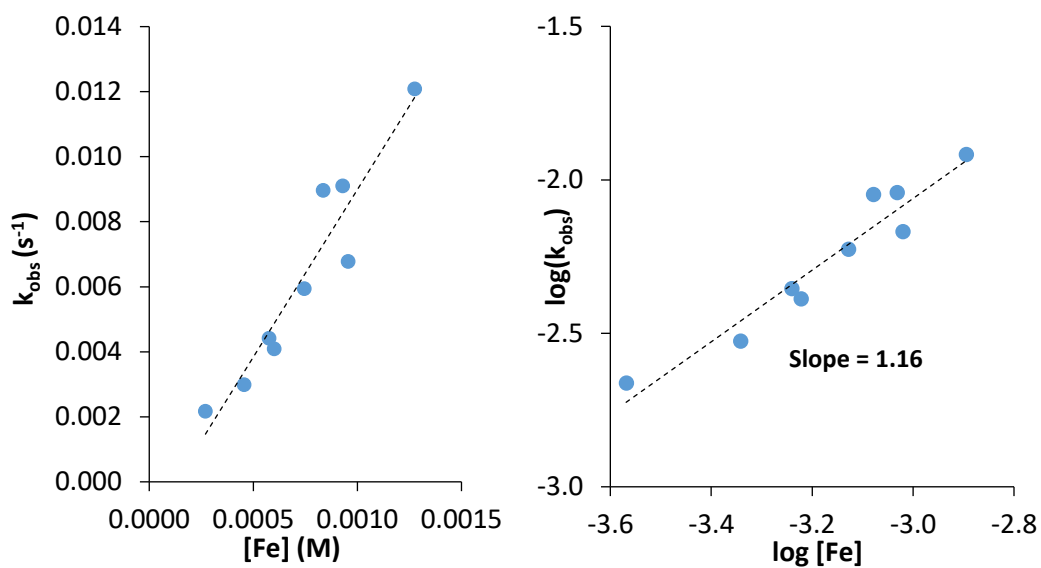


Figure SIV.11. (Left) Rate dependence on $[\text{Fe}]$ for the reaction of $1^{(\text{IV})}=\text{NTs}$ with MeOPhSMe . (Right) $\log(k_{\text{obs}})$ vs $\log([1^{(\text{IV})}=\text{NTs}])$ in the reaction of $1^{(\text{IV})}=\text{NTs}$ with MeOPhSMe .

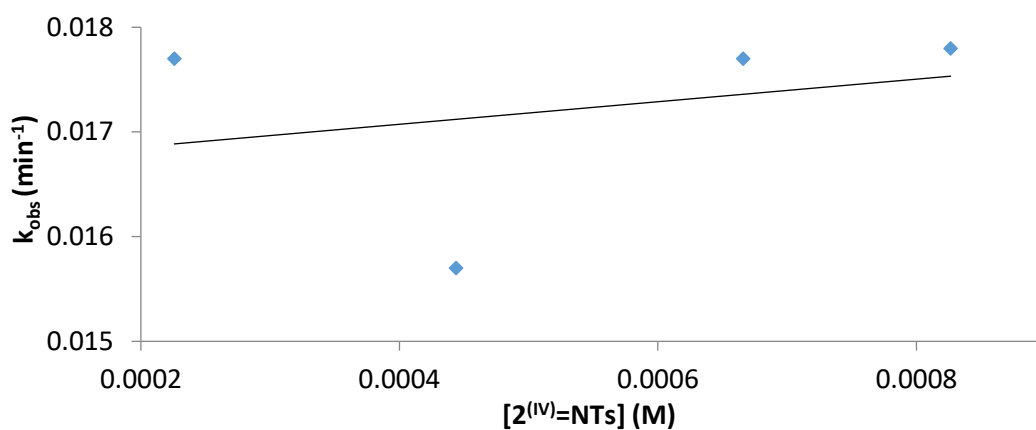


Figure SIV.12. Dependence of k_{obs} on $[\text{Fe}]$ in the reaction of $2^{(\text{IV})}=\text{NTs}$ with ClPhSMe (0.09 M) in MeCN.

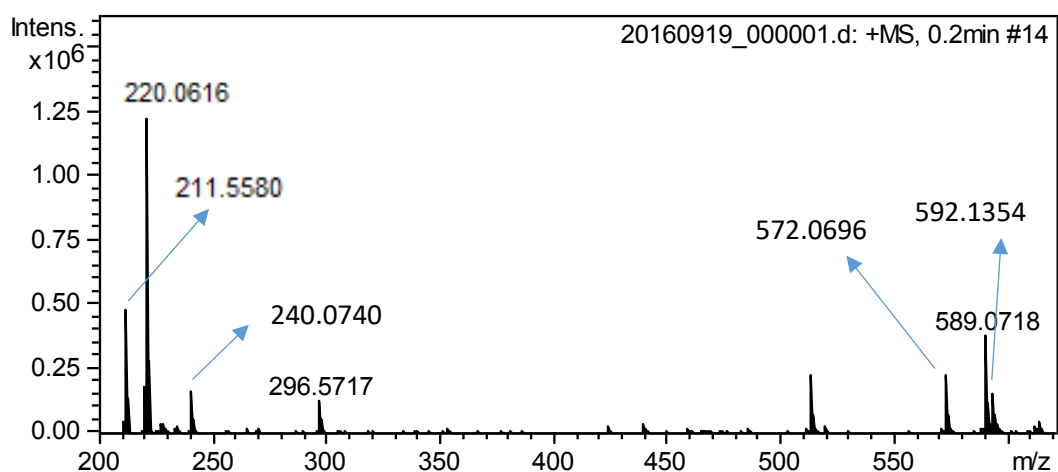
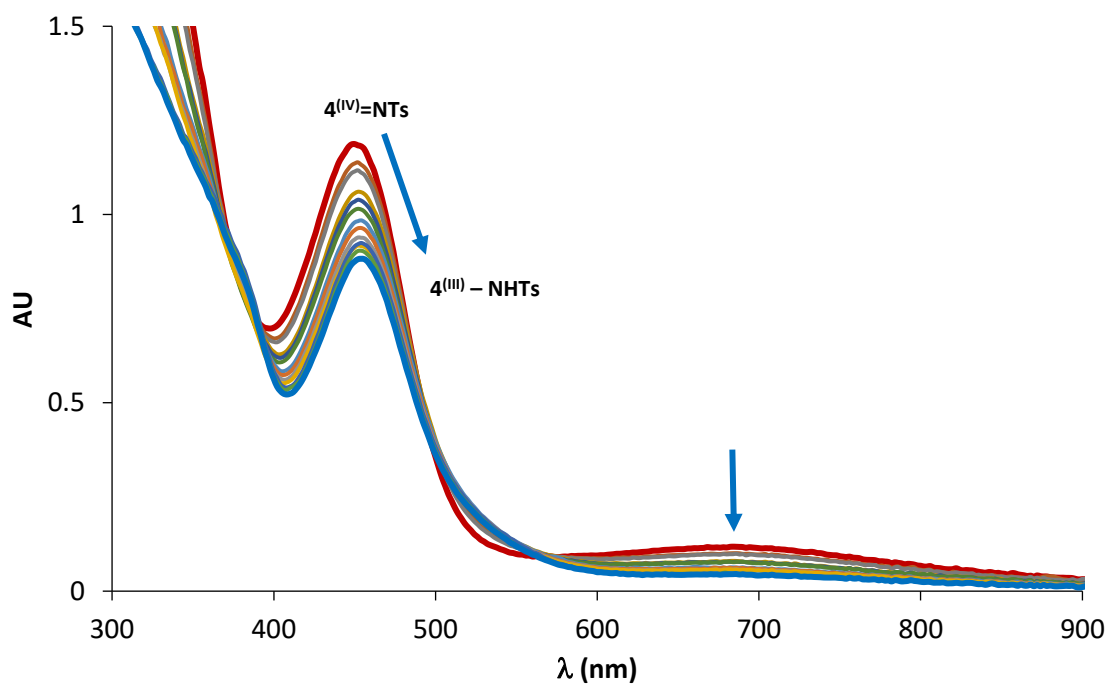
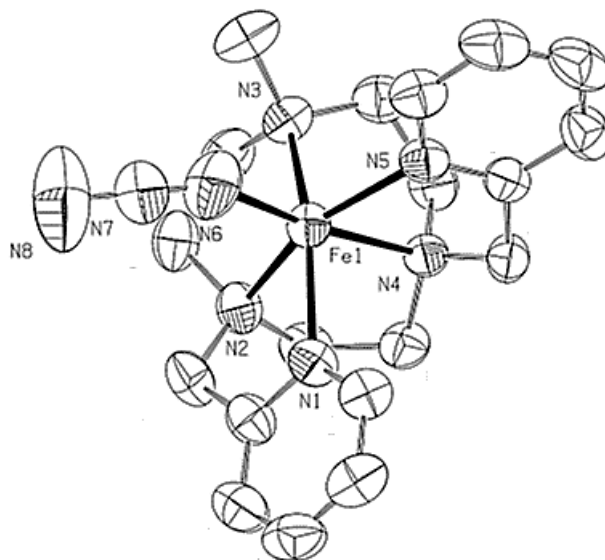


Figure SIV.13. (Top) UV – vis monitoring reduction of $4^{(IV)}=NTs$ to $4^{(III)}-NHTs$ upon addition of one equivalent of ascorbic acid in MeCN. (Below) HR – MS spectrum after addition of 1 eq of ascorbic acid to $4^{(IV)}=NTs$. Ions at $m/z = 296.57$ and 592.13 belong to $[Fe^{III}(NHTs)(N4Py)]^{2+}$ and $[Fe^{III}(NTs)(N4Py)]^+$ respectively. Main ions $m/z = 220.06$ and 589.07 are due to the formation of $[Fe^{III}(OH)(N4Py)]^{2+}$ and $[Fe^{III}(OH)(OTf)(N4Py)]^{2+}$. Ions 211.56 and 572.07 belong to $[Fe^{II}(N4Py)]^{2+}$ and $[Fe^{II}(OTf)(N4Py)]^+$ ions. Ion at 240.07 is $[Fe^{IV}(O)(N4Py)]^{2+}$ formed from traces of water.

Table SIV.4. XYZ coordinates of $1^{(IV)}=NTs$ and $2^{(IV)}=NTs$. $1^{(IV)}=NTs$ S = 1

Fe	-0.293132	0.961073	0.692355	H	2.271245	1.834615	3.439168
N	1.122046	0.002061	-0.295897	C	2.122099	2.341218	1.347459
N	0.997354	2.493884	0.358609	H	2.718321	1.478587	1.046025
N	0.483211	1.031139	2.587536	H	2.757514	3.231398	1.316586
N	-1.549884	2.368436	1.305615	H	0.750771	2.537054	-1.736425
N	-1.184036	-0.472091	1.120089	C	-2.704192	1.500942	-0.621198
C	1.316971	-1.332009	-0.307179	C	-3.725653	1.507530	-1.559474
H	0.691864	-1.911057	0.362024	C	-3.458351	1.085074	-2.859721
C	2.258902	-1.918741	-1.141229	H	-4.715194	1.841514	-1.268989
H	2.385644	-2.995122	-1.123782	C	-1.188700	0.691656	-2.202771
C	3.020718	-1.110070	-1.982336	C	-2.167861	0.676938	-3.185288
H	3.763855	-1.544853	-2.642142	H	-4.245587	1.078314	-3.605655
C	2.822141	0.270316	-1.961801	H	-0.181115	0.359961	-2.417829
H	3.402600	0.932496	-2.594708	H	-1.912826	0.339006	-4.182827
C	1.861728	0.800231	-1.112203	N	-1.445279	1.102545	-0.947002
C	1.528648	2.264837	-1.016466	S	-2.227519	-1.588732	1.530279
H	2.403861	2.893846	-1.204786	O	-1.513965	-2.860867	1.642588
C	0.322333	3.826983	0.552310	O	-2.993998	-1.152403	2.701410
H	0.612724	4.510389	-0.248425	C	-3.346560	-1.699776	0.160528
H	0.683204	4.247418	1.490704	C	-4.674572	-1.291936	0.319046
C	-1.181846	3.642117	0.576005	C	-2.879177	-2.214045	-1.055034
H	-1.680217	4.487778	1.057871	C	-5.550568	-1.417480	-0.757770
H	-1.568800	3.553031	-0.438483	H	-5.012061	-0.902576	1.273266
C	-2.889673	1.933162	0.807138	C	-3.764020	-2.327607	-2.122578
H	-3.611872	2.751867	0.886497	H	-1.845926	-2.530359	-1.155413
H	-3.231501	1.102837	1.431018	C	-5.096815	-1.931282	-1.974482
C	-1.473420	2.528361	2.803311	H	-6.586563	-1.113731	-0.644898
H	-0.961846	3.470918	3.004035	H	-3.415259	-2.725875	-3.070128
H	-2.481052	2.606400	3.216918	H	-5.782328	-2.023189	-2.811389
C	-0.730688	1.350157	3.417146				
H	-1.355223	0.456789	3.427350	$2^{(IV)}=NTs$ S = 1			
H	-0.425009	1.584081	4.442695	Fe	10.455910	7.366840	4.250289
C	1.086948	-0.256437	3.036548	S	9.254597	4.629314	2.974614
H	1.373756	-0.169812	4.089308	O	10.303583	4.353131	1.991925
H	1.973025	-0.460012	2.433871	O	7.900476	4.829341	2.456541
H	0.360317	-1.056852	2.908824	N	12.284535	6.785849	3.752377
C	1.512909	2.122194	2.707695	N	10.430771	8.134948	2.423556
H	1.027078	3.025357	3.077184	N	11.445297	9.052751	4.696083

N	10.615108	6.980524	6.251024	H	11.146725	5.470047	7.638587
N	8.774401	8.415119	4.753465	H	12.284714	5.678264	6.284802
N	9.650388	5.872922	3.890038	H	10.705361	4.887182	6.004390
C	12.779950	5.539182	3.670207	C	11.392263	8.084939	6.938375
H	12.112155	4.735677	3.947950	H	10.683978	8.767761	7.406155
C	14.081561	5.306012	3.242806	H	12.003151	7.653873	7.734174
H	14.447564	4.287257	3.187984	C	12.262572	8.810711	5.934111
C	14.889569	6.385586	2.893989	H	13.123996	8.203896	5.658619
H	15.910315	6.226150	2.563691	H	12.626723	9.761845	6.331894
C	14.371594	7.679892	2.972797	C	9.229648	3.326993	4.167130
H	14.967521	8.546729	2.710677	C	10.310017	2.444856	4.255666
C	13.065412	7.839997	3.401755	H	11.125930	2.509531	3.543362
C	12.304871	9.148312	3.463707	C	10.312221	1.476224	5.255472
H	12.954199	10.024923	3.470830	H	11.148166	0.785582	5.324617
C	11.371316	9.103854	2.279410	C	9.255002	1.377417	6.172325
C	11.493286	9.848480	1.118735	C	8.181922	2.277273	6.060481
H	12.248286	10.623269	1.048026	H	7.353912	2.213226	6.761163
C	10.631131	9.567492	0.057057	C	8.159463	3.248593	5.066966
H	10.697430	10.135093	-0.864801	H	7.323560	3.935901	4.983824
C	9.699379	8.540960	0.191651	C	9.254519	0.311418	7.235079
H	9.031354	8.274528	-0.619137	H	8.742910	0.654927	8.138675
C	9.619865	7.841383	1.390529	H	10.273331	0.009964	7.493206
H	8.910540	7.036137	1.536562	H	8.725058	-0.579877	6.874666
C	10.488312	10.205475	4.885736				
H	10.862154	11.086502	4.358915				
H	10.485509	10.437446	5.951048				
C	9.087055	9.842702	4.408287				
H	8.348387	10.505313	4.870983				
H	8.994073	9.939618	3.327238				
C	7.544005	7.994028	4.021210				
H	6.717005	8.647908	4.315521				
H	7.318513	6.959893	4.274996				
H	7.708112	8.080657	2.949382				
C	8.525449	8.251357	6.234064				
H	8.916048	9.130047	6.748312				
H	7.449537	8.219043	6.417848				
C	9.190572	6.983016	6.717989				
H	8.715268	6.099330	6.287244				
H	9.155331	6.912294	7.810521				
C	11.231673	5.660334	6.563992				

ANNEX CHAPTER V**X – Ray diffraction tables****Table SV.1.** Crystal data and structure refinement for $[\text{Fe}^{\text{II}}(\text{N}_3)(\text{MePy}_2\text{tacn})](\text{OTf})$ (**1a^{II}** – **N₃**) at 298K.

Empirical formula	C ₂₀ H ₂₇ F ₃ Fe N ₈ O ₃ S
Formula weight	572.41
Temperature	298(2) K
Wavelength	0.71073 Å
Crystal system, space group	Monoclinic, P2(1)/n
Unit cell dimensions	a = 7.787(3) Å α = 90 ° b = 17.043(6) Å β = 100.970(6) ° c = 18.996(7) Å γ = 90 °
Volume	2475.0(16) Å ³
Z	4
Final R indices [$I > 2\sigma(I)$]	R1 = 0.0571, wR2 = 0.1441
R indices (all data)	R1 = 0.0895, wR2 = 0.1644

Table SV.2. Selected bond lengths [\AA] and angles [$^\circ$] for $[\text{Fe}^{\text{II}}(\text{N}_3)(\text{MePy}_2\text{tacn})](\text{OTf})$ (**1a^{II}** – **N₃**) at 298K.

Fe(1)-N(6)	2.069(3)
Fe(1)-N(5)	2.148(3)
Fe(1)-N(1)	2.184(3)
Fe(1)-N(2)	2.231(3)
Fe(1)-N(3)	2.248(3)
Fe(1)-N(4)	2.265(2)
N(6)-N(7)	1.042(4)
N(7)-N(8)	1.179(6)
N(6)-Fe(1)-N(5)	95.72(13)
N(6)-Fe(1)-N(1)	91.77(14)
N(5)-Fe(1)-N(1)	103.31(10)
N(6)-Fe(1)-N(2)	109.39(14)
N(5)-Fe(1)-N(2)	154.89(10)
N(1)-Fe(1)-N(2)	76.56(10)
N(6)-Fe(1)-N(3)	101.01(13)
N(5)-Fe(1)-N(3)	96.09(10)
N(1)-Fe(1)-N(3)	155.57(9)
N(2)-Fe(1)-N(3)	79.56(10)
N(6)-Fe(1)-N(4)	172.52(13)
N(5)-Fe(1)-N(4)	77.10(9)
N(1)-Fe(1)-N(4)	91.92(9)
N(2)-Fe(1)-N(4)	77.81(9)
N(3)-Fe(1)-N(4)	77.96(9)
N(7)-N(6)-Fe(1)	132.6(3)
N(6)-N(7)-N(8)	175.3(5)

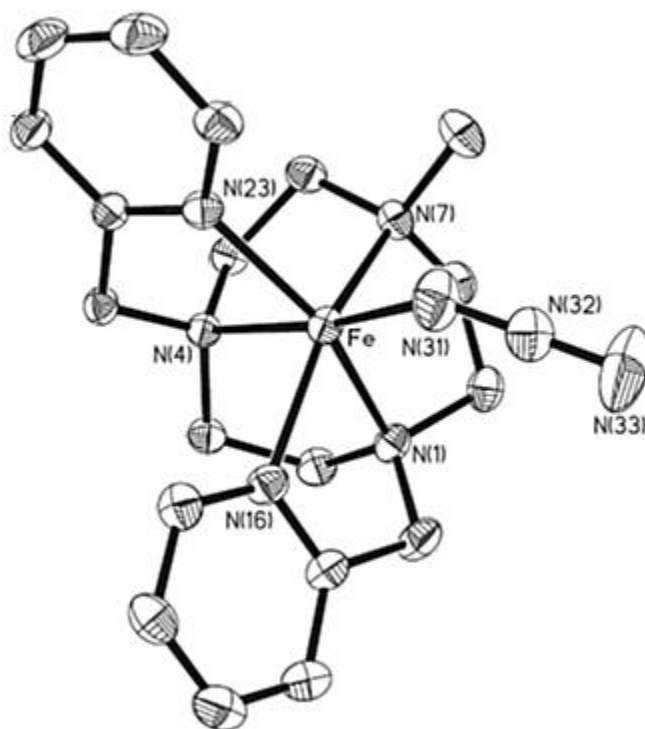


Table SV.3. Selected crystal data and structure refinement for $[\text{Fe}^{\text{II}}(\text{N}_3)(\text{MePy}_2\text{tacn})](\text{OTf})$ ($\mathbf{1a}^{\text{III}} - \text{N}_3$) at 200K.

Empirical formula	$\text{C}_{20} \text{H}_{27} \text{F}_3 \text{Fe} \text{N}_8 \text{O}_3 \text{S}$	
Formula weight	572.40	
Temperature	200(2) K	
Wavelength	0.71073 Å	
Crystal system	Monoclinic	
Space group	$P 2_1/n$, No.14	
Unit cell dimensions	$a = 7.6925(3)$ Å	$\alpha = 90^\circ$
	$b = 16.9959(9)$ Å	$\beta = 101.016(4)^\circ$
	$c = 18.8925(7)$ Å	$\gamma = 90^\circ$
Volume	$2424.51(19)$ Å ³	
Z	4	
Final R indices [$I > 2\sigma(I)$]	$R_1 = 0.0422$, $wR_2 = 0.1009$	
R indices (all data)	$R_1 = 0.0602$, $wR_2 = 0.1136$	

Table SV.4. Selected Bond lengths [Å] and angles [°] for [Fe^{II}(N₃)(MePy₂tacn)](OTf) (**1a^{II}** – N₃) at 200K.

Fe-N(31)	2.0422(16)
Fe-N(23)	2.1400(13)
Fe-N(16)	2.1790(14)
Fe-N(1)	2.2248(13)
Fe-N(7)	2.2390(13)
Fe-N(4)	2.2556(12)
N(31)-Fe-N(23)	94.94(6)
N(31)-Fe-N(16)	92.31(7)
N(23)-Fe-N(16)	103.26(5)
N(31)-Fe-N(1)	109.68(6)
N(23)-Fe-N(1)	155.38(5)
N(16)-Fe-N(1)	76.62(5)
N(31)-Fe-N(7)	100.65(7)
N(23)-Fe-N(7)	96.17(5)
N(16)-Fe-N(7)	155.60(5)
N(1)-Fe-N(7)	79.56(5)
N(31)-Fe-N(4)	171.87(6)
N(23)-Fe-N(4)	77.21(5)
N(16)-Fe-N(4)	91.58(5)
N(1)-Fe-N(4)	78.18(5)
N(7)-Fe-N(4)	78.36(5)
N(32)-N(31)-Fe	131.34(15)
N(31)-N(32)-N(33)	176.9(2)

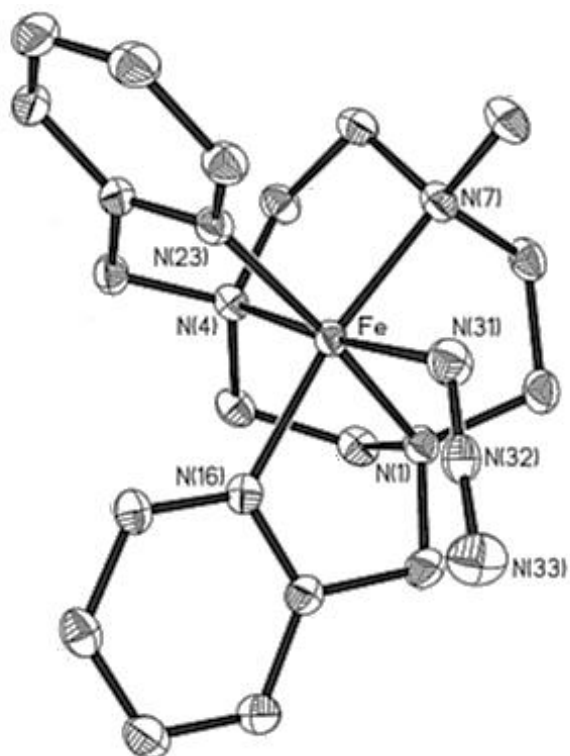


Table SV.5. Crystal data and structure refinement for $[\text{Fe}^{\text{II}}(\text{N}_3)(\text{MePy}_2\text{tacn})](\text{OTf})$ ($\mathbf{1a}^{\text{OTf}} - \text{N}_3$) at 100K.

Empirical formula	$\text{C}_{20} \text{H}_{27} \text{F}_3 \text{Fe} \text{N}_8 \text{O}_3 \text{S}$	
Formula weight	572.40	
Temperature	100(2) K	
Wavelength	0.71073 Å	
Crystal system	Monoclinic	
Space group	P 2 ₁ /n, No.14	
Unit cell dimensions	$a = 8.1408(11)$ Å	$\alpha = 90^\circ$
	$b = 15.519(2)$ Å	$\beta = 101.276(7)^\circ$
	$c = 18.913(2)$ Å	$\gamma = 90^\circ$
Volume	$2343.3(5)$ Å ³	
Z	4	
Final R indices [I > 2σ(I)]	R1 = 0.0375, wR2 = 0.0979	
R indices (all data)	R1 = 0.0443, wR2 = 0.1032	

Table SV.6. Selected bond lengths [Å] and angles [°] for [Fe^{II}(N₃)(MePy₂tacn)](OTf) (**1a^{III}** – N₃) at 100K.

Fe-N(23)	1.9537(10)
Fe-N(16)	1.9702(10)
Fe-N(4)	2.0027(10)
Fe-N(1)	2.0047(10)
Fe-N(31)	2.0153(11)
Fe-N(7)	2.0531(10)
N(31)-N(32)	1.1843(15)
N(32)-N(33)	1.1728(16)
N(23)-Fe-N(16)	95.86(4)
N(23)-Fe-N(4)	84.04(4)
N(16)-Fe-N(4)	95.83(4)
N(23)-Fe-N(1)	169.80(4)
N(16)-Fe-N(1)	83.15(4)
N(4)-Fe-N(1)	85.96(4)
N(23)-Fe-N(31)	94.73(5)
N(16)-Fe-N(31)	89.36(4)
N(4)-Fe-N(31)	174.76(4)
N(1)-Fe-N(31)	95.41(5)
N(23)-Fe-N(7)	94.64(4)
N(16)-Fe-N(7)	169.50(4)
N(4)-Fe-N(7)	85.22(4)
N(1)-Fe-N(7)	86.51(4)
N(31)-Fe-N(7)	89.81(5)
N(32)-N(31)-Fe	126.92(9)
N(33)-N(32)-N(31)	177.98(14)

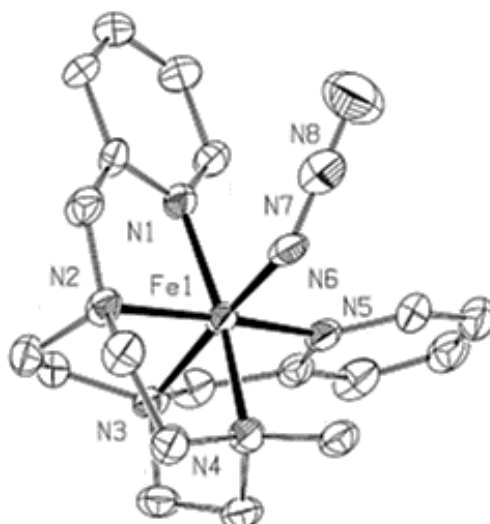


Table SV.7. Crystal data and structure refinement for $[\text{Fe}^{\text{III}}(\text{N}_3)(\text{MePy}_2\text{tacn})](\text{PF}_6)_2$ (**1b^{III}** – **N₃**) at 100 K.

Empirical formula	C ₁₉ H ₂₇ F ₁₂ Fe N ₈ P ₂
Formula weight	713.27
Temperature	100(2) K
Wavelength	0.71073 Å
Crystal system, space group	Monoclinic, P 21/c
Unit cell dimensions	a = 11.312(6) Å α = 90° b = 10.407(5) Å β = 91.837(9)° c = 22.323(11) Å γ = 90°
Volume	2627(2) Å ³
Z	4
Final R indices [I > 2σ(I)]	R1 = 0.0692, wR2 = 0.1558
R indices (all data)	R1 = 0.1589, wR2 = 0.1961

Table SV.8. Selected bond lengths [Å] and angles [°] for [Fe^{III}(N₃)(MePy₂tacn)](PF₆)₂ (**1b**^{III} – N₃) at 100 K.

Fe(1)-N(6)	1.859(5)
Fe(1)-N(5)	1.957(4)
Fe(1)-N(1)	1.974(5)
Fe(1)-N(2)	1.980(4)
Fe(1)-N(4)	2.018(4)
Fe(1)-N(3)	2.030(5)
N(6)-N(7)	1.246(7)
N(7)-N(8)	1.177(8)
N(6)-Fe(1)-N(5)	97.7(2)
N(6)-Fe(1)-N(1)	88.92(19)
N(5)-Fe(1)-N(1)	93.43(19)
N(6)-Fe(1)-N(2)	93.1(2)
N(5)-Fe(1)-N(2)	168.5(2)
N(1)-Fe(1)-N(2)	82.88(19)
N(6)-Fe(1)-N(4)	90.65(19)
N(5)-Fe(1)-N(4)	96.23(18)
N(1)-Fe(1)-N(4)	170.30(18)
N(2)-Fe(1)-N(4)	87.47(19)
N(6)-Fe(1)-N(3)	175.41(18)
N(5)-Fe(1)-N(3)	83.59(19)
N(1)-Fe(1)-N(3)	95.42(18)
N(2)-Fe(1)-N(3)	85.94(19)
N(4)-Fe(1)-N(3)	84.82(18)
N(7)-N(6)-Fe(1)	122.2(4)
N(8)-N(7)-N(6)	176.5(7)

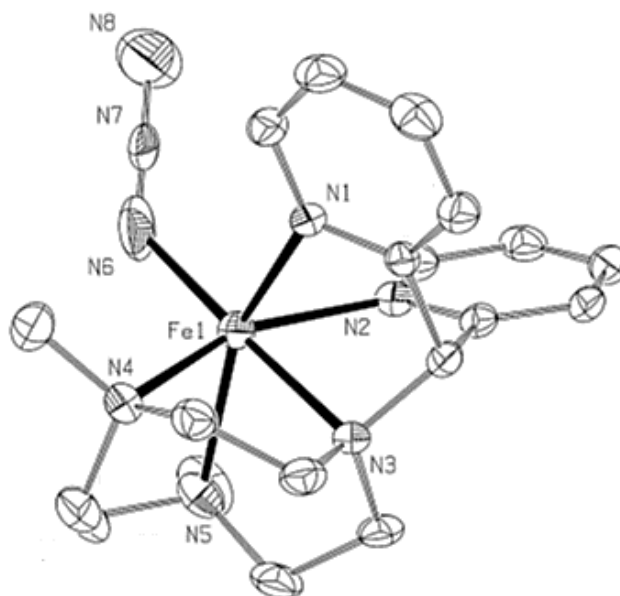


Table SV.9. Crystal data and structure refinement for $[\text{Fe}^{\text{II}}(\text{N}_3)\text{Me}_2(\text{CHPy}_2)\text{tacn}](\text{OTf})$ (**2a^{III}** – **N₃**) at 100K.

Empirical formula	C ₂₀ H ₂₇ F ₃ Fe N ₈ O ₃ S
Formula weight	572.40
Temperature	100(2) K
Wavelength	0.71073 Å
Crystal system, space group	Monoclinic, P 2 ₁ /c
Unit cell dimensions	a = 9.892(7) Å α = 90 ° b = 18.747(14) Å β = 103.439(13) ° c = 13.778(10) Å γ = 90 °
Volume	2485(3) Å ³
Z	4
Final R indices [I > 2σ(I)]	R1 = 0.0892, wR2 = 0.2369
R indices (all data)	R1 = 0.1404, wR2 = 0.2719

Table SV.10. Selected bond lengths [Å] and angles [°] for [Fe^{II}(N₃)Me₂(CHPy₂)tacn](OTf) (**2a^{II}** – N₃) at 100K.

Fe(1)-N(6)	2.011(6)
Fe(1)-N(2)	2.188(5)
Fe(1)-N(3)	2.206(4)
Fe(1)-N(1)	2.221(4)
Fe(1)-N(4)	2.241(5)
Fe(1)-N(5)	2.259(4)
N(6)-N(7)	1.080(7)
N(7)-N(8)	1.218(8)
N(6)-Fe(1)-N(2)	101.7(2)
N(6)-Fe(1)-N(3)	177.6(2)
N(2)-Fe(1)-N(3)	76.07(16)
N(6)-Fe(1)-N(1)	101.7(2)
N(2)-Fe(1)-N(1)	81.28(15)
N(3)-Fe(1)-N(1)	77.11(15)
N(6)-Fe(1)-N(4)	102.5(2)
N(2)-Fe(1)-N(4)	155.62(16)
N(3)-Fe(1)-N(4)	79.67(16)
N(1)-Fe(1)-N(4)	91.01(17)
N(6)-Fe(1)-N(5)	103.7(2)
N(2)-Fe(1)-N(5)	98.51(16)
N(3)-Fe(1)-N(5)	77.64(16)
N(1)-Fe(1)-N(5)	154.01(16)
N(4)-Fe(1)-N(5)	78.50(16)
N(7)-N(6)-Fe(1)	136.0(5)
N(6)-N(7)-N(8)	176.0(8)

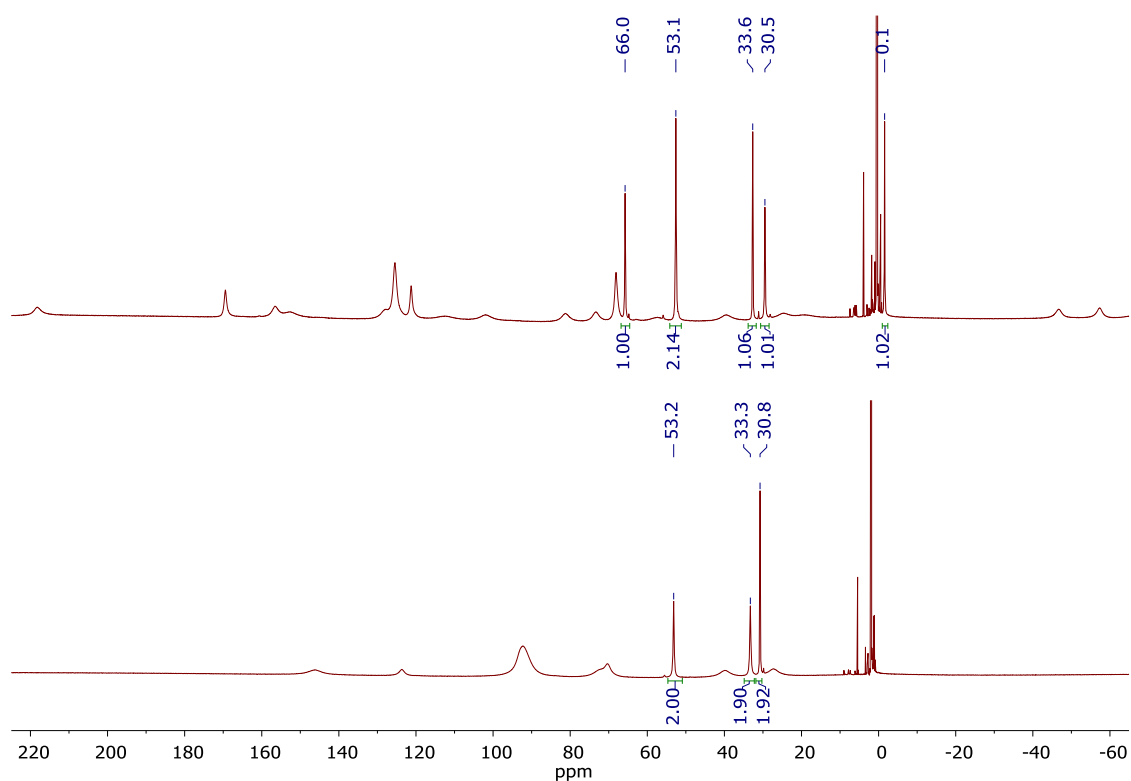
^1H – NMR spectroscopy of $1\text{a}^{\text{II}} - \text{N}_3$ and $2\text{a}^{\text{II}} - \text{N}_3$ 

Figure SV.1. Paramagnetic ^1H -NMR spectrum of $1\text{a}^{\text{II}} - \text{N}_3$ (top) and $2\text{a}^{\text{II}} - \text{N}_3$ (below) in CD_3CN at 273 K.

UV – vis spectroscopy of $1\text{a}^{\text{II}} - \text{N}_3$ and $2\text{a}^{\text{II}} - \text{N}_3$

The UV – vis spectra of iron (II) – azide complexes $1\text{a}^{\text{II}} - \text{N}_3$ and $2\text{a}^{\text{II}} - \text{N}_3$ in acetonitrile are similar to their iron (II) precursors but with lower absorption coefficients (1^{II} and 2^{II} can be found in chapter III). Complex $1\text{a}^{\text{II}} - \text{N}_3$ shows a very intense band at 437 nm ($\epsilon = 1876 \text{ cm}^{-1} \cdot \text{M}^{-1}$) and complex $2\text{a}^{\text{II}} - \text{N}_3$ shows two features at 483 and 397 nm ($\epsilon = 1855$ and $1235 \text{ cm}^{-1} \cdot \text{M}^{-1}$). Both complexes show a similar ϵ with the energy of the maximum more shifted to the red region for $2\text{a}^{\text{II}} - \text{N}_3$. The observed bands are attributed to metal to ligand charge transfer from $d_\pi(\text{Fe})$ to $\pi^*(\text{L})$ of the pyridines.

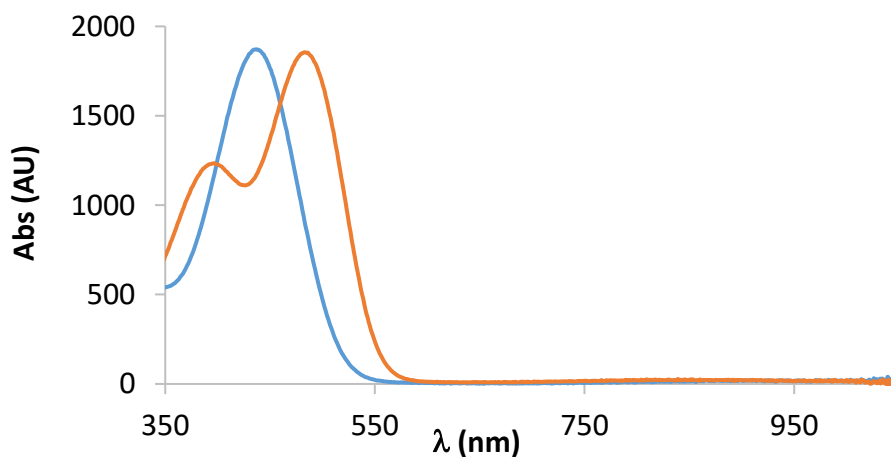


Figure SV.2. UV – vis spectra for complexes $1\text{a}^{\text{II}} - \text{N}_3$ (blue line) and $2\text{a}^{\text{II}} - \text{N}_3$ (orange line) in acetone at 298 K.

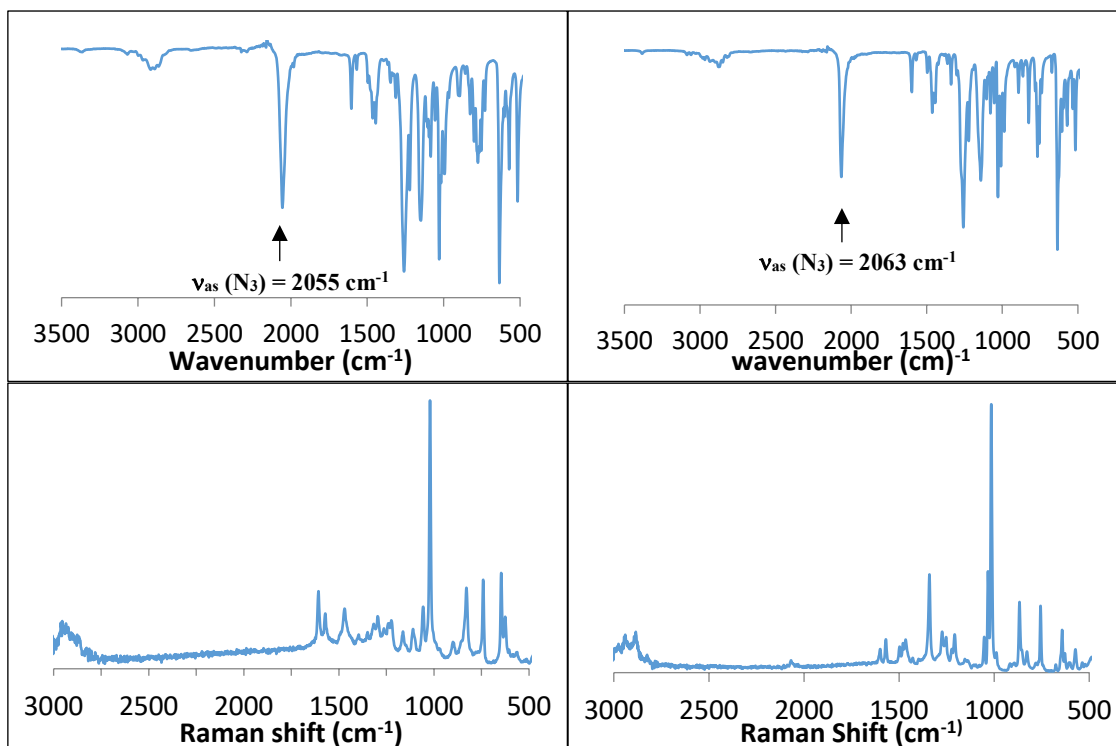
FT – IR and Raman Spectroscopy of $1a^{(II)} - N_3$, $2a^{(II)} - N_3$, $1b^{(III)} - N_3$ and $2b^{(III)} - N_3$


Figure SV.3. Top; IR spectra of iron (II) azide $1a^{(II)} - N_3$ (left) and iron (II) azide $2a^{(II)} - N_3$ (right). Below; Raman spectra of $1a^{(II)} - N_3$ (left) and $2a^{(II)} - N_3$ (right); $\approx 2000 \text{ cm}^{-1}$ features are typical for asymmetric stretching of $Fe - N_3$.³²²

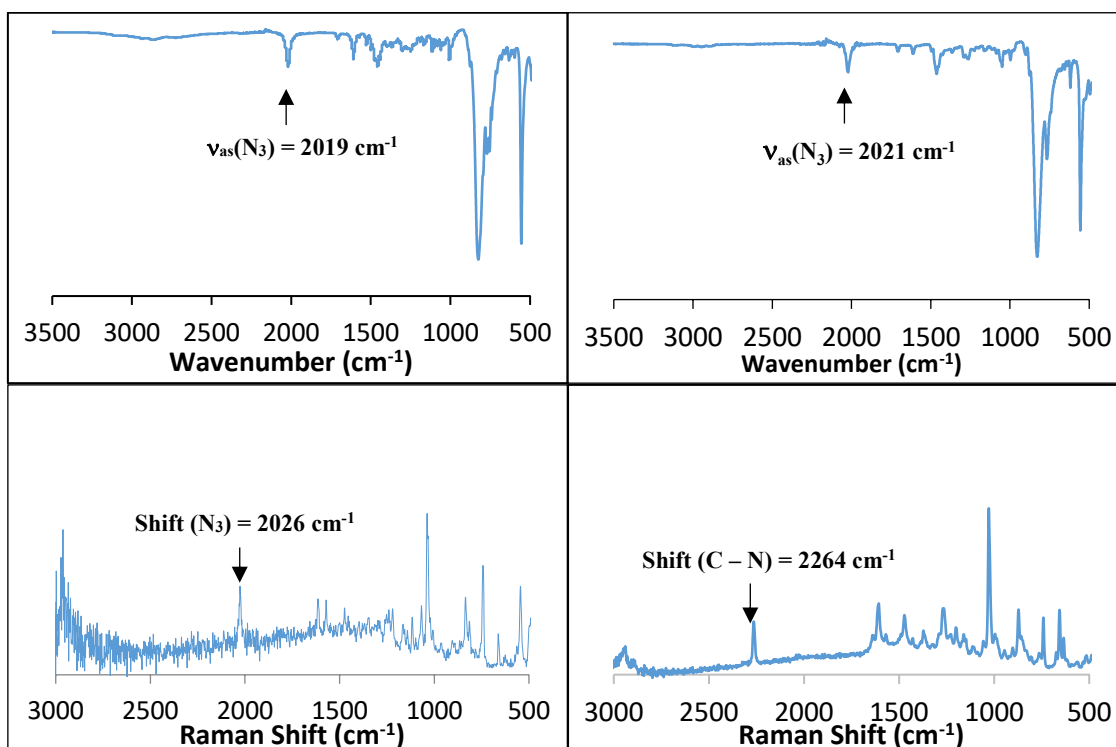


Figure SV.4. Top; IR spectra of iron (II) azide $1b^{(III)} - N_3$ (left) and iron (II) azide $2b^{(III)} - N_3$ (right). Below; Raman spectra of $1b^{(III)} - N_3$ (left) and $2b^{(III)} - N_3$ (right); $\approx 2000 \text{ cm}^{-1}$ features are typical for asymmetric stretching of $Fe - N_3$ while $2200 - 2300 \text{ cm}^{-1}$ features are typical for nitrile species.^{322,374}

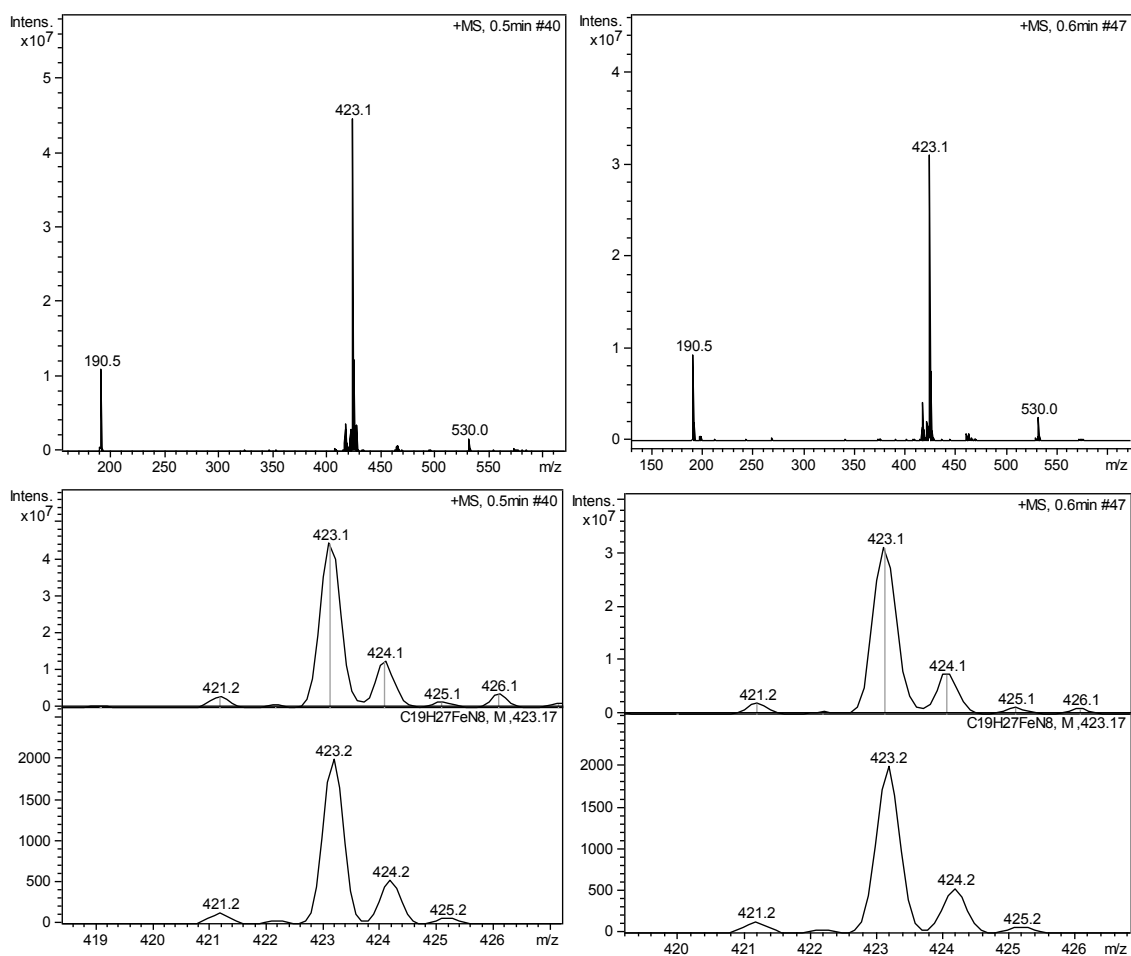
ESI – MS of $1a^{(II)} - N_3$ and $2a^{(II)} - N_3$ 

Figure SV.5. ESI – MS of complex $1a^{(II)} - N_3$ (left) and $2a^{(II)} - N_3$ (right), insets on the right side show the simulated peak for ion $[Fe^{II}(N_3)(L)]^+$. Peaks at $m/z = 190.5$ and 530.0 belong to $[Fe^{II}(L)]^{2+}$ and $[Fe^{II}(OTf)(L)]^+$ respectively. $m/z = 416.1$ corresponds to a minor impurity of $[Fe^{II}(Cl)(L)]^+$. (L) = MePy₂tacn or Me₂(CHPy₂)tacn.

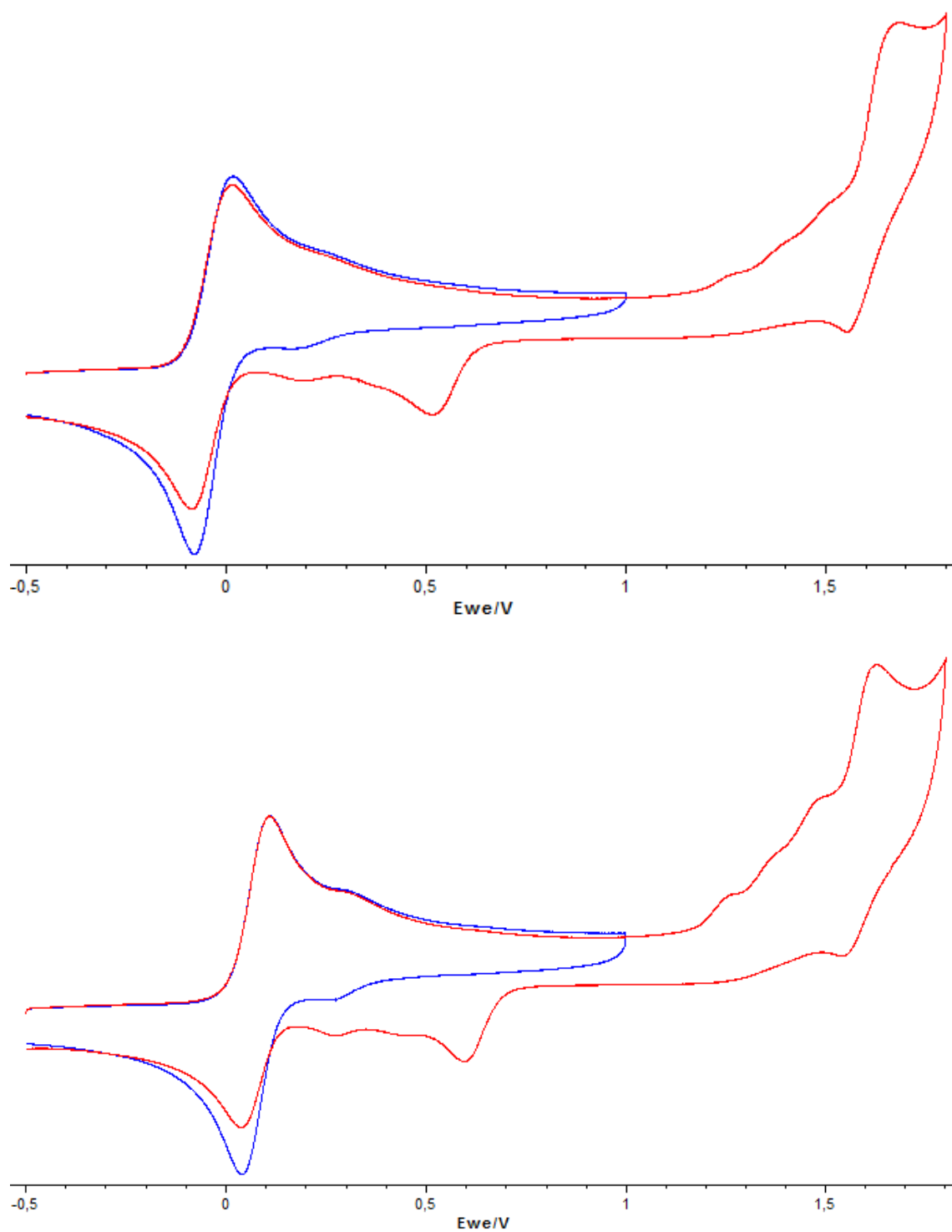
Electrochemistry of $1a^{(II)} - N_3$ and $2a^{(II)} - N_3$ 

Figure SV.6. Cyclic voltammetry of $1a^{(II)} - N_3$ (top) and $2a^{(II)} - N_3$ in acetone (below); $-20\text{ }^\circ\text{C}$ (1 mM Fe and 0.1 M TBAPF₆, values referenced vs. Ag/AgNO₃).

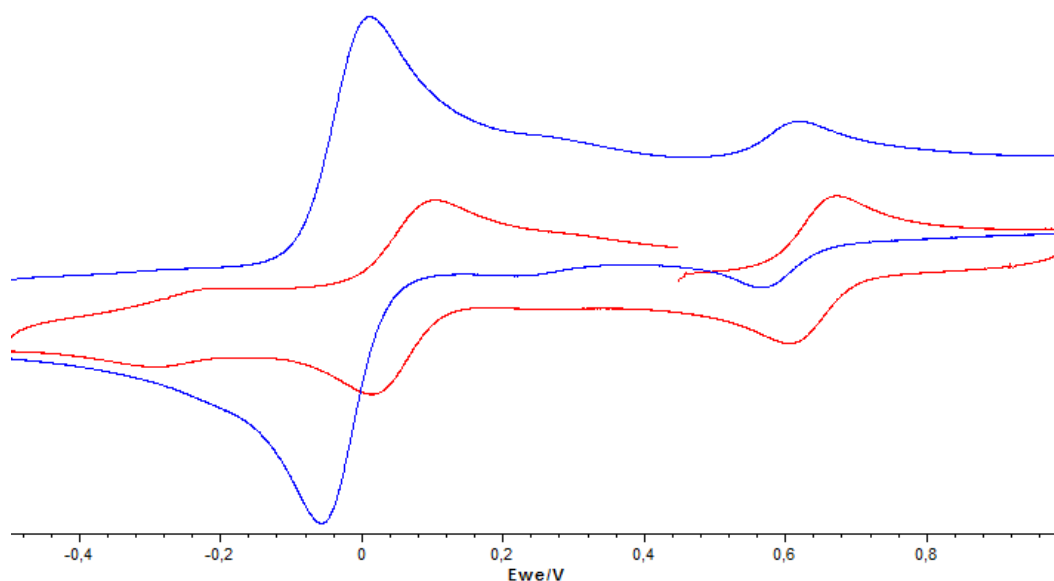


Figure SV.7. Cyclic voltammetry of **1a^(III) – N₃** (blue) and **2a^(III) – N₃** (red) in MeCN; -20 °C (1 mM Fe and 0.1 M TBAPF₆, values referenced vs. Ag/AgNO₃).

Additionally, we performed CV studies to further investigate the purity of **1b^(III) – N₃** and **2b^(III) – N₃**. The spectrum of **1b^(III) – N₃** in acetone showed a reversible wave with $E_{1/2} \approx -0.1$ V while in MeCN an additional tiny couple of Fe^{II/III}(MeCN) was detected. In contrast, complex **2b^(III) – N₃** in MeCN revealed a big wave for Fe^{II/III}(MeCN) couple, in agreement with the important amount of [Fe^{II}(Me₂(CHPy)₂tacn(MeCN))] detected by Mössbauer spectroscopy and Raman resonance.

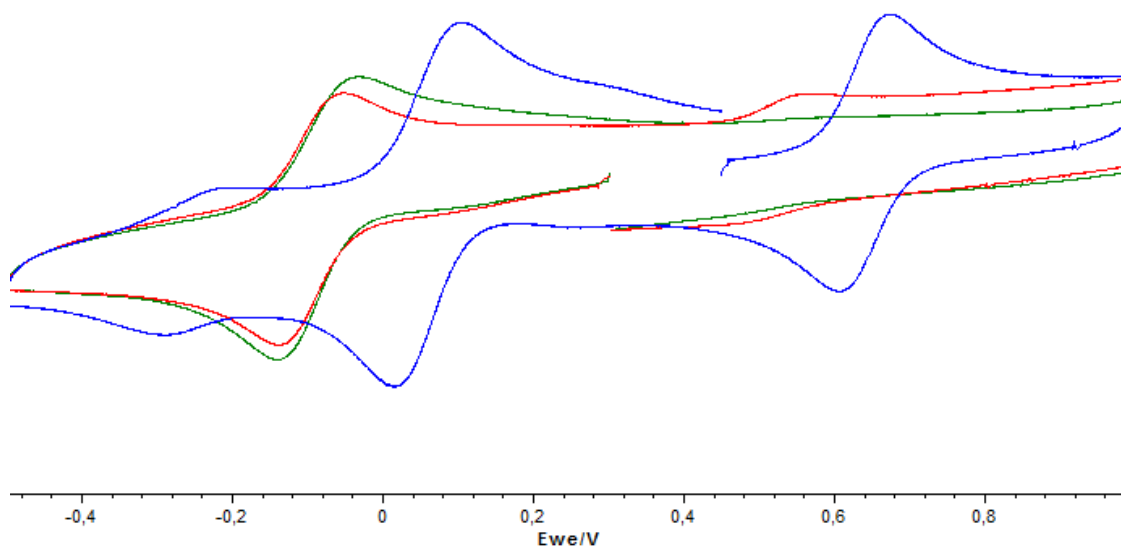


Figure SV.8. Cyclic voltammeteries of complexes **1b^(III) – N₃** in acetone (green) and acetonitrile (red) and **2b^(III) – N₃** (blue) in acetonitrile at -20 °C; 1 mM on iron and 0.2M N(n – Bu)₄PF₆ (values referenced vs. Ag/AgNO₃).

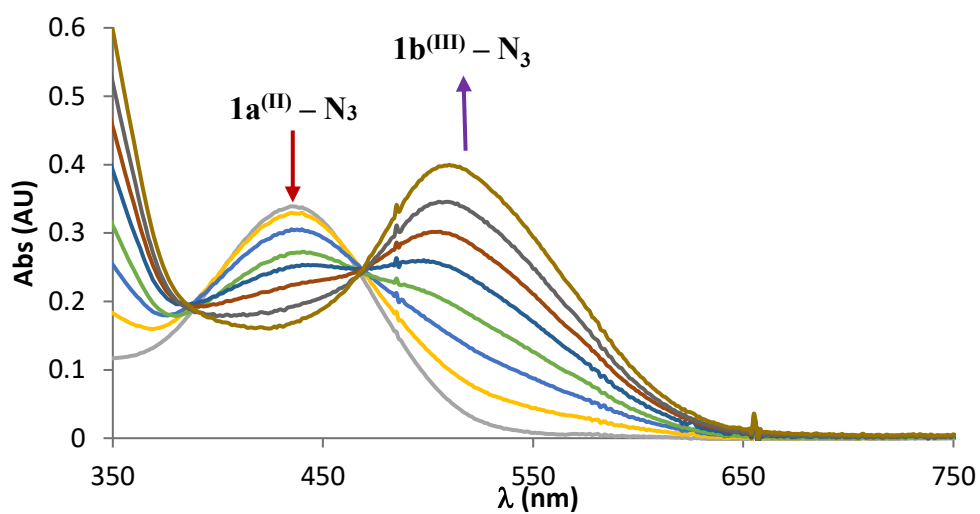


Figure SV.9. Oxidation of $1a^{(II)} - N_3$ to $1b^{(III)} - N_3$ upon applying 0.5 V to the solution (acetone, -20°C , 0.2 mM, 0.2 M TBAPF₆).

Magnetic measurements of $1b^{(III)} - N_3$ and $2b^{(III)} - N_3$

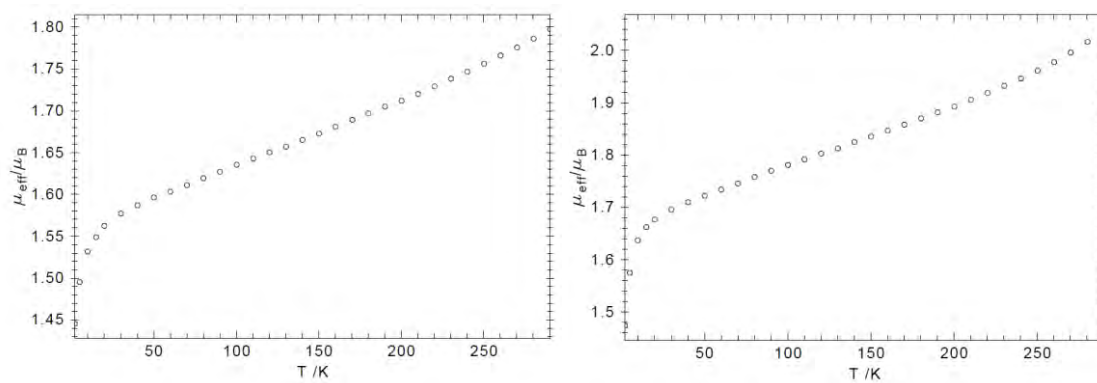


Figure SV.10: Magnetic effective moment dependence on temperature for complex $1b^{(III)} - N_3$ (left) and $2b^{(III)} - N_3$ (right).

UV – vis spectra of $1b^{(III)} - N_3$ and $2b^{(III)} - N_3$

UV – vis spectra of iron (III) complex $1b^{(III)} - N_3$ and $2b^{(III)} - N_3$ in acetone at 25 °C show features with maximum at 512 nm ($\epsilon = 1889 \text{ M}^{-1}\cdot\text{cm}^{-1}$) and 498 ($\epsilon = 2778 \text{ M}^{-1}\cdot\text{cm}^{-1}$) respectively, attributed to metal to ligand charge transfer bands, in good agreement with the spectra of *cis/trans*- $[\text{Fe}^{III}(\text{N}_3)_2(\text{cyclam})]$.¹⁹⁴ Moreover the recording of UV – vis at different temperatures revealed a change in the UV – vis spectra reflecting a change in the spin. This behaviour contrasts with solid state where the change is not observed.

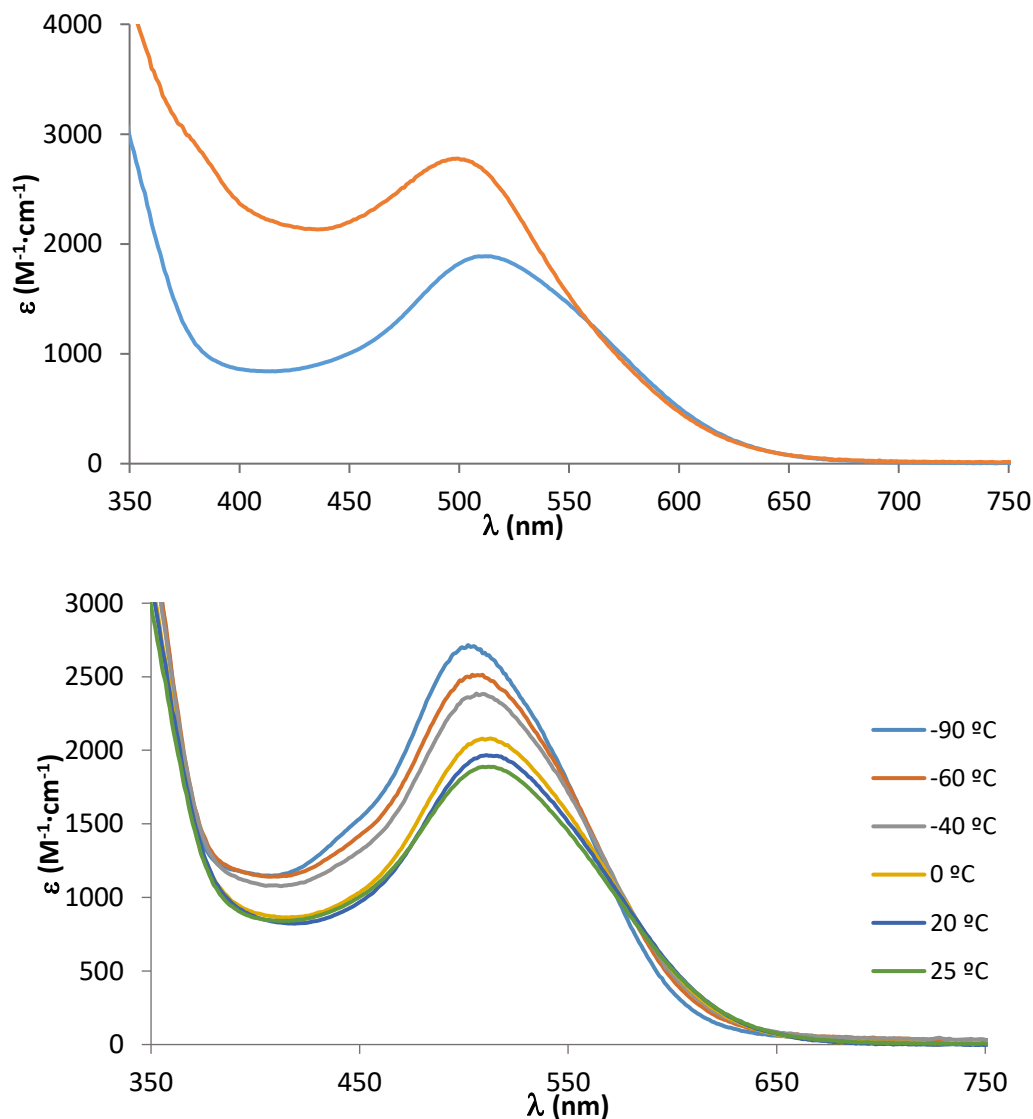


Figure SV.11. (Top) UV – vis spectra for complexes $1b^{(III)} - N_3$ (blue line) and $2b^{(III)} - N_3$ (orange line) in acetone at 298 K. (Below) UV – vis spectra for complex $2b^{(III)} - N_3$ in acetone recorded at different temperatures.

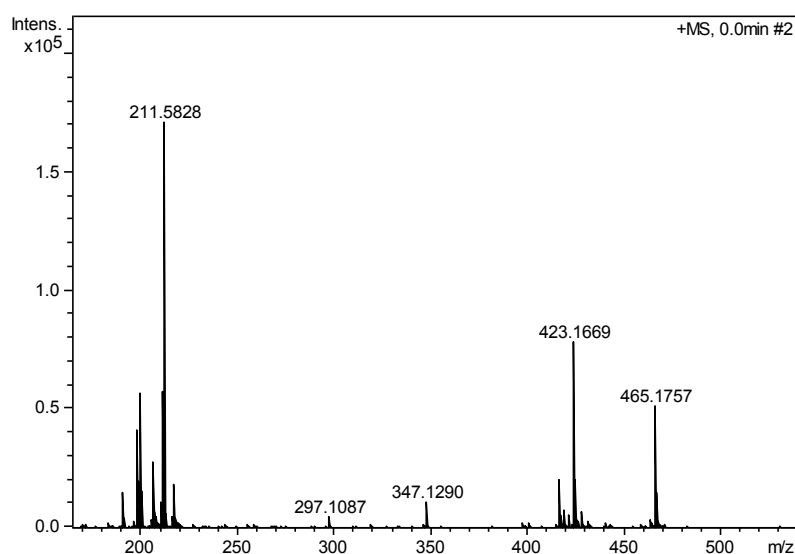
HR – MS of $2b^{(III)} - N_3$ 

Figure SV.12. MS spectrum of $2b^{(III)} - N_3$ in acetone. The main ion peak $m/z = 211.58$ is the $[Fe^{III}(N_3)(Me_2(CHPy)_2)tacn)]^{2+}$ ($2b^{(III)} - N_3$), peaks at $m/z = 423.17$ and 190.08 belong to $[Fe^{II}(N_3)(Me_2(CHPy)_2)tacn)]^+$ and $[Fe^{II}(Me_2(CHPy)_2)tacn)]^{2+}$ respectively. The peak at $m/z = 465.17$ are attributed to aggregates of $[Fe^{III}(N_3)(Me_2(CHPy)_2)tacn)]^+$ with N_3^- anions. Peaks at $m/z = 199.08$ and 197.58 belong to the $[Fe^{III}(OH)(Me_2(CHPy)_2)tacn)]^{2+}$ and the in situ formation of $[Fe^V(N)(Me_2(CHPy)_2)tacn)]^{2+}$ species, respectively.

Photolysis of $1a^{(II)} - N_3$ in solid matrix

2 mM samples of $1a^{(II)} - N_3$ and $2a^{(II)} - N_3$ in acetone were prepared using enriched ^{57}Fe samples. Mössbauer analysis of the initial $1a^{(II)} - N_3$ sample in frozen acetone solution showed a 77% of low – spin iron (II) species (isomer shift $\delta = 0.53 \text{ mm} \cdot \text{s}^{-1}$, quadrupole splitting $\Delta E_Q = 0.53 \text{ mm} \cdot \text{s}^{-1}$) and 23% of high – spin iron (II) species (isomer shift $\delta = 1.10 \text{ mm} \cdot \text{s}^{-1}$, quadrupole splitting $\Delta E_Q = 3.20 \text{ mm} \cdot \text{s}^{-1}$). Ratio of high and low – spin species differences may come from the matrix differences (solid state or frozen solution). Sample was maintained in a Mössbauer cup at 77 K in frozen matrix and photolysed with blue LED (470 nm) for four hours in a liquid nitrogen bath but no change was observed by Mössbauer spectroscopy analysis; the sample was then further irradiated following the same procedure with a green LED (530 nm), but no changes were observed after three more hours of irradiation. Therefore the same sample was further irradiated by using 350 nm lamps in a Rayonet photoreactor for four hours, but no change was observed. Only after irradiating in the photoreactor under 253 nm lamps for 4.5 additional hours the sample slightly changed from orange to brownish and in the Mössbauer spectra was observed a mixture of three species (*vide infra*): 74% of the initial low spin iron (II) and two high – spin iron (II) species (11% of initial high – spin iron (II) species and the remaining 14% a new species consistent with a high – spin iron (II) species (isomer shift $\delta = 1.05 \text{ mm} \cdot \text{s}^{-1}$, quadrupole splitting $\Delta E_Q = 2.99 \text{ mm} \cdot \text{s}^{-1}$).

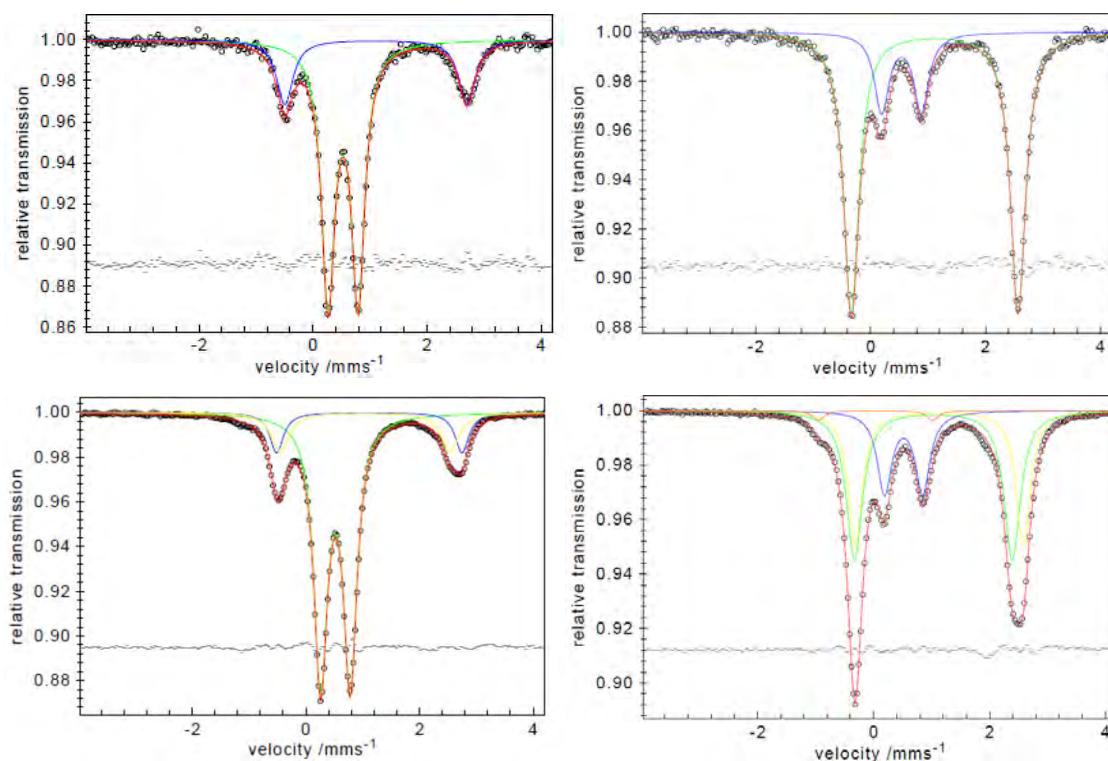


Figure SV.13. Mössbauer spectra of ^{57}Fe enriched samples of $1\mathbf{a}^{\text{(II)}} - \text{N}_3$ (left row) and $2\mathbf{a}^{\text{(II)}} - \text{N}_3$ (right row) in frozen acetone solution. Top spectra are samples before irradiation and below spectra are same samples after irradiation.

The same procedure was followed to study photolysis capability of complex $2\mathbf{a}^{\text{(II)}} - \text{N}_3$. The initial frozen solution also was composed of two iron (II) species. The major component, 80 % of the iron, is the species $2\mathbf{a}^{\text{(II)}} - \text{N}_3$ in high – spin (isomer shift $\delta = 1.11 \text{ mm}\cdot\text{s}^{-1}$, quadrupole splitting $\Delta E_Q = 2.90 \text{ mm}\cdot\text{s}^{-1}$), while the minor component is an iron (II) in low – spin with isomer shift $\delta = 0.54 \text{ mm}\cdot\text{s}^{-1}$, quadrupole splitting $\Delta E_Q = 0.69 \text{ mm}\cdot\text{s}^{-1}$ and accounts for the 20 % of the iron from the sample. Analogously to $1\mathbf{a}^{\text{(II)}} - \text{N}_3$, no high – valent species was formed, when it was irradiated for 7 h at 77 K with blue LED the only change observed was a split of the initial high – spin iron (II) into two doublets, both with similar parameters to the initial $2\mathbf{a}^{\text{(II)}} - \text{N}_3$, while low – spin species remained unchanged. Further irradiation of the same sample in the Rayonet photoreactor with 253 nm lamps for 12 h led to no generation of high – valent iron species (*vide supra*).

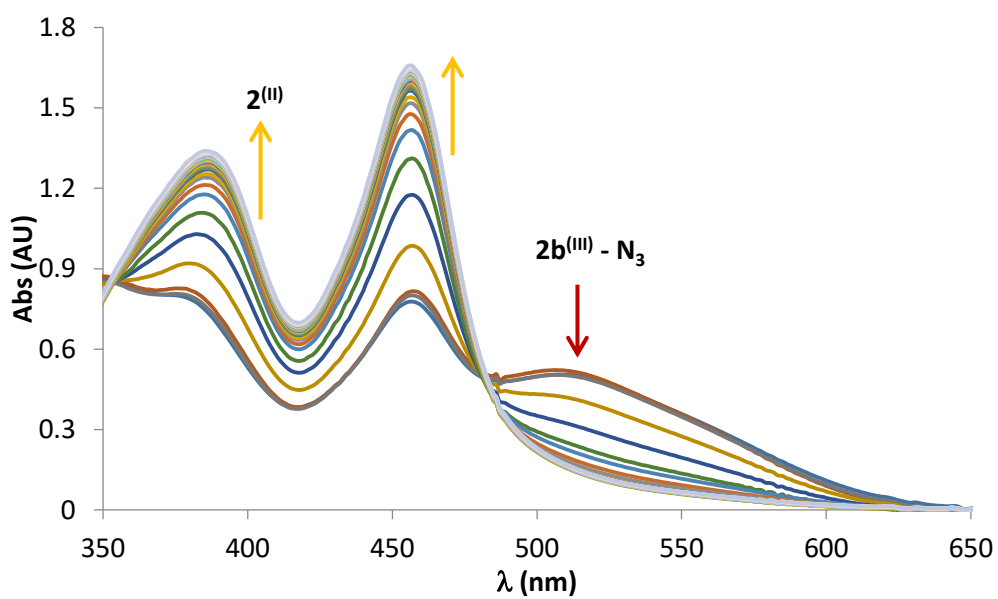
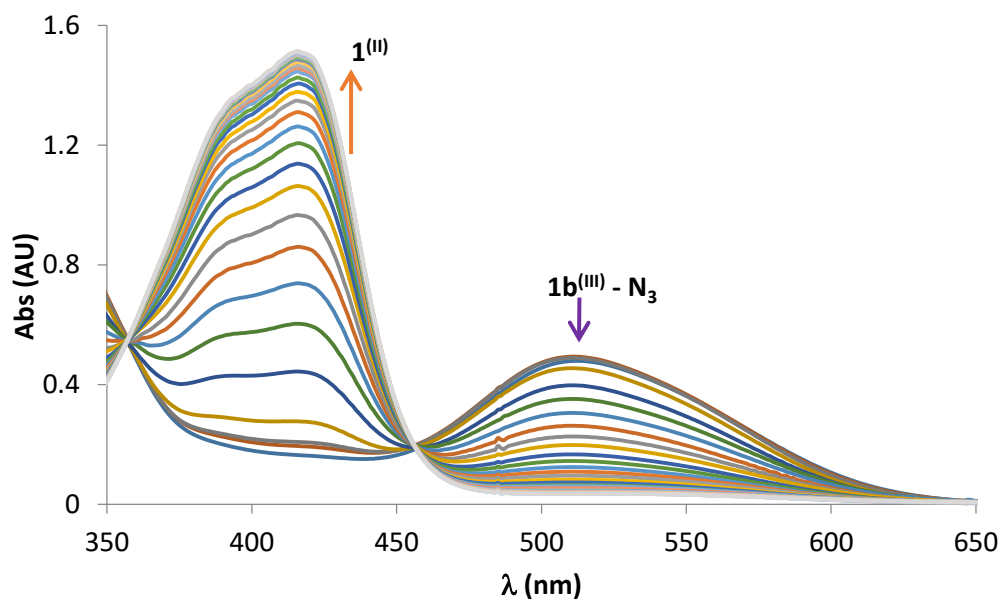
Photolysis of $1b^{(III)} - N_3$ 

Figure SV.14. Photolysis of complex $1b^{(III)} - N_3$ (0.2 mM) and $2b^{(III)} - N_3$ (0.25 mM) with 530 nm LED in acetonitrile at 233 K.

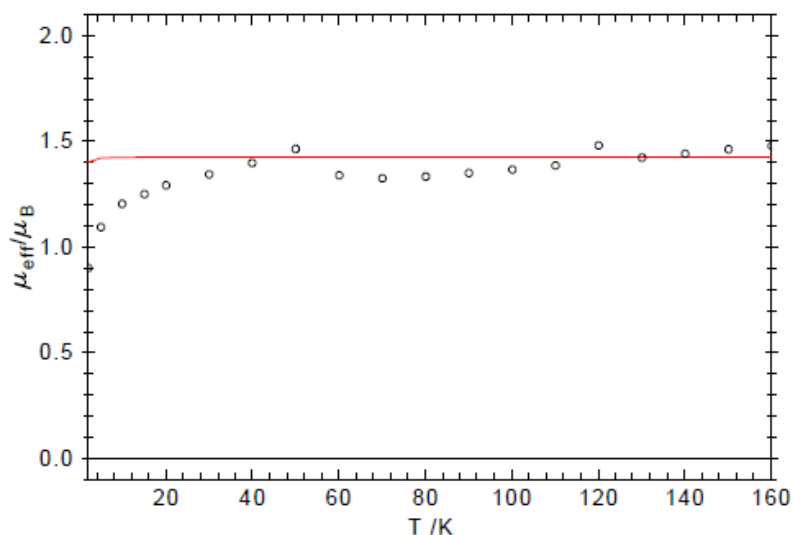


Figure SV.15. SQUID measurement of solid complex $1^{(V)}\text{EN}$ after 4.5 h photolysis at 77 K with a 470 nm LED in a beaker. Red line is the simulation of a mixture of 74 % of an $S = 1/2$ and a 26 % of $S = 2$ species.

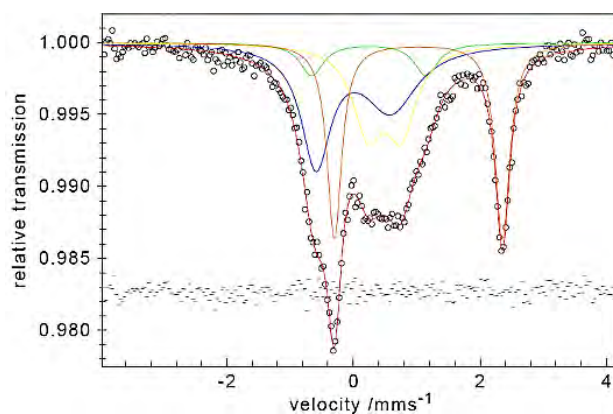


Figure SV.16. Mössbauer spectra of solid sample containing putative $2^{(V)}\text{EN}$ after 2.5 h photolysis at 77 K with a 470 nm LED lamp. Zero – field Mössbauer spectrum of solid sample containing putative $2^{(V)}\text{EN}$ at 77 K. Obtained after 2.5 h of photolysis of a $2\mathbf{b}^{(III)} - \text{N}_3$ sample at 77 K with a 470 nm (blue) LED. The Mössbauer spectrum was fitted with four Lorentzian doublets accounting for i) Iron (III) starting material ($2\mathbf{b}^{(III)} - \text{N}_3$, 8%, in green), ferrous impurities ii) iron (II) HS (30%, in orange) and iii) iron (II) LS (26%, in yellow), and iv) the high – valent photo – product ($2^{(V)}\text{EN}$, 36%, in blue).

XANES Analysis

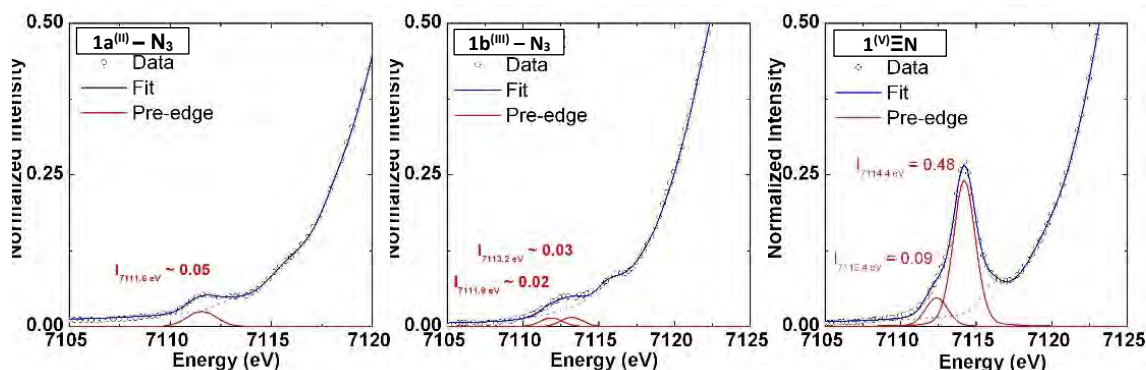


Figure SV.17. Fe K pre – edge XANES region for compounds $1a^{(III)} - N_3$, $1b^{(III)} - N_3$ and $1^{(V)}\Xi N$ highlighting the $1s \rightarrow 3d$ feature fit with a cumulative Gaussian lorentzian sum function having 0.75% Gaussian character.

Table SV.11 Selected EXAFS fits for $1^{(V)}\Xi N$. Fits carried out in r – space ($\Delta k = 2 - 14 \text{ \AA}^{-1}$; $\Delta r = 1 - 3 \text{ \AA}$) with a Hanning window ($dk = 2$), a k – weight = 3 and $S_0 = 0.9$. Bond distances and disorder parameters (Δr_{eff} and σ^2) were allowed to float having initial values of 0.0 \AA and 0.003 \AA^2 respectively, with a universal E_0 initially set to first inflection point of the rising edge and $\Delta E_0 = 0 \text{ eV}$. (Fits highlighted in blue are the best models; values highlighted in red are either statistically or physically erroneous; σ^2 reported as $\times 10^3 \text{ \AA}^2$).

FIT	Δk	Δr	Var.	R_{FACTOR}	χ^2_{ν}	ΔE_0	Fe-N/O*			Fe-N/O*			Fe-N/O*		
							N	$r(\text{\AA})$	σ^2	N	$r(\text{\AA})$	σ^2	N	$r(\text{\AA})$	σ^2
1	2.0-14.0	1.0-3.0	8	0.044	12.5	2.38	1	1.64(1)	2(2)	3	1.98(1)	2(1)	2	2.05(4)	9(6)
2	2.0-14.0	1.0-3.0	6	0.137	30.0	-1.97	-	-	-	4	1.99(2)	3(2)	2	2.03(6)	9(9)
3	2.0-14.0	1.0-3.0	6	0.068	15.0	-0.73	1	1.65(2)	2(2)	-	-	-	5	1.99(1)	5(1)
4	2.0-14.0	1.0-3.0	8	0.036	10.2	3.81	1	1.64(1)	2(1)	2	1.98(1)	0(1)	2	2.05(2)	5(2)
5	2.0-14.0	1.0-3.0	8	0.029	8.1	2.57	1	1.64(1)	3(1)	3	1.98(1)	2(1)	2	2.05(2)	7(3)

FIT	Fe-C			Fe-C			Fe-C-N-Fe			Fe-C-N-Fe		
	N	$r(\text{\AA})$	σ^2	N	$r(\text{\AA})$	σ^2	N	$r(\text{\AA})$	σ^2	N	$r(\text{\AA})$	σ^2
1	8	2.86(4)	9(6)	5	2.96(8)	9(6)	-	-	-	-	-	-
2	8	2.84(6)	9(9)	5	2.95(12)	9(9)	4	3.05(12)	9(9)	4	3.12(12)	9(9)
3	8	2.79(1)	5(1)	5	2.94(3)	5(1)	4	3.05(3)	5(1)	4	3.12(3)	5(1)
4	8	2.86(2)	5(2)	6	3.00(4)	5(2)	4	3.10(4)	5(2)	4	3.17(4)	5(2)
5	8	2.86(2)	7(3)	5	2.99(3)	7(3)	4	3.08(3)	7(3)	4	3.16(3)	7(3)

*Although EXAFS can not differentiate between O/N/C scattering paths, chemical intuition was used for description to facilitate comparison with theoretically derived structure

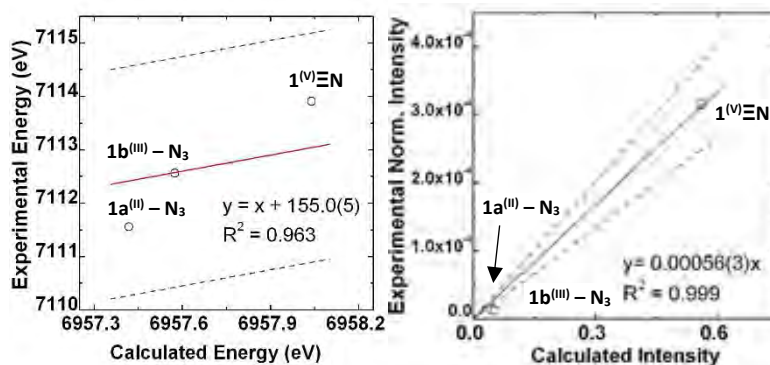


Figure SV.18. Correlation between calculated and experimental Fe K pre – edge intensity averaged energies (left) and total intensities (right) $1a^{(III)} - N_3$, $1b^{(III)} - N_3$ and $1^{(V)}\Xi N$.

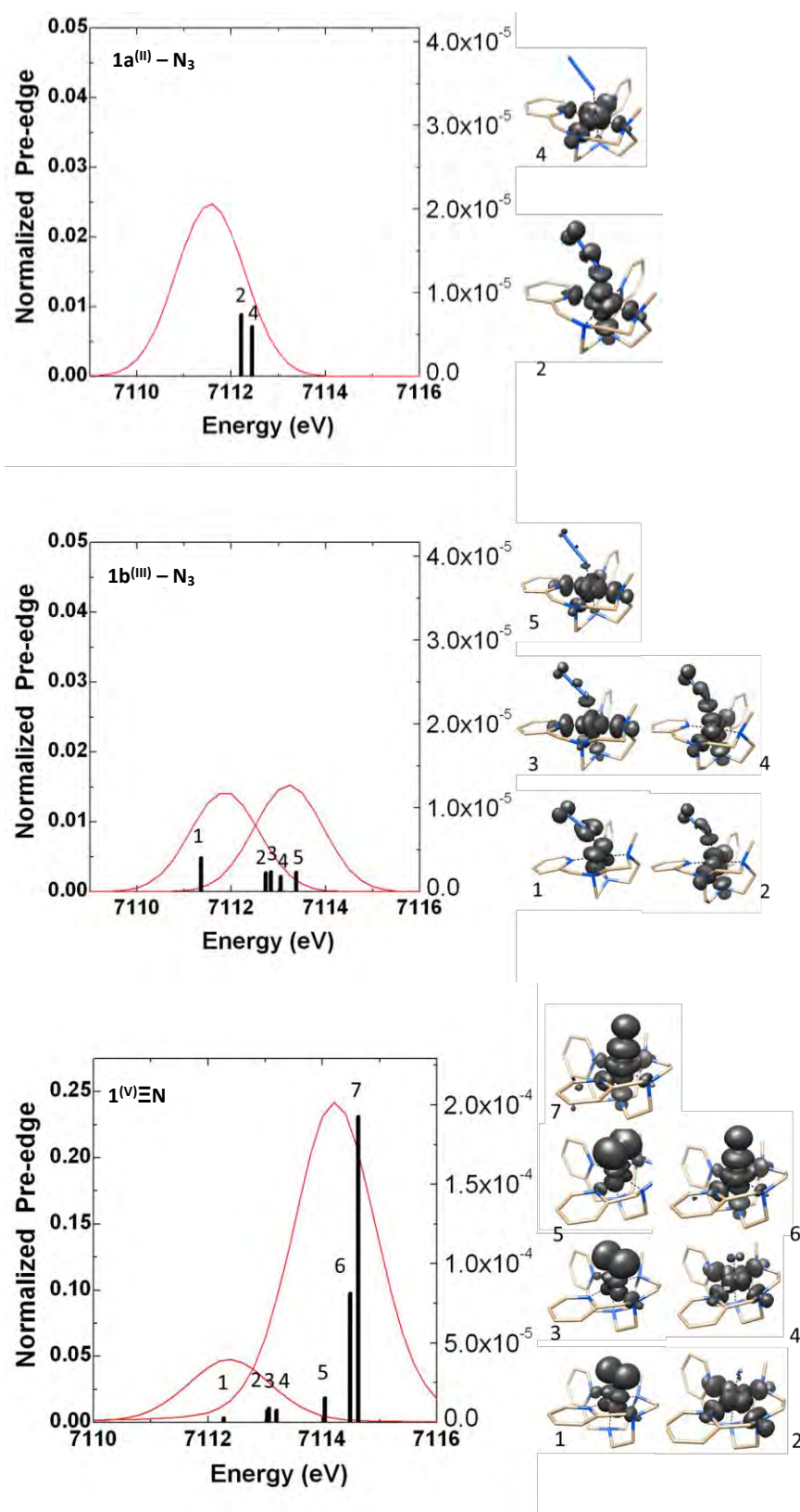


Figure SV.19. Correlation between experimental Fe K pre – edges and calculated transitions including the difference density maps for: $1a^{(III)} - N_3$, $1b^{(III)} - N_3$ and $1^{(V)}EN$. Transitions were shifted by 155.0 eV to match experiment.

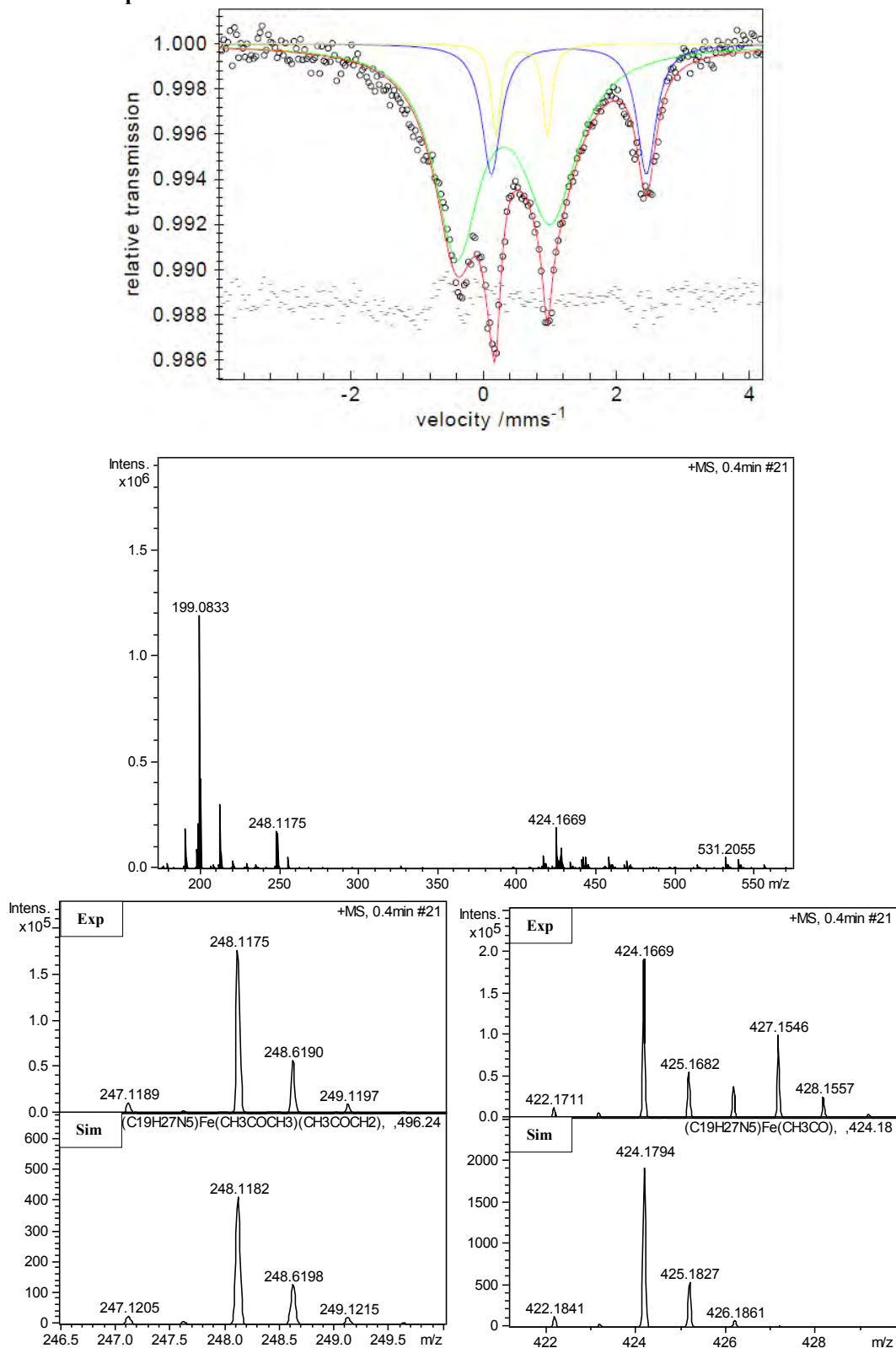
Thermal decomposition of $1^{(V)}\Xi\text{N}$ 

Figure SV.20. (Top) Mössbauer spectra after decomposition of solid $1^{(V)}\Xi\text{N}$ at room temperature under anaerobic conditions. (Below) HR – MS analysis of melted sample after photolysis of $1\text{b}^{(III)} - \text{N}_3$ to $1^{(V)}\Xi\text{N}$ during online mass spectrometry studies; insets show the experimental and simulated ions 248.12 and 424.17, tentatively assigned to species $[\text{Fe}^{\text{II}}(\text{COCH}_3)(\text{MePy}_2\text{tacn})]^+$ and $[\text{Fe}^{\text{III}}(\text{COCH}_3)(\text{CH}_3\text{COCH}_3)(\text{MePy}_2\text{tacn})]^{2+}$ suggesting that $1^{(V)}\Xi\text{N}$ could be reacting with acetone.

Table SV.12. XYZ files of geometry optimized structures.

Compound 1a^(II) – N₃ S = 2				H	3.633646	3.289749	3.485918
Fe	0.493200	4.655523	1.412778	C	2.606700	2.587877	0.660901
N	-0.420727	3.196766	0.105525	H	1.803819	1.937399	0.309842
C	-1.336775	2.272733	0.447838	H	3.509053	1.973476	0.787051
H	-1.564210	2.197453	1.507097	C	2.884779	3.690415	-0.364042
N	1.798949	4.712048	-0.399611	H	3.822077	4.196721	-0.126294
C	-1.958373	1.455390	-0.488321	H	3.012199	3.239741	-1.354645
H	-2.691036	0.722963	-0.167469	C	1.495801	2.187821	2.814983
N	2.108568	6.029665	2.123459	H	2.219934	1.562974	3.353771
C	-1.606351	1.593277	-1.830726	H	0.906323	1.529227	2.166670
H	-2.059870	0.962002	-2.588346	C	0.558428	2.867001	3.781618
N	2.161836	3.177553	1.945302	C	0.351025	2.408365	5.076757
C	-0.661976	2.554162	-2.188862	H	0.920429	1.559428	5.442214
H	-0.367205	2.690306	-3.224554	C	-0.589314	3.047023	5.886576
N	-0.112990	3.935105	3.283078	H	-0.765331	2.704777	6.901253
C	-0.097509	3.350373	-1.196420	C	-1.292766	4.134051	5.367175
C	0.854187	4.482719	-1.510776	H	-2.033687	4.661890	5.957968
H	1.376271	4.294042	-2.457665	C	-1.024941	4.548882	4.069204
H	0.262791	5.397708	-1.633431	H	-1.535699	5.396187	3.621897
N	-0.891967	6.045419	1.038401	Compound 1a^(II) – N₃ S = 0			
N	-1.922841	5.945774	0.426261	Fe	5.047414	3.398126	1.098482
C	2.309046	6.107141	-0.364549	N	5.986802	3.041049	-0.628195
H	1.439308	6.759380	-0.486534	C	7.118874	4.026934	-0.790940
H	3.010629	6.304963	-1.187154	H	7.184711	4.351439	-1.833472
C	2.988826	6.395188	0.971976	H	8.050302	3.509905	-0.555307
H	3.924558	5.838134	1.052683	C	6.927217	5.229812	0.127624
H	3.251566	7.457464	1.020135	H	7.855953	5.808920	0.197575
N	-2.922402	5.879264	-0.166096	H	6.139436	5.885399	-0.245309
C	1.493658	7.239482	2.715296	N	6.493582	4.732558	1.466618
H	2.260850	7.900679	3.141583	C	7.640099	4.087097	2.200855
H	0.799071	6.937538	3.502916	H	8.050598	4.784365	2.936823
H	0.936564	7.770130	1.942040	H	8.428386	3.882082	1.474850
C	2.835228	5.264368	3.165163	C	7.180697	2.804939	2.870915
H	2.152708	5.156238	4.011752	H	8.045968	2.216112	3.201695
H	3.722583	5.811560	3.516641	H	6.560998	3.018947	3.743892
C	3.265913	3.893490	2.648193	N	6.337655	2.024118	1.918310
H	4.098408	3.999726	1.949538				

C	7.182201	1.461463	0.798171	Compound 1b^(III) – N₃S = 1/2			
H	7.387468	0.403382	0.985157	Fe	1.976183	0.378658	13.560691
H	8.144065	1.977840	0.796861	N	3.227752	-1.153380	13.514145
C	6.473739	1.634454	-0.534412	C	4.574691	-1.140139	13.601595
H	7.143342	1.381795	-1.366302	H	5.046105	-0.171563	13.710756
H	5.585651	1.000967	-0.577890	N	0.602760	-1.030675	13.851832
C	4.961947	3.215803	-1.692316	C	5.329048	-2.302713	13.547767
H	4.352453	2.306458	-1.698471	H	6.408395	-2.239406	13.623153
H	5.417252	3.336609	-2.681581	N	2.018942	0.556186	15.569612
C	4.090538	4.381646	-1.328396	C	4.677928	-3.526267	13.401523
C	3.408982	5.151421	-2.260821	H	5.241576	-4.452442	13.367399
H	3.553488	4.956315	-3.318630	N	0.439146	1.712738	13.639829
C	2.543833	6.154616	-1.824436	C	3.289093	-3.543030	13.295499
H	2.001145	6.766231	-2.537485	H	2.745640	-4.473497	13.172768
C	2.390124	6.345991	-0.451879	N	3.409850	1.717370	13.660981
H	1.720743	7.102877	-0.057517	C	2.590195	-2.343895	13.342675
C	3.111727	5.554035	0.429639	N	1.824117	0.298066	11.670091
H	3.010279	5.676002	1.501198	C	1.105476	-2.245558	13.143950
N	3.969311	4.590940	0.015997	H	0.586033	-3.144100	13.487628
C	5.852836	5.790321	2.298410	H	0.893916	-2.109953	12.078674
H	5.291823	6.439356	1.617326	C	0.438719	-1.292095	15.335021
H	6.595748	6.407567	2.814916	H	0.283259	-2.360173	15.501360
C	4.899449	5.137468	3.259173	H	-0.463718	-0.776644	15.662655
C	4.560839	5.669568	4.494915	N	2.690360	-0.117413	10.922143
H	5.044494	6.579895	4.834640	N	3.454886	-0.495443	10.147256
C	3.598902	5.028238	5.277768	C	1.655280	-0.798464	16.099724
H	3.318184	5.429221	6.245975	H	1.446275	-0.746913	17.172794
C	3.009955	3.863021	4.786201	H	2.514616	-1.451473	15.946624
H	2.254515	3.330759	5.354372	C	1.021606	1.598127	16.021748
C	3.402619	3.369602	3.549594	H	0.135159	1.074668	16.380356
H	2.982585	2.463559	3.129192	H	1.435005	2.155427	16.865075
N	4.338157	3.983698	2.785222	C	0.678050	2.525523	14.874022
C	5.693020	0.905430	2.654579	H	-0.208488	3.122526	15.114460
H	6.461640	0.264782	3.104609	H	1.499708	3.209275	14.654227
H	5.079704	0.332867	1.960603	C	0.347108	2.636428	12.471989
H	5.056340	1.316620	3.438777	H	-0.455064	3.359940	12.651433
N	3.703995	1.945988	0.795873	H	0.139728	2.057718	11.573833
N	2.562334	2.104688	0.457819	H	1.293946	3.164436	12.357129
N	1.443954	2.199800	0.132609	C	-0.852062	0.926623	13.756419

H	-1.159988	0.925437	14.802792
H	-1.637427	1.431630	13.189472
C	-0.653708	-0.486852	13.242416
H	-1.510817	-1.120376	13.493167
H	-0.503688	-0.492255	12.161808
C	3.413129	0.944055	15.938097
H	4.020683	0.033305	15.937861
H	3.450416	1.369411	16.944366
C	3.936768	1.894103	14.903254
C	4.916126	2.846157	15.148976
H	5.304423	2.965940	16.154486
C	5.382682	3.629950	14.095010
H	6.147942	4.379335	14.266307
C	4.847026	3.438613	12.822906
H	5.178631	4.025101	11.973883
C	3.859739	2.480832	12.641435
H	3.404390	2.309108	11.674389

Compound 1^(V)EN S = 1/2

Fe	1.976242	0.373452	13.451529
N	3.224483	-1.173234	13.461304
C	4.567241	-1.157360	13.560306
H	5.039887	-0.186720	13.643585
N	0.615134	-1.024975	13.828059
C	5.317102	-2.325571	13.549899
H	6.395955	-2.265649	13.634870
N	2.024859	0.546570	15.599464
C	4.661131	-3.549218	13.433186
H	5.220969	-4.478426	13.431716
N	0.437074	1.728520	13.634655
C	3.272627	-3.564694	13.315287
H	2.726388	-4.496321	13.216610
N	3.389705	1.723271	13.642836
C	2.581121	-2.360702	13.320402
N	1.881237	0.346116	11.852566
C	1.100700	-2.245952	13.113305
H	0.563859	-3.135350	13.453265
H	0.900521	-2.097220	12.047011
C	0.461442	-1.296178	15.314116

H	0.303845	-2.366467	15.463262
H	-0.442208	-0.784449	15.644383
C	1.672284	-0.810320	16.095532
H	1.447691	-0.805112	17.168051
H	2.534532	-1.457840	15.931320
C	1.026419	1.578610	16.031317
H	0.133827	1.058771	16.381567
H	1.418174	2.148148	16.878742
C	0.687499	2.514521	14.883255
H	-0.195537	3.114725	15.129914
H	1.511171	3.197845	14.670278
C	0.331934	2.671521	12.485469
H	-0.482386	3.379303	12.673228
H	0.138790	2.102802	11.576680
H	1.271111	3.215591	12.382023
C	-0.849152	0.933369	13.752072
H	-1.154585	0.930349	14.799102
H	-1.638148	1.434690	13.187055
C	-0.655147	-0.481911	13.239825
H	-1.505326	-1.115532	13.512708
H	-0.528269	-0.494546	12.155604
C	3.408666	0.952676	15.937330
H	4.034755	0.053638	15.936162
H	3.471481	1.396521	16.935826
C	3.913069	1.899954	14.885567
C	4.889404	2.858618	15.125409
H	5.274994	2.982234	16.131530
C	5.355947	3.640706	14.071680
H	6.117412	4.394013	14.243013
C	4.828985	3.439094	12.797067
H	5.164979	4.019175	11.945320
C	3.847743	2.477125	12.616456
H	3.403849	2.280967	11.647849

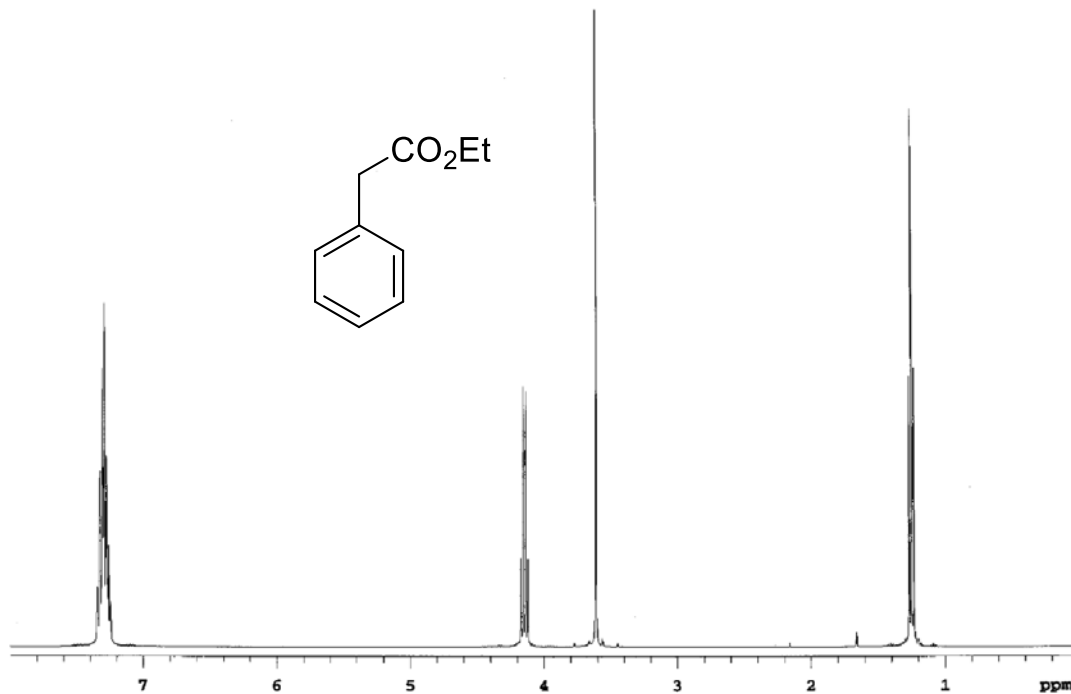
Compound 1^(V)EN S = 3/2

Fe	1.983198	0.391195	13.536031
N	3.200559	-1.178944	13.477052
C	4.545340	-1.159475	13.576302

H	5.016988	-0.191358	13.682442	H	-1.638353	1.437132	13.215244
N	0.616677	-1.026537	13.830579	C	-0.643399	-0.476448	13.229148
C	5.296875	-2.325236	13.538799	H	-1.493267	-1.126023	13.462296
H	6.375372	-2.261287	13.625155	H	-0.484648	-0.455502	12.149251
N	2.020635	0.564968	15.633816	C	3.402991	0.991069	15.963335
C	4.646664	-3.549067	13.396515	H	4.036040	0.097012	15.982774
H	5.210055	-4.475720	13.375328	H	3.462764	1.457728	16.951332
N	0.435569	1.716576	13.660612	C	3.914039	1.921995	14.893736
C	3.258469	-3.565765	13.278278	C	4.886285	2.886201	15.119501
H	2.713831	-4.495781	13.158423	H	5.267814	3.037135	16.123275
N	3.411275	1.721650	13.642432	C	5.355422	3.645205	14.047662
C	2.561877	-2.365962	13.309075	H	6.112385	4.405320	14.209996
N	1.916970	0.345590	11.782126	C	4.845168	3.417965	12.769038
C	1.088291	-2.237029	13.093258	H	5.191076	3.984575	11.912438
H	0.533924	-3.124561	13.408910	C	3.872986	2.445650	12.598946
H	0.904173	-2.057274	12.029166	H	3.433130	2.205280	11.637092
C	0.470678	-1.303994	15.318148				
H	0.335967	-2.377458	15.467331				
H	-0.443763	-0.813203	15.651081				
C	1.672844	-0.801608	16.112457				
H	1.435366	-0.808551	17.182121				
H	2.543918	-1.438301	15.952968				
C	1.009082	1.585629	16.061502				
H	0.119303	1.055363	16.403096				
H	1.387418	2.159420	16.911873				
C	0.672183	2.516388	14.908301				
H	-0.218304	3.110849	15.138810				
H	1.492987	3.203626	14.695823				
C	0.353937	2.636654	12.489533				
H	-0.473153	3.336966	12.645780				
H	0.193211	2.045100	11.588812				
H	1.289863	3.188316	12.402081				
C	-0.852105	0.921470	13.770636				
H	-1.151125	0.902209	14.818854				

ANNEX CHAPTER VI**Table SVI.1.** Distribution of isomers for substituted benzenes as substrates (normalised values for the number of C available, 2 for *ortho*, 2 for *meta* and 1 for *para*).

R substituent	<i>ortho</i>	<i>meta</i>	<i>para</i>
Me	33	21	46
Et	28	28	44
ⁱ Bu	26	30	44
Ph	41	22	37
Cyclopropyl	31	22	46
Cy	33	25	42
^t Bu	12	27	61
MeO	37	7	56
Cl	39	19	42
CF ₃	22	55	23

**Figure SVI.1.** ¹H – NMR spectrum of the benzene derivative (500 MHz, CDCl₃, 20 °C).

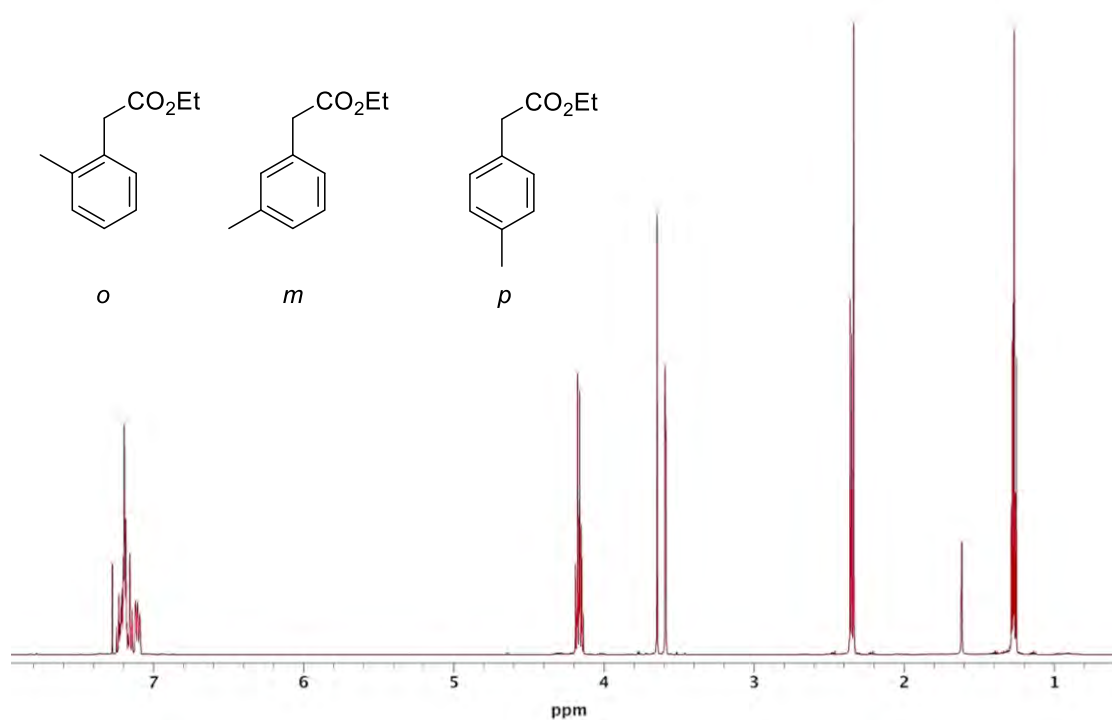


Figure SVI.2. ^1H – NMR spectrum of the toluene derivative (500 MHz, CDCl_3 , 20 °C).

The products have been assigned using NOESY experiments. The figure below shows a portion of the ^1H – NMR spectrum (assigned as *para*, *meta* and *ortho* from left to right) with the resonances of the methyl groups attached to the arene ring, from which the ratio of products has been obtained. In other cases, such ratio is obtained from the benzylic resonances of the $\text{CH}_2\text{CO}_2\text{Et}$ group.

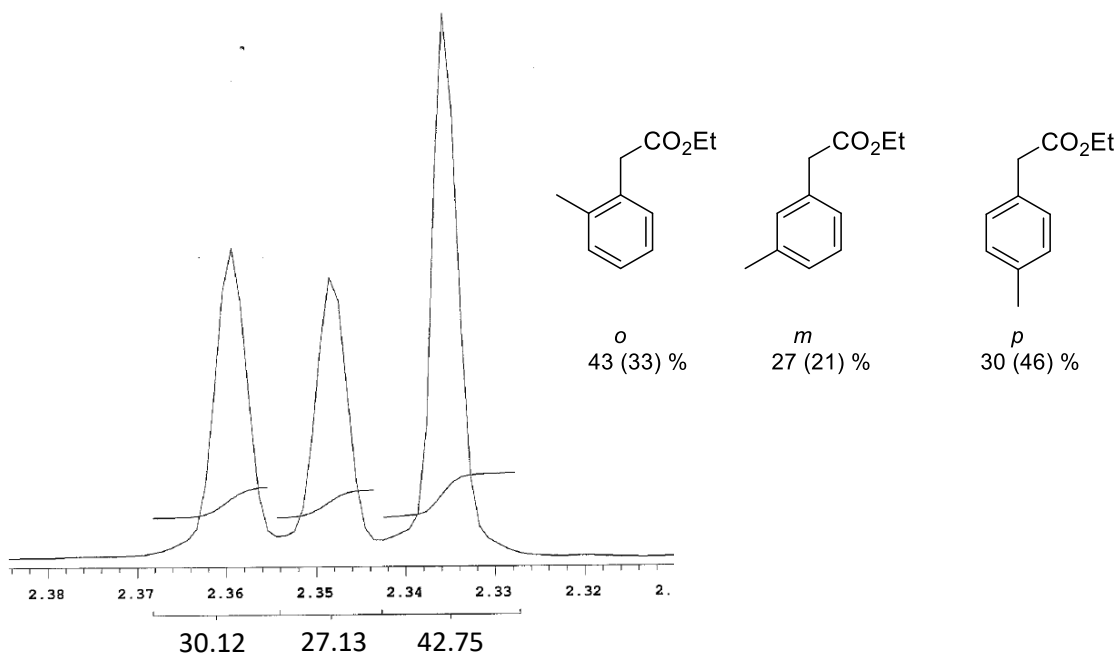


Figure SVI.3. Detail of the ^1H – NMR spectrum of the toluene derivative (500 MHz, CDCl_3 , 20 °C). Values in brackets are the normalised per number of C atoms (2 *ortho*, 2 *meta* and 1 *para*).

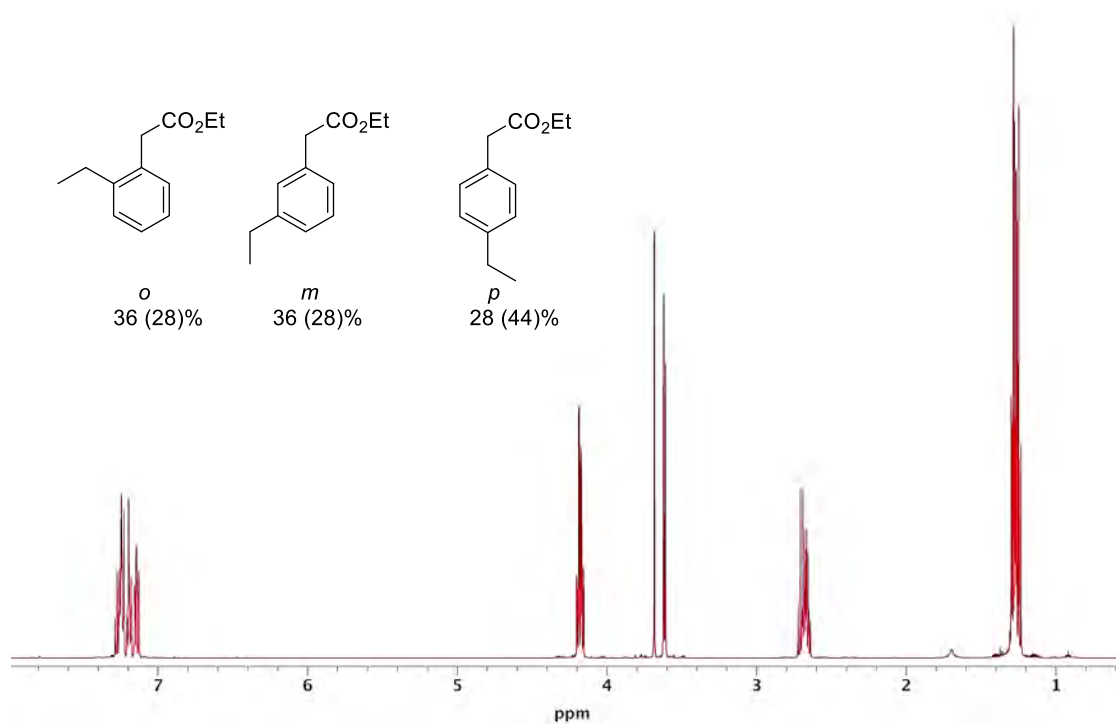


Figure SVI.4. ^1H – NMR spectrum of the ethylbenzene derivative (500 MHz, CDCl_3 , 20 °C). Values in brackets are the normalised per number of C atoms (2 *ortho*, 2 *meta* and 1 *para*).

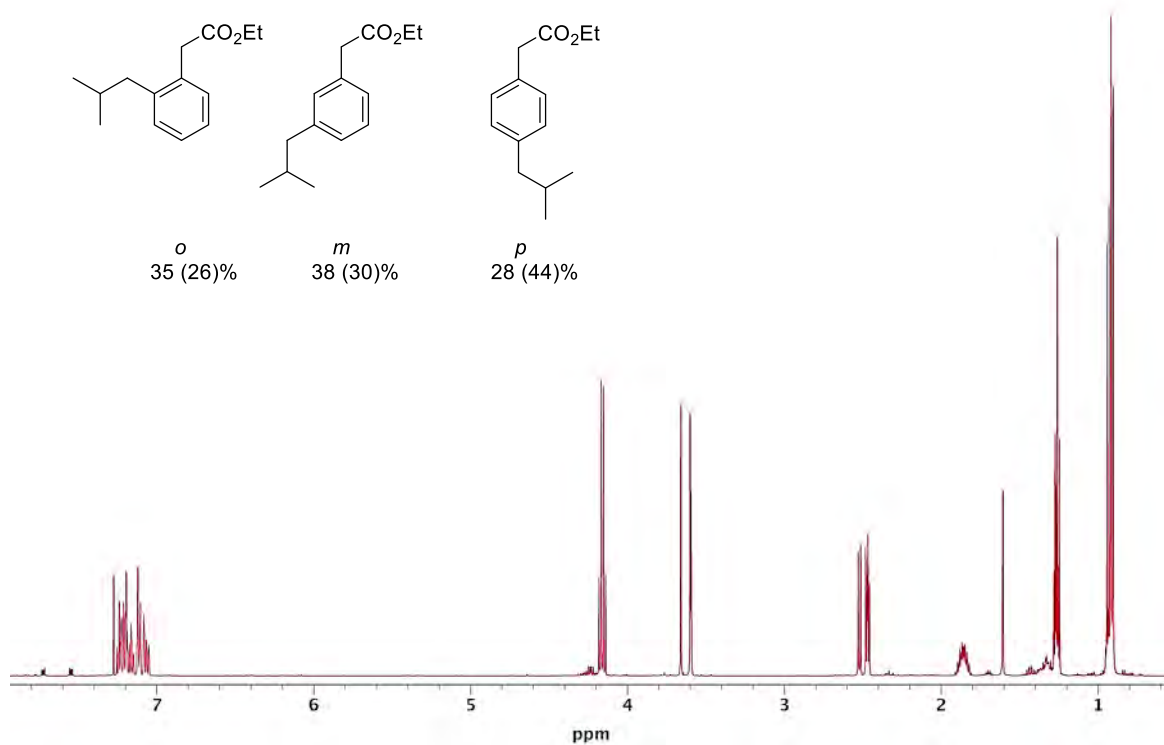


Figure SVI.5. ^1H – NMR spectrum of the isobutylbenzene derivative (500 MHz, CDCl_3 , 20 °C). Values in brackets are the normalised per number of C atoms (2 *ortho*, 2 *meta* and 1 *para*).

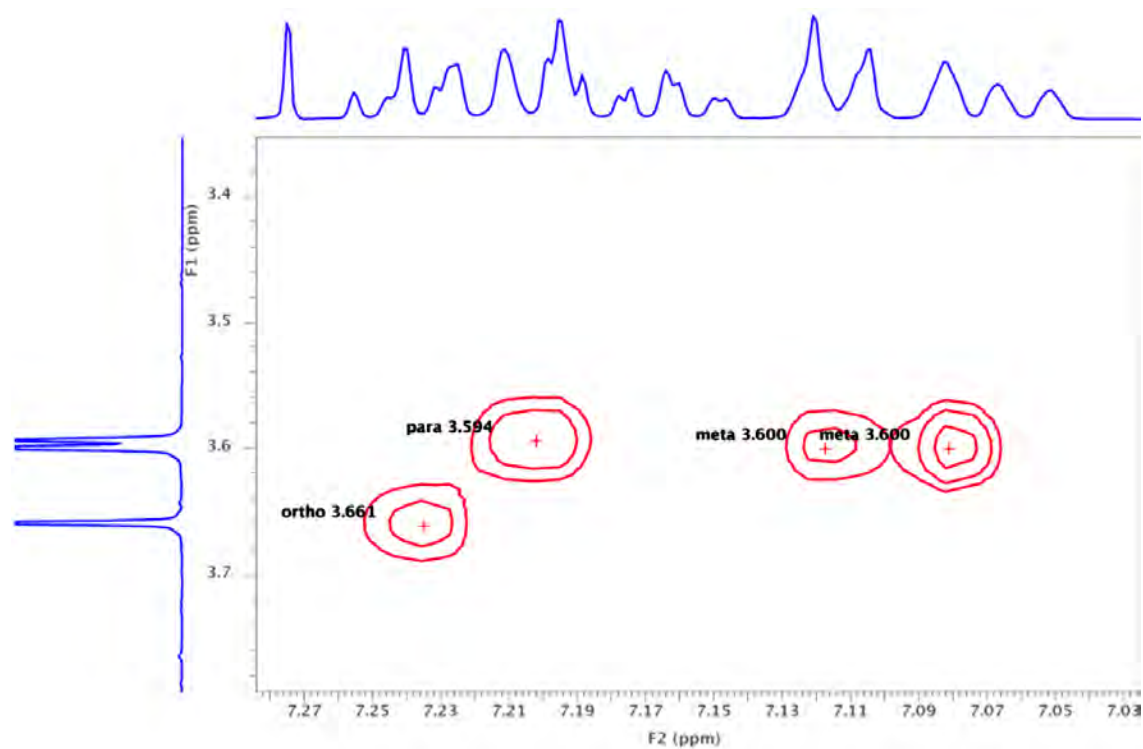


Figure SVI.6. 2D – NOESY spectrum of the isobutylbenzene derivative (500 MHz, CDCl₃, 20 °C).

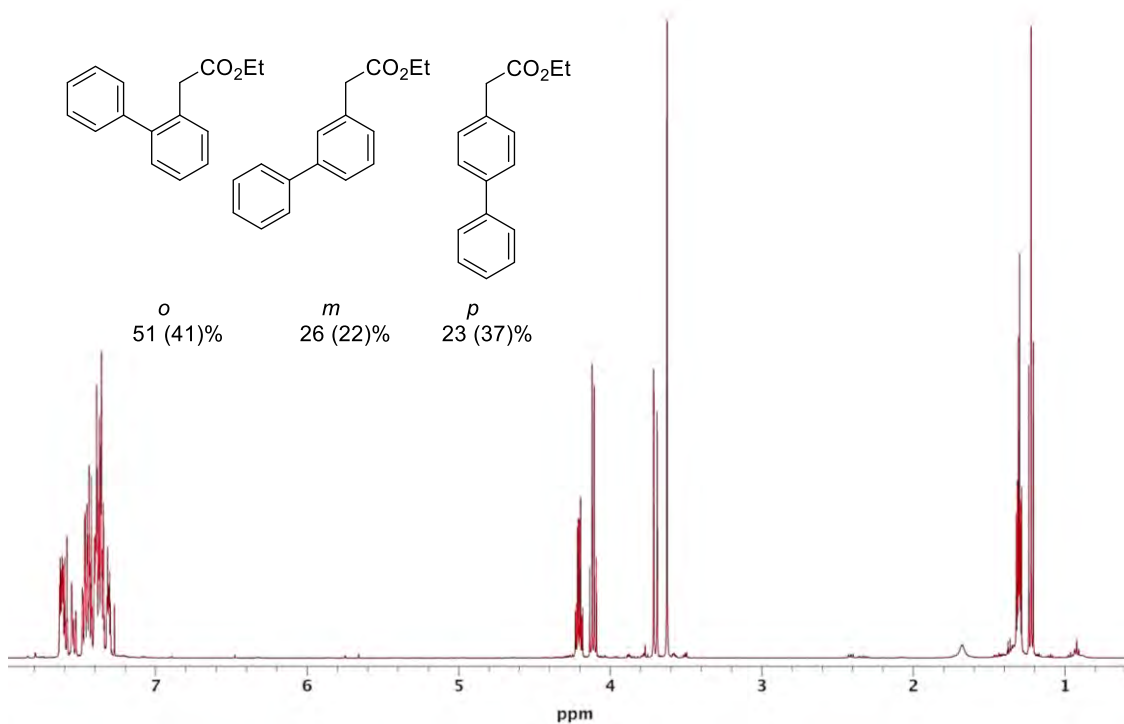


Figure SVI.7. ¹H – NMR spectrum of the biphenyl derivative (500 MHz, CDCl₃, 20 °C). Values in brackets are the normalised per number of C atoms (2 *ortho*, 2 *meta* and 1 *para*).

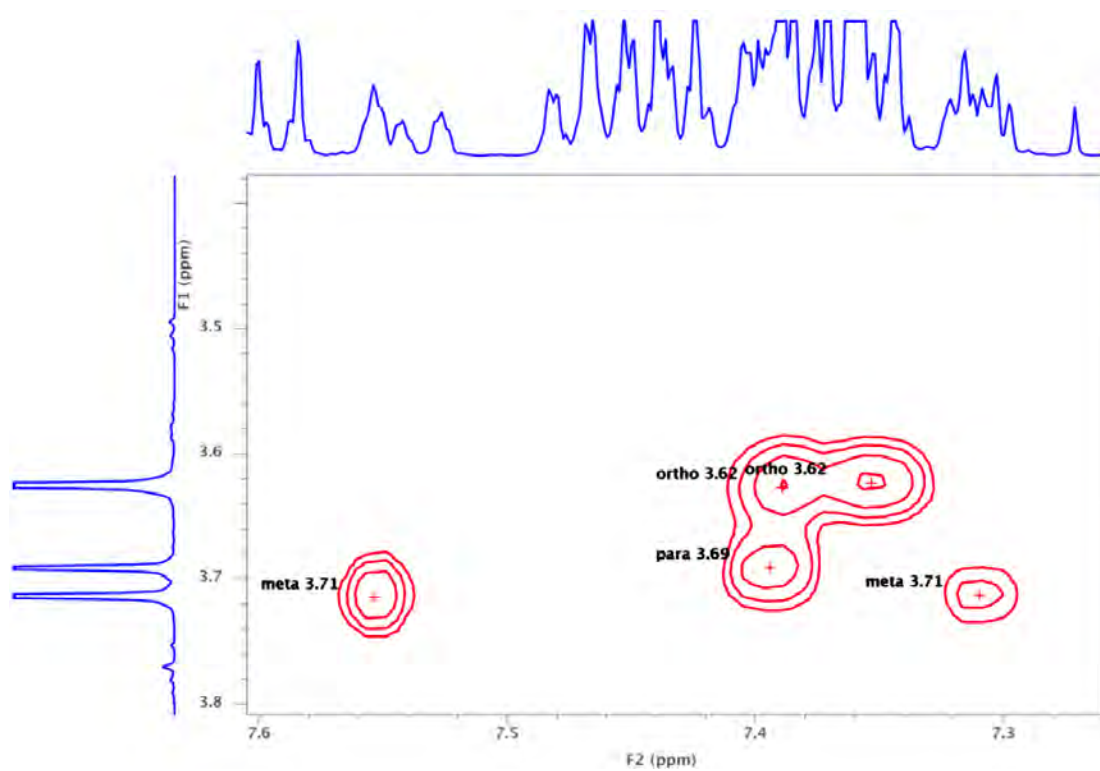


Figure SVI.8. 2D – NOESY spectrum of the biphenyl derivative (500 MHz, CDCl_3 , 20 °C)

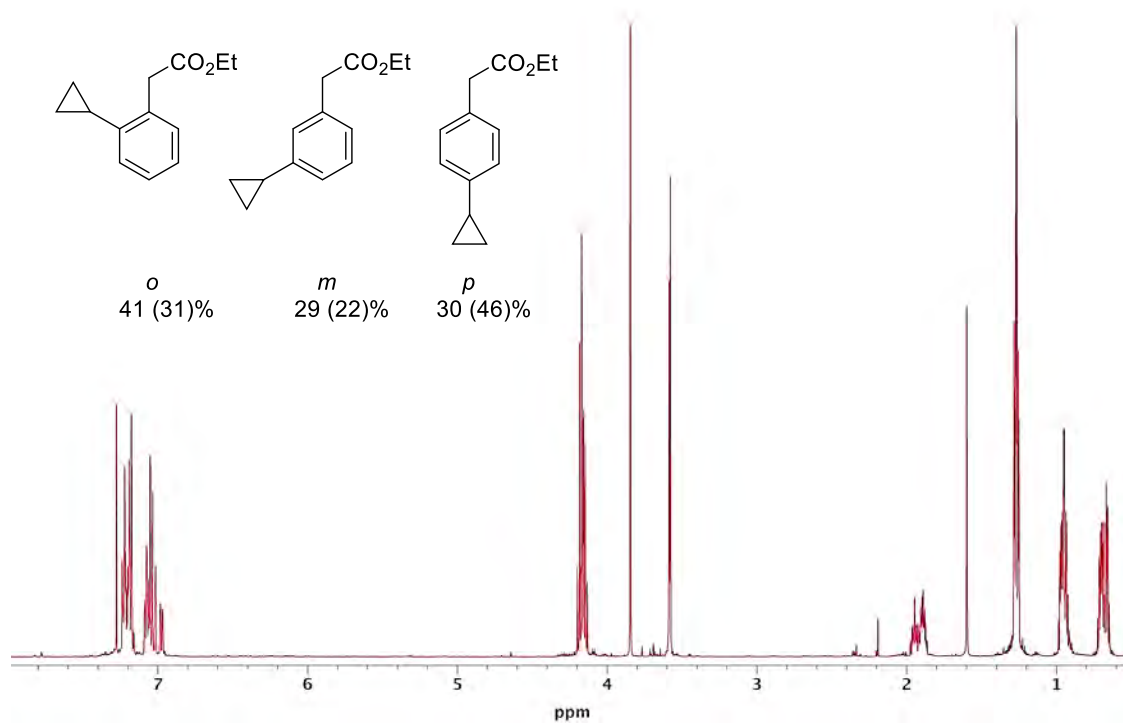
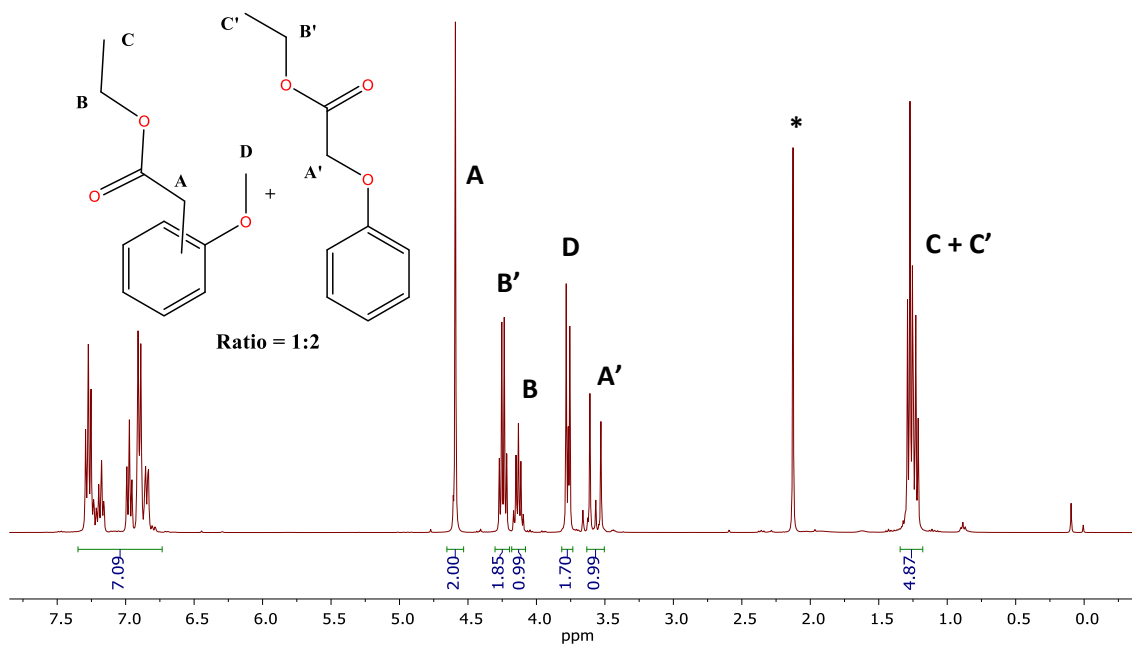


Figure SVI.9. ^1H NMR spectrum of the cyclopropylbenzene derivative (500 MHz, CDCl_3 , 20 °C). Values in brackets are the normalised per number of C atoms (2 *ortho*, 2 *meta* and 1 *para*).



*Residual acetone.

Figure SVI.10. ¹H NMR spectrum of the anisole derivative (400 MHz, CDCl₃, 20 °C). O – Me functionalization product was assigned by comparison with commercially available ethyl phenoxyacetate.

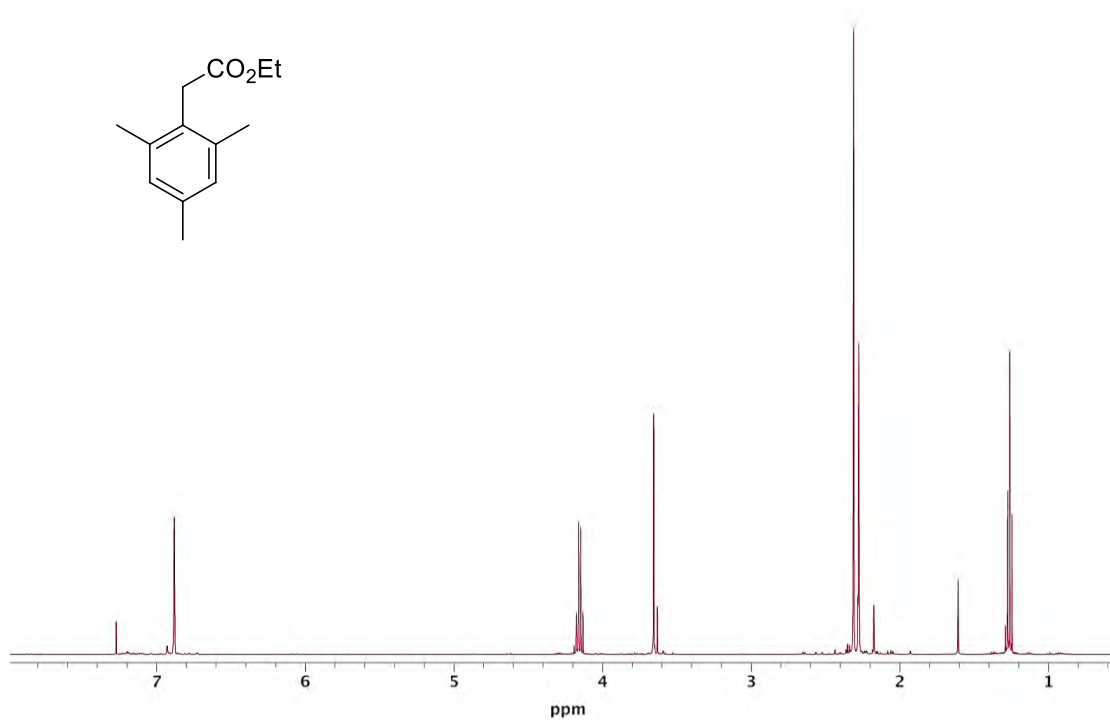


Figure SVI.11. ¹H NMR spectrum of the mesitylene derivative (500 MHz, CDCl₃, 20 °C).

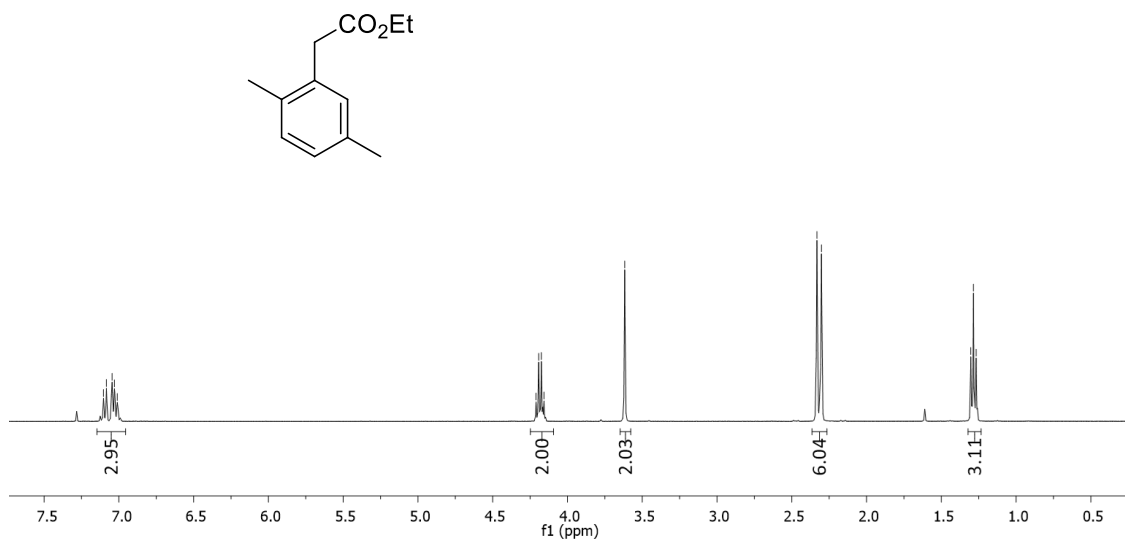


Figure SVI.12. ^1H NMR spectrum of the *p*-xylene derivative (400 MHz, CDCl_3 , 20 °C).

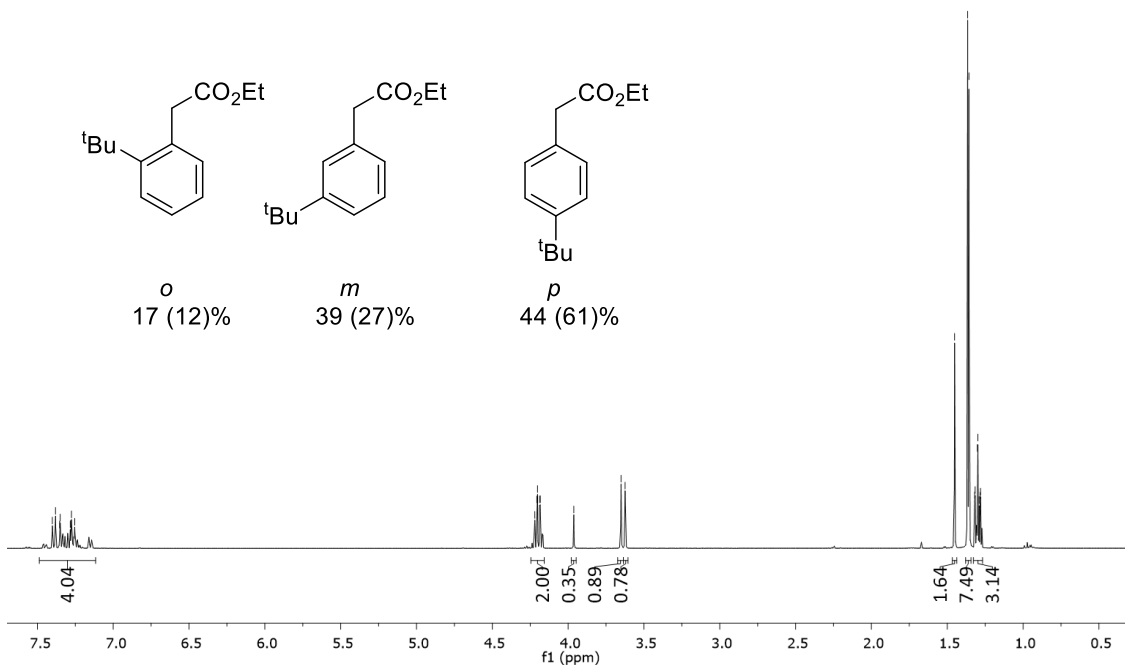


Figure SVI.13. ^1H NMR spectrum of the *tert*-butylbenzene derivatives (400 MHz, CDCl_3 , 20 °C). Values in brackets are the normalised per number of C atoms (2 *ortho*, 2 *meta* and 1 *para*).

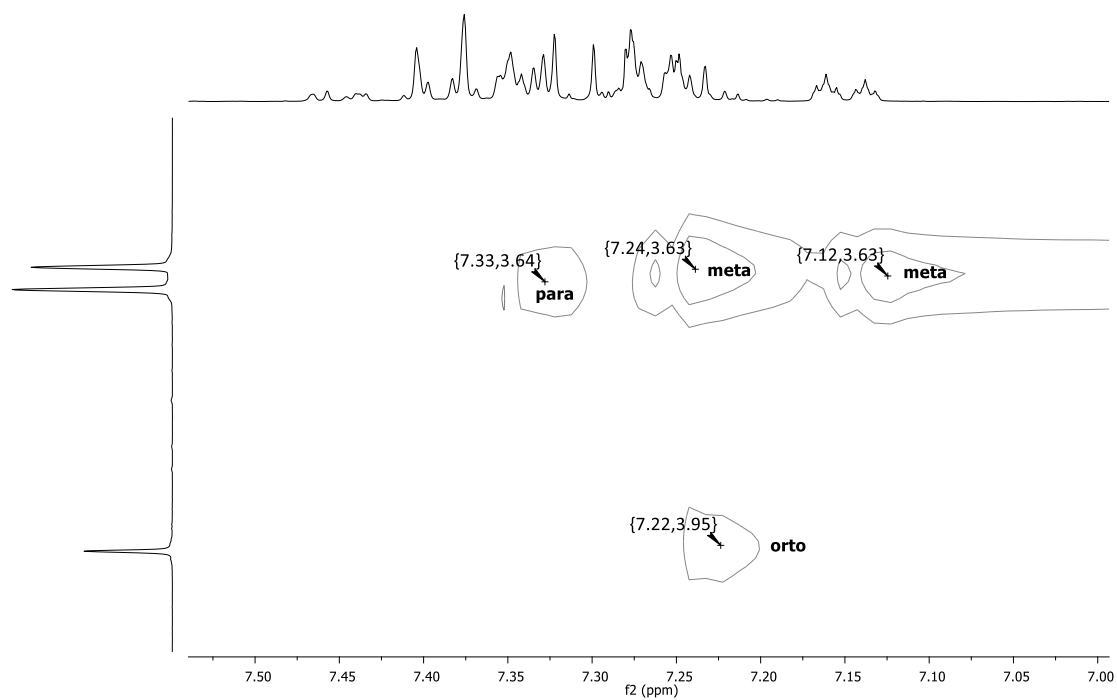


Figure SVI.14. 2D – NOESY spectrum of the *tert* – butylbenzene derivative (300 MHz, CDCl₃, 20 °C).

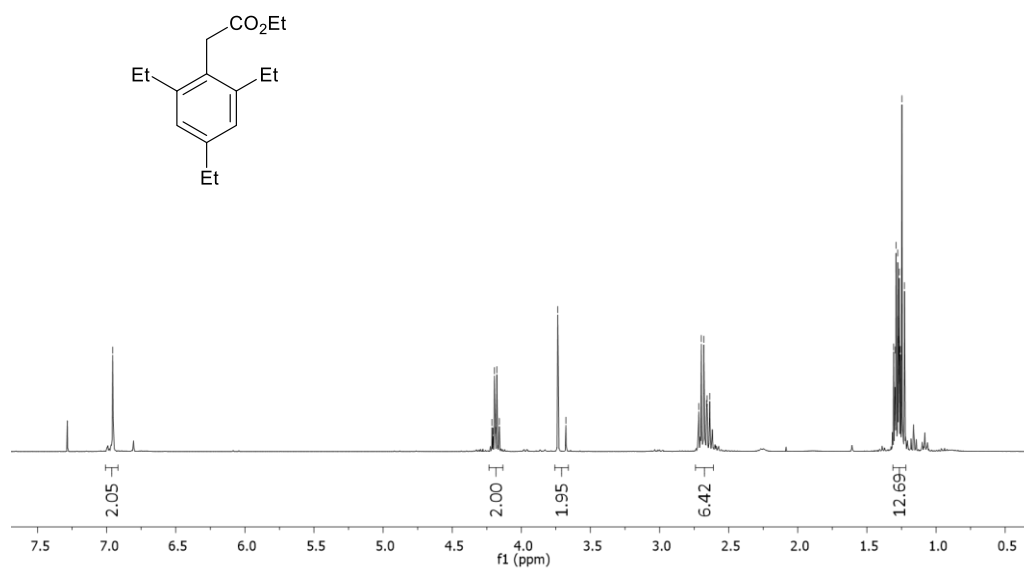


Figure SVI.15. ¹H – NMR spectrum of the 1,3,5 – triethylbenzene derivative (400 MHz, CDCl₃, 20 °C).

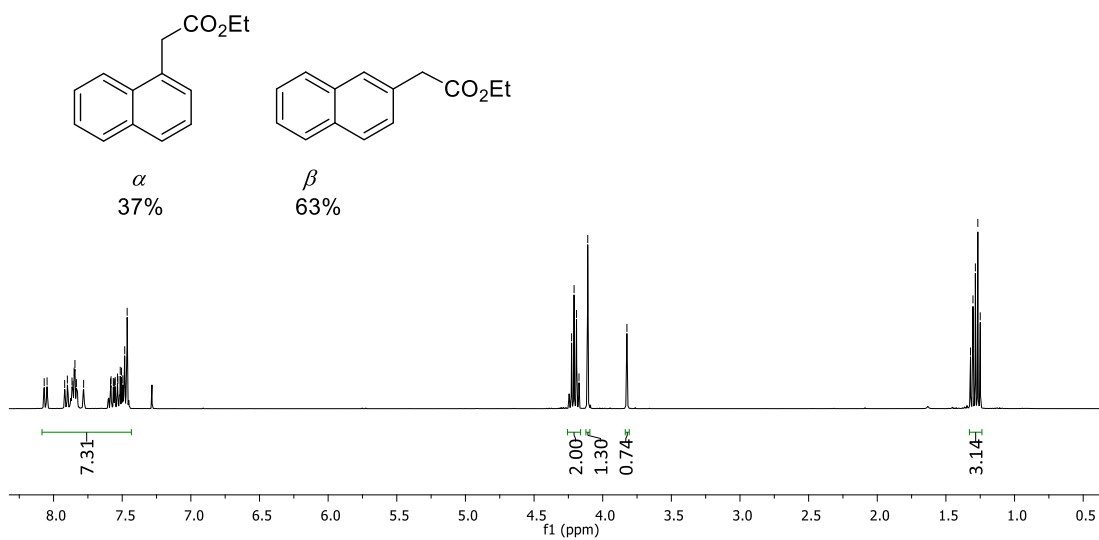


Figure SVI.16. ^1H NMR spectrum of the naphthalene derivatives (400 MHz, CDCl_3 , 20 °C).

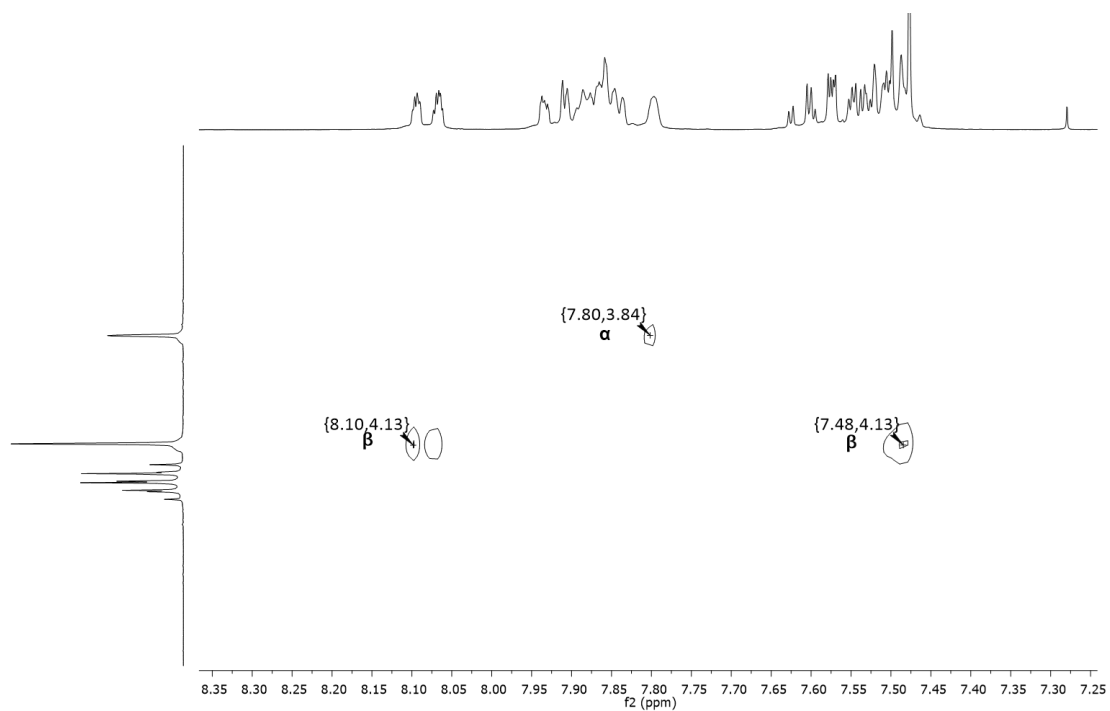


Figure SVI.17. 2D – NOESY spectrum of the naphthalene derivative (400 MHz, CDCl_3 , 20 °C).

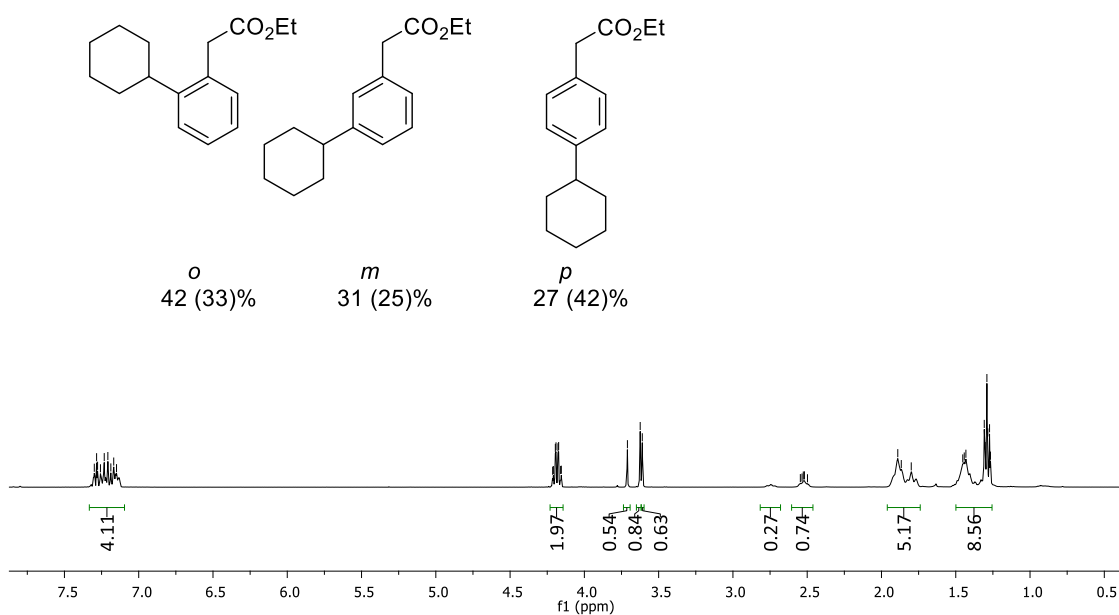


Figure SVI.18. ^1H – NMR spectrum of the phenyl-cyclohexane derivatives (400 MHz, CDCl_3 , 20 °C). Values in brackets are the normalised per number of C atoms (2 *ortho*, 2 *meta* and 1 *para*).

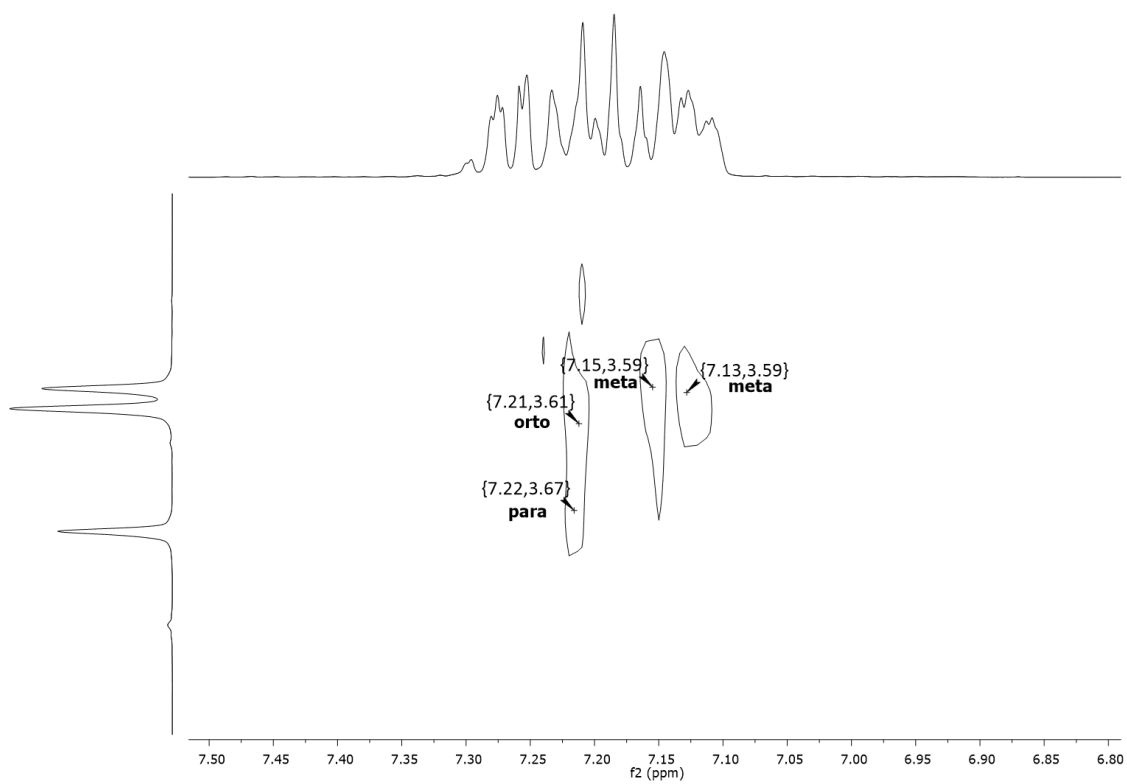


Figure SVI.19. 2D – NOESY spectrum of the cyclohexylbenzene derivative (400 MHz, CDCl_3 , 20 °C).

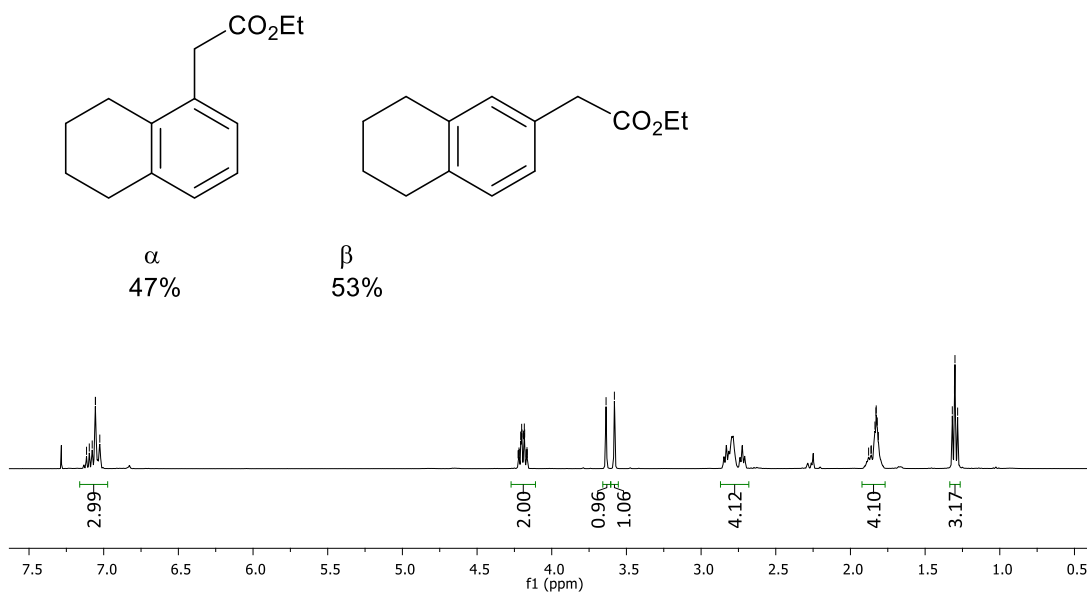


Figure SVI.20. ^1H NMR spectrum of the tetrahydronaphthalene derivatives (400 MHz, CDCl_3 , 20 °C).

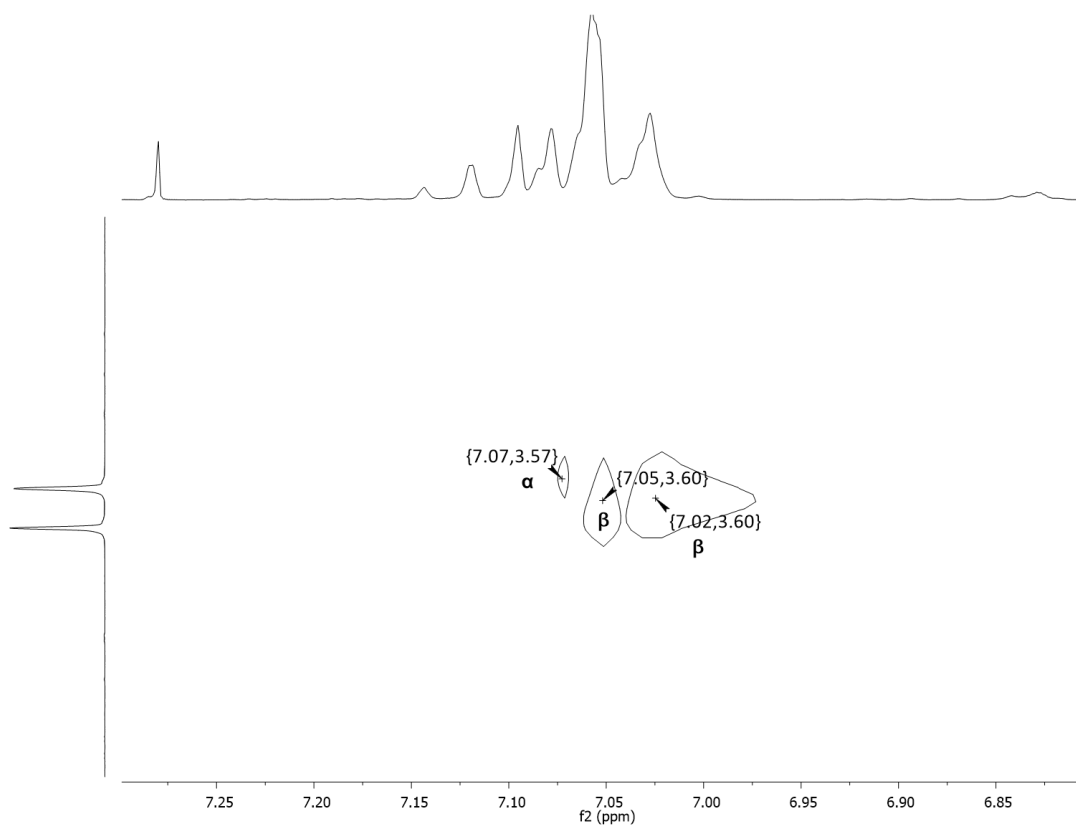


Figure SVI.21. 2D – NOESY spectrum of the tetrahydronaphthalene derivative (400 MHz, CDCl_3 , 20 °C).

REFERENCES

- (1) Labinger, J. A.; Bercaw, J. E. *Nature* **2002**, *417*, 507.
- (2) Chen, K.; Baran, P. S. *Nature* **2009**, *459*, 824.
- (3) Godula, K.; Sames, D. *Science* **2006**, *312*, 67.
- (4) Davies, H. M. L.; Morton, D. J. *Org. Chem.* **2016**, *81*, 343.
- (5) Hartwig, J. F.; Larsen, M. A. *ACS Cent. Sci.* **2016**, *2*, 281.
- (6) Hersleth, H.-P.; Ryde, U.; Rydberg, P.; Görbitz, C. H.; Andersson, K. K. *J. Inorg. Biochem.* **2006**, *100*, 460.
- (7) Krebs, C.; Galonić Fujimori, D.; Walsh, C. T.; Bollinger, J. M. *Acc. Chem. Res.* **2007**, *40*, 484.
- (8) Krebs, C.; Price, J. C.; Baldwin, J.; Saleh, L.; Green, M. T.; Bollinger, J. M. *Inorg. Chem.* **2005**, *44*, 742.
- (9) Price, J. C.; Barr, E. W.; Glass, T. E.; Krebs, C.; Bollinger, J. M. *J. Am. Chem. Soc.* **2003**, *125*, 13008.
- (10) Friedle, S.; Reisner, E.; Lippard, S. J. *Chem. Soc. Rev.* **2010**, *39*, 2768.
- (11) Jung, C. *Biochimica et Biophysica Acta (BBA) - Proteins and Proteomics* **2011**, *1814*, 46.
- (12) Schulz, C. E.; Rutter, R.; Sage, J. T.; Debrunner, P. G.; Hager, L. P. *Biochemistry* **1984**, *23*, 4743.
- (13) Stone, K. L.; Hoffart, L. M.; Behan, R. K.; Krebs, C.; Green, M. T. *J. Am. Chem. Soc.* **2006**, *128*, 6147.
- (14) Behan, R. K.; Hoffart, L. M.; Stone, K. L.; Krebs, C.; Green, M. T. *J. Am. Chem. Soc.* **2006**, *128*, 11471.
- (15) Rittle, J.; Green, M. T. *Science* **2010**, *330*, 933.
- (16) Shu, L.; Nesheim, J. C.; Kauffmann, K.; Münck, E.; Lipscomb, J. D.; Que, L. *Science* **1997**, *275*, 515.
- (17) Banerjee, R.; Proshlyakov, Y.; Lipscomb, J. D.; Proshlyakov, D. A. *Nature* **2015**, *518*, 431.
- (18) Kovaleva, E. G.; Lipscomb, J. D. *Nat. Chem. Biol.* **2008**, *4*, 186.
- (19) Costas, M.; Mehn, M. P.; Jensen, M. P.; Que, L. *Chem. Rev.* **2004**, *104*, 939.
- (20) Sinnecker, S.; Svensen, N.; Barr, E. W.; Ye, S.; Bollinger, J. M.; Neese, F.; Krebs, C. *J. Am. Chem. Soc.* **2007**, *129*, 6168.
- (21) Tinberg, C. E.; Lippard, S. J. *Acc. Chem. Res.* **2011**, *44*, 280.
- (22) Wallar, B. J.; Lipscomb, J. D. *Chem. Rev.* **1996**, *96*, 2625.
- (23) Jayaraj, K.; Gold, A.; Austin, R. N.; Mandon, D.; Weiss, R.; Turner, J.; Bill, E.; Muether, M.; Trautwein, A. X. *J. Am. Chem. Soc.* **1995**, *117*, 9079.
- (24) Cho, K.-B.; Hirao, H.; Shaik, S.; Nam, W. *Chem. Soc. Rev.* **2016**, *45*, 1197.
- (25) Ortiz de Montellano, P. R. *Chem. Rev.* **2010**, *110*, 932.
- (26) Meunier, B.; de Visser, S. P.; Shaik, S. *Chem. Rev.* **2004**, *104*, 3947.
- (27) Urlacher, V. B.; Girhard, M. *Trends Biotechnol.* **2012**, *30*, 26.
- (28) Meunier, B. *Chem. Rev.* **1992**, *92*, 1411.
- (29) Price, J. C.; Barr, E. W.; Tirupati, B.; Bollinger, J. M.; Krebs, C. *Biochemistry* **2003**, *42*, 7497.
- (30) Proshlyakov, D. A.; Henshaw, T. F.; Monterosso, G. R.; Ryle, M. J.; Hausinger, R. P. *J. Am. Chem. Soc.* **2004**, *126*, 1022.
- (31) Riggs-Gelasco, P. J.; Price, J. C.; Guyer, R. B.; Brehm, J. H.; Barr, E. W.; Bollinger, J. M.; Krebs, C. *J. Am. Chem. Soc.* **2004**, *126*, 8108.
- (32) Hoffart, L. M.; Barr, E. W.; Guyer, R. B.; Bollinger, J. M.; Krebs, C. *Proc. Natl. Acad. Sci. U.S.A.* **2006**, *103*, 14738.
- (33) Eser, B. E.; Barr, E. W.; Frantom, P. A.; Saleh, L.; Bollinger, J. M.; Krebs, C.; Fitzpatrick, P. F. *J. Am. Chem. Soc.* **2007**, *129*, 11334.
- (34) Panay, A. J.; Lee, M.; Krebs, C.; Bollinger, J. M.; Fitzpatrick, P. F. *Biochemistry* **2011**, *50*, 1928.

- (35) Panay, A. J.; Fitzpatrick, P. F. *J. Am. Chem. Soc.* **2010**, *132*, 5584.
- (36) Vaillancourt, F. H.; Yeh, E.; Vosburg, D. A.; Garneau-Tsodikova, S.; Walsh, C. T. *Chem. Rev.* **2006**, *106*, 3364.
- (37) Neumann, C. S.; Fujimori, D. G.; Walsh, C. T. *Chemistry & Biology* **2008**, *15*, 99.
- (38) Galonić Fujimori, D.; Barr, E. W.; Matthews, M. L.; Koch, G. M.; Yonce, J. R.; Walsh, C. T.; Bollinger, J. M.; Krebs, C.; Riggs-Gelasco, P. J. *J. Am. Chem. Soc.* **2007**, *129*, 13408.
- (39) Galonic, D. P.; Barr, E. W.; Walsh, C. T.; Bollinger, J. M.; Krebs, C. *Nat. Chem. Biol.* **2007**, *3*, 113.
- (40) Matthews, M. L.; Krest, C. M.; Barr, E. W.; Vaillancourt, F. H.; Walsh, C. T.; Green, M. T.; Krebs, C.; Bollinger, J. M. *Biochemistry* **2009**, *48*, 4331.
- (41) Blasiak, L. C.; Vaillancourt, F. H.; Walsh, C. T.; Drennan, C. L. *Nature* **2006**, *440*, 368.
- (42) Wong, S. D.; Srnc, M.; Matthews, M. L.; Liu, L. V.; Kwak, Y.; Park, K.; Bell Iii, C. B.; Alp, E. E.; Zhao, J.; Yoda, Y.; Kitao, S.; Seto, M.; Krebs, C.; Bollinger, J. M.; Solomon, E. I. *Nature* **2013**, *499*, 320.
- (43) Barry, S. M.; Challis, G. L. *ACS Catal.* **2013**, *3*, 2362.
- (44) Kauppi, B.; Lee, K.; Carredano, E.; Parales, R. E.; Gibson, D. T.; Eklund, H.; Ramaswamy, S. *Structure* **1998**, *6*, 571.
- (45) Chakrabarty, S.; Austin, R. N.; Deng, D.; Groves, J. T.; Lipscomb, J. D. *J. Am. Chem. Soc.* **2007**, *129*, 3514.
- (46) Wolfe, M. D.; Lipscomb, J. D. *J. Biol. Chem.* **2003**, *278*, 829.
- (47) Wackett, L. P.; Kwart, L. D.; Gibson, D. T. *Biochemistry* **1988**, *27*, 1360.
- (48) Baik, M.-H.; Newcomb, M.; Friesner, R. A.; Lippard, S. J. *Chem. Rev.* **2003**, *103*, 2385.
- (49) Lee, S. K.; Fox, B. G.; Froland, W. A.; Lipscomb, J. D.; Munck, E. *J. Am. Chem. Soc.* **1993**, *115*, 6450.
- (50) Que, L.; Tolman, W. B. *Nature* **2008**, *455*, 333.
- (51) Meunier, B. *Biomimetic Oxidations Catalyzed by Transition Metal Complexes*; Imperial College Press, 2000.
- (52) Costas, M. *Coord. Chem. Rev.* **2011**, *255*, 2912.
- (53) Shan, X.; Que Jr, L. *J. Inorg. Biochem.* **2006**, *100*, 421.
- (54) Nam, W. *Acc. Chem. Res.* **2007**, *40*, 522.
- (55) Hohenberger, J.; Ray, K.; Meyer, K. *Nat. Commun.* **2012**, *3*, 720.
- (56) Bryliakov, K. P.; Talsi, E. P. *Coord. Chem. Rev.* **2014**, *276*, 73.
- (57) Klein, J. E. M. N.; Que, L. In *Encyclopedia of Inorganic and Bioinorganic Chemistry*; John Wiley & Sons, Ltd: 2016.
- (58) Groves, J. T.; Haushalter, R. C.; Nakamura, M.; Nemo, T. E.; Evans, B. J. *J. Am. Chem. Soc.* **1981**, *103*, 2884.
- (59) Fujii, H. *Coord. Chem. Rev.* **2002**, *226*, 51.
- (60) Groves, J. T. *J. Inorg. Biochem.* **2006**, *100*, 434.
- (61) Kang, Y.; Chen, H.; Jeong, Y. J.; Lai, W.; Bae, E. H.; Shaik, S.; Nam, W. *Chem. Eur. J.* **2009**, *15*, 10039.
- (62) Shaik, S.; Cohen, S.; Wang, Y.; Chen, H.; Kumar, D.; Thiel, W. *Chem. Rev.* **2010**, *110*, 949.
- (63) Fujii, H.; Ichikawa, K. *Inorg. Chem.* **1992**, *31*, 1110.
- (64) Mandon, D.; Weiss, R.; Jayaraj, K.; Gold, A.; Turner, J.; Bill, E.; Trautwein, A. *Inorg. Chem.* **1992**, *31*, 4404.
- (65) Rohde, J.-U.; In, J.-H.; Lim, M. H.; Brennessel, W. W.; Bukowski, M. R.; Stubna, A.; Münck, E.; Nam, W.; Que, L. *Science* **2003**, *299*, 1037.
- (66) Jackson, T. A.; Rohde, J.-U.; Seo, M. S.; Sastri, C. V.; DeHont, R.; Stubna, A.; Ohta, T.; Kitagawa, T.; Münck, E.; Nam, W.; Que, L. *J. Am. Chem. Soc.* **2008**, *130*, 12394.
- (67) Rohde, J.-U.; Que, L. *Angew. Chem. Int. Ed.* **2005**, *44*, 2255.

- (68) Sastri, C. V.; Park, M. J.; Ohta, T.; Jackson, T. A.; Stubna, A.; Seo, M. S.; Lee, J.; Kim, J.; Kitagawa, T.; Münck, E.; Que, L.; Nam, W. *J. Am. Chem. Soc.* **2005**, *127*, 12494.
- (69) Bell, C. B.; Wong, S. D.; Xiao, Y.; Klinker, E. J.; Tenderholt, A. L.; Smith, M. C.; Rohde, J.-U.; Que, L.; Cramer, S. P.; Solomon, E. I. *Angew. Chem. Int. Ed.* **2008**, *47*, 9071.
- (70) Prakash, J.; Rohde, G. T.; Meier, K. K.; Munck, E.; Que, L., Jr. *Inorg. Chem.* **2015**, *54*, 11055.
- (71) Grapperhaus, C. A.; Mienert, B.; Bill, E.; Weyhermüller, T.; Wieghardt, K. *Inorg. Chem.* **2000**, *39*, 5306.
- (72) Thibon, A.; England, J.; Martinho, M.; Young, V. G.; Frisch, J. R.; Guillot, R.; Girerd, J.-J.; Münck, E.; Que, L.; Banse, F. *Angew. Chem. Int. Ed.* **2008**, *47*, 7064.
- (73) England, J.; Bigelow, J. O.; Van Heuvelen, K. M.; Farquhar, E. R.; Martinho, M.; Meier, K. K.; Frisch, J. R.; Munck, E.; Que, L. *Chem. Sci.* **2014**, *5*, 1204.
- (74) Bukowski, M. R.; Koehntop, K. D.; Stubna, A.; Bominaar, E. L.; Halfen, J. A.; Münck, E.; Nam, W.; Que, L. *Science* **2005**, *310*, 1000.
- (75) Chanda, A.; Shan, X.; Chakrabarti, M.; Ellis, W. C.; Popescu, D. L.; Tiago de Oliveira, F.; Wang, D.; Que, L.; Collins, T. J.; Münck, E.; Bominaar, E. L. *Inorg. Chem.* **2008**, *47*, 3669.
- (76) Popescu, D.-L.; Vrabel, M.; Brausam, A.; Madsen, P.; Lente, G.; Fabian, I.; Ryabov, A. D.; van Eldik, R.; Collins, T. J. *Inorg. Chem.* **2010**, *49*, 11439.
- (77) Company, A.; Prat, I.; Frisch, J. R.; Mas-Ballesté, D. R.; Güell, M.; Juhász, G.; Ribas, X.; Münck, D. E.; Luis, J. M.; Que, L.; Costas, M. *Chem. Eur. J.* **2011**, *17*, 1622.
- (78) Planas, O.; Clemancey, M.; Latour, J.-M.; Company, A.; Costas, M. *Chem. Commun.* **2014**, *50*, 10887.
- (79) Puri, M.; Company, A.; Sabenya, G.; Costas, M.; Que, L. *Inorg. Chem.* **2016**, *55*, 5818.
- (80) Seo, M. S.; Kim, N. H.; Cho, K.-B.; So, J. E.; Park, S. K.; Clemancey, M.; Garcia-Serres, R.; Latour, J.-M.; Shaik, S.; Nam, W. *Chem. Sci.* **2011**, *2*, 1039.
- (81) Kaizer, J.; Klinker, E. J.; Oh, N. Y.; Rohde, J.-U.; Song, W. J.; Stubna, A.; Kim, J.; Münck, E.; Nam, W.; Que, L. *J. Am. Chem. Soc.* **2004**, *126*, 472.
- (82) Klinker, E. J.; Kaizer, J.; Brennessel, W. W.; Woodrum, N. L.; Cramer, C. J.; Que, L., Jr. *Angew. Chem. Int. Ed. Engl.* **2005**, *44*, 3690.
- (83) Wang, D.; Ray, K.; Collins, M. J.; Farquhar, E. R.; Frisch, J. R.; Gomez, L.; Jackson, T. A.; Kerscher, M.; Waleska, A.; Comba, P.; Costas, M.; Que, L. *Chem. Sci.* **2013**, *4*, 282.
- (84) Rohde, J.-U.; Torelli, S.; Shan, X.; Lim, M. H.; Klinker, E. J.; Kaizer, J.; Chen, K.; Nam, W.; Que, L. *J. Am. Chem. Soc.* **2004**, *126*, 16750.
- (85) Company, A.; Sabenya, G.; Gonzalez-Bejar, M.; Gomez, L.; Clemancey, M.; Blondin, G.; Jasniewski, A. J.; Puri, M.; Browne, W. R.; Latour, J. M.; Que, L., Jr.; Costas, M.; Perez-Prieto, J.; Lloret-Fillol, J. *J. Am. Chem. Soc.* **2014**, *136*, 4624.
- (86) Pestovsky, O.; Stoian, S.; Bominaar, E. L.; Shan, X.; Münck, E.; Que, L.; Bakac, A. *Angew. Chem. Int. Ed.* **2005**, *44*, 6871.
- (87) Pestovsky, O.; Bakac, A. *J. Am. Chem. Soc.* **2004**, *126*, 13757.
- (88) Loegager, T.; Holcman, J.; Sehested, K.; Pedersen, T. *Inorg. Chem.* **1992**, *31*, 3523.
- (89) Bataineh, H.; Pestovsky, O.; Bakac, A. *Inorg. Chem.* **2016**, *55*, 6719.
- (90) England, J.; Martinho, M.; Farquhar, E. R.; Frisch, J. R.; Bominaar, E. L.; Münck, E.; Que, L. *Angew. Chem. Int. Ed.* **2009**, *48*, 3622.
- (91) England, J.; Guo, Y.; Farquhar, E. R.; Young, V. G., Jr.; Munck, E.; Que, L., Jr. *J. Am. Chem. Soc.* **2010**, *132*, 8635.
- (92) Lacy, D. C.; Gupta, R.; Stone, K. L.; Greaves, J.; Ziller, J. W.; Hendrich, M. P.; Borovik, A. S. *J. Am. Chem. Soc.* **2010**, *132*, 12188.
- (93) Hill, E. A.; Weitz, A. C.; Onderko, E.; Romero-Rivera, A.; Guo, Y.; Swart, M.; Bominaar, E. L.; Green, M. T.; Hendrich, M. P.; Lacy, D. C.; Borovik, A. S. *J. Am. Chem. Soc.* **2016**.

- (94) Bigi, J. P.; Harman, W. H.; Lassalle-Kaiser, B.; Robles, D. M.; Stich, T. A.; Yano, J.; Britt, R. D.; Chang, C. J. *J. Am. Chem. Soc.* **2012**, *134*, 1536.
- (95) England, J.; Guo, Y.; Van Heuvelen, K. M.; Cranswick, M. A.; Rohde, G. T.; Bominaar, E. L.; Münck, E.; Que, L. *J. Am. Chem. Soc.* **2011**, *133*, 11880.
- (96) Biswas, A. N.; Puri, M.; Meier, K. K.; Oloo, W. N.; Rohde, G. T.; Bominaar, E. L.; Münck, E.; Que, L. *J. Am. Chem. Soc.* **2015**, *137*, 2428.
- (97) Puri, M.; Biswas, A. N.; Fan, R.; Guo, Y.; Que, L. *J. Am. Chem. Soc.* **2016**, *138*, 2484.
- (98) de Oliveira, F. T.; Chanda, A.; Banerjee, D.; Shan, X.; Mondal, S.; Que, L.; Bominaar, E. L.; Münck, E.; Collins, T. J. *Science* **2007**, *315*, 835.
- (99) Kundu, S.; Thompson, J. V. K.; Shen, L. Q.; Mills, M. R.; Bominaar, E. L.; Ryabov, A. D.; Collins, T. J. *Chem. Eur. J.* **2015**, *21*, 1803.
- (100) Ghosh, M.; Singh, K. K.; Panda, C.; Weitz, A.; Hendrich, M. P.; Collins, T. J.; Dhar, B. B.; Sen Gupta, S. *J. Am. Chem. Soc.* **2014**, *136*, 9524.
- (101) Van Heuvelen, K. M.; Fiedler, A. T.; Shan, X.; De Hont, R. F.; Meier, K. K.; Bominaar, E. L.; Münck, E.; Que, L. *Proc. Natl. Acad. Sci. U.S.A.* **2012**, *109*, 11933.
- (102) MacBeth, C. E.; Gupta, R.; Mitchell-Koch, K. R.; Young, V. G.; Lushington, G. H.; Thompson, W. H.; Hendrich, M. P.; Borovik, A. S. *J. Am. Chem. Soc.* **2004**, *126*, 2556.
- (103) MacBeth, C. E.; Golombek, A. P.; Young, V. G.; Yang, C.; Kuczera, K.; Hendrich, M. P.; Borovik, A. S. *Science* **2000**, *289*, 938.
- (104) Fukuzumi, S.; Morimoto, Y.; Kotani, H.; Naumov, P.; Lee, Y.-M.; Nam, W. *Nat. Chem.* **2010**, *2*, 756.
- (105) Prakash, J.; Rohde, G. T.; Meier, K. K.; Jasniewski, A. J.; Van Heuvelen, K. M.; Münck, E.; Que, L. *J. Am. Chem. Soc.* **2015**, *137*, 3478.
- (106) Prakash, J.; Que, L. *Chem. Commun.* **2016**, *52*, 8146.
- (107) Prakash, J.; Rohde, G. T.; Meier, K. K.; Münck, E.; Que, L. *Inorg. Chem.* **2015**, *54*, 11055.
- (108) Que, L. *Acc. Chem. Res.* **2007**, *40*, 493.
- (109) Decker, A.; Rohde, J.-U.; Que, L.; Solomon, E. I. *J. Am. Chem. Soc.* **2004**, *126*, 5378.
- (110) Kotani, H.; Suenobu, T.; Lee, Y.-M.; Nam, W.; Fukuzumi, S. *J. Am. Chem. Soc.* **2011**, *133*, 3249.
- (111) Collins, M. J.; Ray, K.; Que, L. *Inorg. Chem.* **2006**, *45*, 8009.
- (112) Wang, D.; Zhang, M.; Bühlmann, P.; Que, L. *J. Am. Chem. Soc.* **2010**, *132*, 7638.
- (113) Li, F.; England, J.; Que, L. *J. Am. Chem. Soc.* **2010**, *132*, 2134.
- (114) Kim, S. O.; Sastri, C. V.; Seo, M. S.; Kim, J.; Nam, W. *J. Am. Chem. Soc.* **2005**, *127*, 4178.
- (115) Hong, S.; Lee, Y.-M.; Shin, W.; Fukuzumi, S.; Nam, W. *J. Am. Chem. Soc.* **2009**, *131*, 13910.
- (116) Li, F.; Meier, K. K.; Cranswick, M. A.; Chakrabarti, M.; Van Heuvelen, K. M.; Münck, E.; Que, L. *J. Am. Chem. Soc.* **2011**, *133*, 7256.
- (117) Solomon, E. I.; Decker, A.; Lehnert, N. *Proc. Natl. Acad. Sci. U.S.A.* **2003**, *100*, 3589.
- (118) Gómez, L.; Garcia-Bosch, I.; Company, A.; Benet-Buchholz, J.; Polo, A.; Sala, X.; Ribas, X.; Costas, M. *Angew. Chem. Int. Ed.* **2009**, *48*, 5720.
- (119) Serrano-Plana, J.; Aguinaco, A.; Belda, R.; García-España, E.; Basallote, M. G.; Company, A.; Costas, M. *Angew. Chem. Int. Ed.* **2016**, *55*, 6310.
- (120) Serrano-Plana, J.; Oloo, W. N.; Acosta-Rueda, L.; Meier, K. K.; Verdejo, B.; García-España, E.; Basallote, M. G.; Münck, E.; Que, L.; Company, A.; Costas, M. *J. Am. Chem. Soc.* **2015**, *137*, 15833.
- (121) Cussó, O.; Garcia-Bosch, I.; Ribas, X.; Lloret-Fillol, J.; Costas, M. *J. Am. Chem. Soc.* **2013**, *135*, 14871.

- (122) Cusso, O.; Ribas, X.; Costas, M. *Chem. Commun.* **2015**, *51*, 14285.
- (123) Chen, M. S.; White, M. C. *Science* **2007**, *318*, 783.
- (124) Mas-Ballesté, R.; Que, L. *J. Am. Chem. Soc.* **2007**, *129*, 15964.
- (125) Makhlynets, O. V.; Rybak-Akimova, E. V. *Chem. Eur. J.* **2010**, *16*, 13995.
- (126) Yoon, J.; Wilson, S. A.; Jang, Y. K.; Seo, M. S.; Nehru, K.; Hedman, B.; Hodgson, K. O.; Bill, E.; Solomon, E. I.; Nam, W. *Angew. Chem. Int. Ed.* **2009**, *48*, 1257.
- (127) Cho, J.; Jeon, S.; Wilson, S. A.; Liu, L. V.; Kang, E. A.; Braymer, J. J.; Lim, M. H.; Hedman, B.; Hodgson, K. O.; Valentine, J. S.; Solomon, E. I.; Nam, W. *Nature* **2011**, *478*, 502.
- (128) Janardanan, D.; Wang, Y.; Schyman, P.; Que, L.; Shaik, S. *Angew. Chem. Int. Ed.* **2010**, *49*, 3342.
- (129) Shaik, S.; Chen, H.; Janardanan, D. *Nat. Chem.* **2011**, *3*, 19.
- (130) Sastri, C. V.; Lee, J.; Oh, K.; Lee, Y. J.; Lee, J.; Jackson, T. A.; Ray, K.; Hirao, H.; Shin, W.; Halfen, J. A.; Kim, J.; Que, L.; Shaik, S.; Nam, W. *Proc. Natl. Acad. Sci. U.S.A.* **2007**, *104*, 19181.
- (131) Andris, E.; Jašík, J.; Gómez, L.; Costas, M.; Roithová, J. *Angew. Chem. Int. Ed.* **2016**, *55*, 3637.
- (132) McDonald, A. R.; Que Jr, L. *Coord. Chem. Rev.* **2013**, *257*, 414.
- (133) de Visser, S. P.; Rohde, J.-U.; Lee, Y.-M.; Cho, J.; Nam, W. *Coord. Chem. Rev.* **2013**, *257*, 381.
- (134) Jensen, M. P.; Mehn, M. P.; Que, L. *Angew. Chem. Int. Ed.* **2003**, *42*, 4357.
- (135) Jensen, M. P.; Lange, S. J.; Mehn, M. P.; Que, E. L.; Que, L. *J. Am. Chem. Soc.* **2003**, *125*, 2113.
- (136) Meyer, S.; Klawitter, I.; Demeshko, S.; Bill, E.; Meyer, F. *Angew. Chem. Int. Ed.* **2013**, *52*, 901.
- (137) Nam, W.; Lee, Y.-M.; Fukuzumi, S. *Acc. Chem. Res.* **2014**, *47*, 1146.
- (138) Nam, W. *Acc. Chem. Res.* **2015**, *48*, 2415.
- (139) Fillol, J. L.; Codolà, Z.; Garcia-Bosch, I.; Gómez, L.; Pla, J. J.; Costas, M. *Nat. Chem.* **2011**, *3*, 807.
- (140) Codolà, Z.; Gómez, L.; Kleespies, S. T.; Que Jr, L.; Costas, M.; Lloret-Fillol, J. *Nat. Commun.* **2015**, *6*.
- (141) Prat, I.; Mathieson, J. S.; Güell, M.; Ribas, X.; Luis, J. M.; Cronin, L.; Costas, M. *Nat. Chem.* **2011**, *3*, 788.
- (142) Codolà, Z.; Garcia-Bosch, I.; Acuña-Parés, F.; Prat, I.; Luis, J. M.; Costas, M.; Lloret-Fillol, J. *Chem. Eur. J.* **2013**, *19*, 8042.
- (143) Wolfe, M. D.; Parales, J. V.; Gibson, D. T.; Lipscomb, J. D. *J. Biol. Chem.* **2001**, *276*, 1945.
- (144) Que, L.; Ho, R. Y. N. *Chem. Rev.* **1996**, *96*, 2607.
- (145) de Oliveira, F. T.; Chanda, A.; Banerjee, D.; Shan, X.; Mondal, S.; Que, L.; Bominaar, E. L.; Münck, E.; Collins, T. J. *Science* **2007**, *315*, 835.
- (146) Kundu, S.; Thompson, J. V. K.; Ryabov, A. D.; Collins, T. J. *J. Am. Chem. Soc.* **2011**, *133*, 18546.
- (147) Kwon, E.; Cho, K.-B.; Hong, S.; Nam, W. *Chem. Commun.* **2014**, *50*, 5572.
- (148) Chen, K.; Costas, M.; Kim, J.; Tipton, A. K.; Que, L. *J. Am. Chem. Soc.* **2002**, *124*, 3026.
- (149) Chen, K.; Costas, M.; Que, J. L. *J. Chem. Soc., Dalton Trans.* **2002**, 672.
- (150) Oloo, W. N.; Que, L. *Acc. Chem. Res.* **2015**, *48*, 2612.
- (151) McDonald, A. R.; Que, L. *Nat. Chem.* **2011**, *3*, 761.
- (152) Hitomi, Y.; Arakawa, K.; Funabiki, T.; Kodera, M. *Angew. Chem. Int. Ed.* **2012**, *51*, 3448.
- (153) Tse, C.-W.; Chow, T. W.-S.; Guo, Z.; Lee, H. K.; Huang, J.-S.; Che, C.-M. *Angew. Chem. Int. Ed.* **2014**, *53*, 798.
- (154) Chow, T. W.-S.; Wong, E. L.-M.; Guo, Z.; Liu, Y.; Huang, J.-S.; Che, C.-M. *J. Am. Chem. Soc.* **2010**, *132*, 13229.

- (155) Engelmann, X.; Monte-Pérez, I.; Ray, K. *Angew. Chem. Int. Ed.* **2016**, *55*, 7632.
- (156) Jaccob, M.; Rajaraman, G. *Dalton Trans.* **2012**, *41*, 10430.
- (157) Kumar, S.; Faponle, A. S.; Barman, P.; Vardhaman, A. K.; Sastri, C. V.; Kumar, D.; de Visser, S. P. *J. Am. Chem. Soc.* **2014**, *136*, 17102.
- (158) Svastits, E. W.; Dawson, J. H.; Breslow, R.; Gellman, S. H. *J. Am. Chem. Soc.* **1985**, *107*, 6427.
- (159) Breslow, R.; Gellman, S. H. *J. Chem. Soc., Chem. Commun.* **1982**, 1400.
- (160) Breslow, R.; Gellman, S. H. *J. Am. Chem. Soc.* **1983**, *105*, 6728.
- (161) Mansuy, D.; Mahy, J.-P.; Dureault, A.; Bedi, G.; Battioni, P. *J. Chem. Soc., Chem. Commun.* **1984**, 1161.
- (162) Lucas, R. L.; Powell, D. R.; Borovik, A. S. *J. Am. Chem. Soc.* **2005**, *127*, 11596.
- (163) King, E. R.; Betley, T. A. *Inorg. Chem.* **2009**, *48*, 2361.
- (164) Gouré, E.; Avenier, F.; Dubourdeaux, P.; Sénèque, O.; Albrieux, F.; Lebrun, C.; Clémancey, M.; Maldivi, P.; Latour, J.-M. *Angew. Chem. Int. Ed.* **2014**, *53*, 1580.
- (165) Verma, A. K.; Nazif, T. N.; Achim, C.; Lee, S. C. *J. Am. Chem. Soc.* **2000**, *122*, 11013.
- (166) Klinker, E. J.; Jackson, T. A.; Jensen, M. P.; Stubna, A.; Juhász, G.; Bominaar, E. L.; Münck, E.; Que, L. *Angew. Chem. Int. Ed.* **2006**, *45*, 7394.
- (167) Vardhaman, A. K.; Barman, P.; Kumar, S.; Sastri, C. V.; Kumar, D.; de Visser, S. P. *Angew. Chem. Int. Ed.* **2013**, *52*, 12288.
- (168) Vardhaman, A. K.; Lee, Y. M.; Jung, J.; Ohkubo, K.; Nam, W.; Fukuzumi, S. *Angew. Chem. Int. Ed. Engl.* **2016**, *55*, 3709.
- (169) Thomas, C. M.; Mankad, N. P.; Peters, J. C. *J. Am. Chem. Soc.* **2006**, *128*, 4956.
- (170) Nieto, I.; Ding, F.; Bontchev, R. P.; Wang, H.; Smith, J. M. *J. Am. Chem. Soc.* **2008**, *130*, 2716.
- (171) Leeladee, P.; Jameson, G. N. L.; Siegler, M. A.; Kumar, D.; de Visser, S. P.; Goldberg, D. P. *Inorg. Chem.* **2013**, *52*, 4668.
- (172) Searles, K.; Fortier, S.; Khusniyarov, M. M.; Carroll, P. J.; Sutter, J.; Meyer, K.; Mindiola, D. J.; Caulton, K. G. *Angew. Chem. Int. Ed.* **2014**, *53*, 14139.
- (173) Zhang, H.; Ouyang, Z.; Liu, Y.; Zhang, Q.; Wang, L.; Deng, L. *Angew. Chem. Int. Ed.* **2014**, *53*, 8432.
- (174) Bowman, A. C.; Milsman, C.; Bill, E.; Turner, Z. R.; Lobkovsky, E.; DeBeer, S.; Wieghardt, K.; Chirik, P. J. *J. Am. Chem. Soc.* **2011**, *133*, 17353.
- (175) Wang, L.; Hu, L.; Zhang, H.; Chen, H.; Deng, L. *J. Am. Chem. Soc.* **2015**, *137*, 14196.
- (176) Spasyuk, D. M.; Carpenter, S. H.; Kefalidis, C. E.; Piers, W. E.; Neidig, M. L.; Maron, L. *Chem. Sci.* **2016**, *7*, 5939.
- (177) Ni, C.; Fettinger, J. C.; Long, G. J.; Brynda, M.; Power, P. P. *Chem. Commun.* **2008**, 6045.
- (178) Liu, P.; Wong, E. L.-M.; Yuen, A. W.-H.; Che, C.-M. *Org. Lett.* **2008**, *10*, 3275.
- (179) Chen, G.-Q.; Xu, Z.-J.; Liu, Y.; Zhou, C.-Y.; Che, C.-M. *Synlett* **2011**, 2011, 1174.
- (180) King, E. R.; Hennessy, E. T.; Betley, T. A. *J. Am. Chem. Soc.* **2011**, *133*, 4917.
- (181) Paradine, S. M.; White, M. C. *J. Am. Chem. Soc.* **2012**, *134*, 2036.
- (182) Hennessy, E. T.; Betley, T. A. *Science* **2013**, *340*, 591.
- (183) Hennessy, E. T.; Liu, R. Y.; Iovan, D. A.; Duncan, R. A.; Betley, T. A. *Chem. Sci.* **2014**, *5*, 1526.
- (184) Liu, Y.; Guan, X.; Wong, E. L.-M.; Liu, P.; Huang, J.-S.; Che, C.-M. *J. Am. Chem. Soc.* **2013**, *135*, 7194.
- (185) Ertl, G. *Angew. Chem. Int. Ed. Engl.* **1990**, *29*, 1219.
- (186) Jennings, J. R., Ed. *Catalytic Ammonia Synthesis Fundamentals and Practice.*; Springer US: New York, 1991.
- (187) Howard, J. B.; Rees, D. C. *Chem. Rev.* **1996**, *96*, 2965.
- (188) Einsle, O.; Tezcan, F. A.; Andrade, S. L. A.; Schmid, B.; Yoshida, M.; Howard, J. B.; Rees, D. C. *Science* **2002**, *297*, 1696.

- (189) Lancaster, K. M.; Roemelt, M.; Ettenhuber, P.; Hu, Y.; Ribbe, M. W.; Neese, F.; Bergmann, U.; DeBeer, S. *Science* **2011**, *334*, 974.
- (190) Rees, J. A.; Bjornsson, R.; Schlesier, J.; Sippel, D.; Einsle, O.; DeBeer, S. *Angew. Chem. Int. Ed.* **2015**, *54*, 13249.
- (191) MacKay, B. A.; Fryzuk, M. D. *Chem. Rev.* **2004**, *104*, 385.
- (192) Seefeldt, L. C.; Hoffman, B. M.; Dean, D. R. *Annu. Rev. Biochem.* **2009**, *78*, 701.
- (193) Wagner, W. D.; Nakamoto, K. *J. Am. Chem. Soc.* **1989**, *111*, 1590.
- (194) Meyer, K.; Bill, E.; Mienert, B.; Weyhermüller, T.; Wieghardt, K. *J. Am. Chem. Soc.* **1999**, *121*, 4859.
- (195) Aliaga-Alcalde, N.; DeBeer George, S.; Mienert, B.; Bill, E.; Wieghardt, K.; Neese, F. *Angew. Chem. Int. Ed.* **2005**, *44*, 2908.
- (196) Petrenko, T.; DeBeer George, S.; Aliaga-Alcalde, N.; Bill, E.; Mienert, B.; Xiao, Y.; Guo, Y.; Sturhahn, W.; Cramer, S. P.; Wieghardt, K.; Neese, F. *J. Am. Chem. Soc.* **2007**, *129*, 11053.
- (197) Berry, J. F.; DeBeer George, S.; Neese, F. *PCCP* **2008**, *10*, 4361.
- (198) Berry, J. F.; Bill, E.; Bothe, E.; George, S. D.; Mienert, B.; Neese, F.; Wieghardt, K. *Science* **2006**, *312*, 1937.
- (199) Delaude, L.; Laszlo, P. *J. Org. Chem.* **1996**, *61*, 6360.
- (200) Song, Y.-F.; Berry, J. F.; Bill, E.; Bothe, E.; Weyhermüller, T.; Wieghardt, K. *Inorg. Chem.* **2007**, *46*, 2208.
- (201) Krahe, O.; Bill, E.; Neese, F. *Angewandte Chemie International Edition* **2014**, *53*, 8727.
- (202) Torres-Alacan, J.; Das, U.; Filippou, A. C.; Vöhringer, P. *Angew. Chem. Int. Ed.* **2013**, *52*, 12833.
- (203) Schröder, D.; Schwarz, H.; Aliaga-Alcalde, N.; Neese, F. *Eur. J. Inorg. Chem.* **2007**, *2007*, 816.
- (204) Schlangen, M.; Neugebauer, J.; Reiher, M.; Schröder, D.; López, J. P.; Haryono, M.; Heinemann, F. W.; Grohmann, A.; Schwarz, H. *J. Am. Chem. Soc.* **2008**, *130*, 4285.
- (205) Berry, J. F.; Bill, E.; Bothe, E.; Weyhermüller, T.; Wieghardt, K. *J. Am. Chem. Soc.* **2005**, *127*, 11550.
- (206) Betley, T. A.; Peters, J. C. *J. Am. Chem. Soc.* **2004**, *126*, 6252.
- (207) Hendrich, M. P.; Gunderson, W.; Behan, R. K.; Green, M. T.; Mehn, M. P.; Betley, T. A.; Lu, C. C.; Peters, J. C. *Proc. Natl. Acad. Sci. U.S.A.* **2006**, *103*, 17107.
- (208) Rohde, J.-U.; Betley, T. A.; Jackson, T. A.; Saouma, C. T.; Peters, J. C.; Que, L. *Inorg. Chem.* **2007**, *46*, 5720.
- (209) Vogel, C.; Heinemann, F. W.; Sutter, J.; Anthon, C.; Meyer, K. *Angew. Chem. Int. Ed.* **2008**, *47*, 2681.
- (210) Vogel, C., Friedrich-Alexander-University Erlangen-Nürnberg, 2012.
- (211) Scepaniak, J. J.; Fulton, M. D.; Bontchev, R. P.; Duesler, E. N.; Kirk, M. L.; Smith, J. M. *J. Am. Chem. Soc.* **2008**, *130*, 10515.
- (212) Scepaniak, J. J.; Margarit, C. G.; Harvey, J. N.; Smith, J. M. *Inorg. Chem.* **2011**, *50*, 9508.
- (213) Lee, W.-T.; Juarez, R. A.; Scepaniak, J. J.; Muñoz, S. B.; Dickie, D. A.; Wang, H.; Smith, J. M. *Inorg. Chem.* **2014**, *53*, 8425.
- (214) Scepaniak, J. J.; Young, J. A.; Bontchev, R. P.; Smith, J. M. *Angew. Chem. Int. Ed.* **2009**, *48*, 3158.
- (215) Scepaniak, J. J.; Vogel, C. S.; Khusniyarov, M. M.; Heinemann, F. W.; Meyer, K.; Smith, J. M. *Science* **2011**, *331*, 1049.
- (216) Crichton, R. In *Iron Metabolism*; John Wiley & Sons, Ltd: 2009, p 17.
- (217) Ye, T.; McKervey, M. A. *Chem. Rev.* **1994**, *94*, 1091.
- (218) Zhu, S.-F.; Zhou, Q.-L. *Natl. Sci. Rev.* **2014**, *1*, 580.
- (219) Caballero, A.; Diaz-Requejo, M. M.; Fructos, M. R.; Olmos, A.; Urbano, J.; Perez, P. J. *Dalton Trans.* **2015**, *44*, 20295.

- (220) Mansuy, D.; Lange, M.; Chottard, J.-C.; Guerin, P.; Morliere, P.; Brault, D.; Rougee, M. *J. Chem. Soc., Chem. Commun.* **1977**, 648.
- (221) Mansuy, D.; Lange, M.; Chottard, J. C.; Bartoli, J. F.; Chevrier, B.; Weiss, R. *Angew. Chem. Int. Ed. Engl.* **1978**, *17*, 781.
- (222) English, D. R.; Hendrickson, D. N.; Suslick, K. S. *Inorg. Chem.* **1983**, *22*, 367.
- (223) Li, Y.; Huang, J.-S.; Zhou, Z.-Y.; Che, C.-M.; You, X.-Z. *J. Am. Chem. Soc.* **2002**, *124*, 13185.
- (224) Khade, R. L.; Fan, W.; Ling, Y.; Yang, L.; Oldfield, E.; Zhang, Y. *Angew. Chem. Int. Ed.* **2014**, *53*, 7574.
- (225) Mansuy, D.; Guerin, P.; Chottard, J. C. *J. Organomet. Chem.* **1979**, *171*, 195.
- (226) Guerin, P.; Battioni, J.-P.; Chottard, J.-C.; Mansuy, D. *J. Organomet. Chem.* **1981**, *218*, 201.
- (227) Battioni, J.-P.; Dupre, D.; Guerin, P.; Mansuy, D. *J. Organomet. Chem.* **1984**, *265*, 53.
- (228) Ziegler, C. J.; Suslick, K. S. *J. Am. Chem. Soc.* **1996**, *118*, 5306.
- (229) Wolf, J. R.; Hamaker, C. G.; Djukic, J.-P.; Kodadek, T.; Woo, L. K. *J. Am. Chem. Soc.* **1995**, *117*, 9194.
- (230) Plietker, B., Ed. *Iron Catalysis Fundamentals and Applications*; Springer-Verlag Berlin Heidelberg, 2011.
- (231) Hamaker, C. G.; Mirafzal, G. A.; Woo, L. K. *Organometallics* **2001**, *20*, 5171.
- (232) Lai, T.-S.; Chan, F.-Y.; So, P.-K.; Ma, D.-L.; Wong, K.-Y.; Che, C.-M. *Dalton Trans.* **2006**, 4845.
- (233) Tagliatesta, P.; Pastorini, A. *J. Mol. Catal. A: Chem.* **2003**, *198*, 57.
- (234) Morandi, B.; Carreira, E. M. *Angew. Chem. Int. Ed.* **2010**, *49*, 938.
- (235) Morandi, B.; Carreira, E. M. *Science* **2012**, *335*, 1471.
- (236) Baumann, L. K.; Mbuvi, H. M.; Du, G.; Woo, L. K. *Organometallics* **2007**, *26*, 3995.
- (237) Mbuvi, H. M.; Klobukowski, E. R.; Roberts, G. M.; Woo, L. K. *J. Porphyrins Phthalocyanines* **2010**, *14*, 284.
- (238) Mbuvi, H. M.; Keith Woo, L. *J. Porphyrins Phthalocyanines* **2009**, *13*, 136.
- (239) Mbuvi, H. M.; Woo, L. K. *Organometallics* **2008**, *27*, 637.
- (240) Seitz, W. J.; Saha, A. K.; Casper, D.; Hossain, M. M. *Tetrahedron Lett.* **1992**, *33*, 7755.
- (241) Seitz, W. J.; Saha, A. K.; Hossain, M. M. *Organometallics* **1993**, *12*, 2604.
- (242) Seitz, W. J.; Hossain, M. M. *Tetrahedron Lett.* **1994**, *35*, 7561.
- (243) Du, G.; Andrioletti, B.; Rose, E.; Woo, L. K. *Organometallics* **2002**, *21*, 4490.
- (244) Edulji, S. K.; Nguyen, S. T. *Organometallics* **2003**, *22*, 3374.
- (245) Edulji, S. K.; Nguyen, S. T. *Pure Appl. Chem.* **2004**, *76*, 645.
- (246) Yeung, C.-T.; Sham, K.-C.; Lee, W.-S.; Wong, W.-T.; Wong, W.-Y.; Kwong, H.-L. *Inorg. Chim. Acta* **2009**, *362*, 3267.
- (247) Cai, Y.; Zhu, S.-F.; Wang, G.-P.; Zhou, Q.-L. *Adv. Synth. Catal.* **2011**, *353*, 2939.
- (248) Zhu, S.-F.; Cai, Y.; Mao, H.-X.; Xie, J.-H.; Zhou, Q.-L. *Nat. Chem.* **2010**, *2*, 546.
- (249) Lieberman, R. L.; Rosenzweig, A. C. *Crit. Rev. Biochem. Mol. Biol.* **2004**, *39*, 147.
- (250) Chen, K.; Que, L. *J. Am. Chem. Soc.* **2001**, *123*, 6327.
- (251) Blakesley, D. W.; Payne, S. C.; Hagen, K. S. *Inorg. Chem.* **2000**, *39*, 1979.
- (252) Britovsek, G. J. P.; England, J.; White, A. J. P. *Inorg. Chem.* **2005**, *44*, 8125.
- (253) Constable, E. C.; Baum, G.; Bill, E.; Dyson, R.; van Eldik, R.; Fenske, D.; Kaderli, S.; Morris, D.; Neubrand, A.; Neuburger, M.; Smith, D. R.; Wieghardt, K.; Zehnder, M.; Zuberbühler, A. D. *Chem. Eur. J.* **1999**, *5*, 498.
- (254) Diebold, A.; Hagen, K. S. *Inorg. Chem.* **1998**, *37*, 215.
- (255) Simaan, A. J.; Döpner, S.; Banse, F.; Bourcier, S.; Bouchoux, G.; Boussac, A.; Hildebrandt, P.; Girerd, J.-J. *Eur. J. Inorg. Chem.* **2000**, *2000*, 1627.

- (256) Zang, Y.; Kim, J.; Dong, Y.; Wilkinson, E. C.; Appelman, E. H.; Que, L. *J. Am. Chem. Soc.* **1997**, *119*, 4197.
- (257) Lee, Y.-M.; Dhuri, S. N.; Sawant, S. C.; Cho, J.; Kubo, M.; Ogura, T.; Fukuzumi, S.; Nam, W. *Angew. Chem. Int. Ed.* **2009**, *48*, 1803.
- (258) Bernadou, J.; Fabiano, A.-S.; Robert, A.; Meunier, B. *J. Am. Chem. Soc.* **1994**, *116*, 9375.
- (259) Seo, M. S.; In, J.-H.; Kim, S. O.; Oh, N. Y.; Hong, J.; Kim, J.; Que, L.; Nam, W. *Angew. Chem. Int. Ed.* **2004**, *43*, 2417.
- (260) Mi Hee, L.; Jan-Uwe, R.; Audria, S.; Michael, R. B.; Miquel, C.; Raymond, Y. N. H.; Eckard, M.; Wonwoo, N.; Lawrence, Q. J. *Proc. Natl. Acad. Sci. U.S.A.* **2003**, *100*, 3665.
- (261) Weinberg, D. R.; Gagliardi, C. J.; Hull, J. F.; Murphy, C. F.; Kent, C. A.; Westlake, B. C.; Paul, A.; Ess, D. H.; McCafferty, D. G.; Meyer, T. J. *Chem. Rev.* **2012**, *112*, 4016.
- (262) Hashimoto, S.; Tatsuno, Y.; Kitagawa, T. *Proc. Natl. Acad. Sci. U.S.A.* **1986**, *83*, 2417.
- (263) Nam, W.; Valentine, J. S. *J. Am. Chem. Soc.* **1993**, *115*, 1772.
- (264) Prat, I.; Company, A.; Corona, T.; Parella, T.; Ribas, X.; Costas, M. *Inorg. Chem.* **2013**, *52*, 9229.
- (265) Mikhalyova, E. A.; Makhlynets, O. V.; Palluccio, T. D.; Filatov, A. S.; Rybak-Akimova, E. V. *Chem. Commun.* **2012**, *48*, 687.
- (266) Company, A.; Gómez, L.; Güell, M.; Ribas, X.; Luis, J. M.; Que, L.; Costas, M. *J. Am. Chem. Soc.* **2007**, *129*, 15766.
- (267) Sastri, C. V.; Sook Seo, M.; Joo Park, M.; Mook Kim, K.; Nam, W. *Chem. Commun.* **2005**, 1405.
- (268) Goto, Y.; Matsui, T.; Ozaki, S.-i.; Watanabe, Y.; Fukuzumi, S. *J. Am. Chem. Soc.* **1999**, *121*, 9497.
- (269) Kojima, T.; Nakayama, K.; Ikemura, K.; Ogura, T.; Fukuzumi, S. *J. Am. Chem. Soc.* **2011**, *133*, 11692.
- (270) Cho, K.-B.; Wu, X.; Lee, Y.-M.; Kwon, Y. H.; Shaik, S.; Nam, W. *J. Am. Chem. Soc.* **2012**, *134*, 20222.
- (271) Rana, S.; Dey, A.; Maiti, D. *Chem. Commun.* **2015**, *51*, 14469.
- (272) Bryant, J. R.; Matsuo, T.; Mayer, J. M. *Inorg. Chem.* **2004**, *43*, 1587.
- (273) Oh, N. Y.; Suh, Y.; Park, M. J.; Seo, M. S.; Kim, J.; Nam, W. *Angew. Chem.* **2005**, *117*, 4307.
- (274) Fukuzumi, S.; Kotani, H.; Lee, Y.-M.; Nam, W. *J. Am. Chem. Soc.* **2008**, *130*, 15134.
- (275) Comba, P.; Fukuzumi, S.; Kotani, H.; Wunderlich, S. *Angew. Chem. Int. Ed.* **2010**, *49*, 2622.
- (276) Nesheim, J. C.; Lipscomb, J. D. *Biochemistry* **1996**, *35*, 10240.
- (277) *CRC Handbook of Chemistry and Physics; Lide, D. R., Ed.; CRC Press: Boca Raton, FL* **2005**.
- (278) Acuña-Parés, F.; Codolà, Z.; Costas, M.; Luis, J. M.; Lloret-Fillol, J. *Chem. Eur. J.* **2014**, *20*, 5696.
- (279) Campagna, S.; Puntoriero, F.; Nastasi, F.; Bergamini, G.; Balzani, V. *Photochemistry and Photophysics of Coordination Compounds I*; Springer-Verlag Berlin Heidelberg: Verlag Berlin Heidelberg, 2007; Vol. 280.
- (280) Simmons, E. M.; Hartwig, J. F. *Angew. Chem. Int. Ed.* **2012**, *51*, 3066.
- (281) Nehru, K.; Seo, M. S.; Kim, J.; Nam, W. *Inorg. Chem.* **2007**, *46*, 293.
- (282) Stock, P.; Pędziński, T.; Spintig, N.; Grohmann, A.; Hörner, G. *Chem. Eur. J.* **2013**, *19*, 839.
- (283) Enachescu, C.; Hauser, A.; Girerd, J.-J.; Boillot, M.-L. *ChemPhysChem* **2006**, *7*, 1127.
- (284) Canton, S. E.; Zhang, X.; Lawson Daku, M. L.; Liu, Y.; Zhang, J.; Alvarez, S. *J. Phys. Chem. C* **2015**, *119*, 3322.

- (285) Klinker, E. J., University of Minnesota, 2007.
- (286) Mehn, M. P.; Brown, S. D.; Jenkins, D. M.; Peters, J. C.; Que, L. *Inorg. Chem.* **2006**, *45*, 7417.
- (287) Mehn, M. P.; Peters, J. C. *J. Inorg. Biochem.* **2006**, *100*, 634.
- (288) Saouma, C. T.; Peters, J. C. *Coord. Chem. Rev.* **2011**, *255*, 920.
- (289) Nishida, Y.; Kino, K.; Kida, S. *J. Chem. Soc., Dalton Trans.* **1987**, 1157.
- (290) C. Noveron, J.; Herradora, R.; Olmstead, M. M.; Mascharak, P. K. *Inorg. Chim. Acta* **1999**, *285*, 269.
- (291) Soo, H. S.; Sougrati, M. T.; Grandjean, F.; Long, G. J.; Chang, C. J. *Inorg. Chim. Acta* **2011**, *369*, 82.
- (292) McDonald, A. R.; Que, L., Jr. *Coordination Chemistry Reviews* **2013**, *257*, 414.
- (293) Costas, M.; Mehn, M. P.; Jensen, M. P.; Que, L., Jr. *Chem. Rev.* **2004**, *104*, 939.
- (294) Hohenberger, J.; Ray, K.; Meyer, K. *Nat. Commun.* **2012**, *3*, 720.
- (295) Wallar, B. J.; Lipscomb, J. D. *Chem. Rev.* **1996**, *96*, 2625.
- (296) Sahu, S.; Goldberg, D. P. *J. Am. Chem. Soc.* **2016**, *138*, 11410.
- (297) Rittle, J.; Green, M. T. *Science* **2010**, *330*, 933.
- (298) Krebs, C.; Galonić Fujimori, D.; Walsh, C. T.; Bollinger, J. M. *Acc. Chem. Res.* **2007**, *40*, 484.
- (299) Banerjee, R.; Meier, K. K.; Münck, E.; Lipscomb, J. D. *Biochemistry* **2013**, *52*, 4331.
- (300) Zandi, O.; Hamann, T. W. *Nat Chem* **2016**, *8*, 778.
- (301) Codola, Z.; Gomez, L.; Kleespies, S. T.; Que, L., Jr.; Costas, M.; Lloret-Fillol, J. *Nature Communications* **2015**, *6*.
- (302) Panda, C.; Debgupta, J.; Diaz Diaz, D.; Singh, K. K.; Gupta, S. S.; Dhar, B. B. *J. Am. Chem. Soc.* **2014**, *136*, 12273.
- (303) Ertl, G. *The Chemical Record* **2001**, *1*, 33.
- (304) Hoffman, B. M.; Dean, D. R.; Seefeldt, L. C. *Acc. Chem. Res.* **2009**, *42*, 609.
- (305) Hu, Y.; Ribbe, M. W. *Acc. Chem. Res.* **2010**, *43*, 475.
- (306) Howard, J. B.; Rees, D. C. *Chem. Rev.* **1996**, *7*, 2965.
- (307) Smith, J. M.; Subedi, D. *Dalton Trans.* **2012**, *41*, 1423.
- (308) Berry, J. F. *Comments on Inorganic Chemistry* **2009**, *30*, 28.
- (309) Smith, J. M. In *Progress in Inorganic Chemistry, Vol 58*; Karlin, K. D., Ed.; John Wiley & Sons Inc: Hoboken, 2014; Vol. 58, p 417.
- (310) Betley, T. A.; Peters, J. C. *J Am Chem Soc* **2004**, *126*, 6252.
- (311) Scepaniak, J. J.; Fulton, M. D.; Bontchev, R. P.; Duesler, E. N.; Kirk, M. L.; Smith, J. M. *J Am Chem Soc* **2008**, *130*, 10515.
- (312) Scepaniak, J. J.; Bontchev, R. P.; Johnson, D. L.; Smith, J. M. *Angewandte Chemie International Edition* **2011**, *50*, 6630.
- (313) Muñoz, S. B.; Lee, W.-T.; Dickie, D. A.; Scepaniak, J. J.; Subedi, D.; Pink, M.; Johnson, M. D.; Smith, J. M. *Angewandte Chemie International Edition* **2015**, *54*, 10600.
- (314) Meyer, K.; Bill, E.; Mienert, B.; Weyhermüller, T.; Wieghardt, K. *J. Am. Chem. Soc.* **1999**, *121*, 4859.
- (315) Grapperhaus, C. A.; Mienert, B.; Bill, E.; Weyhermüller, T.; Wieghardt, K. *Inorg. Chem.* **2000**, *39*, 5306.
- (316) Berry, J. F.; Bill, E.; Bothe, E.; George, S. D.; Mienert, B.; Neese, F.; Wieghardt, K. *Science* **2006**, *312*, 1937.
- (317) Schlangen, M.; Neugebauer, J.; Reiher, M.; Schröder, D.; López, J. P.; Haryono, M.; Heinemann, F. W.; Grohmann, A.; Schwarz, H. *J Am Chem Soc* **2008**, *130*, 4285.
- (318) Song, Y.-F.; Berry, J. F.; Bill, E.; Bothe, E.; Weyhermüller, T.; Wieghardt, K. *Inorg Chem* **2007**, *46*, 2208.
- (319) Kahn, O. *Molecular Magnetism*; Wiley-VCH: New York, 1993.
- (320) Sorai, M.; Seki, S. *J. Phys. Chem. Solids* **1974**, *35*, 555.

- (321) Dori, Z.; Ziolo, R. F. *Chem. Rev.* **1973**, *73*, 247.
- (322) Nakamoto, K. *Infrared and Raman Spectra of Inorganic and Coordination Compounds. Part B: Application in Coordination, Organometallic, and Bioinorganic Chemistry, 5th Edition*; John Wiley & Sons, Inc.: Hoboken, New Jersey, 2009.
- (323) Römelt, M.; Ye, S.; Neese, F. *Inorganic Chemistry* **2009**, *48*, 784.
- (324) Ye, S.; Tuttle, T.; Bill, E.; Simkhovich, L.; Gross, Z.; Thiel, W.; Neese, F. *Chemistry – A European Journal* **2008**, *14*, 10839.
- (325) Krahe, O. M., Rheinischen Friedrich-Wilhelms-Universität Bonn, 2016.
- (326) Westre, T. E.; Kennepohl, P.; DeWitt, J. G.; Hedman, B.; Hodgson, K. O.; Solomon, E. I. *Journal of the American Chemical Society* **1997**, *119*, 6297.
- (327) DeBeer George, S.; Brant, P.; Solomon, E. I. *Journal of the American Chemical Society* **2005**, *127*, 667.
- (328) Ye, S.; Geng, C.-Y.; Shaik, S.; Neese, F. *Physical Chemistry Chemical Physics* **2013**, *15*, 8017.
- (329) Doyle, M. P.; Duffy, R.; Ratnikov, M.; Zhou, L. *Chem. Rev.* **2010**, *110*, 704.
- (330) Caballero, A.; Despagnet-Ayoub, E.; Mar Díaz-Requejo, M.; Díaz-Rodríguez, A.; González-Núñez, M. E.; Mello, R.; Muñoz, B. K.; Ojo, W.-S.; Asensio, G.; Etienne, M.; Pérez, P. J. *Science* **2011**, *332*, 835.
- (331) Ford, A.; Miel, H.; Ring, A.; Slattery, C. N.; Maguire, A. R.; McKervey, M. A. *Chem. Rev.* **2015**, *115*, 9981.
- (332) Anciaux, A. J.; Demonceau, A.; Noels, A. F.; Hubert, A. J.; Warin, R.; Teyssie, P. J. *Org. Chem.* **1981**, *46*, 873.
- (333) Morilla, M. E.; Díaz-Requejo, M. M.; Belderrain, T. R.; Nicasio, M. C.; Trofimenko, S.; Pérez, P. J. *Organometallics* **2004**, *23*, 293.
- (334) Lovely, C. J.; Browning, R. G.; Badarinarayana, V.; Dias, H. V. R. *Tetrahedron Lett.* **2005**, *46*, 2453.
- (335) Rosenfeld, M. J.; Shankar, B. K. R.; Shechter, H. *J. Org. Chem.* **1988**, *53*, 2699.
- (336) Yang, M.; Webb, T. R.; Livant, P. *J. Org. Chem.* **2001**, *66*, 4945.
- (337) Fructos, M. R.; Belderrain, T. R.; de Frémont, P.; Scott, N. M.; Nolan, S. P.; Díaz-Requejo, M. M.; Pérez, P. J. *Angew. Chem. Int. Ed.* **2005**, *44*, 5284.
- (338) Rivilla, I.; Gómez-Emeterio, B. P.; Fructos, M. R.; Díaz-Requejo, M. M.; Pérez, P. J. *Organometallics* **2011**, *30*, 2855.
- (339) Liu, Y.; Yu, Z.; Zhang, J. Z.; Liu, L.; Xia, F.; Zhang, J. *Chem. Sci.* **2016**, *7*, 1988.
- (340) Fructos, M. R.; Besora, M.; Braga, A. A. C.; Díaz-Requejo, M. M.; Maseras, F.; Pérez, P. J. *Organometallics* **2016**.
- (341) Padwa, A.; Austin, D. J.; Price, A. T.; Semones, M. A.; Doyle, M. P.; Protopopova, M. N.; Winchester, W. R.; Tran, A. *J. Am. Chem. Soc.* **1993**, *115*, 8669.
- (342) Furukawa, T.; Tobisu, M.; Chatani, N. *J. Am. Chem. Soc.* **2015**, *137*, 12211.
- (343) Pérez, P. J.; Díaz-Requejo, M. M.; Rivilla, I. *Beilstein J. Org. Chem.* **2011**, *7*, 653.
- (344) Werlé, C.; Goddard, R.; Fürstner, A. *Angew. Chem. Int. Ed.* **2015**, *54*, 15452.
- (345) Bellow, J. A.; Stoian, S. A.; van Tol, J.; Ozarowski, A.; Lord, R. L.; Groysman, S. J. *Am. Chem. Soc.* **2016**, *138*, 5531.
- (346) Carboni, M.; Clemancey, M.; Molton, F.; Pecaut, J.; Lebrun, C.; Dubois, L.; Blondin, G.; Latour, J. M. *Inorg. Chem.* **2012**, *51*, 10447.
- (347) McLachlan, G. A.; Fallon, G. D.; Martin, R. L.; Moubaraki, B.; Murray, K. S.; Spiccia, L. *Inorg. Chem.* **1994**, *33*, 4663.
- (348) Roelfes, G.; Vrajmasu, V.; Chen, K.; Ho, R. Y. N.; Rohde, J. U.; Zondervan, C.; la Crois, R. M.; Schudde, E. P.; Lutz, M.; Spek, A. L.; Hage, R.; Feringa, B. L.; Munck, E.; Que, L. *Inorg. Chem.* **2003**, *42*, 2639.
- (349) Saltzman, H.; Sharefkin, J. G. In *Organic Syntheses*; Wiley: New York, 1973; Vol. V, p 658.

- (350) Tagore, R.; Chen, H. Y.; Crabtree, R. H.; Brudvig, G. W. *J. Am. Chem. Soc.* **2006**, *128*, 9457.
- (351) Seo, M. S.; In, J.-H.; Kim, S. O.; Oh, N. Y.; Hong, J.; Kim, J.; Que, L., Jr.; Nam, W. *Angew. Chem. Int. Ed.* **2004**, *43*, 2417.
- (352) Roelfes, G.; Vrajmasu, V.; Chen, K.; Ho, R. Y. N.; Rohde, J.-U.; Zondervan, C.; la Crois, R. M.; Schudde, E. P.; Lutz, M.; Spek, A. L.; Hage, R.; Feringa, B. L.; Münck, E.; Que, L. *Inorg. Chem.* **2003**, *42*, 2639.
- (353) Ravel, B.; Newville, M. *Journal of Synchrotron Radiation* **2005**, *12*, 537.
- (354) Newville, M. *Journal of Synchrotron Radiation* **2001**, *8*, 96.
- (355) Rehr, J. J.; Albers, R. C. *Reviews of Modern Physics* **2000**, *72*, 621.
- (356) Martin-Diaconescu, V.; Bellucci, M.; Musiani, F.; Ciurli, S.; Maroney, M. J. *Journal of Biological Inorganic Chemistry* **2012**, *17*, 353.
- (357) Zambelli, B.; Berardi, A.; Martin-Diaconescu, V.; Mazzei, L.; Musiani, F.; Maroney, M. J.; Ciurli, S. *Journal of Biological Inorganic Chemistry* **2014**, *19*, 319.
- (358) Neese, F. *Wiley Interdisciplinary Reviews: Computational Molecular Science* **2012**, *2*, 73.
- (359) Schäfer, A.; Horn, H.; Ahlrichs, R. *The Journal of Chemical Physics* **1992**, *97*, 2571.
- (360) Weigend, F.; Ahlrichs, R. *Physical Chemistry Chemical Physics* **2005**, *7*, 3297.
- (361) Neese, F. *Inorganica Chimica Acta* **2002**, *337*, 181.
- (362) Grimme, S.; Antony, J.; Ehrlich, S.; Krieg, H. *The Journal of Chemical Physics* **2010**, *132*.
- (363) Grimme, S.; Ehrlich, S.; Goerigk, L. *Journal of Computational Chemistry* **2011**, *32*, 1456.
- (364) Klamt, A.; Schuurmann, G. *Journal of the Chemical Society, Perkin Transactions 2* **1993**, 799.
- (365) DeBeer George, S.; Petrenko, T.; Neese, F. *Inorganica Chimica Acta* **2008**, *361*, 965.
- (366) DeBeer George, S.; Petrenko, T.; Neese, F. *Journal of Physical Chemistry A* **2008**, *112*, 12936.
- (367) Prat, I.; Company, A.; Postils, V.; Ribas, X.; Que, L.; Luis, J. M.; Costas, M. *Chem. Eur. J.* **2013**, *19*, 6724.
- (368) Garcia-Bosch, I.; Company, A.; Fontrodona, X.; Ribas, X.; Costas, M. *Org. Lett.* **2008**, *10*, 2095.
- (369) Yakelis, N. A.; Bergman, R. G. *Organometallics* **2005**, *24*, 3579.
- (370) McKervey, M. A.; Russell, D. N.; Twohig, M. F. *J. Chem. Soc., Chem. Commun.* **1985**, 491.
- (371) Kaim, W.; Fiedler, J. *Chem. Soc. Rev.* **2009**, *38*, 3373.
- (372) Yokoi, H.; Hatta, A.; Ishiguro, K.; Sawaki, Y. *J. Am. Chem. Soc.* **1998**, *120*, 12728.
- (373) Ioele, M.; Steenken, S.; Baciocchi, E. *J. Phys. Chem. A* **1997**, *101*, 2979.
- (374) Clarke, R. E.; Ford, P. C. *Inorg. Chem.* **1970**, *9*, 227.

